frontiers | Research Topics

Exploring mechanisms of cardiac rhythm disturbances using novel computational methods: Prediction, classification, and therapy

Edited by
Xin Li, G. Andre Ng, Fernando Soares Schlindwein, Jichao Zhao and Martin Bishop

Published in
Frontiers in Physiology

ISSN 1664-8714
ISBN 978-2-83251-758-1
DOI 10.3389/978-2-83251-758-1

About Frontiers

Frontiers is more than just an open access publisher of scholarly articles: it is a pioneering approach to the world of academia, radically improving the way scholarly research is managed. The grand vision of Frontiers is a world where all people have an equal opportunity to seek, share and generate knowledge. Frontiers provides immediate and permanent online open access to all its publications, but this alone is not enough to realize our grand goals.

Frontiers journal series

The Frontiers journal series is a multi-tier and interdisciplinary set of open-access, online journals, promising a paradigm shift from the current review, selection and dissemination processes in academic publishing. All Frontiers journals are driven by researchers for researchers; therefore, they constitute a service to the scholarly community. At the same time, the *Frontiers journal series* operates on a revolutionary invention, the tiered publishing system, initially addressing specific communities of scholars, and gradually climbing up to broader public understanding, thus serving the interests of the lay society, too.

Dedication to quality

Each Frontiers article is a landmark of the highest quality, thanks to genuinely collaborative interactions between authors and review editors, who include some of the world's best academicians. Research must be certified by peers before entering a stream of knowledge that may eventually reach the public - and shape society; therefore, Frontiers only applies the most rigorous and unbiased reviews. Frontiers revolutionizes research publishing by freely delivering the most outstanding research, evaluated with no bias from both the academic and social point of view. By applying the most advanced information technologies, Frontiers is catapulting scholarly publishing into a new generation.

What are Frontiers Research Topics?

Frontiers Research Topics are very popular trademarks of the *Frontiers journals series*: they are collections of at least ten articles, all centered on a particular subject. With their unique mix of varied contributions from Original Research to Review Articles, Frontiers Research Topics unify the most influential researchers, the latest key findings and historical advances in a hot research area.

Find out more on how to host your own Frontiers Research Topic or contribute to one as an author by contacting the Frontiers editorial office: frontiersin.org/about/contact

Exploring mechanisms of cardiac rhythm disturbances using novel computational methods: Prediction, classification, and therapy

Topic editors

Xin Li — University of Leicester, United Kingdom
G. Andre Ng — University of Leicester, United Kingdom
Fernando Soares Schlindwein — University of Leicester, United Kingdom
Jichao Zhao — The University of Auckland, New Zealand
Martin Bishop — King's College London, United Kingdom

Citation

Li, X., Ng, G. A., Schlindwein, F. S., Zhao, J., Bishop, M., eds. (2023). *Exploring mechanisms of cardiac rhythm disturbances using novel computational methods: Prediction, classification, and therapy*. Lausanne: Frontiers Media SA. doi: 10.3389/978-2-83251-758-1

Table of contents

frontiers | Frontiers in Physiology

TYPE Editorial
PUBLISHED 10 February 2023
DOI 10.3389/fphys.2023.1155857

OPEN ACCESS

EDITED AND REVIEWED BY
Ruben Coronel,
University of Amsterdam, Netherlands

*CORRESPONDENCE
Xin Li,
xl251@le.ac.uk

SPECIALTY SECTION
This article was submitted to Cardiac Electrophysiology, a section of the journal Frontiers in Physiology

RECEIVED 31 January 2023
ACCEPTED 02 February 2023
PUBLISHED 10 February 2023

CITATION
Li X, Schlindwein FS, Zhao J, Bishop M and Ng GA (2023), Editorial: Exploring mechanisms of cardiac rhythm disturbances using novel computational methods: Prediction, classification, and therapy.
Front. Physiol. 14:1155857.
doi: 10.3389/fphys.2023.1155857

Editorial: Exploring mechanisms of cardiac rhythm disturbances using novel computational methods: Prediction, classification, and therapy

Xin Li[1,2,3]*, Fernando S. Schlindwein[1,3], Jichao Zhao[4], Martin Bishop[5] and G. André Ng[2,3]

[1]School of Engineering, University of Leicester, Leicester, United Kingdom, [2]Department of Cardiovascular Sciences, University of Leicester, Leicester, United Kingdom, [3]National Institute for Health Research Leicester Cardiovascular Biomedical Research Centre, Glenfield Hospital, Leicester, United Kingdom, [4]Auckland Bioengineering Institute, University of Auckland, Auckland, New Zealand, [5]School of Biomedical Engineering and Imaging Sciences, King's College London, London, United Kingdom

KEYWORDS

atrial fibrillation, sudden cardiac death, computational methods, machine learning, cardiac arrythmia

Editorial on the Research Topic
Exploring mechanisms of cardiac rhythm disturbances using novel computational methods: Prediction, classification, and therapy

Introduction

Cardiac rhythm disturbances, including arrhythmias and sudden cardiac death (SCD), represent a major worldwide public health problem, accounting for 15%–20% of all deaths (Mehra, 2007; Srinivasan and Schilling, 2018). The electrophysiological mechanisms underlying certain cardiac arrhythmias and SCD are not completely understood. There is still strong debate whether rhythm disturbances such as atrial and ventricular fibrillation are caused entirely by disorganized rhythms, sustained by multiple wavefronts, or if they are caused by organized drivers with subsequent wave breaks and fibrillatory conduction (Nattel, 2003; Nash et al., 2006).

Computational methods for prediction, classification and therapy of cardiac arrhythmias and SCD are of great interest to improve the clinical outcomes of these disorders. However, considerable challenges persist that limit the efficacy and cost-effectiveness of available methodologies. It is therefore vital to develop computational tools to help better understand the underlying mechanisms and improve effectiveness and efficacy of current therapies.

Recent advances in computational power and applications in bioinspired systems including machine learning, big data and statistical mathematics, allow new and more complex architectures with great potential to outperform traditional methods. Novel computational methods applied in electro-anatomic mapping, non-invasive imaging,

cardiac clinical and optical mapping, and biophysical computational models will help to describe the mechanisms causing the arrhythmias. A Research Topic compiling these novel computational methods in complex cardiac arrhythmias and SCD may significantly contribute to shed light on clinical applications in prediction, classification and therapy, providing unique and critical importance for management of these significant public health issues.

This Research Topic includes 17 original papers focusing on technological challenges and breakthroughs for mechanisms of cardiac rhythm disturbances using novel computational methods: prediction, classification, and therapy. The papers were co-authored by 149 authors from various science backgrounds, emphasising the importance of interdisciplinary research, particularly by young researchers, in advancing novel computational methods in cardiac research.

Non-invasive detection, stratification and machine learning

The utilization of machine learning (ML) approaches in the analysis of electrocardiogram (ECG) signals has been proposed as a means of improving the early detection of atrial fibrillation (AF) (Hannun et al., 2019). Studies have demonstrated that these ML algorithms, such as deep learning, decision trees, and support vector machines, possess high accuracy in identifying patterns associated with AF within ECG data (Murat et al., 2021). Additionally, these techniques can also be utilized to predict the likelihood of future events, thereby aiding in risk stratification (Raghunath et al., 2021; Barker et al., 2022). Early detection of AF is crucial for the timely initiation of therapy, as untreated AF can lead to serious complications, including stroke. On this theme, Tseng and Noseworthy reviewed the recent advancements in the use of machine learning techniques in the prediction and screening of atrial fibrillation. They highlighted the effectiveness of various ML algorithms in detecting and predicting AF from ECG signals and how other data such as heart rate variability can also be used for the same purpose. For instance, Valiaho et al. developed a new method for detecting AF that utilizes photoplethysmography (PPG) data. This technique can be integrated into PPG wristbands for AF detection. Mazumder et al. proposed a deep neural architecture for classifying shockable rhythms such as ventricular fibrillation (VF) and ventricular tachycardia (VT) versus other types of non-shockable rhythms. They evaluated their proposed architecture on two open access ECG databases and discovered that the classification accuracy achieved is in compliance with American Heart Association standards for wearable cardioverter defibrillator (WCD). This computational model can also be used for the design and development of personalized WCD vests based on the subject's specific anatomy and pathology, apart from acting as a device validation test-bed. Accurate detection of ectopic beats is a crucial step in ECG processing, Liu et al. developed a beat-by-beat arrhythmia detection method using weakly supervised deep learning. The model was trained to detect ventricular ectopic beats (VEBs) and supraventricular ectopic beats (SVEBs) on five large, coarsely-annotated datasets. The framework has potential applications in both clinical settings and telehealth. For better treatment planning, Li et al. developed a new ECG classification framework that can differentiate between different levels of organization of fibrillation. This method can non-invasively distinguish AF/VF of different global organization levels from the ECG alone. This framework may be useful in guiding patient selection and mechanism-directed tailored treatment strategies. Improved accuracy of detection and stratification of cardiac complexities can be achieved by utilising a deeper understanding of features obtained from ECG time series data; Li et al. conducted a retrospective study on 1024 consecutive patients who underwent cardiac surgery. They described that certain ECG biomarkers, such as the J wave, T peak to end (Tpe) greater than 112.5 ms, and the amplitude of SV1+RV5 (Sokolow Lyon index) greater than 35 mm, were strong predictors of postoperative ventricular arrhythmias (POVAs). For better utilising non-invasive ECG in clinical pathway, Roudijk et al. conducted the first in-human comparison of non-invasive intracardiac electrocardiogram (iECG) and invasive local activation time (LAT) maps on both the endocardial and epicardial surface during sinus rhythm. They found that iECG and LAT-maps showed improved agreement, but there was considerable absolute difference and moderate correlation coefficient. The study concluded that non-invasive iECG still requires further refinements to facilitate clinical implementation and risk stratification.

Catheter ablation in atrial fibrillation

Atrial arrhythmias including AF are commonly treated with catheter ablation when medication fails to maintain a patient in normal rhythm. Characterising the atrial electrical activity and structure in patients may be a key step toward a successful intervention. To determine the arrhythmogenic substrate, this stage largely depends on diverse approaches for mapping electrical activity and tissue properties. In this issue, Liao et al. developed a new deep learning (DL) model that can classify the focal source of human AF with high accuracy. The model is trained on raw unipolar electrogram (EGM) data and can automate the process of identifying the focal source (FaST) sites of AF. FaST sites were determined based on data from a single recording location, rather than the activation pattern obtained from a multi-electrode array. The clinical significance of this method is yet to be determined. Roney et al. developed a new time-averaged wavefront analysis method, which showed that there are preferential pathways of activation during AF. They also proposed a new index that measures the propagation of activation waves from the pulmonary vein antra into the atrial body. This index was significantly higher in patients who responded to pulmonary vein isolation (PVI) treatment compared to those who did not respond.

The dominant frequency (DF) of atrial electrograms during AF reflects the local activation rate of the atria. The highest DF sites may play a key role in the maintenance of AF. From a study on 40 patients who underwent a step-CA (stepwise cavotricuspid isthmus ablation) for persistent atrial fibrillation (persAF), Pithon et al. reported that high baseline DF values are predictive of unfavourable ablation outcomes. They also found that a reduction in LAA DF early in the ablation process following PVI is associated with the termination of AF (atrial fibrillation) and maintenance of sinus rhythm in the long term. Chu et al. conducted a prospective AF ablation study using simultaneous whole-chamber non-contact mapping of the highest dominant frequency (HDF). They concluded that targeting dynamic HDF sites is feasible and can be effective, but it lacks specificity in identifying

relevant persistent atrial fibrillation (persAF) substrate. They also found that spectral organization may have an adjunctive role in preventing unnecessary substrate ablation. Additionally, they concluded that dynamic HDF sites are not associated with observable rotational activity on isopotential mapping, but epi-endocardial breakthroughs could be contributory. Hwang et al. used realistic computational modelling to study 25 AF patients. They studied that the reduction of DF (dominant frequency) with antiarrhythmic drugs (AADs) is more prominent in the PVs (pulmonary veins) and during a high Smax (maximum spatial dispersion of DF) condition, which results in termination or fragmentation of AF. Additionally, they found that a lower DF and spatially unstable (higher DF-COV) condition also leads to AF termination or fragmentation.

Innovative computational methods are critical components in the robust capture of advanced features. Mase et al. introduced a novel methodology for the characterization of wave propagation and the identification of focal drivers in AF, which is based on the reconstruction of CV vector fields and the application of divergence analysis. They stated that divergence analysis was effective in identifying focal drivers in a complex simulated AF pattern. They also applied this method to human AF mapping data and discovered that it consistently detected focal activation in the pulmonary veins and left atrial appendage area. These results suggest the potential of divergence analysis in combination with multipolar mapping to identify critical sites for AF. Siles-Paredes et al. developed a Circle Method for robust estimation of local conduction velocity high-density maps from optical mapping data. This method aims to provide a more accurate representation of the electrical activity in the heart enables quantitatively predictive studies of how local CV changes affect heart electrophysiology.

Computer models can aid in the discovery of underlying mechanisms of complex cardiac arrythmias. Lyon et al. adapted a computer model of mouse ventricular electrophysiology using experimental data and found that beta-adrenergic stimulation and connexin43 hemichannel-mediated calcium entry contribute to the generation of delayed-afterdepolarizations upon loss of plakophilin-2 function. This work provides insights into potential future antiarrhythmic strategies in arrhythmogenic cardiomyopathy due to plakophilin-2 loss-of-function. Jin et al. developed a realistic computational model of AF and uncovered that circumferential PVI was effective in reducing the DF of AF, increasing its spatial heterogeneity in areas outside of the pulmonary veins, and providing better anti-AF effects than ablation in areas outside of the pulmonary veins or the use of additional flecainide in conditions where gaps existed in PVI.

Additionally, Luo et al. explored the electro-characteristics of myocardial pouches and the relationship between steam pops (SPs), pouches, and impedance. They reported that appropriate delta impedance cutoff settings (percentage of delta impedance (PDI): 15%; delta time: 3 s) can reduce the frequency of SPs and improve the safety of radiofrequency ablation (RFA).

Conclusion

Cardiac arrhythmias and sudden cardiac death are a major public health problem and the mechanisms underlying these disorders are not fully understood. Computational methods, such as machine learning, big data, and statistical mathematics, can help to improve the effectiveness and efficacy of current therapies by helping better understanding of the underlying mechanisms. Recent advances in these areas, along with other technologies such as electro-anatomic mapping and non-invasive imaging (Salinet et al., 2021), have the potential to significantly improve the management and treatment of these disorders. The future outlook for the field of Electrophysiology (EP) is very promising with many new and innovative advancements expected to emerge in the coming years. With the growth of data analytics, machine learning, and artificial intelligence, the ability to analyse and understand complex ECG data will increase dramatically. Additionally, new technologies such as wearable ECG monitors, non-invasive EP procedures, and real-time monitoring systems are expected to become increasingly prevalent. These advances will improve the accuracy of arrhythmia detection and stratification, leading to more effective and personalized treatments for cardiac patients. Additionally, the development of new drugs and ablation techniques are also expected to play a critical role in the future of EP. Overall, the next decade promises to be an exciting and transformative period for the EP field, and researchers and practitioners alike are looking forward to the many new innovations and advancements that are yet to come. We are pleased to present a Research Topic of studies describing recent investigations into the mechanisms of cardiac rhythm disturbances using novel computational methods for prediction, classification, and therapy. We hope that scientists, engineers, clinicians, and patients interested in the Research Topic will find this overview of basic, clinical, and translational research trends inspiring and encouraging in the development of novel computational methods in cardiac research.

Author contributions

XL wrote the first draft of the manuscript. All authors contributed to manuscript revision, read, and approved the submitted version.

Funding

XL received research grants from Medical Research Council UK (MRC DPFS ref: MR/S037306/1) and from the British Heart Foundation (BHF Project Grant no. PG/18/33/33780), GN received funding from the British Heart Foundation (BHF Programme Grant, RG/17/3/32774). The authors declare that this study received funding from SJM/Abbott, Medtronic and Biosense Webster. The funders were not involved in the study design, collection, analysis, interpretation of data, the writing of this article or the decision to submit it for publication.

Conflict of interest

The authors declare that the research was conducted in the absence of any commercial or financial relationships that could be construed as a potential conflict of interest.

Publisher's note

References

Barker, J., Li, X., Khavandi, S., Koeckerling, D., Mavilakandy, A., Pepper, C., et al. (2022). Machine learning in sudden cardiac death risk prediction: A systematic review. *EP Eur.* 24, 1777–1787. doi:10.1093/europace/euac135

Hannun, A. Y., Rajpurkar, P., Haghpanahi, M., Tison, G. H., Bourn, C., Turakhia, M. P., et al. (2019). Cardiologist-level arrhythmia detection and classification in ambulatory electrocardiograms using a deep neural network. *Nat. Med.* 25, 65–69. doi:10.1038/s41591-018-0268-3

Mehra, R. (2007). Global public health problem of sudden cardiac death. *J. Electrocardiol.* 40, S118–S122. doi:10.1016/j.jelectrocard.2007.06.023

Murat, F., Sadak, F., Yildirim, O., Talo, M., Murat, E., Karabatak, M., et al. (2021). Review of deep learning-based atrial fibrillation detection studies. *Int. J. Environ. Res. Public Health* 18, 11302. doi:10.3390/ijerph182111302

Nash, M. P., Mourad, A., Clayton, R. H., Sutton, P. M., Bradley, C. P., Hayward, M., et al. (2006). Evidence for multiple mechanisms in human ventricular fibrillation. *Circulation* 114, 536–542. doi:10.1161/CIRCULATIONAHA.105.602870

Nattel, S. (2003). Atrial electrophysiology and mechanisms of atrial fibrillation. *J. Cardiovasc Pharmacol. Ther.* 8 (1), S5–S11. doi:10.1177/107424840300800102

Raghunath, S., Pfeifer, J. M., Ulloa-Cerna, A. E., Nemani, A., Carbonati, T., Jing, L., et al. (2021). Deep neural networks can predict new-onset atrial fibrillation from the 12-lead ECG and help identify those at risk of atrial fibrillation–related stroke. *Circulation* 143, 1287–1298. doi:10.1161/CIRCULATIONAHA.120.047829

Salinet, J., Molero, R., Schlindwein, F. S., Karel, J., Rodrigo, M., Rojo-Álvarez, J. L., et al. (2021). Electrocardiographic imaging for atrial fibrillation: A perspective from computer models and animal experiments to clinical value. *Front. Physiol.* 12, 653013. doi:10.3389/fphys.2021.653013

Srinivasan, N. T., and Schilling, R. J. (2018). Sudden cardiac death and arrhythmias. *Arrhythm. Electrophysiol. Rev.* 7, 111–117. doi:10.15420/aer.2018:15:2

frontiers in Physiology

ORIGINAL RESEARCH
published: 07 May 2021
doi: 10.3389/fphys.2021.654555

Wrist Band Photoplethysmography Autocorrelation Analysis Enables Detection of Atrial Fibrillation Without Pulse Detection

Eemu-Samuli Väliaho[1,2], Pekka Kuoppa[3], Jukka A. Lipponen[3], Juha E. K. Hartikainen[1,4], Helena Jäntti[1,5], Tuomas T. Rissanen[6], Indrek Kolk[4], Hanna Pohjantähti-Maaroos[4], Maaret Castrén[7,8], Jari Halonen[1,4], Mika P. Tarvainen[3,9], Onni E. Santala[1,2] and Tero J. Martikainen[10]*

[1] School of Medicine, Faculty of Health Sciences, University of Eastern Finland, Kuopio, Finland, [2] Doctoral School, Faculty of Health Sciences, University of Eastern Finland, Kuopio, Finland, [3] Department of Applied Physics, University of Eastern Finland, Kuopio, Finland, [4] Heart Center, Kuopio University Hospital, Kuopio, Finland, [5] Center for Prehospital Emergency Care, Kuopio University Hospital, Kuopio, Finland, [6] Heart Center, North Karelia Central Hospital, Joensuu, Finland, [7] Emergency Medicine, Faculty of Medicine, University of Helsinki, Helsinki, Finland, [8] Department of Emergency Medicine and Services, Helsinki University Hospital, Helsinki, Finland, [9] Department of Clinical Physiology and Nuclear Medicine, Kuopio University Hospital, Kuopio, Finland, [10] Department of Emergency Care, Kuopio University Hospital, Kuopio, Finland

OPEN ACCESS

Edited by:
Fernando Soares Schlindwein, University of Leicester, United Kingdom

Reviewed by:
Dewar Finlay, Ulster University, United Kingdom
Fons Schipper, Philips Research, Netherlands

***Correspondence:**
Eemu-Samuli Väliaho
eemuv@uef.fi

Specialty section:
This article was submitted to Cardiac Electrophysiology, a section of the journal Frontiers in Physiology

Received: *16 January 2021*
Accepted: *07 April 2021*
Published: *07 May 2021*

Citation:
Väliaho E-S, Kuoppa P, Lipponen JA, Hartikainen JEK, Jäntti H, Rissanen TT, Kolk I, Pohjantähti-Maaroos H, Castrén M, Halonen J, Tarvainen MP, Santala OE and Martikainen TJ (2021) Wrist Band Photoplethysmography Autocorrelation Analysis Enables Detection of Atrial Fibrillation Without Pulse Detection. Front. Physiol. 12:654555. doi: 10.3389/fphys.2021.654555

Atrial fibrillation is often asymptomatic and intermittent making its detection challenging. A photoplethysmography (PPG) provides a promising option for atrial fibrillation detection. However, the shapes of pulse waves vary in atrial fibrillation decreasing pulse and atrial fibrillation detection accuracy. This study evaluated ten robust photoplethysmography features for detection of atrial fibrillation. The study was a national multi-center clinical study in Finland and the data were combined from two broader research projects (NCT03721601, URL: https://clinicaltrials.gov/ct2/show/NCT03721601 and NCT03753139, URL: https://clinicaltrials.gov/ct2/show/NCT03753139). A photoplethysmography signal was recorded with a wrist band. Five pulse interval variability, four amplitude features and a novel autocorrelation-based morphology feature were calculated and evaluated independently as predictors of atrial fibrillation. A multivariate predictor model including only the most significant features was established. The models were 10-fold cross-validated. 359 patients were included in the study (atrial fibrillation n = 169, sinus rhythm n = 190). The autocorrelation univariate predictor model detected atrial fibrillation with the highest area under receiver operating characteristic curve (AUC) value of 0.982 (sensitivity 95.1%, specificity 93.7%). Autocorrelation was also the most significant individual feature ($p < 0.00001$) in the multivariate predictor model, detecting atrial fibrillation with AUC of 0.993 (sensitivity 96.4%, specificity 96.3%). Our results demonstrated that the autocorrelation independently detects atrial fibrillation reliably without the need of pulse detection. Combining pulse wave morphology-based features such as autocorrelation

with information from pulse-interval variability it is possible to detect atrial fibrillation with high accuracy with a commercial wrist band. Photoplethysmography wrist bands accompanied with atrial fibrillation detection algorithms utilizing autocorrelation could provide a computationally very effective and reliable wearable monitoring method in screening of atrial fibrillation.

Keywords: atrial fibrillation, atrial fibrillation detection, arrhythmia detection, pulse detection, photoplethysmography, autocorrelation, algorithms, stroke

INTRODUCTION

Atrial fibrillation (AF) is the most common tachyarrhythmia and it's prevalence is increasing as the population ages (Morillo et al., 2017). AF is associated with thromboembolic complications, such as stroke (Xiong et al., 2015; Morillo et al., 2017; Pereira et al., 2020). It is estimated that 20–30% of all strokes are due to AF (Kirchhof et al., 2016; Pereira et al., 2020). In addition, 25% of ischaemic strokes are of unknown cause and there is persuasive evidence that most of these are of thromboembolic origin (Hart et al., 2014). Up to two thirds of strokes can be prevented with anticoagulation (Saxena and Koudstaal, 2004; Hart et al., 2007). A clinical challenge is that AF is often asymptomatic or paroxysmal (Xiong et al., 2015) and therefore, difficult to be diagnosed. Intermittent electrocardiograms (ECGs) recorded during clinical visits have a low likelihood of detecting paroxysmal AF. Long-term, continuous monitoring with automatic AF detection would improve AF screening detection allowing appropriate primary and secondary strategies for prevention of stroke (Pereira et al., 2020).

Photoplethysmography (PPG) technology is widely used for welfare or sport-tracking purposes. PPG has also been proven to be promising also in the detection of AF (Tison et al., 2018; Dörr et al., 2019; Fan et al., 2019; Kashiwa et al., 2019; Väliaho et al., 2019; Pereira et al., 2020). Usually, in PPG the rhythm assessment is based on pulse-to-pulse interval detection. However, AF detection with PPG based on pulse-to-pulse (PP) interval irregularity is often challenging. Namely, AF is characterized by poorly coordinated atrial activation, resulting in highly irregular heart rate and variable pulse wave amplitudes. In addition, the signal is susceptible to artifacts caused by motion of the sensor against the skin or poor sensor contact (Pereira et al., 2020). Furthermore, the pulse detection accuracy is lower in patients with AF compared to those in sinus rhythm (SR) and even lower in patients with episodes of short duration of AF (Väliaho et al., 2019). Several companies are currently developing wrist worn PPG devices with arrythmia detection features. Thus, reliable methods for PPG-based AF detection are under strong interest and could lead to improved rhythm diagnostics of AF patients.

In this study we introduce a novel PPG pulse wave morphology-based method which enables AF detection without the need of individual pulse detection. A robust morphology-based PPG-analysis can significantly improve AF detection accuracy of PPG wrist bands.

MATERIALS AND METHODS

Study Design

The study was a national multi-center clinical study implemented in three hospitals in Finland: Kuopio University Hospital (KUH), Helsinki University Hospital (HUS) and North Karelia Central Hospital (NKCH). The data were combined from two studies (Afib study and Single-ECG study), both of which were approved by the Ethics Committee of KUH (237/2017 and 850/2018) and registered in the ClinicalTrials.gov database (NCT03721601[1] and NCT03753139[2]).

The participants were given written and oral information and an opportunity to ask questions about the study. All participants provided written informed consent.

Study Population

A total of 555 patients were screened in the emergency care departments and the cardiological wards of the three participating hospitals (**Figure 1**) in two broader research projects (the Afib study and the Single-ECG study). A total of 295 patients were screened in KUH, HUS and NKCH between May – September 2017 (the Afib study), and 260 patients in KUH between November 2018 – May 2019 (the Single-ECG study).

The inclusion criteria were AF or sinus rhythm (SR) diagnosed by the treating physician from a 12-lead resting ECG. The exclusion criteria were a body mass index (BMI) $\geq$ 33 kg/m^2 (the Afib study) or $\geq$ 35 kg/m^2 (the Single-ECG study), a cardiac pacemaker, a left bundle branch block (LBBB), a right bundle branch block (RBBB), an inconclusive or a non-stable rhythm and a medical condition requiring immediate treatment. In the initial screening 182 patients were excluded; 143 due to not meeting the inclusion criteria, 21 patients declined and 18 were excluded for other reasons. After the 3-lead continuous ECG and PPG recording (see below), additional 14 patients were excluded: six due to inconclusive rhythms, two due to RBBBs and six due to inadequate PPG data. Thus, the final population consisted of 359 patients: 169 AF patients and 190 patients in SR (**Figure 1**).

Data Acquisition

After the initial screening, simultaneous 3-lead ECG and PPG wrist band signals were recorded for at least 5 minutes. The 3-lead ECG was recorded with 1,000 Hz sampling frequency using

[1]https://clinicaltrials.gov/ct2/show/NCT03721601

[2]https://clinicaltrials.gov/ct2/show/NCT03753139

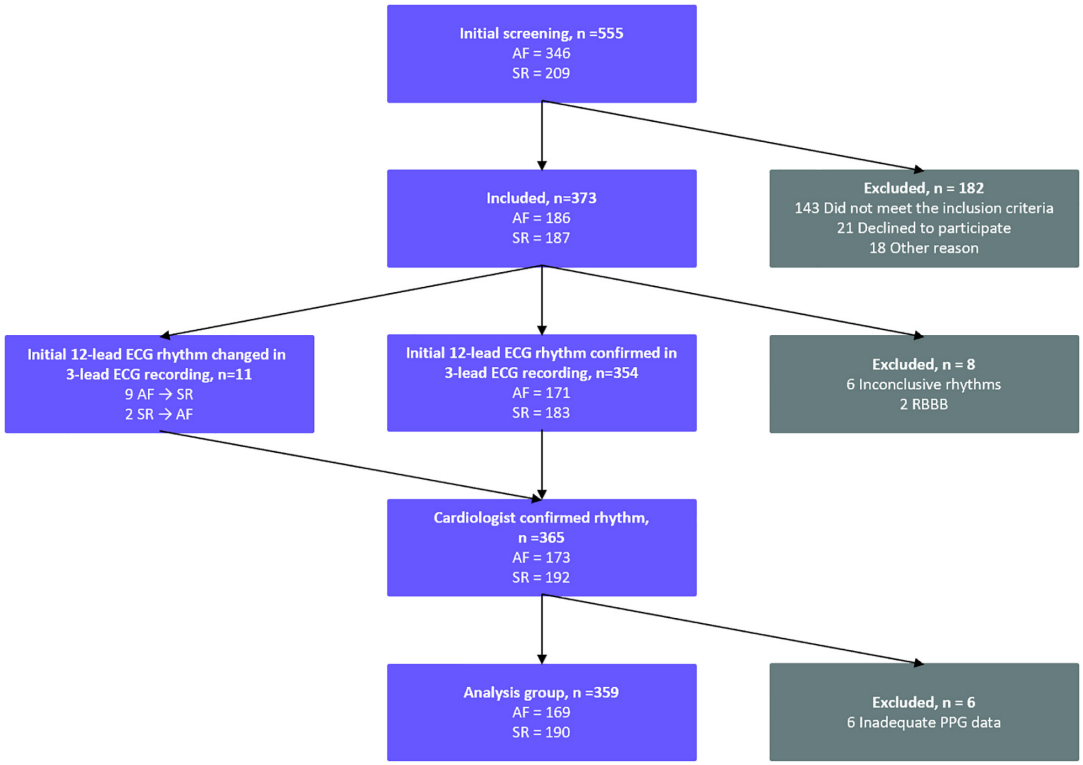

FIGURE 1 | Standards for Reporting Diagnostic Accuracy Studies (STARD) flow diagram of the study patient flow. A total of 555 patients were screened in the participating hospitals KUH, HUS, and NKCH. 359 patients were included in the analysis. AF, atrial fibrillation; ECG, electrocardiogram; SR, sinus rhythm; PPG, photoplethysmography; RBBB, right bundle branch block.

a Holter ECG device (Faros 360, Bittium, Oulu, Finland) with five wet electrodes. A simultaneous PPG signal was recorded using 64 Hz sampling frequency with an Empatica E4 wrist band (Empatica Inc, Cambridge, United States). This wrist band captures optical PPG signal utilizing the blood volume pulse (BVP) method. Before the recordings, patients were resting for at least 2 min. After the rest, the ECG and the PPG signals were recorded simultaneously with the patient in the supine position.

ECG Analysis

The final rhythm classification was based on 3-lead ECG recording interpreted by two experienced cardiologists blinded to the initial 12-lead ECG. The consensus of rhythm interpretation by the two cardiologists served as the "golden standard" for the final rhythm analysis. If no consensus was met, the patient was excluded from the study (**Figure 1**).

PPG Processing and Feature Extraction

The PPG data was transferred to a MATLAB® software (version R2017b) for pre-processing and analysis. The PPG data was first interpolated to 128 Hz to increase the time resolution for the beat detection. A digital zero-phase finite impulse response lowpass filter with order of 256 and a cut-off frequency of 4 Hz was used to remove high frequency noise. A PPG quality algorithm was used to identify a 1-min period of good quality PPG signal from each measurement. Only the first eligible 1-min section of each patients' recording was utilized, and the rest of the recording was discarded. The PPG quality algorithm used acceleration measurement from the wristband to detect stable periods with no movement of the wrist and PPG amplitude variation to detect artifacts from the PPG signal. The first continuous 1-min sample of each PPG recording with at least 55 s fulfilling the above conditions was accepted for the analysis. If a good quality period was not found from the PPG recording, the patient was excluded from the final analysis (**Figure 1**).

A total of ten features were calculated from the PPG signal, from which five were based on pulse interval (PIN, **Figure 2**) detection and four on pulse amplitude (AMP) detection. The five PIN-based variables were: mean PIN, root-mean-square values of successive differences (RMSSD), AFEvidence (AFE), Coefficient of Sample Entropy (COSEn) and turning point ratio (TPR). AFEvidence is based on relative population of segments in a 2D histogram representing dRR-intervals (Sarkar et al., 2008) and COSEn is an estimate of entropy optimized for AF detection (Lake and Moorman, 2011). Four features based on pulse amplitude were: mean AMP, RMSSD, Sample Entropy (SampEn) and TPR. These nine features are more commonly used for AF detection (Tang et al., 2017; Väliaho et al., 2019). In addition, we evaluated the performance of a more novel autocorrelation (AC) feature.

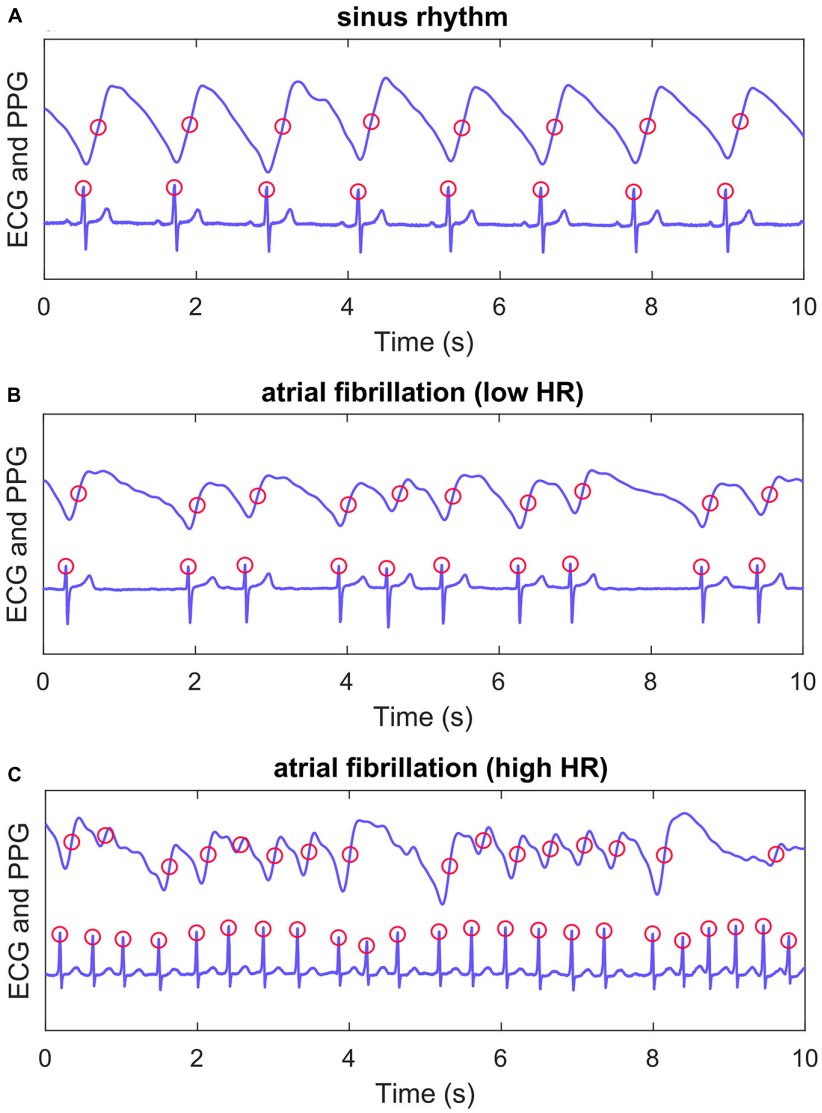

FIGURE 2 | Example recordings. PPG (upper) and ECG (lower) recordings from three patients. Panel **(A)** shows a patient with sinus rhythm, panel **(B)** atrial fibrillation with lenient heart rate and panel **(C)** atrial fibrillation with high heart rate. Algorithm ECG QRS detection points and PPG pulse detection points are marked with red circles. A PIN time series was formed with detected PPG pulses for PIN-based AF detection features. ECG, electrocardiogram; PPG, photoplethysmography; HR, heart rate.

The pulses were detected from the 1-min PPG samples using a method described and validated in our previous study (**Figure 2**; Väliaho et al., 2019). A time series with PINs was formed from the successive pulse detections. The PIN-based features (mean, RMSSD, AFE, COSEn and TPR) were calculated from these time series.

The amplitude of each PPG pulse wave was calculated as difference of maximum and minimum amplitude in a 0.5 s window around the detected pulse. The formed amplitude time series was used to calculate the values for the AMP-based features (mean, RMSSD, SampEn and TPR). The values of TPR and AC features were used as 100-fold for better calculation accuracy (by avoiding dividing by almost 0) and estimation of odds ratios.

AC is a pulse wave morphology-based feature extracted from the PPG signal. It represents the correlation between a signal and its delayed copy as a function of delay. AC describes the regularity of the PPG signal morphology without a need for detection of individual pulses from the time series (**Figure 3**). AC values are decreased if the shape and periodicity of the PPG pulse waves vary. The average of absolute autocorrelation values (performed over different delays) was calculated for 1-min PPG samples of each patient. The normalized value of AC for different delays can be calculated as

$$R_l = \frac{\left(\frac{1}{N}\sum_{t=1}^{N-l} x_t x_{t+l}\right)}{R_0}$$

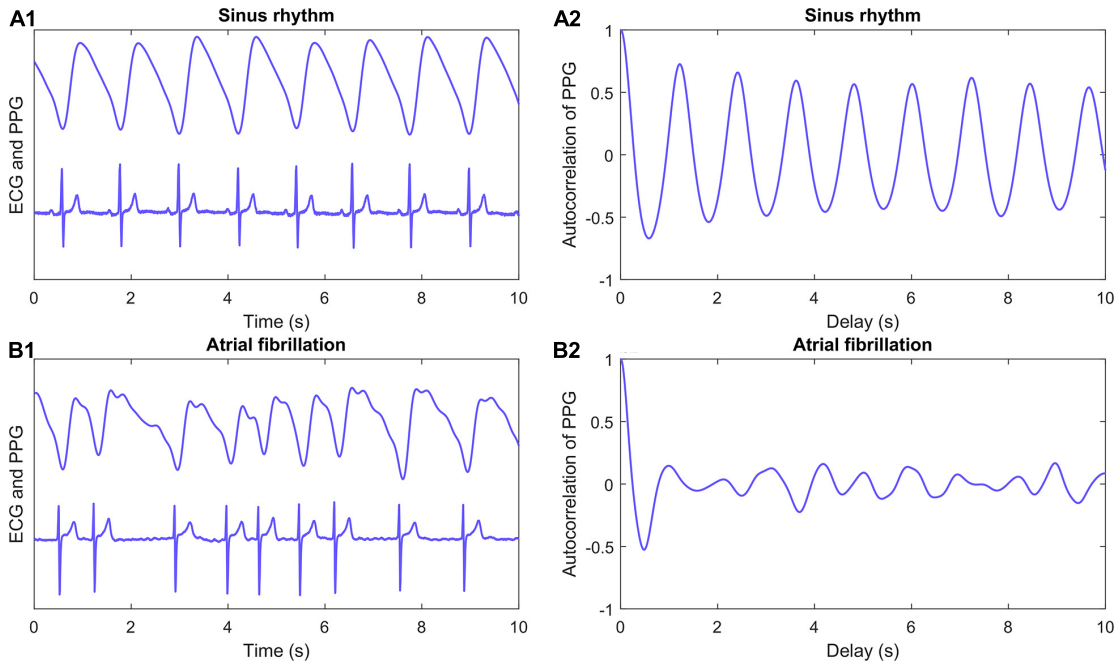

FIGURE 3 | Autocorrelation. PPG (upper) and ECG (lower) recordings from a patient with sinus rhythm **(A1)** and atrial fibrillation **(B1)**. Corresponding autocorrelation values were calculated for 1-min samples of PPG signal for each patient. First 10 s of example recordings and calculated autocorrelation values **(A2** and **B2)** are shown in panels. Autocorrelation is a feature calculated straight from the signal and it requires no pulse detection. It is the correlation between a signal and its delayed copy as a function of delay. ECG, electrocardiogram; PPG, photoplethysmography.

where R_l is the value of AC for delay l, R_0 is the value of AC with no delay, x_t is signal value for time index t and N is total number of samples in the signal.

Atrial Fibrillation Detection With Univariate Predictor Models

To test how all the ten features can individually predict AF, each feature was evaluated as a univariate predictor model for detection of AF. All ten features were established in ten independent linear logistic regression models. The logistic regression uses the features to estimate the probability of the PPG sample being true positive AF. Since our dataset was balanced, the cut-off value of AF detection was set at 0.5. The performance was evaluated with 10-fold cross-validation (see below) and diagnostic performance parameter values were calculated for each univariate predictor model.

Establishing the Multivariate Predictor Model for Atrial Fibrillation Detection

Linear logistic regression with backward feature selection procedure was used to detect independent and statistically significant features for the detection of AF with MATLAB® software version R2017b. Our hypothesis was that the combined performance of some of the features is better than any of these features independently. Backward feature selection method was started with all the ten features using all the data samples and recommended significance level of 0.157 (Heinze et al., 2018). Features were removed from the model one at a time if removing them would not significantly decrease the performance of the model. A logistic regression model including only the most significant features was established. The cut-off value of AF detection was set at 0.5. The performance of this multivariate predictor model was tested with 10-fold cross-validation.

Validation of the Predictor Models

AF data samples (n = 359) were randomly divided into ten sections for 10-fold cross-validation. All ten univariate predictor models and the established multivariate predictor model were validated with this method. Each time nine sections were used to train the model and one section was used to validate the prediction performance. The process was repeated ten times, with each of ten sections used only once as the validation data. The advantage of this validation method is that same samples are not used simultaneously for training and validation (reduce bias) of the predictor model, and each individual sample is used exactly once for validation. The diagnostic performance parameter values were averaged to produce a single estimation of AF prediction, including area under receiver operating characteristic curve (AUC) value, sensitivity, specificity, positive prediction value (PPV), negative prediction value (NPV) and accuracy.

The receiver operating characteristics (ROC) curve was formed for each prediction model by using the average of true and false positive rates from the 10-fold cross validation models.

Statistical Analysis

Clinical characteristic data and PPG feature parameter values were analyzed using IBM SPSS statistics software version 25. Continuous variables between AF and SR patients were analyzed with independent-sample t-tests and categorical variables with χ^2 tests. The significance of differences within AF and SR patients were tested with paired t-tests. All significance tests were two-tailed with $p \leq 0.05$ considered statistically significant.

RESULTS

Clinical Characteristics

The study population consisted of 359 patients (AF $n = 169$, SR $n = 190$). Patients with AF were older, had higher heart rate, more often medical history including earlier AF episodes, congestive heart failure and heart surgery, and were more often on beta-blockers, digoxin or anticoagulation therapy (**Table 1**). There were no adverse events related to the study recordings.

PPG Feature Comparison Between Rhythm Groups

Calculated parameter values of all ten features of the PPG signal differed between AF and SR groups (**Table 2**).

Univariate Predictor Models With Single Features for AF Detection

The novel PPG pulse wave morphology-based AC feature detected AF as a univariate predictor model with highest AUC of 0.982 (sensitivity 95.1%, specificity 93.7%). The PIN-based AFE detected AF with AUC of 0.977 (sensitivity of 96.0%, specificity 92.9%) and PIN-based COSEn with 0.964 (sensitivity of 92.3%, specificity of 92.1%). The other seven univariate predictor models yielded lower AUC values. The averaged 10-fold cross-validated diagnostic performance parameter values for each univariate predictor models are presented in **Table 3**. The ROC curves for each univariate predictor models are presented in **Figure 4**.

AF Detection With the Multivariate Predictor Model

The multivariate predictor model was reduced with the backward feature selection to include only four features: PIN_AFE ($p = 0.007$), PIN_TPR ($p = 0.008$), AMP_mean ($p = 0.031$) and AC ($p < 0.00001$) (**Table 4**).

The multivariate predictor model detected AF with AUC of 0.993, sensitivity of 96.4% and specificity of 96.3%. The diagnostic performance parameters of the validated multivariate predictor model are presented in **Table 5**. The ROC curve for the multivariate prediction model is presented in **Figure 4**.

DISCUSSION

We demonstrated that the novel AC as a univariate predictor model detected AF with high sensitivity (95.1%) and specificity (93.7%) from the PPG wrist band signal. AC had the highest AUC (0.982) of all ten univariate predictor models, each containing only one PPG feature. The advantage of AC is that it requires no individual pulse detection from the PPG signal unlike all other nine features evaluated. To the best of our knowledge, this is the first time AC was assessed and validated as a predictor of AF with a PPG wrist band. The AC feature was also included in the multivariate predictor model with backward feature selection method and it turned out to be the most significant individual feature in the model ($p < 0.00001$).

In addition, our study shows that combining pulse wave morphology-based AC with PIN and AMP-based features improves the diagnostic performance of PPG wrist bands. The multivariate predictor model developed and validated in our study consisting of four PPG features detected AF with higher AUC, sensitivity and specificity (0.993, 96.4%, 96.3%) than any of the ten evaluated features as univariate predictor models independently.

Short-term AC has been used earlier for instantaneous heart rate (IHR) and R-peak detection from the ECG signal due to its noise-tolerant performance (Fujii et al., 2013). In addition, the advantage of short-term AC for wearable ECG monitoring systems is that it has low digital processing capacity requirements (Fujii et al., 2013). From the PPG signal, short-term AC has been used to estimate pulse-to-pulse interval with short 4-s time windows because it has more instability tolerance (Kashiwa et al., 2019). PPG pulse waves frequently have low peaks or varying amplitude in AF patients. This is due to loss of atrial-ventricular synchrony, impaired ventricular diastolic filling, and irregular ventricular rate. As a result, the PPG pulse detection sensitivity in patients with AF is lower compared to patients with SR, and even lower if the AF has lasted for less than 48 h (Väliaho et al., 2019). Autocorrelation as a robust and computationally very effective method can detect the absence of this morphology regularity. An obvious advantage of AC is that it recognizes AF without pulse detection.

Yan et al. used a smartphone camera to measure the PPG from the fingertip and contact-free from the face (Yan et al., 2018). They used a smartphone application utilizing a support vector machine (SVM) with the AC to detect AF from the PPG signal (Yan et al., 2018). The SVM is a machine learning technique (Kwon et al., 2019). The sensitivity and specificity were 94.7 and 95.8% for facial PPG and 94.7 and 93.0% for the fingertip PPG (Yan et al., 2018). Recently Kwon et al. reported that the SVM with the AC to detected AF with sensitivity of 93.26% and specificity of 89.60% with a pulse oximeter from the fingertip (Kwon et al., 2019). In our study the multivariate predictor model including the AC feature achieved higher sensitivity and specificity compared to both studies. Also, the method of measuring PPG was different in these studies as compared to the wrist band that was used here.

In our study we assessed the feasibility of a PPG wrist band, a commonly used method for sport and welfare purposes, for AF detection. A wide range of other devices such as smartwatches (Tison et al., 2018; Dörr et al., 2019; Guo et al., 2019; Perez et al., 2019), smartphone applications (Yan et al., 2018; Kwon et al., 2019), and chest strap ECGs (Hartikainen et al., 2019)

TABLE 1 | Clinical characteristics of the patients.

	AF group,	SR group,	Significance	Mean difference and
	***n* = 169**	***n* = 190**	**(2-sided)**	**[95% CI of the difference]**
Characteristics				
Age, years	72.2 ± 14.3	57.9 ± 18.8	<0.001	14.29 [10.85 to 17.73]*
BMI, kg/m^2	26.0 ± 3.9	25.8 ± 3.7	0.635	0.19 [−0.60 to 0.99]*
Sex, male	87 (51.5)	97 (51.1)	0.936	0.43 [−9.83 to 10.67]
PPG				
Mean heart rate, min^{-1}	84.4 ± 15.0	69.8 ± 13.6	<0.001	14.59 [11.62 to 17.56]*
Medical history				
Atrial fibrillation	128 (75.7)	44 (23.2)	<0.001	52.58 [43.04 to 60.56]
Hypertension	112 (66.3)	96 (50.5)	0.003	15.75 [5.53 to 25.47]
Coronary artery disease	48 (28.4)	41 (21.6)	0.135	6.82 [−2.12 to 15.75]
Congestive heart failure	46 (27.2)	6 (3.2)	<0.001	24.06 [16.96 to 31.42]
Diabetes	30 (17.8)	29 (15.3)	0.525	2.49 [−5.18 to 10.31]
Cardiac surgery	22 (13.0)	9 (4.7)	0.005	8.28 [2.42 to 14.59]
Other arrhythmia	16 (9.5)	21 (11.1)	0.622	−1.59 [−7.93 to 4.93]
Structural heart disease	14 (8.3)	9 (4.7)	0.171	3.55 [−1.64 to 9.15]
Medication				
Anticoagulation	131 (77.5)	42 (22.1)	<0.001	55.41 [46.01 to 63.16]
Beta-blocker	125 (74.0)	74 (38.9)	<0.001	35.02 [24.99 to 43.99]
Digoxin	22 (13.0)	1 (0.5)	<0.001	12.49 [7.60 to 18.41]
Anti-arrhythmic drugs	9 (5.3)	4 (2.1)	0.103	3.22 [−0.83 to 7.88]

Values are mean ± standard deviation and number (percentages). In the last column values are mean difference and [95% Confidence Interval of the Difference]. Values for dicotomical variables in this column (e.g., sex or hypertension) are percentages.
AF, atrial fibrillation; CI, confidence interval; HR, heart rate; PPG, photoplethysmography and SR, sinus rhythm.
**Mean difference and [95% confidence interval of the difference] values for Age, BMI, and HR are years, kg/m^2 and min^{-1}.*

TABLE 2 | Comparison of feature parameter values between atrial fibrillation and sinus rhythm groups.

Feature	AF group	SR group	Significance	Mean difference and
	***n* = 169**	***n* = 190**	**(2-sided)**	**[95% CI of the difference]**
	Mean ± SD	**Mean ± SD**		
Pulse-interval				
PIN_mean	0.734 ± 0.134	0.892 ± 0.166	<0.00001	−0.158 [−0.189 to −0.126]
PIN_RMSSD	0.281 ± 0.102	0.122 ± 0.111	<0.00001	0.159 [0.136 to 0.181]
PIN_AFE	58.201 ± 13.838	−26.111 ± 36.605	<0.00001	84.312 [78.432 to 90.191]
PIN_COSEn	−0.411 ± 0.554	−1.981 ± 0.511	<0.00001	1.570 [1.459 to 1.680]
PIN_TPR	61.751 ± 6.059	48.836 ± 10.984	<0.00001	12.915 [11.054 to 14.776]
Amplitude				
AMP_mean	64.380 ± 46.774	90.082 ± 57.042	<0.00001	−25.703 [−36.612 to −14.794]
AMP_RMSSD	27.782 ± 20.453	17.072 ± 16.800	<0.00001	10.710 [6.841 to 14.580]
AMP_SampEn	2.217 ± 1.073	1.774 ± 0.664	<0.00001	0.443 [0.260 to 0.626]
AMP_TPR	65.716 ± 6.536	57.169 ± 8.565	<0.00001	8.547 [6.951 to 10.144]
Morphology				
AC	4.790 ± 1.544	14.723 ± 5.306	<0.00001	−9.933 [−10.766 to −9.101]

Values were calculated for each PPG feature for each patient individually in both rhythm groups. Numbers are mean ± standard deviation. Significance is between groups. AC, autocorrelation; AF, atrial fibrillation; AFE, AFEvidence; AMP, peak amplitude; CI, confidence interval; COSEn, coefficient of sample entropy; PIN, pulse interval; PPG, photoplethysmography; RMSSD, root mean square of successive pulse-to-pulse differences; SampEn, sample entropy; SD, standard deviation; SR, sinus rhythm and TPR, turning point ratio.

have also been evaluated for AF detection. Recently, in the Huawei Heart study 187 912 participants were monitored with a PPG wrist band or a wristwatch (Guo et al., 2019). During the monitoring, 424 (0.23%) subjects received an irregular pulse notification and of those 262 were followed up with an ECG or 24-h Holter (Guo et al., 2019). AF was ECG-confirmed

TABLE 3 | Averaged 10-fold cross-validated univariate predictor model diagnostic performance values for detection of atrial fibrillation.

Univariate predictor models	AUC*	Sensitivity	Specificity	PPV	NPV	Accuracy
Pulse-interval						
PIN_mean	0.780	72.2	72.2	69.6	75.0	72.1
PIN_RMSSD	0.867	77.4	80.9	78.5	79.8	78.8
PIN_AFE	0.977	96.0	92.9	93.1	97.0	94.7
PIN_COSEn	0.964	92.3	92.1	91.4	93.2	92.2
PIN_TPR	0.841	80.1	72.3	71.7	81.1	76.0
Amplitude						
AMP_mean	0.659	59.7	60.4	57.3	63.0	59.6
AMP_RMSSD	0.726	46.0	82.6	70.7	63.2	65.0
AMP_SampEn	0.680	48.1	72.8	61.0	61.6	61.3
AMP_TPR	0.792	72.2	73.1	71.1	74.7	72.7
Morphology						
AC	0.982	95.1	93.7	93.5	96.2	94.4

AC, autocorrelation; AF, atrial fibrillation; AFE, AFEvidence; AMP, peak amplitude; AUC, area under the curve; CI, confidence interval; COSEn, coefficient of sample entropy; NPV, negative predictive value; PIN, pulse interval; PPG, photoplethysmography; PPV, positive predictive value; RMSSD, root mean square of successive pulse-to-pulse differences; SampEn, sample entropy; SD, standard deviation; SR, sinus rhythm and TPR, turning point ratio.
**The values are percent (%) except AUC is absolute value.*

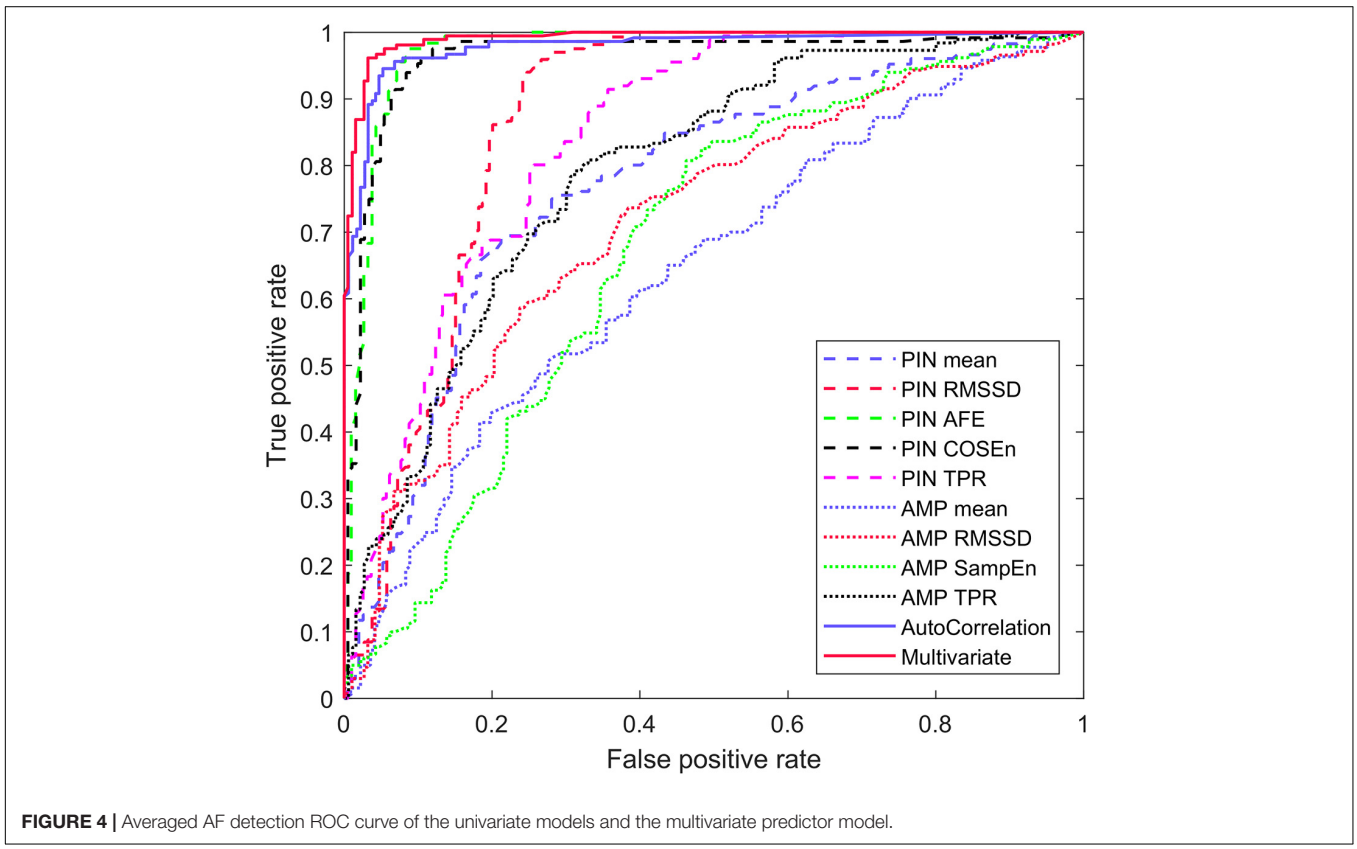

FIGURE 4 | Averaged AF detection ROC curve of the univariate models and the multivariate predictor model.

in 227 (87%) cases with the PPV 91.6% for the PPG-based algorithm (Guo et al., 2019). Correspondingly, in the Apple Heart Study PPG was recorded with a smartwatch from 419 093 participants (Perez et al., 2019). 2161 (0.52%) of subjects received PPG-based irregular pulse notifications and of those 450 were monitored with ECG patches for an average of 6.3 days (Perez et al., 2019). AF was found in 153 (34%) of the subjects (Perez et al., 2019). Only 86 individuals had irregular PPG pulse notifications during simultaneous use of an ECG patch, and AF was confirmed in 72 of these cases resulting in a PPV of 84% with the PPG smartwatch (Perez et al., 2019). Because of the study designs in both Huawei Heart Study and Apple Heart Study, sensitivity could not be assessed and thus compared to the results of our study. Perez et al. state that their PPG-based irregular pulse detection algorithm was designed to minimize false positive findings of AF and should

not be used for AF screening (Perez et al., 2019). However, our algorithm produced high sensitivity (96.4%), specificity (96.3%) and PPV (96.1%) indicating PPG wrist bands could enable reliable detection of AF.

Kashiwa et al. developed a wrist band pulse wave monitor for long-term PPG monitoring that detects AF with PPG pulse frequency-based analysis (Kashiwa et al., 2019). Their AF detection was based on two statistical values: the coefficient of variation (CV) of PP values and Kolmogorov-Smirnov (KS) difference (Kashiwa et al., 2019). They detected AF with a patient average sensitivity of 81.0%, specificity of 96.4% and PPV of 86.6% with AF episodes lasting over 6 min (Kashiwa et al., 2019). Compared to Kashiwa et al., in our study, using the multivariate predictor model, the sensitivity and the PPV were higher (96.4 and 96.1%) and the specificity was equal (96.3%). Fan et al. used a novel algorithm utilizing combined PPG morphology and pulse frequency analysis to detect AF with a PPG wrist band (Fan et al., 2019). The quality of the PPG signal was assessed with a mobile phone application, and in case of rejected recording the measurement was retaken (Fan et al., 2019). In line with us, they analyzed also 1-min samples, but they extracted three samples from each patient, yielding a sensitivity of 95.36%, a specificity of 99.70% and a PPV of 99.63% for AF detection (Fan et al., 2019). The sensitivity of the multivariate predictor model in our study was slightly better but the specificity and the PPV were lower.

Recently, Tison et al. reported that PPG smartwatch was able to detect AF utilizing a deep neural network with sensitivity of 98.0%, specificity of 90.2% and PPV of 90.9% (Tison et al., 2018). They trained their method in 6,682 patients and validated it in 51 patients (Tison et al., 2018). The algorithm-based multivariate predictor model developed in our study achieved significantly higher specificity (96.3%) and PPV (96.1%) with only slightly lower sensitivity (96.4%). Also, Dörr et al. showed that an AF detection algorithm detected AF with a PPG smartwatch with a sensitivity of 93.7%, a specificity of 98.2% and a PPV of 97.8% calculated from high quality samples (Dörr et al., 2019). As compared to the other studies Dörr et al. reported high number of non-interpretable samples, more than 20% of their 1-min PPG samples remained without rhythm interpretation (Dörr et al., 2019). Our method yielded higher sensitivity and slightly lower specificity and PPV, however, by using our method there were only six (1.6%) samples which rhythm could not be interpreted.

TABLE 4 | Features in the multivariate predictor model.

Feature		Estimate	SE	OR	Significance (2-sided)*
Any	(Intercept)	−3.723	2.671	0.024	0.163
Pulse-interval	PIN_AFE	0.045	0.017	1.046	0.007
	PIN_TPR	0.126	0.047	1.135	0.008
Amplitude	AMP_mean	0.016	0.008	1.017	0.031
Morphology	AC	−0.771	0.171	0.463	<0.00001

All features included in the established multivariate predictor model were statistically significant with $p < 0.05$. Intercept is the constant of the linear logistic regression model.
AC, autocorrelation; AFE, AFEvidence; AMP, peak amplitude; OR, odds ratio; PIN, pulse interval; SE, standard error and TPR, turning point ratio.
**For logistic regression model including all four features.*

TABLE 5 | Multivariate predictor model 10-fold cross-validation diagnostic performance results in detection of atrial fibrillation.

	Mean	Min	Max
Multivariate			
AUC	0.993	0.987	1.000
Sensitivity	96.4	88.9	100.0
Specificity	96.3	90.0	100.0
PPV	96.1	88.9	100.0
NPV	96.9	88.9	100.0
Accuracy	96.4	91.7	100.0

The multivariate prediction model consisted of PIN_AFE, PIN_TPR, AMP_mean and AC features. Mean values are averaged from ten validations with subsections. The values are percent (%) except AUC are absolute values (number).
AFE, AFEvidence; AMP, peak amplitude; AUC, area under the curve; Max, maximum; Min, minimum; NPV, negative predictive value; PPV, positive predictive value; PIN, pulse interval and TPR, turning point ratio.

Limitations

AF detection was performed from 1-min PPG samples of good quality data. These samples were selected automatically by the quality algorithm. The PPG signal is susceptible to disturbances caused by movement of the optical sensor against the skin, blood pressure changes and vascular elasticity fluctuations. In our study, the PPG signal was recorded only for 5 min and from stationary patients. For detection of paroxysmal atrial fibrillation, the technology should allow longer rhythm monitoring in ambulatory patients. The quality of the data can be improved by using PPG wrist bands equipped with acceleration sensors programmed to accept only PPG signal for AF analysis when the patient is at rest and the hand is stable position. Further clinical studies are needed to assess the utility of PPG wristband in the detection of AF in long-term monitoring of ambulatory patients. The capability of the AF detection algorithms should be evaluated in a setting where the PPG signal is exposed to the artifacts caused by e.g., motion, thus describing the actual practical capability of the AF detection method in patients' daily situations.

The effect of premature atrial (PAC) and ventricular contractions (PVC) on the AF detection was not examined in this study. The presence of premature contractions could affect the AF detection and probably impair AF detection specificity as they are probable to cause irregularity in both ECG and PPG signals. Irregular pulse during sinus rhythm with premature contractions could be falsely detected as atrial fibrillation by automated algorithms based on pulse irregularity or altering the PPG morphology.

CONCLUSION

We demonstrated that the novel AC feature based on pulse wave morphology detects AF independently with high sensitivity and specificity without the need of pulse detection. In addition, we

proved that combining pulse wave morphology-based features such as AC with information from pulse-interval variability it is possible to detect AF with high accuracy by using a commercial PPG wrist band.

Results indicate that PPG wrist bands accompanied with AF detection algorithm could provide an easy-access and a reliable wearable monitoring method in search of paroxysmal or asymptomatic AF.

DATA AVAILABILITY STATEMENT

The raw data supporting the conclusions of this article will be made available by the authors, without undue reservation.

ETHICS STATEMENT

The studies involving human participants were reviewed and approved by The Ethics Committee of Kuopio University Hospital (approval number: 237/2017, 850/2018). The patients/participants provided their written informed consent to participate in this study.

AUTHOR CONTRIBUTIONS

E-SV, PK, JL, JH, HJ, TR, JH, MT, OS, and TM contributed to the design of the study. E-SV, TR, MC, OS, and TM contributed to the collection of the data. E-SV, PK, JL, JH, IK, HP-M, and OS performed the data analysis. E-SV and PK performed the statistical analysis. E-SV drafted the manuscript. All authors have contributed to the manuscript and approved the final version.

FUNDING

This work was supported by the Research Committee of the Kuopio University Hospital Catchment Area for the State Research Funding (project 5101137, Kuopio, Finland), the Helena Vuorenmies Foundation, the Finnish Medical Foundation, the Ida Montin Foundation, the Finnish Cultural Foundation (North-Savo Regional Fund, A. A. Laaksonen Fund) and the Antti and Tyyne Soininen Foundation. E-SV received travel grants from the Finnish Society of Cardiology. PK, JL, MT, JH, and HJ report personal fees from Heart2Save.

ACKNOWLEDGMENTS

We thank the medical and nursing staff of the participating hospitals, and especially B. M. Lasse Pörsti, B. M. Eveliina Hirvijärvi, B. M. Noora Naukkarinen, B. M. Olli Rantula, and B. H. C. Hannah Karhu for their help with data acquisition, and M.Sc. Tuomas Selander for statistical consultancy.

SUPPLEMENTARY MATERIAL

The Supplementary Material for this article can be found online at: https://www.frontiersin.org/articles/10.3389/fphys.2021.654555/full#supplementary-material

Supplementary Material 1 | STARD 2015 Checklist and information about STARD 2015.

REFERENCES

Dörr, M., Nohturfft, V., Brasier, N., Bosshard, E., Djurdjevic, A., Gross, S., et al. (2019). The watch AF trial: smart watches for detection of atrial fibrillation. *JACC Clin. Electrophys.* 5, 199–208. doi: 10.1016/j.jacep.2018.10.006

Fan, Y. Y., Li, Y. G., Li, J., Cheng, W. K., Shan, Z. L., Wang, Y. T., et al. (2019). Diagnostic performance of a smart device with photoplethysmography technology for atrial fibrillation detection: pilot study (Pre-mAFA II Registry). *JMIR Mhealth Uhealth* 7:e11437. doi: 10.2196/11437

Fujii, T., Nakano, M., Yamashita, K., Konishi, T., Izumi, S., Kawaguchi, H., et al. (2013). Noise-tolerant instantaneous heart rate and R-peak detection using short-term autocorrelation for wearable healthcare systems. *Conf. Proc. IEEE Eng. Med. Biol. Soc.* 2013, 7330–7333. doi: 10.1109/EMBC.2013.6611251

Guo, Y., Wang, H., Zhang, H., Liu, T., Liang, Z., Xia, Y., et al. (2019). MAFA II investigators, "mobile photoplethysmographic technology to detect atrial fibrillation. *J. Am. Coll. Cardiol.* 74, 2365–2375. doi: 10.1016/j.jacc.2019.08.019

Hart, R. G., Diener, H. C., Coutts, S. B., Easton, J. D., Granger, C. B., O'Donnell, M. J., et al. (2014). Cryptogenic stroke / ESUS international working group, "embolic strokes of undetermined source: the case for a new clinical construct. *Lancet Neurol.* 13, 429–438. doi: 10.1016/S1474-4422(13)70310-7

Hart, R. G., Pearce, L. A., and Aguilar, M. I. (2007). Meta-analysis: antithrombotic therapy to prevent stroke in patients who have nonvalvular atrial fibrillation. *Ann. Intern. Med.* 146, 857–867. doi: 10.7326/0003-4819-146-12-200706190-00007

Hartikainen, S., Lipponen, J. A., Hiltunen, P., Rissanen, T. T., Kolk, I., Tarvainen, M. P., et al. (2019). Effectiveness of the chest strap electrocardiogram to detect atrial fibrillation. *Am. J. Cardiol.* 123, 1643–1648. doi: 10.1016/j.amjcard.2019.02.028

Heinze, G., Wallisch, C., and Dunkler, D. (2018). Variable selectiona review and recommendations for the practicing statistician. *Biom. J.* 60, 431–449. doi: 10.1002/bimj.201700067

Kashiwa, A., Koyama, F., Miyamoto, K., Kamakura, T., Wada, M., Yamagata, K., et al. (2019). Performance of an atrial fibrillation detection algorithm using continuous pulse wave monitoring. *Ann. Noninvasive Electrocardiol.* 24:e12615. doi: 10.1111/anec.12615

Kirchhof, P., Benussi, S., Kotecha, D., Ahlsson, A., Atar, D., Casadei, B., et al. (2016). 2016 ESC guidelines for the management of atrial fibrillation developed in the collaboration with EACTS. *Eur. J. Cardiothorac. Surg.* 50, e1–e88. doi: 10.1093/ejcts/ezw313

Kwon, S., Hong, J., Choi, E. K., Lee, E., Hostallero, D. E., Kang, W. J., et al. (2019). Deep learning approaches to detect atrial fibrillation using photoplethysmographic signals: algorithms development study. *JMIR Mhealth Uhealth* 7:e12770. doi: 10.2196/12770

Lake, D. E., and Moorman, J. R. (2011). Accurate estimation of entropy in very short physiological time series: the problem of atrial fibrillation detection in implanted ventricular devices. *Am. J. Physiol. Heart Circ. Physiol.* 300, H319–H325. doi: 10.1152/ajpheart.00561.2010

Morillo, C. A., Banerjee, A., Perel, P., Wood, D., and Jouven, X. (2017). Atrial fibrillation: the current epidemic. *J. Geriatr. Cardiol.* 14, 195–203. doi: 10.11909/j.issn.1671-5411.2017.03.011

Pereira, T., Tran, N., Gadhoumi, K., Pelter, M. M., Do, D. H., Lee, R. J., et al. (2020). Photoplethysmography based atrial fibrillation detection: a review. *NPJ Digit. Med.* 3:eCollection. doi: 10.1038/s41746-019-0207-9

Perez, M. V., Mahaffey, K. W., Hedlin, H., Rumsfeld, J. S., Garcia, A., Ferris, T., et al. (2019). Apple heart study investigators, "large-scale assessment of a smartwatch to identify atrial fibrillation. *N. Engl. J. Med*. 381, 1909–1917. doi: 10.1056/NEJMoa1901183

Sarkar, S., Ritscher, D., and Mehra, R. (2008). A detector for a chronic implantable atrial tachyarrhythmia monitor. *IEEE Trans. Biomed. Eng.* 55, 1219–1224. doi: 10.1109/TBME.2007.903707

Saxena, R., and Koudstaal, P. J. (2004). Anticoagulants versus antiplatelet therapy for preventing stroke in patients with nonrheumatic atrial fibrillation and a history of stroke or transient ischemic attack. *Cochrane Database Syst. Rev.* CD000187. doi: 10.1002/14651858.CD000187

Tang, S.-C., Huang, P.-W., Hung, C.-S., Shan, S.-M., Lin, Y.-H., Shieh, J.-S., et al. (2017). Identification of atrial fibrillation by quantitative analyses of fingertip photoplethysmogram. *Sci. Rep*. 7:45644. doi: 10.1038/srep45644

Tison, G. H., Sanchez, J. M., Ballinger, B., Singh, A., Olgin, J. E., Pletcher, M. J., et al. (2018). Passive detection of atrial fibrillation using a commercially available smartwatch. *JAMA Cardiol*. 3, 409–416. doi: 10.1001/jamacardio.2018.0136

Väliaho, E.-S., Kuoppa, P., Lipponen, J. A., Martikainen, T. J., Jäntti, H., Rissanen, T. T., et al. (2019). Wrist band photoplethysmography in detection of individual pulses in atrial fibrillation and algorithm-based detection of atrial fibrillation. *EP Eur.* 21, 1031–1038. doi: 10.1093/europace/euz060

Xiong, Q., Proietti, M., Senoo, K., and Lip, G. Y. (2015). Asymptomatic versus symptomatic atrial fibrillation: a systematic review of age/gender differences and cardiovascular outcomes. *Int. J. Cardiol.* 191, 172–177. doi: 10.1016/j.ijcard.2015.05.011

Yan, B. P., Lai, W. H. S., Chan, C. K. Y., Chan, S. C., Chan, L. H., Lam, K. M., et al. (2018). Contact-free screening of atrial fibrillation by a smartphone using facial pulsatile photoplethysmographic signals. *J. Am. Heart Assoc.* 7:e008585. doi: 10.1161/JAHA.118.008585

Conflict of Interest: JL, TR, TM, HJ, JH, and MT are shareholders of Heart2Save company that designs ECG-based software for medical equipment. JL, MT, and HJ have a patent pending.

The remaining authors declare that the research was conducted in the absence of any commercial or financial relationships that could be construed as a potential conflict of interest.

frontiers in Physiology

ORIGINAL RESEARCH
published: 30 July 2021
doi: 10.3389/fphys.2021.704122

Deep Learning Classification of Unipolar Electrograms in Human Atrial Fibrillation: Application in Focal Source Mapping

Shun Liao[1], Don Ragot[1], Sachin Nayyar[1], Adrian Suszko[1], Zhaolei Zhang[2], Bo Wang[1] and Vijay S. Chauhan[1]**

[1] Peter Munk Cardiac Centre, Division of Cardiology, Toronto General Hospital, University Health Network, Toronto, ON, Canada, [2] Department of Computer Science, University of Toronto, Toronto, ON, Canada

Focal sources are potential targets for atrial fibrillation (AF) catheter ablation, but they can be time-consuming and challenging to identify when unipolar electrograms (EGM) are numerous and complex. Our aim was to apply deep learning (DL) to raw unipolar EGMs in order to automate putative focal sources detection. We included 78 patients from the Focal Source and Trigger (FaST) randomized controlled trial that evaluated the efficacy of adjunctive FaST ablation compared to pulmonary vein isolation alone in reducing AF recurrence. FaST sites were identified based on manual classification of sustained periodic unipolar QS EGMs over 5-s. All periodic unipolar EGMs were divided into training (n = 10,004) and testing cohorts (n = 3,180). DL was developed using residual convolutional neural network to discriminate between FaST and non-FaST. A gradient-based method was applied to interpret the DL model. DL classified FaST with a receiver operator characteristic area under curve of 0.904 ± 0.010 (cross-validation) and 0.923 ± 0.003 (testing). At a prespecified sensitivity of 90%, the specificity and accuracy were 81.9 and 82.5%, respectively, in detecting FaST. DL had similar performance (sensitivity 78%, specificity 89%) to that of FaST re-classification by cardiologists (sensitivity 78%, specificity 79%). The gradient-based interpretation demonstrated accurate tracking of unipolar QS complexes by select DL convolutional layers. In conclusion, our novel DL model trained on raw unipolar EGMs allowed automated and accurate classification of FaST sites. Performance was similar to FaST re-classification by cardiologists. Future application of DL to classify FaST may improve the efficiency of real-time focal source detection for targeted AF ablation therapy.

Keywords: atrial fibrillation, unipolar electrogram, focal sources, machine learning, catheter ablation

OPEN ACCESS

Edited by:
G. Andre Ng,
University of Leicester,
United Kingdom

Reviewed by:
Elena Tolkacheva,
University of Minnesota Twin Cities,
United States
Candido Cabo,
The City University of New York,
United States

****Correspondence:***
Bo Wang
bo.wang@uhnresearch.ca
Vijay S. Chauhan
vijay.chauhan@uhn.ca

Specialty section:
This article was submitted to Cardiac Electrophysiology, a section of the journal Frontiers in Physiology

Received: *01 May 2021*
Accepted: *02 July 2021*
Published: *30 July 2021*

Citation:
Liao S, Ragot D, Nayyar S, Suszko A, Zhang Z, Wang B and Chauhan VS (2021) Deep Learning Classification of Unipolar Electrograms in Human Atrial Fibrillation: Application in Focal Source Mapping. Front. Physiol. 12:704122. doi: 10.3389/fphys.2021.704122

INTRODUCTION

The pathogenesis of atrial fibrillation (AF) is complex, potentially involving localized drivers and abnormal atrial substrate outside the pulmonary veins (Heijman et al., 2016), which may account for the poor long-term success of pulmonary vein isolation (PVI) alone (Ganesan et al., 2013). Using panoramic high-resolution mapping, localized drivers, including focal electrical sources have been observed to sustain experimental AF (Lee et al., 2013, 2020), but their relevance in the pathogenesis of human AF is less clear. Detecting focal electrical sources

in humans is challenging owing to the low spatial resolution of mapping techniques (Roney et al., 2017) and complex electrogram (EGM) features (DeBakker and Wittkampf, 2010).

To address these challenges, we have developed a pragmatic focal source detection algorithm, known as Focal Source and Trigger (FaST) mapping, where bipolar and unipolar EGMs are analyzed for periodicity and unipolar QS features as footprints of centrifugal wave propagation (Gizurarson et al., 2016; Kochhauser et al., 2017). In a randomized controlled trial, FaST sites were widely distributed in PV and extra-PV regions in all patients, and their ablation reduced AF recurrence compared to PVI alone (Chauhan et al., 2020; Nayyar et al., 2020). In FaST mapping, the accurate detection of sustained, periodic unipolar QS electrograms is critical and requires over reading by the cardiologist after the onset of the unipolar electrograms has been annotated by the FaST algorithm to guide morphology classification. This can be challenging when unipolar EGMs appear fractionated and non-stationary over 5-s recordings.

In this regard, machine learning, and more specifically deep learning (DL), has been used recently to automate classification of complex biomedical signals from ECG recordings (Hannun et al., 2019; Chang et al., 2021), but the utility of DL in raw EGM classification during AF has not been explored (Feeny et al., 2020). DL has the advantage of automatically learning features from raw signals without the need for *a priori* manual features engineering. We hypothesized that automating the detection of sustained, periodic unipolar QS EGMs using DL will improve the reliability and efficiency of FaST mapping for cardiologists performing AF driver catheter ablation. Our objective was to develop a DL model trained on raw unipolar EGMs to allow automated and accurate identification of FaST sites during AF as putative focal source targets for ablation.

MATERIALS AND METHODS

Patient Population

The FaST randomized controlled trial evaluated the efficacy of FaST ablation as an adjunct to PVI in reducing AF recurrence compared to PVI alone in 80 patients with drug-refractory, high-burden paroxysmal or persistent AF (Chauhan et al., 2020). Real-time endocardial mapping of the left atrium (LA) during sustained AF was completed in 78 patients, who comprised the cohort for the present study. The study was approved by the University Health Network Research Ethics Board and all patients provided written, informed research consent.

AF Mapping

The FaST mapping protocol and ablation outcomes have been previously described (Chauhan et al., 2020). Briefly, anti-arrhythmic drugs were held for 5 half-lives with the exception of amiodarone which was discontinued 1 month before mapping. LA mapping was performed during either spontaneous AF or induced AF using burst atrial pacing at CL 180–250 ms, and if necessary, intravenous isoprenaline (0.5–1 μg/min). Electroanatomic data was acquired using the CARTO^{TM} 3 (Biosense Webster, Diamond Bar, CA, United States) system and a roving 20-pole circular catheter (Lasso^{TM} Nav Variable, 15–25 mm diameter, 1 mm electrodes at 2–6–2 mm spacing, Biosense Webster, Diamond Bar, CA, United States). Stable catheter-tissue contact and signal quality were ensured before recording 5-s bipolar (bandpass 30–500 Hz) and unipolar EGMs (bandpass 0.05–500 Hz) at a sampling rate of 1,000 Hz. Unipolar EGMs were recorded only from one electrode of the bipolar electrode pair. All EGMs were exported for off-line analysis of FaST sites using custom software written in Matlab^{TM} (MathWorks Inc., Natick, MA, United States). Noisy EGMs with low signal:noise and EGMs recorded >5 mm from the LA endocardium were excluded to minimize far-field signal contamination.

FaST Sites

The hierarchical algorithm for FaST detection has been previously reported (Dalvi et al., 2016; Gizurarson et al., 2016; Chauhan et al., 2020; Nayyar et al., 2020) and is summarized in **Figure 1**. Briefly, each 5-s bipolar EGM underwent fast Fourier transformation after bandpass filtering (40–250 Hz followed by 0.5–20 Hz) and rectification. Periodicity was present if the spectral frequency with the largest spectral power contained at least 10% of the total spectral power. The corresponding periodicity CL was defined as the inverse of this frequency. Among bipolar EGMs demonstrating periodicity within a CL ranging from 100 to 250 ms (i.e., physiologic atrial refractory period), local bipolar periodic activations were annotated using a graph search function. For this purpose, candidate local activations were automatically selected provided their amplitude was above a noise threshold of 0.05 mV and a slew rate >0.014 mV/ms. Local periodic activations across the 5-s bipolar EGM were identified as those with the greatest number of consecutive candidate activations having the extracted periodicity CL, which satisfied the lowest cost of a matrix containing the difference between each candidate activation and the extracted periodicity CL (see **Supplementary Methods**) (Dalvi et al., 2016). This ensured that sustained periodic activations with predefined periodicity CL were identified regardless of their EGM amplitude, which itself is not a pre-requisite for defining local activation. These local periodic bipolar activations were then transposed to the corresponding unipolar EGMs in order to annotate unipolar EGM onset and thereby facilitate manual classification of unipolar morphology as QS or non-QS. FaST was defined based on the presence of sustained bipolar EGM periodicity and a dominant unipolar QS pattern (i.e., R/S ratio < 0.1) in >90% of EGMs over the 5-s recording, which was assigned manually by two cardiologists in real-time before ablation. Any disagreement in FaST classification by the cardiologists was resolved by consensus. FaST sites were classified as PV vs. extraPV and they were considered to be anatomically distinct if >7 mm from one another.

Patient Cohorts and Data Augmentations

Patients were randomly divided into a training and testing cohort, and all periodic unipolar EGMs from both cohorts were firstly down-sampled to 200 Hz using fast Fourier transformation. Then, their magnitudes were normalized through a min-max

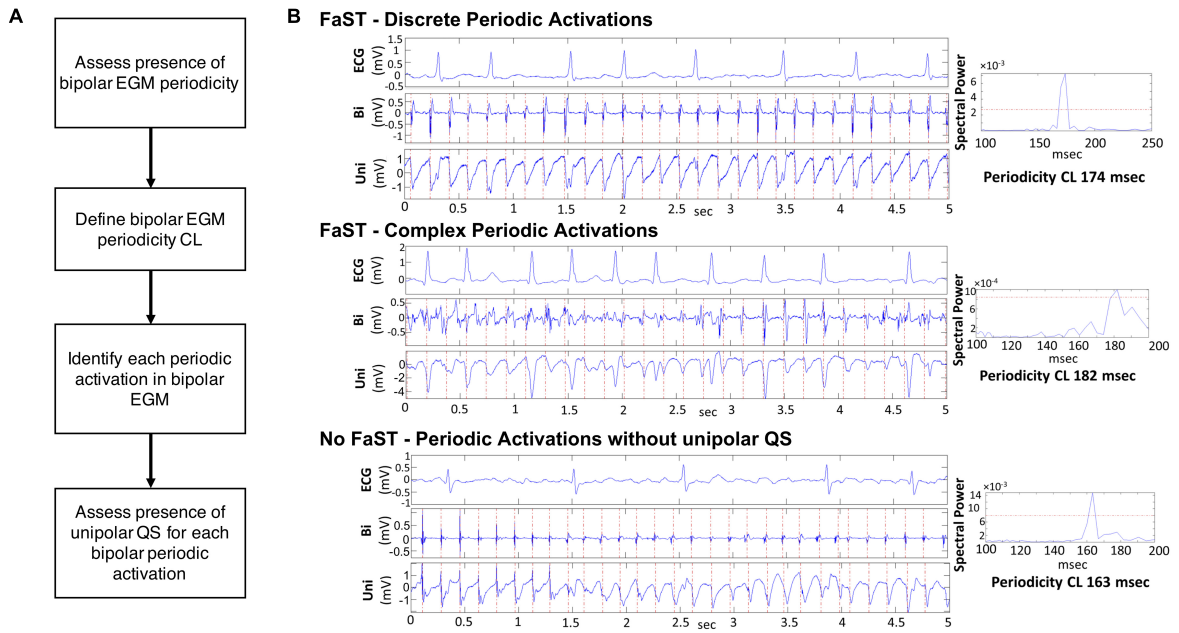

FIGURE 1 | FaST Algorithm. **(A)** Hierarchical steps in FaST classification. **(B)** Representative examples of bipolar and unipolar EGMs from three different left atrial sites. In each example, the power spectral plot of the bipolar EGM indicates the presence of periodicity (i.e., spectral peak above threshold red horizontal line). The periodicity cycle length is calculated from the spectral peak (right panels). The first two examples are classified as FaST sites by the FaST algorithm based on the presence of bipolar EGM periodicity and sustained unipolar QS complexes for the duration of the 5-s recording. The top example shows discrete bipolar EGM complexes while the bottom example also contains complex, fractionated bipolar EGM complexes. In contrast, the third example is classified as No FaST because the unipolar EGM does not manifest sustained QS complexes for the duration of the 5-s recording, even though there is bipolar EGM periodicity. The first 1.4 s of the unipolar EGM manifests RS complexes, followed by QS complexes.

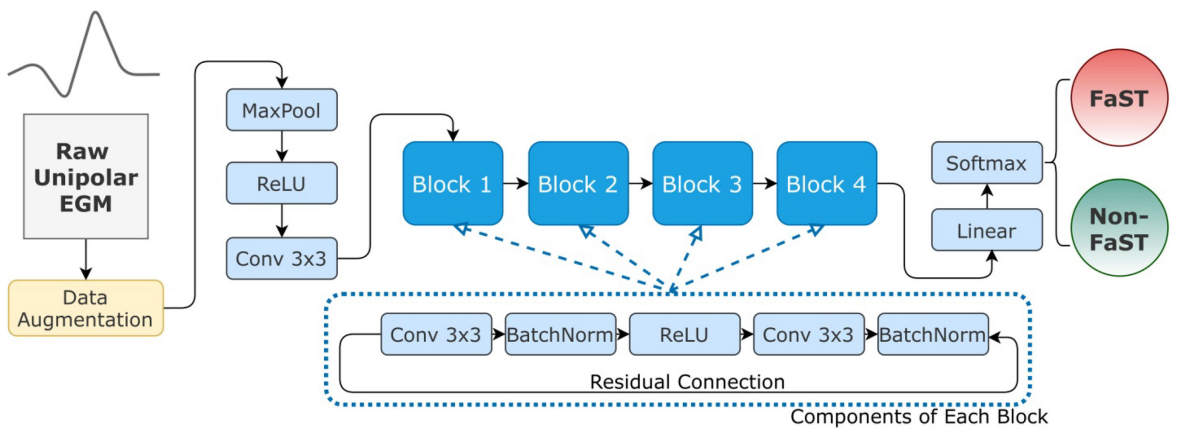

FIGURE 2 | Convolutional Neural Network Architecture. The DL model inputs raw unipolar EGM **(right)** and outputs a binary decision as FaST vs. non-FaST **(left)**. For robust training, the raw inputs are normalized and augmented as described in the text. The architecture of the proposed network is inherited from ResNet-18, which has 4 residual blocks. Each block consists of 2 convolutional, 2 batch normalization, and one ReLU layers. Abbreviations: Conv – convolutional layer, MaxPool – 1-D max-pooling layer.

feature scaling. To improve the generalizability of the model, four artificial data augmentations were implemented, namely baseline shifting, Gaussian noise, cropping and resampling. Baseline shifting added constant noise to the EGM signal, where the constant is sampled from a normal distribution. Gaussian noise added normal noise, sampled from a Gaussian distribution, to the EGM. Cropping randomly replaced a segment of data with zeros, while resampling further removed a data segment, but unsampled the shorter signal to the original length (Perez and Wang, 2017). A hyper-parameter was introduced to track the probability of augmentation and to ensure that both clean and noised examples were observed during training. The effectiveness of augmentation is demonstrated in the **Supplementary Methods** and **Supplementary Figures 1, 2**.

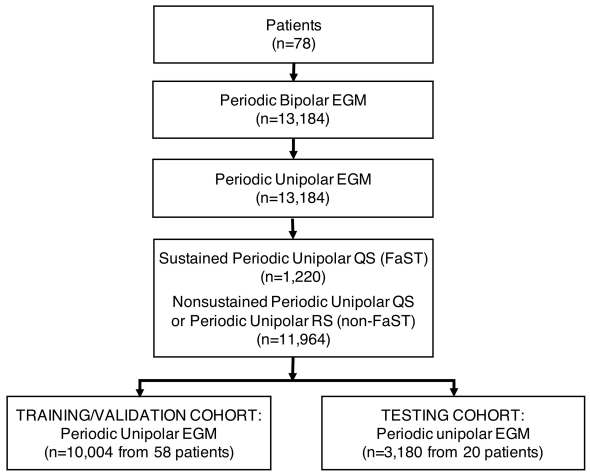

FIGURE 3 | Consort Diagram for DL Training and Testing Cohorts. Patients (n = 78) were divided into a training/validation cohort (n = 58) and test cohort (n = 20). The number of periodic unipolar EGMs in each cohort is indicated.

One-Dimensional Residual Convolutional Neural Network

The DL model was designed to take the raw periodic unipolar EGM as input, and then output the probability of FaST on a continuous scale from 0 to 1. The model is a one-dimensional (1-D) residual, convolutional, deep neural network (CNN) which is implemented through PyTorch (Paszke et al., 2019). The network architecture is inspired by ResNet-18 for image recognition, which has been credible in a large number of datasets (He et al., 2016). In brief, it is an 18 layer neural network consisting of five residual convolutional blocks and one fully connected layer. Each block abstracts the features gradually from raw inputs to a higher level representation (LeCun et al., 2015). Specifically, each residual convolutional block consists of a convolutional layer, a pooling, a batch normalization, a dropout, a non-linear activation and a residual connection (LeCun et al., 2015). Notably, our EGM network replaces the 2-D convolution filters in each block of ResNet-18 by 1-D filters so that the architecture becomes suitable for unipolar EGM analysis. Our DL architecture is illustrated in **Figure 2**.

Due to similar structure, our DL model shares the same hyper-parameter settings with ResNet-18, such as kernel size, stride size and dropout rate (He et al., 2016). Although larger networks (e.g., ResNet-50, ResNet-101) and different architectures (e.g., EfficientNet) were also explored, we found ResNet-18 achieved the best testing performance in classifying FaST as shown in **Supplementary Table 1**. To prevent model overfitting, we searched a small subset of hyper-parameters, including batch size, initial learning rate and the learning rate scheduler. The best hyper-parameter combination was found through grid search with a three-fold cross-validation, which was then applied to the whole training cohort to train the DL model. The trained DL model was finally evaluated in the testing cohort. In terms of optimization details, the network is initialized by He-initialization and optimized by Adam (Kingma and Ba, 2014; He et al., 2015).

In addition, we investigated the performance of classic machine learning models to classify FaST, including logistic regression, support vector machine (SVM) and k nearest neighbor (KNN). Compared to DL, these classic models have a lower model complexity, which limits their ability to analyze complex data, such as EGMs. We reported the SVM and KNN with two different hyper-parameters, where the polynomial degree is either 3 or 10 for SVM, and the number of k neighbors is either 10 or 50 for KNN. These classic models were implemented through scikit-learn (Pedregosa et al., 2011).

DL Model Discretization to Explain Classification

To explain DL classification as FaST vs. non-FaST, we adopted a gradient-weighted class activation mapping method (Guided Grad-CAM) to probe important features (Selvaraju et al., 2017). Grad-CAM is commonly used in computer vision to provide a contextual explanation for model decisions. Briefly, Grad-CAM defines the importance of a feature based on the changes in the classification output in response to a small variance or gradient in the feature. A larger change in output indicates that this feature is more important. For our study, Grad-CAM was applied because of similar architecture between our model and models in vision. Specifically, the gradient in the convolutional layer of the residual blocks of our model were probed. The importance of features was visualized as a 1-D importance plot where peaks indicated more importance.

FaST Re-Classification by Cardiologists

Manual classification of FaST using the FaST algorithm at the time of PVI served as the gold standard. Subsequently, two cardiologists (VC, SN) independently performed blinded re-classification of periodic unipolar EGMs as FaST vs. non-FaST using the FaST algorithm in a subset of 100 EGMs, which included 50 random EGMs and 50 EGMs falsely classified by DL. The sensitivity and specificity of FaST re-classification by the cardiologists was evaluated relative to the gold standard. Inter- and intraobserver agreement among the cardiologists in FaST re-classification was assessed using the kappa statistic.

Statistical Analysis

Continuous variables are presented as mean ± standard deviation. Comparison between patient cohorts was done using an unpaired t-test or Mann-Whitney U test where appropriate. Receiver operator characteristic (ROC) analysis was performed to evaluate the diagnostic performance of the DL algorithm for detecting FaST with results presented as area under the curve (AUC) and 95th percentile confidence interval (95% CI). Specificity was calculated at prespecified sensitivities of 85, 90, and 95% as well as the sensitivity of cardiologists re-classifying a subset of 50 random periodic unipolar EGMs. In order to complement ROC analysis for class-imbalanced datasets, the performance of DL was evaluated using the F1-score which is a harmonic mean of the positive predictive value and sensitivity

TABLE 1 | Baseline patient characteristics.

	All patients (n = 78)	Training/ validation cohort (n = 58)	Testing cohort (n = 20)	p-value
Age, years	61 ± 10	61 ± 10	59 ± 8	0.229
Male, n (%)	58 (74)	42 (72)	16 (80)	0.503
Body mass index, kg/m^2	29 ± 5	30 ± 5	29 ± 5	0.598
LVEF,%	59 ± 8	58 ± 9	61 ± 4	0.097
LA dimensions				
LA diameter, mm	42 ± 7	42 ± 6	40 ± 8	0.383
LA volume, ml	90 ± 35	90 ± 33	91 ± 39	0.893
LA volume index, ml/m^2	44 ± 16	43 ± 16	44 ± 16	0.811
AF characteristics				
High-burden paroxysmal, n (%)	40 (51)	29 (50)	11 (55)	0.700
Persistent, n (%)	38 (49)	29 (50)	9 (45)	0.700
Duration of AF, years	5.6 ± 5.0	5.9 ± 5.0	4.6 ± 3.4	0.245
Comorbidities				
Diabetes, n (%)	4 (5)	2 (3)	2 (10)	0.270
Hypertension, n (%)	37 (47)	25 (43)	12 (60)	0.192
Sleep apnea, n (%)	25 (32)	19 (33)	6 (30)	0.820
Obesity, n (%)	29 (37)	23 (40)	6 (30)	0.441
Coronary artery disease, n (%)	2 (3)	2 (3)	0 (0)	1.000
Current antiarrhythmic drugs				
Flecainide or propafenone, n (%)	29 (37)	26 (45)	3 (15)	0.017
Sotalol, n (%)	6 (8)	5 (9)	1 (5)	1.000
Amiodarone, n (%)	21 (27)	14 (24)	7 (35)	0.345
β-blocker, n (%)	37 (47)	28 (48)	9 (45)	0.800
Calcium channel blocker, n (%)	15 (19)	9 (16)	6 (30)	0.192
Number of failed AAD	1.7 ± 0.9	1.7 ± 1.0	1.6 ± 0.8	0.482

AAD, antiarrhythmic drugs; CL, cycle length; LA, left atrium; LVEF, left ventricular ejection fraction; obesity–BMI > 30 kg/m^2; renal dysfunction–eGFR < 50 ml/min/1.72 m^2.

(Saito and Rehmsmeier, 2015). A two-tailed p-value < 0.05 was considered statistically significant. Statistical analyses were performed using scikit-learn (Pedregosa et al., 2011).

RESULTS

Patient and FaST Characteristics

Seventy-eight patients (age 61 ± 10 years, 74% males) were included with either high-burden paroxysmal AF (51%) or persistent AF (49%). The LA volume and LV ejection fraction were 44 ± 16 ml/m^2 and 59 ± 8%, respectively (**Table 1**). Mapping was performed during spontaneous AF in 36 (46%) patients and after inducing sustained AF with programmed atrial stimulation in the remaining 42 (54%) patients. On average, 340 ± 60 LA sites from 60 ± 8 circular catheter acquisitions were analyzed per patient after excluding overlapping points and those with poor endocardial contact. FaST sites were identified in all patients (4.9 ± 1.9 per patient), including 2.1 ± 1.1 PV FaST and 2.8 ± 1.4 extra-PV FaST per patient.

Performance of Deep Learning and Classic Machine Learning Models

Among the 78 patients, a total of 13,184 periodic unpolar EGMs were recorded of which 1,220 (9.2%) had a dominant, sustained QS morphology (i.e., FaST) and the remaining 11,964 (90.7%) were non-FaST (**Figure 3**). The DL model was trained and validated using 10,004 periodic unipolar EGMs from a cohort of 58 patients, where the prevalence of FaST EGMs was 9.2%. Cross-validation in this cohort was achieved using five different random seeds, such that each seed produced a different validation cohort and a different network initialization (i.e., three-fold cross validation performed five times). The final DL model was then tested using 3,180 periodic unipolar EGMs from a testing cohort of 20 patients, where the prevalence of FaST EGMs was 9.4%. The clinical characteristics of the validation and testing cohorts were similar as shown in **Table 1**. The performance of DL in classifying FaST for the three-fold cross-validation and testing cohorts is demonstrated by the ROC curve in **Figure 4A**. The DL model achieved a high ROC AUC of 0.904 (95% CI 0.884, 0.924) and 0.923 (95% CI 0.917, 0.929) in cross-validation and testing cohorts, respectively. The AUC variance for the test cohort was < 0.5% demonstrating robustness of the DL model. In contrast, the performance of classic machine learning models, including logistic regression, SVM and KNN, was inferior to that of DL based on a lower ROC AUC, specificity and F1-score as shown in **Figure 4B** and **Supplementary Table 2**.

The performance of DL in classifying FaST was also evaluated using different prediction thresholds. Because the DL model has continuous output, ranging from 0 to 1, the prediction was classified as FaST when the DL output was above a threshold, which was based on achieving a predefined sensitivity of 85,

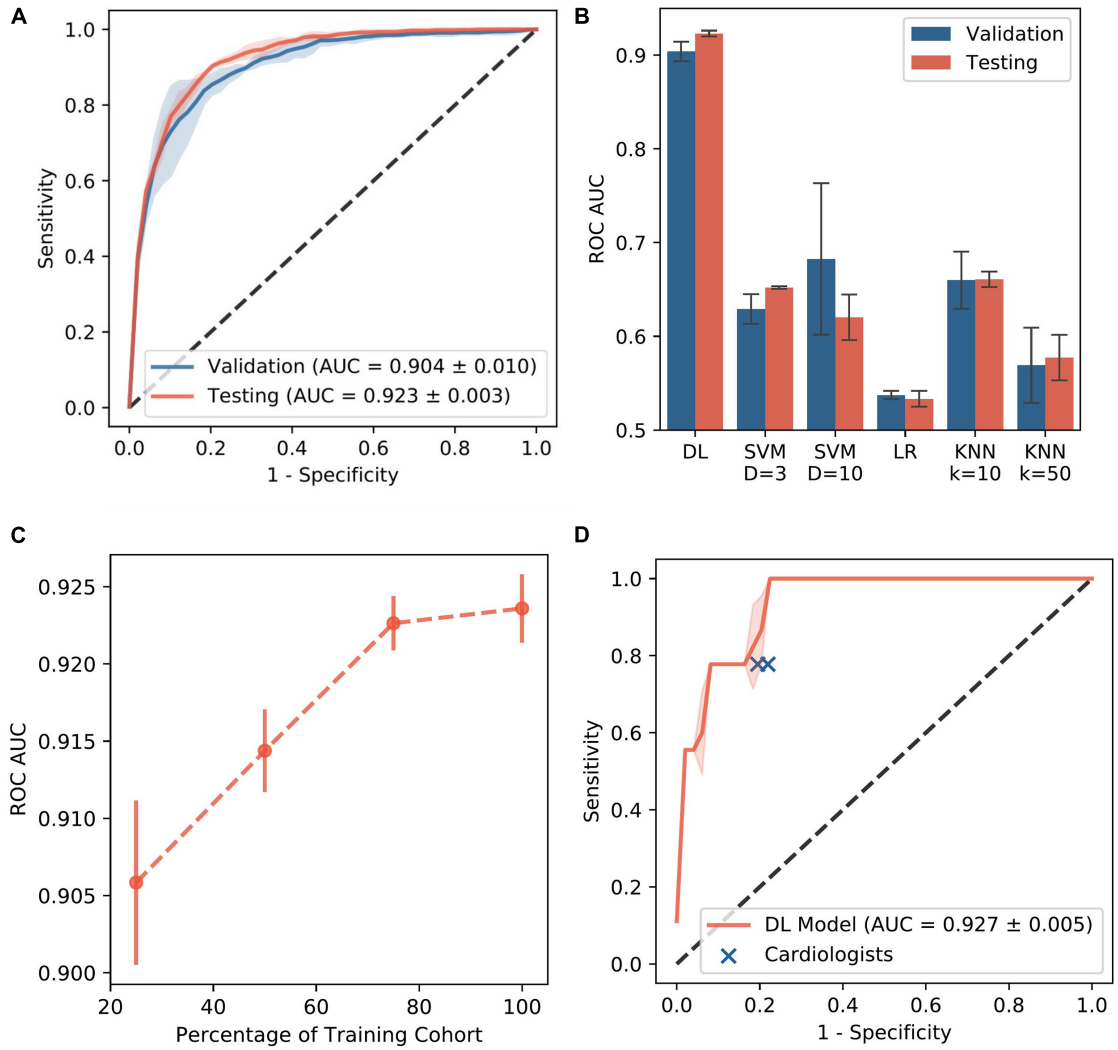

FIGURE 4 | Performance of DL Model. **(A)** ROC curve is shown for FaST classification using DL model in the validation and testing cohorts. **(B)** ROC AUC is shown for DL and classic machine learning models. The error bars indicate standard deviation of different random seeds. **(C)** ROC AUC for DL is shown as a function of the training cohort size. **(D)** ROC curve is shown for FaST classification using DL model in a random sample of 50 periodic unipolar EGMs. The performance of two cardiologists for FaST re-classification is also plotted for comparison. AUC – area under curve; KNN – k nearest neighbor (either 10 or 50); LR – logistic regression; ROC – receiver operator characteristic; SVM – support vector machine (D refers to polynomial degree).

90, or 95% in detecting FaST. The respective specificity, positive predictive value (PPV), negative predictive value (NPV), F1-score and accuracy are shown in **Table 2**. DL had reasonably high specificity for each predefined sensitivity. In the case of 90% sensitivity, DL achieved a specificity of 81.9% (95% CI 81.8 – 82.0%), PPV of 33.6% (95% CI 33.3 – 33.9%), NPV of 98.5% (CI 95% 98.4 – 98.6%), F1-score of 0.486 (CI 95% 0.481 – 0.491), and an accuracy of 82.5% (95% CI 82.3, 82.6). Because DL performance improves with larger training datasets (LeCun et al., 2015), the performance of our DL model was further evaluated using smaller training cohorts. As shown in **Figure 4C**, the ROC AUC significantly improved when the test cohort size was increased from 25 to 75% of the original sample size. However, a further increase from 75 to 100% was associated with a marginal change in ROC AUC from 0.921 to 0.923, respectively, suggesting that our training cohort of 58 patients was adequately sized.

Performance of Deep Learning Compared to Re-Classification by Cardiologists

The reliability in FaST re-classification was evaluated in a random sample of 50 periodic unipolar EGMs from 18 patients by two cardiologists. In this 50 EGM subset, the proportion with FaST was modest at 18%. Intra- and interobserver variability was moderate based on a kappa of 0.43 and 0.46, respectively, but intraobserver variability improved (kappa 0.81) after the cardiologists reviewing their disagreements and retrained. Among these 50 EGMs, the DL model's classification of FaST had

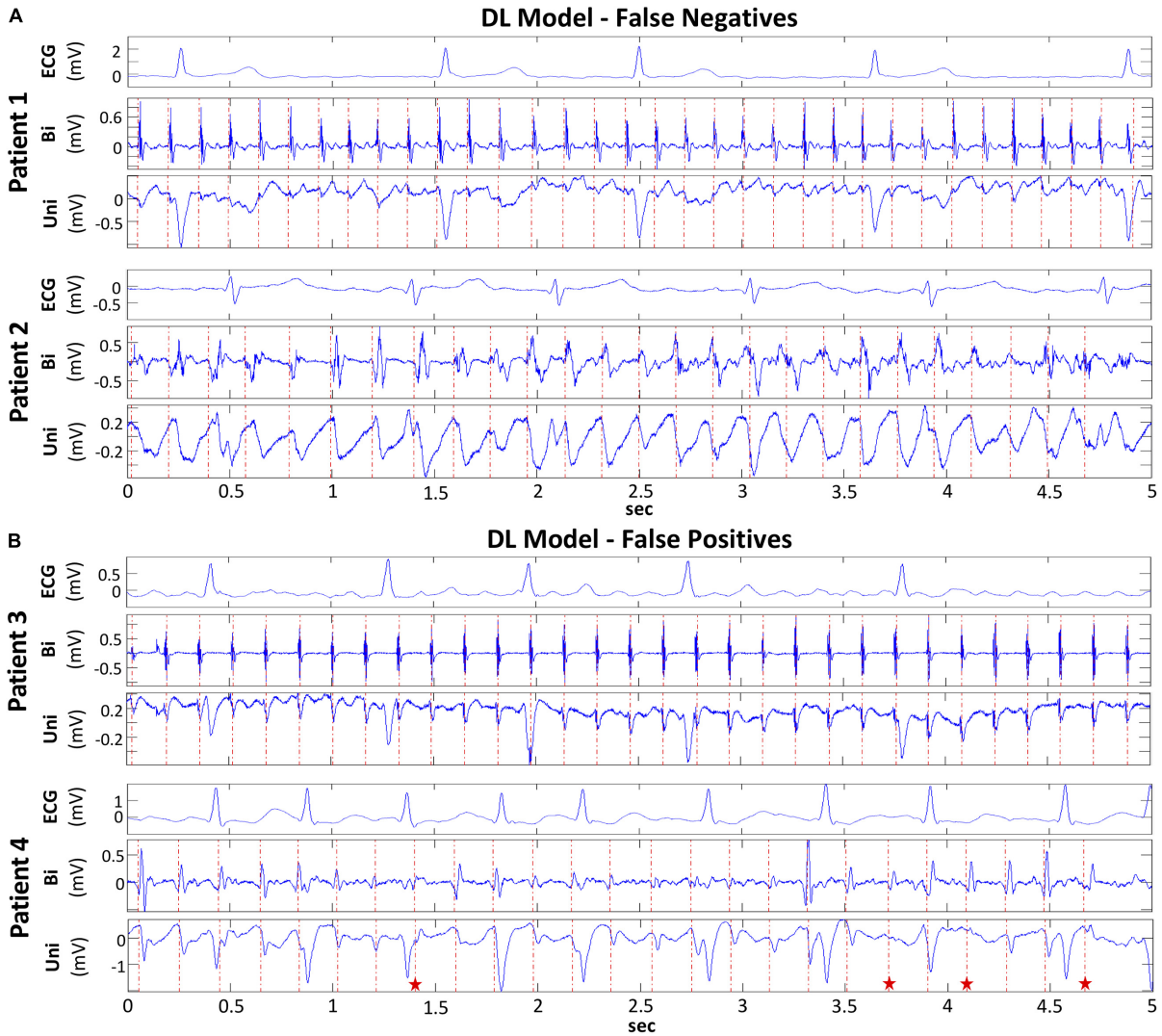

FIGURE 5 | False Classification of FaST and non-FaST using DL Model. **(A)** False negative classification of FaST using DL due to low-amplitude, sustained periodic unipolar QS complexes near PV ostium (Patient 1, top panel) and broad, slurred unipolar QS complexes (Patient 2, bottom panel). **(B)** False positive classification of FaST using DL due to sustained unipolar rS complexes with small r waves (Patient 3, top panel) and near-sustained periodic unipolar QS complexes (red stars – rS complexes) (Patient 4, bottom panel).

an ROC AUC of 0.927 (95th CI 0.916, 0.938) (**Figure 4D**), which was similar to that of the whole periodic unipolar EGM dataset. In the subset of 50 random EGMs, the sensitivity and specificity in classifying FaST with DL was 78.1 (95th CI 77.6, 78.7) and 82.2 (95th CI 80.0, 84.4), respectively, which was similar to that of the cardiologists (sensitivity 77.8, specificity 79.0) (**Figure 4D**). Among the EGMs with interobserver agreement (n = 35 of 50), the DL model's classification of FaST had a higher ROC AUC of 0.980 (95th CI 0.980, 0.986).

Characterizing False Classifications by Deep Learning

In order to evaluate the basis for the false classification of FaST and non-FaST by DL, a subset of 50 periodic unipolar EGMs were selected, which comprised 25 false negative EGMs with the lowest DL predicted probability for FaST, and 25 false positive EGMs with the highest DL predicted probability for FaST. False positive classification by DL was commonly due to borderline EGMs with small rS complexes or non-sustained periodicity. In contrast, false negative cases by DL were most often the result of EGM fractionation or low amplitude/slewed QS complexes, such as near the PV ostium as shown in **Figure 5**. Given the complexity of these EGMs, the reliability in FaST re-classification was assessed by two cardiologists. In this 50 EGM subset, the proportion with FaST was 50%, which included all 25 false negative EGMs. Intra- and interobserver variability in FaST re-classification was poor based on a kappa of −0.08 and −0.02, respectively, which was concordant with the false classification or

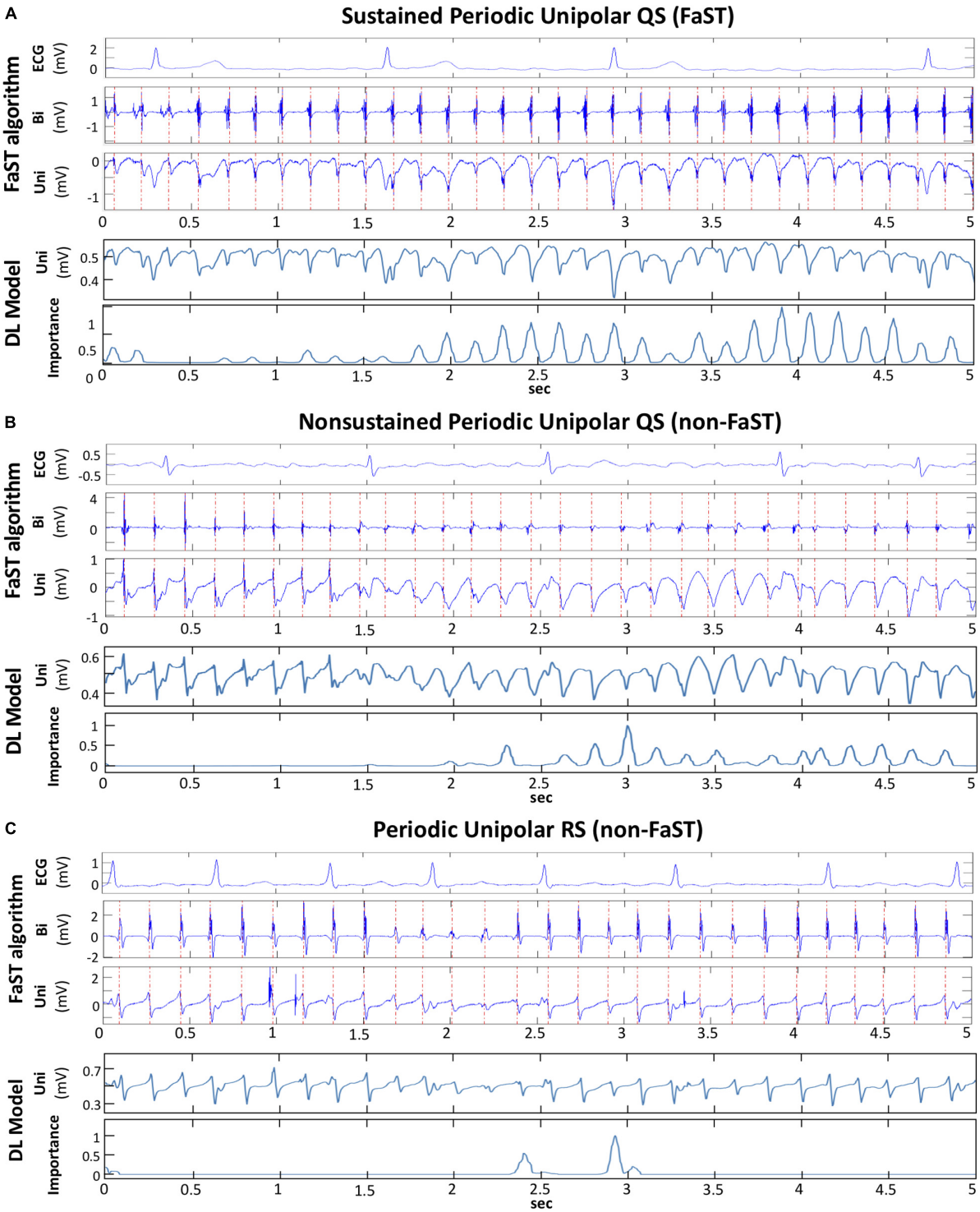

FIGURE 6 | Discretization of DL model to explain classification. **(A)** FaST site defined by the FaST algorithm based on sustained, periodic unipolar QS for 5-s. Bipolar EGM and unipolar EGM are shown with dashed, red vertical lines annotating periodic activations. The DL model inputs the raw unipolar EGM without annotations and the importance plot from convolutional layer 3.0 demonstrates peaks corresponding to the majority of atrial unipolar QS complexes, but not the far-field ventricular complexes during the 5-s recording. **(B)** Non-FaST site defined by the FaST algorithm based on non-sustained periodic unipolar QS. The first 8 complexes are unipolar RS, while the rest are unipolar QS. The importance plot from the DL model's convolutional layer 3.0 demonstrates peaks corresponding to the majority of atrial unipolar QS complexes, but not the atrial unipolar RS complexes. **(C)** Non-FaST site defined by the FaST algorithm based on the absence of unipolar QS complexes. Accordingly, the importance plot from the DL model's convolutional layer 3.0 demonstrates virtually no peaks. There are 2 peaks which correspond to atrial unipolar rS complexes, similar in morphology to QS complexes.

disagreement with DL. However, intraobserver agreement among the two cardiologists improved (kappa 0.71) after they reviewed disagreements and retrained.

Discretization of Deep Learning to Explain FaST Classification

From the subset of 100 periodic unipolar EGMs used above to evaluate observer reliability and false classification of FaST, a random sample of 10 EGMs were input into Grad-CAM in order to determine which convolutional layers of the DL model best tracked unipolar QS complexes. Our results suggest that Grad-CAM's importance plot from convolutional layer 3 identified atrial unipolar QS complexes most consistently in all 10 EGMs. **Figure 6** shows three examples of periodic unipolar EGMs from FaST and non-FaST sites where EGM onset is annotated with a vertical red line using the FaST algorithm. In each example, the importance plot from convolutional layer 3 demonstrates periodic peaks of importance that coincide temporally to most atrial unipolar QS complexes, while ignoring atrial unipolar RS complexes and far-field ventricular unipolar QS complexes. These importance plots provide a visual explanation of DL's classification of FaST vs. non-FaST.

DISCUSSION

Our DL model automatically classified periodic unipolar EGMs with sustained QS complexes (i.e., FaST) during AF without the requisite for EGM segmentation or annotation. The DL model's accuracy in FaST classification was 82.5% (ROC AUC of 92.3), which is high considering the low prevalence of FaST EGMs (9%) and the spatiotemporal variability in unipolar EGM morphologies. False detection of FaST was attributed to ambiguous, time-varying unipolar EGM signal features, but in these instances the reliability in re-classifying FaST was also poor among cardiologists, indicating that DL's performance was on par with that of the cardiologists. For select EGMs, introspection of the DL convolutions identified the layer that tracked individual periodic unipolar QS EGMs, thereby providing visual verification of DL performance.

Focal sources are a well-established mechanism of AF, and have been demonstrated in a canine model of vagal AF (Lee et al., 2013, 2020) as well as in human AF (Lee et al., 2015, 2017). Using 512-electrode, high-density, biatrial activation mapping, Lee et al. (2015, 2017) demonstrated focal sources lasting up to 30 s during AF. At their epicenter, focal sources manifested fairly discrete, periodic unipolar QS EGMs. Our FaST algorithm searches for similar signal features to identify putative focal sources, but to improve specificity, unipolar QS periodicity must be sustained for 5-s. To avoid ambiguity in unipolar morphology classification, the onset of the unipolar EGM is annotated based on a graph search function whose input is the respective periodic bipolar EGM. However, unipolar QS classification is still performed manually and therefore susceptible to interpretation by the cardiologist, especially when morphology features are ambiguous, albeit periodic. This accounts for the moderate intra- and interobserver agreement in FaST re-classification in a random subset of periodic unipolar EGMs (kappa 0.43–0.47), and essentially no intra- or interobserver agreement in a subset falsely classified by DL. However, intraobserver agreement did improve (kappa 0.71–0.81) after cardiologists were retrained. These findings highlight the modest precision in the manual interpretation and classification of periodic unipolar QS EGMs during AF.

Despite this inherent limitation, DL achieved reasonable performance in classifying FaST based on an ROC AUC > 90% in the training and testing cohorts. This performance was similar when assessed in 75% of the training cohort indicating that data satisfaction was reached and that a larger training cohort would be unlikely to significantly improve classification accuracy. Based on ROC AUC, this performance was also comparable to re-classification by the cardiologists. False negative classification of FaST by DL was commonly due to fractionation at unipolar EGM onset and low amplitude/slew unipolar EGMs near the PV ostia. In false positive cases, periodic unipolar EGMs manifested small rS complexes or were non-sustained for only a few beats such that

TABLE 2 | Performance of DL model.

	FaST Prevalence	Predefined Sensitivity	Specificity	PPV	NPV	F1-score	Accuracy
Cross-Validation Cohort	9.2% (*n* = 1,220)	78*	87.3 (81.0 – 93.5)	40.0 (30.9 – 49.1)	97.4 (97.0 – 97.9)	0.528 (0.448 – 0.607)	86.4 (80.7 – 92.1)
		85	81.2 (75.9 – 86.6)	32.1 (28.7 – 35.6)	97.9 (97.6 – 98.3)	0.464 (0.429 – 0.499)	81.5 (76.8 – 86.2)
		90	73.7 (69.7 – 77.7)	26.3 (22.9 – 29.8)	98.5 (98.3 – 98.6)	0.406 (0.365 – 0.447)	75.2 (71.7 – 78.7)
		95	60.3 (54.9 – 65.7)	20.0 (18.8 – 21.2)	99.0 (98.7 – 99.3)	0.330 (0.313 – 0.347)	63.6 (58.9 – 68.2)
Testing Cohort	9.4% (*n* = 300)	78*	88.8 (87.4 – 90.3)	42.3 (39.1 – 45.5)	97.5 (97.5 – 97.6)	0.549 (0.522 – 0.576)	87.9 (86.5 – 89.2)
		85	85.0 (83.2 – 86.9)	36.7 (34.2 – 39.2)	98.0 (97.7 – 98.3)	0.509 (0.486 – 0.532)	84.9 (83.3 – 86.4)
		90	81.9 (81.8 – 82.0)	33.6 (33.3 – 33.9)	98.5 (98.4 – 98.6)	0.486 (0.481 – 0.491)	82.5 (82.3 – 82.6)
		95	68.7 (61.4 – 76.1)	24.1 (19.8 – 28.4)	99.1 (99.1 – 99.2)	0.383 (0.330 – 0.437)	71.1 (64.6 – 77.7)

**Sensitivity of cardiologist re-classifying FaST from a subset of 50 random periodic unipolar EGMs; NPV, negative predictive value; PPV, positive predictive value; 95% confidence intervals presented in parentheses.*

the prespecified criteria of >90% temporal stability for 5-s was not met.

Comparison With Previous Machine Learning Studies

Deep learning has recently been applied to arrhythmia classification, but primarily in ECG recordings. Hannun et al. (2019) used residual CNN to classify a finite number of arrhythmias from a single-lead ECG strip, while Chang et al. (2021) employed the bi-directional long short term memory (LSTM) network to classify the same arrhythmias from a 12-lead ECG. To our knowledge, our study is the first application of DL to classify raw, intracardiac EGMs during AF. Similar to Hannun et al. (2019), we adopt residual CNN because all EGM signals were of the same duration, so that LSTM was not required. Machine learning models have also been developed to detect rotational activation during human AF, but the input training dataset was either color-coded phase maps (Alhusseini et al., 2020) or EGM frequency spectral features (Zolotarev et al., 2020) from a multielectrode array, and not raw EGMs as in our study. In the CNN model by Alhusseini et al. (2020), rotational activation was detected with an accuracy of 95%, while more classic machine learning models by Zolotarev et al. (2020) achieved an accuracy of 80–90% depending on size of the multi-electrode mapping array input into the model. In our study, the performance of classic machine learning models, such as logistic regression, SVM and KNN, in classifying FaST sites was inferior to that of DL, which highlights the computational proficiency of DL in EGM classification without the requisite for discrete feature input, such as unipolar EGM onset.

Explainability of DL Model

Several techniques have been proposed to interpret machine learning classification in electrophysiology. We used Grad-CAM to evaluate explainability because the whole EGM signal is considered and the contribution of DL convolutional layers are weighted to generate visually interpretable importance plots (Selvaraju et al., 2017). Other approaches have been described, such as "occlusion mapping," where portions of the signal are systematically deleted to assess the effect on DL performance (Bleijendaal et al., 2021), but this cannot be applied to our dataset because the entire 5-s EGM recording requires classified. Our findings with Grad-CAM suggested that the higher convolutional layers are more relevant in periodic unipolar QS classification, and in distinguishing atrial EGMs from far-field ventricular EGMs. These layers also detect the presence of sustained periodicity, which adds temporal dimensionality to the detection of individual unipolar QS complexes (**Figure 6**).

Clinical Implications

Focal sources may be a relevant mechanism sustaining AF in some patients, which provides the rationale for accurate mapping. Given the complexity and non-stationarity of AF EGMs, automating focal source detection is difficult using multisite EGM recordings and conventional time-frequency domain analysis. Manual overreading may improve the robustness of focal source detection, but this is time-consuming and still susceptible to imprecision. In our randomized controlled trial, FaST sites were identified manually from an automated list of candidate periodic unipolar EGMs. FaST ablation terminated AF in 30% of patients, prolonged AF cycle length by 20 ± 14 ms among those with AF termination, and reduced AF recurrence by 48% at 1-year follow (Chauhan et al., 2020), suggesting that FaST sites defined with our non-DL FaST algorithm may identify focal sources. In the present study, FaST detection with DL using a training set of periodic unipolar EGMs was accurate, and the fully automated approach will ultimately improve interobserver variability and reduce FaST mapping time. As a clinical mapping tool, high sensitivity is important to identify the majority of putative focal sources, but equally important is the need to visually verify the EGM output so false positives are discarded. At a prespecified sensitivity of 90%, the specificity and accuracy of FaST detection with DL was high at 82 and 83%, respectively. Thus, DL has the potential to improve clinical AF mapping workflow by efficiently generating a comprehensive list of FaST sites, which can then be manually overread by the cardiologist. In addition, explainability of DL is essential to demystify the "black box" and facilitate adoption as a *bone fid* mapping tool in AF given the ambiguity of many EGMs and the uncertainty in their classification. Explainability was demonstrated with the importance plots using Grad-CAM for a subset of periodic unipolar EGMs in our study. Ultimately, our DL model may provide a more standardized approach to FaST detection as an adjunctive ablation strategy to PVI.

Limitations

There are several limitations to acknowledge. First, FaST sites were defined based on a single recording site and not the activation pattern from a multielectrode array, but this was intentional to avoid the ambiguity of activation mapping in AF. Although unipolar QS are markers of focal sources, passive activation from epicardial-endocardial breakthrough or source-sink mismatch may also produce similar unipolar EGM morphology, but sustained periodicity would be unlikely. It is possible that DL training with neighboring unipolar EGMs from a multielectrode array will improve the specificity focal source detection (Zolotarev et al., 2020). Second, EGMs were rcorded for 5-s, but longer recordings could increase the sensitivity and specificity of FaST detection as putative AF sources. This was not performed to avoid circular catheter instability and poor EGM quality in some mapping region. Prior studies with ≥ 30 s recordings have been performed with a 64-electrode basket catheter, but this approach is disadvantaged by poor electrode-tissue contact and lower spatial resolution compared to FaST mapping. Third, our study population and periodic unipolar EGM dataset is relatively small and sourced from a single center. The performance of our DL model requires external validation in a larger patient cohort. The prevalence of FaST was also low, which can create class imbalance and a lower PPV and F1-score. To address this, we evaluated the performance of the DL model based on a number of predefined sensitivities and benchmarked this performance to cardiologists with good results as shown in **Table 2** and **Figure 4D**. Fourth, our DL model, although

comprehensive, has limitations in robustness and explainability, which are common to other DL algorithms (LeCun et al., 2015). Robustness was optimized by training the DL model on different sets of patients each with different random seeds, but this may still not be sufficient to address systematic noise (e.g., far-field ventricular EGM) or adversarial EGMs (e.g., borderline unipolar QS cases) (Papernot et al., 2016). For explainability, Grad-CAM was applied to probe the importance of features, but the analysis was qualitative because there are no clear metrics for quantitative benchmarking. Finally, DL was not used to guide real-time FaST ablation, however its reliability and efficiency will be evaluated in a future multicenter, randomized trial.

CONCLUSION

Our novel DL model trained on raw unipolar EGMs in AF accurately identified FaST EGMs in patients with drug-refractory AF. Performance was similar to FaST re-classification by cardiologists. Explainability analysis showed that our DL model temporally tracked the hallmark periodic unipolar QS complexes that define FaST. DL is a promising computational tool to automate AF EGM classification and improve the efficiency of FaST detection, which may facilitate focal source mapping and ablation.

DATA AVAILABILITY STATEMENT

The raw data supporting the conclusions of this article will be made available by the authors upon reasonable request.

ETHICS STATEMENT

The studies involving human participants were reviewed and approved by the University Health Network Research Ethics Board. The patients/participants provided their written informed consent to participate in this study.

AUTHOR CONTRIBUTIONS

SL: methodology design, data analysis, figure, and the manuscript preparation. DR: the figure preparation. SN: data analysis and critical review of manuscript. AS: data preparation. ZZ: critical review of the manuscript. BW: methodology design and critical review of the manuscript. VC: study conceptualization, methodology design, data analysis, the figure, and the manuscript preparation. All authors contributed to the article and approved the submitted version.

FUNDING

This study was supported by the Heart and Stroke Foundation of Ontario Career Award (MC 7577) and MaRS Innovation and the Pennycook Arrhythmia Research Fund to VC.

SUPPLEMENTARY MATERIAL

The Supplementary Material for this article can be found online at: https://www.frontiersin.org/articles/10.3389/fphys.2021.704122/full#supplementary-material

REFERENCES

Alhusseini, M. I., Abuzaid, F., Rogers, A. J., Zaman, J. A. B., Baykaner, T., Clopton, P., et al. (2020). Machine learning to classify intracardiac electrical patterns during atrial fibrillation: machine learning of atrial fibrillation. *Circ. Arrhythm Electrophysiol.* 13:e008160.

Bleijendaal, H., Ramos, L. A., Lopes, R. R., Verstraelen, T. E., Baalman, S. W. E., Oudkerk Pool, M. D., et al. (2021). Computer versus cardiologist: is a machine learning algorithm able to outperform an expert in diagnosing a phospholamban p.Arg14del mutation on the electrocardiogram? *Heart Rhythm* 18, 79–87. doi: 10.1016/j.hrthm.2020.08.021

Chang, K. C., Hsieh, P. H., Wu, M. Y., Wang, Y. C., Chen, J. Y., Tsai, F. J., et al. (2021). Usefulness of machine learning-based detection and classification of cardiac arrhythmias with 12-lead electrocardiograms. *Can. J. Cardiol.* 37, 94–104. doi: 10.1016/j.cjca.2020.02.096

Chauhan, V. S., Verma, A., Nayyar, S., Timmerman, N., Tomlinson, G., Porta-Sanchez, A., et al. (2020). Focal source and trigger mapping in atrial fibrillation: randomized controlled trial evaluating a novel adjunctive ablation strategy. *Heart Rhythm* 17(5 Pt A), 683–691. doi: 10.1016/j.hrthm.2019.12.011

Dalvi, R., Suszko, A., and Chauhan, V. S. (2016). Identification and annotation of multiple periodic pulse trains using dominant frequency and graph search: applications in atrial fibrillation rotor detection. *Annu. Int. Conf. IEEE Eng. Med. Biol. Soc.* 2016, 3572–3575.

DeBakker, J. M., and Wittkampf, F. H. (2010). The pathophysiologic basis of fractionated and complex electrograms and the impact of recording techniques on their detection and interpretation. *Circ. Arrhythm Electrophysiol.* 3, 204–213. doi: 10.1161/circep.109.904763

Feeny, A. K., Chung, M. K., Madabhushi, A., Attia, Z. I., Cikes, M., Firouznia, M., et al. (2020). Artificial intelligence and machine learning in arrhythmias and cardiac electrophysiology. *Circ. Arrhythm Electrophysiol.* 13:e007952.

Ganesan, A. N., Shipp, N. J., Brooks, A. G., Kuklik, P., Lau, D. H., Lim, H. S., et al. (2013). Long-term outcomes of catheter ablation of atrial fibrillation: a systematic review and meta-analysis. *J. Am. Heart Assoc.* 2:e004549.

Gizurarson, S., Dalvi, R., Das, M., Ha, A. C. T., Suszko, A., and Chauhan, V. S. (2016). Hierarchical schema for identifying focal electrical sources during human atrial fibrillation: implications for catheter-based atrial substrate ablation. *JACC Clin. Electrophysiol.* 2, 656–666. doi: 10.1016/j.jacep.2016.02.009

Hannun, A. Y., Rajpurkar, P., Haghpanahi, M., Tison, G. H., Bourn, C., Turakhia, M. P., et al. (2019). Cardiologist-level arrhythmia detection and classification in ambulatory electrocardiograms using a deep neural network. *Nat. Med.* 25, 65–69. doi: 10.1038/s41591-018-0268-3

He, K., Zhang, X., Ren, S., and Sun, J. (2015). "Delving deep into rectifiers: surpassing human-level performance on imagenet classification," in *Proceedings of the IEEE international conference on computer vision*, Santiago, 1026–1034.

He, K., Zhang, X., Ren, S., and Sun, J. (2016). "Identity mappings in deep residual networks," in *Proceedings of the European conference on computer vision* (Cham: Springer), 630–645. doi: 10.1007/978-3-319-46493-0_38

Heijman, J., Algalarrondo, V., Voigt, N., Melka, J., Wehrens, X. H., Dobrev, D., et al. (2016). The value of basic research insights into atrial fibrillation mechanisms as a guide to therapeutic innovation: a critical analysis. *Cardiovasc. Res.* 109, 467–479. doi: 10.1093/cvr/cvv275

Kingma, D. P., and Ba, J. (2014). Adam: a method for stochastic optimization. *arXiv* [Preprint] arXiv:1412 6980,

Kochhauser, S., Verma, A., Dalvi, R., Suszko, A., Alipour, P., Sanders, P., et al. (2017). Spatial relationships of complex fractionated atrial electrograms and continuous electrical activity to focal electrical sources: implications for substrate ablation in human atrial fibrillation. *JACC Clin. Electrophysiol.* 3, 1220–1228. doi: 10.1016/j.jacep.2017.05.013

LeCun, Y., Bengio, Y., and Hinton, G. (2015). Deep learning. *Nature* 521, 436–444.

Lee, S., Khrestian, C. M., Sahadevan, J., and Waldo, A. L. (2020). Reconsidering the multiple wavelet hypothesis of atrial fibrillation. *Heart Rhythm* 17, 1976–1983. doi: 10.1016/j.hrthm.2020.06.017

Lee, S., Sahadevan, J., Khrestian, C. M., Cakulev, I., Markowitz, A., and Waldo, A. L. (2015). Simultaneous biatrial high-density (510-512 electrodes) epicardial mapping of persistent and long-standing persistent atrial fibrillation in patients: new insights into the mechanism of its maintenance. *Circulation* 132, 2108–2117. doi: 10.1161/circulationaha.115.017007

Lee, S., Sahadevan, J., Khrestian, C. M., Durand, D. M., and Waldo, A. L. (2013). High density mapping of atrial fibrillation during vagal nerve stimulation in the canine heart: restudying the Moe hypothesis. *J. Cardiovasc. Electrophysiol.* 24, 328–335. doi: 10.1111/jce.12032

Lee, S., Sahadevan, J., Khrestian, C. M., Markowitz, A., and Waldo, A. L. (2017). Characterization of foci and breakthrough sites during persistent and long-standing persistent atrial fibrillation in patients: studies using high-density (510-512 Electrodes) biatrial epicardial mapping. *J. Am. Heart Assoc.* 17:6.

Nayyar, S., Ha, A. C. T., Timmerman,N., Suszko, A., Ragot, D., and Chauhan, V. S. (2020). Focal and pseudo/rotational activations in human atrial fibrillation defined with automated periodicity mapping. *J. Cardiovasc.Electrophysiol.* 32, 212–223. doi: 10.1111/jce.14812

Papernot, N., McDaniel, P., Jha, S., Fredrikson, M., Celik, Z. B., and Swami, A. (2016). The limitations of deep learning in adversarial settings. *IEEE Eur. Symp. Secur. Privacy* 21, 372–387.

Paszke, A., Gross, S., Massa, F., Lerer, A., Bradbury, J., Chanan, G., et al. (2019). "Pytorch: an imperative style, high-performance deep learning library," in *Proceedings of the Advances in Neural Information Processing Systems 32: Annual Conference on Neural Information Processing Systems*, eds H. M. Wallach, H. Larochelle, A. Beygelzimer, F. d'Alché-Buc, E. B. Fox, and R. Garnett (Vancouver, BC: NeuroIPS), 8026–8037.

Pedregosa, F., Varoquaux, G., Gramfort, A., Michel, V., Thirion, B., Grisel, O., et al. (2011). Scikit-learn: machine learning in python. *J. Mach. Learn. Res.* 12, 2825–2830.

Perez, L., and Wang, J. (2017). The effectiveness of data augmentation in image classification using deep learning. *arXiv* [Preprint] arXiv: 1712 04621,

Roney, C. H., Cantwell, C. D., Bayer, J. D., Qureshi, N. A., Lim, P. B., Tweedy, J. H., et al. (2017). Spatial resolution requirements for accurate identification of drivers of atrial fibrillation. *Circ. Arrhythm Electrophysiol.* 10:e004899.

Saito, T., and Rehmsmeier, M. (2015). The precision-recall plot is more informative than the ROC plot when evaluating binary classifiers on imbalanced datasets. *PLoS One* 10:e0118432. doi: 10.1371/journal.pone.0118432

Selvaraju, R. R., Cogswell, M., Das, A., Vedantam, R., Parikh, D., and Batra, D. (2017). "Grad-CAM: Visual Explanations from Deep Networks via Gradient-based Localization," in *Proceedings of the IEEE International Conference on Computer Vision*, Venice, 618–626.

Zolotarev, A. M., Hansen, B. J., Ivanova, E. A., Helfrich, K. M., Li, N., Janssen, P. M. L., et al. (2020). Optical mapping-validated machine learning improves atrial fibrillation driver detection by multi-electrode mapping. *Circ. Arrhythm Electrophysiol.* 13:e008249.

Conflict of Interest: VC is the author of FaST mapping intellectual property (US 10,111,598 B2) owned by University Health Network, Toronto, ON, Canada. The study sponsors were not responsible for machine learning/mapping algorithm development, data collection, analysis or the manuscript preparation.

The remaining authors declare that the research was conducted in the absence of any commercial or financial relationships that could be construed as a potential conflict of interest.

Publisher's Note: All claims expressed in this article are solely those of the authors and do not necessarily represent those of their affiliated organizations, or those of the publisher, the editors and the reviewers. Any product that may be evaluated in this article, or claim that may be made by its manufacturer, is not guaranteed or endorsed by the publisher.

frontiers in Physiology

ORIGINAL RESEARCH
published: 24 September 2021
doi: 10.3389/fphys.2021.733543

Spatial Changes in the Atrial Fibrillation Wave-Dynamics After Using Antiarrhythmic Drugs: A Computational Modeling Study

*Inseok Hwang, Ze Jin, Je-Wook Park, Oh-Seok Kwon, Byounghyun Lim, Jisu Lee, Hee-Tae Yu, Tae-Hoon Kim, Boyoung Joung and Hui-Nam Pak**

Yonsei University Health System, Seoul, South Korea

Background: We previously reported that a computational modeling-guided antiarrhythmic drug (AAD) test was feasible for evaluating multiple AADs in patients with atrial fibrillation (AF). We explored the anti-AF mechanisms of AADs and spatial change in the AF wave-dynamics by a realistic computational model.

Methods: We used realistic computational modeling of 25 AF patients (68% male, 59.8 ± 9.8 years old, 32.0% paroxysmal AF) reflecting the anatomy, histology, and electrophysiology of the left atrium (LA) to characterize the effects of five AADs (amiodarone, sotalol, dronedarone, flecainide, and propafenone). We evaluated the spatial change in the AF wave-dynamics by measuring the mean dominant frequency (DF) and its coefficient of variation [dominant frequency-coefficient of variation (DF-COV)] in 10 segments of the LA. The mean DF and DF-COV were compared according to the pulmonary vein (PV) vs. extra-PV, maximal slope of the restitution curves (Smax), and defragmentation of AF.

Results: The mean DF decreased after the administration of AADs in the dose dependent manner ($p < 0.001$). Under AADs, the DF was significantly lower ($p < 0.001$) and COV-DF higher ($p = 0.003$) in the PV than extra-PV region. The mean DF was significantly lower at a high Smax (≥1.4) than a lower Smax condition under AADs. During the episodes of AF defragmentation, the mean DF was lower ($p < 0.001$), but the COV-DF was higher ($p < 0.001$) than that in those without defragmentation.

Conclusions: The DF reduction with AADs is predominant in the PVs and during a high Smax condition and causes AF termination or defragmentation during a lower DF and spatially unstable (higher DF-COV) condition.

Keywords: atrial fibrillation, computational modeling, antiarrhythmic drug, dominant frequency, spatial changes

Edited by:
Martin Bishop,
King's College London,
United Kingdom

Reviewed by:
Caroline Helen Roney,
King's College London,
United Kingdom
Edward Joseph Vigmond,
Université de Bordeaux, France
Oleg Aslanidi,
King's College London,
United Kingdom

***Correspondence:**
Hui-Nam Pak
hnpak@yuhs.ac

Specialty section:
This article was submitted to Computational Physiology and Medicine, a section of the journal Frontiers in Physiology

Received: *30 June 2021*
Accepted: *02 September 2021*
Published: *24 September 2021*

Citation:
Hwang I, Jin Z, Park J-W, Kwon O-S, Lim B, Lee J, Yu H-T, Kim T-H, Joung B and Pak H-N (2021) Spatial Changes in the Atrial Fibrillation Wave-Dynamics After Using Antiarrhythmic Drugs: A Computational Modeling Study. Front. Physiol. 12:733543. doi: 10.3389/fphys.2021.733543

INTRODUCTION

Atrial fibrillation (AF) is a common arrhythmia, with a prevalence of more than 1.6% of the total population, and the prevalence continues to increase in the aging society (Kim et al., 2018). Antiarrhythmic drugs (AADs) are the most commonly used first-line treatment for AF rhythm control. However, inadvertent use of AADs can increase the mortality (Cardiac-Arrhythmia-Suppression-Trial-(CAST)-Investigators, 1989; The-AFFIRM-Investigators, 2004) and has the risk

of various side effects (Chandhok and Schwartzman, 2007). After the establishment of the guidelines of AF management on the use of AADs, the safety of AADs has been improving, and early rhythm control using AADs ensures a better prognosis in AF patients (Kirchhof et al., 2020; Hindricks et al., 2021). Nevertheless, as AADs are ion channel blockers, their efficacy highly varies from person to person due to the interaction of multiple ion channels and the genetic influence (Darbar and Roden, 2013) and remains unsatisfactory (Roy et al., 2000). Many experimental studies have conducted to investigate the effects of AADs, however, most of the studies were results of animal studies (Varela et al., 2016). Previous study indicated that APD heterogeneity promoted substrate for arrhythmogenic re-entrant waves during AF initiation and maintenance. Amiodarone has shown anti-AF effect by increasing atrial APD and reducing APD heterogeneity. Increasing atrial APD and reduced APD heterogeneity were effective in controlling arrhythmogenic reentry (Varela et al., 2016). If the rhythm control effect of AADs can be predicted through simulation modeling, an efficient selection of AADs might be possible and can reduce the adverse effects or trial and error. We recently reported that the virtual AAD test can be performed through computational modeling reflecting the personalized atrial anatomy, histology, and electrophysiology of AF patients (Hwang et al., 2021). Computational modeling can evaluate the efficacy of multiple AADs under the same condition and can quantify the mechanistic effects of AADs using very high-spatiotemporal resolution maps (Loewe et al., 2014; Li et al., 2016; Lim et al., 2020b; Bai et al., 2021; Hwang et al., 2021). This virtual AAD test does not have any ethical problems because it allows testing of multiple drugs with variable doses without the risk of adverse events (Hwang et al., 2021). This study analyzed the mechanism of the AAD effects on the AF wave-dynamics using an AF computational modeling that reflected the anatomical, histological, and electrophysiological characteristics of 25 patients with AF. The purpose of this study was to quantify the dominant frequency (DF) and its spatial heterogeneity after using AADs (Jarman et al., 2012; Kogawa et al., 2015; Li et al., 2016) and to compare the regional differences between the pulmonary veins (PVs) and extra-PV regions and differences according to the AF wave-break conditions (Li et al., 2016). In addition, we compared the characteristics of the wave-dynamics in episodes of AF termination or defragmentation under AAD use.

MATERIALS AND METHODS

Ethical Approval

The study protocol followed the Declaration of Helsinki and was approved by the Institutional Review Board of the Severance Cardiovascular Hospital, Yonsei University Health System. All participants were included in Yonsei AF Ablation Cohort Database (ClinicalTrials.gov Identifier: NCT02138695) and provided written consent to participate in the study.

Activation Time Matching

First, electroanatomical modeling using patient voltage data was conducted. Over 500 bipolar voltage data points that included sequential recordings of electrograms at a 500 ms cycle length were obtained from the surface of the individual atria during AF catheter ablation (**Figure 1**). The individual CT images were merged with the voltage data to produce the personalized electroanatomical environment of each patient. The inverse distance weighting (IDW) method (Ugarte et al., 2015) was used to interpolate the clinical voltage signal for a simulation. The interpolation was based on the IDW method (Ugarte et al., 2015) and was within a 10-mM radius from the region of interest. Interpolation of the clinical voltage data produced a virtual voltage map with an amplitude. The detailed equation for the IDW was as follows:

$$W_{ij} = \frac{{d_{ij}}^{-a}}{\sum_{k}^{n_j} d_{kj}}, R_j = \sum_{i=1}^{n_j} w_{ij} R_{ij}$$

where W demonstrated the weighted average of neighboring values; i and j represented the unknown and known values of the respective points; ${d_{ij}}^{-a}$ was the distance between unknown and known points; R_j represented the interpolation value at unknown point j; and R_{ij} indicated the known point of the value. The 3D left atrium (LA) model was created using the interpolated voltage map and CT images through the Ensite Navx system (Abbott Inc., Lake Bluff, IL, United States). Accurate matching of the voltage and CT images data on the 3D LA model was conducted using rotation and translation. We interpolated a clinical voltage map to produce a virtual voltage map on 3D model. The registration of the electro-anatomical maps onto the CT models involved the four following steps: geometry, trimming, field scaling, and alignment. The registration error could occur during such steps. Each step was conducted manually by an operator therefore possible human error potentially existed (Lim et al., 2020a). The fiber orientation involved two states: tracking and visualization. Tracking was a parallel task making it effective for graphic processing unit (GPU)-based fiber tracking. The conductivity varied due to the direction of the vector. A vector pointing perpendicular to the direction of conductivity indicated slower conductivity compared with a vector pointing the same direction as the conductivity. The fiber orientation was produced by simulating a clinical local activation map as well as the atlas-based mesh of atrial geometry. The fiber orientation was produced by simulating a clinical local activation map as well as the atlas-based mesh of atrial geometry (Pashakhanloo et al., 2016; Lim et al., 2020a). We estimated personalized fiber orientations using an atlas-based method (Niederer et al., 2019; Roney et al., 2021) to reflect anisotropic conduction from isotropic triangular mesh with 300 μM edges. Then, we adjusted the fiber orientation based on the clinical LAT map. The conductivity of our model (Zahid et al., 2016) was applied 0.1264 S/m (non-fibrotic longitudinal cell), 0.0546 S/m (fibrotic longitudinal cell), 0.0252 S/m (non-fibrotic transverse cell), and 0.0068 S/m (fibrotic transverse cell). Fibrosis areas were estimated based on the clinical bipolar map. Fibrosis was determined using a non-linear relationship of the

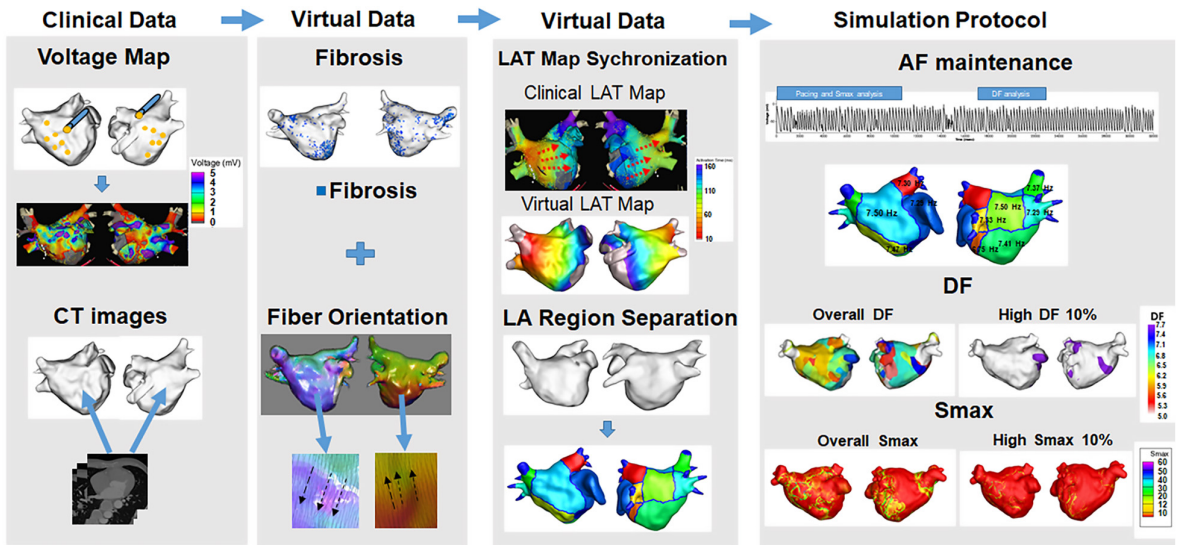

FIGURE 1 | Computational modeling of the left atrium with atrial fibrillation (AF). Realistic left atrium (LA) modeling was conducted using an interpolation of the voltage map and merging with the CT images. Fibrosis and the fiber orientation were implemented. The LAT map synchronization and AF simulation protocol were conducted for the analyses.

bipolar voltage and the probability of fibrosis. The equation for the probability of fibrosis was described as follows (Hwang et al., 2019):

$$P_{fibrosis} = \begin{cases} 1, & X < 0 \\ -40.0X^3 + 155X^2 - 206X + 99.8 & 0 \le X \le 1.74 \\ 0, & 1.74 < X \end{cases}$$

where X is the bipolar voltage at each node, and it was ranged from 0 to 1.74 mV. If X is >1.74 mV, then $P_{fibrosis}$ would be zero. The probability of fibrosis was determined using clinical bipolar voltage data.

Fiber tracking was performed to determine the direction of the conduction. Fibrosis was represented using the relationship between the probability of fibrosis and bipolar voltage values (Zahid et al., 2016). The diffusion coefficient was calibrated by synchronization of the clinical and virtual conduction velocity. Before a preliminary simulation, conduction velocity was calculated by using the distance from the pacing location to the LA appendage and divided it by the travel time to get the conduction velocity. We then matched conduction velocity from the simulation to clinical conduction velocity by modulating the diffusion coefficient (Lim et al., 2020a). A color scale indicating the conduction time was compared between the clinical and virtual activation time maps for matching to produce an accurate conduction environment for each patient.

Virtual Antiarrhythmic Drug Intervention

The human atrial myocyte model (Courtemanche et al., 1998) was used for normal sinus rhythm, and an AF state was created by modifying that model (Lee et al., 2016). For the baseline AF state, the I_{Na}, I_{to}, I_{CaL}, I_{Kur}, and I_{Caup} were decreased by 10, 70, 70, 50, and 20%, and the I_{K1} was increased by 110% as compared to that of the Courtemanche model (Lee et al., 2016). Five types of AADs were used for the study. Class III included amiodarone, sotalol, and dronedarone, and class IC indicated flecainide, and propafenone. High dose included amiodarone 10 μM, sotalol 10 mM, dronedarone 10 μM, flecainide 15 μM, and propafenone 10 μM. Low dose included amiodarone 5 μM, sotalol 60 μM, dronedarone 3 μM, flecainide 5 μM, and propafenone 5 μM. All the ionic changes for each drug were derived from previously reported references. Our AAD references used IC50 values. We used such references and make percent changes relative to the Courtemanche-Ramirez-Nattel model (Courtemanche et al., 1998). The reduction of channel conductance was calculated to reflect the ion channel blocking effect at the considered concentration. For the implementation of ion currents for each dose, we conducted the literature search and implemented such information to construct the ion currents for each dose as previously reported in our study (Hwang et al., 2021). As the Courtemanche-Ramirez-Nattel model (Sossalla et al., 2010; Grandi et al., 2011) being the baseline, the effects of each dose were implemented by applying the blockage of specific ion channels. **Supplementary Tables 1**, **2** showed detailed descriptions of the ion current changes from baseline in response to the different AADs references including the class IC and class III drugs as well as each dose.

Atrial Fibrillation Induction, Dominant Frequency, and Smax Analyses

Our GPU-based customized software (CUVIA ver. 2.5, Model: SH01; Laonmed Inc., Seoul, South Korea) was used virtually to induce and apply appropriate ion currents for AADs. The DF and

TABLE 1 | Effects of antiarrhythmic drugs (AADs) on the electrophysiological and fibrillatory wave-dynamics parameters.

	Baseline (†*n* = 25)	Overall AADs (†*n* = 250)	*P*-value	Class IC AADs (†*n* = 100)	Class III AADs (†*n* = 150)	*P*-value	Low dose AADs (†*n* = 125)	High dose AADs (†*n* = 125)	*P*-value
APD_{90} (ms)	233.000 (231.000, 239.000)	273.000 (263.000, 295.000)	<0.001	269.000 (256.000, 290.000)	277.000 (265.000, 303.000)	0.002	267.000 (261.000, 273.000)	293.000 (271.000, 309.000)	<0.001
CV (m/s)	0.750 (0.617, 0.906)	0.612 (0.411, 0.741)	0.007	0.598 (0.474, 0.732)	0.618 (0.395, 0.745)	0.615	0.674 (0.484, 0.826)	0.526 (0.346, 0.685)	<0.001
Mean AFCL (ms)	135.616 (130.526, 150.303)	159.344 (145.632, 176.964)	<0.001	156.508 (140.000, 171.579)	162.312 (150.923, 183.952)	0.038	153.750 (140.000, 172.281)	164.167 (156.508, 192.404)	<0.001
Mean Smax	0.785 (0.656, 0.963)	0.802 (0.635, 1.009)	0.899	0.851 (0.639, 1.027)	0.744 (0.629, 0.998)	0.136	0.730 (0.628, 0.916)	0.851 (0.677, 1.106)	0.003
Mean DF (Hz)	7.025 (6.097, 7.379)	5.722 (1.286, 6.553)	<0.001	6.148 (5.315, 6.922)	5.170 (1.200, 6.145)	<0.001	6.121 (5.082, 6.874)	5.101 (1.200, 6.098)	<0.001
COV-DF (%)	NA	141.421 (105.265, 173.205)	NA	149.079 (108.095, 173.205)	141.421 (102.270, 170.349)	0.001	141.000 (120.000, 141.000)	141.000 (119.000, 141.000)	0.918

APD_{90}, Action potential duration 90%; CV, Conduction velocity; AFCL, AF cycle length; Smax, The Maximal slope of the restitution curves; DF, Dominant frequency; COV-DF, Coefficient of Variation-Dominant Frequency.
Patients who did not sustain proper normal sinus rhythm and an atrial fibrillation (AF) status were excluded from the analysis.
Median (IQ1, IQ3) was displayed in the Table.
†n = The number of patients × AAD × Dose.

Smax were analyzed using this same GPU-based software. AF was initiated in a pacing location using AF pacing from 200 to 120 ms with eight beats per cycle using ion currents for specific AADs. Virtual pacing location was matched with clinical activation time map for a realistic LA modeling. Before AF induction simulation, clinical and virtual pacing sites were matched to reflect the personalized LA model. Successful AF induction was determined during AF pacing by observing electrogram in the 3D LA map (**Supplementary Figure 1**). Defragmentation of AF includes termination of AF and conversion of AF to atrial tachycardia. Defragmentation was determined by visually assessing the electrogram and 3D activation map of each case. If there were <2 spiral waves, we determined it as a defragmented state. Once AF was induced successfully, maintenance of AF was observed up to 32 s. During the maintenance period, the DF was calculated from 17 to 23 s. APD_{90} was a normal sinus rhythm measured at a pacing cycle length of 600 ms. We calculated using non-linear fitting of APD_{90} and diastolic interval (Shattock et al., 2017) from over 400,000 nodes during single-site pacing. Smax values were defined at every node in LA regions per patient. For the regional analyses of the Smax and DF, the LA was divided into 10 regions. 10 regions of LA were decided based on the previous clinical study (Park et al., 2009). We used 3D spiral CT images of LA to divide LA portions according to the embryological origin. The portions include the venous LA (posterior LA including the antrum and posterior wall), anterior LA (excluding LA appendage), and LAA. We also divided PV antrum, posterior inferior wall, and septum along the posterior inferior line and septal line. The mean DF and mean Smax were calculated using the results of all 10 regions. A high DF and high Smax were defined as the respective top 10% of the values (**Supplementary Figures 2**, **3**). For the stability of the DF and Smax after AADs, the coefficient of variation (COV) of the high DF and high Smax were calculated as the standard deviation divided by the mean:

$$COV = \frac{\sigma}{\bar{x}}$$

σ represented the standard deviation, and $\bar{x}$ indicated the mean value.

Statistical Analyses

The continuous variables were represented as the median and interquartile range. A comparison of the DF, Smax, and COV was conducted using a *t*-test and Mann-Whitney test depending on the distribution. A p-value < 0.05 was considered statistically significant. Any case in which the DF terminated before 17 s was excluded from the study. Statistical analyses were conducted using SPSS (IBM Corp., IBM SPSS Statistics for Windows, Version 21.0) and RStudio [RStudio Team (2020). RStudio: Integrated Development for R. RStudio, PBC, Boston, MA][1] software.

RESULTS

Effects of Antiarrhythmic Drugs on the Atrial Fibrillation Wave-Dynamics

The patient group consisted of 25 AF patients (68.0% male, 59.8 ± 9.8 years old, 32.0% paroxysmal AF) who had undergone radiofrequency catheter ablation (**Supplementary Table 3**). **Table 1** compared the effects of AADs on the electrophysiological

[1]http://www.rstudio.com/

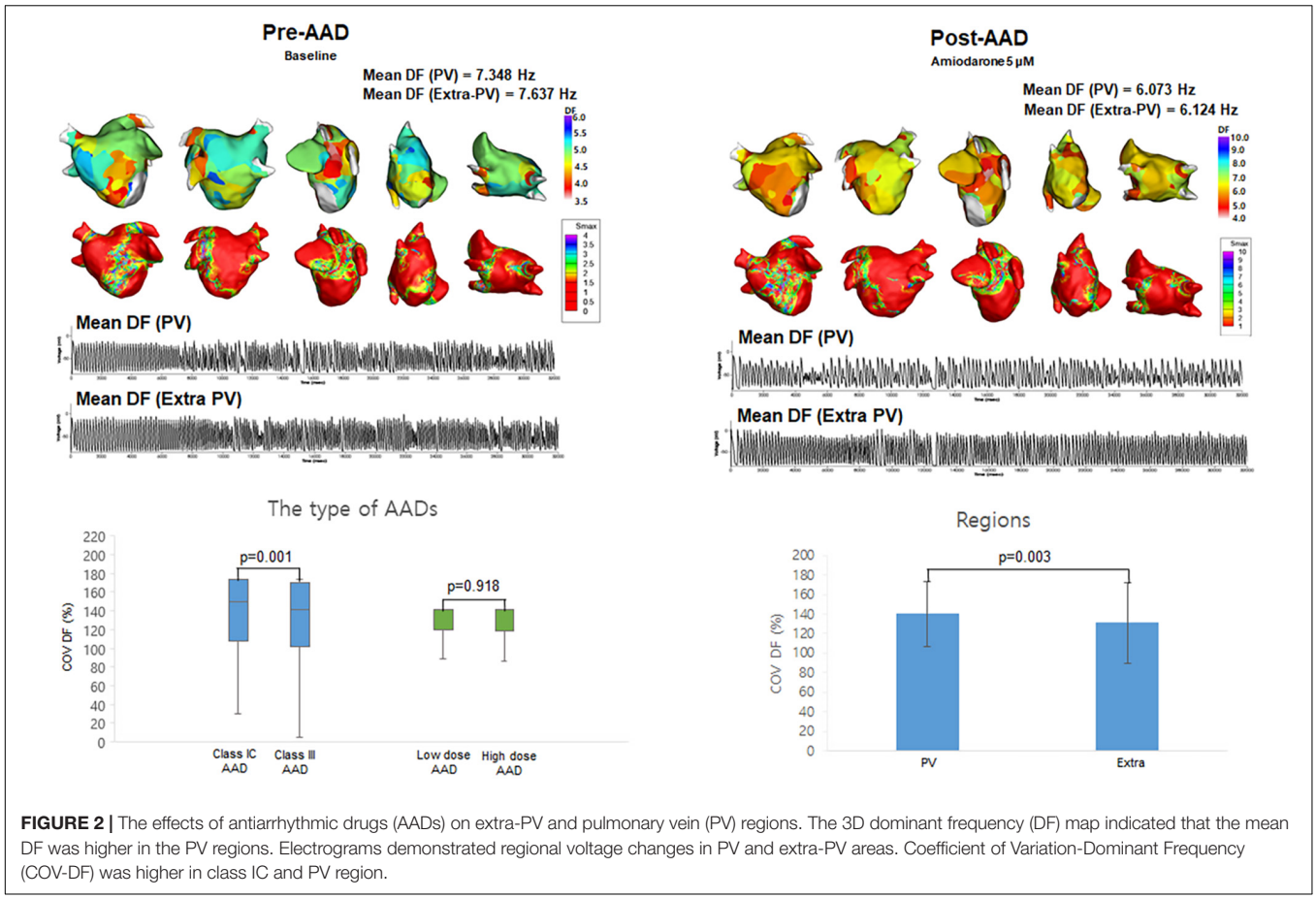

FIGURE 2 | The effects of antiarrhythmic drugs (AADs) on extra-PV and pulmonary vein (PV) regions. The 3D dominant frequency (DF) map indicated that the mean DF was higher in the PV regions. Electrograms demonstrated regional voltage changes in PV and extra-PV areas. Coefficient of Variation-Dominant Frequency (COV-DF) was higher in class IC and PV region.

parameters and wave-dynamic parameters. Overall (2 class IC and 3 class III AADs, low and high doses for each drug), the AADs prolonged the action potential duration for the 90% repolarization (APD_{90}, $p < 0.001$) and mean AF cycle length (AFCL, $p < 0.001$) and reduced the conduction velocity (CV, $p = 0.007$), but did not change the Smax ($p = 0.899$). The DF ($p < 0.001$) and COV-DF ($p = 0.001$, **Figure 2**) reduction effects of the class III AAD were more significant than those of the class IC AADs (**Table 1**). AADs dose-dependently changed the APD_{90} ($p < 0.001$), AFCL ($p < 0.001$), and CV ($p < 0.001$), and the DF reduction was more pronounced at high doses than low doses ($p < 0.001$, **Table 1**).

Different Antiarrhythmic Drug Effects on the Pulmonary Vein and Extra-Pulmonary Vein Regions

Among the 10 segments of the LA, we compared the areas of the PV antrum and extra-PV regions (**Table 2**). The Smax and DF did not differ between the PV antrum and extra-PV LA regions during the baseline AF. After the administration of the AADs, the mean DF became lower ($p < 0.001$, **Figure 2**) and COV-DF higher ($p = 0.003$, **Figure 2**) at the PV antrum than in extra-PV LA regions, which suggested a lower and unstable DF on the PV antrum after AADs.

Post-antiarrhythmic Drug Mean Dominant Frequency Depending on the Smax

We compared the changes in the mean DF and COV-DF at a Smax value of 1.4, based on a previous clinical study for human atrial restitution (**Table 3**). In **Table 3**, we used the baseline Smax values threshold for baseline mean DF, and post-AAD Smax threshold for post-AAD mean DF. At a Smax ≥1.4, the post-AAD mean DF was significantly lower than that at a Smax <1.4 ($p = 0.014$, **Figure 3**). The pattern of a higher mean DF during a Smax <1.4 condition was consistent in the PV ($p = 0.039$, **Figure 3**) and extra-PV areas ($p = 0.002$, **Figure 3**). However, the COV-DFs did not differ depending on the Smax value. Additionally, we differentiated especially **Table 3** into subgroups as indicated in **Supplementary Table 4**. DF was higher in dronedarone 3 μM and amiodarone 5 μM at low Smax.

Termination or Defragmentation of Atrial Fibrillation Depending on the Dominant Frequency and Coefficient of Variation-Dominant Frequency

Table 4 shows the electrophysiological characteristics of the termination and defragmentation episodes of AF after the AAD administration. In the episodes of AF defragmentation within

TABLE 2 | Effects of antiarrhythmic drugs (AADs) on the pulmonary vein (PV) vs. Extra-PV tissue.

	Baseline			AAD		
	PV (†*n* = 25)	**Extra-PV (†*n* = 25)**	***P*-value**	**PV (†*n* = 750)**	**Extra-PV (†*n* = 500)**	***P*-value**
Mean Smax	1.258 (1.060, 1.619)	1.418 (1.006, 1.729)	0.541	1.264 (0.802, 1.659)	1.290 (0.892, 1.663)	0.541
ΔMean Smax	NA	NA	NA	−0.027 (−0.219, 0.170)	0.006 (−0.326, 0.250)	0.692
Mean DF (Hz)	7.567 (6.246, 8.186)	7.916 (7.383, 8.595)	0.086	6.464 (5.246, 7.170)	7.029 (6.209, 7.659)	<0.001
ΔMean DF	NA	NA	NA	−0.820 (−1.275, −0.236)	−0.848 (−1.368, −0.298)	0.238
COV-DF (%)	NA	NA	NA	141.421 (117.963, 173.205) ‡140.446 ± 33.227	141.421 (97.825, 172.515) ‡130.932 ± 41.633	0.003

Smax, The Maximal slope of the restitution curves; ΔMean Smax, Changes of Smax; DF, Dominant Frequency; ΔMean DF, Changes of DF; COV-DF, Coefficient of Variation-Dominant Frequency.
Patients who did not sustain proper normal sinus rhythm and an atrial fibrillation (AF) status were excluded from the analysis.
Median (IQ1, IQ3) was displayed in the Table.
†*n = The number of patients × AAD × Dose.*
‡*Mean ± SD.*

32 s after the AAD administration, the mean DF was significantly lower ($p < 0.001$, **Table 4** and **Figure 4**), and the COV-DF was significantly higher ($p < 0.001$, **Figure 5**) than that in those with sustained AF. In the AF termination episodes, the mean DF was consistently lower ($p < 0.001$, **Table 4**) and COV-DF higher ($p < 0.001$, **Figure 5**). The tendency of a low DF and unstable (higher) COV-DF in the AF defragmentation episodes was consistent regardless of the class IC or class III AAD (**Table 4**).

DISCUSSION

Main Findings

We evaluated the spatial changes in the AF wave-dynamics reflected by the mean DF and COV-DF after using AADs in a realistic computational model that reflected 25 AF patients' LA geometry, histology, and electrophysiology. The AAD classes and doses apparently affected the AF wave-dynamics, and those effects differed between the PV and extra-PV regions depending on the Smax. The AADs easily caused defragmentation or termination at a reduced mean DF and spatially unstable DF (high COV-DF). Realistic AF computational modeling was a feasible approach to study the regional effect of AADs or electrophysiological changes.

Anti-atrial Fibrillation Effects of Antiarrhythmic Drugs on the Pulmonary Vein or Extra-Pulmonary Vein Regions

The mechanism of the AADs involves the blocking of specific *trans*-membrane ion channels to inhibit the initiation or maintenance mechanisms of fibrillation. Class IC drugs function by blocking the rapid inward sodium current that slows the rate of the increasing action potential, and class III AADs block the outward potassium current, lengthening the repolarization and refractoriness (Kowey, 1998). However, it is not known how AADs act on different regions of the atrium and how the wave-dynamics react according to the anatomical structure. There have been many studies on the role of the PVs in the mechanism of AF (Khan, 2004). The PVs have a venous atrium origin that differs from that of other parts of the atrium in terms of the embryological development (Sherif, 2013) and are influenced highly by AF-associated genes such as *PITX2* (Wang et al., 2010). For this reason, the electrical isolation of the PV antrum is the most important target for AF catheter ablation (Chen et al., 1999). PV isolation blocks not only the triggers from the PVs, but also the cardiac autonomic nerves located in the PV antrum and reduces the atrial critical mass. In this study, AADs reduced the mean DF and its spatial instability (COV-DF) more significantly in the PV area than non-PV area. That suggested that the anti-AF effect of AADs mainly is responsible for the lower and spatially unstable DFs in the PV area than in the extra-PV areas. Investigation of the select effects of AADs on the LA regions can have a significant impact on the treatment of AF.

Atrial Fibrillation Mechanisms of Multiple Wavelet or Focal Sources

The focal source hypothesis and multiple wavelet hypothesis have been considered as mechanisms of AF initiation and maintenance (Saad et al., 2009; Narayan and Jalife, 2014). The focal source hypothesis indicates that a special form of a reentry pattern of activation produced by rotors drives the AF mechanism. The multiple wavelet hypothesis explains the AF mechanism as spontaneous wave-breaks that constantly generate randomly wandering daughter wavelets. These wave-breaks collide, are disrupted, coalesce, or give rise to new wavelets in a self-sustaining turbulent process (Chen et al., 2000). High DF areas were used to locate the source of AF drivers or rotors (Hwang et al., 2016), and high Smax areas represent the vulnerable condition of AF wave-breaks in the AF maintenance mechanism (Kalifa et al., 2006). Therefore, the DF is a representative parameter for the focal source hypothesis, and the Smax advocates the multiple wavelet theory. Wu et al. (2002) reported that the focal source and multiple wavelets interact and maintain fibrillation according to the tissue conditions such as the conduction velocity. The present study demonstrated for the first time that the Smax has a direct effect on the DF wave-dynamics in AF and anti-AF mechanisms. Although the

TABLE 3 | Atrial fibrillation (AF) wave-dynamics depending on the Smax values.

	Overall		*P*-value	PV		*P*-value	Extra-PV		*P*-value
	Smax < 1.4 (†*n* = 13)	Smax ≥ 1.4 (†*n* = 12)		Smax < 1.4 (†*n* = 13)	Smax ≥ 1.4 (†*n* = 12)		Smax < 1.4 (†*n* = 13)	Smax ≥ 1.4 (†*n* = 12)	
Baseline mean DF (Hz)	7.958 (7.138, 8.485)	7.708 (7.194, 8.013)	0.650	7.797 (6.246, 8.243)	7.338 (6.382, 8.061)	0.689	8.103 (7.796, 8.599)	7.836 (7.220, 8.385)	0.503
Post-AAD Mean DF (Hz)	6.986 (6.011, 7.677)	6.584 (5.801, 7.015)	0.014	6.732 (5.013, 7.534)	5.963 (5.430, 6.815)	0.039	7.225 (6.411, 7.781)	6.818 (5.859, 7.168)	0.002
Post-AAD COV-DF (%)	141.000 (104.000, 141.000)	141.000 (110.000, 141.000)	0.656	141.000 (116.500, 141.000)	141.000 (131.500, 141.000)	0.532	141.000 (96.600, 141.000)	140.000 (91.900, 141.000)	0.371

DF, Dominant Frequency; COV-DF, Coefficient of Variation-Dominant Frequency.
Patients who did not sustain proper normal sinus rhythm and an AF status were excluded from the analysis.
Median (IQ1, IQ3) was displayed in the Table.
†*n = The number of patients × AAD × Dose.*

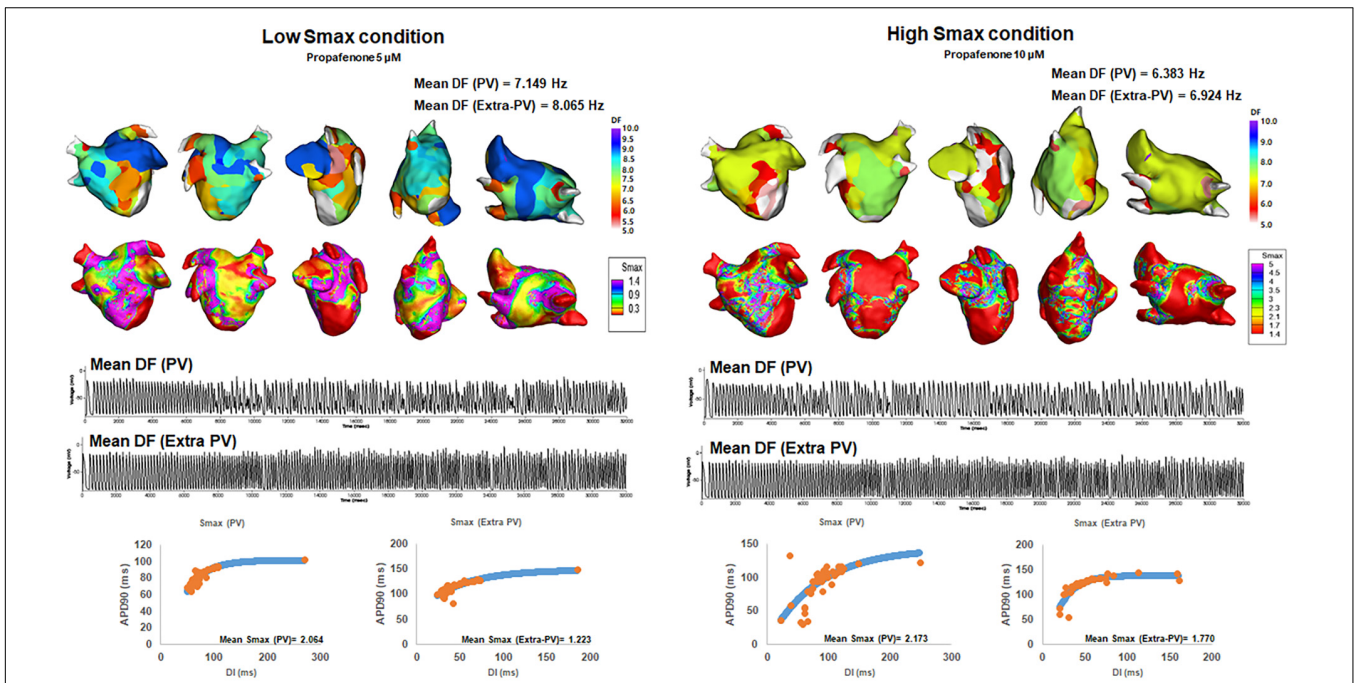

FIGURE 3 | Changes in the dominant frequency (DF) during a high and low Smax. The 3D DF map indicated that the mean DF was inversely related to the mean Smax. Regional voltage changes in pulmonary vein (PV) and extra-PV areas were demonstrated in electrograms.

AADs did not decrease the Smax, the focal source mechanism represented by the DF was predominant in maintaining AF in atrial tissue with a low Smax. At a low Smax, the mean DF was high in both the PV and extra-PV regions, whereas the mean DF was low when the Smax was high. Therefore, the DF and Smax exhibited an inverse relationship.

Sufficient Conditions for Atrial Fibrillation Defragmentation or Termination

Many studies (Pandit et al., 2005; Jarman et al., 2012; Sánchez et al., 2012) have been conducted over the years to understand spiral wave meander and AF termination in various ways. After the AADs, the continuous wave-breaks and reentrant behaviors could not be sustained, resulting in termination or defragmentation. Though a spiral meandering and reentry termination are challenging to study quantitatively (Pandit et al., 2005), we analyzed the DF and Smax changes during the AF defragmentation using realistic computational modeling of AF. This is because the computational modeling enabled spatiotemporally high-resolution mapping while repeatedly being performed (Li et al., 2016; Hwang et al., 2021). In this study, the changes in the DF wave-dynamics had a close relationship with the AF defragmentation. The defragmented AF episodes after the virtual AAD intervention exhibited a reduced mean DF and high COV-DF (spatial instability of DF) regardless of the type of AAD. These changes in the DF were consistently observed in the AF termination episodes. The change in the Smax did not

TABLE 4 | Electrophysiological characteristics terminated atrial fibrillation (AF) after antiarrhythmic drugs (AADs).

Defragmentation	**Overall AADs**			**Class IC**			**Class III**		
	Defragmented (†*n* = 290)	**Not defragmented (†*n* = 2210)**	***P*-value**	**Defragmented (†*n* = 60)**	**Not defragmented (†*n* = 940)**	***P*-value**	**Defragmented (†*n* = 230)**	**Not defragmented (†*n* = 1270)**	***P*-value**
Mean Smax	1.254 (1.022, 1.526)	1.263 (0.923, 1.675)	0.777	1.275 (0.920, 1.509)	1.271 (0.901, 1.549)	0.894	1.238 (1.036, 1.507)	1.255 (0.941, 1.856)	0.729
Mean DF (Hz)	5.476 (1.299, 6.706)	6.913 (6.233, 7.466)	<0.001	5.770 (5.201, 6.563)	7.118 (6.527, 7.860)	0.029	5.262 (1.299, 6.640)	6.710 (5.992, 7.227)	<0.001
COV-DF (%)	141.000 (139.000, 141.000) ‡126.166 ± 33.607	141.000 (108.500, 141.000) ‡117.571 ± 39.203	<0.001	141.000 (140.750, 141.000) ‡136.285 ± 10.847	141.000 (109.750, 141.000) ‡117.432 ± 39.783	<0.001	141.000 (138.250, 141.000) ‡123.734 ± 36.821	141.000 (98.625, 141.000) ‡115.311 ± 40.276	0.008
Termination	**Overall AADs**			**Class IC**			**Class III**		
	Terminated (†*n* = 230)	**Not Terminated (†*n* = 2270)**	***P*-value**	**Terminated (†*n* = 30)**	**Not Terminated (†*n* = 970)**	***P*-value**	**Terminated (†*n* = 200)**	**Not Terminated (†*n* = 1300)**	***P*-value**
Mean Smax	1.265 (1.041, 1.437)	1.263 (0.901, 1.675)	0.704	0.812 (0.809, 1.059)	1.264 (0.900, 1.552)	0.281	1.294 (1.089, 1.481)	1.255 (0.941, 1.856)	0.885
Mean DF (Hz)	5.295 (1.299, 6.677)	6.889 (6.170, 7.465)	<0.001	5.041 (3.170, 6.896)	7.101 (6.469, 7.843)	0.385	5.476 (1.299, 6.677)	6.170 (5.507, 6.684)	0.084
COV-DF (%)	141.000 (139.500, 141.000) ‡126.312 ± 33.185	141.000 (103.000, 141.000) ‡116.545 ± 40.083	<0.001	141.000 (136.000, 141.000) ‡131.124 ± 19.179	141.000 (113.000, 141.000) ‡118.718 ± 38.890	0.199	141.000 (141.000, 141.000)	138.000 (85.750, 141.000)	<0.001

Smax, The Maximal slope of the restitution curves; DF, Dominant Frequency; COV-DF, Coefficient of Variation-Dominant Frequency.
Defragmentation: Termination + Atrial Tachycardia.
Patients who did not sustain proper normal sinus rhythm and an AF status were excluded from the analysis.
Median (IQ1, IQ3) was displayed in the Table.
†*n = The number of patients × AAD × Dose.*
‡*Mean ± SD.*

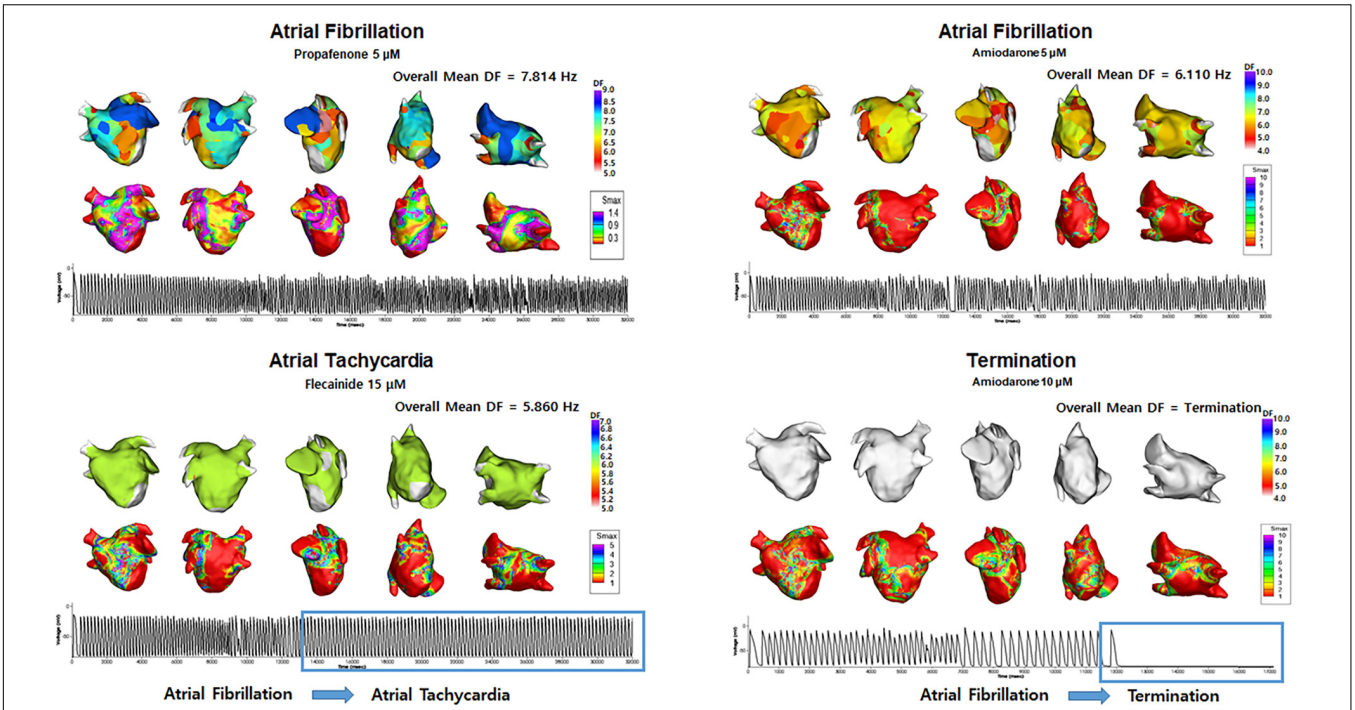

FIGURE 4 | Changes in the dominant frequency (DF) during Termination and Atrial Tachycardia. The 3D DF map indicated that the mean DF was lower during AT episodes, and AF termination episodes. Electrograms demonstrated AT and AF termination episodes.

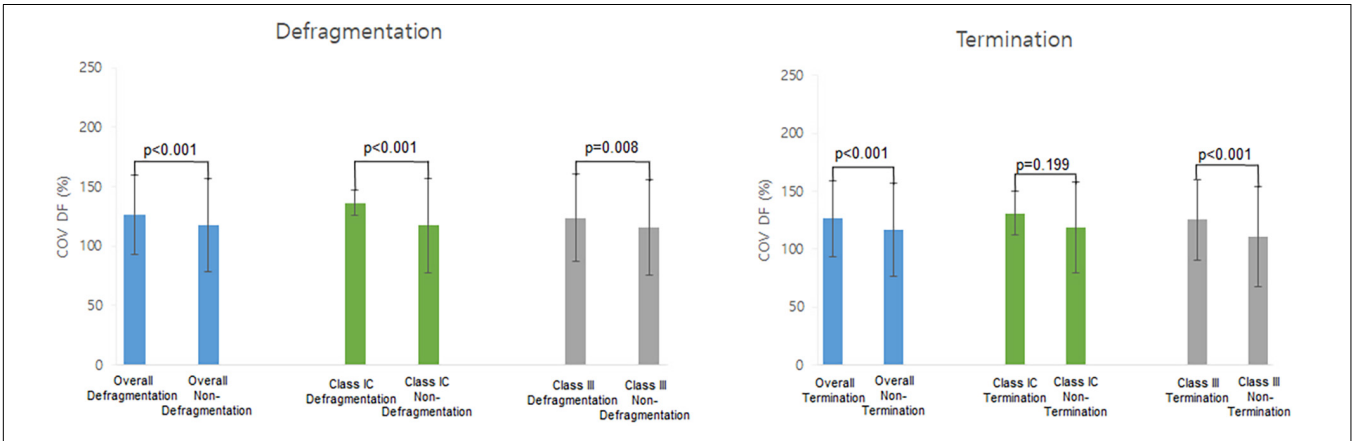

FIGURE 5 | Heterogeneity of dominant frequency (DF). Heterogeneity of DF was observed in overall defragmentation as well as termination group.

have a direct effect on the AF termination, which was presumably because the AADs did not significantly change the Smax.

Limitations

Right atrium (RA) was omitted from the study. The biatrial model is premature to be applied in personalized modeling because current image resolution cannot define the personalized interatrial connections. Heterogeneity due to nervous influence has been neglected. The fiber orientation layer was a monolayer. The LA wall thickness can be implemented to reflect a more clinically acceptable LA model. Bipolar voltage was not a feasible marker for fibrosis, and fiber orientation was not measured in a patient-specific manner. To incorporate a clinical electroanatomical map to the high-resolution computational modeling, we heavily extrapolated the limited number of bipolar electrograms. We measured DF at a fixed time window and it did not change over time. Regions especially PV specific ionic currents were not applied in this study due to lack of reference for ion currents effects of AADs on PV cells. No focal triggers were simulated in this study. The personalized LA model consisted of a monolayer. The LA wall thickness can be implemented to reflect a more clinically acceptable LA model. Multiple induction sites can reflect the complex mechanism of AF initiation (Prakosa et al., 2018).

Although there are some differences in the rate-dependent action potential changes, restitution, and calcium dynamics among different human myocardial cell models (Nygren et al., 1998; Maleckar et al., 2009; Grandi et al., 2011; Koivumäki et al., 2011), the Courtemanche-Ramirez-Nattel model (Sossalla et al., 2010; Grandi et al., 2011) accurately represented the mathematical modeling of human atrial myocyte as indicated in our previous studies (Hwang et al., 2016, 2019, 2021; Lee et al., 2016; Lim et al., 2020a,b). The ion currents conductance values might not be an accurate representation of the effects of AADs in human atrial myocytes, however, the amount of uncertainty was minimal since large mammals were selected for references (**Supplementary Table 2**). Invasive mapping data were used for the analysis. Non-invasive late gadolinium enhancement of the cardiac magnetic resonance imaging data can be used for further analysis (Lopez-Perez et al., 2015).

CONCLUSION

A DF reduction due to AADs is predominantly observed in the PV regions, and the AAD-induced low and heterogeneous DF condition during a high Smax condition was associated with AF termination or defragmentation. Personalized AF computational modeling provided evidence of how AADs exhibit anti-AF effects according to the atrial region or electrophysiological condition.

DATA AVAILABILITY STATEMENT

The original contributions presented in the study are included in the article/**Supplementary Material**, further inquiries can be directed to the corresponding author/s.

ETHICS STATEMENT

The studies involving human participants were reviewed and approved by the Institutional Review Board of the Severance Cardiovascular Hospital. The patients/participants provided their written informed consent to participate in this study.

AUTHOR CONTRIBUTIONS

IH and ZJ contributed to the data, statistical analyses, and writing of the manuscript. J-WP contributed to the statistical analyses and data acquisition. O-SK contributed to the software programming and data acquisition. BL confirmed the data acquisition and references. JL provided support for the software programming. H-TY, T-HK, and BJ contributed to the clinical data acquisition and interpretation of clinical data. H-NP contributed to the study design, clinical data acquisition, data interpretation, and revision of manuscript. All authors contributed to the article and approved the submitted version.

FUNDING

This work was supported by Grants (HI19C0114) and (HI21C0011) from the Ministry of Health and Welfare and a Grant (NRF-2020R1A2B01001695) from the Basic Science Research Program by the National Research Foundation of Korea, which is funded by the Ministry of Science, ICT and Future Planning. This work also was supported by the Brain Korea 21 PLUS Project for Medical Science, Yonsei University.

ACKNOWLEDGMENTS

We would like to thank John Martin for his linguistic assistance.

SUPPLEMENTARY MATERIAL

The Supplementary Material for this article can be found online at: https://www.frontiersin.org/articles/10.3389/fphys.2021.733543/full#supplementary-material

REFERENCES

Bai, J., Zhu, Y., Lo, A., Gao, M., Lu, Y., Zhao, J., et al. (2021). In silico assessment of class I Antiarrhythmic drug effects on Pitx2-induced atrial fibrillation: insights from populations of electrophysiological models of human atrial cells and tissues. *Int. J. Mol. Sci.* 22:1265. doi: 10.3390/ijms22031265

Cardiac-Arrhythmia-Suppression-Trial-(CAST)-Investigators (1989). Preliminary report: effect of encainide and flecainide on mortality in a randomized trial of arrhythmia suppression after myocardial infarction. *N. Engl. J. Med.* 321, 406–412. doi: 10.1056/nejm198908103210629

Chandhok, S., and Schwartzman, D. (2007). Amiodarone therapy for atrial rhythm control: insights gained from a single center experience. *J. Cardiovasc. Electrophysiol.* 18, 714–718. doi: 10.1111/j.1540-8167.2007.00847.x

Chen, J., Mandapati, R., Berenfeld, O., Skanes, A. C., Gray, R. A., and Jalife, J. (2000). Dynamics of wavelets and their role in atrial fibrillation in the isolated sheep heart. *Cardiovasc. Res.* 48, 220–232. doi: 10.1016/s0008-6363(00)00177-2

Chen, S. A., Hsieh, M. H., Tai, C. T., Tsai, C. F., Prakash, V. S., Yu, W. C., et al. (1999). Initiation of atrial fibrillation by ectopic beats originating from the pulmonary veins: electrophysiological characteristics, pharmacological responses, and effects of radiofrequency ablation. *Circulation* 100, 1879–1886. doi: 10.1161/01.cir.100.18.1879

Courtemanche, M., Ramirez, R. J., and Nattel, S. (1998). Ionic mechanisms underlying human atrial action potential properties: insights from a mathematical model. *Am. J. Physiol.* 275, H301–H321.

Darbar, D., and Roden, D. M. (2013). Genetic mechanisms of atrial fibrillation: impact on response to treatment. *Nat. Rev. Cardiol.* 10, 317–329. doi: 10.1038/nrcardio.2013.53

Grandi, E., Pandit, S. V., Voigt, N., Workman, A. J., Dobrev, D., Jalife, J., et al. (2011). Human atrial action potential and Ca2+ model: sinus rhythm and chronic atrial fibrillation. *Circ. Res.* 109, 1055–1066. doi: 10.1161/circresaha.111.253955

Hindricks, G., Potpara, T., Dagres, N., Arbelo, E., Bax, J. J., Blomström-Lundqvist, C., et al. (2021). 2020 ESC guidelines for the diagnosis and management of atrial fibrillation developed in collaboration with the European Association

for Cardio-Thoracic Surgery (EACTS): the Task Force for the diagnosis and management of atrial fibrillation of the European Society of Cardiology (ESC) developed with the special contribution of the European Heart Rhythm Association (EHRA) of the ESC. *Eur. Heart J.* 42, 373–498.

Hwang, I., Park, J.-W., Kwon, O.-S., Lim, B., Hong, M., Kim, M., et al. (2021). Computational modeling for antiarrhythmic drugs for atrial fibrillation according to genotype. *Front. Physiol.* 12:650449. doi: 10.3389/fphys.2021.650449

Hwang, M., Kim, J., Lim, B., Song, J.-S., Joung, B., Shim, E. B., et al. (2019). Multiple factors influence the morphology of the bipolar electrogram: an in silico modeling study. *PLoS Computat. Biol.* 15:e1006765. doi: 10.1371/journal.pcbi.1006765

Hwang, M., Song, J.-S., Lee, Y.-S., Li, C., Shim, E. B., and Pak, H.-N. (2016). Electrophysiological rotor ablation in in-silico modeling of atrial fibrillation: comparisons with dominant frequency, shannon entropy, and phase singularity. *PLoS One* 11:e0149695. doi: 10.1371/journal.pone.0149695

Jarman, J. W., Wong, T., Kojodjojo, P., Spohr, H., Davies, J. E., Roughton, M., et al. (2012). Spatiotemporal behavior of high dominant frequency during paroxysmal and persistent atrial fibrillation in the human left atrium. *Circ. Arrhythm. Electrophysiol.* 5, 650–658. doi: 10.1161/circep.111.967992

Kalifa, J., Tanaka, K., Zaitsev, A. V., Warren, M., Vaidyanathan, R., Auerbach, D., et al. (2006). Mechanisms of wave fractionation at boundaries of high-frequency excitation in the posterior left atrium of the isolated sheep heart during atrial fibrillation. *Circulation* 113, 626–633. doi: 10.1161/circulationaha.105.575340

Khan, R. (2004). Identifying and understanding the role of pulmonary vein activity in atrial fibrillation. *Cardiovasc. Res.* 64, 387–394. doi: 10.1016/j.cardiores.2004.07.025

Kim, D., Yang, P. S., Jang, E., Yu, H. T., Kim, T. H., Uhm, J. S., et al. (2018). 10-year nationwide trends of the incidence, prevalence, and adverse outcomes of non-valvular atrial fibrillation nationwide health insurance data covering the entire Korean population. *Am. Heart J.* 202, 20–26. doi: 10.1016/j.ahj.2018.04.017

Kirchhof, P., Camm, A. J., Goette, A., Brandes, A., Eckardt, L., Elvan, A., et al. (2020). Early rhythm-control therapy in patients with atrial fibrillation. *New Engl. J. Med.* 383, 1305–1316.

Kogawa, R., Okumura, Y., Watanabe, I., Kofune, M., Nagashima, K., Mano, H., et al. (2015). Spatial and temporal variability of the complex fractionated atrial electrogram activity and dominant frequency in human atrial fibrillation. *J. Arrhythm.* 31, 101–107. doi: 10.1016/j.joa.2014.08.004

Koivumäki, J. T., Korhonen, T., and Tavi, P. (2011). Impact of sarcoplasmic reticulum calcium release on calcium dynamics and action potential morphology in human atrial myocytes: a computational study. *PLoS Computat. Biol.* 7:e1001067. doi: 10.1371/journal.pcbi.1001067

Kowey, P. R. (1998). Pharmacological effects of antiarrhythmic drugs: review and update. *Archiv. Intern. Med.* 158, 325–332. doi: 10.1001/archinte.158.4.325

Lee, Y. S., Hwang, M., Song, J. S., Li, C., Joung, B., Sobie, E. A., et al. (2016). The contribution of ionic currents to rate-dependent action potential duration and pattern of reentry in a mathematical model of human atrial fibrillation. *PLoS One* 11:e0150779. doi: 10.1371/journal.pone.0150779

Li, C., Lim, B., Hwang, M., Song, J.-S., Lee, Y.-S., Joung, B., et al. (2016). The spatiotemporal stability of dominant frequency sites in in-silico modeling of 3-Dimensional left atrial mapping of atrial fibrillation. *PLoS One* 11:e0160017. doi: 10.1371/journal.pone.0160017

Lim, B., Kim, J., Hwang, M., Song, J.-S., Lee, J. K., Yu, H.-T., et al. (2020a). In situ procedure for high-efficiency computational modeling of atrial fibrillation reflecting personal anatomy, fiber orientation, fibrosis, and electrophysiology. *Sci. Rep.* 10:2417.

Lim, B., Park, J. W., Hwang, M., Ryu, A. J., Kim, I. S., Yu, H. T., et al. (2020b). Electrophysiological significance of the interatrial conduction including cavo-tricuspid isthmus during atrial fibrillation. *J. Physiol.* 598, 3597–3612. doi: 10.1113/jp279660

Loewe, A., Lutz, Y., Wilhelms, M., Sinnecker, D., Barthel, P., Scholz, E. P., et al. (2014). In-silico assessment of the dynamic effects of amiodarone and dronedarone on human atrial patho-electrophysiology. *Europace* 16(Suppl. 4), iv30–iv38.

Lopez-Perez, A., Sebastian, R., and Ferrero, J. M. (2015). Three-dimensional cardiac computational modelling: methods, features and applications. *Biomed. Eng.* 14:35.

Maleckar, M. M., Greenstein, J. L., Giles, W. R., and Trayanova, N. A. (2009). K+ current changes account for the rate dependence of the action potential in the human atrial myocyte. *Am. J. Physiol. Heart Circ. Physiol.* 297, H1398–H1410.

Narayan, S. M., and Jalife, J. (2014). CrossTalk proposal: rotors have been demonstrated to drive human atrial fibrillation. *J. Physiol.* 592, 3163–3166. doi: 10.1113/jphysiol.2014.271031

Niederer, S. A., Lumens, J., and Trayanova, N. A. (2019). Computational models in cardiology. *Nat. Rev. Cardiol.* 16, 100–111. doi: 10.1038/s41569-018-0104-y

Nygren, A., Fiset, C., Firek, L., Clark, J. W., Lindblad, D. S., Clark, R. B., et al. (1998). Mathematical model of an adult human atrial cell. *Circ. Res.* 82, 63–81. doi: 10.1161/01.res.82.1.63

Pandit, S. V., Berenfeld, O., Anumonwo, J. M., Zaritski, R. M., Kneller, J., Nattel, S., et al. (2005). Ionic determinants of functional reentry in a 2-D model of human atrial cells during simulated chronic atrial fibrillation. *Biophys. J.* 88, 3806–3821. doi: 10.1529/biophysj.105.060459

Park, J. H., Pak, H.-N., Choi, E. J., Jang, J. K., Kim, S. K., Choi, D. H., et al. (2009). The Relationship between endocardial voltage and regional volume in electroanatomical remodeled left atria in patients with atrial fibrillation: comparison of three-dimensional computed tomographic images and voltage mapping. *J. Cardiovasc. Electrophysiol.* 20, 1349–1356. doi: 10.1111/j.1540-8167.2009.01557.x

Pashakhanloo, F., Herzka, D. A., Ashikaga, H., Mori, S., Gai, N., Bluemke, D. A., et al. (2016). Myofiber architecture of the human atria as revealed by submillimeter diffusion tensor imaging. *Circ. Arrhythm. Electrophysiol.* 9:e004133.

Prakosa, A., Arevalo, H. J., Deng, D., Boyle, P. M., Nikolov, P. P., Ashikaga, H., et al. (2018). Personalized virtual-heart technology for guiding the ablation of infarct-related ventricular tachycardia. *Nat. Biomed. Eng.* 2, 732–740. doi: 10.1038/s41551-018-0282-2

Roney, C. H., Bendikas, R., Pashakhanloo, F., Corrado, C., Vigmond, E. J., Mcveigh, E. R., et al. (2021). Constructing a human atrial fibre atlas. *Ann. Biomed. Eng.* 49, 233–250. doi: 10.1007/s10439-020-02525-w

Roy, D., Talajic, M., Dorian, P., Connolly, S., Eisenberg, M. J., Green, M., et al. (2000). Amiodarone to prevent recurrence of atrial fibrillation. *New Engl. J. Med.* 342, 913–920.

RStudio Team (2020). *Rstudio: Integrated Development for R. RStudio*, Boston, MA: RStudio, PBC.

Saad, M. N., Morin, D. P., and Khatib, S. (2009). Atrial fibrillation: current perspective. *Ochsner. J.* 9, 241–247.

Sánchez, C., Corrias, A., Bueno-Orovio, A., Davies, M., Swinton, J., Jacobson, I., et al. (2012). The Na+/K+ pump is an important modulator of refractoriness and rotor dynamics in human atrial tissue. *Am. J. Physiol. Heart Circ. Physiol.* 302, H1146–H1159.

Shattock, M. J., Park, K. C., Yang, H.-Y., Lee, A. W. C., Niederer, S., Macleod, K. T., et al. (2017). Restitution slope is principally determined by steady-state action potential duration. *Cardiovasc. Res.* 113, 817–828. doi: 10.1093/cvr/cvx063

Sherif, H. M. (2013). The developing pulmonary veins and left atrium: implications for ablation strategy for atrial fibrillation. *Eur. J. Cardiothorac. Surg.* 44, 792–799. doi: 10.1093/ejcts/ezt098

Sossalla, S., Kallmeyer, B., Wagner, S., Mazur, M., Maurer, U., Toischer, K., et al. (2010). Altered Na+Currents in atrial fibrillation: effects of ranolazine on arrhythmias and contractility in human atrial myocardium. *J. Am. Coll. Cardiol.* 55, 2330–2342.

The-AFFIRM-Investigators (2004). Relationships between sinus rhythm, treatment, and survival in the atrial fibrillation follow-up investigation of rhythm management (AFFIRM) study. *Circulation* 109, 1509–1513. doi: 10.1161/01.cir.0000121736.16643.11

Ugarte, J. P., Tobón, C., Orozco-Duque, A., Becerra, M. A., and Bustamante, J. (2015). Effect of the electrograms density in detecting and ablating the tip of the

rotor during chronic atrial fibrillation: an in silico study. *Europace* 17(Suppl. 2), ii97–ii104.

Varela, M., Colman, M. A., Hancox, J. C., and Aslanidi, O. V. (2016). Atrial heterogeneity generates re-entrant substrate during atrial fibrillation and anti-arrhythmic drug action: mechanistic insights from canine atrial models. *PLoS Comput. Biol.* 12:e1005245. doi: 10.1371/journal.pcbi.1005245

Wang, J., Klysik, E., Sood, S., Johnson, R. L., Wehrens, X. H. T., and Martin, J. F. (2010). Pitx2 prevents susceptibility to atrial arrhythmias by inhibiting left-sided pacemaker specification. *Proc. Natl. Acad. Sci. U.S.A.* 107, 9753–9758. doi: 10.1073/pnas.0912585107

Wu, T.-J., Lin, S.-F., Weiss, J. N., Ting, C.-T., and Chen, P.-S. (2002). Two types of ventricular fibrillation in isolated rabbit hearts. *Circulation* 106, 1859–1866. doi: 10.1161/01.cir.0000031334.49170.fb

Zahid, S., Cochet, H., Boyle, P. M., Schwarz, E. L., Whyte, K. N., Vigmond, E. J., et al. (2016). Patient-derived models link re-entrant driver localization in atrial fibrillation to fibrosis spatial pattern. *Cardiovasc. Res.* 110, 443–454. doi: 10.1093/cvr/cvw073

Conflict of Interest: The authors declare that the research was conducted in the absence of any commercial or financial relationships that could be construed as a potential conflict of interest.

Publisher's Note: All claims expressed in this article are solely those of the authors and do not necessarily represent those of their affiliated organizations, or those of the publisher, the editors and the reviewers. Any product that may be evaluated in this article, or claim that may be made by its manufacturer, is not guaranteed or endorsed by the publisher.

frontiers | Frontiers in Physiology

TYPE Correction
PUBLISHED 15 December 2022
DOI 10.3389/fphys.2022.992000

OPEN ACCESS

EDITED AND REVIEWED BY
Martin Bishop,
King's College London, United Kingdom

*CORRESPONDENCE
Hui-Nam Pak,
hnpak@yuhs.ac

SPECIALTY SECTION
This article was submitted to Computational Physiology and Medicine, a section of the journal Frontiers in Physiology

RECEIVED 12 July 2022
ACCEPTED 21 November 2022
PUBLISHED 15 December 2022

CITATION
Hwang I, Jin Z, Park J-W, Kwon O-S, Lim B, Lee J, Yu H-T, Kim T-H, Joung B and Pak H-N (2022), Corrigendum: Spatial changes in the atrial fibrillation wave-dynamics after using antiarrhythmic drugs: A computational modeling study.
Front. Physiol. 13:992000.
doi: 10.3389/fphys.2022.992000

Corrigendum: Spatial changes in the atrial fibrillation wave-dynamics after using antiarrhythmic drugs: A computational modeling study

Inseok Hwang, Ze Jin, Je-Wook Park, Oh-Seok Kwon, Byounghyun Lim, Jisu Lee, Hee-Tae Yu, Tae-Hoon Kim, Boyoung Joung and Hui-Nam Pak*

Yonsei University Health System, Seoul, South Korea

KEYWORDS

atrial fibrillation, computational modeling, antiarrhythmic drug, dominant frequency, spatial changes

A Corrigendum on
Spatialc hanges in the trial fibrillation wave-dynamics after using antiarrhythmic drugs: A computational modeling study

by Hwang I, Park J-W, Kwon O-S, Lim B, Lee J, Jin Z, Yu H-T, Kim T-H, Joung B and Pak H-N (2021). Front. Physiol. 12:733543. doi: 10.3389/fphys.2021.733543

In the published article, there was an error in the **Author** list. Author "Ze Jin" was erroneously excluded. The corrected **Author** list appears below:

"Inseok Hwang, Ze Jin, Je-Wook Park, Oh-Seok Kwon, Byounghyun Lim, Jisu Lee, Hee-Tae Yu, Tae-Hoon Kim, Boyoung Joung, Hui-Nam Pak."

In the published article, there was an error in Supplementary Table S1. The ion currents for baselines and AADs were described incorrectly. The correct Supplementary Table S1 appears in the Supplementary material.

In the published article, the **Author Contributions** were described incorrectly:

"IH contributed to the data, statistical analyses, and writing of the manuscript. J-WP contributed to the statistical analyses and data acquisition. O-SK contributed to the software programming and data acquisition. BL confirmed the data acquisition and references. JL provided the support for the software programming. ZJ contributed the clinical data acquisition. H-TY, T-HK, and BJ contributed to the clinical data acquisition and interpretation of clinical data. H-NP contributed to the study design, clinical data acquisition, data interpretation, and revision of manuscript. All authors contributed to the article and approved the submitted version."

The corrected **Author Contributions** statement appears below:

"IH and ZJ contributed to the data, statistical analyses, and writing of the manuscript. J-WP contributed to the statistical analyses and data acquisition. O-SK contributed to the software programming and data acquisition. BL confirmed the data acquisition and references. JL provided support for the software programming. H-TY, T-HK, and BJ contributed to the clinical data acquisition and interpretation of clinical data. H-NP contributed to the study design, clinical data acquisition, data interpretation, and revision of manuscript. All authors contributed to the article and approved the submitted version."

The authors apologize for these errors and state that this does not change the scientific conclusions of the article in any way. The original article has been updated.

Publisher's note

Supplementary material

The Supplementary Material for this article can be found online at: https://www.frontiersin.org/articles/10.3389/fphys.2022.992000/full#supplementary-material

frontiers in Physiology

ORIGINAL RESEARCH
published: 24 September 2021
doi: 10.3389/fphys.2021.732573

In silico Identification of Disrupted Myocardial Calcium Homeostasis as Proarrhythmic Trigger in Arrhythmogenic Cardiomyopathy

Aurore Lyon[1], Chantal J. M. van Opbergen[2], Mario Delmar[2], Jordi Heijman[3†] and Toon A. B. van Veen[1†]*

[1] Division of Heart and Lungs, Department of Medical Physiology, University Medical Center Utrecht, Utrecht, Netherlands,
[2] The Leon Charney Division of Cardiology, New York University Grossmann School of Medicine, New York, NY, United States,
[3] Department of Cardiology, Cardiovascular Research Institute Maastricht, Maastricht University, Maastricht, Netherlands

OPEN ACCESS

Edited by:
Jichao Zhao,
The University of Auckland,
New Zealand

Reviewed by:
Sanjay Ram Kharche,
Western University, Canada
Shanna Hamilton,
The Ohio State University,
United States

***Correspondence:**
Aurore Lyon
a.lyon@maastrichtuniversity.nl;
a.a.p.lyon@umcutrecht.nl

† These authors share senior authorship

Specialty section:
This article was submitted to Cardiac Electrophysiology, a section of the journal Frontiers in Physiology

Received: *29 June 2021*
Accepted: *27 August 2021*
Published: *24 September 2021*

Citation:
Lyon A, van Opbergen CJM, Delmar M, Heijman J and van Veen TAB (2021) In silico Identification of Disrupted Myocardial Calcium Homeostasis as Proarrhythmic Trigger in Arrhythmogenic Cardiomyopathy. Front. Physiol. 12:732573. doi: 10.3389/fphys.2021.732573

Background: Patients with arrhythmogenic cardiomyopathy may suffer from lethal ventricular arrhythmias. Arrhythmogenic cardiomyopathy is predominantly triggered by mutations in plakophilin-2, a key component of cell-to-cell adhesion and calcium cycling regulation in cardiomyocytes. Calcium dysregulation due to plakophilin-2 mutations may lead to arrhythmias but the underlying pro-arrhythmic mechanisms remain unclear.

Aim: To unravel the mechanisms by which calcium-handling abnormalities in plakophilin-2 loss-of-function may contribute to proarrhythmic events in arrhythmogenic cardiomyopathy.

Methods: We adapted a computer model of mouse ventricular electrophysiology using recent experimental calcium-handling data from plakophilin-2 conditional knock-out (PKP2-cKO) mice. We simulated individual effects of beta-adrenergic stimulation, modifications in connexin43-mediated calcium entry, sodium-calcium exchanger (NCX) activity and ryanodine-receptor 2 (RyR2) calcium affinity on cellular electrophysiology and occurrence of arrhythmogenic events (delayed-afterdepolarizations). A population-of-models approach was used to investigate the generalizability of our findings. Finally, we assessed the potential translation of proposed mechanisms to humans, using a human ventricular cardiomyocyte computational model.

Results: The model robustly reproduced the experimental calcium-handling changes in PKP2-cKO cardiomyocytes: an increased calcium transient amplitude (562 vs. 383 nM), increased diastolic calcium (120 vs. 91 nM), reduced L-type calcium current (15.0 vs. 21.4 pA/pF) and an increased free SR calcium (0.69 vs. 0.50 mM). Under beta-adrenergic stimulation, PKP2-cKO models from the population of models ($n = 61$) showed a higher susceptibility to delayed-afterdepolarizations compared to control (41 vs. 3.3%). Increased connexin43-mediated calcium entry further elevated the number of delayed-afterdepolarizations (78.7%, 2.5-fold increase in background calcium influx). Elevated diastolic cleft calcium appeared responsible for the increased RyR2-mediated calcium leak, promoting delayed-afterdepolarizations occurrence. A reduction in RyR2

calcium affinity prevented delayed-afterdepolarizations in PKP2-cKO models (24.6 vs. 41%). An additional increase in I_{NCX} strongly reduced delayed-afterdepolarizations occurrence, by lowering diastolic cleft calcium levels. The human model showed similar outcomes, suggesting a potential translational value of these findings.

Conclusion: Beta-adrenergic stimulation and connexin43-mediated calcium entry upon loss of plakophilin-2 function contribute to generation of delayed-afterdepolarizations. RyR2 and NCX dysregulation play a key role in modulating these proarrhythmic events. This work provides insights into potential future antiarrhythmic strategies in arrhythmogenic cardiomyopathy due to plakophilin-2 loss-of-function.

Keywords: arrhythmogenic cardiomyopathy (ACM), plakophilin-2, computational modeling, calcium handling, arrhythmia

INTRODUCTION

Arrhythmogenic cardiomyopathy (ACM) is an inherited cardiac disease characterized by fibrofatty replacement of the cardiac muscle, predominantly in the right ventricle. Individuals with ACM suffer from an increased risk of ventricular arrhythmias and sudden cardiac death (SCD), often occurring in young adults during exercise, in early (asymptomatic) stages of the disease (Corrado et al., 2017). However, disease penetrance is incomplete, and imaging techniques are at present unable to detect subclinical stages of the disease (Philips and Cheng, 2016), making early detection of ACM to prevent SCD challenging (Groeneweg et al., 2015). A better understanding of the mechanisms underlying ACM is needed to identify markers of early disease and predict potential arrhythmic events.

ACM can be caused by mutations in genes coding for desmosomal proteins. Among these, one of the most affected genes is *PKP2*, coding for the protein plakophilin-2 (PKP2). PKP2 is a desmosomal protein present in the intercalated disks of cardiac cells. As such, it plays a role in cell to cell adhesion, but as a component of the connexome, it also influences various molecular pathways. A dysfunction of these mechanisms would disrupt transcriptional events in the cardiomyocyte. The consequences of PKP2 deficiency in the cardiomyocyte remain poorly known, but recent studies have shown the crucial role of PKP2 in the translation of signals originating at the cell junction into intracellular signals controlling structural and electrical cardiomyocyte components, especially connexin43 (Oxford et al., 2007), voltage-gated sodium channel (Sato et al., 2009), and calcium cycling (Cerrone et al., 2017; Austin et al., 2019). This influence on calcium homeostasis suggests a key role for PKP2 loss-of-function in arrhythmogenicity, even in absence of structural disease (Cerrone et al., 2017).

A cardiomyocyte-specific PKP2 conditional knockout (PKP2-cKO) mouse model has previously been used to study the role of PKP2 in cardiomyocyte pathophysiology, and seemed to replicate critical components of ACM disease onset and progression in humans (Cerrone et al., 2017). This model can therefore serve as helpful tool to investigate early cellular events that trigger arrhythmia upon loss of PKP2 function. Among other things, these studies have revealed that PKP2 loss-of-function promotes disruption of intracellular calcium handling, resulting in an increased susceptibility toward arrhythmias induced by beta adrenergic stimulation (Cerrone et al., 2017; van Opbergen et al., 2019). Important proarrhythmic modifications include increased permeability of connexin43 (Cx43) hemichannels for calcium ions, potentially because of a weakened intercellular adhesion, leading to an increased calcium influx into cardiomyocytes (Kim et al., 2019). In addition, a reduced expression of the ryanodine receptor (RyR2), in combination with an increased calcium sensitivity of the channel, has been reported in PKP2-cKO hearts (Kim et al., 2019). RyR2 is an important regulator of sarcoplasmic reticulum (SR) calcium release and its activity is modulated by the cytoplasmic calcium concentration (Eisner et al., 2004). Therefore, RyR2 dysfunction predisposes to spontaneous SR calcium release events, playing a key role in arrhythmogenicity (Kim et al., 2019). However, the relative contribution of these calcium-handling alterations (Cx43-permeability and RyR2 calcium leak) to arrhythmia initiation, as well as the modulatory role of BARS in this model remain incompletely understood.

Computational models provide a controlled environment to evaluate the influence of distinct parameters on cellular electrophysiology and thereby may be very helpful to uncover mechanisms contributing to the arrhythmogenicity of PKP2-cKO cardiomyocytes. Computational models have shown to be effective at providing mechanistic insights into the dysregulation of cardiomyocyte calcium-handling (Sutanto et al., 2020). Previous studies have used computer models to demonstrate the role of aberrant sodium-current kinetics in facilitating reentry-based arrhythmias upon reduced presence of PKP2 (Deo et al., 2011), or to confirm the experimentally observed calcium-handling abnormalities (Cerrone et al., 2017). However, none of these studies focused on the underlying mechanisms by which calcium-handling abnormalities due to PKP2 loss-of-function may lead to arrhythmias.

Abbreviations: ACM, arrhythmogenic cardiomyopathy; AP, action potential; APD, action potential duration; BARS, beta-adrenergic stimulation; Cx43, connexin43; DAD, delayed afterdepolarization; HF, heart failure; NCX, sodium-calcium exchanger; PKP2, plakophilin-2; PKP2-cKO, PKP2 conditional knockout; RMP, resting membrane potential; RyR2, ryanodine receptors 2; SCD, sudden cardiac death; SR, sarcoplasmic reticulum; WT, wildtype.

In this paper, we adapted a computer model of mouse cardiac electrophysiology (Morotti et al., 2014), based on recent experimental data, to better understand how BARS and increased calcium influx through Cx43 hemichannels may contribute to proarrhythmic events in PKP2-cKO cardiomyocytes. Using a population-of-models approach (Britton et al., 2013), we show the synergistic effects of BARS and Cx43-mediated calcium entry in the generation of proarrhythmic delayed-afterdepolarizations (DADs), as well as the role of RyR2 and sodium-calcium exchanger (NCX) dysregulation in modulating these events. In PKP2-cKO cardiomyocytes, an increased diastolic cleft calcium was responsible for an increased RyR2-mediated calcium leak under BARS, leading to the occurrence of DADs. Reducing the affinity of RyR2 for calcium prevented the occurrence of DADs. In addition, increasing NCX activity further reduced DAD occurrence by lowering diastolic cleft calcium levels. Similar results were obtained in a human ventricular cardiomyocyte model. These cellular data provide initial insights into potential future antiarrhythmic strategies in ACM due to loss-of-function of PKP2.

MATERIALS AND METHODS

The overall methodology is illustrated in **Figure 1**. Details are provided in the subsections below.

Experimental Calcium-Handling Data: PKP2 Conditional Knock-Out Mouse Model

Calcium imaging and patch-clamp data were obtained from previously published studies using a cardiomyocyte-specific, tamoxifen-activated, PKP2-cKO mouse model (Cerrone et al., 2017; Kim et al., 2019). Published differences in levels of proteins involved in calcium-handling, action potentials (AP) characteristics and calcium-transient properties were incorporated. In addition, the arrhythmia susceptibility upon an isoproterenol challenge was evaluated.

PKP2-cKO Computer Simulations

Computer simulations of cardiomyocyte electrophysiology were performed using a validated state-of-the-art mouse ventricular cardiomyocyte model by Morotti et al. (2014), which also incorporates BARS signaling. Experimental characteristics from PKP2-cKO mouse cardiomyocytes were modeled as described below, following the mathematical simulations presented in Cerrone et al. (2017). Calsequestrin concentration was reduced to 45.3% of its original value. The closing rate of the L-type calcium channels was reduced to 75% of its original value and the current density of the L-type calcium current to 50% of its original value. Maximal calcium flux through the RyR2 and junctional volume were adjusted to 60% of their original value to account for RyR2 decreased expression. Model changes are summarized in **Table 1**.

The effect of increased calcium influx via Cx43 hemichannels (reported in Cerrone et al., 2017; Kim et al., 2019) was assessed by varying the maximum conductance of the background calcium current (I_{CaB}). In the simulations presented here, PKP2-cKO Cx43 hemichannel-mediated calcium entry is modeled by a 1.5-fold increase in I_{CaB} (as reported in Kim et al., 2019). To assess the potential impact of this influx on electrophysiological properties, simulations without I_{CaB} increase as well as with a larger Cx43 hemichannel-mediated calcium entry (simulated as a 2.5-fold increase in I_{CaB}) were also performed. In addition, the effect of BARS on electrophysiological properties of PKP2 cardiomyocytes was modeled as described in Morotti et al. (2014).

Models were paced at 1 Hz for 500 s and AP and calcium-handling properties were recorded. The presence of DADs was quantified as secondary calcium transients with an amplitude > 100 nM after $t = 400$ ms. The model was implemented in MATLAB and solved using ODE15s and is available for download at https://github.com/aurora2093.

Population-of-Models Approach

To evaluate the generalizability of the findings from the single model, take into account the effect of inter-subject variability on the electrophysiological properties modeled in this study, and quantify the relative contribution of modulating factors involved in DAD generation, we used a population-of-models approach (Britton et al., 2013; Muszkiewicz et al., 2016). The maximum conductances of eight major ionic currents (I_{Na}, I_{NaL}, I_{CaL}, I_{Kr}, I_{K1}, I_{to}, I_{NCX}, I_{NaK}) and the activity of RyR2 and SERCA2a were scaled using Latin-hypercube sampling as previously described (Britton et al., 2013; Ledezma et al., 2018). Five-hundred models were generated, and this control population was calibrated based on AP properties. Models were considered physiological if AP duration was between 20 and 80 ms, peak membrane potential larger than 25 mV, resting membrane potential (RMP) lower than −75 mV, upstroke duration lower than 10 ms and if the membrane potential was lower than RMP + 2 mV after 400 ms. Non-physiological models were rejected. In total, 61 out of 500 models that met these criteria were included in the analysis and the PKP2 remodeling as presented in section PKP2-cKO Computer Simulations was applied to these models.

Human Model

To assess the translatability of our findings to human cellular electrophysiology, we simulated, as a proof-of-principle, the effects of the PKP2-cKO alterations detailed in section PKP2-cKO Computer Simulations in a human ventricular cardiomyocyte model. We adapted the Grandi et al. model (Grandi et al., 2010) which exhibits a similar structure as the Morotti et al. mouse model (especially in terms of RyR2 description). BARS and Cx43-mediated calcium influx were modeled as in section PKP2-cKO Computer Simulations.

Statistical Analysis

Continuous variables with normal distribution are expressed as mean ± standard deviation. Categorical variables are presented as observed number with percentage. Normally distributed data were compared using *t*-tests. Non-normally distributed data were compared using the Mann–Whitney U-test. Statistical

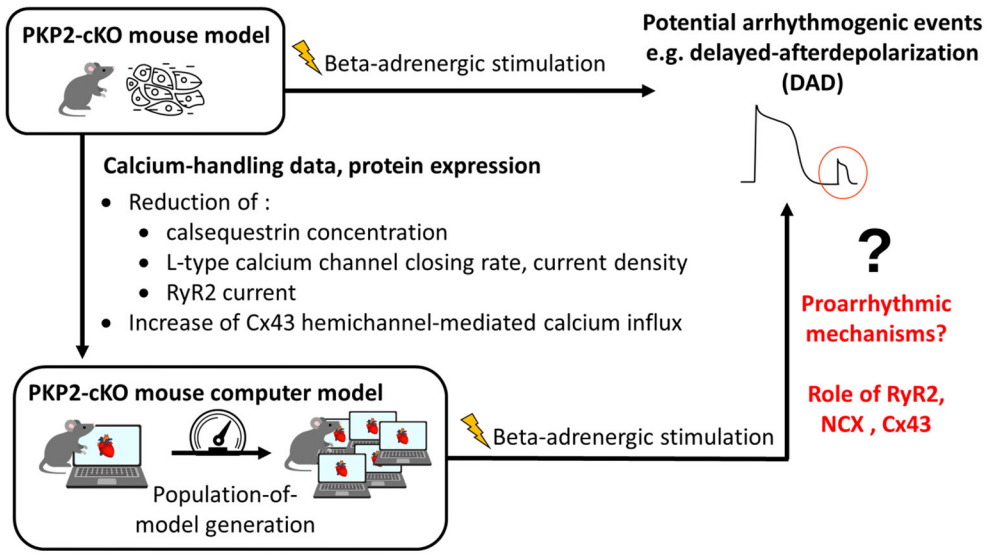

FIGURE 1 | Methodology of combining experimental data with computational modeling to understand proarrhythmic mechanisms due to loss of plakophilin-2 (PKP2). PKP2-cKO, PKP2 conditional knock-out; RyR2, ryanodine receptors 2; Cx43, connexin43; NCX, sodium-calcium exchanger.

TABLE 1 | Summary table of the parameters changed in the original model (Morotti et al., 2014) to simulate the PKP2-cKO experimental characteristics, their interpretation, their values in the original WT and PKP2-cKO model and the relative change between WT and PKP2-cKO.

Model parameter	Interpretation	WT value	PKP2-cKO value	Relative change
Vjunc	Junctional volume	1.78e-14 L	1.07e-14 L	×60%
Bmax_Csqn	Calsequestrin buffer concentration	2.7 mM	1.22 mM	×45.3%
ICa_scale	Scaling of $I_{Ca,L}$	1	0.5	×50%
r2m2	L-type calcium channel (LTCC) closing rate	0.38 ms^{-1}	0.28 ms^{-1}	×75%
ks	SR Ca release rate	25 ms^{-1}	15 ms^{-1}	×60%
kleak	SR Ca passive leak rate	1.22.10^{-05} ms^{-1}	7.32. 10^{-06} ms^{-1}	×60%

significance was assumed when $p < 0.05$. Statistical tests were performed using MATLAB.

RESULTS

The Computer Model Recapitulates Experimentally-Measured Calcium-Handling Properties

PKP2-cKO changes were incorporated in the model as described in Methods. The model was able to recapitulate the experimentally observed changes in calcium-handling properties (Cerrone et al., 2017). The PKP2 model displayed an increased calcium transient amplitude compared to control (562 vs. 383 nM), as well as increased diastolic calcium levels (120 vs. 91 nM). Peak L-type calcium current was reduced (15.0 vs. 21.4 pA/pF) and the amount of free calcium in the SR was increased (0.69 vs. 0.50 mM), due to the reduced SR calcium buffering capacity by calsequestrin (**Figure 2**). Simulations revealed that the increased background calcium influx via Cx43 hemichannels (I_{CaB}) contributed largely to the increased calcium transient amplitude, which was observed experimentally in PKP2-cKO cardiomyocytes (**Figure 3**).

Beta-Adrenergic Stimulation and Cx43-Mediated Calcium Entry Contribute to DAD Occurrence

Simulating BARS in the PKP2-cKO cell model without Cx43 calcium influx led to an increased calcium transient peak (448 vs. 355 nM), a reduction in calcium transient duration (550 vs. 681 ms) and a reduction in diastolic calcium levels (66 vs. 103 nM). In combination with an increased Cx43 calcium influx, BARS promoted spontaneous diastolic SR calcium-release events, which translated into the occurrence of DADs (occurring at $t =$ 713 ms) (**Figure 4A**, top). **Figure 4A** (bottom) shows the calcium transient and AP traces in all models from the population of models. Of note, a larger (2.5-fold instead of 1.5-fold) increase in I_{CaB} was sufficient to induce DADs in the PKP2-cKO model, even in the absence of BARS (**Figure 4B**).

Subsequently, we employed a population-of-models approach to assess the generalizability of our findings. This approach

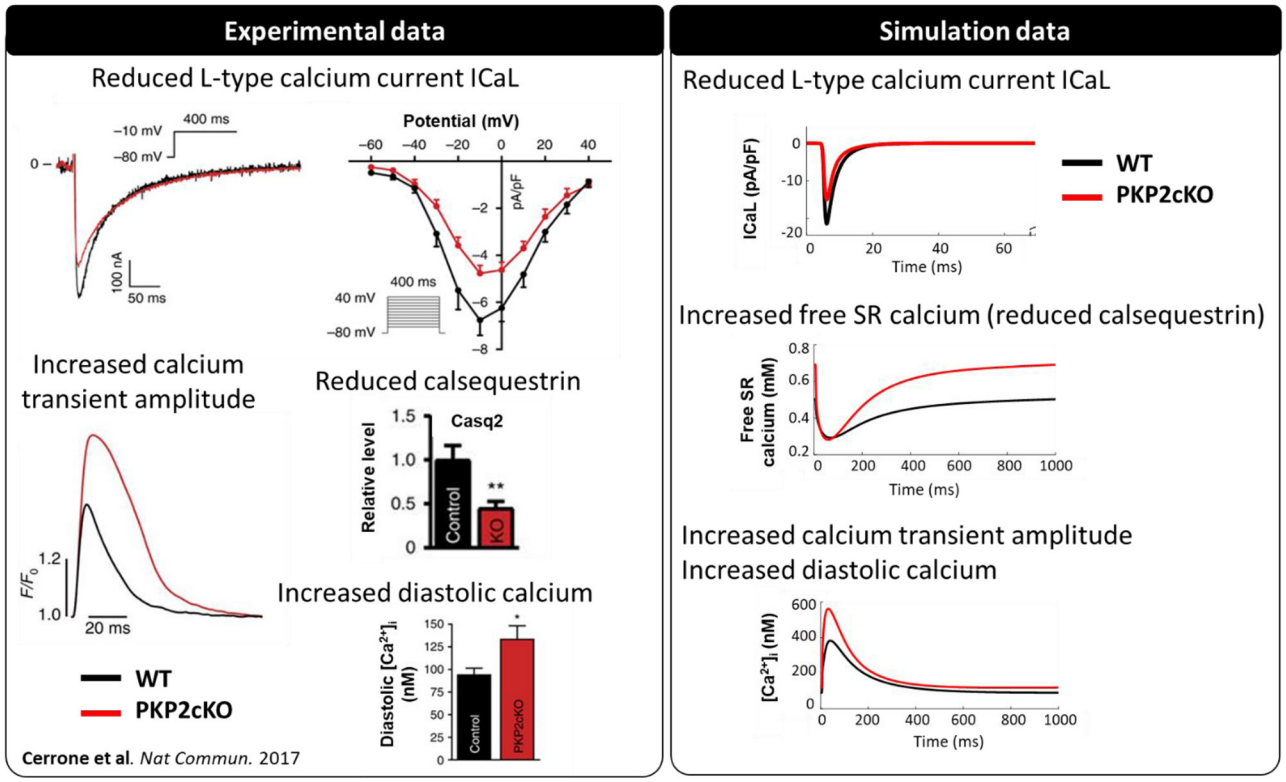

FIGURE 2 | Calcium-handling properties [L-type calcium current ($I_{Ca,L}$), calsequestrin protein levels, calcium transient and diastolic calcium concentrations] measured experimentally (modified from Cerrone et al., 2017) ($^{**}p < 0.01$) in wildtype (WT) (black) and PKP2-cKO (red) cardiomyocytes (left), and corresponding simulated data [$I_{Ca,L}$, free sarcoplasmic reticulum (SR) calcium concentration, calcium transient] (right).

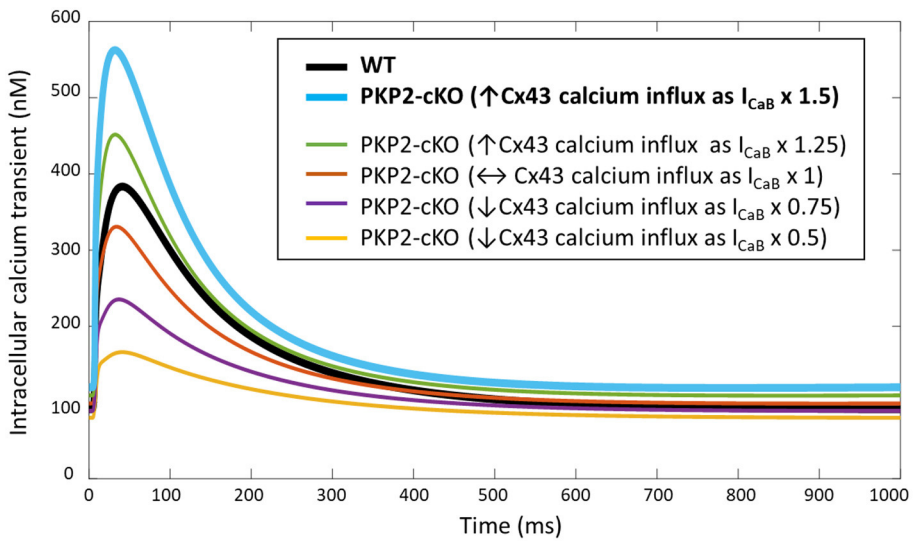

FIGURE 3 | Intracellular calcium transient in WT and PKP2-cKO models with varying scaling of I_{CaB} (1.5 – baseline model, and 1, 0.5, 0.75, 1.25), to mimic different magnitudes of background calcium influx *via* Cx43 hemichannels.

confirmed the synergistic effects of BARS and increased Cx43-mediated calcium entry on the occurrence of DADs. At baseline, DADs were observed in 3.3% ($n = 2$) of control models and 13.1% ($n = 8$) of PKP2-cKO models without Cx43 calcium influx. Under BARS, 11.4% ($n = 7$) of controls and 16.4% ($n = 10$) of the PKP2-cKO models without Cx43 calcium influx showed DADs.

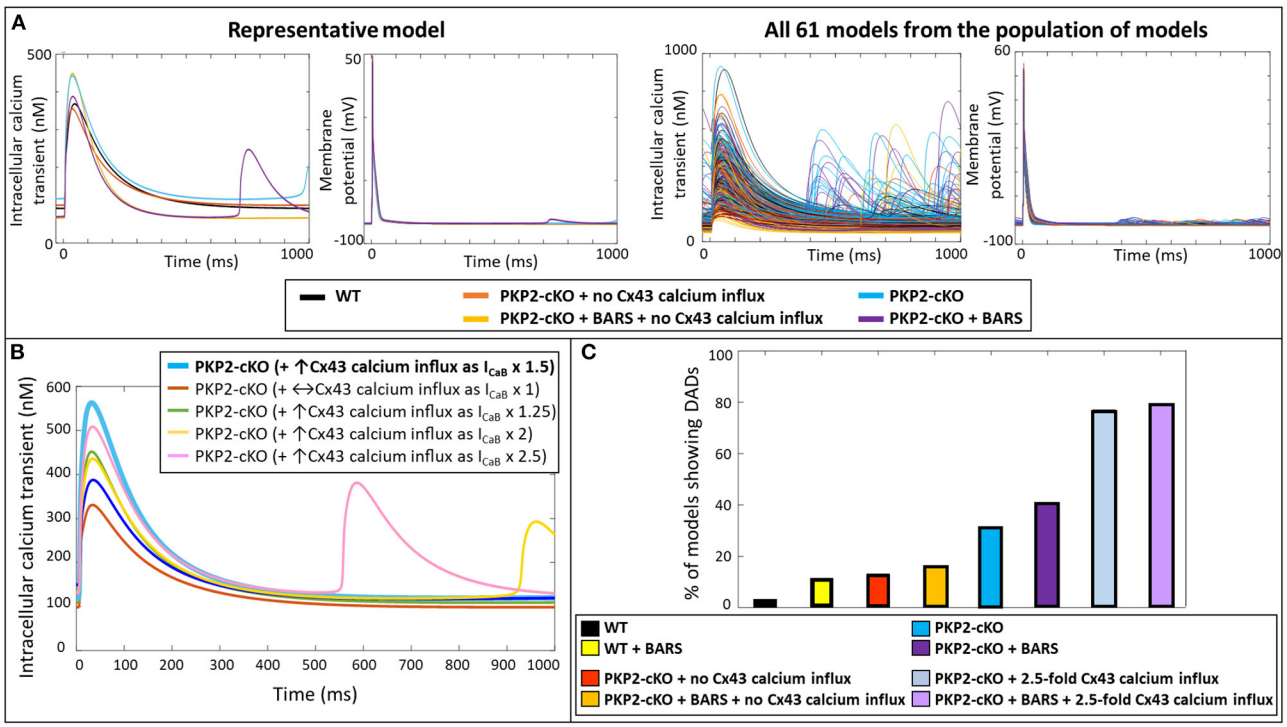

FIGURE 4 | (A) Top: Representative calcium transient and membrane potential traces of the wildtype (WT) and PKP2-cKO model, with and without BARS and the PKP2-cKO model with no Cx43 hemichannels-mediated calcium influx, with and without BARS. Please note the occurrence of a DAD-like event in the presence of PKP2-cKO under BARS (purple line) but absence of these events without Cx43 hemichannels-mediated calcium influx. Bottom: Calcium transient and membrane potential traces for all models from the population of models in the five situations described above. **(B)** Calcium transient in PKP2-cKO models with various increments of Cx43 hemichannel-mediated calcium influx showing the occurrence of DADs from I_{CaB} x 2. **(C)** Percentage of models showing DADs under control (wildtype, WT) conditions with and without BARS, PKP2-cKO conditions with no Cx43 hemichannel-mediated calcium influx with and without BARS, PKP2-cKO conditions (1.5-fold increase in Cx43 hemichannel-mediated calcium influx) with and without BARS, and PKP2-cKO conditions in addition of an even larger increase in Cx43 hemichannel-mediated calcium influx (2.5-fold) with and without BARS.

Upon a 1.5-fold increased Cx43 hemichannel mediated calcium influx, 31.2% ($n = 19$) of the PKP2-cKO models showed DADs, vs. 41% ($n = 25$) under BARS (**Figure 4C**). With an even larger increase in calcium influx (2.5-fold), the contribution of BARS to the occurrence of DADs became smaller (77.1%, $n = 47$ without BARS vs. 78.7%, $n = 48$ with BARS).

Ryanodine Receptor Dysfunction Contributes to the Occurrence of DADs

Using the ability of computer modeling to investigate the contribution of individual parameters in the model, we compared the specific configurational changes in RyR2 states (inactive, open, recovered) at the onset of the DAD between control and PKP2-cKO with BARS. The RyR2 open probability was increased in the PKP2-cKO model compared to control, leading to an increased RyR2-mediated SR calcium leak. This resulted in increased cleft calcium levels, which in turn promoted further RyR2 opening, spontaneous SR calcium release events and the appearance of the DADs (**Figure 5A**).

To confirm the causal link between RyR2 hyperactivity and PKP2-cKO-related calcium-handling abnormalities, we reduced the RyR2 calcium affinity by 80% in our population of models, thereby lowering the sensitivity of RyR2 channels to increased cleft calcium concentrations. This reduction led to a decrease in the number of models that showed DADs (**Figure 5B**). This was effective in PKP2-cKO models with BARS without Cx43 calcium influx (6.6%, $n = 4$ vs. 16.4%, $n = 10$), in the PKP2-cKO models with BARS (1.5-fold increased Cx43 hemichannel-mediated calcium influx) (24.6%, $n = 15$ vs. 41%, $n = 25$), as well as in the PKP2-cKO models with BARS plus an even larger (2.5-fold) increase in Cx43 hemichannel-mediated calcium influx (54.1%, $n = 33$ vs. 78.7%, $n = 48$). **Figure 5C** shows a representative example of the effect of reducing RyR2 calcium affinity on calcium transient characteristics, clearly preventing DADs.

Reduced NCX Activity Promotes DADs by an Increase in Diastolic Cleft Calcium

To further understand why the reduction in RyR2 calcium affinity did not remove the occurrence of DADs in all models with elevated Cx43 hemichannel-mediated calcium influx (2.5-fold) (54.1%, $n = 33$, **Figure 5B**), we analyzed the parameters that varied during the construction of the population of models. We compared the models in which reducing RyR2 calcium affinity removed the occurrence of DADs (RyR2-sensitive), with

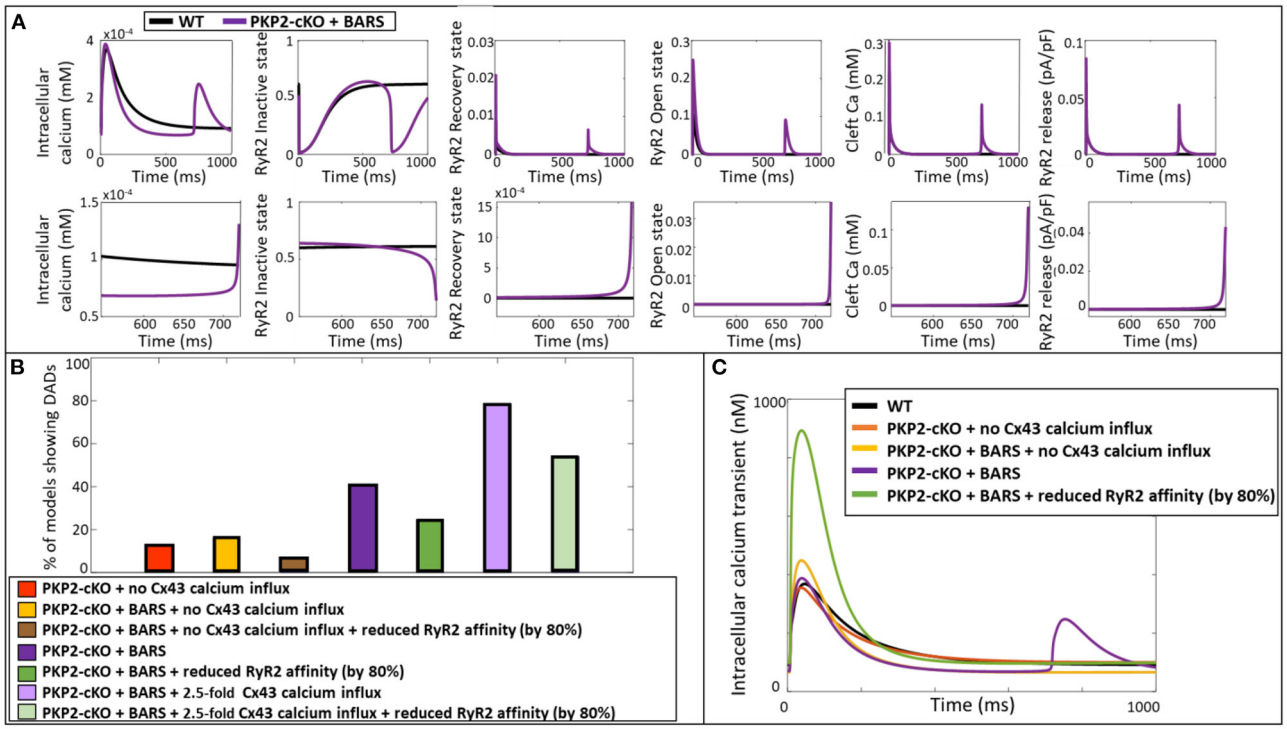

FIGURE 5 | (A) Representation of the intracellular calcium transient, RyR2 configuration (inactive, recovery and open state), cleft calcium levels and RyR2-mediated calcium release in the wildtype model (blue) and PKP2-cKO model with BARS (1.5-fold Cx43 hemichannel-mediated calcium influx incorporated) (purple). Bottom: Zoom-in on the zone of DAD occurrence. **(B)** Percentage of models showing DAD-like events when comparing PKP2-cKO model with no Cx43 hemichannel-mediated calcium influx with and without BARS, with or without reduced RyR2 affinity, PKP2-cKO model plus BARS (1.5-fold Cx43 hemichannel-mediated calcium influx incorporated), with or without reduced RyR2 affinity, as well as the PKP2-cKO model plus BARS and 2.5-fold Cx43 hemichannel-mediated calcium influx, with or without reduced RyR2 affinity. **(C)** Representative calcium transient traces of the different models. Please note the disappearance of DADs when reducing the RyR2 calcium affinity in the PKP2-cKO model in presence BARS (1.5-fold Cx43 hemichannel-mediated calcium influx still incorporated).

the models that still exhibited a DAD after a reduction in RyR2 calcium affinity (RyR2-insensitive). Significant parameter differences were observed in the scaling multipliers of RyR2 ($p = 0.004$, **Figure 6A**) and I_{NCX} ($p < 0.001$, **Figure 6A**). RyR2-insensitive models had a lower I_{NCX} maximum conductance multiplier compared to the RyR2-sensitive models (0.72 ± 0.15 vs. 1.18 ± 0.21, $p < 0.001$), suggesting an additional and modulating role for NCX in development of spontaneous SR calcium release events.

To analyze the role of NCX in modulating the occurrence of spontaneous calcium releases and DADs in the PKP2-cKO model plus BARS (including 1.5 fold Cx43 hemichannel-mediated calcium influx), we doubled I_{NCX} in the models from the RyR2-insensitive group. This greatly reduced the number of models showing DADs; 3.3% ($n = 2$), upon doubled I_{NCX} vs. 54.1% ($n = 33$), with RyR2 calcium affinity reduction only). In line with this observation, a 50% reduction in I_{NCX} in RyR2-sensitive models greatly increased the occurrence of spontaneous calcium releases (83.6%, $n = 51$, **Figure 6B**).

We analyzed the mechanisms by which an increase in I_{NCX} may help to reduce the occurrence of spontaneous calcium releases by comparing the diastolic cleft calcium concentration with and without an increase in I_{NCX}. Diastolic cleft calcium level was much lower with increased I_{NCX} (471 ± 150 nM), compared to baseline I_{NCX} (758 ± 195 nM; **Figure 7A**), suggesting that an NCX-mediated lowering of diastolic cleft calcium level underlies the potential antiarrhythmic effects of increased NCX. In agreement, **Figure 7B** shows the relationship between diastolic calcium levels and likelihood of DADs in the various situations [PKP2-cKO with BARS without Cx43 calcium influx, PKP2-cKO with BARS (1.5-fold Cx43 hemichannel-mediated calcium influx), PKP2-cKO with BARS, 1.5-fold Cx43 calcium influx and reduced RyR2 calcium affinity, and PKP2-cKO with BARS, 1.5-fold calcium influx, reduced RyR2 calcium affinity and increased NCX]. This analysis revealed an increased occurrence of DADs with larger diastolic calcium levels (78.7% at 799 nM in PKP2-cKO plus BARS and 1.5-fold Cx43-mediated calcium influx vs. 3.3% at 473 nM in PKP2-cKO plus BARS, 1.5-fold calcium influx, reduced RyR2 calcium affinity and increased I_{NCX} in RyR2-insensitive models, correlation coefficient $r = 0.861$). A reduction in RyR2 calcium affinity and an increase in I_{NCX} apparently facilitate a reduction in diastolic cleft calcium level, thereby reducing the number of models showing DADs.

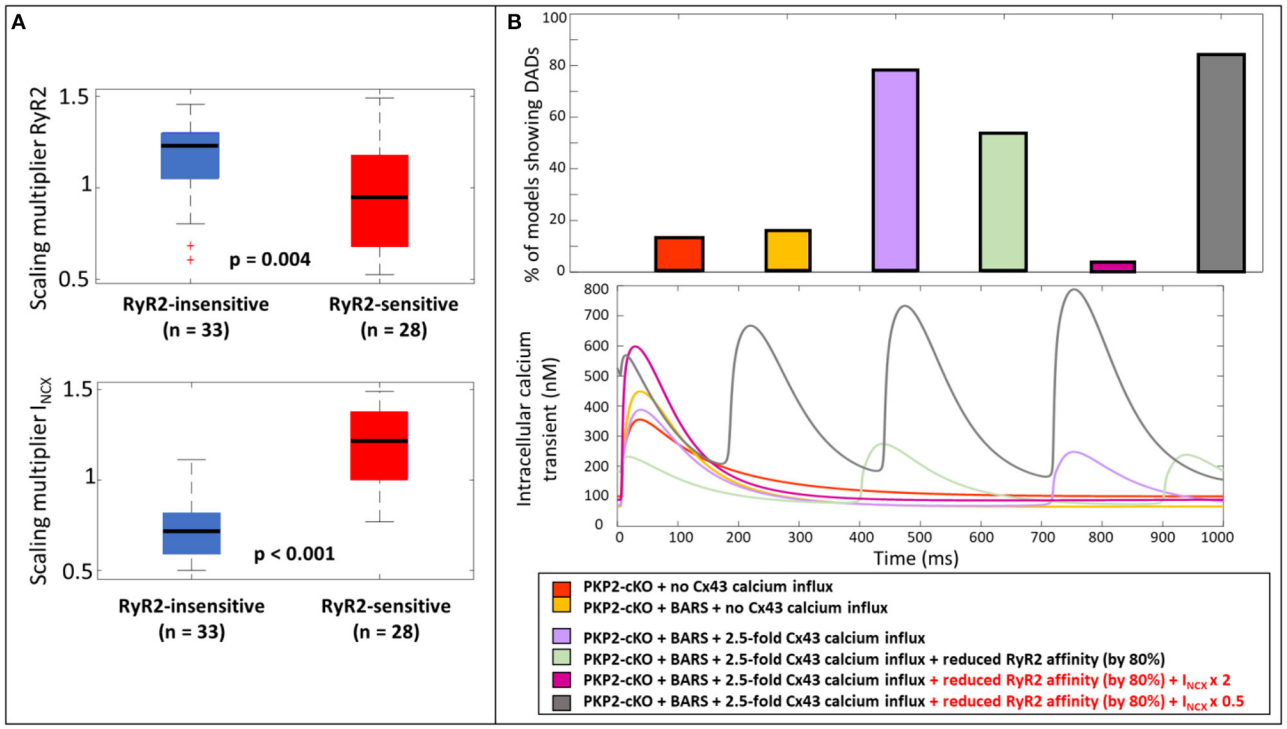

FIGURE 6 | (A) Scaling multiplier of RyR2 and I_{NCX} between models that still show DADs after a reduction in RyR2 calcium affinity (RyR2-insensitive, blue) and the ones who do not show DADs after reduction (RyR2-sensitive, red). **(B)** Percentage of models showing DADs when comparing; the PKP2-cKO model with no Cx43 hemichannel-mediated calcium influx, PKP2-cKO model plus BARS (1.5-fold Cx43 hemichannel-mediated calcium influx incorporated), with or without reduced RyR2 affinity, the PKP2-cKO model plus BARS (1.5-fold Cx43 hemichannel-mediated calcium influx), with or without reduced RyR2 activity, doubled I_{NCX} in the RyR2-insensitive group or a 50% reduction of I_{NCX} in the RyR2-sensitive group (top); the corresponding calcium traces (bottom).

Translation to Humans

As a proof-of-principle for the translational relevance of our computational findings, based on experimental mouse data, for human ACM pathophysiology, we incorporated the measured PKP2-cKO changes in a human ventricular cardiomyocyte computer model. Increasing the Cx43 hemichannel-mediated calcium entry in WT (via an increase in I_{CaB}) modulated the amplitude of the the calcium transient, like in the mouse. However, contrary to the mouse model, a 2.5-fold increase in I_{CaB} did not lead to an increased calcium transient amplitude in the human PKP2-cKO model, compared to control (**Figure 8A**). Under BARS and increased Cx43 hemichannel-mediated calcium entry (5-fold increase in I_{CaB}), DADs occurred (yellow trace, **Figure 8B**). A reduction in RyR2 calcium affinity removed the DADs (purple trace) but increased the amplitude of the calcium transient considerably. An increase in NCX activity (2-fold) also removed the DADs, as seen in the murine PKP2-cKO computational model.

DISCUSSION

Pathophysiological remodeling of the heart is a complex orchestration of molecular alterations which, together, gradually may deteriorate normal performance toward heart failure (HF). The magnitude and importance of different underlying molecular mechanisms often changes during the transition toward HF, which makes it extremely difficult to pinpoint the most relevant ones for cardiac deterioration. This also applies to pathological alterations in the cardiac calcium homeostasis that gradually compromise contractility, but also enhance the susceptibility to arrhythmias. Pathophysiological mechanisms are often studied using experimental models like (transgenic) mice or human induced pluripotent stem cells-derived cardiomyocytes. In previous studies we have used the PKP2-cKO mouse model to study the endophenotype of PKP2 and ACM disease progression. This work identified disturbed calcium homeostasis as a major contributor toward cardiac arrhythmias in the early stage of the disease, and disease progression in general. To better understand and specify the molecular events contributing to the disturbed calcium handling in these cardiomyocytes, we employed the computational approach described in the current study. Using a combination of mouse-specific computer modeling and experimental data obtained from the PKP2-cKO mouse model, our work highlights the contribution of BARS and Cx43 hemichannel-mediated calcium entry in the generation of proarrhythmic DADs in this mouse model. Our simulations uncovered RyR2 and NCX dysregulation as important modulators of these proarrhythmic events. In PKP2-cKO cardiomyocytes, an increased diastolic

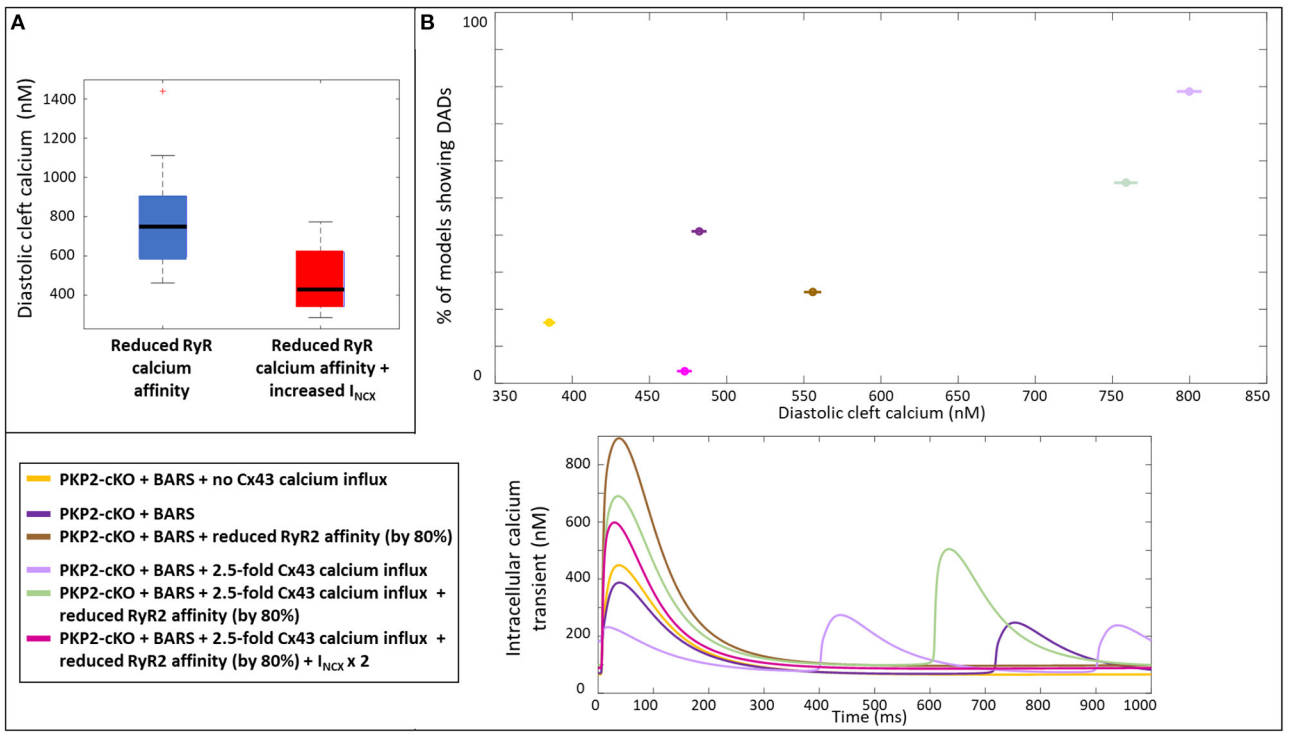

FIGURE 7 | (A) Diastolic cleft calcium levels upon a reduced RyR2 calcium affinity (blue) and on top of that an increased I_{NCX} (red). **(B)** Percentage of models showing DADs, plotted against the diastolic cleft calcium levels presented for six different situations in the PKP2-cKO model (top); Corresponding calcium traces (bottom).

cleft calcium was responsible for an increased RyR2-mediated calcium leak, leading to the occurrence of DADs. Reducing the affinity of RyR2 for cytosolic calcium prevented the occurrence of DADs. In addition, a further increase in NCX activity reduced the likelihood of DADs, by lowering the Cx43 hemichannel-mediated elevation of diastolic cleft calcium level. These cellular data provide initial insights into potential future antiarrhythmic strategies in ACM, due to loss-of-function of PKP2.

PKP2-cKO Cellular Changes Are Captured by the Computer Model and the Population-of-Models Approach Captures Cell Variability

Our computer model convincingly reproduced the cellular changes measured in the PKP2-cKO mouse model; a reduced L-type calcium current, increased SR calcium load, increased calcium transient amplitude and increased diastolic calcium levels. Our simulations suggested that Cx43 hemichannel-mediated calcium entry is a key modulator of calcium transient amplitude in PKP2-cKO computational models. An increased Cx43 hemichannel-mediated calcium entry upon loss-of-function of PKP2 in mice has been demonstrated in previous studies (Kim et al., 2019; van Opbergen et al., 2019) and is likely the result of a disrupted cell-to-cell adhesion and/or orphan Cx43 hemichannels, allowing influx of calcium into the cardiomyocytes.

Interestingly, the effects of this Cx43 hemichannel related calcium entry were different in the human model, likely due to inter-species differences in cellular electrophysiology (discussed in more detail in section Translation to Human). The population-of-models approach allowed us to assess the generalizability of our findings by generating 61 different models with slightly varying baseline electrophysiological properties. This helped us to uncover an additional and potential key role for NCX by comparing the electrophysiological properties of the models that did, and those that did not, respond to a RyR2 calcium affinity reduction, and linked that to the occurrence of DADs.

BARS and Cx43 Hemichannels-Mediated Calcium Entry Contribute to Arrhythmogenicity by PKP2-cKO

BARS and Cx43 hemichannel-mediated calcium entry both contributed to arrhythmogenic events in the PKP2-cKO computational models. This was illustrated by the number of models showing DADs under the conditions of PKP2-cKO plus BARS with and without Cx43 hemichannel-mediated calcium entry. This is in agreement with an enhanced susceptibility to isoproterenol induced arrhythmias in PKP2-cKO hearts (Kim et al., 2019). Cx43-mediated calcium entry had a larger contribution to the number of DADs than BARS, with a smaller increase in DAD occurrence with BARS in the presence of large Cx43-mediated calcium entry (2.5-fold increase in I_{CaB}). In agreement, a large (2-fold) increase in Cx43-mediated calcium

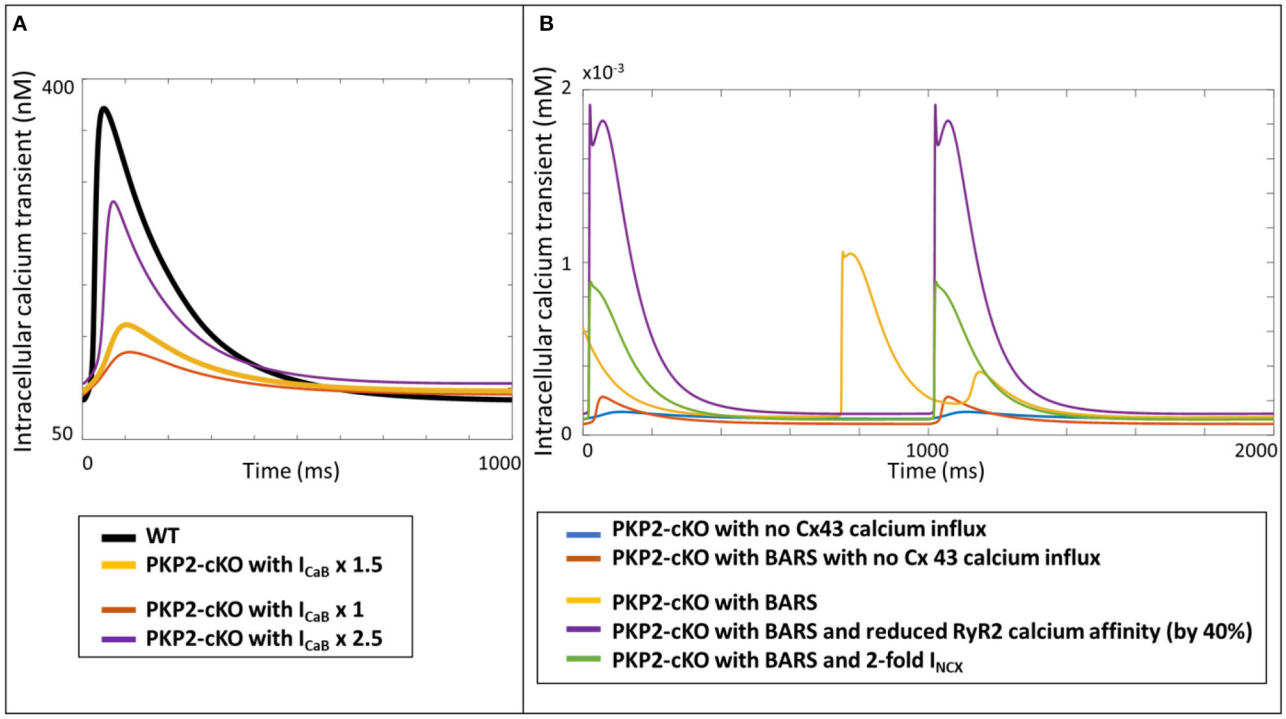

FIGURE 8 | (A) Calcium transients in the human WT, PKP2-cKO and PKP2-cKO model, with various increments of Cx43 hemichannels-mediated calcium entry, applied in the Grandi human ventricular cardiomyocyte model. **(B)** Calcium transients in the PKP2-cKO model with no Cx43 calcium influx with and without BARS, and PKP2-cKO model plus BARS, RyR2 calcium affinity reduction and increased I_{NCX}.

entry was sufficient to induce DADs even in the absence of BARS. This is in line with the experimental data reported in Kim et al. (2019), showing a larger amount of early and delayed after-transients in PKP2-cKO cardiomyocytes, even in the absence of BARS. This role of Cx43 hemichannel-mediated calcium entry in PKP2-cKO arrhythmogenesis is also consistent with recent studies showing its pro-arrhythmic effect (van Opbergen et al., 2019), and has been reported in other conditions such as heart failure (Smet et al., 2021) and muscular dystrophy (Patrick Gonzalez et al., 2015). Importantly, blocking Cx43 hemichannels with GAP19 normalized intracellular calcium homeostasis and reduced the occurrence of calcium sparks in PKP2-cKO cardiomyocytes (Kim et al., 2019), confirming the proarrhythmic effects of Cx43-mediated calcium entry.

RyR2 and NCX Dysfunction Modulate the Occurrence of DADs in PKP2-cKO Models by Increasing Diastolic Calcium Levels

In the simulations, DADs occurred as a direct consequence of RyR2 dysfunction. The RyR2 open probability was increased in the PKP2-cKO model compared to control, leading to an increased RyR2-mediated SR calcium leak. Resulting from that, the diastolic cleft calcium levels were increased, promoting further opening of RyR2 channels, spontaneous SR calcium release and the development of DADs. Our modeling confirmed that a reduction in the calcium affinity of RyR2 decreased the number of PKP2-cKO models showing DADs, even back to baseline values.

A reduction in RyR2 calcium affinity was not sufficient to remove all DADs when the magnitude of Cx43 hemichannel calcium entry was so large that DADs occurred without BARS. An increase in I_{NCX}, however, reduced the diastolic cleft calcium levels and removed any remaining DADs. Our previous experimental studies did not discover changes in I_{NCX}, NCX protein levels and NCX mRNA levels in PKP2-cKO hearts (Kim et al., 2019). However, the population-of-models approach uncovered that NCX dysfunction, in addition to electrophysiological remodeling upon loss-of-function of PKP2, may act as a potential additional proarrhythmogenic factor. In a more general setting of HF, both unchanged and enhanced activity have been reported (Flesch et al., 1996; Schwinger et al., 1999; Sipido et al., 2002). Interestingly, unchanged NCX activity was associated with diastolic dysfunction whereas diastolic function in the case of enhanced NCX activity remained normal (Hasenfuss et al., 1999). This suggests that an enhanced NCX activity may be a biological compensatory mechanism to temper calcium handling dysregulation in the heart (Louch et al., 2010), substantiating our computational findings in this regard.

In our simulations, the DADs observed in PKP2-cKO cells originated from increased diastolic calcium levels. Thus, reducing the RyR2 calcium affinity and increasing I_{NCX} helped lowering diastolic calcium and preventing the occurrence of DADs. Increasing I_{NCX} was particularly powerful in reducing diastolic

calcium levels, even removing DADs in the models that did not respond to the RyR2 inhibition alone. This highlights the complementary effects of reducing both the cytosolic influx of calcium from the SR (RyR2 effect) and normalizing diastolic cleft calcium levels (NCX effect). Interestingly, no particular role of intracellular sodium was found in our simulations, reinforcing the influence of calcium handling disturbances in arrhythmogenicity induced by loss-of-function of PKP2.

Translation to Human

In order to investigate the translational value of our findings in mouse models, to human pathophysiology of ACM, we introduced the PKP2-cKO alterations in our human computational electrophysiology model. These simulations suggested that the mechanisms presented in this study have potential translational value, in spite of differences between murine and human electrophysiology. We observed that in human the calcium amplitude remained lower in the PKP2-cKO model, compared to control, despite an increased Cx43 hemichannel-mediated calcium entry. This could be caused by a difference in the balance in transsarcolemmel (I_{CaL} and NCX) and SR (SERCA) calcium fluxes between mice and human. Reducing I_{CaL} had more impact on the calcium transient amplitude in the PKP2-cKO human model, because I_{CaL} has a more profound role in calcium entry in human cardiomyocytes when compared to that in mice (Bers, 2008). However, despite these inter-species differences, the simulations showed that DADs caused by BARS and Cx43 hemichannel-mediate calcium entry were suppressed by a reduction in RyR2 calcium affinity, similar to what was shown in the mouse models. This suggests that the mechanisms presented here potentially translate to humans, which could open doors for future clinical management of patients with ACM. These results also reinforce the potential of computer modeling in translating experimental findings to patients, thereby hopefully bridging the gap in knowledge regarding the molecular mechanisms involved in the pathogenesis of ACM in humans. The latter being obviously compromised by the fact that human cardiac specimen to study these molecular alterations are virtually absent, especially when it comes to patients in the concealed phase of the disease, who might be at high risk for major arrhythmic events and SCD.

Clinical Impact

Here, we propose a role for RyR2 dysfunction and NCX modulation as potential targets for the prevention/treatment of arrhythmias resulting from loss of PKP2 function. We suggest that a reduction in the calcium affinity of RyR2 and an increase in NCX activity may help to reduce the occurrence of arrhythmogenic events. This can have implications for potential therapeutic strategies, for example drugs modulating RyR2 activity, such as ent-*verticilide* (Batiste et al., 2019). Interestingly, our simulations suggest an additional anti-arrhythmic role for NCX stimulators, which would inhibit the reverse-mode of NCX. This could be further investigated experimentally in the PKP2-cKO mice. This is in agreement with previous studies reporting a cardioprotective effect of NCX stimulatory drugs like flecainide, although flecainide also is known to modulate RyR2 and the sodium current (Watanabe, 2019). Flecainide was effective in suppressing arrhythmic events through direct modulation of I_{NCX} in Andersen-Tawil syndrome-induced pluripotent stem cells-derived cardiomyocytes (Kuroda et al., 2017). Interestingly, patients with ACM do respond positively to flecainide (Ermakov et al., 2017; Bouvier et al., 2018) and this is current subject of an ongoing clinical trial (Zareba, 2021). This highlights the potential effect of the drug on calcium handling disturbances and includes modulation of NCX as a potential antiarrhythmic mechanism. In addition, our simulations suggested that Cx43-mediated calcium entry may be a major proarrhythmic trigger. Correcting this increased calcium entry could therefore be an additional potential therapeutic strategy.

Limitations and Future Directions

In the simulations, we mimicked Cx43 hemichannel-mediated calcium entry by an increase in background calcium current. This reproduced a general entry of calcium in the cell, but the localization of the channel, residing in the perimeter of the gap junctions, as well as the entry of other ions like sodium were not included in the model. Future work may focus on describing in more detail the action of Cx43 hemichannels to investigate the influence of potential other factors (dynamically regulating calcium entry) in the mechanisms proposed here.

In addition, a thorough analysis of the mechanisms in humans is beyond the scope of this study, but our simulations show a promising translation of the mechanisms we propose here to human. Future work will focus on investigating the role of BARS, Cx43-mediated calcium entry, RyR2 and NCX dysfunction in humans. Finally, these results provide insights in cellular proarrhythmic events in PKP2 loss-of-function, but arrhythmias are inherently multicellular phenomena and extrapolation across these spatial scales remains challenging and beyond the scope of the current study.

CONCLUSIONS

Using computer modeling combined with experimental data from mouse models, we uncovered the contribution of BARS and Cx43 hemichannel-mediated calcium entry in generation of proarrhythmic DADs in the PKP2-cKO model. In these cardiomyocytes, an increased diastolic cleft calcium was responsible for increased RyR2-mediated calcium leak, leading to the occurrence of DADs. A reduction in RyR2 calcium affinity prevented the occurrence of DADs and an increased NCX activity further reduced DAD occurrence by lowering diastolic cleft calcium levels. By uncovering additional mechanisms underlying arrhythmogenicity in PKP2-cKO cardiomyocytes, this work provides potential insights into future antiarrhythmic strategies in ACM due to dysfunction of PKP2.

DATA AVAILABILITY STATEMENT

The datasets presented in this study can be found in online repositories. The names of the repository/repositories and

accession number(s) can be found at: https://github.com/aurora2093/FrontiersinPhysiology2021_PKP2.

AUTHOR CONTRIBUTIONS

AL, JH, and TV conceived the study, performed the data analysis, and drafted the manuscript. AL performed the computational simulations. MD, CO, and TV generated the used experimental data. AL, CO, MD, JH, and TV critically revised the manuscript. All authors approved the final version.

FUNDING

This work was supported by Netherlands Cardiovascular Research Initiative: an initiative with support of the Dutch Heart Foundation (CVON 2015-12 eDETECT. 2018-30 PREDICT2 to TV), by a grant from the UU-3R Stimulation Fund (to AL), by NIH grants RO1-HL134328, RO1-HL136179 and RO1-HL145911 (MD), a Transatlantic Network of Excellence from the Leducq Foundation (MD), the Wilton W. Webster Fellowship in Pediatric Electrophysiology from Heart Rhythm Society (CO) and by the Netherlands Organization for Scientific Research NWO/ZonMW Vidi 09150171910029 to JH.

REFERENCES

Austin, K. M., Trembley, M. A., Chandler, S. F., Sanders, S. P., Saffitz, J. E., Abrams, D. J., et al. (2019). Molecular mechanisms of arrhythmogenic cardiomyopathy. *Nat. Rev. Cardiol.* 16, 519–537. doi: 10.1038/s41569-019-0200-7

Batiste, S. M., Blackwell, D. J., Kim, K., Kryshtal, D. O., Gomez-Hurtado, N., Rebbeck, R. T., et al. (2019). Unnatural verticilide enantiomer inhibits type 2 ryanodine receptor-mediated calcium leak and is antiarrhythmic. *Proc. Natl. Acad. Sci.* 116, 4810–4815. doi: 10.1073/pnas.1816685116

Bers, D. M. (2008). Calcium cycling and signaling in cardiac myocytes. *Annu. Rev. Physiol.* 70, 23–49. doi: 10.1146/annurev.physiol.70.113006.100455

Bouvier, F., Maupain, C., Roche, N. C., Fiorina, L., Poindron, D., Moini, C., et al. (2018). Effectiveness and safety of flecainide in arrhythmogenic right ventricular cardiomyopathy. *Arch. Cardiovasc. Dis. Suppl.* 10, 98–99. doi: 10.1016/j.acvdsp.2017.11.260

Britton, O. J., Bueno-Orovio, A., Van Ammel, K., Lu, H. R., Towart, R., Gallacher, D. J., et al. (2013). Experimentally calibrated population of models predicts and explains intersubject variability in cardiac cellular electrophysiology. *Proc. Natl. Acad. Sci. U. S. A.* 110, E2098–2105. doi: 10.1073/pnas.1304382110

Cerrone, M., Montnach, J., Lin, X., Zhao, Y.-T., Zhang, M., Agullo-Pascual, E., et al. (2017). Plakophilin-2 is required for transcription of genes that control calcium cycling and cardiac rhythm. *Nat. Commun.* 8:106. doi: 10.1038/s41467-017-00127-0

Corrado, D., Link, M. S., and Calkins, H. (2017). Arrhythmogenic right ventricular cardiomyopathy. *N. Engl. J. Med.* 376, 61–72. doi: 10.1056/NEJMra1509267

Deo, M., Sato, P. Y., Musa, H., Lin, X., Pandit, S. V., Delmar, M., et al. (2011). Relative contribution of changes in sodium current vs intercellular coupling on reentry initiation in two dimensional preparations of Plakophilin-2-deficient cardiac cells. *Heart Rhythm Off. J. Heart Rhythm Soc.* 8, 1740–1748. doi: 10.1016/j.hrthm.2011.06.029

Eisner, D. A., Diaz, M. E., O'Neill, S. C., and, Trafford, A. W. (2004). Physiological and pathological modulation of ryanodine receptor function in cardiac muscle. *Cell Calcium* 35, 583–589. doi: 10.1016/j.ceca.2004.01.012

Ermakov, S., Gerstenfeld, E. P., Svetlichnaya, Y., and Scheinman, M. M. (2017). Use of flecainide in combination antiarrhythmic therapy in patients with arrhythmogenic right ventricular cardiomyopathy. *Heart Rhythm* 14, 564–569. doi: 10.1016/j.hrthm.2016.12.010

Flesch, M., Schwinger, R. H., Schiffer, F., Frank, K., Südkamp, M., Kuhn-Regnier, F., et al. (1996). Evidence for functional relevance of an enhanced expression of the Na(+)-Ca2+ exchanger in failing human myocardium. *Circulation* 94, 992–1002. doi: 10.1161/01.CIR.94.5.992

Grandi, E., Pasqualini, F. S., and Bers, D. M. (2010). A novel computational model of the human ventricular action potential and Ca transient. *J. Mol. Cell. Cardiol.* 48, 112–121. doi: 10.1016/j.yjmcc.2009.09.019

Groeneweg, J. A., Bhonsale, A., James, C. A., te Riele, A. S., Dooijes, D., Tichnell, C., et al. (2015). Clinical presentation, long-term follow-up, and outcomes of 1001 arrhythmogenic right ventricular dysplasia/cardiomyopathy patients and family members. *Circ. Cardiovasc. Genet.* 8, 437–446. doi: 10.1161/CIRCGENETICS.114.001003

Hasenfuss, G., Schillinger, W., Lehnart, S. E., Preuss, M., Pieske, B., Maier, L. S., et al. (1999). Relationship between Na+-Ca2+-exchanger protein levels and diastolic function of failing human myocardium. *Circulation* 99, 641–648. doi: 10.1161/01.CIR.99.5.641

Kim, J.-C., Pérez-Hernández, M., Alvarado, F. J., Maurya, S. R., Montnach, J., Yin, Y., et al. (2019). Disruption of Ca2+i homeostasis and connexin 43 hemichannel function in the right ventricle precedes overt arrhythmogenic cardiomyopathy in plakophilin-2-deficient mice. *Circulation* 140, 1015–1030. doi: 10.1161/CIRCULATIONAHA.119.039710

Kuroda, Y., Yuasa, S., Watanabe, Y., Ito, S., Egashira, T., Seki, T., et al. (2017). Flecainide ameliorates arrhythmogenicity through NCX flux in Andersen-Tawil syndrome-iPS cell-derived cardiomyocytes. *Biochem. Biophys. Rep.* 9, 245–256. doi: 10.1016/j.bbrep.2017.01.002

Ledezma, C. A., Kappler, B., Meijborg, V., Boukens, B., Stijnen, M., Tan, P. J., et al. (2018). Bridging organ- and cellular-level behavior in *ex vivo* experimental platforms using populations of models of cardiac electrophysiology. *J. Eng. Sci. Med. Diagn. Ther.* 1:041003. doi: 10.1115/1.4040589

Louch, W. E., Hougen, K., Mørk, H. K., Swift, F., Aronsen, J. M., Sjaastad, I., et al. (2010). Sodium accumulation promotes diastolic dysfunction in end-stage heart failure following Serca2 knockout. *J. Physiol.* 588, 465–478. doi: 10.1113/jphysiol.2009.183517

Morotti, S., Edwards, A. G., McCulloch, A. D., Bers, D. M., and Grandi, E. (2014). A novel computational model of mouse myocyte electrophysiology to assess the synergy between Na+ loading and CaMKII. *J. Physiol.* 592, 1181–1197. doi: 10.1113/jphysiol.2013.266676

Muszkiewicz, A., Britton, O. J., Gemmell, P., Passini, E., Sánchez, C., Zhou, X., et al. (2016). Variability in cardiac electrophysiology: using experimentally-calibrated populations of models to move beyond the single virtual physiological human paradigm. *Prog. Biophys. Mol. Biol.* 120, 115–127. doi: 10.1016/j.pbiomolbio.2015.12.002

Oxford, E. M., Musa, H., Maass, K., Coombs, W., Taffet, S. M., and Delmar, M. (2007). Connexin43 remodeling caused by inhibition of plakophilin-2 expression in cardiac cells. *Circ. Res.* 101, 703–711. doi: 10.1161/CIRCRESAHA.107.154252

Patrick Gonzalez, J., Ramachandran, J., Xie, L.-H., Contreras, J. E., and Fraidenraich, D. (2015). Selective connexin43 inhibition prevents isoproterenol-induced arrhythmias and lethality in muscular dystrophy mice. *Sci. Rep.* 5:13490. doi: 10.1038/srep15315

Philips, B., and Cheng, A. (2016). 2015 update on the diagnosis and management of arrhythmogenic right ventricular cardiomyopathy. *Curr. Opin. Cardiol.* 31, 46–56. doi: 10.1097/HCO.0000000000000240

Sato, P. Y., Musa, H., Coombs, W., Guerrero-Serna, G., Patiño, G. A., Taffet, S. M., et al. (2009). Loss of plakophilin-2 expression leads to decreased sodium current and slower conduction velocity in cultured cardiac myocytes. *Circ. Res.* 105, 523–526. doi: 10.1161/CIRCRESAHA.109.201418

Schwinger, R. H., Wang, J., Frank, K., Müller-Ehmsen, J., Brixius, K., McDonough, A. A., et al. (1999). Reduced sodium pump alpha1, alpha3, and beta1-isoform protein levels and Na+,K+-ATPase activity but unchanged Na+-Ca2+ exchanger protein levels in human heart failure. *Circulation* 99, 2105–2112. doi: 10.1161/01.CIR.99.16.2105

Sipido, K. R., Volders, P. G. A., Vos, M. A., and Verdonck, F. (2002). Altered Na/Ca exchange activity in cardiac hypertrophy and heart failure: a new target for therapy? *Cardiovasc. Res.* 53, 782–805. doi: 10.1016/S0008-6363(01)00470-9

Smet, M. A. J. D., Lissoni, A., Nezlobinsky, T., Wang, N., Dries, E., Pérez-Hernández, M., et al. (2021). Cx43 hemichannel microdomain signaling at the intercalated disc enhances cardiac excitability. *J. Clin. Invest*. 131:e137752. doi: 10.1172/JCI137752

Sutanto, H., Lyon, A., Lumens, J., Schotten, U., Dobrev, D., and Heijman, J. (2020). Cardiomyocyte calcium handling in health and disease: Insights from *in vitro* and *in silico* studies. *Prog. Biophys. Mol. Biol*. 157, 54–75. doi: 10.1016/j.pbiomolbio.2020.02.008

van Opbergen, C. J. M., Noorman, M., Pfenniger, A., Copier, J. S., Vermij, S. H., Li, Z., et al. (2019). Plakophilin-2 haploinsufficiency causes calcium handling deficits and modulates the cardiac response towards stress. *Int. J. Mol. Sci*. 20:4076. doi: 10.3390/ijms20174076

Watanabe, Y. (2019). Cardiac Na + /Ca 2+ exchange stimulators among cardioprotective drugs. *J. Physiol. Sci*. 69, 837–849. doi: 10.1007/s12576-019-00721-5

Zareba, W. (2021). *Pilot Randomized Trial With Flecainide in ARVC Patients*. Report No.: NCT03685149. Available online at: https://clinicaltrials.gov/ct2/show/NCT03685149 (accessed June 22, 2021).

Conflict of Interest: The authors declare that the research was conducted in the absence of any commercial or financial relationships that could be construed as a potential conflict of interest.

Publisher's Note: All claims expressed in this article are solely those of the authors and do not necessarily represent those of their affiliated organizations, or those of the publisher, the editors and the reviewers. Any product that may be evaluated in this article, or claim that may be made by its manufacturer, is not guaranteed or endorsed by the publisher.

frontiers in Physiology

ORIGINAL RESEARCH
published: 27 September 2021
doi: 10.3389/fphys.2021.707189

Time-Averaged Wavefront Analysis Demonstrates Preferential Pathways of Atrial Fibrillation, Predicting Pulmonary Vein Isolation Acute Response

Caroline H. Roney[1], Nicholas Child[1], Bradley Porter[1], Iain Sim[1], John Whitaker[1], Richard H. Clayton[2], Jacob I. Laughner[3], Allan Shuros[3], Petr Neuzil[4], Steven E. Williams[1], Reza S. Razavi[1], Mark O'Neill[1], Christopher A. Rinaldi[5], Peter Taggart[6], Matt Wright[5], Jaswinder S. Gill[5†] and Steven A. Niederer[1†]*

[1] School of Biomedical Engineering and Imaging Sciences, King's College London, London, United Kingdom, [2] INSIGNEO Institute for In Silico Medicine and Department of Computer Science, University of Sheffield, Sheffield, United Kingdom, [3] Boston Scientific Corp, St. Paul, MN, United States, [4] Department of Cardiology, Na Holmolce Hospital, Prague, Czechia, [5] Department of Cardiology, Guy's and St Thomas' Hospital, London, United Kingdom, [6] Institute of Cardiovascular Science, University College London, London, United Kingdom

Electrical activation during atrial fibrillation (AF) appears chaotic and disorganised, which impedes characterisation of the underlying substrate and treatment planning. While globally chaotic, there may be local preferential activation pathways that represent potential ablation targets. This study aimed to identify preferential activation pathways during AF and predict the acute ablation response when these are targeted by pulmonary vein isolation (PVI). In patients with persistent AF ($n = 14$), simultaneous biatrial contact mapping with basket catheters was performed pre-ablation and following each ablation strategy (PVI, roof, and mitral lines). Unipolar wavefront activation directions were averaged over 10 s to identify preferential activation pathways. Clinical cases were classified as responders or non-responders to PVI during the procedure. Clinical data were augmented with a virtual cohort of 100 models. In AF pre-ablation, pathways originated from the pulmonary vein (PV) antra in PVI responders (7/7) but not in PVI non-responders (6/6). We proposed a novel index that measured activation waves from the PV antra into the atrial body. This index was significantly higher in PVI responders than non-responders (clinical: 16.3 vs. 3.7%, $p = 0.04$; simulated: 21.1 vs. 14.1%, $p = 0.02$). Overall, this novel technique and proof of concept study demonstrated that preferential activation pathways exist during AF. Targeting patient-specific activation pathways that flowed from the PV antra to the left atrial body using PVI resulted in AF termination during the procedure. These PV activation flow pathways may correspond to the presence of drivers in the PV regions.

Keywords: atrial fibrillation mechanisms, catheter ablation, pulmonary vein isolation, computational modelling, signal processing

OPEN ACCESS

Edited by:
Xin Li,
University of Leicester,
United Kingdom

Reviewed by:
Miguel Rodrigo Bort,
Universitat Politècnica de València, Spain
João Salinet,
Federal University of ABC, Brazil
Juan Pablo Martínez,
University of Zaragoza, Spain

****Correspondence:***
Caroline H. Roney
caroline.roney@kcl.ac.uk

† These authors have contributed equally to this work and share the last authorship

Specialty section:
This article was submitted to Cardiac Electrophysiology, a section of the journal Frontiers in Physiology

Received: *09 May 2021*
Accepted: *24 August 2021*
Published: *27 September 2021*

Citation:
Roney CH, Child N, Porter B, Sim I, Whitaker J, Clayton RH, Laughner JI, Shuros A, Neuzil P, Williams SE, Razavi RS, O'Neill M, Rinaldi CA, Taggart P, Wright M, Gill JS and Niederer SA (2021) Time-Averaged Wavefront Analysis Demonstrates Preferential Pathways of Atrial Fibrillation, Predicting Pulmonary Vein Isolation Acute Response. Front. Physiol. 12:707189. doi: 10.3389/fphys.2021.707189

INTRODUCTION

Patients with persistent atrial fibrillation (AF) are a diverse population. Some patients with persistent AF require multiple catheter ablation procedures with more extensive ablation strategies, which may still be ultimately unsuccessful, while for other patients, isolation of the pulmonary veins (PVs) is a sufficient treatment approach (Verma et al., 2015). Identifying appropriate ablation strategies for specific patients with persistent AF, including stratifying patients for whom pulmonary vein isolation (PVI) will be sufficient treatment, remains a clinical challenge (Johner et al., 2019). If solved, this could lead to improved safety and better patient selection, as well as decreased time and cost for procedures. Determining the optimal catheter ablation therapy for patients with persistent AF requires an understanding of the patient-specific mechanisms that sustain AF (Calkins et al., 2017).

It can be challenging to characterise mechanisms sustaining AF because AF appears chaotic and disorganised (Lee et al., 2014). In particular, the Signal Transfer of Atrial Fibrillation to Guide Human Treatment (STARLIGHT) clinical study, which analysed AF complexity from basket mapping catheters, found no evidence for electrical drivers of persistent AF within the mapping field and instead demonstrated multiple wavelets of activation (Child et al., 2018). In the current study, we hypothesised that while globally chaotic, there may be local preferential activation pathways that can be identified by analysing AF activation sequences probabilistically over time. We further hypothesised that the features of these activation pathways can be used to predict PVI ablation response.

In this study, we aimed to develop a technique for identifying preferential pathways of activation by analysing AF wavefront patterns over time. Then, we aimed to use this information to predict PVI acute ablation response, with the hypothesis that in cases where PVI terminated AF during the procedure, the source of preferential pathways, whether re-entrant or focal, should originate from the PVs. We performed this analysis on recordings from patients with persistent AF collected using simultaneous biatrial contact mapping with 64 electrode constellation catheters. To test the sensitivity of the algorithm to driver type, catheter size, and catheter contact, we used synthetic signals obtained from AF simulations for a virtual patient cohort in which the underlying AF mechanisms are known.

METHODS

Clinical Basket Recordings

This study assessed 14 patients with persistent AF from the STARLIGHT clinical trial (NCT01765075) (Child et al., 2018). These patients had a mean age of 61 ± 8 years, mean duration of persistent AF of 20.2 ± 6.7 months, mean left ventricular ejection fraction of 59 ± 10%, mean left atrium (LA) size of 46 × 55 mm, and mean right atrium (RA) size of 42 × 55 mm. Other properties are as follows: five patients had hypertension; three had obstructive sleep apnoea; seven had a body mass index > 30.

All patients gave informed consent and the study was approved by the local ethics committee. Simultaneous biatrial contact mapping was performed with two 64 electrode Constellation catheters (size, 48, 60, and 75 mm; Boston Scientific, Saint Paul, Minnesota), using the Ensite Velocity cardiac mapping system (St. Jude Medical, St. Paul, MN, USA). The recordings were performed pre-ablation, post-PVI, and post each subsequent lesion set. The recordings were sampled at a rate of 2.0345 kHz and the recording duration was in the range from 49.8 to 245 s (mean: 147.4 ± 74.6 s). Acute PVI responders were patients who went into sinus rhythm or an atrial tachycardia or flutter following PVI, while acute PVI non-responders remained in AF. Seven of the patients were PVI responders, six were non-responders to PVI, and one patient presented with atrial tachycardia, which provided data for validating the algorithms on a simpler rhythm. The ablation protocol used isolated the PV first and secondary lines were only applied if the patient remained in AF after PVI.

Simulation Data: Constructing a Virtual Patient Cohort

Imaging data for 25 patients with persistent AF were used to construct a virtual patient cohort; ethical approval was granted by the regional ethics committee (17/LO/0150 and 15/LO/1803). This dataset was a separate clinical imaging cohort from the STARLIGHT cohort. These cases have a range of atrial sizes from 90.8 to 244.9 cm^2 (mean 143.4 ± 30.5 cm^2) and LA fibrosis surface areas ranging from 5.16 to 46.3 cm^2 (mean 20.7 ± 13.5 cm^2). We combined different anatomies with different fibrosis maps from the dataset to create a virtual cohort of patients, covering the range of atrial sizes, morphologies, anisotropies, and fibrosis distributions that were seen in patients with AF (Sim et al., 2019). AF simulations for these models have different underlying AF mechanisms, cycle lengths, and arrhythmia complexities. As such, we tested PVI response across a range of different structural and electrical AF properties.

For each case, the left atrium was segmented from contrast-enhanced magnetic resonance angiogram (CE-MRA) scans and registered with late-gadolinium enhancement magnetic resonance imaging (LGE-MRI) scans using CEMRGApp software (https://cemrg.com/software/cemrgapp.html) King's College London, London, UK (Razeghi et al., 2020). Segmented meshes were re-meshed to produce a regular edge length of 0.34 mm, using mmgtools software (www.mmgtools.org) (Dapogny et al., 2014). Simulations were run for monolayer left atrial models using the Cardiac Arrhythmia Research Package (CARPentry) simulator, with the monodomain model for excitation propagation and the Courtemanche-Ramirez-Nattel human atrial ionic model (Courtemanche et al., 1998), and with modifications to represent the effects of AF electrical remodelling (Courtemanche et al., 1999; Vigmond et al., 2003). Longitudinal conductivity was assigned as 0.4 S/m and transverse as 0.1 S/m (Bayer et al., 2016). Models were constructed with repolarization heterogeneity by labelling each PV and the LA appendage using Paraview software, Kitware (https://www.paraview.org/) and assigning different ionic conductances, following our previous studies (Roney et al., 2018, 2019). Fibrotic remodelling was incorporated in each mesh according to the LGE-MRI intensity values, which were assigned as the maximum value through the wall (Sim et al., 2019).

Fibrotic effects were incorporated as regions of conduction slowing [100% conduction velocity (CV) in regions of 0–56% normalised LGE intensity, 80% CV for 56–60% LGE; 60% CV for 60–64% LGE, and 40% CV for > 64% normalised LGE intensity]. The ionic properties were also modified in fibrotic regions to represent the effects of elevated TGF-β1 (maximal ionic conductances were rescaled in regions with LGE intensity > 3 standard deviations above the mean of the blood pool as follows: 50% gK1, 60% gNa, and 50% gCaL) (Roney et al., 2016; Zahid et al., 2016; Krueger et al., 2014).

Simulations were run for each anatomy, with or without patient-specific fibrosis and with two further different fibrosis maps randomly selected from the remaining 24 fibrosis maps to create a virtual patient cohort of 100 models. These 100 models were used for testing the preferential pathways analysis algorithms. Fibrosis distributions were mapped between atrial anatomies by expressing all anatomies in universal atrial coordinates, following our previous methodology (Roney et al., 2019).

To investigate the effects of fibre field on simulated preferential pathways and PVI acute response, fibrosis model simulations with three different fibre fields were compared. The baseline fibre field incorporated in all model set-ups (the 100 models described above) was the rule-based LA endocardial fibre field in the study of Labarthe et al. (2014). Additional simulations were performed for the 25 different anatomies incorporating patient-specific fibrosis with a diffusion tensor MRI (DTMRI) human atrial fibre field (dataset number 1 from Roney et al., 2020b) or an average LA endocardial field constructed from seven DTMRI datasets (Roney et al., 2020b available to download at https://zenodo.org/record/3764917). For each case, atrial fibres were mapped to each atrial mesh using the universal atrial coordinate system (Roney et al., 2019).

Simulation Data: AF Initiation, Post-processing, and Modelling PVI Ablation

Atrial fibrillation was induced through burst pacing, and basket catheter electrode signals were simulated across the atria, as shown in **Figure 1**. For each model, AF was induced through burst pacing the right superior pulmonary vein (RSPV) at a cycle length of 155 ms for five beats following sinus rhythm (Roney et al., 2018). To investigate the effects of AF initiation pacing protocol on preferential pathways and PVI outcome, we considered two additional pacing protocols for the 25 models with patient-specific fibrosis and the rule-based LA endocardial fibre field (Roney et al., 2020a). These methods and results are presented in detail in the **Supplementary Material**.

Atrial fibrillation transmembrane potential data were analysed at points that correspond to a constellation basket catheter configuration, using the same methodology that was used for the clinical data. Our previous study compared simulated unipolar electrogram phase and bipolar electrogram phase to action potential phase to demonstrate a good agreement (phase singularity trajectory distance < 0.8 mm) (Roney et al., 2017b). To construct a basket arrangement of points in each anatomy, the recording locations from one of the clinical cases were aligned with a simulation mesh such that the largest separation between splines was across the mitral valve annulus (see **Figure 1**). These locations were then rescaled by two scaling factors to represent a larger and smaller basket and assigned to the closest points on the atrial geometry. Finally, to transfer the basket electrode locations to each atrial geometry, electrode locations were expressed in universal atrial coordinates (Roney et al., 2019) and mapped to the corresponding atrial coordinates on the target anatomy.

Pulmonary vein isolation, which was modelled as two non-conducting rings (tissue conductivity of 0.001 S/m) around the left and right LA-PV junctions, was applied 5 s post-AF initiation for all AF simulations. Pulmonary vein isolation outcome was visually classified at 2 s post-PVI as responder (macro-reentry or termination) or non-responder (AF continues).

Simulation Data: Biatrial Bilayer Simulations of Different Atrial Rhythms

To test the preferential pathways methodology on different atrial rhythms, we used simulation data from a previously published biatrial bilayer model (Labarthe et al., 2014). Left and right atrial baskets were positioned in each atrium by rescaling, rotation, and translation of clinical basket electrode locations. Atrial flutter was initiated by applying a line stimulus from the tricuspid valve to the inferior vena cava and temporarily adding a line of the block along the crista terminalis. After five re-entry circuits, this line of the block was removed and the re-entry was sustained. The focal activity was simulated by stimulating a region on the posterior wall of the left atrium at a cycle length of 200 ms.

Electrogram Processing

Unipolar electrogram signals were processed to calculate a normalised derivative signal and a phase signal using a sequence of steps, shown in **Supplementary Figure 1**. First, QRS subtraction was applied to unipolar electrograms to remove any ventricular artefacts from the signals (Shkurovich et al., 1998). Following QRS subtraction, electrograms were differentiated and the derivative signal was filtered using a sequence of filters typically used prior to dominant frequency analysis to make the signal more sinusoidal (Ng et al., 2007). For each of the 64 electrodes on each basket catheter, filtered derivative signals were normalised and the unipolar phase was also calculated, following our previously validated methodology (Roney et al., 2017b) (for further details see the **Supplementary Material**). The mean cycle length (CL) was calculated for each electrogram by taking the mean of all the time intervals between peaks of the normalised filtered derivative signal. The mean of all LA or RA electrogram CLs was calculated to give the mean LA or RA CL for each patient.

Normalised filtered derivative signals were then displayed in a 9 × 8 arrangement corresponding to the eight splines of the basket catheter, which each have eight electrodes, with the anterior mitral valve (MV) spline duplicated at the posterior MV side of the grid, following the study of Child et al. (2018) (see **Figure 2**). The visualisation used has the posterior MV at the bottom of the grid, the anterior MV at the top, and the left PV (lateral wall) and right PV (septal wall) on the left and right of the grid, respectively. Correspondingly for the right atrium (RA), the inferior vena cava (IVC) is displayed at the bottom

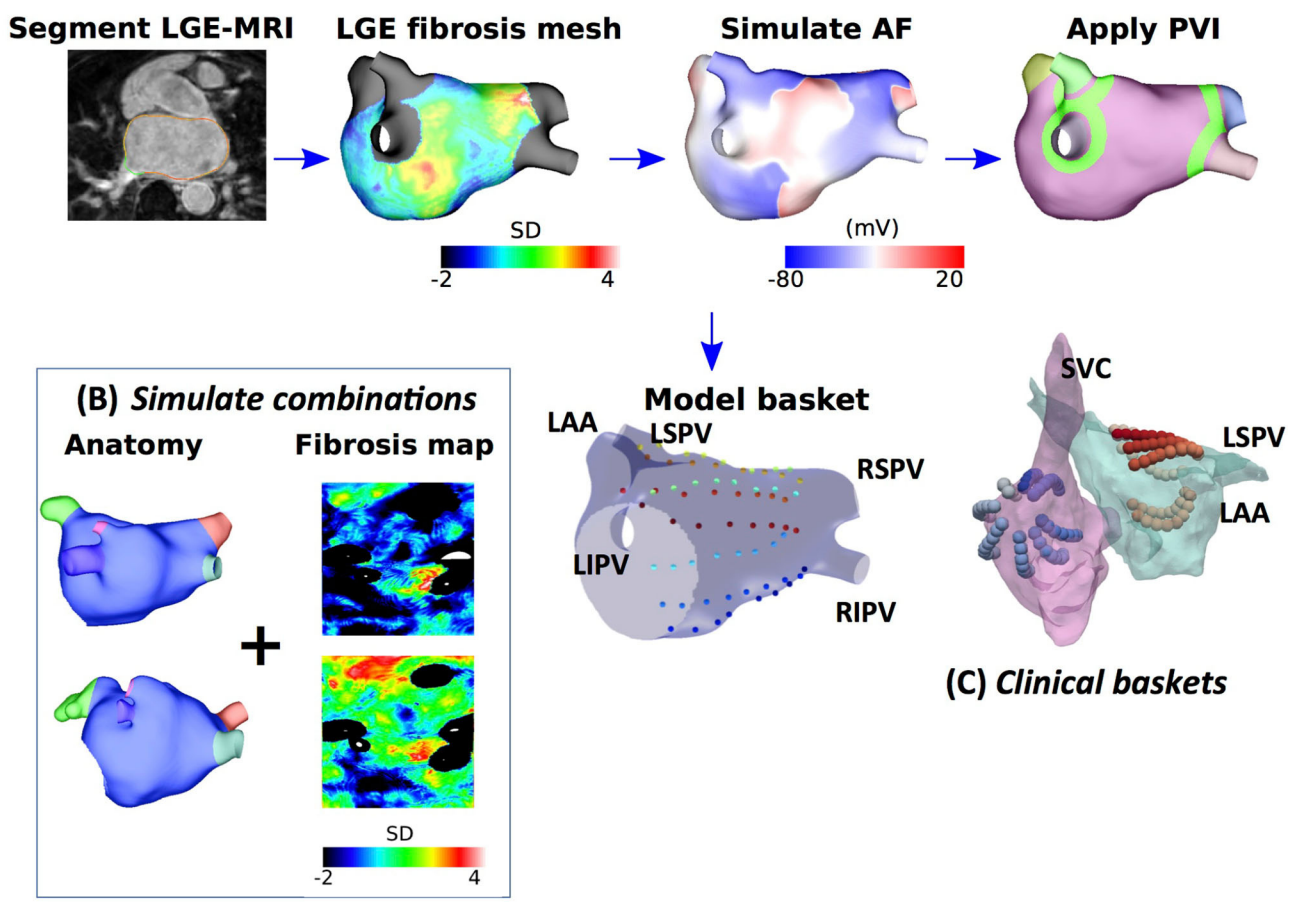

FIGURE 1 | Schematic showing the steps in model construction, simulation, and post-processing. **(A)** Imaging data were segmented, and simulation meshes were created incorporating conductivity and ionic changes in areas of fibrotic tissue identified using LGE-MRI intensity values. Atrial fibrillation (AF) was simulated and analysed at a basket arrangement of points modelled based on clinical electrode locations. Pulmonary vein isolation (PVI) was applied after 5 s. **(B)** Models were generated for different combinations of anatomy and fibrosis distribution to build a virtual patient cohort of 100 models. **(C)** Simultaneous biatrial contact mapping was performed with two 64 electrode Constellation catheters.

of the grid, the superior vena cava (SVC) at the top, the septal tricuspid valve (TV) on the left, and the lateral TV on the right. This 2D arrangement was performed on a case-by-case basis depending on the spline arrangement in relation to the MV and TV location. Finally, these data were linearly interpolated to a higher resolution grid with an additional two points introduced between every two points on the original grid (Roney et al., 2017a).

Vector Mapping, Streamline Visualisation, and Statistics Over Time

To track the direction of propagation of activation wavefronts, the optical flow of the interpolated grid of normalised filtered derivative signals was calculated. Specifically, a displacement vector was calculated for each normalised filtered derivative pixel at each time frame analysed to show where that pixel is found in the next time frame, i.e., the direction of flow. This was performed at an increment of 40 frames (approximately 20 ms) to allow for sufficient movement of pixels between frames. This implementation followed Horn and Schunck (1981). These optical flow vectors were then averaged for activation wavefronts, which were identified as isolines of 0.9 normalised filtered derivative with greater than three connected pixels (Kay and Gray et al., 2005), as shown in **Figure 2**. This averaging was performed over 10 s windows using vector addition.

For visualisation of these average optical flow vectors and identification of preferential pathways, activation streamlines were constructed. Activation streamlines were calculated using an adaptation of the technique as proposed in the study of Saliani et al. (2019). Specifically, a Delaunay triangulation of the recording points was calculated to construct a mesh, and streamlines were initially calculated from seeds at each mesh element. This construction progressed both forward and backward along the vector field direction, subject to an

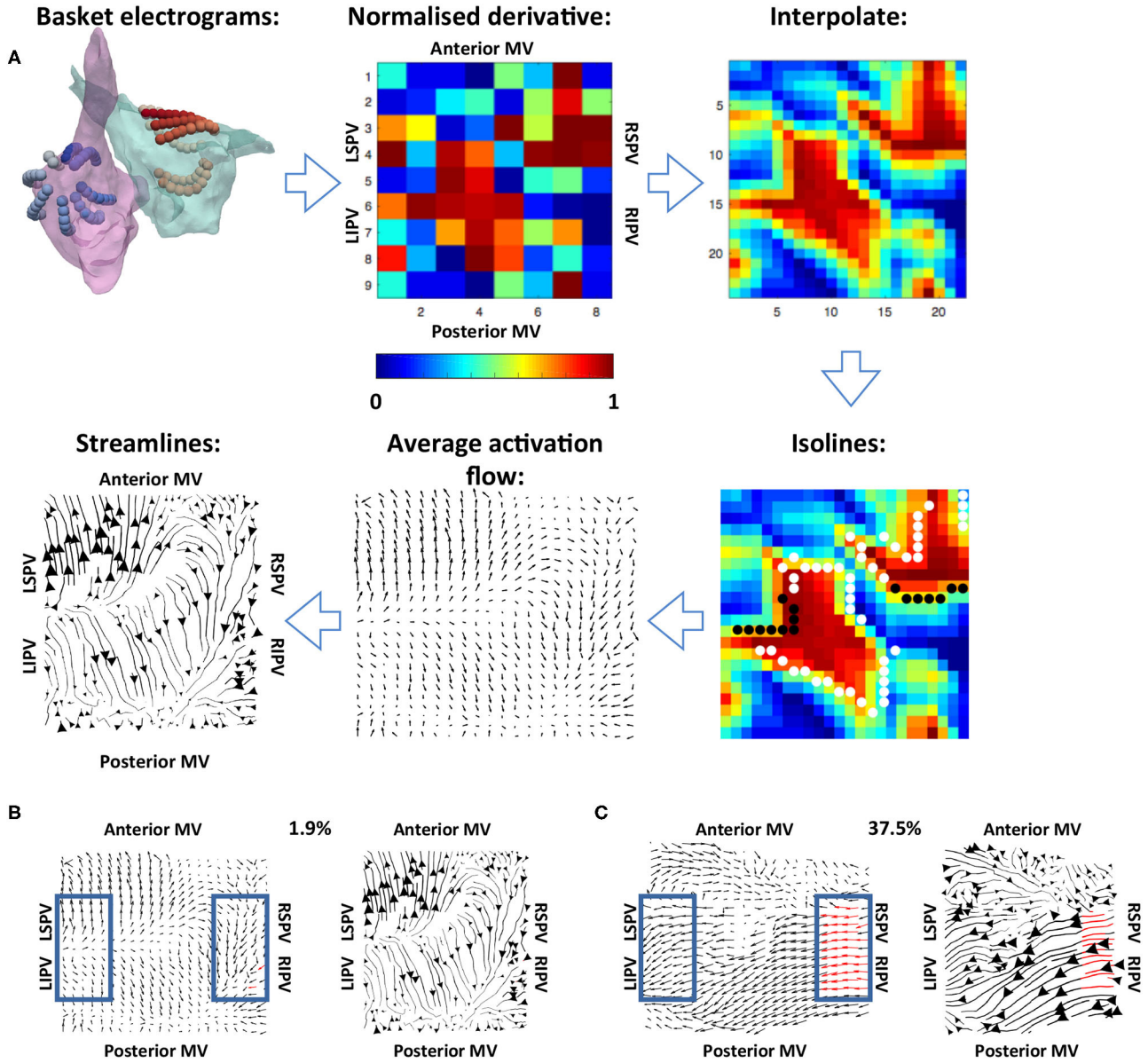

FIGURE 2 | Methodology used for calculating the average activation flow vector field from unipolar electrograms. **(A)** The normalised filtered derivative signal for each electrode on the basket catheter was displayed in a regular 9 × 8 grid. These signals were interpolated to a higher resolution grid, and optical flow vectors were calculated. The vectors were averaged over time for isolines of constant normalised filtered derivative signal (indicated by white and black dots; wavefront and wave back). Finally, streamlines were calculated from average optical flow vectors to visualise activation pathways. The normalised derivative, interpolate and isoline plots are snapshots representing the wavefronts at a given time in the recording, while the average activation flow and streamlines are calculated as an average across the 10 s recording. **(B)** Example PV activation flow calculation for a case with low PV activation flow. Vectors within the blue boxes were assessed, with red vectors tagged as PV antra to LA activation flow. **(C)** Example PV activation flow calculation for a case with high PV activation flow.

angular stopping criterion of 0.7 radians. Finally, a set of these streamlines was built iteratively at the desired spacing by adding streamlines to the set by order of decreasing streamline length subject to a minimum distance criterion (0.5 pixels). Each streamline is plotted with thickness dependent on the magnitude of the underlying average vector field to indicate how often a direction is repeated. The direction of the centre of each streamline is marked with an arrow, again with magnitude proportional to the magnitude of the average vector field at that point. An example is shown in the final subplot of **Figure 2**.

To quantify the degree of PV antra to LA body activation flow, the percentage of optical flow vectors that were of threshold magnitude and directed into the LA were calculated. This analysis was performed for vectors within a box close to the left PV and a box close to the right PV, indicated in blue in **Figures 2B,C**. Specifically, vectors within these boxes were tagged as PV to LA activation flow in the case that their magnitude was larger than

the mean magnitude across the array to represent a degree of repeatability, and that their direction was within a 90° range into the body. These vectors were identified for both the left PV and the right PV antra, and an activation flow metric was calculated for each box separately as the percentage of all vectors in the boxes tagged as representing PV to LA activation flow. The PV activation flow metric was then calculated as the maximum of the left PV and right PV activation flow metrics. To compare PV activation flow metrics between PVI responders and PVI non-responders, we performed the Wilcoxon signed-rank test and calculated the following metrics: sensitivity; specificity; area under the receiver operating characteristic curve.

Calculation of vector maps and activation flow maps was performed blinded to acute PVI response.

RESULTS

Testing on Simulated Atrial Re-entry and Focal Activation

Simulations of atrial re-entry and focal activation resulted in activation flow patterns that qualitatively reflected the underlying activation, as shown in **Figure 3** for the biatrial bilayer model. Simulation data corresponding to an RA atrial flutter is shown in **Figure 3A** with wavefront propagation from the IVC along the septal wall to the RAA and SVC, which then propagated along the lateral wall from the RAA and the SVC to the IVC. This wavefront propagation, from the IVC to SVC along the septal wall and from the SVC to IVC along the lateral wall, has formed a re-entrant circuit.

The activation streamlines constructed from the average optical flow field vector map show this activation pattern, with the wavefront propagation direction indicated by the green arrows. A re-entrant pattern is visible on the roof of the right atrium because there is a driving pattern around the TV that propagated along the septal wall from the IVC to SVC, and then along the lateral wall from the SVC to the IVC. This resulted in the discontinuity in the streamlines along the roof as one end of the reentrant wavefront travels along the roofline and did not propagate to the other wall as it is still refractory from the previous propagation. A further simulation example representing a fixed focal source is shown in **Figure 3B**, with an activation streamline map that is divergent from the source location. This demonstrated that the methodology correctly identifies re-entrant and focal mechanisms.

Testing on Clinical Atrial Tachycardia Data

To validate the developed algorithms on clinical data, we applied the techniques to a typical clinical tachycardia case. Macro-reentrant tachycardia generated a regular activation, which should manifest as clear lines following the activation path, providing suitable data for validating our algorithms. Clinical atrial tachycardia data for one patient with re-entry on the posterior LA wall and passive RA activation, previously analysed in the study of Child et al. (2018), were used to test our preferential pathways methodology. **Figure 4A** shows phase maps for the unipolar electrogram recordings, together with the normalised filtered derivative signals interpolated to a regular grid on which re-entry on the posterior LA wall is observed and regular passive RA activation. Streamlines that were constructed from the average optical flow activation vector fields for this case had demonstrated a re-entrant activation pattern on the LA posterior wall and regular RA activation starting at the septal RA wall following activation from the LA, offering testing of the technique. **Figure 4B** shows LA basket electrograms at four locations indicated by the locations E1–E4. These electrograms are sequentially activated, demonstrating the presence of re-entry.

Testing on Simulated AF Data: Pathway Analysis and PV Activation Flow Metrics for PVI Responders vs. Non-responders

Preferential pathway analysis was next applied to simulated pre-ablation AF recordings across the cohort of 100 models. AF was initiated in the same way for each model through burst pacing the RSPV, while maintenance mechanisms varied between the models, exhibiting different numbers, stability, and locations of drivers. **Figure 5A** shows example simulated isopotential maps for AF pre-ablation for a case in which PVI terminated AF, and **Figure 5B** shows an AF example pre-ablation in which AF continued post-PVI. For the PVI responder case (**Figure 5A**), re-entry around the right PV drove the AF pre-ablation, with secondary rotational activity and break-up below the left inferior pulmonary vein (LIPV) in an area of fibrotic remodelling. It is challenging to determine the dominant arrhythmia driver from the isopotential maps, but right PV driver dominance was evident on the average optical flow activation map, for which 22% of PV vectors represented activation flow from the PV antra to the LA body. For the PVI non-responder case (**Figure 5B**), there were multiple drivers in the LA body pre-ablation as well as break-up due to fibrosis, with no clear drivers in the PV regions. The optical flow map is more chaotic, with only 4% of PV vectors representing PV activation flow. Splitting the pre-ablation simulations into PVI responder and non-responder cases results in significantly different PV activation flow metric values, shown in **Figure 5C**. The results are as follows: median for responder 21.1% vs. non-responder 14.1%; $p = 0.018$ (Wilcoxon signed-rank); sensitivity = 0.79; specificity = 0.58; area under the receiver operating characteristic curve = 0.69.

Fibre field does not have a large impact on simulated acute response or PV activation flow metric in models incorporating fibrotic remodelling (86.7% of model PV activation flow metrics for the two fibre fields were within ±10% of baseline fibre field, see **Supplementary Material**). These simulations were for the 25 anatomies with patient-specific fibrosis with three different fibre field maps. Overall, this provided a confirmation of the PV activation flow metric for a virtual patient cohort.

Application to Clinical AF Data: Pathway Analysis and PV Activation Flow Metrics for PVI Responders vs. Non-responders

Vector maps calculated on pre-ablation clinical recordings for PVI responder cases are shown in **Figure 6**. These maps visually demonstrated preferential flow from the PV antra regions, which

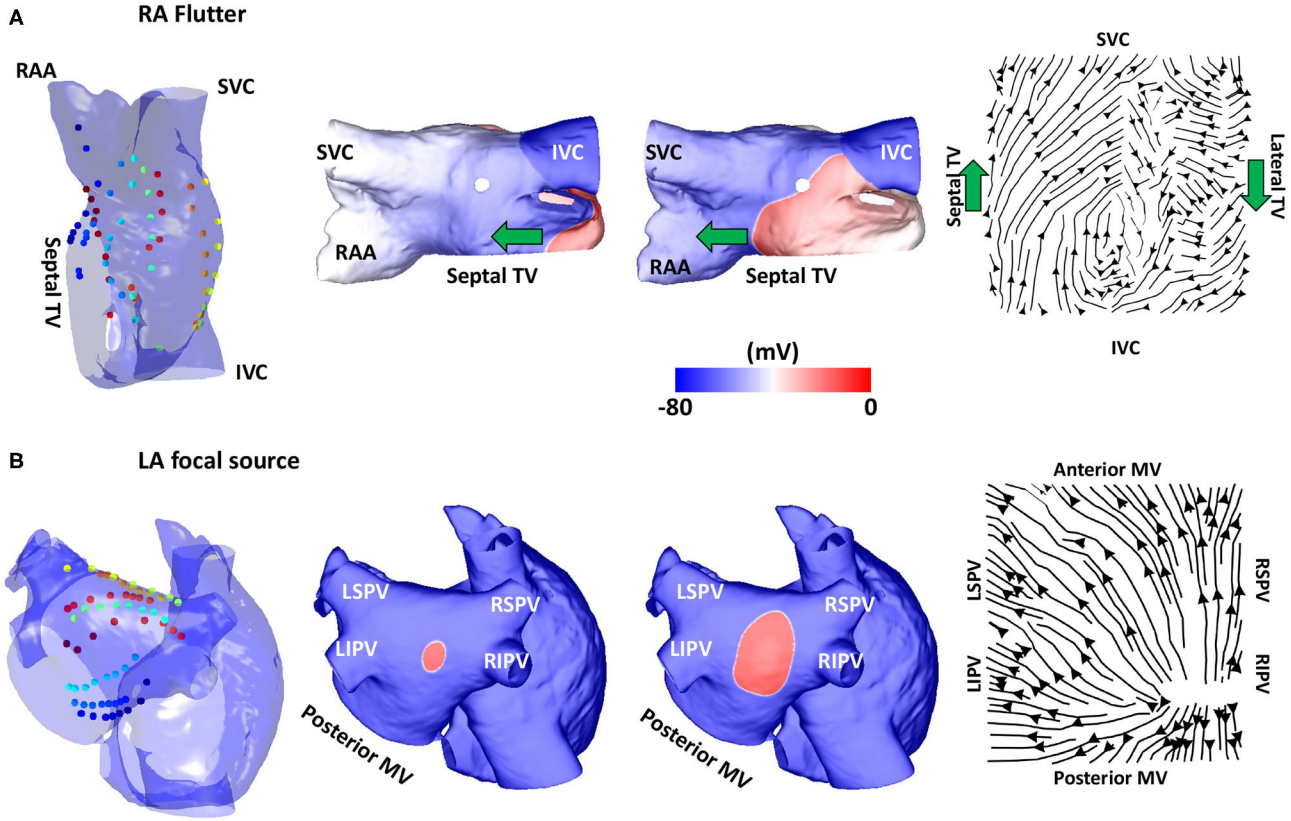

FIGURE 3 | Validation using simulated data: flutter and focal activity. **(A)** Simulated atrial flutter with activation streamlines from the IVC to SVC along the septal wall and from the SVC to IVC along the lateral wall, to complete the re-entry circuit. Basket location, isopotential plots and the activation streamlines are shown. The wavefront propagation path direction is indicated by the green arrows. The orientation of the RA in each sub-figure was chosen to offer easier visualisation of the electrode locations and the wavefront propagation direction. **(B)** A simulated repetitive focal source manifests as a divergent activation streamline field. TV, tricuspid valve; SVC, superior vena cava; IVC, inferior vena cava; RAA, right atrial appendage; MV, mitral valve; LSPV, left superior pulmonary vein; LIPV, left inferior pulmonary vein; RIPV, right inferior pulmonary vein; RSPV, right superior pulmonary vein; LA, left atrium; RA, right atrium.

were marked as left inferior PV (LIPV), left superior PV (LSPV), right inferior PV (RIPV), and RSPV, into the atrial body. The activation of the atrial body from the PV regions was quantified using the PV activation flow metric. In the pre-ablation cases shown in **Figure 6**, this was 37.5, 28.8, 26.9, 16.4, 12.5, 10.6, and 5.8%. Conversely, pre-ablation recordings for which PVI ablation did not terminate AF, as shown in **Figure 7**, did not visually demonstrate a preferential activation flow from the PV antra into the atrial body. Instead, recordings demonstrated a range of repeatability over time: some recordings exhibited the presence of repeated re-entrant activity within the atrial body, while others were more chaotic. The pulmonary vein activation flow metric for these cases pre-ablation are as follows: 0, 1.9, 2.9, 4.5, 6.7, and 27.9%. The average optical flow vector fields with PV activation flow vectors indicated in red are shown for PVI responders in **Supplementary Figure 2** and PV non-responders in **Supplementary Figure 3**.

Figure 8A shows that for the clinical dataset, the PV activation flow pre-ablation was significantly higher for PVI responders than PVI non-responder cases. The results are as follows: median 16.3 vs. 3.7%; $p = 0.035$, (Wilcoxon signed-rank); sensitivity = 0.86; specificity = 0.83; area under the receiver operating characteristic curve = 0.86. Other metrics including LA cycle length (**Figure 8B**: median 182 ms for PVI responder, 173 ms for PVI non-responder) and RA cycle length (**Figure 8C**: median 183 ms for PVI responder, 176 ms for PVI non-responder) were not significantly different between the PVI responder and non-responder groups.

Algorithm Sensitivity to Recording Window Choice and Duration Assessed Using Clinical Recordings

To test the effects of recording duration on measured preferential pathways, average optical flow maps were constructed and the PV flow metric was calculated for one clinical case using between 5 and 120 s of data (with 5 s increment). The pulmonary vein flow metric was within a small range of 35–40.4%, and so did not depend on recording duration. We also tested whether the choice of 10 s segment used for analysis from the AF episode affected the PV flow metric by analysing 10 intervals of 10 s spaced at regular intervals through an AF

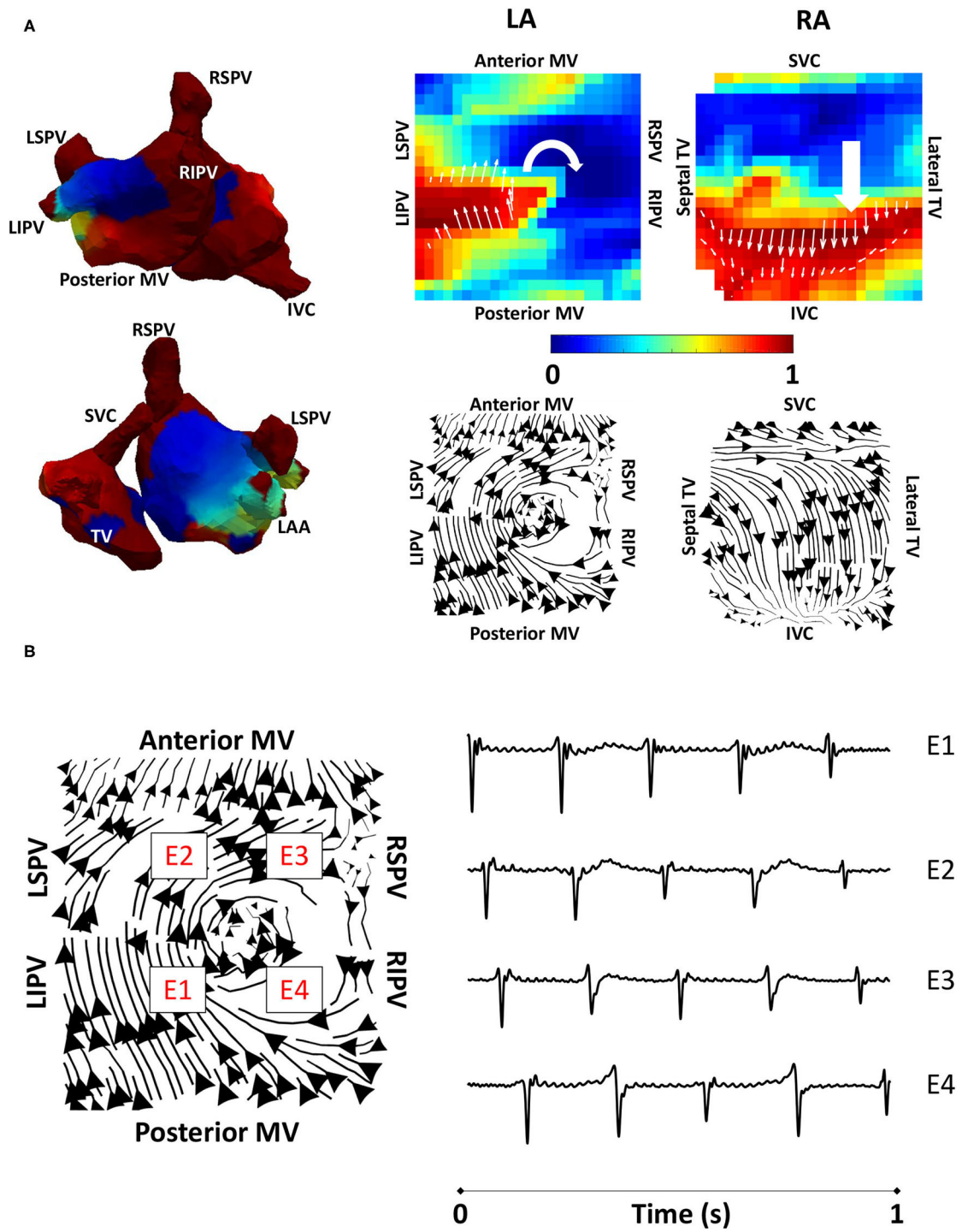

FIGURE 4 | Algorithm validation using clinical atrial tachycardia data. **(A)** Clinical atrial tachycardia phase maps, exhibiting re-entry on the LA posterior wall and passive RA activation are shown on the left of the figure. Normalised filtered derivative signals interpolated to a regular grid are shown on the top right for a single time point to show LA re-entry. Streamlines constructed from the average optical flow activation field for this clinical atrial tachycardia case demonstrate a re-entrant activation pattern on the LA posterior wall, and regular RA activation starting at the RA septal wall as it is activated from the LA. **(B)** Four LA basket electrograms are shown at the grid locations indicated by boxes with E1 to E4 on the streamline map. Locations E1-E4 are sequentially activated, demonstrating the presence of reentry. TV, tricuspid valve; SVC, superior vena cava; IVC, inferior vena cava; RAA, right atrial appendage; MV, mitral valve; LSPV, left superior pulmonary vein; LIPV, left inferior pulmonary vein; RIPV, right inferior pulmonary vein; RSPV, right superior pulmonary vein; LA, left atrium; RA, right atrium.

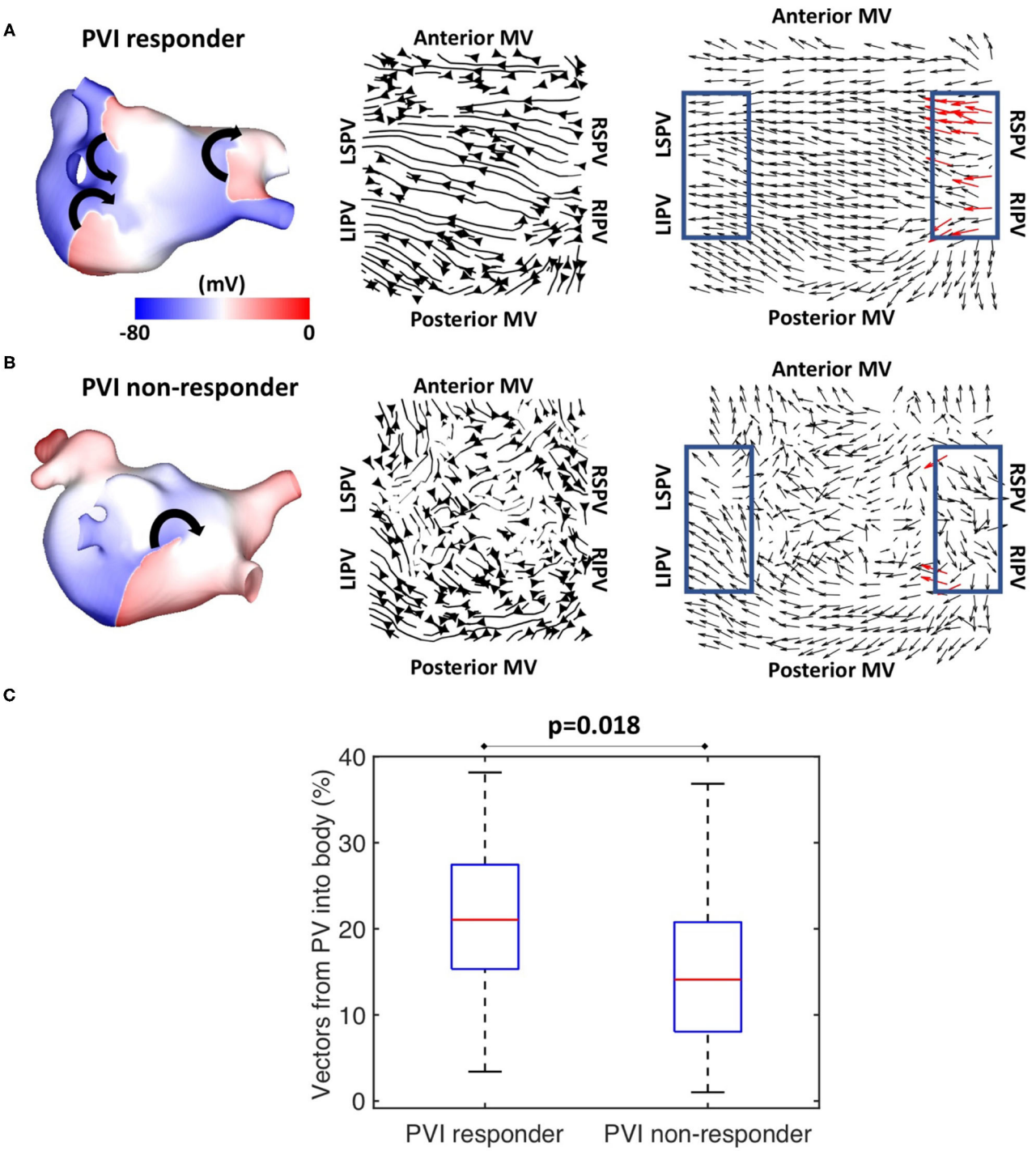

FIGURE 5 | Simulated data PV activation flow metric is significantly different for PVI responder and non-responder cases. Isopotential snapshots (left), streamlines (middle), and optical activation flow (right) plots for examples of **(A)** PVI responder and **(B)** PVI non-responder. PV activation flow was quantified as % of vectors pointing into the LA body in a 90° range within the PV regions (blue boxes). PV activation flow vectors are shown in red. **(A)** For this simulation, re-entry around the right PV drives AF pre-ablation and PVI terminates AF (an example of a responder), with a PV activation flow metric of 22.2%. **(B)** For this simulation, multiple drivers exist in the LA body pre-ablation, and PVI did not terminate AF (an example of a non-responder); the PV activation flow metric is 4.4%. **(C)** Simulated PV activation flow metric is significantly different pre-ablation for PVI responder and non-responder cases (median 21.1 vs. 14.1%, $p = 0.018$, Wilcoxon signed rank).

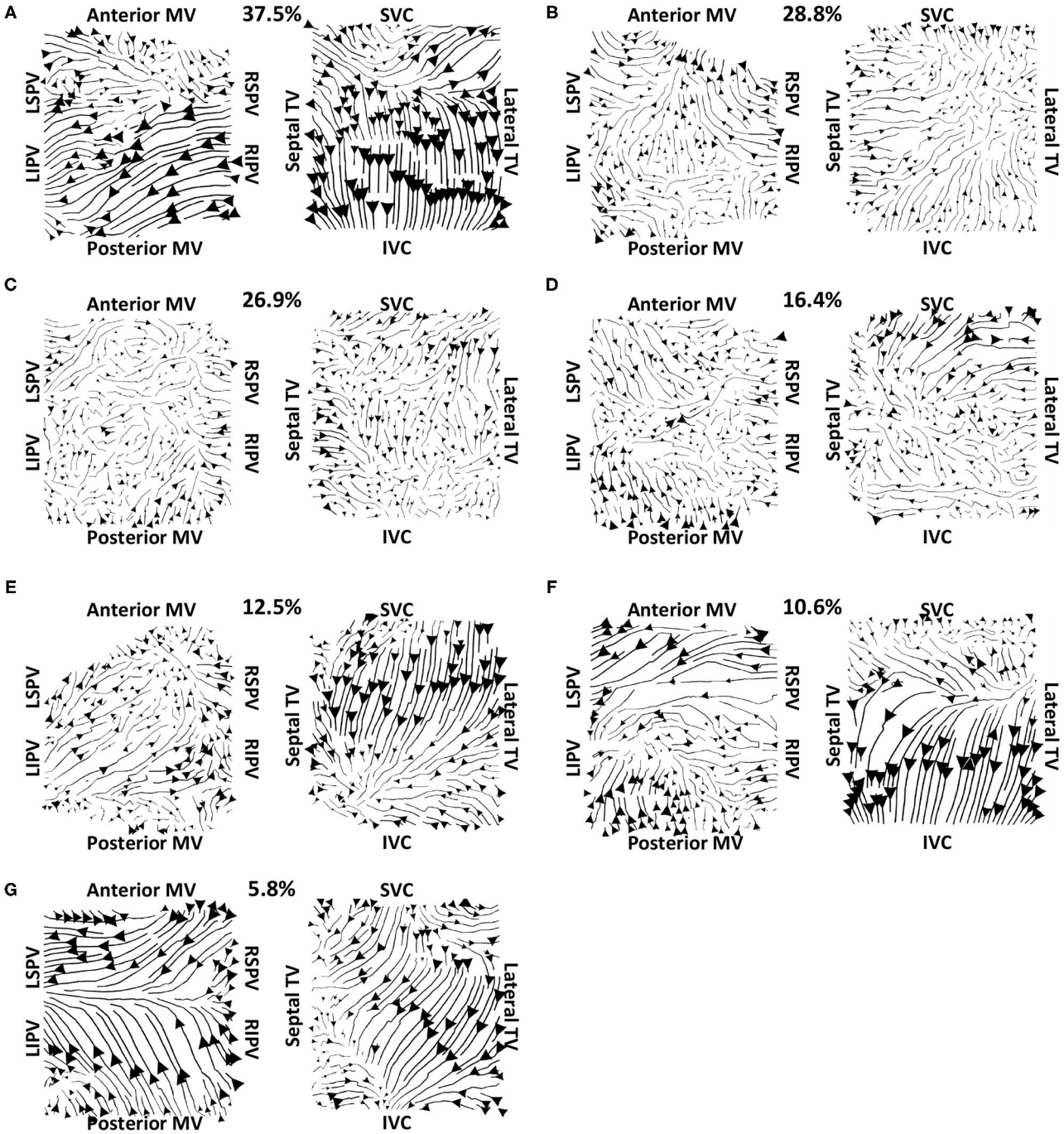

FIGURE 6 | Clinical average vector fields demonstrate activation flow from the PV antra into the atrial body for PVI responder cases pre-ablation. Paths are shown for the left and right atria as streamlines with the magnitude dependent on the magnitude of the underlying average vector field, signifying how often a direction is repeated. The direction of the centre of each streamline is also indicated. Cases are arranged in order of decreasing PV activation flow metric: **(A)** 37.5%, **(B)** 28.8%, **(C)** 26.9%, **(D)** 16.4%, **(E)** 12.5%, **(F)** 10.6%, and **(G)** 5.8%.

recording. **Figure 9** shows example activation streamline maps for different recording segments within a single AF episode. This example AF recording was 217.8 s, and so all intervals represent separate segments with no overlap (approximately 20 s between the start of each interval). For this example, 9 out of the 10 intervals which were assessed had demonstrated visually similar activation, with PV activation flow metric within ±10% of the first interval. Preferential activation pathways were seen from the right PV antra to the LA body for nine of the recordings (for example **Figures 9A,C,D**), while one interval

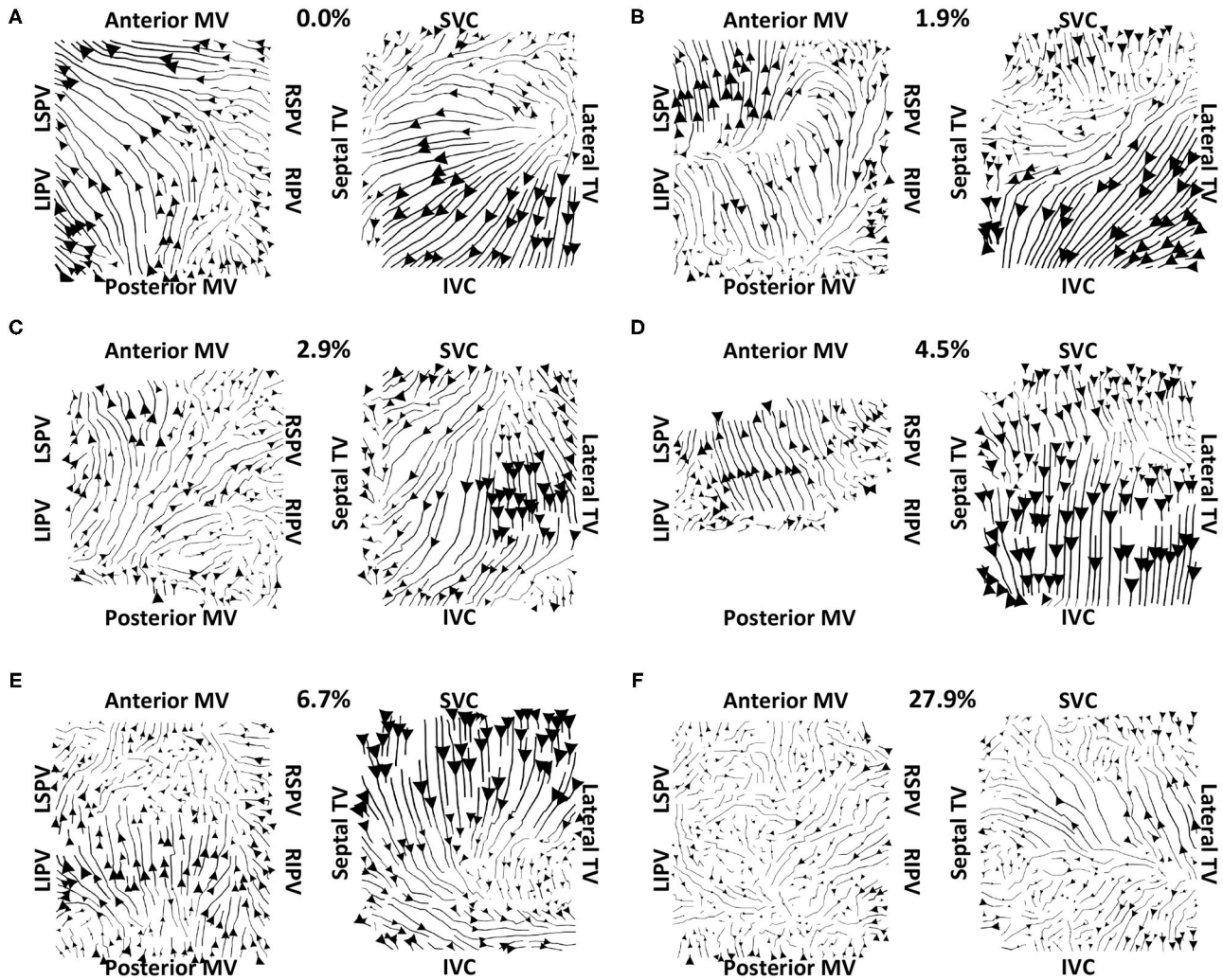

FIGURE 7 | Clinical average vector fields did not demonstrate activation flow from the PV antra into the atrial body for PVI non-responder cases pre-ablation. Visualisation details are as in **Figure 6**. Cases are arranged in order of increasing PV activation flow metric: **(A)** 0, **(B)** 1.9, **(C)** 2.9, **(D)** 4.5, **(E)** 6.7, and **(F)** 27.9%. For case **(D)**, multiple splines of the LA basket were not in contact and so these were excluded from the analysis.

instead demonstrated flow from the left PV antra to the LA body (**Figure 9B**).

Comparing the PV activation flow metric for the 10 s segments to the PV activation flow metric for the first window across all clinical cases, showed that 79.2% of PV activation flow metrics for the different windows were within ±10% of the first window (77.1% for PVI responders and 81.7% for PVI non-responders).

Algorithm Sensitivity to Catheter Size and Contact Tested Through Simulations

This study further investigated the effects of basket size and contact on the preferential activation flow calculation and the PV activation flow metric using simulation. Decreasing the basket size from an average spline length of 50 to 35.7 mm for the same simulation set as in section Testing on Simulated AF Data: Pathway Analysis and PV Activation Flow Metrics for PVI Responders vs. Non-responders resulted in a PV activation flow metric difference that is no longer significant (larger basket: median 21.1 vs. 14.1%, $p = 0.018$, Wilcoxon signed-rank median; smaller basket: 24 vs. 17.7%, not significant, see **Figure 10**). This demonstrated that catheter coverage is important, as well as recording distance from the PVs. The baseline simulated basket size was similar to the smallest of the clinical baskets (simulated: 50 mm; clinically used basket sizes were 48, 60, and 75 mm).

Our current methodology assumes basket recordings are located on a regular grid. However, for catheter recordings in patients, inter-spline distances vary. The study of Laughner et al. (2016) showed that inter-spline distances exhibit large variations for basket catheters, depending on deployment. In addition, multiple studies have shown that spatial resolution affects the analysis of arrhythmia mechanisms (Roney et al., 2017a). To test

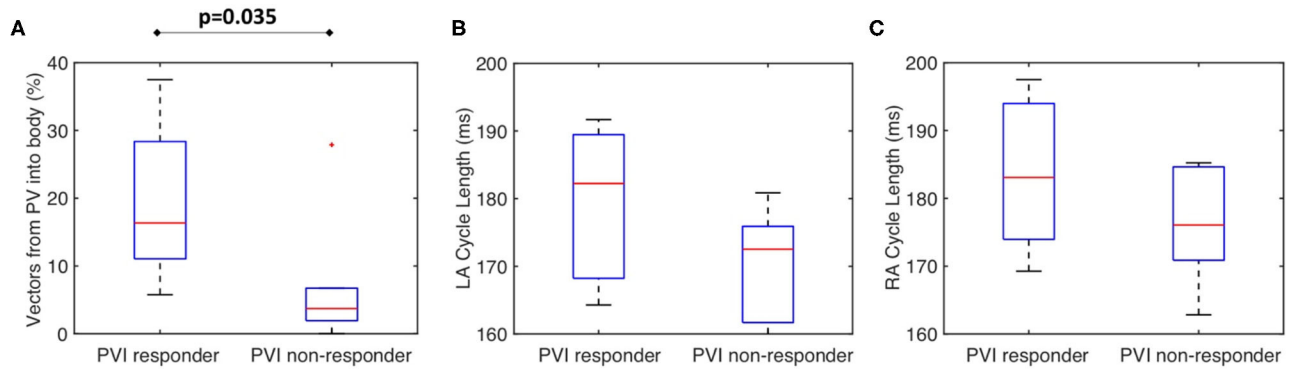

FIGURE 8 | The clinical PV activation flow metric is significantly different for PVI responder and non-responder cases. **(A)** Clinical PV activation flow (%) pre-ablation was significantly higher for PVI responder than PVI non-responder cases (PVI responder: 16.3% vs. non-responder: 3.71%, $p = 0.035$). **(B)** LA cycle length was not significantly different between groups (Wilcoxon signed-rank). **(C)** RA cycle length was not significantly different between groups.

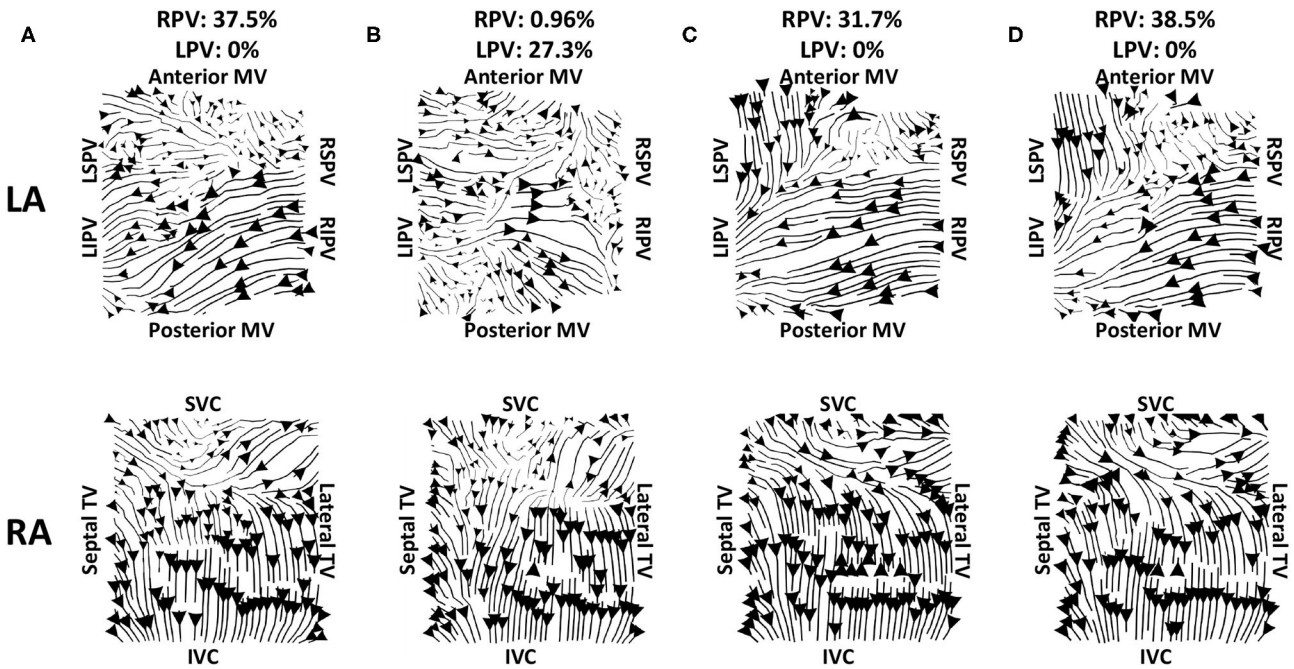

FIGURE 9 | Effects of recording duration on streamlines for example AF episode. Streamlines are shown for 10 s recordings taken from intervals spread through the entire recording. The top row shows the left atrium, and the bottom row shows the right atrium. The streamline plots in **(A)** show the original interval; panels **(C,D)** are visually similar to **(A)**, while the LA for **(B)** demonstrates larger differences. The PV activation flow metrics from the right PV are as follows: **(A)** 37.5%, **(B)** 96%, **(C)** 31.7%, **(D)** 38.5%. There were 9 out of 10 recordings that had no activation flow from the left PV to the LA body, while **(B)** has a PV activation flow metric from the left PV of 27.3%. The start times for these recordings are 0, 6, 125, and 187 s.

these effects on our current analysis, we simulated the effects of removing electrode recordings from the analysis across the 100 atrial models. The effects of poor electrode contact were simulated by randomly removing electrogram recordings from the analysis across all simulations. The percentage of points removed was varied in the range of 10–50%. The pulmonary vein activation flow metric was higher for PVI responder cases than for PVI non-responder cases when the analysis was performed with all electrodes, 90 or 75% of electrodes, although these differences were only significant for the case of all electrodes. It was not possible to differentiate between the PVI responder and PVI non-responder groups when only 50% of electrodes were included in the analysis; shown in **Figure 11.** We next considered that electrode locations in poor contact are likely to be spatially correlated, and so we considered randomly removing one spline, two splines, or four splines of data from the analysis. These results are shown in **Supplementary Figure 4**. As for the case of randomly removing electrodes, the PV activation flow metric was

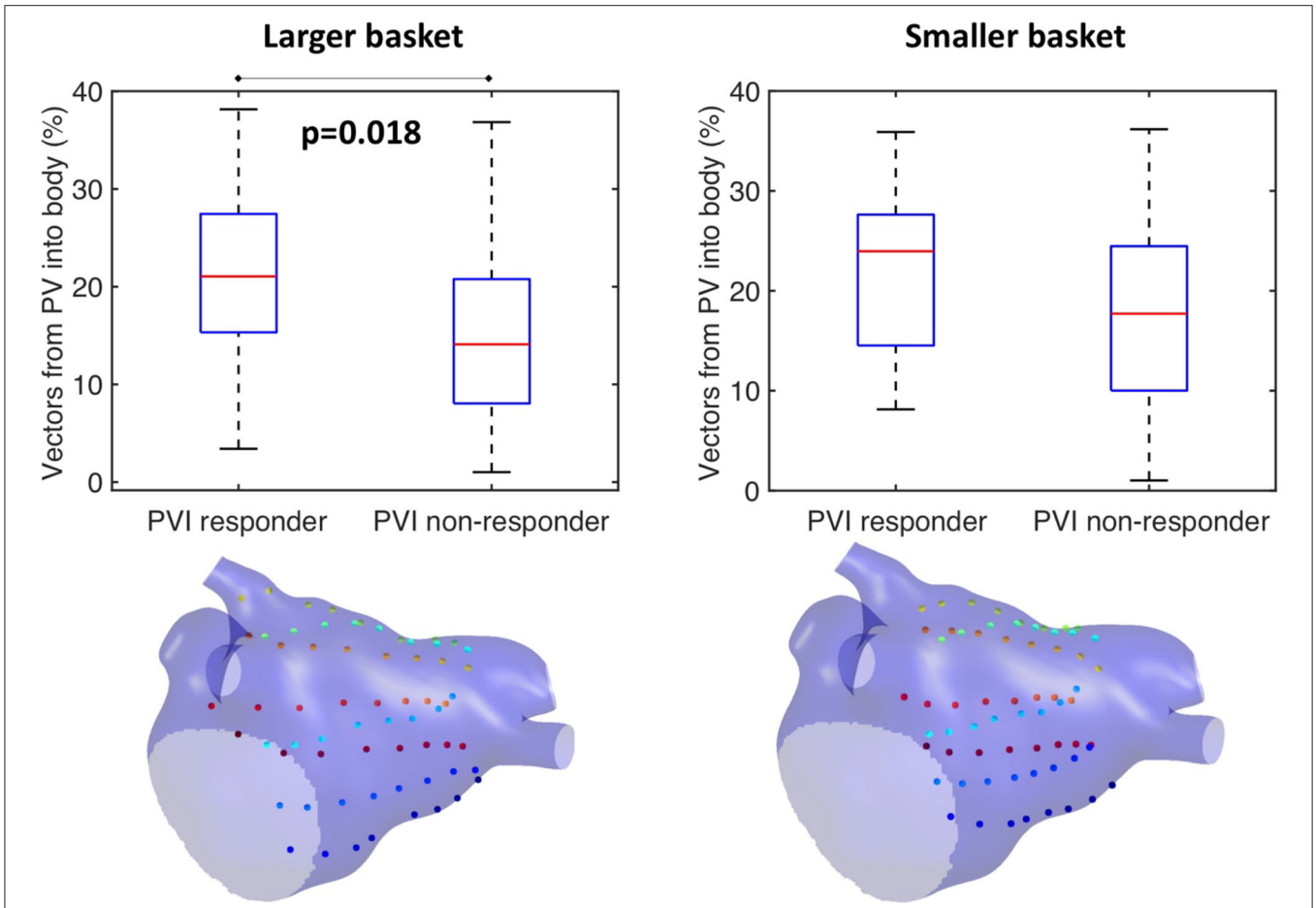

FIGURE 10 | Effects of basket size on preferential pathways. Reducing the basket size changed the significance of the PV flow metric: larger basket: median 21.1 vs. 14.1%, $p = 0.018$, Wilcoxon signed-rank median; smaller basket: 24 vs. 17.7%, not significant.

higher for PVI responder cases than for PVI non-responder cases when the analysis was performed with all splines, one missing spline or two missing splines. For the case of four missing splines, i.e., only 50% of electrodes included, it was again not possible to differentiate between the two groups.

Algorithm Sensitivity to Driver Type Tested Through Simulations

We tested if the mechanistic source of PV activation flow affected our results. In doing this, simulated cases without fibrosis for which PVI terminated AF ($n = 6$) were selected from the dataset and simulated AF pre-ablation was compared with simulating a repeated PV trigger (through pacing the RSPV at 155 ms for 5 beats). The left side of **Figure 12** shows examples (**Figure 12A**) isopotential maps, (**Figure 12B**) average optical activation flow vector fields, and (**Figure 12C**) activation streamlines for a simulation sustained by PV triggers. In this case, preferential activation flow is from the PV antra to the LA body and the PV activation flow metric is 31.7%. The right side of **Figure 12** shows the same anatomy but for a simulation where re-entry around the PV antra drives AF, with a PV activation flow metric of 25.5%. The streamline map for the PV trigger case is more organised than the streamline map for the PV rotational driver. Collating the simulations, the PV activation flow metric for PV triggers and PV re-entry cases are not significantly different (mean triggers: 26 $\pm$ 8.3 %, mean PV re-entry: 26.5 $\pm$ 3.9 %, a paired *t*-test showed not significantly different).

DISCUSSION

Main Findings

In this study, we proposed and tested a methodology for detecting preferential activation pathways in patients with persistent AF. We tested the methodology on simulated data and a clinical atrial tachycardia dataset. The technique developed in this study identified patients likely to respond to PVI during the ablation procedure as those with preferential activation flow from the PV antra to the left atrial body. We hypothesised that this activation flow may correspond to the presence of drivers in PV regions. We simulated AF sustained by either PV triggers or by PV rotational drivers to demonstrate that both mechanisms result in a similar PV flow metric. As such, this suggested that

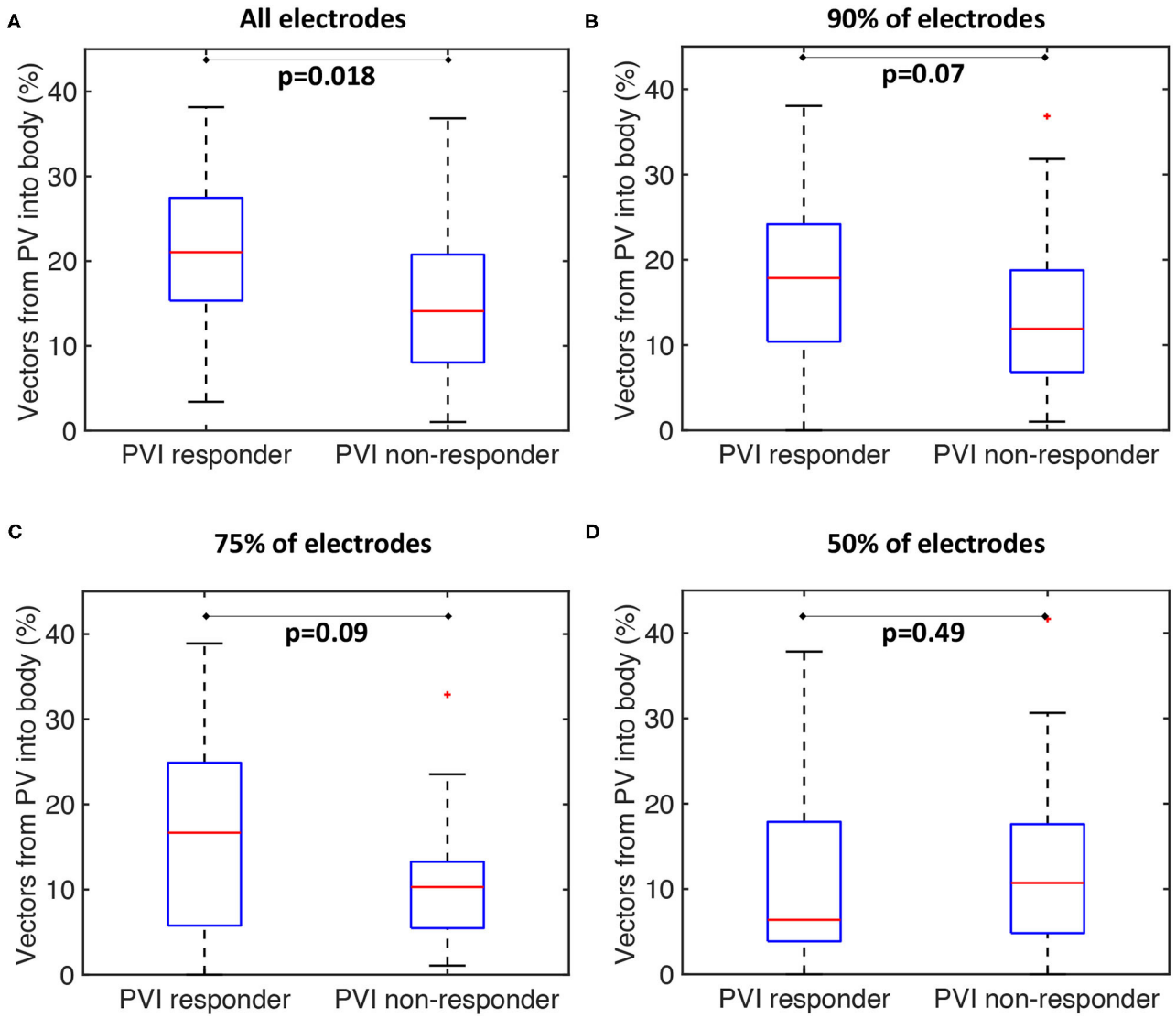

FIGURE 11 | Effects of basket contact on preferential pathways. Effects of poor contact on preferential pathway analysis. PV activation flow metrics are shown for cases with 10–50% of electrodes removed. **(A)** All electrodes: median 21.1 vs. 14.1%, $p = 0.018$, Wilcoxon signed rankmedian. **(B)** 90% of electrodes included: 17.9 vs. 11.9%, $p = 0.07$. **(C)** 75% of electrodes included: 16.7 vs. 10.3%, $p = 0.09$. **(D)** 50% of electrodes included: 6.4 vs. 10.7%, $p = 0.49$.

isolating the PV antrum is more important in some patients than others when the mechanism for maintaining persistent AF in the atria has preferential pathways using the area around the PVs. Our study could motivate a prospective clinical study to confirm the relationship between preferential flow and long-term PVI outcome.

Comparison to Other Methodologies

Phase mapping for this dataset did not identify stable rotational activity (Child et al., 2018), suggesting anarchic fibrillation. Instead, analysing these data probabilistically over time identified preferential pathways of activation, indicating a degree of hierarchy.

Our preferential pathway technique has identified repeated structures in the activation patterns. The study of Vandersickel et al. proposed a directed network for identifying repeated activation patterns in the specific case of tachycardia arrhythmias (Vandersickel et al., 2019). Their technique worked on atrial surface meshes rather than projecting to a two-dimensional grid, but this requires a higher resolution data set. Both approaches determine likely circuits of activation. On one hand, the directed network approach in the study of Vandersickel et al. (2019) assumed a stable re-entry circuit, for example, an atrial tachycardia (Van Nieuwenhuyse et al., 2021). On the other hand, our technique also worked for fibrillatory data. As such, we have proposed a novel general tool for identifying critical paths of activation during atrial arrhythmia, which can be applied to atrial

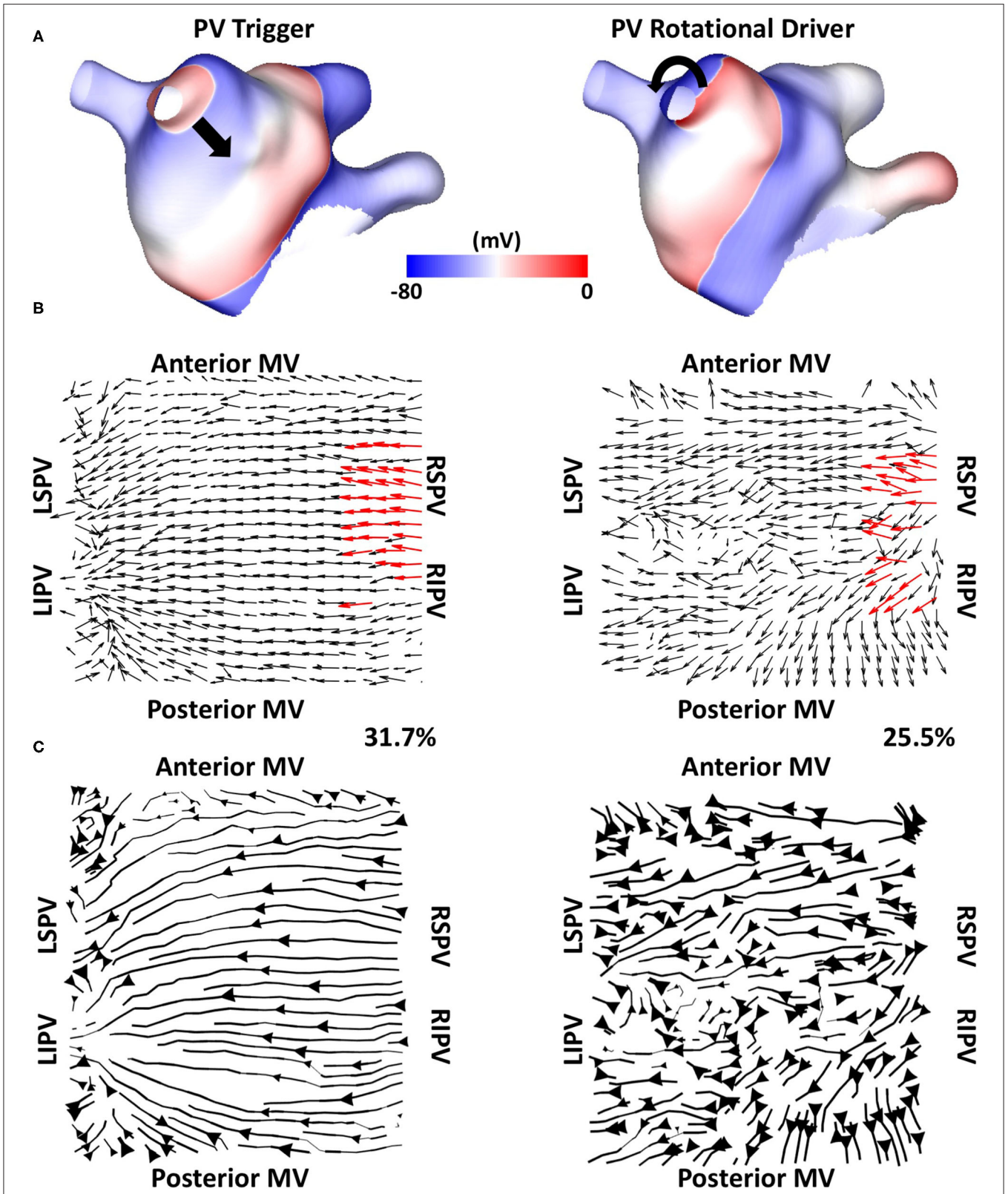

FIGURE 12 | Simulating PV triggers vs. PV rotational drivers. **(A)** Isopotential plots, **(B)** average optical flow activation vector fields and **(C)** activation streamlines are shown for a case sustained by PV triggers (left) and for a PV rotational driver (right).

macro-reentrant tachycardia (**Figure 4**) or fibrillation (**Figures 6, 7**). Similarly, the study of Bellmann et al. (2018) has published an electrographic flow mapping technique to identify electrical sources within the mapping field and classify them as either active or passive. Our technique could be used similarly, but we found no evidence of drivers in the mapping field in this patient cohort. Instead, we utilised the activation flow direction to identify preferential pathways and to assess the arrhythmia, in which we hypothesised that PV triggers or drivers exist for cases in which activation flow occurred from the PV antra to the LA body (**Figure 6**). Our current methodology assumed global biatrial recordings, and our future work will aim to adapt this technique to work with sequentially acquired data, with a focus on recording at the PV antra.

Relation to Other AF Mechanisms

Our study demonstrated the importance of activation from the PV in predicting acute PVI response, wherein PVI responder cases had a significantly higher PV activation flow metric pre-ablation than PVI non-responder cases (**Figure 8**). Similarly, the study of Navara et al. (2018) demonstrated using two mapping methodologies (Rhythmview from Abbott and phase mapping) rotational activity and focal activity in PV antral regions in patients for whom AF terminated during the PVI procedure, which would manifest as preferential activation flow from the PV antra to the LA body. These results agree with our findings. For cases in which activation flow was from the PV antra to the LA body, we found that this was from either the left or right PV, and the utilised PV did not change over time. Previous studies have hypothesised that the smooth PV antra may act as an anchor for rotors (Hocini et al., 2002), which agrees with our simulation studies. Our previous simulation study showed that high PV phase singularity density may indicate the likelihood of a positive PVI response (Roney et al., 2018). Our current study extended our previously proposed metric to one that does not require PV recordings, greatly increasing clinical applicability. Our current simulations suggested that clinical basket sizes are sufficient for PVI ablation outcome prediction using the PV activation flow metric (**Figure 10**). The simulations also showed that the PV activation flow metric cannot differentiate between PV triggers and PV rotational drivers using LA body recordings alone (**Figure 12**). Although this distinction is mechanistically important, the PVI outcome is the same in either case.

The examples shown in **Figure 6G** (PVI responder) and **Figure 7F** (PVI non-responder) represent outliers. For the PVI responder case (**Figure 6G**), the optical flow vectors (shown in **Supplementary Figure 2G**) visually demonstrate flow from the right PV antra to the LA body. However, the magnitudes of these vectors were less than the mean magnitude and so these did not count toward the PV activation flow metric. In this case, the activation flow away from the PV demonstrated a high degree of repeatability. Modifying the threshold magnitude for when to include activation vectors in the PV activation flow metric would increase the value for this outlier. In contrast, the magnitude of repeated directions across the basket device is small for the PVI non-responder case (**Figure 7F** and **Supplementary Figure 3F**). For this case, the PV activation flow metric is high even though PV activation flow is not visually evident on the activation streamline map, due to the small vector magnitude in the LA body. It is possible that PV isolation was incomplete for this patient resulting in AF maintenance post-PVI ablation. The other PVI non-responder cases in **Figure 7** demonstrated preferential paths in the LA body, distinct from any PV activation flow.

The study of Dharmaprani et al. (2019) characterised AF dynamics through calculating the lifetimes of wavelets and phase singularities demonstrating exponential lifetimes, which was also seen in the study conducted by Child et al. (2018). Our current study demonstrated preferential flow from the PV antra when activation directions were averaged over time. This is compatible with an exponential distribution of phase singularity lifetimes, suggesting that wavefront propagation may demonstrate preferential directions over time.

An alternative AF sustaining mechanism is the presence of re-entry in the RA. For example, the study of Hansen et al. (2015) has demonstrated the presence of intramural re-entry along fibrotic tracks in the human RA. These re-entries were detectable using sub-endocardial mapping for 80% of re-entries, but only for 40% of sub-epicardial re-entries, using FIRM mapping (Zhao et al., 2017). We did not find any evidence of such RA re-entries in this patient cohort using our methodology.

Simulation Limitations

We used a monolayer model for the simulations in this study. The monolayer is an approximation, like all models, of the atrial activation patterns observed clinically. We chose to use a monolayer model as its complexity reflected the available data. While wall thickness and transmural fibrosis distribution may contribute to atrial arrhythmias and ablation outcomes (Csepe et al., 2017; Roy et al., 2018; Ali et al., 2019), these cannot be reliably measured using standard clinical LGE-MRI. We did not account for these features, and this is an inherent limitation of building models from routine clinical data. The AF simulations in this study were initiated through pacing the RSPV. To investigate the effects of AF initiation protocol on preferential pathways and the PV activation flow metric, we also simulated AF initiation through burst pacing the LSPV or using initial conditions corresponding to four spiral wave re-entries. We found that the AF initiation pacing protocol used affected the preferential pathways and PV activation flow metric, where AF wavefront patterns were generally different for AF initiated using each of the AF initiation protocols for the same model (see **Supplementary Figure 5**). Despite this, it was still the case that the PV activation flow metric was higher for PVI responders compared with non-responders: for LSPV pacing: 15.6 vs. 5.3% ($p = 0.06$) and for initiation with four spiral wave re-entries: 19.6 vs. 9.6% ($p = 0.03$). These results are presented in the **Supplementary Material**. Our future work will extend this to systematically investigate the effects of initiation location on preferential pathways and will test this metric for different AF induction protocols (for example, following the studies of Azzolin et al., 2021 and Boyle et al., 2018).

To test whether the PV activation flow metric defined in this study could be used to predict acute PVI response in simulations, we post-processed transmembrane potential signals from AF

simulations. Similar to the previous studies (Boyle et al., 2018; Roy et al., 2018; Azzolin et al., 2021), we chose to analyse transmembrane potential signals to eliminate the complexities associated with the effects of wavefront direction on electrogram complexity. However, to demonstrate the full applicability of our pipeline in the clinical environment, it is necessary to also test it on electrogram signals. To test whether the choice of the signal used to calculate preferential pathways affected our simulation results, we compared PV activation flow metrics calculated using transmembrane potential signals to those from unipolar electrogram signals for the LSPV paced dataset. These results are presented in the **Supplementary Material** where we found that the PV activation flow metric for unipolar signals was similarly higher for PVI responders compared with non-responders, with the same significance value as for the transmembrane potential analysis ($p = 0.06$ for both data types). This suggested the method was not significantly affected by the choice of the input signal, agreeing with our previous study (Roney et al., 2017b). However, these simulations do not include the effects of several clinical complexities, including electrode size, orientation, and noise on the electrogram signals (Potse, 2018).

A further analysis choice or assumption is how to treat data at the mitral and tricuspid valves. We chose to follow the study of Child et al. (2018) and duplicated the anterior MV spline at the posterior side of the grid (using a similar approach for the TV), working on a 9 × 8 grid. This captured that there may be areas where propagation occurred across these splines. An alternative approach was to work on an 8 × 8 grid (Narayan et al., 2012). To test the effects of grid choice, we compared the PV activation flow metric for an 8 × 8 grid to the default 9 × 8 grid analysis. This analysis is presented in the **Supplementary Material**. Using an 8 × 8 grid, the PV activation flow metric was also significantly higher for the PVI responder cases with a p-value of 0.012 (21.4 vs. 14.0%), similar to the results for the 9 × 8 dataset (21.1 vs. 14.1%, $p = 0.018$). The difference between activation flow metrics calculated with or without spline duplication was small, with a mean absolute difference of 1.4%.

Clinical Limitations

This study has further limitations clinically. We had applied a new method to a limited number of patients in an acute study. The proportion of acute PVI responders is likely to be different in a larger patient population (Verma et al., 2015). A limitation of this study is that patients did not receive the same ablation procedure. All patients had PVI at the start of their ablation, but subsequent ablations were at the discretion of the operator. This was accounted for by assessing acute PVI ablation outcome during the procedure, which while correlated with long-term outcome, is not a surrogate for a long-term outcome (Lim et al., 2015; Kochhäuser et al., 2017; Singh et al., 2017). This study motivated the application of this technique to a larger patient cohort in a prospective trial with standardised ablation procedures and long-term follow-up to determine applicability for general clinical practise. Temporally averaging and spatially coarsening the data to calculate preferential pathways may lose information on individual wavefronts. The technique presented here could be extended to assess the role of the left atrial appendage (Romero et al., 2020), and to identify the intermittent driver or focal regions by analysing shorter recording segments (Gerstenfeld et al., 1992). Future work will compare pathways to atrial fibre structures, including the crista terminalis and septopulmonary bundle (Pashakhanloo et al., 2016; Roney et al., 2020b). Further work should investigate alternative mechanisms for PVI response, for example, by reducing the critical mass of tissue available for fibrillation. The effects of additional ablation lesions on preferential pathways could be investigated in future studies.

CONCLUSIONS

Preferential pathways of activation exist during AF. Our novel technique identified patients that were likely to respond to PVI during an ablation procedure as those with preferential activation flow from the PV antra to the LA body. This flow may correspond to the presence of drivers in the PV regions. We proposed that the metric should be applied in a prospective study, with high-density catheter recordings in the PV at the LA-PV junction, to confirm the relationship between preferential flow, AF mechanisms, and long-term PVI outcome.

DATA AVAILABILITY STATEMENT

The data analysed in this study is subject to the following licenses/restrictions: The clinical data underlying this article cannot be shared publicly due to privacy reasons. The signal processing codes developed in this article will be shared on github or through openEP (https://openep.io). Requests to access these datasets should be directed to Caroline Roney, caroline.roney@kcl.ac.uk.

ETHICS STATEMENT

The studies involving human participants were reviewed and approved by Regional Ethics Committee (17/LO/0150 and 15/LO/1803). The patients/participants provided their written informed consent to participate in this study.

AUTHOR CONTRIBUTIONS

CHR, NC, JG, and SN conceived and designed the study. CHR drafted the manuscript, constructed atrial models, ran the simulations, developed the preferential pathways analysis technique, and analysed the clinical and simulation data. NC, BP, RC, JL, AS, PN, RR, MO'N, CAR, PT, MW, and JG collected, annotated, and analysed the STARLIGHT dataset. IS, JW, and SW collected and segmented atrial imaging data. SN and JG provided the supervision. All authors contributed to the article and approved the submitted version.

FUNDING

CHR acknowledges a Medical Research Council Skills Development Fellowship (MR/S015086/1). This study was supported by the UK Engineering and Physical Sciences Research

Council (EP/P010741/1, EP/F043929/1, EP/P01268X/1). This study was supported by the Wellcome Trust Center for Medical at King's College London, and the Department of Health via the National Institute for Health Research Biomedical Research Centre award to Guy's & St Thomas' NHS Foundation Trust in partnership with King's College London and King's College Hospital NHS Foundation Trust; the London Medical Imaging and AI Centre for Value-Based Healthcare and the King's College London BHF centre of research excellence. This work was supported by the Wellcome/EPSRC Centre for Medical Engineering [WT 203148/Z/16/Z]. NC was funded by an education grant from St Jude Medical (Abbott).

SUPPLEMENTARY MATERIAL

The Supplementary Material for this article can be found online at: https://www.frontiersin.org/articles/10.3389/fphys.2021.707189/full#supplementary-material

REFERENCES

Ali, R. L., Hakim, J. B., Boyle, P. M., Zahid, S., Sivasambu, B., Marine, J. E., et al. (2019). Arrhythmogenic propensity of the fibrotic substrate after atrial fibrillation ablation: a longitudinal study using magnetic resonance imaging-based atrial models. *Cardiovasc. Res.* 115, 1757–1765. doi: 10.1093/cvr/cvz083

Azzolin, L., Schuler, S., Dössel, O., and Loewe, A. (2021). A reproducible protocol to assess arrhythmia vulnerability *in silico*: pacing at the end of the effective refractory period. *Front. Physiol.* 12:656411. doi: 10.3389/fphys.2021.656411

Bayer, J. D., Roney, C. H., Pashaei, A., Jaïs, P., and Vigmond, E. J. (2016). Novel Radiofrequency Ablation Strategies for Terminating Atrial Fibrillation in the Left Atrium: A Simulation Study. *Front. Physiol.* 7:108. doi: 10.3389/fphys.2016.00108

Bellmann, B., Lin, T., Ruppersberg, P., Zettwitz, M., Guttmann, S., Tscholl, V., et al. (2018). Identification of active atrial fibrillation sources and their discrimination from passive rotors using electrographical flow mapping. *Clin. Res. Cardiol.* 107, 1021–1032. doi: 10.1007/s00392-018-1274-7

Boyle, P. M., Hakim, J. B., Zahid, S., Franceschi, W. H., Murphy, M. J., Vigmond, E. J., et al. (2018). Comparing reentrant drivers predicted by image-based computational modeling and mapped by electrocardiographic imaging in persistent atrial fibrillation. *Front. Physiol.* 9:414. doi: 10.3389/fphys.2018.00414

Calkins, H., Hindricks, G., Cappato, R., Kim, Y. H., Saad, E. B., Aguinaga, L., et al. (2017). 2017 HRS/EHRA/ECAS/APHRS/SOLAECE expert consensus statement on catheter and surgical ablation of atrial fibrillation. *Europace* 20, e1–e160. doi: 10.1093/europace/eux274

Child, N., Clayton, R. H., Roney, C. H., Laughner, J. I., Shuros, A., Neuzil, P., et al. (2018). Unraveling the underlying arrhythmia mechanism in persistent atrial fibrillation: results from the STARLIGHT study. *Circ. Arrhythmia Electrophysiol.* 11:e005897. doi: 10.1161/CIRCEP.117.005897

Courtemanche, M., Ramirez, R. J., and Nattel, S. (1998). Ionic mechanisms underlying human atrial action potential properties: insights from a mathematical model. *Am. J. Physiol.* 275, H301–H321. doi: 10.1152/ajpheart.1998.275.1.H301

Courtemanche, M., Ramirez, R. J., and Nattel, S. (1999). Ionic targets for drug therapy and atrial fibrillation-induced electrical remodeling: insights from a mathematical model. *Cardiovasc. Res.* 42, 477–489. doi: 10.1016/s0008-6363(99)00034-6

Csepe, T. A., Hansen, B. J., and Fedorov, V. V. (2017). Atrial fibrillation driver mechanisms: insight from the isolated human heart. *Trends Cardiovasc. Med.* 27, 1–11. doi: 10.1016/j.tcm.2016.05.008

Dapogny, C., Dobrzynski, C., Frey, P. (2014). Three-dimensional adaptive domain remeshing, implicit domain meshing, and applications to free and moving boundary problems. *J. Comput. Phys.* 262, 358–378. doi: 10.1016/j.jcp.2014.01.005

Dharmaprani, D., Schopp, M., Kuklik, P., Chapman, D., Lahiri, A., Dykes, L., et al. (2019). Renewal theory provides a universal quantitative framework to characterise the continuous regeneration of rotational events in cardiac fibrillation. *Circ Arrhythm Electrophysiol.* 12:e007569. doi: 10.1161/CIRCEP.119.007569

Gerstenfeld, E. P., Sahakian, A. V., and Swiryn, S. (1992). Evidence for transient linking of atrial excitation during atrial fibrillation in humans. *Circulation* 86, 375–382. doi: 10.1161/01.CIR.86.2.375

Hansen, B. J., Zhao, J., Csepe, T. A., Moore, B. T., Li, N., Jayne, L. A., et al. (2015). Atrial fibrillation driven by micro-anatomic intramural re-entry revealed by simultaneous sub-epicardial and sub-endocardial optical mapping in explanted human hearts. *Eur. Heart J.* 36, 2390–2401. doi: 10.1093/eurheartj/ehv233

Hocini, M., Ho, S. Y., Kawara, T., Linnenbank, A. C., Potse, M., Shah, D., et al. (2002). Electrical conduction in canine pulmonary veins: electrophysiological and anatomic correlation. *Circulation* 105, 2442–2448. doi: 10.1161/01.CIR.0000016062.80020.11

Horn, B. K., and Schunck, B. G. (1981). Determining optical flow. *Artif. Intell.* 17, 185–203.

Johner, N., Namdar, M., and Shah, D. C. (2019). Individualised approaches for Catheter ablation of AF: patient selection and procedural endpoints. *Arrhythmia Electrophysiol. Rev.* 8, 184–190. doi: 10.15420/aer.2019.33.2

Kay, M. W., and Gray, R. A. (2005). Measuring curvature and velocity vector fields for waves of cardiac excitation in 2-D media. *IEEE Trans. Biomed. Eng.* 52, 50–63. doi: 10.1109/TBME.2004.839798

Kochhäuser, S., Jiang, C. Y., Betts, T. R., Chen, J., Deisenhofer, I., Mantovan, R., et al. (2017). Impact of acute atrial fibrillation termination and prolongation of atrial fibrillation cycle length on the outcome of ablation of persistent atrial fibrillation: a substudy of the STAR AF II trial. *Heart Rhythm* 14, 476–483. doi: 10.1016/j.hrthm.2016.12.033

Krueger, M. W., Rhode, K. S., O'Neill, M. D., Rinaldi, C. A., Gill, J., Razavi, R., et al. (2014). Patient-specific modeling of atrial fibrosis increases the accuracy of sinus rhythm simulations and may explain maintenance of atrial fibrillation. *J. Electrocardiol.* 47, 324–328. doi: 10.1016/j.jelectrocard.2013.11.003

Labarthe, S., Bayer, J., Coudière, Y., Henry, J., Cochet, H., Jaïs, P., et al. (2014). A bilayer model of human atria: mathematical background, construction, and assessment. *Europace* 16(Suppl 4), iv21–iv29. doi: 10.1093/europace/euu256

Laughner, J., Shome, S., Child, N., Shuros, A., Neuzil, P., Gill, J., et al. (2016). Practical considerations of mapping persistent atrial fibrillation with whole-chamber basket catheters. *JACC Clin. Electrophysiol.* 2, 55–65. doi: 10.1016/j.jacep.2015.09.017

Lee, G., Kumar, S., Teh, A., Madry, A., Spence, S., Larobina, M., et al. (2014). Epicardial wave mapping in human long-lasting persistent atrial fibrillation: transient rotational circuits, complex wavefronts, and disorganized activity. *Eur. Heart J.* 35, 86–97. doi: 10.1093/eurheartj/eht267

Lim, H. S., Derval, N., Komatsu, Y., Zellerhoff, S., Denis, A., Shah, A. J., et al. (2015). Is ablation to termination the best strategy for ablation of persistent atrial fibrillation. *Circ. Arrhythmia Electrophysiol.* 8, 963–970. doi: 10.1161/CIRCEP.114.001721

Narayan, S. M., Patel, J., Mulpuru, S., and Krummen, D. E. (2012). Focal impulse and rotor modulation ablation of sustaining rotors abruptly terminates persistent atrial fibrillation to sinus rhythm with elimination on follow-up: a video case study. *Heart Rhythm* 9, 1436–1439. doi: 10.1016/j.hrthm.2012.03.055

Navara, R., Leef, G., Shenasa, F., Kowalewski, C., Rogers, A. J., Meckler, G., et al. (2018). Independent mapping methods reveal rotational activation near pulmonary veins where atrial fibrillation terminates before pulmonary vein isolation. *J. Cardiovasc. Electrophysiol.* 29, 687–695. doi: 10.1111/jce.13446

Ng, J., Kadish, A. H., and Goldberger, J. J. (2007). Technical considerations for dominant frequency analysis. *J. Cardiovasc. Electrophysiol.* 18, 757–764. doi: 10.1111/j.1540-8167.2007.00810.x

Pashakhanloo, F., Herzka, D. A., Ashikaga, H., Mori, S., Gai, N., Bluemke, D. A., et al. (2016). Myofiber architecture of the human atria as revealed by submillimeter diffusion tensor imaging. *Circ. Arrhythmia Electrophysiol.* 9, 1–9. doi: 10.1161/CIRCEP.116.004133

Potse, M. (2018). Scalable and accurate ECG simulation for reaction-diffusion models of the human heart. *Front. Physiol.* 9:370. doi: 10.3389/fphys.2018.00370

Razeghi, O., Solís-Lemus, J. A., Lee, A. W. C., Karim, R., Corrado, C., Roney, C. H., et al. (2020). CemrgApp: An interactive medical imaging application with image processing, computer vision, and machine learning toolkits for cardiovascular research. *SoftwareX*, 12:100570. doi: 10.1016/j.softx.2020.100570

Romero, J., Di Biase, L., Mohanty, S., Trivedi, C., Patel, K., Parides, M., et al. (2020). Long-term outcomes of left atrial appendage electrical isolation in patients with nonparoxysmal atrial fibrillation: a propensity score-matched analysis. *Circ. Arrhythmia Electrophysiol.* 13:e008390. doi: 10.1161/CIRCEP.120.008390

Roney, C. H., Bayer, J. D., Cochet, H., Meo, M., Dubois, R., Jaïs, P., et al. (2018). Variability in pulmonary vein electrophysiology and fibrosis determines arrhythmia susceptibility and dynamics. *PLoS Comput. Biol.* 14:e1006166. doi: 10.1371/journal.pcbi.1006166

Roney, C. H., Bayer, J. D., Zahid, S., Meo, M., Boyle, P. M., Trayanova, N. A., et al. (2016). Modelling methodology of atrial fibrosis affects rotor dynamics and electrograms. *Europace*. 18, iv146–iv155. doi: 10.1093/europace/euw365

Roney, C. H., Beach, M. L., Mehta, A. M., Sim, I., Corrado, C., Bendikas, R., et al. (2020a). *In silico* comparison of left atrial ablation techniques that target the anatomical, structural, and electrical substrates of atrial fibrillation. *Front. Physiol.* 11:572874. doi: 10.3389/fphys.2020.572874

Roney, C. H., Bendikas, R., Pashakhanloo, F., Corrado, C., Vigmond, E. J., McVeigh, E. R., et al. (2020b). Constructing a human atrial fibre atlas. *Ann. Biomed. Eng.* 49, 233–250. doi: 10.1007/s10439-020-02525-w

Roney, C. H., Cantwell, C. D., Bayer, J. D., Qureshi, N. A., Lim, P. B., Tweedy, J. H., et al. (2017a). Spatial resolution requirements for accurate identification of drivers of atrial fibrillation. *Circ. Arrhythmia Electrophysiol.* 10:e004899. doi: 10.1161/CIRCEP.116.004899

Roney, C. H., Cantwell, C. D., Qureshi, N. A., Chowdhury, R. A., Dupont, E., Lim, P. B., et al. (2017b). Rotor tracking using phase of electrograms recorded during atrial fibrillation. *Ann. Biomed. Eng.* 45, 910–923. doi: 10.1007/s10439-016-1766-4

Roney, C. H., Pashaei, A., Meo, M., Dubois, R., Boyle, P. M., Trayanova, N. A., et al. (2019). Universal atrial coordinates applied to visualisation, registration and construction of patient specific meshes. *Med. Image Anal.* 55, 65–75. doi: 10.1016/j.media.2019.04.004

Roy, A., Varela, M., and Aslanidi, O. (2018). Image-based computational evaluation of the effects of atrial wall thickness and fibrosis on re-entrant drivers for atrial fibrillation. *Front. Physiol.* 9:1352. doi: 10.3389/fphys.2018.01352

Saliani, A., Tsikhanovich, A., and Jacquemet, V. (2019). Visualization of interpolated atrial fiber orientation using evenly-spaced streamlines. *Comput. Biol. Med.* 111:103349. doi: 10.1016/j.compbiomed.2019.103349

Shkurovich, S., Sahakian, A. V., and Swiryn, S. (1998). Detection of atrial activity from high-voltage leads of implantable ventricular defibrillators using a cancellation technique. *IEEE Tran. Biomed. Eng.* 45, 229–234. doi: 10.1109/10.661270

Sim, I., Razeghi, O., Karim, R., Chubb, H., Whitaker, J., O'Neill, L., et al. (2019). Reproducibility of atrial fibrosis assessment using CMR imaging and an open source platform. *JACC Cardiovasc. Imaging* 12, 2076–2077. doi: 10.1016/j.jcmg.2019.03.027

Singh, S. M., D'Avila, A., Kim, Y. H., Aryana, A., Mangrum, J. M., Michaud, G. F., et al. (2017). Termination of persistent atrial fibrillation during pulmonary vein isolation: insight from the MAGIC-AF trial. *Europace* 19, 1657–1663. doi: 10.1093/europace/euw266

Van Nieuwenhuyse, E., Strisciuglio, T., Lorenzo, G., El Haddad, M., Goedgebeur, J., Van Cleemput, N., et al. (2021). Evaluation of directed graph-mapping in complex atrial tachycardias. *JACC Clin. Electrophysiol.* 936–949. doi: 10.1016/j.jacep.2020.12.013

Vandersickel, N., Van Nieuwenhuyse, E., Van Cleemput, N., Goedgebeur, J., El Haddad, M., De Neve, J., et al. (2019). Directed networks as a novel way to describe and analyze cardiac excitation: directed graph mapping. *Front. Physiol.* 10:1138. doi: 10.3389/fphys.2019.01138

Verma, A., Jiang, C.-Y., Betts, T. R., Chen, J., Deisenhofer, I., Mantovan, R., et al. (2015). Approaches to catheter ablation for persistent atrial fibrillation. *N. Engl. J. Med.* 372, 1812–1822. doi: 10.1056/NEJMoa1408288

Vigmond, E. J., Hughes, M., Plank, G., and Leon, L. J. (2003). Computational tools for modeling electrical activity in cardiac tissue. *J. Electrocardiol.* 36(Suppl):69–74. doi: 10.1016/j.jelectrocard.2003.09.017

Zahid, S., Cochet, H., Boyle, P. M., Schwarz, E. L., Whyte, K. N., Vigmond, E. J., et al. (2016). Patient-derived models link re-entrant driver localization in atrial fibrillation to fibrosis spatial pattern. *Cardiovasc. Res.* 110, 443–454. doi: 10.1093/cvr/cvw073

Zhao, J., Hansen, B. J., Wang, Y., Csepe, T. A., Sul, L. V., Tang, A., et al. (2017). Three-dimensional integrated functional, structural, and computational mapping to define the structural "fingerprints" of heart-specific atrial fibrillation drivers in human heart *ex vivo*. *J. Am. Heart Assoc.* 6:e005922. doi: 10.1161/JAHA.117.005922

Conflict of Interest: JL and AS were employed by Boston Scientific Corp.

The remaining authors declare that the research was conducted in the absence of any commercial or financial relationships that could be construed as a potential conflict of interest.

Publisher's Note: All claims expressed in this article are solely those of the authors and do not necessarily represent those of their affiliated organizations, or those of the publisher, the editors and the reviewers. Any product that may be evaluated in this article, or claim that may be made by its manufacturer, is not guaranteed or endorsed by the publisher.

frontiers in Physiology

BRIEF RESEARCH REPORT
published: 04 October 2021
doi: 10.3389/fphys.2021.730736

Comparing Non-invasive Inverse Electrocardiography With Invasive Endocardial and Epicardial Electroanatomical Mapping During Sinus Rhythm

*Robert W. Roudijk[1†], Machteld J. Boonstra[1†], Rolf Brummel[1], Wil Kassenberg[1], Lennart J. Blom[1], Thom F. Oostendorp[2], Anneline S. J. M. te Riele[1], Jeroen F. van der Heijden[1], Folkert W. Asselbergs[1,3,4], Peter M. van Dam[1,5] and Peter Loh[1]**

[1] Division Heart and Lungs, Department of Cardiology, University Medical Center Utrecht, Utrecht University, Utrecht, Netherlands, [2] Radboud University Nijmegen Medical Centre, Donders Institute for Brain, Cognition and Behaviour, Nijmegen, Netherlands, [3] Faculty of Population Health Sciences, Institute of Cardiovascular Science, University College London, London, United Kingdom, [4] Health Data Research UK, Institute of Health Informatics, University College London, London, United Kingdom, [5] ECG Excellence BV, Nieuwerbrug, Netherlands

OPEN ACCESS

Edited by:
Jichao Zhao,
The University of Auckland,
New Zealand

Reviewed by:
Emilio Macchi,
University of Parma, Italy
Jan E. Azarov,
Komi Scientific Center (RAS), Russia

***Correspondence:**
Peter Loh
p.loh@umcutrecht.nl

[†] These authors have contributed equally to this work and share first authorship

Specialty section:
This article was submitted to Cardiac Electrophysiology, a section of the journal Frontiers in Physiology

Received: 25 June 2021
Accepted: 01 September 2021
Published: 04 October 2021

Citation:
Roudijk RW, Boonstra MJ, Brummel R, Kassenberg W, Blom LJ, Oostendorp TF, te Riele ASJM, van der Heijden JF, Asselbergs FW, van Dam PM and Loh P (2021) Comparing Non-invasive Inverse Electrocardiography With Invasive Endocardial and Epicardial Electroanatomical Mapping During Sinus Rhythm. Front. Physiol. 12:730736. doi: 10.3389/fphys.2021.730736

This study presents a novel non-invasive equivalent dipole layer (EDL) based inverse electrocardiography (*i*ECG) technique which estimates both endocardial and epicardial ventricular activation sequences. We aimed to quantitatively compare our *i*ECG approach with invasive electro-anatomical mapping (EAM) during sinus rhythm with the objective of enabling functional substrate imaging and sudden cardiac death risk stratification in patients with cardiomyopathy. Thirteen patients (77% males, 48 ± 20 years old) referred for endocardial and epicardial EAM underwent 67-electrode body surface potential mapping and CT imaging. The EDL-based *i*ECG approach was improved by mimicking the effects of the His-Purkinje system on ventricular activation. EAM local activation timing (LAT) maps were compared with *i*ECG-LAT maps using absolute differences and Pearson's correlation coefficient, reported as mean ± standard deviation [95% confidence interval]. The correlation coefficient between *i*ECG-LAT maps and EAM was 0.54 ± 0.19 [0.49–0.59] for epicardial activation, 0.50 ± 0.27 [0.41–0.58] for right ventricular endocardial activation and 0.44 ± 0.29 [0.32–0.56] for left ventricular endocardial activation. The absolute difference in timing between *i*ECG maps and EAM was 17.4 ± 7.2 ms for epicardial maps, 19.5 ± 7.7 ms for right ventricular endocardial maps, 27.9 ± 8.7 ms for left ventricular endocardial maps. The absolute distance between right ventricular endocardial breakthrough sites was 30 ± 16 mm and 31 ± 17 mm for the left ventricle. The absolute distance for latest epicardial activation was median 12.8 [IQR: 2.9–29.3] mm. This first in-human quantitative comparison of

*i*ECG and invasive LAT-maps on both the endocardial and epicardial surface during sinus rhythm showed improved agreement, although with considerable absolute difference and moderate correlation coefficient. Non-invasive *i*ECG requires further refinements to facilitate clinical implementation and risk stratification.

Keywords: inverse problem of electrocardiography, sudden cardiac death, electrocardiographic imaging (ECGI), equivalent dipole layer, cardiac arrhythmia, electroanatomical mapping, non-invasive mapping

INTRODUCTION

Non-invasive imaging of cardiac depolarization and repolarization sequences, known as electrocardiographic imaging, is based on body surface potentials maps and cardiovascular imaging (Huiskamp and Van Oosterom, 1988; Ramanathan et al., 2004; van Dam et al., 2009; Rudy, 2013). Two major methods have been introduced: (1) the potential based Equivalent Potential Distribution (EPD) method (Ramanathan et al., 2004; Sapp et al., 2012; Rudy, 2013; Cluitmans et al., 2017; Duchateau et al., 2019; Graham et al., 2019; Hohmann et al., 2019), which estimates electrograms on the epicardium in a linear relation whereof activation and recovery timings are determined on the epicardium, and (2) the wave-front formulation based on the equivalent dipole layer (EDL) (Huiskamp and Van Oosterom, 1988; van Dam et al., 2009; van Oosterom, 2014; Oosterhoff et al., 2016). The EDL-based method, used in this study and referred to as inverse electrocardiography (*i*ECG), calculates transmembrane potentials at both the endocardium and epicardium as a local source, whereof activation and recovery times are derived (van Dam et al., 2009; van Oosterom, 2014). More precisely, these transmembrane potentials represented in the EDL-based method create currents that are proportional to the second derivative of the local transmembrane potentials (Leon and Witkowski, 1995). Since the relation between the transmembrane potentials and the body surface potential map is non-linear, an initial estimation of the activation sequence is required (Huiskamp and Van Oosterom, 1988; van Dam et al., 2009; Oosterhoff et al., 2016).

The implementation of electrocardiographic imaging in clinical practice is limited, which may partly be explained by poor results for estimations during sinus rhythm (Cluitmans et al., 2018). Whereas estimation of rhythms with a single ventricular focus, i.e., ventricular pacing or premature ventricular complexes, is promising (Rudy, 2013; Oosterhoff et al., 2016; Cluitmans et al., 2018; Duchateau et al., 2019; Graham et al., 2019; Hohmann et al., 2019). Estimation of ventricular activation during sinus rhythm is complicated by the nearly simultaneous initiation of activation waves from multiple endocardial sites mediated by the His-Purkinje system (Durrer et al., 1970). Quantitative comparison studies during sinus rhythm are limited and have shown poor performance, represented by low correlation coefficients between non-invasive estimations and invasive mapping (Duchateau et al., 2019).

The proposed *i*ECG method mimics the effects of the His-Purkinje system on the initiation of ventricular activation waves to improve accuracy of estimation during sinus rhythm (van Dam et al., 2009; Sapp et al., 2012; Rudy, 2013; van Oosterom, 2014; Cluitmans et al., 2017; Duchateau et al., 2019; Graham et al., 2019). With improved accuracy of estimation during sinus rhythm, *i*ECG techniques may enable functional imaging of electro-anatomical substrates on both the epicardium and endocardium and aid early detection and non-invasive risk stratification of patients with cardiomyopathies (Tung et al., 2020). Therefore, a quantitative comparison of this novel *i*ECG method for estimation of ventricular activation during sinus rhythm was performed. In this study, invasive endocardial and epicardial high-resolution local activation timing (LAT) maps obtained during electro-anatomical mapping (EAM) were compared to non-invasively estimated activation patterns.

MATERIALS AND METHODS

Patient Population

Patients referred for endocardial and epicardial EAM and ablation were enrolled. Epicardial mapping was indicated because of either recurrent ventricular tachycardia with a suspected epicardial substrate or symptomatic premature ventricular complexes with a prior failed endocardial ablation. Anti-arrhythmic drugs, except amiodarone, were discontinued for a minimum of three half-lives prior to the ablation procedure. Amiodarone was continued because of its long half-life. The study protocol was approved by the local institutional review board (University Medical Center Utrecht, Utrecht, Netherlands; protocol nr.17/628). The study was conducted according to the declaration of Helsinki and all patients gave informed consent prior to non-invasive and invasive mapping.

Data Acquisition

The workflow of the study is depicted in **Figure 1**. Patients underwent 67-electrode body surface potential mapping (sampling frequency 2048 Hz, Biosemi, Amsterdam, Netherlands) prior to the invasive mapping procedure and the electrode positions were captured using a 3-dimensional camera (Intel Realsense D435, Santa Clara, CA, United States) (Hoekema et al., 1999). Per patient, cardiac computed tomography (CT, Philips Healthcare, Best, Netherlands) was performed to manually create patient specific anatomical models of the ventricles with both epicardial and endocardial surfaces, ventricular blood pool, lungs and thorax. The ventricular anatomical models were supplemented with patient specific endocardial structures associated with early ventricular activation through the His-Purkinje system (e.g., the left ventricular papillary muscles and right ventricular moderator band) (Durrer et al., 1970). Electrode positions were

reconstructed by registering 3-dimensional images to the thorax model. The volume conductor model was computed using the boundary element method. Conductivity values of 0.2 S/m for the thorax and ventricular tissue, 0.04 S/m for the lungs and 0.6 S/m for the blood cavities were used (**Supplementary Methods**).

Signal Processing

Baseline drift and 50 Hz noise were removed from the body surface potential map signals. Per patient, five subsequent sinus rhythm complexes were selected to be analyzed in the *i*ECG procedure. Premature ventricular complexes and sinus rhythm complexes prior to premature ventricular complexes were excluded from analysis. The root mean square of all recorded signals was used to annotate QRS onset, J-point and T-wave end. One lead from the standard 12-lead ECG was used as timing reference to allow comparison of absolute timings between *i*ECG estimations and invasive EAM timings.

Inverse Electrocardiographic Imaging Procedure

The novel *i*ECG method has been described in more detail in the **Supplementary Methods** (Greensite et al., 1990; Huiskamp and Greensite, 1997; van Dam et al., 2009; van Oosterom, 2014). In short: the *i*ECG method simulates body surface potential maps using the patient specific EDL cardiac source model, the patient specific volume conductor model and the estimated ventricular activation sequence. Nine regions containing potential foci were localized: four at the left ventricular septum, two at the base of both the posterior and anterior papillary muscles of the left ventricle, two at the right ventricular septum and one at the insertion of the moderator band at the right ventricular free wall free wall (Durrer et al., 1970). The fastest route algorithm was used to compute activation sequences emerging from these locations and combinations of foci (van Dam et al., 2009). All possible combinations of foci were tested as the initial estimation (**Supplementary Methods**). The activation sequence from the initial estimation with the highest correlation between the simulated body surface potential map and the recorded body surface potential map, was selected as input for the optimization step (**Supplementary Methods**) (van Dam et al., 2009). The optimized activation sequence was used to assign LAT to each node in the patient specific ventricular anatomical model (**Figure 1** and **Supplementary Figure 1**).

Invasive Electro-Anatomical Mapping

Invasive EAM was performed under general anesthesia during sinus rhythm or atrial pacing. Ventricular paced complexes and premature ventricular complexes were excluded from analysis. Epicardial access was obtained by percutaneous subxiphoid approach (Sosa et al., 1996) and endocardial access was obtained through the right femoral vein. Access to the left ventricle was gained through a transseptal puncture, using a steerable sheath (Mobicath, Biosense-Webster Inc. Irvine, CA, United States). Anatomical coordinates, LAT maps and voltage maps were automatically created with EAM systems (Carto-3, Biosense-Webster Inc. Irvine, CA, United States or EnSite Precision, Abbott, Chicago, IL, United States) without prior integration of cardiac CT images. Endocardial and epicardial EAM was performed with multi-electrode catheters (PENTARAY® catheter, Biosense-Webster Inc. Irvine, United States or ADVISOR^{TM} HD Grid mapping Catheter, Abbott, Chicago, Il, United States). Unipolar and bipolar electrograms were simultaneously recorded with standard 12-lead ECG (band pass filters 30–500 Hz, sampling frequency 1000 Hz), and one of these leads was used as timing reference for electrograms. Post-procedure, bipolar and corresponding unipolar electrograms were manually reviewed by investigators who were blinded to the information from the corresponding *i*ECG map. LAT was set at the maximal amplitude of the bipolar signal, corresponding to maximum downslope (dV/dt) in unipolar electrograms (see **Figure 2** for examples) (Cantwell et al., 2015). In case of doubt, recordings from neighboring electrograms were taken into consideration to determine LAT. Epicardial and endocardial myocardium with abnormal voltage electrograms was defined as bipolar voltage amplitude < 1.5 mV.

Comparison of Non-invasive Mapping and Invasive Mapping

Anatomical coordinates with corresponding annotated LAT and bipolar voltage, obtained during EAM, were exported (MATLAB-2017a, The Mathworks Inc, Natick, United States). These anatomical coordinates were semi-automatically aligned to the CT-based ventricular anatomical model, according to anatomical landmarks (right ventricular outflow tract and the apex of the ventricles, **Figure 1**). Endocardial alignment was optimized using a closest point matching algorithm (Bergquist et al., 2019). Surface Laplacian interpolation was used for areas with incomplete EAM, within a distance of 10 mm. To reduce misalignment errors, invasively collected datapoints for myocardial surfaces were projected onto the nearest node of the CT-based model and all projections per node were averaged. *i*ECG-LAT maps were referenced to the same timing reference used during the EAM procedure. Pearson's inter-map correlation coefficient and inter-map absolute difference in milliseconds (ms) were determined for the epicardium, right ventricular endocardium and left ventricular endocardium. Breakthrough of activation was defined as nodes with the lowest LAT value, and sites of latest activation were defined as the node with the highest LAT value. Euclidian distances between sites of earliest and latest activation were determined in millimeters (mm). Myocardial conduction velocity over surfaces was calculated as the minimum positive velocity between nodes, velocities more than 3 mm/ms were excluded. A relatively high cut-off of 3 mm/ms was used to account for velocities observed in regions with a high density of Purkinje-myocardial junctions as the conduction velocity of Purkinje fibers ranges between 2 and 3 mm/ms. This cut-off was used to take into account that the electrical pulse may spread via the Purkinje fibers to the neighboring myocardial tissue instead of via the myocardial tissue itself. Ventricular activation sequences were presented in right anterior oblique, left anterior oblique and inferior views (Cosio et al., 1999).

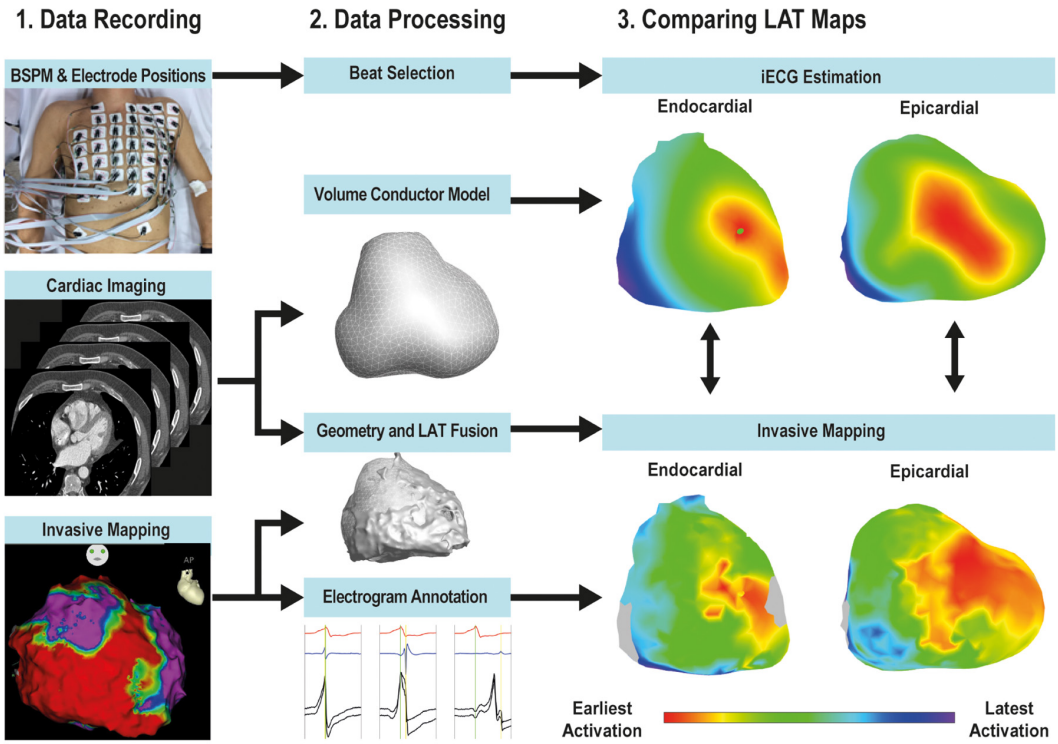

FIGURE 1 | Workflow. The workflow of the study consisted of data recording (left panel), data processing (middle panel) and quantitative comparison (right panel). Body surface potential mapping (BSPM) using 67-electrodes was performed. CT imaging of the thorax and cardiac anatomy was performed and used to construct patient specific anatomical models and compute the volume conductor. The EAM anatomical point clouds were registered to the CT-based ventricular anatomy and LAT and bipolar values were projected on the CT-based anatomy. EAM-LAT maps were quantitatively compared to *i*ECG-LAT maps.

Statistical Analysis

Data were presented as mean ± standard deviation or median [interquartile range], supplemented with 95% confidence interval (CI). Continuous data were compared using (un)paired Student's *t*-test or Mann–Whitney *U* test as appropriate. Differences between *i*ECG-LAT maps and EAM-LAT maps were presented as absolute difference in ms for timings or absolute difference in mm for differences in sites of breakthrough, earliest activation or latest activation. *i*ECG-LAT and EAM-LAT maps were compared with Pearson's linear correlation and presented as correlation coefficient. Agreement between *i*ECG and EAM-LAT timings was quantitatively compared by Bland-Altman plots. A 2-sided *P*-value of <0.05 was considered significant. Statistical analysis was performed in MATLAB (MATLAB 2017a, The Mathworks Inc, Natick, MA, United States).

RESULTS

Study Population

Thirteen patients (77% males, age 48 ± 20 years) referred for epicardial and endocardial mapping and ablation of ventricular tachycardia (n = 10) or symptomatic premature ventricular complexes (n = 3) were included. Patients were diagnosed with arrhythmogenic cardiomyopathy (n = 5), dilated cardiomyopathy (n = 2), symptomatic premature ventricular complexes (n = 3), or ventricular arrhythmias after healed myocarditis (n = 3). Patients had either sinus rhythm (n = 10) or atrial pacing by an implanted permanent pacemaker (n = 3) during body surface potential recording and the EAM procedure, see **Supplementary Table 1** for a summary of the included population and **Supplementary Table 2** for a detailed description per included patient.

Electrocardiographic Imaging Procedure Quality

The patient cardiac anatomical models had an inter-node spatial resolution of 8 ± 1 mm. The QRS complex morphology of the recorded body surface potential maps correlated with the QRS complex morphology of the simulated body surface potential maps in the *i*ECG procedure (correlation coefficient = 0.97 ± 0.02). The QRS morphology of the timing reference lead during EAM correlated with the timing reference lead of the recorded body surface potential map (correlation coefficient = 0.94 ± 0.02).

Electro-Anatomical Mapping Quality

Epicardial EAM was performed in all patients, right ventricular endocardial EAM in 10 patients and left ventricular endocardial EAM in four patients. EAM consisted of median 4611 [3369–5633] epicardial electrograms, 910 [280–1638] right ventricular

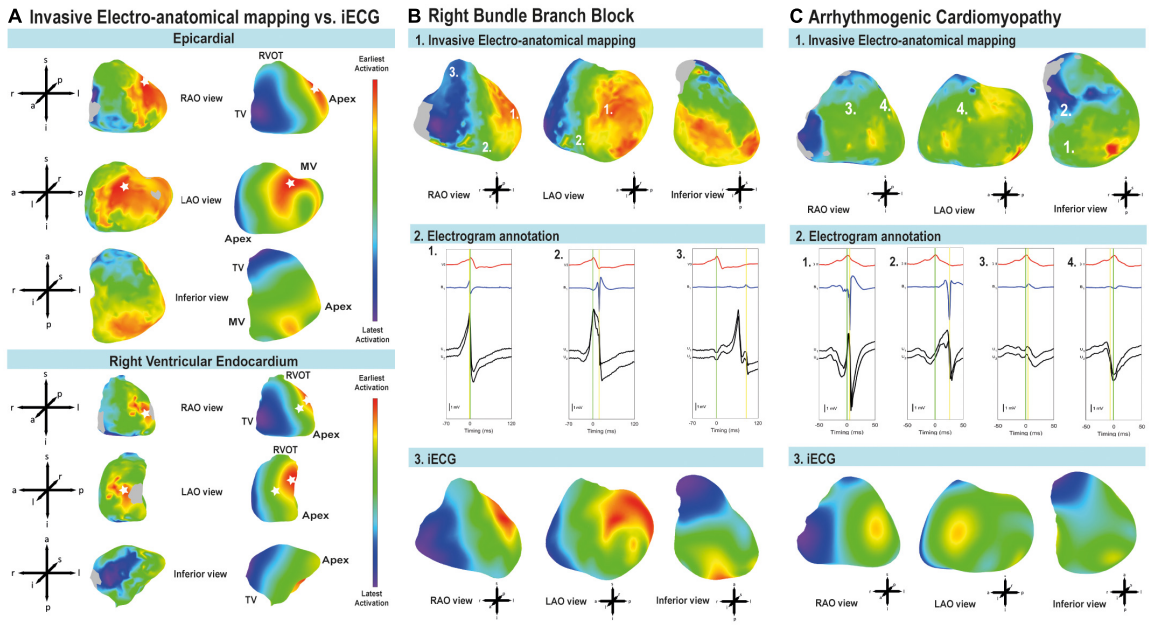

FIGURE 2 | Comparison of early and latest activated myocardium and annotation of local activation timing. **(A)** LAT maps derived from iECG and EAM from early (red) to late (blue) activation. Breakthroughs of ventricular activation are indicated with a white asterisk. Epicardium: both EAM and iECG estimation showed breakthrough of activation at the right ventricular free wall and the left ventricular free wall. Endocardial activation of the right ventricular free wall: iECG estimation corresponds to EAM, intraventricular septum activation was located more toward the apex in the EAM. Imaging views are based on the anatomical approach for EAM (Cosio et al., 1999). MV, mitral valve; RVOT, right ventricular outflow tract; TV, tricuspid valve. **(B)** Patient with healed myocarditis and right bundle branch block. Imaging views are based on the anatomical approach for EAM (Cosio et al., 1999). 1: Epicardial EAM-LAT map from early (red) to late (blue) activation. The early regions in the left ventricle and late regions in the right ventricle suggest a right bundle branch block. 2: EGM annotation of bipolar electrograms. The green line corresponds to the timing reference. The yellow line shows annotation to the maximal amplitude of the bipolar signal. 3: *i*ECG-LAT map of epicardial activation from early (red) to late (blue) activation. **(C)** Epicardial activation and electrogram annotation in a patient with arrhythmogenic cardiomyopathy. Imaging views are based on the anatomical approach for EAM (Cosio et al., 1999). 1: EAM-LAT maps from early (red) to latest (blue) activation. 2: Electrogram annotation of bipolar signals. The green line corresponds to the timing reference. The yellow line shows annotation to the maximal amplitude of the bipolar signal. 3: *i*ECG-LAT map from early (red) to late (blue) activation.

endocardial electrograms and 605 [247–1412] left ventricular endocardial electrograms. The number of annotations per square mm was 20 ± 11 for the epicardium, 10 ± 5 for the right ventricular endocardium and 8 ± 4 for the left ventricular endocardium. The percentage of EAM per surface was on average 67 [range: 48–82]% of anatomical nodes for the epicardium, 45 [range: 15–79]% for the right ventricular endocardium and 48 [range: 22–71]% for the left ventricular endocardium. The anatomical EAM model was limited to the locations where the catheter had been positioned during the EAM procedure.

Local Activation Timing

Figure 2A shows an example of the comparison of *i*ECG and EAM for LAT maps, and the comparison between earliest and latest activated nodes for both the epicardium and endocardium. The ranges between earliest and latest ventricular activation were not significantly different between *i*ECG-LAT maps and EAM-LAT maps (111 ± 23 vs. 124 ± 39 ms, $p = 0.311$). The ranges of earliest and latest activation per patient are included in **Supplementary Table 3**. **Figure 2B** shows an example of the *i*ECG and the EAM approach in a patient with a healed myocarditis with right bundle branch block. The fast and His-Purkinje mediated activation of the left ventricular myocardium is shown in contrast to the relatively slower activation of the right ventricle due to the right bundle branch block. **Figure 2C** shows an example of the activation pattern and epicardial electrogram annotation in a patient with arrhythmogenic cardiomyopathy. Furthermore, all LAT and voltage maps of each included patient are available as **Supplementary Figure 1**. The mean correlation coefficient between *i*ECG-LAT maps and EAM-LAT maps was 0.54 ± 0.19; [95% CI: 0.49–0.59] for epicardial maps, 0.50 ± 0.27; [95% CI: 0.41–0.58] for endocardial right ventricular maps and 0.44 ± 0.29; [95% CI: 0.32–0.56] for endocardial left ventricular maps (**Table 1**). The moderate agreement of LAT between *i*ECG and EAM maps is shown in **Figure 3A** for all included electrograms on the epicardium ($R = 0.632$, $p < 0.001$), right ventricular endocardium ($R = 0.597$, $p < 0.001$) and left ventricular endocardium ($R = 0.546$, $p < 0.001$). **Figure 3B** shows that a prolonged QRS duration of the included complexes did not affect correlation coefficient or absolute difference. **Figure 3C** suggest that a higher density of mapped electrograms per mm2 reduces the scatter of correlation coefficients. The absolute difference for epicardial LAT maps was 17.4 ± 7.2 ms; [95% CI: 15.6–19.2], for endocardial right ventricular maps 19.5 ± 7.7 ms; [95% CI: 17.2–21.7], and for endocardial left ventricular maps 27.9 ± 8.7 ms; [95% CI: 24.2–31.5]. The relation between

TABLE 1 | Comparison between *i*ECG and EAM.

Parameters	Mean ± SD	Median [IQR]
Epicardium		
Correlation coefficient	54.1 ± 19.0	51.0 [44.0 – 71.5]
Absolute difference (ms)	17.4 ± 7.2	15.1 [12.8 – 19.6]
Absolute difference earliest breakthrough (mm)	42.1 ± 18.6	37.9 [28.4 – 58.5]
Absolute difference terminal site of activation (mm)	54.1 ± 26.9	51.0 [33.4 - 69.6]
Absolute difference timing of latest activation (ms)	19.1 ± 20.9	12.8 [2.9 – 29.3]
EAM breakthroughs (n)	3.15 ± 0.9	3.0 [2.5 - 4.0]
*i*ECG breakthroughs (n)	3.3 ± 0.8	3.4 [2.9 – 4.0]
Right ventricular endocardium		
Correlation coefficient	49.6 ± 27.3	55.5 [46.0 – 62.0]
Absolute difference (ms)	19.5 ± 7.7	17.4 [13.2 - 24.4]
Absolute difference earliest breakthrough (mm)	29.9 ± 16.0	28.3 [22.3 - 47.4]
Absolute difference terminal site of activation (mm)	46.7 ± 28.8	37.0 [24.5 - 69.4]
Absolute difference timing of latest activation (ms)	20.4 ± 16.7	15.2 [10.1 - 28.7]
EAM breakthroughs (n)	2.1 ± 0.6	2.0 [2.0 - 2.25]
*i*ECG breakthroughs (n)	1.8 ± 0.6	2.0 [1.2 - 2.3]
Left ventricular endocardium		
Correlation coefficient	44.0 ± 28.8	53.5 [13.5 - 65.0]
Absolute difference (ms)	27.9 ± 8.7	27.3 [20.1 - 36.2]
Absolute difference earliest breakthrough (mm)	31.0 ± 16.8	31.1 [14.7 - 47.1]
Absolute difference terminal site of activation (mm)	32.7 ± 17.2	39.2 [14.8 – 44.1]
Absolute difference timing of latest activation (ms)	29.5 ± 26.3	20.8 [10.4 - 57.3]
EAM breakthroughs (n)	1.8 ± 1.0	1.5 [1.0 - 2.8]
*i*ECG breakthroughs (n)	1.8 ± 0.5	2.0 [1.3 - 2.0]

the percentage of mapped anatomical points during EAM and the agreement for LAT values is shown in **Figure 3D**. The correlation coefficient between *i*ECG-LAT maps and EAM-LAT maps was not significantly affected by the absolute number of EAM electrograms ($p = 0.324$), the number of electrograms with abnormal voltage ($p = 0.306$) or the QRS duration ($p = 0.485$) (see **Supplementary Figure 2**). However, the annotation density and the percentage of mapped anatomical points per map affected the agreement between *i*ECG and EAM. In maps with a low annotation density or lower percentage of mapped anatomical points the correlation coefficients were low (**Figures 3C,D**). This may have negatively affected the observed correlation coefficients in this study because endocardial EAM was often limited to either the right ventricular or left ventricular surface. The *i*ECG estimations were based on five QRS complexes selected from the body surface potential maps, but a Bland-Altman analysis did not result in divergent results per included QRS complex. These scatter plots and Bland-Altman plots for each included patient are available in **Supplementary Figure 3**.

Localization of Earliest Breakthrough and Areas of Latest Activation

The number of endocardial breakthrough points was similar when comparing *i*ECG-LAT maps and EAM-LAT maps: 3.3 ± 0.8 vs. 3.2 ± 0.9 for epicardial maps, 1.8 ± 0.6 vs. 2.1 ± 0.6 for right ventricular endocardial maps and 1.8 ± 0.5 vs. 1.8 ± 1.0 for left ventricular endocardial maps (**Table 1**). These findings were in line with the observations of Durrer et al. and the assumptions of the *i*ECG initial estimation (Durrer et al., 1970). Epicardial breakthrough of activation had an absolute difference between *i*ECG-LAT maps and EAM-LAT maps of 42.1 ± 18.6 mm; [95% CI: 36.7–47.5]. For endocardial breakthrough of activation, the absolute difference was 29.9 ± 16.0 mm; [95% CI: 25.1–34.8] for the right ventricular endocardium and 31.0 ± 16.8 mm; [95% CI: 23.8–38.1] for the left ventricular endocardium. The latest activated nodes had an absolute difference between *i*ECG and EAM of 54.1 ± 26.9 mm; [95% CI: 47.5–60.7] for epicardial maps, 46.7 ± 28.8 mm; [95% CI: 38.8–54.7] for right ventricular endocardial maps and 32.7 ± 17.2mm; [95% CI: 25.1–40.4] for left ventricular endocardial maps (**Table 1**). The timing of the latest activated nodes differed 12.8 [2.9–29.3] ms; [95% CI: 6.4–31.7] for epicardial maps, 15.2 [10.1–28.7] ms; [95% CI: 8.5–32.5] for right ventricular endocardial maps and 20.8 [10.4–57.3] ms; [95% CI: 12.5–71.4] for left ventricular endocardial maps. The myocardial conduction velocity was not significantly different between *i*ECG and EAM maps for, respectively, the epicardium (1.26 ± 0.16 vs. 1.26 ± 0.20 m/s, $p > 0.999$), right ventricular endocardium (1.13 ± 0.09 vs.. 0.94 ± 0.17 m/s, $p = 0.069$) or left ventricular endocardium (1.03 ± 0.11 vs. 0.92 ± 0.07 m/s, $p = 0.968$).

DISCUSSION

This is the first study to quantitatively compare non-invasive, EDL-based *i*ECG estimation of ventricular activation sequences during sinus rhythm with invasive high density endocardial and epicardial EAM in humans. Comparison of agreement between *i*ECG-LAT maps with EAM-LAT maps showed moderate agreement. However, this observed agreement (correlation coefficient = 0.54 ± 0.19) was remarkably higher compared to a recent validation study (correlation coefficient = −0.04 ± 0.3) performed during sinus rhythm (Duchateau et al., 2019). Mimicking the effects of the His-Purkinje system on ventricular activation in the *i*ECG method resulted in activation patterns corresponding to observations of Durrer et al. in experiments with explanted human hearts (Durrer et al., 1970). In contrast to prior EPD-based studies which were limited to estimations on the epicardium, estimation of both the endocardial and epicardial activation sequences was achieved. Although accuracy and spatial resolution require further improvement before implementation of this diagnostic tool in clinical practice, these findings may be of clinical importance for functional non-invasive substrate imaging during sinus rhythm to improve the value of ECG screening and risk stratification of sudden cardiac death (Tung et al., 2020).

Quantitative Comparison

Previous quantitative EPD-based validation studies showed higher agreement between ventricular paced complexes and EAM, compared to sinus rhythm complexes (Duchateau et al., 2019; Graham et al., 2019). Duchateau et al. (2019) showed poor epicardial inter-map correlation coefficient (−0.04 ± 0.3) during

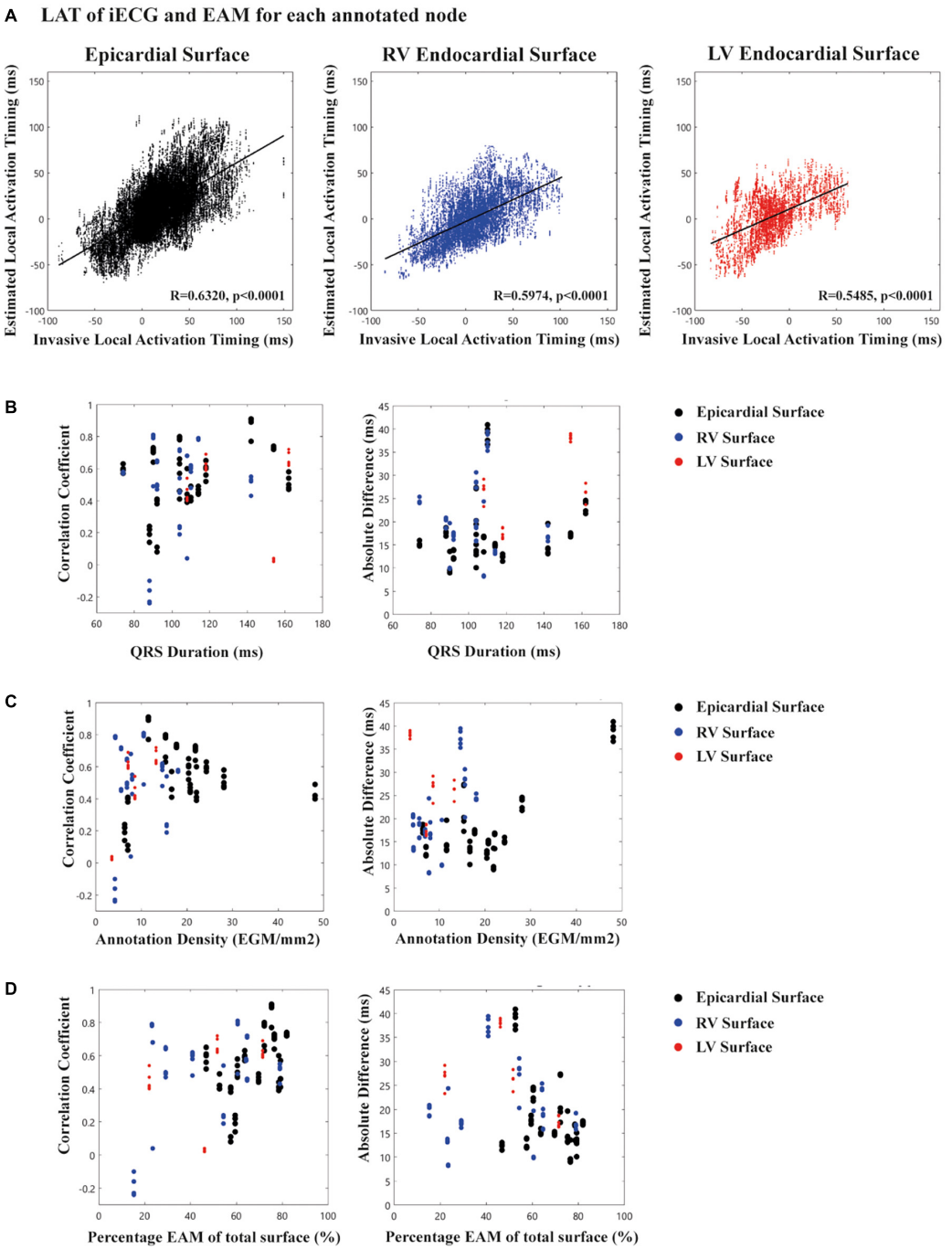

FIGURE 3 | Scatter plots of local activation timing stratified for epicardial and endocardial surfaces. **(A)** For each node in the ventricular anatomy the EAM-LAT values (*X*-axis) are scattered against *i*ECG-LAT values (*Y*-axis). The black line in each plot represents the linear regression line and R-value and *p*-value are shown in each plot. **(B)** Relation between QRS duration (*X*-axis) for the 5 selected complexes in the *i*ECG procedure and correlation coefficient/absolute difference for the LAT values (*Y*-axis). **(C)** Relation between annotation density (*X*-axis) per mm^2 and correlation coefficient/absolute difference for LAT values for the 5 selected complexes in the *i*ECG procedure (*Y*-axis). **(D)** Relation between percentage of EAM of the total surface (*X*-axis) and correlation coefficient/absolute difference for LAT values (*Y*-axis).

sinus rhythm, although correlation coefficients increased with increasing QRS duration. This relation is most likely explained by the complexity of multiple simultaneous ventricular activation waveforms occurring during sinus rhythm, which decreases in rhythms with a single focus (Duchateau et al., 2019). In the present study, a considerably higher agreement (correlation

coefficient 0.54 ± 0.19) between EAM and the novel *i*ECG-LAT maps was observed during sinus rhythm. This improved performance is attributed to the incorporation of the effects of the His-Purkinje system on the initiation of ventricular activation (Oosterhoff et al., 2016). Previously reported absolute difference for breakthrough of epicardial pacing was smaller compared to the present study (13.2–20.7 mm vs. 42.1 ± 18.6 mm) (Oosterhoff et al., 2016; Graham et al., 2019; Hohmann et al., 2019). However, previously reported absolute difference for epicardial breakthrough during sinus rhythm was higher compared to our results (75.6 ± 38.1 mm vs. 42.1 ± 18.6 mm) (Duchateau et al., 2019). Again, these differences may be explained by estimations of rhythms originating from a single ventricular focus and sinus rhythm. Thus, spatial resolution observed in this study was comparable to the earlier studies in paced complexes (Cluitmans et al., 2017; Hohmann et al., 2019). Due to the complex nature of the His-Purkinje system and the Purkinje-myocardial coupling, the implemented methods remain an approximation of the true myocardial activation and His-Purkinje physiology (Durrer et al., 1970; Myerburg, 1971; Veenstra et al., 1984).

We observed a high agreement between estimated and measured body surface potential maps, whereas the inter-map agreement was less. As the inverse problem is ill-posed, completely different ventricular activation sequences can result in similar body surface potential map waveforms, consequently we found a high agreement between body surface potential maps but a lower agreement in myocardial activation patterns.

The conduction velocities calculated on the epicardial and endocardial surfaces in this study for both the EAM-LAT maps and *i*ECG-LAT maps were quite high (>1 m/s). However, we note that these conduction velocities are mostly determined by the velocity estimated at the surface of the myocardium. Consequently, in a Purkinje dense region, surface velocity may appear high because it also reflects the effect of the activation spread by the Purkinje fibers and not only by the myocardial tissue at the endocardial surface. Furthermore, at the epicardial surface, velocities may appear high due to the occurrence of transmural waves.

Modeling the Effects of the His-Purkinje System During Sinus Rhythm

In this study, initial sites of activation were determined in the *i*ECG method based on the observations of Durrer et al. and nine possible sites of early activation were localized (Durrer et al., 1970). Sets of these initial sites of activation were tested based on the correlation coefficient between the computed and recorded body surface potential maps, as described in more detail in the **Supplementary Methods**. This hypothesis was partially tested by comparing the EAM-LAT maps to the *i*ECG-LAT maps. However, as endocardial EAM-LAT maps were often either of the right or the left endocardial surface and also did not cover the complete endocardial surface for each patient, the comparison between the number of identified EAM foci and *i*ECG foci was hampered. This was also reflected in the absolute difference in location of identified foci of approximately 30 mm comparing *i*ECG foci to EAM foci.

Previous versions of EDL-based methods estimating His-Purkinje mediated activation (e.g., sinus rhythm) were based on a multi-focal search algorithm over the complete endocardium and epicardium, where the first identified focus was chosen based on the highest correlation between recorded and simulated body surface potentials (van Dam et al., 2009; Oosterhoff et al., 2016). Consequently, this algorithm directly assumed that by using one focus, most of the underlying activation sequence could be 'explained'. However, sinus rhythm, and especially narrow QRS complex sinus rhythm is an interplay between multiple activation wavefronts. Implementation of the His-Purkinje system excludes these unrealistic estimates and provides the possibility to test multiple near simultaneous foci. At the same time the initial estimation is restricted to the physiologically realistic anatomical areas and the computational burden of the *i*ECG algorithm is minimized.

Post-processing and Reference Standard

Post-processing of ECG signals, electrogram signals, and cardiac imaging influences *i*ECG accuracy (Cluitmans et al., 2018; Graham et al., 2019). To achieve high quality EAM-LAT maps, which were used as gold standard for comparison, electrograms derived from multi-electrode catheters required re-annotation using bipolar and unipolar signals and timing to a timing reference (Cantwell et al., 2015; Graham et al., 2019). However, inhomogeneity in LAT distributions of EAM-LAT maps were observed even after re-annotation, which may have influenced the observed agreement between *i*ECG and EAM-LAT maps. Both the epicardial and endocardial surfaces had an adequate spatial distribution of electrograms as reflected in the number of LAT per mm2 (see **Figure 3C**). Furthermore, the percentage of mapped surfaces was variable and some EAM procedures resulted in incomplete endocardial EAM anatomical point clouds, which affects calculated inter-map correlation coefficient (see **Figures 3C,D**).

Clinical Implications and Future Directions

Despite a considerable improvement of the *i*ECG approach for sinus rhythm, the technique requires further adaptations and refinements that will facilitate implementation in clinical practice. Further integration of cardiovascular imaging techniques may improve performance and spatial resolution (Tung et al., 2020). Currently, the patient specific anatomical models were limited in spatial resolution by the computational models of the *i*ECG procedure, allowing at maximum 3000 cardiac nodes, which directly affects the resolution of the cardiac anatomical model resulting in an inter-node spatial resolution of 8 ± 1mm. Diffuse or local myocardial fibrosis affects ventricular activation patterns in structurally diseased hearts. Integration of these structural abnormalities in the *i*ECG method and refinement of the cardiac anatomical models is likely to improve imaging of electro-anatomical substrates (van Dam et al., 2009; Oosterhoff et al., 2016; Tung et al., 2020). Since electro-anatomical substrates are not limited to solely

the epicardium or endocardium, *i*ECG may allow functional imaging of such 3-dimentional substrates in patients with arrhythmias or cardiomyopathy (Tung et al., 2020). Besides diagnostic implications, non-invasive sinus rhythm *i*ECG may play a role in the monitoring of disease progression and in sudden cardiac death risk stratification in patients with complex electroanatomical substrates, such as inherited cardiomyopathies. Eventually, reducing the number of electrodes of the body surface potential map that currently ranges from 67 to 256 electrodes, may improve clinical applicability (Hoekema et al., 1999). For EDL-based studies, also this study, the 64-electrode setup is often used (van Dam et al., 2009; Oosterhoff et al., 2016). Mathematically this setup suffices, as the number of independent signals is adequately captured using this number of electrodes and additionally, the electrodes are distributed with a high resolution in the high-gradient potential regions on the surface of the thorax (Hoekema et al., 1999).

Limitations

This single center study with a small sample size included patients with structural heart disease, which may influence the generalizability of the results. Additionally, we used a set conduction velocity over the model to determine the initial estimation. This assumption may not hold in the presence of pathologies or myocardial scarring after prior ablation, but the EDL holds for homogeneous anisotropic tissue (Geselowitz, 1992).

Electro-anatomical mapping procedures and body surface potential maps were not simultaneously recorded, but in similar conditions especially concerning anti-arrhythmic drugs. During EAM, complexes were selected using dedicated Carto/Ensite EAM systems. Furthermore, sinus rhythm complexes directly following a premature ventricular complex were excluded for analysis in both the EAM and *i*ECG-LAT map. However, a possible influence of variations in heart rate, autonomic tonus or general anesthesia cannot be excluded. The quality of gold standard EAM may have been influenced by vendor specific algorithms within the EAM systems and regional mapping by the operator during the procedure. Inherent to invasive electrophysiological studies, EAM maps consisted of electrograms recorded from consecutive sinus rhythm complexes, whereas *i*ECG maps were derived from five sinus rhythm complexes selected from the body surface potential map.

Conclusion

Quantitative comparison of EDL-based *i*ECG during sinus rhythm in patients undergoing invasive endocardial and epicardial electro-anatomical mapping showed improved agreement when compared to prior validation studies, although with considerable absolute difference in both timing and breakthrough of ventricular activation. Non-invasive *i*ECG of both the epicardium and endocardium may prove valuable as a diagnostic tool for functional imaging of electro-anatomical substrates in sinus rhythm where activation always starts at the endocardial surface, to improve the value of the ECG in screening for cardiomyopathy and sudden cardiac death risk stratification. Future research should focus on improving accuracy and spatial resolution before implementation into clinical practice to enable imaging of functional electro-anatomical substrates.

DATA AVAILABILITY STATEMENT

The raw data supporting the conclusions of this article will be made available by the authors, without undue reservation.

ETHICS STATEMENT

The studies involving human participants were reviewed and approved by METC UMC Utrecht. Written informed consent to participate in this study was provided by the participants' legal guardian/next of kin.

AUTHOR CONTRIBUTIONS

RR, MB, JH, TO, FA, PD, and PL contributed to conception and design of the study. RB, WK, LB, RR, and MB organized the database. RR and MB performed the statistical analysis. RR wrote the first draft of the manuscript. RR, MB, PD, and PL wrote sections of the manuscript. All authors contributed to manuscript revision, read, and approved the submitted version.

FUNDING

This work was supported by the Dutch Heart Foundation (grant numbers CVON2015-12 eDETECT to FA and QRS-Vision 2018B007 to PD and PL). FA was supported by UCL Hospitals NIHR Biomedical Research Centre.

ACKNOWLEDGMENTS

The authors want to thank Adriaan van Oosterom for laying the foundation of the used inverse ECG methods.

SUPPLEMENTARY MATERIAL

The Supplementary Material for this article can be found online at: https://www.frontiersin.org/articles/10.3389/fphys.2021.730736/full#supplementary-material

Supplementary Figure 1 | All *i*ECG, EAM maps, and voltage maps.

Supplementary Figure 2 | Factors associated with correlation coefficients and absolute differences.

Supplementary Figure 3 | Scatterplot and Bland-Altman plot per included patient.

Supplementary Table 1 | Summary data of the study population.

Supplementary Table 2 | Detailed study population per included patient.

Supplementary Table 3 | Ranges of earliest and latest activation per subject.

Supplementary Methods | Detailed methods section on *i*ECG multi-wave initial estimation.

REFERENCES

Bergquist, J. A., Good, W. W., Zenger, B., Tate, J. D., and MacLeod, R. S. (2019). GRÖMeR: a pipeline for geodesic refinement of mesh registration. *Funct. Imaging Model. Heart* 11504, 37–45. doi: 10.1007/978-3-030-21949-9_5

Cantwell, C. D., Roney, C. H., Ng, F. S., Siggers, J. H., Sherwin, S. J., and Peters, N. S. (2015). Techniques for automated local activation time annotation and conduction velocity estimation in cardiac mapping. *Comput. Biol. Med.* 65, 229–242. doi: 10.1016/j.compbiomed.2015.04.027

Cluitmans, M., Brooks, D. H., MacLeod, R., Dossel, O., Guillem, M. S., van Dam, P. M., et al. (2018). Validation and opportunities of electrocardiographic imaging: from technical achievements to clinical applications. *Front. Physiol.* 9:1305. doi: 10.3389/fphys.2018.01305

Cluitmans, M. J. M., Bonizzi, P., Karel, J. M. H., Das, M., Kietselaer, B., de Jong, M. M. J., et al. (2017). In vivo validation of electrocardiographic imaging. *JACC Clin. Electrophysiol.* 3, 232–242. doi: 10.1016/j.jacep.2016.11.012

Cosio, F. G., Anderson, R. H., Kuck, K. H., Becker, A., Borggrefe, M., Campbell, R. W., et al. (1999). Living anatomy of the atrioventricular junctions. A guide to electrophysiologic mapping. A consensus statement from the cardiac nomenclature study group, working group of arrhythmias, European society of cardiology, and the task force on cardiac nomenclature from NASPE. *Circulation* 100, e31–e37.

Duchateau, J., Sacher, F., Pambrun, T., Derval, N., Chamorro-Servent, J., Denis, A., et al. (2019). Performance and limitations of noninvasive cardiac activation mapping. *Heart Rhythm* 16, 435–442. doi: 10.1016/j.hrthm.2018.10.010

Durrer, D., van Dam, R. T., Freud, G. E., Janse, M. J., Meijler, F. L., and Arzbaecher, R. C. (1970). Total excitation of the isolated human heart. *Circulation* 41, 899–912. doi: 10.1161/01.cir.41.6.899

Geselowitz, D. B. (1992). Description of cardiac sources in anisotropic cardiac muscle. Application of bidomain model. *J. Electrocardiol.* 25, 65–67. doi: 10.1016/0022-0736(92)90063-6

Graham, A. J., Orini, M., Zacur, E., Dhillon, G., Daw, H., Srinivasan, N. T., et al. (2019). Simultaneous comparison of electrocardiographic imaging and epicardial contact mapping in structural heart disease. *Circ. Arrhythm Electrophysiol.* 12:e007120.

Greensite, F., Huiskamp, G., and van Oosterom, A. (1990). New quantitative and qualitative approaches to the inverse problem of electrocardiology: their theoretical relationship and experimental consistency. *Med. Phys.* 17, 369–379. doi: 10.1118/1.596568

Hoekema, R., Uijen, G. J., and van Oosterom, A. (1999). On selecting a body surface mapping procedure. *J. Electrocardiol.* 32, 93–101. doi: 10.1016/s0022-0736(99)90088-2

Hohmann, S., Rettmann, M. E., Konishi, H., Borenstein, A., Wang, S., Suzuki, A., et al. (2019). Spatial accuracy of a clinically established noninvasive electrocardiographic imaging system for the detection of focal activation in an intact porcine model. *Circ. Arrhythm. Electrophysiol.* 12:e007570.

Huiskamp, G., and Greensite, F. (1997). A new method for myocardial activation imaging. *IEEE Trans. Biomed. Eng.* 44, 433–446. doi: 10.1109/10.581930

Huiskamp, G., and Van Oosterom, A. (1988). The depolarization sequence of the human heart surface computed from measured body surface potentials. *IEEE Trans. Biomed. Eng.* 35, 1047–1058.

Leon, L. J., and Witkowski, F. X. (1995). Calculation of transmembrane current from extracellular potential recordings: a model study. *J. Cardiovasc. Electrophysiol.* 6, 379–390. doi: 10.1111/j.1540-8167.1995.tb00411.x

Myerburg, R. J. (1971). The gating mechanism in the distal atrioventricular conducting system. *Circulation* 43, 955–960. doi: 10.1161/01.cir.43.6.955

Oosterhoff, P., Meijborg, V. M., van Dam, P. M., van Dessel, P. F., Belterman, C. N., Streekstra, G. J., et al. (2016). Experimental validation of noninvasive epicardial and endocardial activation imaging. *Circ. Arrhythm. Electrophysiol.* 9:e004104.

Ramanathan, C., Ghanem, R. N., Jia, P., Ryu, K., and Rudy, Y. (2004). Noninvasive electrocardiographic imaging for cardiac electrophysiology and arrhythmia. *Nat. Med.* 10, 422–428. doi: 10.1038/nm1011

Rudy, Y. (2013). Noninvasive electrocardiographic imaging of arrhythmogenic substrates in humans. *Circ. Res.* 112, 863–874. doi: 10.1161/circresaha.112.279315

Sapp, J. L., Dawoud, F., Clements, J. C., and Horacek, B. M. (2012). Inverse solution mapping of epicardial potentials: quantitative comparison with epicardial contact mapping. *Circ. Arrhythm Electrophysiol.* 5, 1001–1009. doi: 10.1161/circep.111.970160

Sosa, E., Scanavacca, M., d'Avila, A., and Pilleggi, F. (1996). A new technique to perform epicardial mapping in the electrophysiology laboratory. *J. Cardiovasc. Electrophysiol.* 7, 531–536. doi: 10.1111/j.1540-8167.1996.tb00559.x

Tung, R., Raiman, M., Liao, H., Zhan, X., Chung, F. P., Nagel, R., et al. (2020). Simultaneous endocardial and epicardial delineation of 3D reentrant ventricular tachycardia. *J. Am. Coll. Cardiol.* 75, 884–897. doi: 10.1016/j.jacc.2019.12.044

van Dam, P. M., Oostendorp, T. F., Linnenbank, A. C., and van Oosterom, A. (2009). Non-invasive imaging of cardiac activation and recovery. *Ann. Biomed. Eng.* 37, 1739–1756. doi: 10.1007/s10439-009-9747-5

van Oosterom, A. (2014). A comparison of electrocardiographic imaging based on two source types. *Europace* 16 (Suppl. 4), iv120–iv128.

Veenstra, R. D., Joyner, R. W., and Rawling, D. A. (1984). Purkinje and ventricular activation sequences of canine papillary muscle. Effects of quinidine and calcium on the Purkinje-ventricular conduction delay. *Circ. Res.* 54, 500–515. doi: 10.1161/01.res.54.5.500

Conflict of Interest: PD is owner of ECG Excellence BV.

The remaining authors declare that the research was conducted in the absence of any commercial or financial relationships that could be construed as a potential conflict of interest.

Publisher's Note: All claims expressed in this article are solely those of the authors and do not necessarily represent those of their affiliated organizations, or those of the publisher, the editors and the reviewers. Any product that may be evaluated in this article, or claim that may be made by its manufacturer, is not guaranteed or endorsed by the publisher.

frontiers in Physiology

ORIGINAL RESEARCH
published: 12 October 2021
doi: 10.3389/fphys.2021.731917

Dynamics of Intraprocedural Dominant Frequency Identifies Ablation Outcome in Persistent Atrial Fibrillation

Alain Pithon[1], Anna McCann[2], Andréa Buttu[2], Jean-Marc Vesin[2], Patrizio Pascale[1], Mathieu Le Bloa[1], Claudia Herrera[1], Chan-Il Park[3], Laurent Roten[4], Michael Kühne[5], Florian Spies[5], Sven Knecht[5], Christian Sticherling[5], Etienne Pruvot[1†] and Adrian Luca[1†]*

[1] Service of Cardiology, Lausanne University Hospital, University of Lausanne, Lausanne, Switzerland, [2] Applied Signal Processing Group, Swiss Federal Institute of Technology, Lausanne, Switzerland, [3] Department of Cardiology, Hôpital de La Tour, Geneva, Switzerland, [4] Department of Cardiology, Inselspital, Bern University Hospital, University of Bern, Bern, Switzerland, [5] Department of Cardiology, University Hospital of Basel, Basel, Switzerland

Background: The role of dominant frequency (DF) in tracking the efficiency of a stepwise catheter ablation (step-CA) in persistent atrial fibrillation (peAF) remains poorly studied. We hypothesized that the DF time-course during step-CA displays divergent patterns between patients in whom a step-CA successfully restores long-term sinus rhythm (SR) and those with recurrence.

Methods: This study involved 40 consecutive patients who underwent a step-CA for peAF (sustained duration 19 ± 11 months). Dominant frequency was computed on electrograms recorded from the right and left atrial appendages (RAA; LAA) and the coronary sinus before and during the step-CA synchronously to the 12-lead ECG. Dominant frequency was defined as the highest peak within the power spectrum.

Results: Persistent atrial fibrillation was terminated by a step-CA in 28 patients [left-terminated (LT)], whereas 12 patients remaining in AF after ablation [not left-terminated (NLT)] were cardioverted. Over a mean follow-up of 34 ± 14 months, all NLT patients had a recurrence. Among the 28 LT patients, 20 had a recurrence, while 8 remained in SR throughout follow-up. The RAA and V_1 DF had the best predictive values of the procedural failure to terminate AF (area under the curve; AUC 0.84, $p < 0.05$). A decision tree model including a decrease in LAA DF $\geq$ 6.61% during the first 20 min following pulmonary vein isolation (PVI) and a baseline RAA DF < 5.6 Hz predicted long-term SR restoration with a sensitivity of 83% and a specificity of 93% ($p < 0.05$).

Conclusion: This study found that high baseline DF values are predictive of unfavorable ablation outcomes. The reduction of the LAA DF at early ablation steps following PVI is associated with procedural AF termination and long-term SR maintenance.

Keywords: atrial fibrillation, catheter ablation, dominant frequency, intracardiac electrogram, surface electrocardiogram, decision tree model

OPEN ACCESS

Edited by:
G. Andre Ng,
University of Leicester,
United Kingdom

Reviewed by:
Martin Stiles,
The University of Auckland,
New Zealand
Maria S. Guillem,
Universitat Politècnica de València, Spain
João Salinet,
Federal University of ABC, Brazil

***Correspondence:**
Adrian Luca
adrian.luca@chuv.ch

[†]These authors share senior authorship

Specialty section:
This article was submitted to Cardiac Electrophysiology, a section of the journal Frontiers in Physiology

Received: *28 June 2021*
Accepted: *06 September 2021*
Published: *12 October 2021*

Citation:
Pithon A, McCann A, Buttu A, Vesin J-M, Pascale P, Le Bloa M, Herrera C, Park C-I, Roten L, Kühne M, Spies F, Knecht S, Sticherling C, Pruvot E and Luca A (2021) Dynamics of Intraprocedural Dominant Frequency Identifies Ablation Outcome in Persistent Atrial Fibrillation. Front. Physiol. 12:731917. doi: 10.3389/fphys.2021.731917

INTRODUCTION

Pulmonary vein isolation has emerged as an effective treatment for patients suffering from paroxysmal atrial fibrillation (AF), while its success rate in persistent AF (peAF) is significantly lower (Brooks et al., 2010). An extra-pulmonary vein (PV) substrate ablation, including the ablation of complex fractionated atrial electrograms (CFAEs) and/or the creation of linear lesions, may be beneficial (Nademanee et al., 2008; Brooks et al., 2010), but extensive ablation lesions are associated with increased procedural time and a high incidence of post-procedural atrial tachycardia.

It has been shown that the clinical efficacy of a stepwise catheter ablation (step-CA) is associated with a decrease in AF complexity as indicated by changes in the dominant frequency (DF) of AF (Lemola et al., 2006; Johner et al., 2020; Ma et al., 2021). However, whether the time-course of AF organization throughout an ablation may serve as an indicator of the efficacy of the procedure remains to be determined.

We recently showed that patients with peAF that are unresponsive to step-CA displayed higher AF complexity at baseline as indicated by higher DF values (Luca et al., 2020) and lower ECG-based organization indices (Buttu et al., 2016; McCann et al., 2021) than patients with successful ablation. Furthermore, we found that a step-CA led to increases in surface ECG AF organization in most patients (McCann et al., 2021), without significant differences between patients who remained in sinus rhythm (SR) in the long term and those who did not. In this study, we hypothesized that combining baseline intracardiac DF and its time-course throughout an ablation may be used to track the efficacy of step-CA *en route* to long-term SR restoration in peAF.

METHODS

Patient Population and Ablation Procedure

This study has been performed within the framework of an ongoing project (REORGANIZE-AF) that is aimed at assessing the level of ECG and intracardiac electrogram (EGM) organization in peAF to improve the selection of patients for ablation. The study group consisted of 40 consecutive patients with peAF referred for a first step-CA. The patients suffered from AF for 6 ± 4 years, sustained for 19 ± 11 months before the ablation, and were resistant to pharmacological or electrical cardioversion. The details of the clinical characteristics of the study population are provided in **Table 1**.

All patients underwent a step-CA procedure consisting of pulmonary vein isolation (PVI), followed by left atrial (LA) CFAEs ablation and linear ablation (roof and mitral isthmus). The stepwise ablation protocol has been described previously (Buttu et al., 2016; Luca et al., 2020). The details of the ablation procedure are also provided in the **Supplementary Material**. The procedural endpoint was reached when AF terminated in SR or atrial tachycardia (AT). Patients with non-terminated peAF were electrically cardioverted. After the index ablation, all patients were followed and data were recorded at 3, 6, 12, 18, and 24 months, then every year. Recurrence was defined as AF or AT lasting more than 30 s (Calkins et al., 2017). All patients provided written informed consent, and the study was approved by the Human Research Ethics Committee of the Lausanne University Hospital.

Based on procedural and clinical outcomes, the study population was divided into three subgroups. Subgroup 1 ($n = 8$) consisted of patients in whom peAF was terminated into SR or AT by ablation and who remained arrhythmia free throughout the follow-up (left-terminated without recurrence—LT_SR). Subgroup 2 ($n = 20$) consisted of patients in whom peAF was terminated by ablation and who had a recurrence after the first step-CA procedure (left-terminated with recurrence—LT_Rec). Subgroup 3 ($n = 12$) consisted of patients in whom the step-CA procedure failed to terminate peAF (not left-terminated—NLT), all with recurrence during follow-up.

Electrophysiological Study

More details are available in the **Supplementary Material**. The following catheters were introduced *via* the left and right femoral veins: a 3.5-mm cooled-tip catheter for mapping and ablation (Navistar Thermocool, Biosense Webster®, Irwindale, California), a circumferential duodecapolar Lasso® catheter (electrode spacing 2-6-2 mm, Biosense Webster®, Irwindale, California) within the LA, a quadripolar catheter (electrode spacing 5-5-5 mm, 4 mm electrode tip size, Supreme St Jude Medical®, Saint Paul, Minnesota) placed into the right atrial appendage (RAA), and a steerable decapolar catheter (electrode spacing 2-8-2 mm, 1 mm electrode tip size, Biosense Webster®, Irwindale, California) placed into the coronary sinus (CS), with the proximal electrode at the ostium. The ECG chest lead V_6 was placed on the back (V_{6b}) of the patients, within the cardiac silhouette, in order to better record LA activity (Luca et al., 2020). Furthermore, EGMs were synchronously recorded from the left atrial appendage (LAA), RAA, and CS at baseline, i.e., before the ablation, during PVI, and throughout CFAEs and the linear ablation. Surface ECG was continuously monitored at baseline and during the entire step-CA procedure. The ECG and EGM signals were recorded using an Axiom Sensis XP® System (Siemens®, Munich, Germany) at a sample rate of 2 kHz and bandpass filter settings of 0.5–200 and 30–400 Hz, respectively.

Data Processing

The ECG and EGM signals were retrospectively processed using MatLab (The Mathworks Inc., Natick, MA, USA).

The EGM signals were rectified and bandpass filtered at 1–20 Hz (Botteron and Smith, 1995; Ng and Goldberger, 2007). Frequency spectra were estimated using the fast Fourier transform, and DF was identified as the highest peak frequency between 3 and 15 Hz. The EGMs with a DF power (1-Hz band centered at the DF peak) lower than 20% of the total power in the 3- to 15-Hz band were reviewed to exclude spurious DF values (Sanders et al., 2005). The surface ECG signals were bandpass filtered (1–50 Hz) to remove baseline wander and power line interference. Surface ECG DF estimation was preceded by ventricular activity cancelation in order to ensure the reliability of the ECG analysis during AF. The single beat method, in which the QRS and T waves are treated

TABLE 1 | Clinical characteristics.

	All ***n* = 40**	**NLT** ***n* = 12**	**LT_Rec** ***n* = 20**	**LT_SR** ***n* = 8**	***p*-value[a]**	***p*-value[b]**	***p*-value[c]**
Age (yrs)	63 (56; 65)	63 (58; 64)	63 (53; 67)	60 (58; 63)	0.98	0.56	0.65
Sex (male/female)	38/2	12/0	18/2	8/0	0.26	-	0.35
AF duration (yrs)	6 (2; 8)	5 (2; 7)	5 (3; 6)	9 (6; 11)	0.74	0.03	0.07
Duration of sustained AF (mo)	15 (12; 24)	22 (14; 39)	13 (12; 24)	20 (10; 24)	0.05	0.28	0.60
BMI (kg/m^2)	30 (25; 31)	30 (24; 31)	30 (25; 34)	29 (27; 30)	0.63	0.94	0.72
High blood pressure	27 (68)	8 (67)	13 (65)	6 (75)	0.72	0.69	0.68
Valvular disease	6 (15)	1 (8)	3 (15)	2 (25)	0.58	0.31	0.53
Diabetes	6 (15)	2 (17)	3 (15)	1 (13)	0.90	0.80	0.86
Tobacco	8 (20)	2 (17)	4 (20)	2 (25)	0.81	0.65	0.77
Hypercholesterolemia	18 (45)	6 (50)	9 (45)	3 (38)	0.78	0.58	0.72
Coronary artery disease	0 (0)	0 (0)	0 (0)	0 (0)	-	-	-
Sleep apnea syndrome	23 (58)	6 (50)	13 (65)	4 (50)	0.40	>0.99	0.46
Chronic kidney disease	1 (3)	0 (0)	1 (5)	0 (0)	0.43	-	0.52
CHA_2DS_2-Vasc score	1 (1; 2)	1 (0; 1)	2 (1; 2)	1 (1; 2)	0.12	0.41	0.47
Dilated cardiomyopathy	14 (35)	3 (25)	9 (45)	2 (25)	0.26	>0.99	0.33
Hypertrophic cardiomyopathy	3 (8)	0 (0)	2 (10)	1 (13)	0.26	0.21	0.85
Left ventricular fraction ejection (%)	50 (40; 60)	55 (50; 60)	50 (35; 56)	55 (44; 55)	0.18	0.50	0.47
Left atrial volume (*ml*)	168 (143; 193)	174 (160; 193)	162 (140; 190)	167 (139; 204)	0.41	0.64	0.90
During stepwise catheter ablation							
Cumulative ablation time (min)							
Total	56 (48; 68)	76 (61; 81)	55 (50; 60)	40 (29; 54)	<0.01	<0.01	0.04
PVI	22 (18; 26)	19 (16; 23)	25 (20; 28)	22 (16; 25)	0.11	0.76	0.39
CFAEs and linear ablation	33 (21; 49)	55 (48; 59)	26 (20; 40)	19 (5; 30)	<0.01	<0.01	0.09
Beta-blockers	28 (70)	7 (58)	15 (75)	6 (75)	0.33	0.44	>0.99
Calcium channel blockers	8 (20)	2 (17)	4 (16)	2 (25)	0.82	0.65	0.77
Amiodarone	7 (18)	1 (8)	4 (16)	2 (25)	0.38	0.31	0.77
Other antiarrhythmics	5 (13)	3 (25)	2 (10)	0 (0)	0.26	0.13	0.35
No. of antiarrhythmics drugs	2 (1; 3.5)	2 (2; 3)	3 (2; 3)	2 (2; 2)	0.03	0.27	0.43
Statins	5 (13)	3 (25)	2 (10)	0 (0)	0.26	0.13	0.35
Recurrence type at follow-up							
Persistent AF	4	3	1				
Paroxysmal AF	3	0	3				
ATs	25	9	16				
Sites of AF termination							
Roof	4		3	1			
Left atrial appendage	2		0	2			
Coronary sinus	4		3	1			
Mitral isthmus	8		6	2			
Pulmonary veins	2		0	2			
Septum	7		7	0			
Left lateral wall	1		1	0			

Values are median with 25th and 75th percentiles or n (%).

[a] *NLT vs. LT_Rec.*

[b] *NLT vs. LT_SR.*

[c] *LT_Rec vs. LT_SR.*

AF, atrial fibrillation; AT, atrial tachyarrhythmia; CFAEs, complex fractionated atrial electrograms; LT_Rec/LT_SR, left-terminated with/without recurrence at follow-up; NLT, not left-terminated; PVI, pulmonary veins isolation.

separately, was used as originally described by our group (Lemay et al., 2007). Following QRST cancellation, the power spectrum of each atrial ECG signal was computed using Welch's method (2.5-s Hamming window, 50% overlap) and the DF was defined as the frequency of the highest peak between 3 and 15 Hz.

The ECG and EGM signals were analyzed at different steps of the procedure: (i) baseline, (ii) during PVI, and (iii) during CFAEs and the linear ablation (LA ablation). The EGM DFs were computed on the distal dipole of the RAA catheter, on the Lasso® catheter placed within the LAA as the average DF of the 10 dipoles, and on the CS catheter as the average DF of the 5 dipoles. Because the atrial activity is best recognized in the leads V_1 and V_{6b} (Luca et al., 2020), the ECG DFs were computed only on these two leads. The ECG and EGM signals were divided into 10-s epochs. Hence, for each 10-s epoch, a single DF value was available for each catheter (1 for the RAA distal dipole, 1 for the Lasso® catheter, and 1 for the CS catheter) and each ECG lead per patient. Interatrial EGM and ECG left-to-right DF gradients were obtained as the difference between LAA and RAA DFs and between V_{6b} and V_1 DFs, respectively. **Figure 1** shows an illustrative example of DF estimation on 10-s epochs simultaneously recorded from the LAA, RAA, and the ECG leads V_1 and V_{6b} in an LT_SR patient at baseline and after 20 min of cumulative CFAEs and linear ablation. For each ECG recording, the atrial V_1 and V_{6b} signals represent the ECG leads V_1 and V_{6b} devoid of ventricular activity.

Statistical Analysis

Continuous variables were expressed as the median and interquartile range (IQR) and categorical variables as numbers and percentages. The significance of any difference between subgroups was analyzed with the Mann–Whitney *U*-test for continuous variables and with the Fisher's exact test for categorical variables. A receiver-operator characteristic (ROC) analysis was performed to assess the performance of ECG and EGM DFs as predictors of ablation outcomes. The optimal ROC curve cutoff was defined as the combination of the highest sensitivity and specificity. A logistic regression analysis was used to determine the predictors of ablation outcomes and to compute the respective odds ratios (OR). Freedom from atrial arrhythmias >30 s during follow-up was analyzed using the Kaplan–Meier method, and a log-rank test was applied to compare differences between subgroups. A decision tree model based on baseline DF and its relative evolution during LA ablation were developed to intra-procedurally predict ablation outcomes. The statistical significance was set at $p < 0.05$. Analyses were performed using XLSTAT (ADDINSOFT®, Paris, France) or MatLab.

RESULTS

Study Population

Persistent AF was terminated by ablation within the LA in 28 out of 40 patients (70%, LT group). Twelve patients (30%, NLT group) remained in AF at the end of the procedure and required electrical cardioversion to restore SR. The termination of AF occurred during PVI in 2 patients, during ablation of CFAEs in 14 patients, and after PVI plus CFAEs and linear ablation in 12 patients. After a single step-CA procedure, all 12 NLT patients developed a recurrence. Among the 28 LT patients, 20 had a recurrence (LT_Rec group), while 8 remained in SR throughout follow-up (LT_SR group). In the NLT and LT_Rec groups, recurrence occurred as AF ($n = 7$) and as ATs ($n = 25$) on average 7 ± 10 months after the index procedure. The baseline characteristics of the subgroups are presented in **Table 1**. A gradual and significant decrease in total ablation time was observed between the subgroups, with the longest time in NLT patients, intermediate in LT_Rec patients, and the shortest time in LT_SR patients (76 vs. 55 vs. 40 min, respectively; $p < 0.05$). Moreover, NLT patients had significantly longer ablation times during CFAEs and linear ablation than LT_Rec and LT_SR patients (55 vs. 26 vs. 19 min, respectively; $p < 0.01$). Clinical parameters and PVI ablation times were similar between subgroups. The mean follow-up duration for the study population was 34 ± 14 months, and at the end of the follow-up period, 34 (85%) patients were in SR without (28 out of 34, 82%) and with (6 out of 34, 18%) amiodarone, with a mean number of 2 ± 1 ablation procedures per patient.

Baseline ECG and EGM DF Values

Table 2 shows the DF values computed at baseline (before ablation) on RAA, LAA, CS EGMs, and on ECG leads V_1 and V_{6b} for the entire population and the three subgroups. Both ECG and EGM DFs were uniformly higher in NLT patients than in LT patients. Although there was no significant difference in DF between the LT_Rec and LT_SR patients, graded DF values were observed among the three subgroups, starting with the highest ones for NLT patients to the lowest ones for LT_SR patients. Particularly, NLT patients also displayed a negative LAA-to-RAA DF gradient [median (IQR): −0.32 (−0.58; 0.09) Hz], while that of LT patients was positive [LT_Rec: 0.19 (−0.04; 0.34) Hz; LT_SR: 0.28 (−0.23; 0.39) Hz]. In contrast, the surface V_{6b}-to-V_1 DF gradient was similar between the three subgroups. Altogether these results show that ECG and EGM DFs have the potential to refine the selection of patients with peAF unresponsive to ablation (NLT group).

Baseline DF as a Predictor of Ablation Outcomes

Table 3 reports the predictive performances of baseline ECG and EGM DFs for the pre-ablation selection of NLT patients. A univariate logistic regression analysis showed that an increased DF in the RAA (OR 10.9), in LAA (OR 3.7), and on lead V_1 (OR 8.5) and lead V_{6b} (OR 7.8), and a negative LAA-to-RAA DF gradient (OR 0.8) were all significantly ($p < 0.05$) associated with an unfavorable procedural outcome. The ROC curve analysis showed that an RAA DF ≥ 5.92 Hz (area under the curve; AUC = 0.86; **Figure 2A**) or a V_1 DF ≥ 5.86 Hz (AUC = 0.84; **Figure 2C**) predicted the procedural outcome ($p < 0.05$) with a sensitivity of 91%, a specificity of 68%, and a PPV and NPV of 53 and 95%, respectively. **Figures 2B,D** show the distribution of DF values from the RAA and lead V_1, respectively, grouped by procedural and clinical outcomes. **Supplementary Table 1** shows the predictive performance of baseline ECG and EGM DFs for the pre-ablation identification of patients with long-term SR maintenance after a single CA procedure (LT_SR subgroup). No significant association was found between baseline DF and the restoration of long-term SR. In summary, high surface and intracardiac DF values and a negative LAA-to-RAA DF gradient

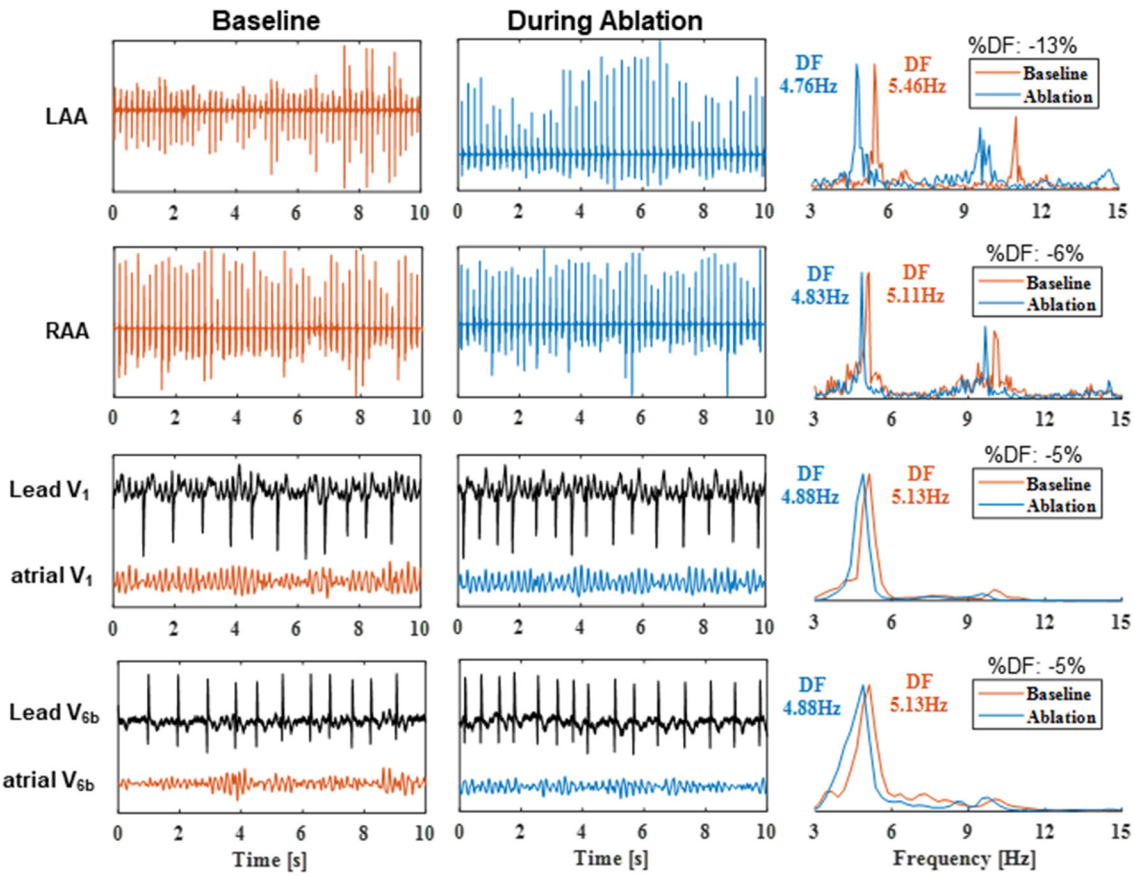

FIGURE 1 | Dominant frequency estimation on 10-s epochs recorded from the LAA, RAA, and the ECG leads V_1 and V_{6b} in an LT_SR patient at baseline and after 20 min of cumulative CFAEs and linear ablation. For the surface ECG recordings, the atrial V_1 and V_{6b} signals represent the ECG leads V_1 and V_{6b} devoid of ventricular activity. The corresponding power spectral densities (normalized by their maximum value) and the estimated DFs are illustrated in the right column. DF, dominant frequency; %DF, relative change in DF during ablation compared with baseline DF values. Other abbreviations as in previous tables.

before ablation are associated with the procedural failure to terminate AF.

Effect of Ablation on DF

To assess the cumulative effect of ablation on AF organization, ECG and EGM DFs were computed during PVI and LA ablation (CFAEs and linear ablation) until AF termination or cardioversion. For each patient, DFs were first computed on 10-s epochs and then averaged over all available epochs at the end of PVI (end_PVI), during the first 10, 20, and 30 min of cumulative ablation following PVI, and the last 3 min of ablation (end_ABL). The relative change in DF was calculated as the percentage deviation of the average DF from the baseline DF value.

The only divergent patterns of DF values between the three subgroups during LA ablation were observed in the LAA. The temporal evolution of RAA, CS, V_1, and V_{6b} DF was similar between subgroups (**Figure 3**). **Supplementary Figure 2** shows that the subgroups displayed a similar decrease in DF at end_ABL compared with the baseline DF values. **Supplementary Figure 3** shows that, for LT patients, the extra-PV substrate ablation led to the durable abolition of the baseline positive LAA-to-RAA DF gradient. In contrast, for NLT patients, after a transient phase of null LAA-to-RAA DF gradient during the first 30 min of LA ablation, the baseline negative LAA-to-RAA DF gradient was re-established at end_ABL.

Figure 4 shows an illustrative example of the temporal evolution of DF estimated on 10-s epochs acquired from the LAA at baseline, during PVI, and during LA ablation in an LT_SR, an LT_Rec, and an NLT patient. The average DF at baseline and during the first 10, 20, and 30 min of cumulative ablation within LA are indicated by horizontal blue, red, green, and magenta lines, respectively. For the LT_SR patient, the ablation led to the progressive reduction of the LAA DF from end_PVI throughout the LA ablation ($\Delta DF_{BL-10min}$ −6.6%, $\Delta DF_{BL-20min}$ −8.9%, $\Delta DF_{BL-30min}$ −10.2%). For the LT_Rec patient, the reduction in LAA DF only occurred after 20 min of CFAE ablation ($\Delta DF_{BL-10min}$ +1%, $\Delta DF_{BL-20min}$ −2.3%, $\Delta DF_{BL-30min}$ −4.3%), while for the NLT patient, no significant changes in DF occurred during the first 30 min of ablation. These specific findings were confirmed for the three subgroups (**Figure 3A**). The subgroup comparison shows that the relative changes in LAA DF at end_PVI and after the first 10 min

TABLE 2 | Surface ECG and intracardiac electrogram (EGM) DF values at baseline.

	All ($n = 40$)	NLT ($n = 12$)	LT_Rec ($n = 20$)	LT_SR ($n = 8$)	p-value[a]	p-value[b]	p-value[c]
RAA	5.74 (5.32; 6.42)	6.69 (6.13; 7.12)	5.62 (5.25; 6.08)	5.37 (5.14; 5.80)	<0.001	<0.005	0.51
LAA	5.74 (5.55; 6.50)	6.26 (5.70; 6.79)	5.69 (5.42; 6.52)	5.57 (5.42; 5.91)	0.08	<0.05	0.5
CS	5.47 (4.88; 6.00)	5.73 (5.61; 6.07)	5.12 (4.83; 5.87)	5.26 (4.86; 5.69)	0.09	0.10	0.85
V_1	5.78 (5.13; 6.35)	6.23 (5.98; 6.77)	5.49 (5.10; 5.92)	5.31 (5.13; 5.83)	<0.005	<0.01	0.95
V_{6b}	5.49 (5.13; 5.86)	5.86 (5.55; 6.41)	5.19 (4.88; 5.62)	5.37 (5.13; 5.86)	<0.01	0.06	0.51
LAA-to-RAA DF gradient	0.14 (−0.32; 0.34)	–0.32 (−0.58; 0.09)	0.19 (−0.04; 0.34)	0.28 (−0.23; 0.39)	<0.05	0.11	0.99
V_{6b}-to-V_1 DF gradient	0.00 (−0.49; 0.06)	0.00 (−0.67; 0.00)	0.00 (−0.37; 0.03)	0.00 (−0.43; 0.24)	0.78	0.42	0.48

Values are median (25th and 75th percentiles) Hz.
[a]NLT vs. LT_Rec.
[b]NLT vs. LT_SR.
[c]LT_Rec vs. LT_SR.
*CS, coronary sinus; DF, dominant frequency; LAA, left atrial appendage; RAA, right atrial appendage; other abbreviations as in **Table 1**.*

TABLE 3 | Baseline ECG and EGM DFs as predictors of procedural ablation outcomes (NLT patients vs. LT_Rec + LT_SR patients).

	Odds ratio			ROC analysis					
	OR	95% CI	p-value	AUC (95% CI)	Optimal cutoff	Se	Sp	PPV	NPV
RAA	10.9	2.3–53.6	0.003	86% (0.78–0.94)	≥5.92 Hz	91%	68%	53%	95%
LAA	3.7	1.2–11.6	0.025	72% (0.57–0.88)	≥5.64 Hz	91%	50%	42%	93%
CS	2.65	0.89–7.92	0.07	70% (0.58–0.82)	≥5.61 Hz	82%	68%	50%	90%
V_1	8.5	1.9–37.3	0.005	84% (0.75–0.93)	≥5.86 Hz	91%	68%	53%	95%
V_{6b}	7.8	1.7–35.6	0.008	80% (0.67–0.93)	≥5.49 Hz	91%	61%	48%	94%
LAA-to-RAA DF gradient	0.80	0.66–0.97	0.02	74% (0.56–0.92)	≤-0.44 Hz	45%	93%	71%	81%

*AUC, area under the curve; CI, confidence interval; NPV, negative predictive value; OR, odds ratio; ROC, receiver operating characteristic; PPV, positive predictive value; Se, sensitivity; Sp, specificity; other abbreviations as in **Table 2**.*

of LA ablation were not significantly different. However, the LT_SR subgroup displayed significantly higher reduction of DF than the other two subgroups after 20 min of ablation within LA (LT_SR vs. LT_Rec vs. NLT: −8.73 vs. −3.78 vs. −2.25%, $p < 0.05$; **Figure 3A**). Altogether, these results suggested that tracking intracardiac DF in the LAA during complex ablation procedures may help identify patients without recurrence at follow-up.

Changes in DF During Ablation as a Predictor of Clinical Outcome

The ROC analysis of the relative change in LAA DF after 20 min of LA ablation (time point of significant difference between subgroups) showed that a decrease in LAA DF ≥ 6.61% predicted long-term maintenance of SR, with 83% sensitivity, 74% specificity, 38% PPV, and 96% NPV (AUC = 0.75, 95% CI 0.64–0.86, $p < 0.05$; **Supplementary Table 2**; **Supplementary Figure 4A**). **Supplementary Figure 4B** shows that patients with an LAA DF decrease of ≥6.61% displayed a trend toward a lower recurrence rate than those with a decrease of <6.61% (40 vs. 5%; $p = 0.055$). Relative changes in RAA, CS, V_1, and V_{6b} DF after 20 min of cumulative ablation within LA were not associated with the long-term maintenance of SR (**Supplementary Table 2**).

A decision tree model combining the relative change in LAA DF during ablation within LA and baseline RAA DF was developed to improve the prediction performances for long-term ablation outcomes (**Figure 5A**). This model was based on two steps: (1) a decrease of <6.61% in LAA DF after a 20-min ablation was associated with recurrence; (2) a baseline RAA DF <5.6 Hz in patients displaying an LAA DF decrease of ≥6.61% identified cases with the lowest risk of recurrence as shown by the Kaplan–Meier analysis (AF-free rate: 62 vs. 4%, $p < 0.01$; **Figure 5B**), with a sensitivity of 83%, a specificity of 93%, and a PPV and an NPV of 63 and 97%, respectively.

In summary, progressive LAA organization during ablation and low baseline RAA DF values are associated with the long-term maintenance of SR. These findings suggest that tracking

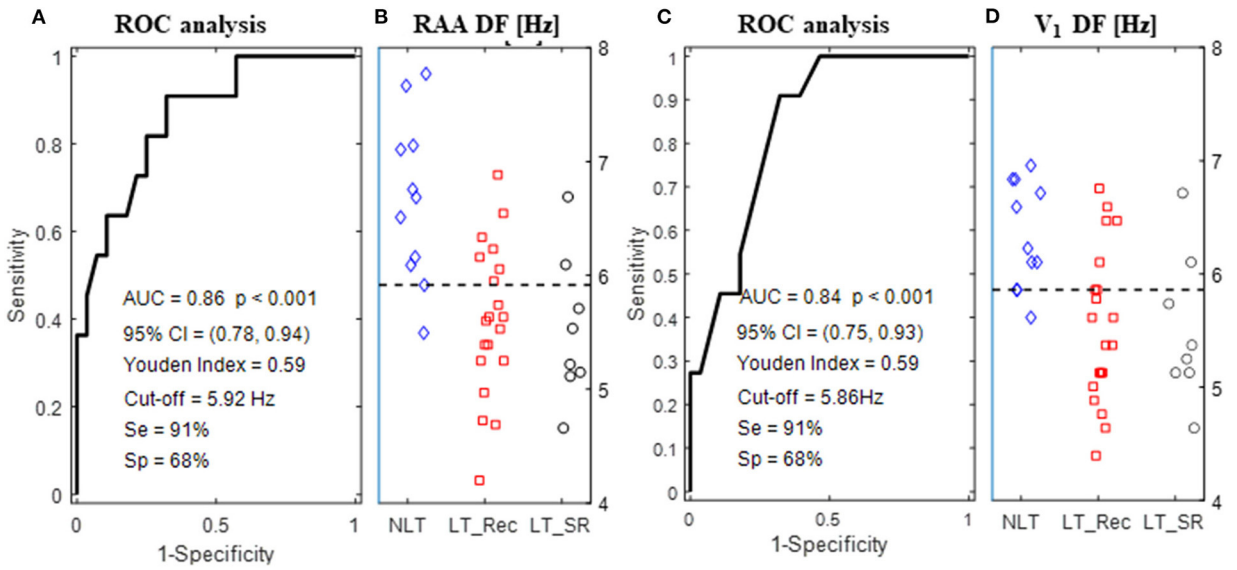

FIGURE 2 | ROC curve for baseline DF computed from the RAA **(A)** and lead V_1 **(C)**. **(B,D)** Show the distribution of RAA and V_1 DF values, respectively, grouped by the procedural outcome (NLT, LT_Rec, and LT_SR). The horizontal dashed lines indicate the optimal cutoff points for DF above which both procedural AF termination and SR maintenance at follow-up were less likely to be achieved by ablation. Abbreviations as in **Table 3**.

the LAA DF during ablation may help define procedural ablation endpoints.

DISCUSSION

Main Findings

This study presented new information regarding the clinical role of DF in predicting ablation outcomes and tracking of the efficacy of complex ablation procedures. First, the study confirmed that high surface and intracardiac DFs and a negative LAA-to-RAA DF gradient before ablation are associated with the procedural failure to terminate AF and high recurrence rates at follow-up. Second, it demonstrated that patients with a significant decrease in LAA DF during ablation and low RAA DF at baseline were more likely to remain in SR after a single ablation procedure. Altogether, these findings suggested that monitoring the intra-procedural evolution of DF may help assess the amount of ablation required to restore long-term SR in patients with long-standing peAF.

High Baseline DF and Negative LAA-to-RAA DF Gradient Are Predictive of Unfavorable Procedural Ablation Outcomes

Extensive atrial remodeling is associated with suboptimal outcomes of catheter ablation in peAF (Nademanee et al., 2008; Brooks et al., 2010). Intracardiac DF is an acceptable surrogate for the degree of atrial remodeling, with high DF values indicative of advanced remodeling (Lemola et al., 2006; Brooks et al., 2010). Our group has recently shown that patients with peAF unresponsive to stepwise ablation had advanced bi-atrial and CS remodeling as shown by high surface and intracardiac DFs (Luca et al., 2020). The clinical role of DF in predicting procedural ablation outcomes has been investigated by several groups. Yoshida et al. (2011) found that patients without AF termination after both PVI and CFAE ablation had higher DFs in the LAA and on lead V_1 than patients with procedural AF termination. Lo et al. (2009) showed that low bi-atrial DFs were associated with acute AF termination. Our study confirms that high DFs in the RAA, LAA, and ECG leads V_1 and V_{6b} were associated with the procedural failure to terminate AF. Another important finding is that the RAA DF had the highest predictive accuracy, which is in line with previous studies reporting that non-PV foci such as in the right atrium (RA) can maintain peAF (Narayan et al., 2012; Hasebe et al., 2016). Narayan et al. (2012) in the CONFIRM trial found that up to one-third of the identified AF rotors or drivers were located in the RA. Hasebe et al. (2016) showed that AF initiated by RA triggers had a baseline positive RA-to-LA DF gradient. In our study, patients without AF termination by ablation within the LA had higher RAA and LAA DFs, negative LAA-to-RAA DF gradients, and longer ablation times than those of patients with successful ablation. These results supported the hypothesis of a high number of bi-atrial AF drivers in patients in whom AF persists despite extensive LA ablation. In summary, our findings suggested that bi-atrial DF values before ablation may help predict the procedural outcome.

Temporal Evolution of DF During Stepwise Ablation

Extensive ablation has been shown to affect the atrial fibrillatory activity. Yokokawa et al. (2010) showed that linear ablation upon PVI resulted in a significant decrease both in the prevalence of

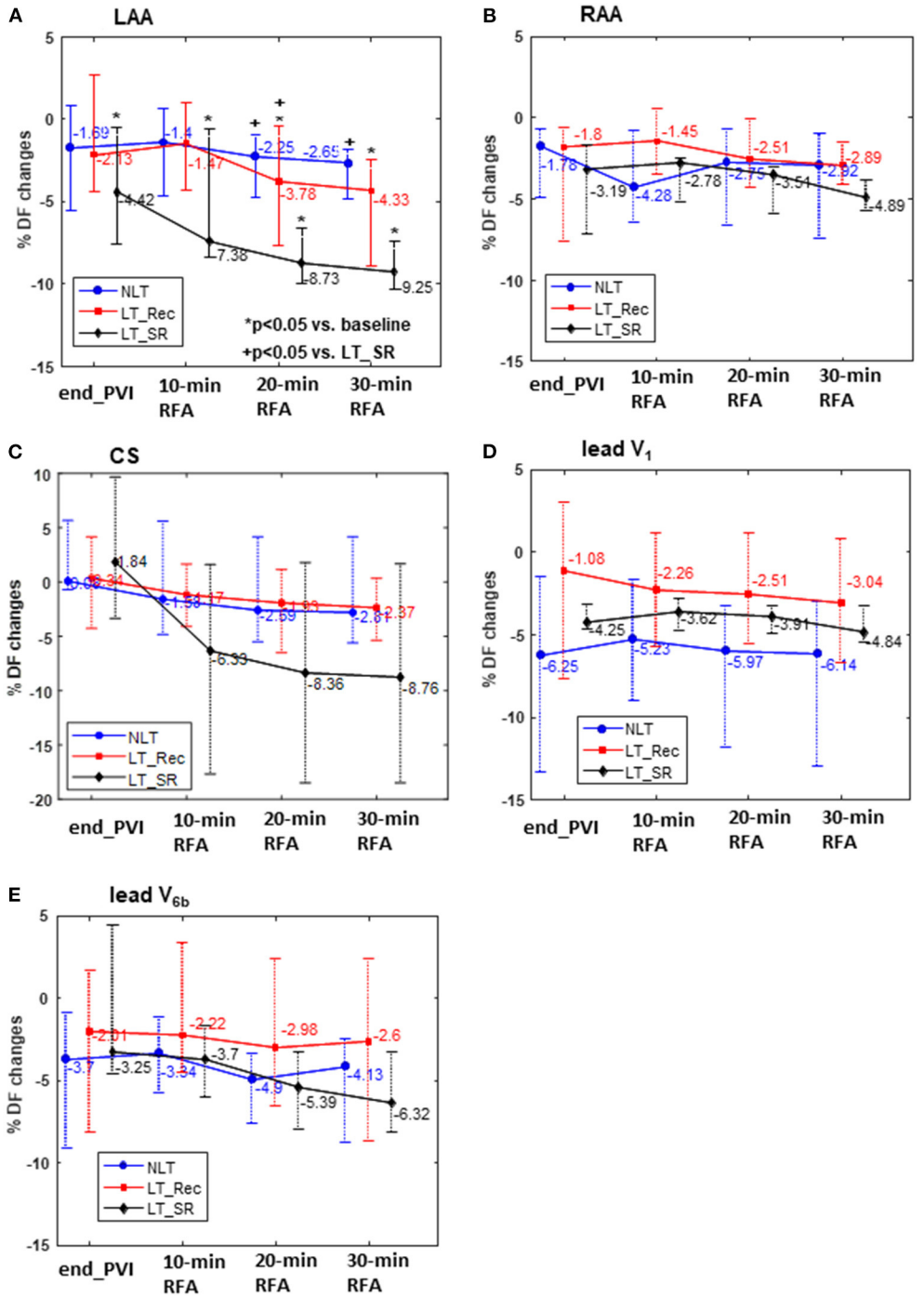

FIGURE 3 | Relative changes (%) in DF compared with the baseline DF at the end of PVI (endPVI) and during the first 10, 20, and 30 min of cumulative ablation following PVI. DF was measured within the LAA, RAA, CS, and on the ECG leads V_1 and V_{6b}. RFA, radiofrequency ablation. Abbreviations as in previous tables and figures.

major spectral components and in the DF of lead V_1 and the CS. Johner et al. (2020) recently showed that stepwise extra-PV AF substrate ablation significantly affects the CS and RA DF. Our study evaluated the effect of PVI followed by CFAEs and linear ablation on the DF measured from RAA, LAA, CS, and ECG leads V_1 and V_{6b}. Surface and intracardiac DFs significantly dropped from baseline to the end of ablation for all the subgroups of patients. Importantly, the time-course of relative changes in the

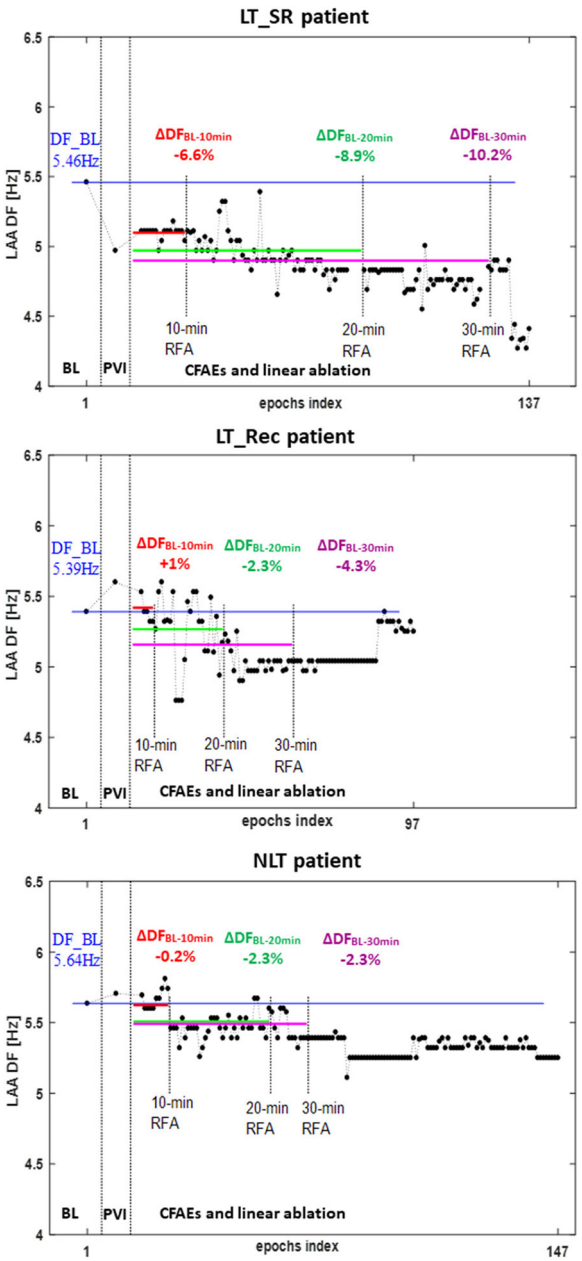

FIGURE 4 | Temporal evolution of DF measured on 10-s epochs recorded from the LAA in an LT_SR patient (top), an LT_Rec patient (middle), and an NLT patient (bottom) at baseline (BL), at the end of PVI (end_PVI), and during LA ablation (CFAEs and linear ablation). Each dot represents the DF value computed on a single 10-s epoch. Average DFs at baseline and during the first 10, 20, and 30 min of cumulative ablation following PVI are represented by the horizontal blue, red, green, and magenta lines, respectively. PVI, pulmonary vein isolation; RFA, radiofrequency ablation; ΔDF, relative change in DF during ablation compared with the baseline DF value. Other abbreviations as in previous tables and figures.

DF during ablation was significantly different between subgroups only for the DF measured in the LAA. In particular, LT_SR patients displayed a progressive reduction in the LAA DF during LA ablation, while NLT patients showed a decrease in the LAA DF only toward the end of ablation. In contrast, LT_Rec patients displayed an intermediate pattern. A few possibilities may explain the high sensitivity of LAA DF to cumulative ablation in the LT_SR group. LT_SR patients had short CFAEs ablation time and positive LAA-to-RAA DF gradient, suggesting a limited number of critical AF drivers within the LA (Haissaguerre et al., 2014). In contrast, patients without AF termination (NLT group) underwent extensive LA ablation before the occurrence of DF changes, suggestive of multiple bi-atrial AF drivers. A failure to decrease the LAA DF at the early stages of ablation may reflect the insufficient elimination of LA AF drivers. Recently, Honarbakhsh et al. (2018) reported that the ablation of AF drivers (rotational and focal) corresponding to sites of high atrial organization was more likely to cause LAA cycle length prolongation or AF termination. Altogether, these findings suggested that the intra-procedural evolution of LAA DF may be a useful marker of ablation efficacy *en route* to restoring long-term SR in peAF.

Intracardiac DF and Long-Term Ablation Outcome

The present study showed that a ≥6.61% decrease in the LAA DF after 20 min of CFAE ablation was associated with long-term SR after a single ablation procedure. We found that a decision tree model combining the level of LAA DF decreases and baseline RAA DF values improves the specificity of SR maintenance. Among the patients with a decrease in LAA DF ≥6.61%, only those with baseline RAA DF <5.6 Hz had the lowest risk of arrhythmia recurrence. While the decrease in LAA DF may reflect the efficient elimination of LA AF drivers, a low baseline RAA DF value fits with mild RA remodeling, while high baseline RAA DF suggests multiple RA drivers (Narayan et al., 2012). In summary, a decision tree model combining the changes in LAA DF during ablation and baseline RAA DF values appears promising in guiding complex ablation procedures for restoring long-term SR in peAF.

Clinical Implications

A prior study found that a ≥11% decrease in DF of lead V_1 after PVI and CFAE ablation was as predictive of freedom from recurrences as AF termination (Yoshida et al., 2010). Acute AF termination may reflect the elimination of AF critical drivers (Oral et al., 2008; Honarbakhsh et al., 2018) and has long been thought of as an optimal ablation endpoint in peAF. Studies reporting the association of AF termination with long-term clinical success have shown conflicting results. While in the study of Scherr et al. (2015), procedural AF termination improved long-term outcomes in patients undergoing substrate-based ablation, in a substudy of the STAR AF II trial, acute termination did not predict long-term AF freedom (Kochhäuser et al., 2017). In our study, 70% of patients with AF termination developed a recurrence. Importantly, these patients did not display any significant decrease in LAA DF during the first 20 min of CFAE ablation, which is suggestive of our inability to eliminate critical AF drivers (Lemola et al., 2006). Moreover,

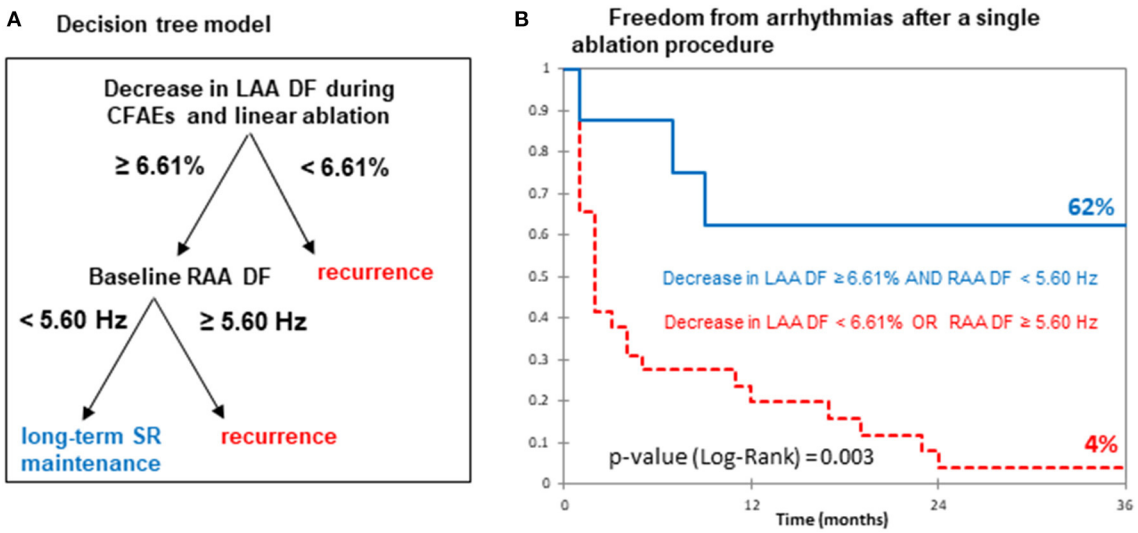

FIGURE 5 | Predictive performance of DF for long-term SR maintenance. **(A)** Decision tree model based on the relative changes in LAA DF after the first 20 min of LA ablation and baseline RAA DF. **(B)** Kaplan–Meier curves for freedom from AF recurrence after catheter ablation. Abbreviations as in previous figures.

these patients had longer ablation times than those without AF recurrence, suggesting that extensive LA substrate modification does not improve ablation success despite acute AF termination. These findings add to the bulk of studies showing the lack of long-term clinical benefit of stepwise ablation (Verma et al., 2015; Kochhäuser et al., 2017). In a previous study, Atienza et al. (2009) found in a mixed paroxysmal and persistent AF population undergoing ablation of DFmax sites and PVI that only those patients showing significant reductions in both LA and RA DFs with the abolition of the baseline LA-to-RA DF gradient remained free from AF. In our study, among patients displaying both baseline positive LAA-to-RAA DF gradient and its abolition by extra-PV substrate ablation, only those with significant reductions of the LAA DF at the early steps of ablation had the lowest risk of arrhythmia recurrence (LT_SR group). In conclusion, significant LAA DF reductions during ablation may be used as an indicator of the elimination of the AF drivers and ablation efficacy, but further studies are needed to validate this parameter in real-time settings.

Limitations

First, this study is limited by the small size of the population, which might have resulted in overestimated performances of the predictive models. However, the patients were consecutively included, and the analysis was performed offline, preventing any selection bias. Second, the tracking of AF organization was performed on EGMs from a limited number of atrial sites (LAA, RAA, and CS). Because of the stepwise ablation at multiple LA sites, the LAA was intently chosen as the site for the tracking of AF organization as no ablation was applied in this structure. It is possible that other atrial sites would have identified different intraprocedural dynamics and threshold values for DF. Third, patients in whom AF was terminated by a step-CA also had shorter ablation times than those without AF termination. We intentionally did not include cumulative ablation time in our decision tree model because it may not reflect the efficacy of ablation as no contact force measurements were available at the time of the study. In contrast, the reduction of the LAA DF at the early steps of ablation may reflect the adequate elimination of critical AF drivers (Lemola et al., 2006; Honarbakhsh et al., 2018). Finally, we acknowledge that the DFs estimated by the Fourier analysis may lack temporal stability due to the non-stationarity of EGM signals during AF (Salinet et al., 2014). To address this potential limitation, the DFs were first computed on 10-s epochs and then averaged over multiple epochs, which has been shown to improve the DF reproducibility (Ng and Goldberger, 2007).

CONCLUSION

This study showed that high surface and intracardiac DF values, and a negative LAA-to-RAA DF gradient before ablation are associated with the procedural failure to terminate AF and high recurrence rates at follow-up. Patients who achieved both a significant increase in LAA organization within 20 min of ablation following PVI and a low baseline RAA DF seem to benefit most from additional non-PV substrate modifications.

DATA AVAILABILITY STATEMENT

The original contributions presented in the study are included in the article/**Supplementary Material**, further inquiries can be directed to the corresponding author.

ETHICS STATEMENT

The studies involving human participants were reviewed and approved by Human Research Ethics Committee of the Lausanne University Hospital. The patients/participants provided their written informed consent to participate in this study.

AUTHOR CONTRIBUTIONS

AP, J-MV, EP, and AL conceived and designed the study, analyzed the results, and drafted the manuscript. AP, AB, and AL performed the data analysis, statistics, and off-line database construction. EP and AL supervised the work and contributed to the final manuscript. AM, PP, ML, CH, C-IP, LR, MK, FS, SK, CS, and EP contributed to data collection and/or critical revision of the manuscript. All authors contributed to the article and approved the submitted version.

FUNDING

This study was supported by Grant 18265.1 PFLS-LS from the Commission for Technology and Innovation (CTI), Switzerland and Grants SNF 205321 - 129876/1 and 146811/1 from the Swiss National Science Foundation.

ACKNOWLEDGMENTS

The authors would like to thank Biosense Webster Switzerland for their technical assistance.

SUPPLEMENTARY MATERIAL

The Supplementary Material for this article can be found online at: https://www.frontiersin.org/articles/10.3389/fphys.2021.731917/full#supplementary-material

REFERENCES

Atienza, F., Almendral, J., Jalife, J., Zlochiver, S., Ploutz-Snyder, R., Torrecilla, E. G., et al. (2009). Real-time dominant frequency mapping and ablation of dominant frequency sites in atrial fibrillation with left-to-right frequency gradients predicts long-term maintenance of sinus rhythm. *Heart Rhythm* 6, 33–40. doi: 10.1016/j.hrthm.2008.10.024

Botteron, G. W., and Smith, J. M. (1995). A technique for measurement of the extent of spatial organization of atrial activation during atrial fibrillation in the intact human heart. *IEEE Trans. Biomed. Eng.* 42, 579–586. doi: 10.1109/10.387197

Brooks, A. G., Stiles, M. K., Laborderie, J., Lau, D. H., Kuklik, P., Shipp, N. J., et al. (2010). Outcomes of long-standing persistent atrial fibrillation ablation: a systematic review. *Heart Rhythm* 7, 835–846. doi: 10.1016/j.hrthm.2010.01.017

Buttu, A., Vesin, J.-M., Zaen, J. V., Ballabeni, P., Pascale, P., Forclaz, A., et al. (2016). A high baseline electrographic organization level is predictive of successful termination of persistent atrial fibrillation by catheter ablation. *JACC Clin. Electrophysiol.* 2, 746–755. doi: 10.1016/j.jacep.2016.05.017

Calkins, H., Hindricks, G., Cappato, R., Kim, Y.-H., Saad, E. B., Aguinaga, L., et al. (2017). 2017 HRS/EHRA/ECAS/APHRS/SOLAECE expert consensus statement on catheter and surgical ablation of atrial fibrillation. *Heart Rhythm* 14, e275–e444. doi: 10.1016/j.hrthm.2017.05.012

Haissaguerre, M., Hocini, M., Denis, A., Shah, A. J., Komatsu, Y., Yamashita, S., et al. (2014). Driver domains in persistent atrial fibrillation. *Circulation* 130, 530–538. doi: 10.1161/CIRCULATIONAHA.113.005421

Hasebe, H., Yoshida, K., Iida, M., Hatano, N., Muramatsu, T., and Aonuma, K. (2016). Right-to-left frequency gradient during atrial fibrillation initiated by right atrial ectopies and its augmentation by adenosine triphosphate: Implications of right atrial fibrillation. *Heart Rhythm* 13, 354–363. doi: 10.1016/j.hrthm.2015.09.030

Honarbakhsh, S., Schilling, R. J., Providencia, R., Keating, E., Chow, A., Sporton, S., et al. (2018). Characterization of drivers maintaining atrial fibrillation: correlation with markers of rapidity and organization on spectral analysis. *Heart Rhythm* 15, 1296–1303. doi: 10.1016/j.hrthm.2018.04.020

Johner, N., Namdar, M., and Shah, D. C. (2020). Right atrial complexity evolves with stepwise left-sided persistent atrial fibrillation substrate ablation and predicts outcomes. *JACC Clin. Electrophysiol.* 6, 1619–1630. doi: 10.1016/j.jacep.2020.06.021

Kochhäuser, S., Jiang, C.-Y., Betts, T. R., Chen, J., Deisenhofer, I., Mantovan, R., et al. (2017). Impact of acute atrial fibrillation termination and prolongation of atrial fibrillation cycle length on the outcome of ablation of persistent atrial fibrillation: a substudy of the STAR AF II trial. *Heart Rhythm* 14, 476–483. doi: 10.1016/j.hrthm.2016.12.033

Lemay, M., Vesin, J.-M., van Oosterom, A., Jacquemet, V., and Kappenberger, L. (2007). Cancellation of ventricular activity in the ECG: evaluation of novel and existing methods. *IEEE Trans. Biomed. Eng.* 54, 542–546. doi: 10.1109/TBME.2006.888835

Lemola, K., Ting, M., Gupta, P., Anker, J. N., Chugh, A., Good, E., et al. (2006). Effects of two different catheter ablation techniques on spectral characteristics of atrial fibrillation. *J. Am. Coll. Cardiol.* 48, 340–348. doi: 10.1016/j.jacc.2006.04.053

Lo, L.-W., Tai, C.-T., Lin, Y.-J., Chang, S.-L., Udyavar, A. R., Hu, Y.-F., et al. (2009). Predicting factors for atrial fibrillation acute termination during catheter ablation procedures: implications for catheter ablation strategy and long-term outcome. *Heart Rhythm* 6, 311–318. doi: 10.1016/j.hrthm.2008.11.013

Luca, A., Pittet, A., Buttu, A., McCann, A., Vesin, J.-M., Pascale, P., et al. (2020). Severe and uniform bi-atrial remodeling measured by dominant frequency analysis in persistent atrial fibrillation unresponsive to ablation. *J. Interv. Card. Electrophysiol.* 59, 431–440. doi: 10.1007/s10840-019-00681-1

Ma, Y., Zaman, J. A. B., Shi, R., Karim, N., Panikker, S., Chen, Z., et al. (2021). Spectral characterization and impact of stepwise ablation protocol including LAA electrical isolation on persistent AF. *Pacing Clin. Electrophysiol.* 44, 318–326. doi: 10.1111/pace.14151

McCann, A., Vesin, J.-M., Pruvot, E., Roten, L., Sticherling, C., and Luca, A. (2021). ECG-based indices to characterize persistent atrial fibrillation before and during stepwise catheter ablation. *Front. Physiol.* 12:654053. doi: 10.3389/fphys.2021.654053

Nademanee, K., Schwab, M. C., Kosar, E. M., Karwecki, M., Moran, M. D., Visessook, N., et al. (2008). Clinical outcomes of catheter substrate ablation for high-risk patients with atrial fibrillation. *J. Am. Coll. Cardiol.* 51, 843–849. doi: 10.1016/j.jacc.2007.10.044

Narayan, S. M., Krummen, D. E., Shivkumar, K., Clopton, P., Rappel, W.-J., and Miller, J. M. (2012). Treatment of atrial fibrillation by the ablation of localized sources: CONFIRM (conventional ablation for atrial fibrillation with or without focal impulse and rotor modulation) trial. *J. Am. Coll. Cardiol.* 60, 628–636. doi: 10.1016/j.jacc.2012.05.022

Ng, J., and Goldberger, J. J. (2007). Understanding and interpreting dominant frequency analysis of AF electrograms. *J. Cardiovasc. Electrophysiol.* 18, 680–685. doi: 10.1111/j.1540-8167.2007.00832.x

Oral, H., Chugh, A., Good, E., Crawford, T., Sarrazin Jean, F., Kuhne, M., et al. (2008). Randomized evaluation of right atrial ablation after left atrial ablation of complex fractionated atrial electrograms for long-lasting persistent atrial fibrillation. *Circ. Arrhythm. Electrophysiol.* 1, 6–13. doi: 10.1161/CIRCEP.107.748780

Salinet, J. L., Tuan, J. H., Sandilands, A. J., Stafford, P. J., Schlindwein, F. S., and Ng, G. A. (2014). Distinctive patterns of dominant frequency trajectory behavior in drug-refractory persistent atrial fibrillation: preliminary

characterization of spatiotemporal instability. *J. Cardiovasc. Electrophysiol.* 25, 371–379. doi: 10.1111/jce.12331

Sanders, P., Berenfeld, O., Hocini, M., Jaïs, P., Vaidyanathan, R., Hsu, L.-F., et al. (2005). Spectral analysis identifies sites of high-frequency activity maintaining atrial fibrillation in humans. *Circulation* 112, 789–797. doi: 10.1161/CIRCULATIONAHA.104.517011

Scherr, D., Khairy, P., Miyazaki, S., Aurillac-Lavignolle, V., Pascale, P., Wilton, S. B., et al. (2015). Five-year outcome of catheter ablation of persistent atrial fibrillation using termination of atrial fibrillation as a procedural endpoint. *Circ. Arrhythm. Electrophysiol.* 8, 18–24. doi: 10.1161/CIRCEP.114.001943

Verma, A., Jiang, C., Betts, T. R., Chen, J., Deisenhofer, I., Mantovan, R., et al. (2015). Approaches to catheter ablation for persistent atrial fibrillation. *N. Engl. J. Med.* 372, 1812–1822. doi: 10.1056/NEJMoa1408288

Yokokawa, M., Chugh, A., Ulfarsson, M., Takaki, H., Han, L., Yoshida, K., et al. (2010). Effect of linear ablation on spectral components of atrial fibrillation. *Heart Rhythm* 7, 1732–1737. doi: 10.1016/j.hrthm.2010.05.040

Yoshida, K., Chugh, A., Good, E., Crawford, T., Myles, J., Veerareddy, S., et al. (2010). A critical decrease in dominant frequency and clinical outcome after catheter ablation of persistent atrial fibrillation. *Heart Rhythm* 7, 295–302. doi: 10.1016/j.hrthm.2009.11.024

Yoshida, K., Rabbani, A. B., Oral, H., Bach, D., Morady, F., and Chugh, A. (2011). Left atrial volume and dominant frequency of atrial fibrillation in patients undergoing catheter ablation of persistent atrial fibrillation. *J. Interv. Card. Electrophysiol. Int. J. Arrhythm. Pacing* 32, 155–161. doi: 10.1007/s10840-011-9590-0

Conflict of Interest: The authors declare that the research was conducted in the absence of any commercial or financial relationships that could be construed as a potential conflict of interest.

Publisher's Note: All claims expressed in this article are solely those of the authors and do not necessarily represent those of their affiliated organizations, or those of the publisher, the editors and the reviewers. Any product that may be evaluated in this article, or claim that may be made by its manufacturer, is not guaranteed or endorsed by the publisher.

frontiers in Physiology

REVIEW
published: 28 October 2021
doi: 10.3389/fphys.2021.752317

Prediction of Atrial Fibrillation Using Machine Learning: A Review

*Andrew S. Tseng and Peter A. Noseworthy**

Department of Cardiovascular Diseases, Mayo Clinic, Rochester, MN, United States

There has been recent immense interest in the use of machine learning techniques in the prediction and screening of atrial fibrillation, a common rhythm disorder present with significant clinical implications primarily related to the risk of ischemic cerebrovascular events and heart failure. Prior to the advent of the application of artificial intelligence in clinical medicine, previous studies have enumerated multiple clinical risk factors that can predict the development of atrial fibrillation. These clinical parameters include previous diagnoses, laboratory data (e.g., cardiac and inflammatory biomarkers, etc.), imaging data (e.g., cardiac computed tomography, cardiac magnetic resonance imaging, echocardiography, etc.), and electrophysiological data. These data are readily available in the electronic health record and can be automatically queried by artificial intelligence algorithms. With the modern computational capabilities afforded by technological advancements in computing and artificial intelligence, we present the current state of machine learning methodologies in the prediction and screening of atrial fibrillation as well as the implications and future direction of this rapidly evolving field.

Keywords: atrial fibrillation, electrocardiogram, echocardiography, risk factor, prediction, deep learning, machine learning

OPEN ACCESS

Edited by:
G. Andre Ng,
University of Leicester,
United Kingdom

Reviewed by:
Candido Cabo,
The City University of New York,
United States
Kamalan Jeevaratnam,
University of Surrey, United Kingdom

***Correspondence:**
Peter A. Noseworthy
Noseworthy.peter@mayo.edu

Specialty section:
This article was submitted to Cardiac Electrophysiology, a section of the journal Frontiers in Physiology

Received: *02 August 2021*
Accepted: *04 October 2021*
Published: *28 October 2021*

Citation:
Tseng AS and Noseworthy PA (2021) Prediction of Atrial Fibrillation Using Machine Learning: A Review. Front. Physiol. 12:752317. doi: 10.3389/fphys.2021.752317

INTRODUCTION

Atrial fibrillation (AF) is the most common arrhythmia worldwide with its burden expected to continue to increase with the aging population. AF is diagnosed clinically, requiring detection of the arrhythmia on formal electrocardiographic testing. Improvements in monitoring technology, including high-fidelity long-term monitors, have increased the yield for the detection of AF, thereby enhancing our knowledge of the true clinical burden of AF.

Beyond detection, there has been immense interest in prediction of AF using both clinical risk factors as well as objective testing. Numerous clinical risk scores have been proposed, incorporating readily available variables from the patient's medical history, such as age, ethnicity, height, weight, blood pressure, smoking status, medication use, and comorbidities (Schnabel et al., 2009; Chamberlain et al., 2011; Alonso et al., 2013; Suenari et al., 2017; Li et al., 2019; Hu and Lin, 2020; Lip et al., 2020; Himmelreich et al., 2021). Abnormalities in both cardiac and inflammatory biomarkers have been shown to augment the predictive ability of clinical prediction scores (O'Neal et al., 2016). Structural cardiac abnormalities, including atrial fibrosis and atrial enlargement, as well as associated manifestations on physiologic parameters such as mitral inflow Doppler and atrial strain have been shown to be predictive of AF (De Vos et al., 2009; Caputo and Mondillo, 2012; Hwang et al., 2015). Likewise, electrocardiographic (ECG), particularly P wave morphology, has been well-studied and shown to have predictive utility. Overall, there is an abundance of clinical variables that have been shown to be predictive of AF, individually or in limited pairings.

With advancements in artificial intelligence technology and the rapid accumulation of digital clinical data, machine learning has the potential to analyze and synthesize seemingly disparate variables to predict AF in such a way that vastly surpasses conventional methods (Siontis et al., 2020). Machine learning algorithms can not only assist in processing imaging or electrocardiographic data, but it may also be able to incorporate and interpret large amounts of clinical data and discover new clinical patterns and concepts. We seek to present the latest review of conventional and machine learning methodologies in the prediction of AF.

THE PRESENT STATE OF MACHINE LEARNING TECHNIQUES

At the core of machine learning is the convergence of statistical analytics and computer engineering. Machine learning algorithms are able to process complex inputs, such as images, and discern subtle relationships that may not be evident with traditional statistical methods. Machine learning techniques can be categorized broadly into three categories: supervised learning, unsupervised learning, and reinforcement learning. Supervised learning requires labels during training, such as the presence or absence of incident AF. Therefore, the algorithm is provided with both the input variables as well as outcome labels. Unsupervised learning seeks to identify relationships within the data without the assistance of labels. Various methods such as clustering have been described for this method of learning. Reinforcement learning uses the concept of reward maximization, in which the machine learning algorithm assumes the role of an agent that receives either positive or negative reinforcement to guide decision making (Thrun and Littman, 2000; Koohy, 2017; Géron, 2019). For the purposes of this review, we will discuss the most used learning method, supervised learning.

Supervised learning itself utilizes different methods including regression modeling, random forests, and neural networks. In regression modeling, both with and without machine learning, preselected variables undergo regression analysis to determine their ability to predict an outcome. Machine learning improves upon these traditional modeling techniques by its ability to analyze large and complex datasets. Techniques include classification algorithms such as Support Vector Machine and K-Nearest Neighbor (Sultana et al., 2016). Random forests utilize branching decision trees, empirically deriving thresholds to determine how the data should be split (Koohy, 2017; Géron, 2019; Uddin et al., 2019).

Neural networks have fundamentally changed the machine learning landscape. Fundamentally, the network architecture is comprised of layers and processing units within each layer called nodes. Data is analyzed in one layer and then transmitted to the next layer, such that a node in a deeper layer receives inputs from one or more nodes in the prior layer. All neural networks have an input layer to process input data and an output layer while a deep neural network continues numerous "hidden" intermediary layers and nodes. Convolutional neural networks utilize the concept of "convolutions," whereby nodes in a deeper layer only receive input from select subset of nodes from the previous layer. Therefore, these networks seek to identify local correlations and preserve local special dependences, which is particularly important for image processing. It also allows for more efficient computational processing by reducing the input data into smaller localized convolved features via methods of dimensionality reduction (Stankovic and Mandic, 2021).

There are a vast array of different machine learning techniques, which by themselves can be the subject of reviews and textbooks. For the clinician, we have summarized the different supervised machine learning techniques, including names of techniques one might encounter, as well as the general advantages and disadvantages in **Table 1**.

FROM CLINICAL DATA

Validated clinical risk scores to predict AF, such as the FHS, ARIC, CHARGE-AF, C2HEST, and HATCH score, utilize readily obtainable clinical variables, such as age, ethnicity, height, weight, blood pressure, smoking status, antihypertensive medication use, history of diabetes, heart failure myocardial infarction, etc. Based on these readily available variables from the patient history, these risk scores have shown adequate model discrimination for the prediction of incident AF (area under the receiver operator curve, AUCs, generally around 0.70) (Schnabel et al., 2009; Chamberlain et al., 2011; Alonso et al., 2013; Suenari et al., 2017; Li et al., 2019; Hu and Lin, 2020; Lip et al., 2020; Himmelreich et al., 2021). AUCs, or c-statistic, are commonly used in studies of diagnostic test performance as an overall indicator of test performance (Bradley, 1997). Other measures of test performance, though not universally reported, include accuracy (proportion of correct assessments), precision (or positive predictive value), and recall (or sensitivity). Due to inconsistencies with reporting these other measures of test performance, which limits comparison among studies, we will largely focus on AUCs. The studies for these validated clinical risk scores to predict AF are summarized in **Table 2**.

The addition of serologic testing of common cardiac biomarkers, including natriuretic peptides and C-reactive protein, has been shown to enhance the predictive ability of such clinical risk scores (Sinner et al., 2014). Additional markers of chronic kidney disease, such as Cystatin C, and endothelial dysfunction have also been shown to be associated with AF, though no studies have been shown that the addition of these parameters enhances the predictive ability of existing clinical risk scores (O'Neal et al., 2016).

With the abundance of clinical and laboratory data available in digital format, recent investigators have started to evaluate the use of machine learning in predicting AF using the electronic health record. To facilitate this, organizations have developed a common data models for analysis, one prime example being the Observational Medical Outcomes Partnership Common Data Model in an effort to synchronize data from disparate sources for systematic analysis (FitzHenry et al., 2015). In a recent large study of nearly 2 million patients from the University of Colorado health systems by Tiwari et al. (2020) investigators applied a

TABLE 1 | Advantages and disadvantages of different supervised machine learning techniques.

Examples	Advantages	Disadvantages
Linear/logistic regression	Simple and easy to implement	Reduced accuracy with variables with complex relationships
k-Nearest Neighbor	Simple and can handle noisy instances or instances with missing attribute value	Computationally taxing, does not identify variables that are important for classification
Support vector machines	More robust than ordinary regression and can classify semi-structured/unstructured data	Computationally taxing, does not handle data noise well
Random forests	Performs well in large datasets and identifies variables that are important for classification	Computationally taxing, easy to overfit
Neural networks	Detects complex non-linear relationships between variables	Computationally taxing, cannot access decision making process ("blackbox")

TABLE 2 | Original and validation studies of clinical AF risk scores.

Clinical AF risk score	Original study	Example validation*
FHS (Age, sex, BMI, SBP, hypertension treatment, PR interval, clinically significant cardiac murmur, CHF)	4,764 patients from the United States AUC 0.78 (95% CI 0.76–0.80) (Schnabel et al., 2009)	49,599 patients from the United States 0.734 (0.724–0.744) (Shulman et al., 2016)
ARIC (Age, race, height, SBP, hypertension treatment, smoking status, precordial murmur, left ventricular hypertrophy, left atrial enlargement, DM, CAD, CHF)	14,546 patients from the United States AUC 0.765; 95% CI, 0.748–0.781 (Chamberlain et al., 2011)	None
CHARGE-AF (Age, ethnicity, height, weight, blood pressure, smoking, antihypertensive use, DM, CHF, MI)	18,556 patients from the United States AUC 0.765 (95% CI: 0.748–0.781) (Alonso et al., 2013)	114,475 patients from the Netherlands AUC 0.74 (95% CI: 0.73–0.74) (Himmelreich et al., 2021)
C2HEST (CAD/COPD, hypertension, age, CHF, hyperthyroidism)	471,446 patients from China AUC 0.75 (95% CI: 0.73–0.77) (Li et al., 2019)	1,047,330 patients from Denmark AUC 0.588 (95% CI: 0.585–0.591) (Lip et al., 2020)
HATCH (Hypertension, age, stroke/TIA, COPD, CHF)	670,804 patients from Taiwan AUC 0.716 (95% CI: 0.710–0.723 (Suenari et al., 2017)	692,691 patients from Taiwan AUC 0.771 (no CI provided) (Hu and Lin, 2020)

AF, atrial fibrillation; AUC, area under the curve; BMI, body mass index; CAD, coronary artery disease; CHF, congestive heart failure; COPD, chronic obstructive pulmonary disease; DM, diabetes mellitus; MI, myocardial infraction; SBP, systolic blood pressure; TIA, transient ischemic attack.
**Studies selected for explanatory purposes and may not be an exhaustive list.*

machine learning model to over 200 most common health record features, including demographics and comorbidity data, and derived a model with an AUC of 0.79 to detect incident AF in a 6 month timeframe, which is in line with non-machine learning clinical AF risk scores. In another study of over 2 million primary care patients from the United Kingdom by Sekelj et al. (2021) another machine learning algorithm achieved an AUC of 0.83 in the development dataset and 0.87 in the validation dataset to detect incident AF in a registry that spanned 7 years, indicating better performance compared to traditional risk scores.

When comparing the AI algorithms to the traditional risk scores, many factors may impact and limit the interpretation of the test performance. Firstly, there is significant variation in the duration of follow-up for each study, ranging from as short as 6 months to more than 10 years. This clearly significantly impacted the proportion of patients at study termination with incident AF (1% vs. 10%, respectively) (Schnabel et al., 2009; Tiwari et al., 2020). It is possible that limited follow-up such as 6 months in the Tiwari AI study may have reduced the test performance in part due to the limited duration of follow-up, where "false positives" (i.e., AI screening positive, AF negative at 6 months) would have been "true positives" if given sufficient time to manifest or vice versa with "true negatives" at the end of study turning into "false negatives" (Tiwari et al., 2020).

In a recent study by Hill et al. (2019) of nearly 3 million patients in the United Kingdom, the investigators compared a machine learning algorithm with time-varying covariates to the CHARGE-AF risk score. The use of time-varying covariates represents yet another technique in neural networks, in which the input covariates are not static but are allowed to be incorporated into the model at varying time points during the study period. This means that the temporal association between a covariate and the outcome becomes another critical factor during the development of these neural networks. In this study, the found that the time-varying model had an AUC of 0.827 while the traditional CHARGE-AF risk score applied to the same population had an AUC of 0.725. Using the time-varying methodology, they were able to determine that congestive heart failure diagnosed within the most recent 91-day quarter contributed the most to the prediction of incident AF. This study

not only showed the benefits of using different machine learning techniques to extract potentially clinically relevant predictors (such as time-dependent variables), but also that the machine learning algorithms performed more robustly than traditional risk scores (Hill et al., 2019). While these algorithms have not been tested prospectively nor have they been validated in external health systems, the size and scale of these massive projects far exceed previous studies of conventional clinical risk scores for AF, and shows the increasing promise of utilizing easily accessible data from the electronic health record to predict the risk of incident AF.

FROM CARDIAC IMAGING DATA

AF is often associated with distinct structural heart abnormalities that are apparent on cardiac imaging, including echocardiography, CT and MRI. Oftentimes, these structural abnormalities result from conditions that predispose patients to AF, such as diastolic dysfunction, but AF can also itself lead to valvular regurgitation. From an echocardiography perspective, previous studies have shown that left atrial volumes, measures of diastolic dysfunction, ventricular wall thickness, strain echocardiography can be associated with the risk of new-onset AF (Xu et al., 2011; Caputo and Mondillo, 2012; Hirose et al., 2012). Newer, non-conventional measurements such as the total atrial conduction time, as a marker of atriopathy, was also shown to be associated with development of AF in a smaller cohort of 249 patients (De Vos et al., 2009). Cardiac CT to evaluate the left atrial appendage have demonstrated mixed results on prediction of AF after AF ablation (Ebersberger et al., 2020). However, left atrial thickness as a marker of atriopathy on cardiac CT has been shown to be associated with increased risk of transition for paroxysmal AF to chronic AF as well as low-voltage areas as potential sites of ablation (Nakamura et al., 2011; Nakatani et al., 2020). Given the unique ability of MRI to evaluate tissue characteristics, left atrial fibrosis by late gadolinium enhancement on cardiac MRI has been shown to be associated with new-onset AF. One study with 182 patients evaluated the predictive ability of left atrial fibrosis>6% and derived an AUC of 0.67, which was further enhanced to 0.80 after adding history of hypertension and left ventricular ejection fraction (Siebermair et al., 2019). Overall, the use of these imaging parameters to predict AF have largely been restricted to small association and procedural studies, and there has not been systematic use of imaging data to develop or refine existing risk scores for predicting AF.

Machine learning has likewise begun to make headway in image analysis. Unlike the categorical or numerical input of data from the electronic health records, images require additional sophisticated methodologies when applying machine learning, yet the fundamental theory remains similar (Fu et al., 2019). Small-scale studies have started to investigate the use of machine learning on cardiac imaging. In a small study on cardiac CT using machine learning to evaluate left atrial and pulmonary vein morphology in 203 patients undergoing AF ablation, the machine learning algorithm was able to predict AF recurrence after ablation using these CT images with an AUC of overall AUC of 0.87 (Firouznia et al., 2021). A similar study of 68 patients using cardiac CT left atrial morphology to predict AF recurrence after ablation demonstrated an AUC of 0.78 when combining imaging and clinical features (Atta-Fosu et al., 2021).

However, there have not been investigations in the use of machine learning in cardiac imaging to predict new-onset AF. Given multiple factors, including the complexity of image processing, machine learning in cardiac imaging has focused on image acquisition, processing, and basic interpretation (Chang et al., 2020). Future studies will be needed to develop the role of machine learning in prognosis and detection of non-imaging diagnoses such as AF. As such, large population-based studies may not be feasible, related to the costs of screening asymptomatic patients with imaging and significant selection bias for patients who have indications to undergo cardiac imaging tests. Nonetheless, machine learning in cardiac imaging for AF will undoubtedly play an important role in periprocedural prognosis and management, and perhaps with well-designed studies can help with the prediction of AF.

FROM ELECTROPHYSIOLOGICAL DATA

Pathophysiologic changes in AF can also manifest itself as abnormalities on electrophysiology testing, such as electrocardiography and invasive intracardiac electrograms. Previous studies have shown that ECG findings, such as P-wave duration, dispersion and amplitude as well as premature atrial contraction morphology and frequency, have been shown to be predictive of incident AF, achieving AUCs ranging from 0.69 to 0.87 (Dilaveris et al., 2000; Thong et al., 2004; Yoshizawa et al., 2014). One study evaluated premature atrial contraction characteristics and percent burden as a risk factor for AF among 652 patients who underwent Holter monitoring, with an AUC of 0.58 (Im et al., 2018).

Intracardiac electrograms are generally obtained during an electrophysiology study in patients with known or suspected arrhythmia. Therefore, there have not been studies specifically evaluating the predictive ability of electrogram features on new-onset AF. However, elements of the intracardiac electrogram have been shown to be correlated with the risk of AF recurrence after ablation. For example, in one study on 140 patients, multiple electrogram characteristics including dominant frequency, regularity index and organizational index of fibrillatory electrograms have shown predictive value for AF recurrence after AF ablation (Szilagyi et al., 2018).

The use of machine learning on the ECG to predict new-onset AF has been the subject of immense inquiry recently. Unlike the use of machine learning to process cardiac imaging, the processing of electrocardiographic signals is highly standardized using a static time series dataset and more easily interpretable compared to a series of images, including moving images like in echocardiography. In a large study from the Mayo Clinic of over

600,000 ECGs in normal sinus rhythm, a convolutional neural network was developed with a robust AUC of 0.87 for predicting new-onset AF, with further augmentation of the AUC to 0.90 for patients with multiple ECGs (Attia et al., 2019). A small study by Ebrahimzadeh et al. (2018) in 53 patients of extended ECG recordings sought to evaluate different machine learning techniques using heart rate variability analysis in extended ECG monitoring to predict initiation of AF. In this self-controlled study, all patients had an episode of paroxysmal AF, in which a 5-min ECG segment obtained 30 min prior to the onset of AF ("AF" label) was compared to a 5-min ECG segment obtained 45 min after termination of AF ("non-AF" label). Unlike the convolutional neural network used in the Mayo Clinic study in which the features of the neural network are hidden, the investigators identified multiple features from the heart rate variability signal, including linear, non-linear and time frequency features, in order to develop the machine learning model. They found that the combined machine learning approach performed better than traditional machine learning classifiers (Multilayer Perceptron, K-Nearest Neighbor, Support Vector Machine) (accuracy of 98.21% vs. 91.90–93.76%, respectively) (Ebrahimzadeh et al., 2018).

Thus, there are numerous techniques in machine learning being explored for the use of electrophysiological data to predict AF. These techniques range from different "traditional" machine learning classification algorithms to convolutional neural networks. No direct comparison between traditional models and machine learning models in ECG interpretation have been performed to date. However, machine learning methodologies allow analysis of large quantities of ECG data that may be too cumbersome and time consuming to perform manually and has thus far allowed for the development of prediction models with strong diagnostic performance.

FUTURE DIRECTION

As the reader considers the various sections in this review from clinical data to electrophysiological data, we can see that machine learning, while still in its infancy, has begun to drastically improve our ability to predict AF. There are current worldwide efforts and clinical trials to prospectively test and harness the potential of AI in clinical practice for AF. In the United States, the Batch Enrollment for AI-Guided Intervention to Lower Neurologic Events in Unrecognized AF, or BEAGLE trial, seeks to assess the performance of AI on detecting AF on normal sinus ECGs in adult patients who do not have a previous diagnosis of AF and are eligible for anticoagulation based on standard stroke risk stratification (Yao et al., 2021). Similar efforts are being undertaken in France, United Kingdom, the Netherlands, Finland, and Germany, some also testing the utility of AI applied to ECGs obtained by portable devices (ClinicalTrials.gov, 2021a,b,c,d,e).

Despite these important advancements, there is still significant room for growth within this space.

(1) Integration of all modalities of data: While siloed approaches are often necessary in the beginning to refine specific methodologies as it pertains to different modalities of data, we have seen from conventional studies that the combination of data (e.g., clinical, laboratory, imaging, etc.) often leads to the highest predictive ability for any clinical risk score. This same principle should be applied to machine learning algorithms, such that the development of a machine learning algorithm that can incorporate all modalities of data, likely further enhancing the powerful predictive performance of the existing AI algorithms.
(2) Advancements in our understanding and methodologies of machine learning: At this early stage, due to the nature of many advanced types of machine learning, including convolutional neural networks, the signal features selected by the AI as important predictive features in an algorithm cannot be known (the so-called "black box"). It is possible that future techniques will allow the algorithms to be more explicit and informative about its own methodologies, both to inform clinicians on novel patterns that may advance human understanding but also to inform researchers on potential troubleshooting issues, such as the inadvertent use of non-medical or unrelated data in their predictive algorithms.
(3) Implications of machine learning algorithms on management: While the overall aim of this review is to evaluate the role of AI in predicting AF, future studies should undoubtedly evaluate the prospective use of these algorithms to determine optimal management strategies for patients. In AF, for example, there is significant implication with AF diagnosis regarding stroke prevention via the use of anticoagulation. Could there be important changes to clinical outcomes and patient management based on the results of the algorithm that can be eventually be actionable, perhaps even before a clinical diagnosis?

CONCLUSION

There is no doubt that artificial intelligence will play a greater role in medicine as the technology continues to advance and our understanding of its applications continues to grow. While still in its early stages and still flawed by inherent limitations, machine learning shows great promise in improving our ability to predict AF. The future integration of clinical, imaging and electrophysiological data will certainly improve the performance of these machine learning algorithms, and ultimately improve the care of patients worldwide.

AUTHOR CONTRIBUTIONS

PN formulated the concept and format of the article and made critical revisions to the manuscript. AT wrote and revised the manuscript. Both authors contributed to the article and approved the submitted version.

REFERENCES

Alonso, A., Krijthe, B. P., Aspelund, T., Stepas, K. A., Pencina, M. J., Moser, C. B., et al. (2013). Simple risk model predicts incidence of atrial fibrillation in a racially and geographically diverse population: the CHARGE-AF consortium. *J. Am. Heart Assoc.* 2:e000102. doi: 10.1161/JAHA.112.000102

Atta-Fosu, T., LaBarbera, M., Ghose, S., Schoenhagen, P., Saliba, W., Tchou, P. J., et al. (2021). A new machine learning approach for predicting likelihood of recurrence following ablation for atrial fibrillation from CT. *BMC Med. Imaging.* 21:45. doi: 10.1186/s12880-021-00578-4

Attia, Z. I., Noseworthy, P. A., Lopez-Jimenez, F., Asirvatham, S. J., Deshmukh, A. J., Gersh, B. J., et al. (2019). An artificial intelligence-enabled ECG algorithm for the identification of patients with atrial fibrillation during sinus rhythm: a retrospective analysis of outcome prediction. *Lancet* 394, 861–867. doi: 10.1016/S0140-6736(19)31721-0

Bradley, A. P. (1997). The use of the area under the ROC curve in the evaluation of machine learning algorithms. *Pattern Recogn.* 30, 1145–1159. doi: 10.1016/S0031-3203(96)00142-2

Caputo, M., and Mondillo, S. (2012). Echocardiography in the prediction of atrial fibrillation recurrence: a review. *J. Atr. Fibrillation.* 5:675.

Chamberlain, A. M., Agarwal, S. K., Folsom, A. R., Soliman, E. Z., Chambless, L. E., Crow, R., et al. (2011). A clinical risk score for atrial fibrillation in a biracial prospective cohort (from the Atherosclerosis Risk in Communities [ARIC] study). *Am. J. Cardiol.* 107, 85–91. doi: 10.1016/j.amjcard.2010.08.049

Chang, A., Cadaret, L. M., and Liu, K. (2020). Machine learning in electrocardiography and echocardiography: technological advances in clinical cardiology. *Curr. Cardiol. Rep.* 22:161. doi: 10.1007/s11886-020-01416-9

ClinicalTrials.gov (2021a). *Artificial Intelligence Use for the Detection of Atrial Fibrillation Drivers*. Available online at: https://ClinicalTrials.gov/show/NCT03401931 (accessed June 1, 2021).

ClinicalTrials.gov (2021c). *Predicting Patient-level New Onset Atrial Fibrillation.* Available online at: https://ClinicalTrials.gov/show/NCT04657900 (accessed June 1, 2021).

ClinicalTrials.gov (2021e). *Portable Measurement Methods Combined With Artificial Intelligence in Detection of Atrial Fibrillation*. Available online at: https://ClinicalTrials.gov/show/NCT04917653 (accessed June 1, 2021).

ClinicalTrials.gov (2021b). *Exploratory Study of Apple Watch Electrocardiographic Diagnostic Performance Enhanced by an Artificial Intelligence Algorithm.* Available online at: https://ClinicalTrials.gov/show/NCT04792905 (accessed June 1, 2021).

ClinicalTrials.gov (2021d). *Prevention of Stroke and Sudden Cardiac Death by Recording of 1-Channel Electrocardiograms*. Available online at: https://ClinicalTrials.gov/show/NCT04637230 (accessed June 1, 2021).

De Vos, C. B., Weijs, B., Crijns, H. J., Cheriex, E. C., Palmans, A., Habets, J., et al. (2009). Atrial tissue Doppler imaging for prediction of new-onset atrial fibrillation. *Heart* 95, 835–840. doi: 10.1136/hrt.2008.148528

Dilaveris, P. E., Gialafos, E. J., Andrikopoulos, G. K., Richter, D. J., Papanikolaou, V., Poralis, K., et al. (2000). Clinical and electrocardiographic predictors of recurrent atrial fibrillation. *Pacing Clin. Electrophysiol.* 23, 352–358. doi: 10.1111/j.1540-8159.2000.tb06761.x

Ebersberger, U., Bernard, M. L., Schoepf, U. J., Wince, W. B., Litwin, S. E., Wang, Y., et al. (2020). Cardiac computed tomography for atrial fibrillation patients undergoing ablation: implications for the prediction of early recurrence. *J. Thorac. Imaging* 35, 186–192. doi: 10.1097/RTI.0000000000000425

Ebrahimzadeh, E., Kalantari, M., Joulani, M., Shahraki, R. S., Fayaz, F., and Ahmadi, F. (2018). Prediction of paroxysmal Atrial Fibrillation: a machine learning based approach using combined feature vector and mixture of expert classification on HRV signal. *Comput. Methods Programs Biomed.* 165, 53–67. doi: 10.1016/j.cmpb.2018.07.014

Firouznia, M., Feeny, A. K., LaBarbera, M. A., McHale, M., Cantlay, C., Kalfas, N., et al. (2021). Machine learning-derived fractal features of shape and texture of the left atrium and pulmonary veins from cardiac computed tomography scans are associated with risk of recurrence of atrial fibrillation postablation. *Circ. Arrhythm. Electrophysiol.* 14:e009265. doi: 10.1161/CIRCEP.120.009265

FitzHenry, F., Resnic, F. S., Robbins, S. L., Denton, J., Nookala, L., Meeker, D., et al. (2015). Creating a common data model for comparative effectiveness with the observational medical outcomes partnership. *Appl. Clin. Inform.* 6, 536–547. doi: 10.4338/ACI-2014-12-CR-0121

Fu, G. S., Levin-Schwartz, Y., Lin, Q. H., and Zhang, D. (2019). Machine learning for medical imaging. *J. Healthcare Eng.* 2019:9874591. doi: 10.1155/2019/9874591

Géron, A. (2019). *Hands-on Machine Learning with Scikit-Learn, Keras, and TensorFlow: Concepts, Tools, and Techniques to Build Intelligent Systems*. Newton, MA: O'Reilly Media.

Hill, N. R., Ayoubkhani, D., McEwan, P., Sugrue, D. M., Farooqui, U., Lister, S., et al. (2019). Predicting atrial fibrillation in primary care using machine learning. *PLoS One* 14:e0224582. doi: 10.1371/journal.pone.0224582

Himmelreich, J. C. L., Lucassen, W. A. M., Harskamp, R. E., Aussems, C., van Weert, H., and Nielen, M. M. J. (2021). CHARGE-AF in a national routine primary care electronic health records database in the Netherlands: validation for 5-year risk of atrial fibrillation and implications for patient selection in atrial fibrillation screening. *Open Heart* 8:e001459. doi: 10.1136/openhrt-2020-001459

Hirose, T., Kawasaki, M., Tanaka, R., Ono, K., Watanabe, T., Iwama, M., et al. (2012). Left atrial function assessed by speckle tracking echocardiography as a predictor of new-onset non-valvular atrial fibrillation: results from a prospective study in 580 adults. *Eur. Heart J. Cardiovasc. Imaging* 13, 243–250. doi: 10.1093/ejechocard/jer251

Hu, W. S., and Lin, C. L. (2020). Prediction of new-onset atrial fibrillation for general population in Asia: a comparison of C2HEST and HATCH scores. *Int. J. Cardiol.* 313, 60–63. doi: 10.1016/j.ijcard.2020.03.036

Hwang, S. H., Oh, Y. W., Lee, D. I., Shim, J., Park, S. W., and Kim, Y. H. (2015). Relation between left atrial wall composition by late gadolinium enhancement and complex fractionated atrial electrograms in patients with persistent atrial fibrillation: influence of non-fibrotic substrate in the left atrium. *Int. J. Cardiovasc. Imaging* 31, 1191–1199. doi: 10.1007/s10554-015-0675-1

Im, S. I., Park, D. H., Kim, B. J., Cho, K. I., Kim, H. S., and Heo, J. H. (2018). Clinical and electrocardiographic characteristics for prediction of new-onset atrial fibrillation in asymptomatic patients with atrial premature complexes. *Int. J. Cardiol. Heart Vasc.* 19, 70–74. doi: 10.1016/j.ijcha.2018.05.002

Koohy, H. (2017). The rise and fall of machine learning methods in biomedical research. *F1000Res.* 6:2012. doi: 10.12688/f1000research.13016.1

Li, Y. G., Pastori, D., Farcomeni, A., Yang, P. S., Jang, E., Joung, B., et al. (2019). A Simple Clinical Risk Score (C2HEST) for Predicting Incident Atrial Fibrillation in Asian Subjects: Derivation in 471,446 Chinese Subjects. With Internal Validation and External Application in 451,199 Korean Subjects. *Chest* 155, 510–518. doi: 10.1016/j.chest.2018.09.011

Lip, G. Y. H., Skjoth, F., Nielsen, P. B., and Larsen, T. B. (2020). Evaluation of the C2HEST Risk Score as a Possible Opportunistic Screening Tool for Incident Atrial Fibrillation in a Healthy Population (From a Nationwide Danish Cohort Study). *Am. J. Cardiol.* 125, 48–54. doi: 10.1016/j.amjcard.2019.09.034

Nakamura, K., Funabashi, N., Uehara, M., Ueda, M., Murayama, T., Takaoka, H., et al. (2011). Left atrial wall thickness in paroxysmal atrial fibrillation by multislice-CT is initial marker of structural remodeling and predictor of transition from paroxysmal to chronic form. *Int. J. Cardiol.* 148, 139–147. doi: 10.1016/j.ijcard.2009.10.032

Nakatani, Y., Sakamoto, T., Yamaguchi, Y., Tsujino, Y., Kataoka, N., and Kinugawa, K. (2020). Left atrial wall thickness is associated with the low-voltage area in patients with paroxysmal atrial fibrillation. *J. Interv. Card. Electrophysiol.* 58, 315–321. doi: 10.1007/s10840-019-00611-1

O'Neal, W. T., Venkatesh, S., Broughton, S. T., Griffin, W. F., and Soliman, E. Z. (2016). Biomarkers and the prediction of atrial fibrillation: state of the art. *Vasc. Health Risk Manag.* 12, 297–303. doi: 10.2147/VHRM.S75537

Schnabel, R. B., Sullivan, L. M., Levy, D., Pencina, M. J., Massaro, J. M., D'Agostino, R. B. Sr., et al. (2009). Development of a risk score for atrial fibrillation (Framingham Heart Study): a community-based cohort study. *Lancet* 373, 739–745. doi: 10.1016/S0140-6736(09)60443-8

Sekelj, S., Sandler, B., Johnston, E., Pollock, K. G., Hill, N. R., Gordon, J., et al. (2021). Detecting undiagnosed atrial fibrillation in UK primary care: validation of a machine learning prediction algorithm in a retrospective cohort study. *Eur. J. Prev. Cardiol.* 28, 598–605. doi: 10.1177/2047487320942338

Shulman, E., Kargoli, F., Aagaard, P., Hoch, E., Di Biase, L., Fisher, J., et al. (2016). Validation of the Framingham heart study and CHARGE-AF risk scores for

atrial fibrillation in Hispanics, African-Americans, and Non-Hispanic Whites. *Am. J. Cardiol.* 117, 76–83. doi: 10.1016/j.amjcard.2015.10.009

Siebermair, J., Suksaranjit, P., McGann, C. J., Peterson, K. A., Kheirkhahan, M., Baher, A. A., et al. (2019). Atrial fibrosis in non-atrial fibrillation individuals and prediction of atrial fibrillation by use of late gadolinium enhancement magnetic resonance imaging. *J. Cardiovasc. Electrophysiol.* 30, 550–556. doi: 10.1111/jce.13846

Sinner, M. F., Stepas, K. A., Moser, C. B., Krijthe, B. P., Aspelund, T., Sotoodehnia, N., et al. (2014). B-type natriuretic peptide and C-reactive protein in the prediction of atrial fibrillation risk: the CHARGE-AF Consortium of community-based cohort studies. *Europace* 16, 1426–1433. doi: 10.1093/europace/euu175

Siontis, K. C., Yao, X., Pirruccello, J. P., Philippakis, A. A., and Noseworthy, P. A. (2020). How will machine learning inform the clinical care of atrial fibrillation? *Circ. Res.* 127, 155–169. doi: 10.1161/CIRCRESAHA.120.316401

Stankovic, L., and Mandic, D. (2021). Convolutional neural networks demystified: a matched filtering perspective based tutorial. *arXiv* [Preprint]. Available online at: https://arxiv.org/pdf/2108.11663.pdf (accessed June 1, 2021).

Suenari, K., Chao, T. F., Liu, C. J., Kihara, Y., Chen, T. J., and Chen, S. A. (2017). Usefulness of HATCH score in the prediction of new-onset atrial fibrillation for Asians. *Medicine (Baltimore).* 96, e5597. doi: 10.1097/MD.0000000000005597

Sultana, N., Kamatham, Y., and Kinnara, B. (eds) (2016). "Performance analysis of artificial neural networks for cardiac arrhythmia detection," in *Proceedings of the 2016 IEEE 6th International Conference on Advanced Computing (IACC)*, Bhimavaram. doi: 10.1109/IACC.2016.84

Szilagyi, J., Walters, T. E., Marcus, G. M., Vedantham, V., Moss, J. D., Badhwar, N., et al. (2018). Surface ECG and intracardiac spectral measures predict atrial fibrillation recurrence after catheter ablation. *J. Cardiovasc. Electrophysiol.* 29, 1371–1378. doi: 10.1111/jce.13699

Thong, T., McNames, J., Aboy, M., and Goldstein, B. (2004). Prediction of paroxysmal atrial fibrillation by analysis of atrial premature complexes. *IEEE Trans. Biomed. Eng.* 51, 561–569. doi: 10.1109/TBME.2003.821030

Thrun, S., and Littman, M. L. (2000). *Reinforcement Learning: An Introduction*. Cambridge, MA: The MIT Press.

Tiwari, P., Colborn, K. L., Smith, D. E., Xing, F., Ghosh, D., and Rosenberg, M. A. (2020). Assessment of a machine learning model applied to harmonized electronic health record data for the prediction of incident atrial fibrillation. *JAMA Netw. Open* 3:e1919396. doi: 10.1001/jamanetworkopen.2019.19396

Uddin, S., Khan, A., Hossain, M. E., and Moni, M. A. (2019). Comparing different supervised machine learning algorithms for disease prediction. *BMC Med. Inform. Decis. Mak.* 19:1–16. doi: 10.1186/s12911-019-1004-8

Xu, H. F., He, Y. M., Qian, Y. X., Zhao, X., Li, X., and Yang, X. J. (2011). Left ventricular posterior wall thickness is an independent risk factor for paroxysmal atrial fibrillation. *West. Indian Med. J.* 60, 647–652.

Yao, X., Attia, Z. I., Behnken, E. M., Walvatne, K., Giblon, R. E., Liu, S., et al. (2021). Batch enrollment for an artificial intelligence-guided intervention to lower neurologic events in patients with undiagnosed atrial fibrillation: rationale and design of a digital clinical trial. *Am. Heart J.* 239, 73–79. doi: 10.1016/j.ahj.2021.05.006

Yoshizawa, T., Niwano, S., Niwano, H., Igarashi, T., Fujiishi, T., Ishizue, N., et al. (2014). Prediction of new onset atrial fibrillation through P wave analysis in 12 lead ECG. *Int. Heart J.* 55, 422–427. doi: 10.1536/ihj.14-052

Conflict of Interest: PN receives research funding from National Institutes of Health [NIH, including the National Heart, Lung, and Blood Institute (NHLBI, R21AG 62580-1, R01HL 131535-4, R01HL 143070-2) the National Institute on Aging (NIA, R01AG 062436-1)], Agency for Healthcare Research and Quality (AHRQ, R01HS 25402-3), Food and Drug Administration (FDA, FD 06292), and the American Heart Association (18SFRN34230146, AHA). PN was a study investigator in an ablation trial sponsored by Medtronic. PN and Mayo Clinic were involved in potential equity/royalty relationship with AliveCor. PN has served on an expert advisory panel for Optum. PN and Mayo Clinic have filed patents related to the application of AI to the ECG for diagnosis and risk stratification.

The remaining author declares that the research was conducted in the absence of any commercial or financial relationships that could be construed as a potential conflict of interest.

Publisher's Note: All claims expressed in this article are solely those of the authors and do not necessarily represent those of their affiliated organizations, or those of the publisher, the editors and the reviewers. Any product that may be evaluated in this article, or claim that may be made by its manufacturer, is not guaranteed or endorsed by the publisher.

frontiers in Physiology

ORIGINAL RESEARCH
published: 11 November 2021
doi: 10.3389/fphys.2021.712454

Classification of Fibrillation Organisation Using Electrocardiograms to Guide Mechanism-Directed Treatments

*Xinyang Li[1], Xili Shi[1], Balvinder S. Handa[1], Arunashis Sau[1], Bowen Zhang[1], Norman A. Qureshi[1], Zachary I. Whinnett[1], Nick W. F. Linton[2], Phang Boon Lim[1], Prapa Kanagaratnam[1], Nicholas S. Peters[1] and Fu Siong Ng[1]**

[1] National Heart and Lung Institute, Imperial College London, London, United Kingdom, [2] Department of Bioengineering, Imperial College London, London, United Kingdom

OPEN ACCESS

Edited by:
G. Andre Ng,
University of Leicester,
United Kingdom

Reviewed by:
Flavia Ravelli,
University of Trento, Italy
Remi Dubois,
Institut de rythmologie et modélisation cardiaque (IHU-Liryc), France

***Correspondence:**
Fu Siong Ng
f.ng@imperial.ac.uk

Specialty section:
This article was submitted to Cardiac Electrophysiology, a section of the journal Frontiers in Physiology

Received: 20 May 2021
Accepted: 29 September 2021
Published: 11 November 2021

Citation:
Li X, Shi X, Handa BS, Sau A, Zhang B, Qureshi NA, Whinnett ZI, Linton NWF, Lim PB, Kanagaratnam P, Peters NS and Ng FS (2021) Classification of Fibrillation Organisation Using Electrocardiograms to Guide Mechanism-Directed Treatments. Front. Physiol. 12:712454. doi: 10.3389/fphys.2021.712454

Background: Atrial fibrillation (AF) and ventricular fibrillation (VF) are complex heart rhythm disorders and may be sustained by distinct electrophysiological mechanisms. Disorganised self-perpetuating multiple-wavelets and organised rotational drivers (RDs) localising to specific areas are both possible mechanisms by which fibrillation is sustained. Determining the underlying mechanisms of fibrillation may be helpful in tailoring treatment strategies. We investigated whether global fibrillation organisation, a surrogate for fibrillation mechanism, can be determined from electrocardiograms (ECGs) using band-power (BP) feature analysis and machine learning.

Methods: In this study, we proposed a novel ECG classification framework to differentiate fibrillation organisation levels. BP features were derived from surface ECGs and fed to a linear discriminant analysis classifier to predict fibrillation organisation level. Two datasets, single-channel ECGs of rat VF ($n = 9$) and 12-lead ECGs of human AF ($n = 17$), were used for model evaluation in a leave-one-out (LOO) manner.

Results: The proposed method correctly predicted the organisation level from rat VF ECG with the sensitivity of 75%, specificity of 80%, and accuracy of 78%, and from clinical AF ECG with the sensitivity of 80%, specificity of 92%, and accuracy of 88%.

Conclusion: Our proposed method can distinguish between AF/VF of different global organisation levels non-invasively from the ECG alone. This may aid in patient selection and guiding mechanism-directed tailored treatment strategies.

Keywords: fibrillation, cardiac arrhythmia, electrocardiography, electrograms, ablation

1. INTRODUCTION

Atrial fibrillation (AF) and ventricular fibrillation (VF) are complex heart rhythm disorders with an increasing prevalence (Zheng et al., 2001; Morillo et al., 2017; Martín-Yebra et al., 2019). Both AF and VF show beat-to-beat variability in electrical propagation through the myocardium and the mechanisms that initiate and sustain these rhythms are not entirely understood.

The limited insight into mechanisms of myocardial fibrillation stems primarily from *ex vivo* optical mapping studies of the transmembrane potentials with potentiometric dyes (Laughner et al., 2012), which have shown several competing mechanisms (Handa et al., 2021). The multiple wavelet hypothesis proposes that fibrillation is a chaotic disorganised rhythm sustained by multiple wavelets of electrical activity that meander, collide, and continuously regenerate (Moe et al., 1964; Krummen et al., 2016). The competing hypothesis is that fibrillation is a spatiotemporally organised phenomenon sustained by one or more rotational drivers (RDs). RDs are scroll waves of electrical propagation that perpetuate around a point of phase singularity, that can anchor to specific regions and/or meander through the myocardium, generating fibrillation wavefronts (Pandit and Jalife, 2013). Multiple disorganised rapidly discharging foci within the myocardium have also been shown to sustain fibrillation (Lee et al., 2015), while, more recently, a more complex mechanism of asynchronous endo-epicardial disassociation of fibrillatory conduction has been proposed in AF (de Groot et al., 2016).

Treatment options for patients at risk of VF and those suffering from AF are empirical at present and not targeted towards the specific mechanism of fibrillation. VF survivors who are at further risk of future episodes are conventionally offered implantable cardioverter defibrillation to terminate VF episodes, while pulmonary vein isolation (PVI) to electrically disconnect the atrial body from the pulmonary veins (where rapid firing can trigger AF) is the only proven efficacious treatment in AF (Sau et al., 2019). The absence of any mechanism-directed treatment for patients with AF in particular has led to limited success rates in catheter ablation for persistent AF (Schreiber et al., 2015). There is a pressing need to move beyond the one-size-fits-all approach of empirical treatment towards mechanism-directed treatments.

We recently showed that there is a range of AF and VF mechanisms, with varying degrees of the global organisation, using *ex vivo* optical mapping of explanted perfused hearts and invasive intracardiac mapping in patients undergoing AF ablation (Handa et al., 2020). Only some forms of AF are globally organised and driven by stable RDs, and these would be potentially amenable to ablation targeting RDs, while other forms of AF are globally disorganised with no clear drivers and as such may respond to compartmentalisation of the atria. A possible approach to individualised tailored therapy would be to select the appropriate treatments based on the specific electrophysiological mechanisms sustaining fibrillation in each specific patient (Ng et al., 2020). Ideally, we would be able to identify the mechanism non-invasively.

The electrocardiogram (ECG) is an integral part of cardiac diagnostics and routine care. With the advent of machine learning, there has been increasing interest in extending the diagnostic abilities of ECGs beyond qualitative human assessment (Fan et al., 2018). Signal processing of ECGs has been implemented in AF (Meo et al., 2013), where certain features of ECG complexity have been shown to correlate with the long-term success of catheter ablation (Lankveld et al., 2016). Conventional signal processing techniques, in the form of dominant frequency (DF) analysis (Uetake et al., 2014) and entropy analysis (Alcaraz and Rieta, 2012) have been utilised to analyse AF surface ECGs, in addition to more novel techniques such as fibrillation-wave power (FWP) and fibrillation-wave amplitude (FWA) analysis (Lankveld et al., 2016) to predict treatment outcomes. A recent study employed convolutional neural networks to identify the ECG signatures of AF from normal sinus rhythm ECGs alone with an accuracy of 83.3% and proposed it as a tool to eliminate the need for expensive long-duration ECG monitoring to diagnose AF (Attia et al., 2019).

In this study, we sought to investigate whether the degree of the global organisation of VF and AF and the underlying fibrillation mechanisms itself can be detected with a machine learning classification framework based on the non-invasive ECG recording alone. First, epicardial VF activity was recorded in *ex vivo* explanted perfused rat hearts with high spatial resolution optical mapping. The mechanism was classified using phase analysis as either globally chaotic and driven by multiple wavelets, or globally organised and driven by RDs. This characterisation was designated as ground truth for labelling the corresponding single channel ECG recorded during the optical mapping studies and to train a machine learning model (Li et al., 2019; Handa et al., 2020). After developing and validating our characterisation of VF mechanisms from ECGs, we trained the model on human AF surface ECGs in patients with persistent AF to determine the prediction accuracy in the classification of the underlying AF organisation/mechanism as determined by invasive intracardiac mapping. For both data sets, the proposed classification frameworks were evaluated in a leave-one-out (LOO) manner, and classification results showed that the proposed method correctly predicted organisation level from rat VF ECGs sensitivity of 75%, specificity of 80%, and accuracy of 78%, and from clinical AF ECG with the sensitivity of 80%, specificity of 92%, and accuracy of 88%. Accurate classification of fibrillation organisation and mechanism using the ECG may allow for more tailored treatments based on the specific arrhythmia mechanism.

2. DATA ACQUISITION AND DATA LABELLING

The objective of the proposed classification framework is to differentiate between organised and disorganised forms of fibrillation from surface ECG. Organised fibrillation is usually driven by RDs while disorganised fibrillation is by multiple wavelets (Handa et al., 2020). This novel technique could be ultimately used to guide patient selection for individualised treatment options. The two data sets used for the model evaluation were derived from a recent study by our group, and the methodology for data acquisition has previously been described in detail (Handa et al., 2020). Optical mapping VF data were obtained by performing *ex vivo* perfused rat heart optical mapping of the transmembrane potential and the clinical AF data were acquired from patients in persistent AF using intracardiac multipolar catheter recordings of electrograms (EGMs) during catheter ablation procedures. Concurrent surface ECGs were also recorded for rat VF and human AF.

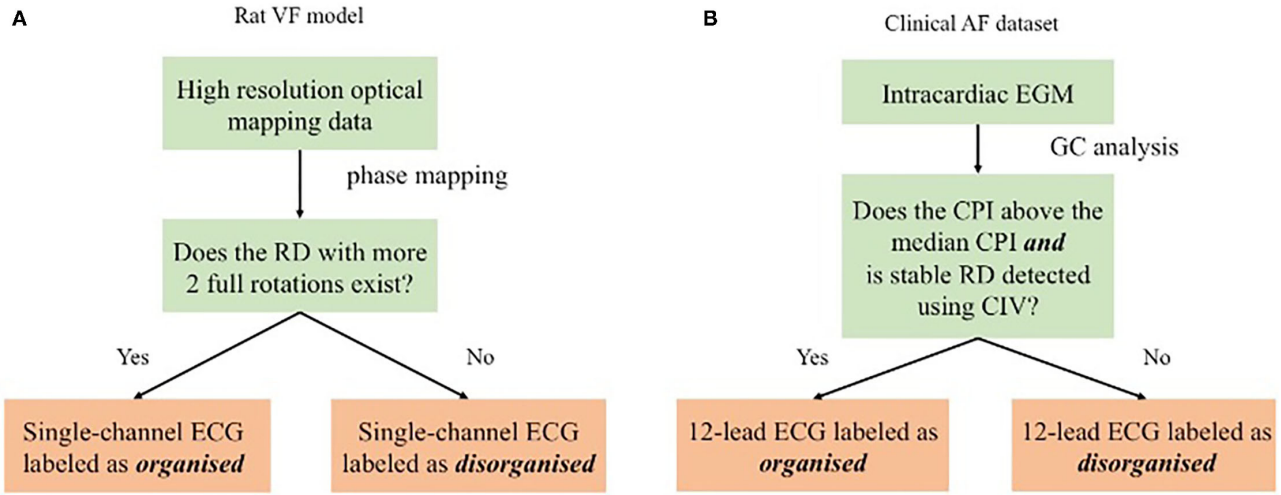

FIGURE 1 | Schematic showing the proposed method evaluated by different sets. For the rat ventricular fibrillation (VF) data, as shown in **(A)**, the ECG was labelled by the rotational driver (RD) detection results from phase mapping. For the clinical atrial fibrillation (AF) data, as shown in **(B)**, GC analysis of the electrogram (EGM) data was the surrogate organisation label for the ECG classification.

For the rat VF model, the labelling of the fibrillation organisation level was conducted using phase mapping, described below. For the clinical AF data, where the high-resolution recording was not available, a Granger causality (GC) analysis of the intracardiac EGM data was used for labelling the clinical ECG. A schematic of the study design is shown in **Figure 1**. The methodology for phase analysis and GC analysis has been described in detail (Handa et al., 2020). Details of the analysis techniques and labelling are presented briefly in the following section.

Data for the AF mapping studies were collected in the cardiac electrophysiology lab, Hammersmith Hospital. Approval was given by the Local Research and Ethics Committee for Imperial College Healthcare NHS Trust and written informed consent was obtained from all patients. LA mapping data were obtained for 17 patients with persistent AF. Electroanatomical mapping data were collected using the EnSite™ Velocity™ system (Abbott Inc, Minnesota, USA). On the day of the procedure, all patients were presented in AF. Left atrial access was gained with a transeptal puncture. A 20-ring electrode A-Focus II™ (Abbot Inc., Minnesota, USA) mapping catheter (double loop, 1 mm length electrodes, 4 mm interelectrode spacing) was used to acquire LA geometry and EGM. EGM were collected with stable tissue contact at the endocardial surface. Data from pulmonary veins and left atrial appendage were excluded from the analysis. Data were collected in both persistent AF and a subset of patients in sinus rhythm after direct current cardioversion. The bipolar EGMs were filtered at 30–500 Hz bandpass filtering. The endocardial area subtended by the A-FocusII™ mapping catheter was termed a 'kernel'. For each given kernel, 20 s of data were subsequently analysed.

The number of kernels collected and subsequently the number of segments analysed in this paper varied between patients due to differing left atrial geometry and catheter stability. An attempt was made to map the left atrium extensively for all subjects, thus, the impact of the heterogeneity will be minimised in the final analysis. A summary of patient characteristics can be found in **Table 1**.

TABLE 1 | Patient characteristics of invasive clinical data-set.

Patient characteristics (*n* = 17)	
Age (years)	66±7
Male	10
Mean left atrium size on TTE (mm)	44±5
Mean CHA_2DS_2VASc score	2.5(0-6)
Hypertension	7
Diabetes Mellitus	4
Cerebrovascular Disease	2
History of heart failure	3
Duration of persistent AF (months)	20.5±9

2.1. Phase Mapping of Rat VF Data

For the rat VF model, nine *ex vivo* perfused rat hearts underwent high-resolution optical mapping of the left ventricular epicardial surface after VF induction with programmed electrical stimulation, and the single-channel ECG was recorded simultaneously, with a sampling rate of 1,000 Hz.

Phase analysis is a gold standard technique for the analysis of fibrillatory signals (Nattel et al., 2017). Phase mapping was applied to the optical mapping data to identify phase singularities (PS) and RDs for further labelling. All our methods for analysing optical mapping fluorescence data have been previously described in detail (Ng et al., 2013, 2016; Roney et al.,

2017; Li et al., 2019; Handa et al., 2020). In this study, a RD was defined as a PS with more than two full rotations. **Figure 1A** shows the ECG labelling based on the RD identification: ECGs are identified as organised if spatiotemporally stable RDs sustained VF on optical mapping and disorganised if VF was driven by chaotic wavefronts with no identifiable stable RD.

2.2. GC Analysis of Clinical AF Data

For clinical AF data (17 subjects), alternative analysis techniques based on GC analysis were used to classify organisational levels of fibrillation recordings as phase analysis of intracardiac EGMs is confounded by several issues, including the low spatial resolution of clinical data (Roney et al., 2017).

Granger causality is a measurement of signal inter-dependency and has been previously used to delineate dominant patterns of wavefront propagation in fibrillation (Luengo et al., 2016, 2018; Rodrigo et al., 2016; Alcaine et al., 2017). In our previous study, two measurements derived from GC, causality pairing index (CPI) and circular interdependence value (CIV) were applied to intra-cardiac EGM to quantify the AF organisation level, detect RDs, and identify the likely mechanism sustaining fibrillation (Handa et al., 2020). In this study, the CPI and CIV calculated from intra-cardiac electrogram data (EGM) were used to label the corresponding surface ECGs as organised or disorganised fibrillation. To make this work self-contained, the calculation of CPI and CIV will be presented in the following section.

2.2.1. Causality Pairing Index

From the multi-variate cardiac signal, $\mathbf{x}(t) \in \mathcal{R}^{n_c}$ at time t of the dimension of n_c, GC is inferred by fitting an auto-regressive (AR) model to $\mathbf{x}(t)$ as

$$\hat{A}(\tau) = \arg\min_{A(\tau)} \sum_{t=L+1}^{n_t} ||\mathbf{x}(t) - \sum_{\tau=1}^{L} A(\tau)^{\top} \mathbf{x}(t-\tau)||_2 + \lambda \sum_{\tau=1}^{L} ||A(\tau)||_1, \quad \tau = 1, \ldots, L \tag{1}$$

$A(\tau) \in \mathcal{R}^{n_c \times n_c}$ is the AR coefficient matrix, τ is the time lag, L is the maximal time lag of the model, and λ is a regularisation coefficient. Let $x_i(t)$ be the i-th row of $\mathbf{x}(t)$. The element of the i-th row and j-th column, $A(\tau, i, j)$, reflects the strength of the $x_i(t-\tau)$ in predicting $x_j(t)$, or in other words, the temporal dependency between $x_i(t)$ and $x_j(t)$.

The optimisation problem in Equation 1 is usually termed as the Lasso-Granger approach (Valdés-Sosa et al., 2005; Arnold et al., 2007; Song and Bickel, 2011). With the l_1-norm-based regularisation term $\sum_{\tau=1}^{L} ||A(\tau)||_1$, the Lasso-Granger approach yields a more sparse and robust Granger causality estimation. In this study, Forward Backward Lasso Granger Causality is applied to solve (Equation 1), which is faster and more robust (Cheng et al., 2014).

With the l_1-norm sparsity constraint, solving (Equation 1) drives all elements in $\hat{A}(\tau)$ to be zero unless the casual relationships between certain pairs of signals are very strong. Therefore, a measurement of the organisation was calculated as the percentage of the non-zero pairings between different signals.

To be specific, define $\mathcal{S}$ as the set containing all the non-zero elements in $\hat{A}(\tau)$, i.e.,

$$\mathcal{S} = \{\hat{a}(\tau, i, j) \mid a(\tau, i, j) > 0,\ i \neq j, \ \tau = 1, \ldots, L, \text{ and } i, j = 1, \ldots, n_c\} \tag{2}$$

where $\hat{a}(\tau, i, j)$ is the element of i-th row and j-th column in $\hat{A}(\tau)$. The CPI is obtained as the following by

$$CPI = \frac{|\mathcal{S}|}{L(n_c^2 - n_c)} \tag{3}$$

where $|\cdot|$ is the cardinal number of a set.

By Equation (3), CPI quantifies the global fibrillatory organisation by calculating the number of possible Granger-causal signal pairs in fibrillation between which there are propagational effects on a normalised scale of 0–1, where 0 is defined as no possible pairing having causal dependency (most disorganised) and 1 where all possible pairings have causal dependency (most disorganised).

2.2.2. Circular Interdependence Value

Circular interdependence value is an analytical tool for localising RDs from regional analysis of cardiac signals from the flow directions indicated by $\hat{A}(\tau)$. Let $\mathbf{x}_i(t)$ be the i-th signal of $\mathbf{x}(t)$. The major source index s_i for $\mathbf{x}_i(t)$ is defined as the signal with the strongest causal influence on $\mathbf{x}_i(t)$, i.e.,

$$s_i = \arg\max_j \sum_{\tau} \hat{A}(\tau, i, j), \quad j = 1, \ldots, n_c \text{ and } j \neq i \tag{4}$$

Let $\mathbf{p}_{s_i}$ and $\mathbf{p}_i$ be the coordinates of the locations corresponding to $\mathbf{x}_i(t)$ and $\mathbf{x}_{s_i}(t)$ in a global coordinate, respectively, and the GC vector for $\mathbf{x}_i(t)$, $\mathbf{g}_i$, is calculated as the following

$$\mathbf{g}_i = \begin{cases} \mathbf{p}_{s_i} - \mathbf{p}_i & \text{if } \sum_{\tau} \hat{A}(\tau, i, s_i) > 0. \\ \mathbf{0} & \text{otherwise.} \end{cases} \tag{5}$$

The GC vector $\mathbf{g}_i$ in Equation (5) can be regarded as the source-to-sink vector for electrode i, pointing from its source electrode s_i to electrode i. Let $\mathbf{p}_0$ be the coordinates of the location of interest. Then, then rotational direction for $\mathbf{p}_i$ relative to $\mathbf{p}_0$ could be calculated as the cross product of $\mathbf{p}_i - \mathbf{p}_0$ and $\mathbf{g}_i$ after normalisation, i.e.,

$$\mathbf{r}_i = \frac{\mathbf{p}_i - \mathbf{p}_0}{||\mathbf{p}_i - \mathbf{p}_0||} \times \frac{\mathbf{g}_i}{||\mathbf{g}_i||} \equiv r_{i,1}\boldsymbol{i} + r_{i,2}\boldsymbol{j} + r_{i,3}\boldsymbol{k} \tag{6}$$

where $\boldsymbol{i}$, $\boldsymbol{j}$, and $\boldsymbol{k}$ are the standard basis vectors corresponding to the x-, y-, and z-axis in the global coordinate, respectively. Suppose a local coordinate where the x-y plane is specified by $\mathbf{p}_0$, $\mathbf{p}_i$, and $\mathbf{p}_{s_i}$ with standard basis vectors $\tilde{\boldsymbol{i}}$, $\tilde{\boldsymbol{j}}$, and $\tilde{\boldsymbol{k}}$ corresponding to the x-, y-, and z-axis, respectively. Define the origin of the local coordinate as $\mathbf{p}_0$, and

$$\tilde{\boldsymbol{i}} \equiv \frac{\mathbf{p}_i - \mathbf{p}_0}{||\mathbf{p}_i - \mathbf{p}_0||} \tag{7}$$

Then, the rotational direction $\mathbf{r}_i$ could be written as

$$\mathbf{r}_i = \tilde{r}_{i,1}\tilde{\boldsymbol{i}} + \tilde{r}_{i,2}\tilde{\boldsymbol{j}} + \tilde{r}_{i,3}\tilde{\boldsymbol{k}} \tag{8}$$

where $\tilde{r}_{i,1}$ and $\tilde{r}_{i,2}$ are equal to 0, and the sign of $\tilde{r}_{i,3}$ indicates the direction of possible rotational activities. If the rotation with the centre as $\mathbf{p}_0$ is clockwise, $\tilde{r}_{i,3} < 0$ and vice versa.

Remark 1. *$\tilde{\boldsymbol{i}}$, $\tilde{\boldsymbol{j}}$, and $\tilde{\boldsymbol{k}}$ may vary depending on the locations $\boldsymbol{p}_0$, $\boldsymbol{p}_i$, and $\boldsymbol{p}_{s_i}$ for $i = 1, \ldots, n_c$. For spiral catheters (e.g., Lasso, Biosense Webster), ideally all recording points are in the same x-y plane, and $\tilde{\boldsymbol{k}}$ are the same for all $i = 1, \ldots, n_c$. Thus, the global coordinate and local coordinates could be represented by just one coordinate for simplification. However, the simplification is not applicable for basket catheters.*

With Equations (6) and (8), CIV is calculated as

$$CIV = \frac{|\sum_i \text{sign}(\tilde{r}_{i,3})|}{\text{n}_n(\mathbf{p}_0)} \tag{9}$$

where $\text{n}_n(\mathbf{p}_0)$ is the number of available neighbouring recordings around $\mathbf{p}_0$ to quantify the rotational activity. CIV ranges from 0 to 1 and measures the circulatory propagation patterns, whereby spatially stable RD yield a high CIV and meandering unstable RDs a low value. Details of using CIV for RD detection and its validation can be found in the method section and in our recent study by Handa et al. (2020).

2.2.3. Labelling

In the patient with persistent AF group, each subject underwent detailed intracardiac mapping in the atrium with a 20-electrode AFocusII mapping catheter, (St Jude Medical, MN, USA). Multiple areas were mapped within the atrium with the catheter recording 20 separate EGMs at a time. CPI, a measure of organisation of fibrillation, was calculated for each set of AFocusII recordings in a given region. Global CPI was calculated as the average of the CPI of all the regional AFocusII recordings for the subjects. The criteria for binarising the 17 subjects in the clinical AF data sets is shown in **Figure 1B**. In particular, those with RD-positive areas and CPI above the median CPI were labelled as organised, and those without any RD-positive areas or CPI below the median CPI as disorganised.

3. METHOD

3.1. QRS Subtraction

The frequency spectrum of the individual QRS complex is often found in a range of 10∼30 Hz (Bollmann et al., 2006), and the frequencies characterising the atrial signal are mostly confined to the interval of 5∼12 Hz (Lin, 2008). Due to this overlap between atria electrical activity and QRS complexes, QRS subtraction was applied to the clinical AF ECG data set. In particular, QRS detection followed by linear interpolation proposed in Ahmad et al. (2011) was adopted. Normal QRS duration is between 0.08 and 0.10 s. To ensure ventricular activity fully removed, points corresponding to a QRS duration of 0.10 s were subtracted and replaced with linearly interpolated points with a ratio of 5:6, i.e. with 5/11 points before and 6/11 points after the peak detection, as described in Ahmad et al. (2011). Two examples of QRS subtraction are shown in **Figure 2**.

3.2. Feature Extraction

In this study, we propose to use the band-power (BP) feature, i.e., the power of the ECG signals corresponding to different frequency bands, to classify the organisation type. Given the heart rate in rats is markedly higher than in humans, in this study, different bands and data segmentation settings were selected for rat VF and clinical AF ECG feature extraction.

For the rat VF model, the single-channel continuous ECG recordings were sampled at a sampling rate of 1,000 Hz and segmented by a 2 s window with a window shift of 1 s. The DF of rat VF ranges from 10∼20 Hz (Handa et al., 2018). Thus, the segmented data were filtered with eight temporal philters with a bandwidth of 4 Hz ranging from 2∼3 4Hz (2∼6 Hz, 6∼10 Hz, … 30∼34 Hz, fourth-order band-pass Butterworth philters with an allowance of 2 Hz). In addition to band-power, an AR model was applied to boost the number of features for the single-channel rat VF ECG. The AR coefficients with the order of 20 together with the BP of the eight bands were concatenated and used as the feature vector. Thus, the total number of features for rat VF ECG was 28.

For the clinical AF dataset, the continuous 12-lead ECG recordings were sampled with a sampling rate of 2034.5 Hz and segmented by an 8 s window with a window shift of 4 s. The segmented data were then filtered into four bands, i.e., 5∼15 Hz, 15∼25 Hz, 25∼50 Hz, and 50∼100 Hz (fourth order band-pass Butterworth philters with an allowance of 2 Hz). The DF of AF was found to be within the frequency spectrum of 3∼12 Hz. Thus, most of the AF components can be covered by the band 5∼15 Hz. The other three higher bands are selected to capture subtle high-frequency characteristics of the signals. For each band and each lead, the band-power was calculated then normalised by the total power of the signal of a broad band 2∼200 Hz. With four normalised BP features extracted for each lead, the total number of features for a clinical AF ECG segment was 48.

3.3. Feature Selection

Mutual information is a measurement of the dependence between features and class labels and has been successfully applied for feature selection of BP features of time series (Ang et al., 2012). Thus, in this study, mutual information was adopted for feature selection.

Given the feature f and class label c, the mutual information is formulated as below:

$$I(f, c) = H(c) - H(c|f) \tag{10}$$

where $H(c)$ is the individual entropy of class label c and $H(c|f)$ is the conditional entropy of class label c given feature vector f. It could be interpreted as the amount of uncertainty reduced in the class label c through observing feature f Ang et al. (2012).

In this study, the class label c was the organisation level. For each BP or AR feature, its mutual information with class label c was calculated during the training stage. The top 50% of features with the highest mutual information were selected and used in the classification step.

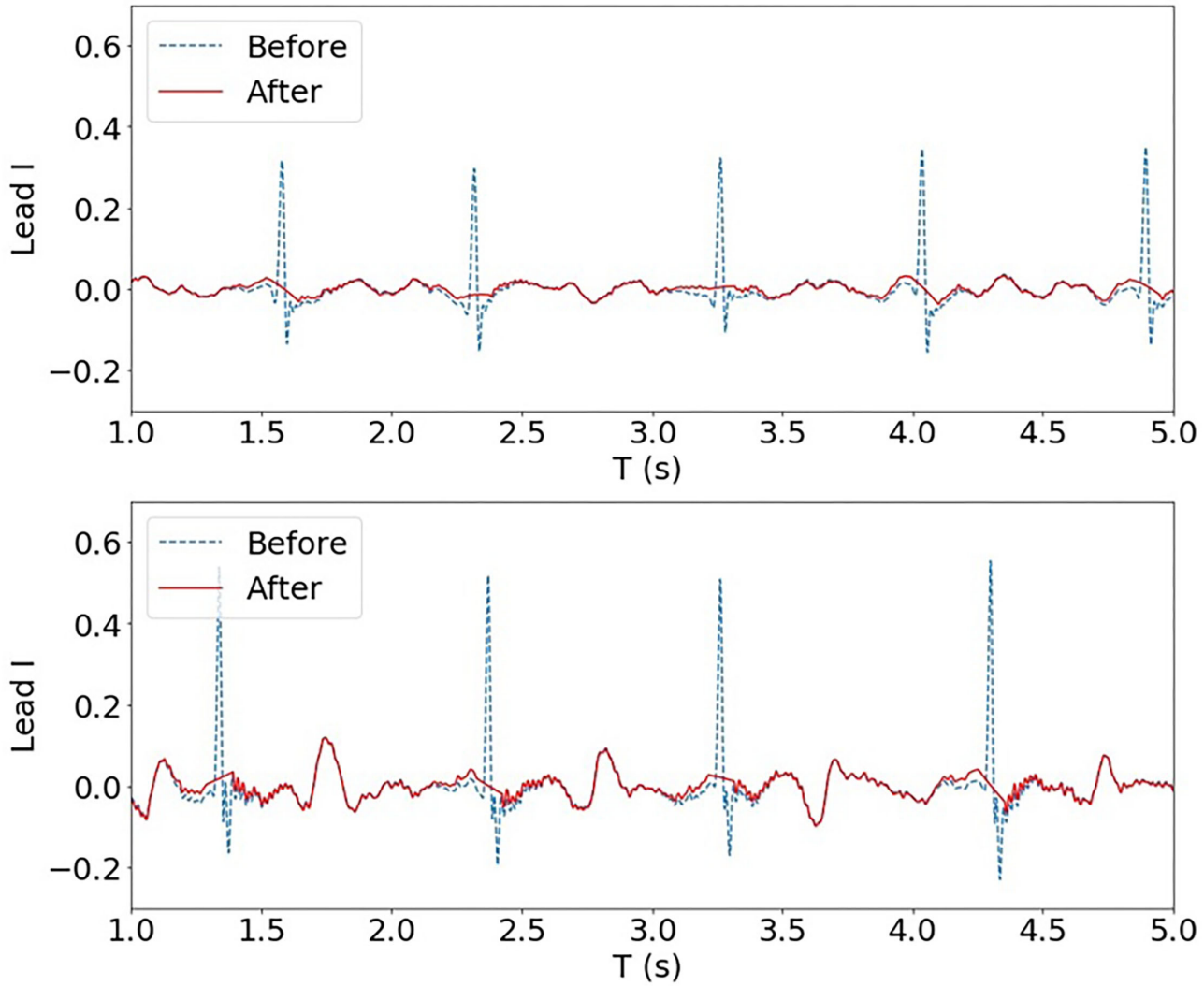

FIGURE 2 | Two examples of QRS subtraction applied to the AF ECG data set (Lead I). Upon QRS detection, points corresponding to a QRS duration of 0.10 s were replaced with linearly interpolated points.

3.4. Classification

In this study, binarised linear discriminative analysis (LDA) and a linear regression model were adopted for the organisation level prediction. During the model training and testing, features from 2 s segments of ECG were used. With the prediction results at the segment level, the final organisation level prediction of each subject was obtained by voting or averaging. For each subject, the final class label was the class label that was predicted most frequently during the segment classification. The subject was predicted as organised if more than half of the segments were predicted to be organised. For clinical AF data, a linear regression model was also tested for continuous organisation level prediction. With the regression model, the mean predicted value of all segments was used as the final prediction of the subject.

The whole evaluation ran in LOO manner, whereby the feature selection and classification framework were trained by data segments from eight out of nine subjects (rat VF ECG) or 16 out of 17 subjects (clinical AF ECG) and evaluated on segments from the remaining subject. Thus, for different subjects, different features could have been selected in the training. In this way, the data segments for each subject were not used to train the model that they were tested with.

4. EXPERIMENTAL RESULTS

4.1. GC Analysis of Clinical AF Data

Figure 3A shows an example of a source-to-sink vector map constructed for a set of intracardiac multipolar (AFocusII) catheter recordings in AF. It shows a site with a stable RD

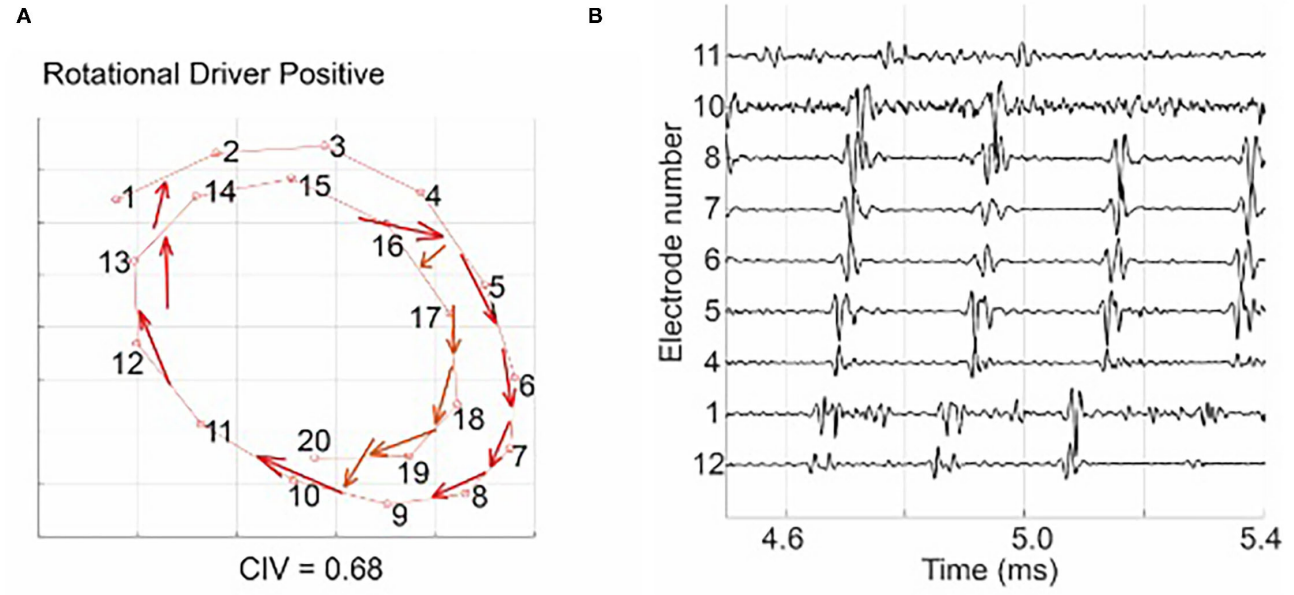

FIGURE 3 | (A) shows a source-to-sink vector map constructed from the intra-cardiac EGM signal, indicating a site with a stable RD with a high circular interdependence value (CIV). The arrows show the directions of the source-to-sink vectors. The corresponding EGMs in **(B)** show organised clockwise rotational activation: electrode 12 was activated first, followed by electrodes 1, 4–8, 10, and 11, and the activation of the electrode 11 was followed by the next activation of electrode 12. Figure reproduced from Handa et al. (2020) (CC BY 4.0).

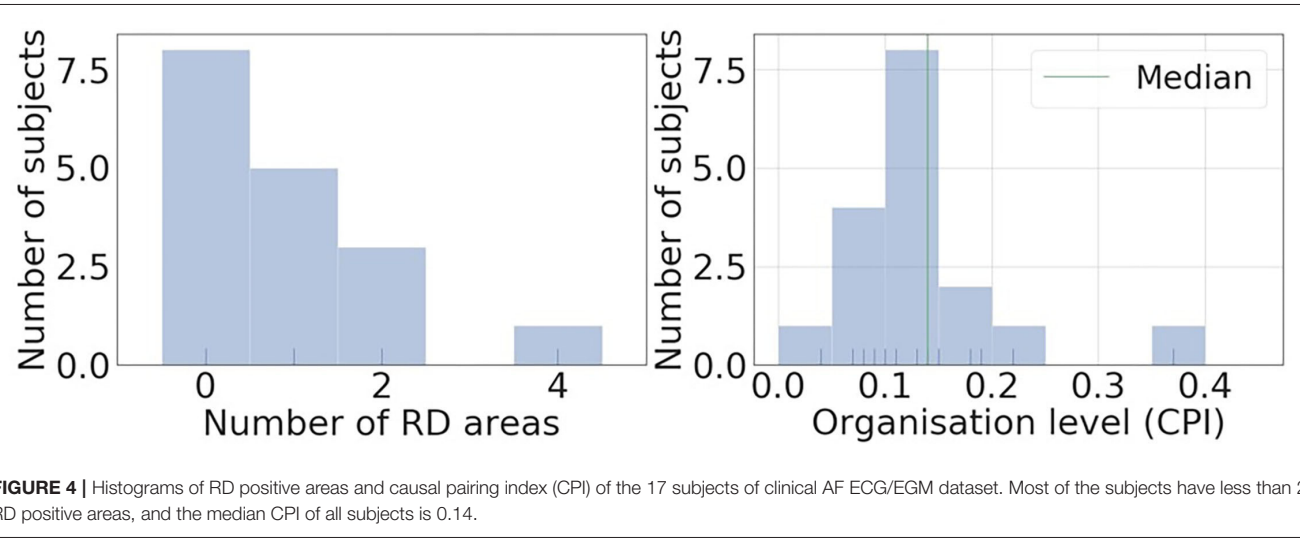

FIGURE 4 | Histograms of RD positive areas and causal pairing index (CPI) of the 17 subjects of clinical AF ECG/EGM dataset. Most of the subjects have less than 2 RD positive areas, and the median CPI of all subjects is 0.14.

with a high CIV driving a globally organised form of AF. The arrows show the directions of the source-to-sink vectors. The corresponding EGMs show organised clockwise rotational activation. For this example, the CIV of 0.68 was above the threshold of 0.60, which is the operating point obtained using rat VF data in our previous study for classifying an RD-positive area (Handa et al., 2020).

Figure 4 shows histograms of RD-positive areas (**Figure 4A**) and CPI (**Figure 4B**) of the 17 subjects of the clinical AF ECG/EGM dataset. For this data set, 8 out of 17 subjects have no RD-positive area, and the maximum number of RD-positive areas identified with intracardiac mapping is 4. The median CPI of all subjects is 0.14. Among the nine subjects with RD-positive areas, the five subjects with CPI above 0.14 were labelled as organised, and those without any RD-positive areas or CPI below the median CPI as disorganised.

4.2. Statistical Correlation Analysis

To investigate whether the surface ECG BP reflected the AF organisation level measured invasively, Pearson correlation analysis was performed to test the correlation between normalised band-power features and the organisation level as quantified by CPI for the clinical AF ECG. Logarithm was

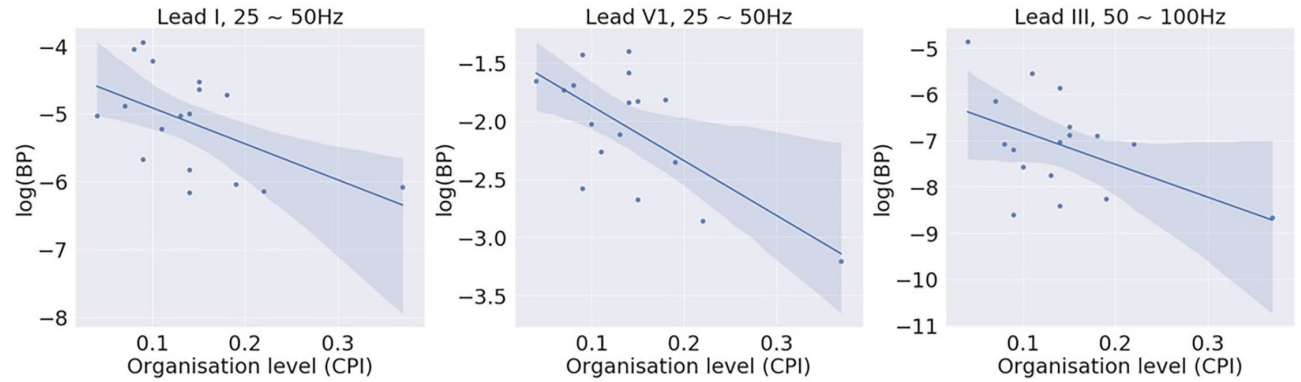

FIGURE 5 | Correlation between log (band power) of different bands and the global fibrillatory organisation level measured with causal pairing index (CPI). Significant correlations were found for higher frequency bands 25∼50 Hz and 50∼100 Hz with certain leads.

TABLE 2 | Correlation results with clinical atrial fibrillation (AF) data.

Band	Lead	β
25∼50 Hz	I	–0.53*
25∼50 Hz	aVL	–0.56*
25∼50 Hz	V1	–0.67**
50∼100 Hz	III	–0.49*
50∼100 Hz	aVL	–0.59*

*$\alpha = 0.05$, **$\alpha = 0.01$.

applied to make the BP distribution normal distribution. A p-value smaller than 0.05 was considered statistically significant.

Figure 5 shows examples of the correlation results of leads I, V1, and III, with each closed circle representing one subject. **Table 2** summarises all significant correlations with $p < 0.05$. The significant correlations were found in two relatively higher bands, 25∼50 Hz and 50∼100 Hz. The correlation was the strongest with BP of lead V1, 25∼50 Hz ($\beta = -0.67$; $p < 0.01$). No significant correlation was found with bands of lower frequencies, i.e., 5∼15 Hz and 15∼25 Hz. The correlation analysis demonstrates that there is a negative correlation between the amount of high-frequency components in the signal and the level of global fibrillatory organisation for certain leads.

4.3. Organisation Level Classification of ECG

The proposed method was evaluated by LOO, and subsequently, the numbers for the training and test data passed to the classifier varied. For the rat VF classification, the number of training samples ranges from 1,856 to 2,416, and that of the test from 17 to 577. For the clinical AF data, the number of training samples ranges from 1,368 to 1,491, and that of the test from 37 to 160. The LOO classification results for both rat VF and clinical AF data are summarised in **Table 3**, where c and $\hat{c}$ are the true and predicted class labels, respectively, and '**O**' and '**D**' represent the organised and disorganised classes, respectively. n_{seg} is the total number of the data segments per subject, and for the clinical AF data, the number of areas being mapped n_k was also included.

TABLE 3 | Leave-one-out (LOO) classification results (%).

Subject ID	n_{seg} (n_k)	c	$\hat{c}$	P_w (%)
Rat-1	168	O	D	76.78
Rat-2	196	O	**O**	73.98
Rat-3	439	O	**O**	98.61
Rat-4	577	O	**O**	100.54
Rat-5	162	D	**D**	71.43
Rat-6	179	D	**D**	77.09
Rat-7	17	D	O	100.00
Rat-8	434	D	**D**	82.10
Rat-9	261	D	**D**	93.87
Clinical-1	160 (21)	D	**D**	63.12
Clinical-2	47 (8)	D	**D**	100.00
Clinical-3	44 (9)	D	**D**	100.00
Clinical-4	85 (16)	D	**D**	100.00
Clinical-5	148 (28)	D	**D**	68.24
Clinical-6	76 (15)	D	**D**	59.21
Clinical-7	53 (9)	D	**D**	100.00
Clinical-8	131 (20)	D	**D**	87.79
Clinical-9	97 (16)	D	O	91.75
Clinical-10	67 (9)	O	D	100.00
Clinical-11	123 (25)	O	**O**	98.37
Clinical-12	151 (27)	O	**O**	97.35
Clinical-13	80 (10)	D	**D**	61.25
Clinical-14	40 (6)	D	**D**	87.50
Clinical-15	91 (25)	O	**O**	98.90
Clinical-16	98 (15)	D	**D**	100.00
Clinical-17	37 (6)	O	**O**	54.05

Bold values indicate correct predictions by the machine learning algorithm. i.e. $c = \hat{c}$.

For each subject, the final prediction was calculated by voting: the subject would be organised if more than 50% of the segments were predicted as organised, and disorganised if below (or equal to) 50%. In **Table 3**, $P_{\mathbf{w}}$ is also presented, which is the percentage of segments classified as the winner class during voting. The confusion matrices of the classification at segment and subject

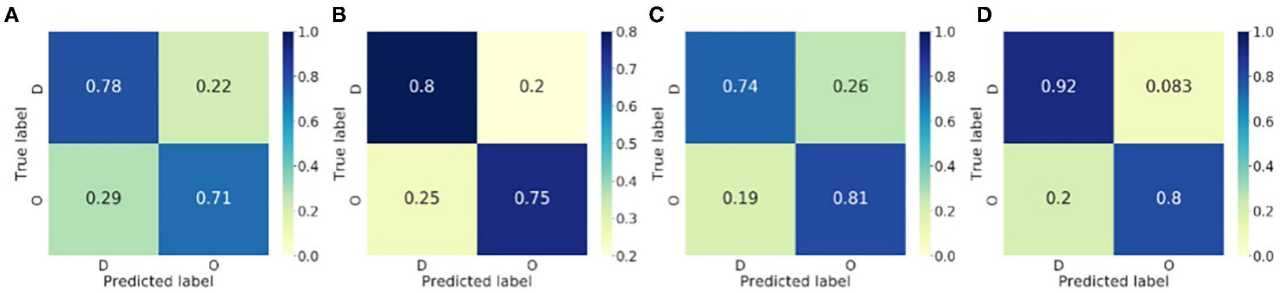

FIGURE 6 | Confusion matrices of the binary classification of the fibrillatory organisation level of the rat VF and clinical AF data. **(A)** Rat VF ECG, segment level. **(B)** Rat VF ECG, Subject level. **(C)** Clinical AF ECG, segment level. **(D)** Clinical AF ECG, subject level.

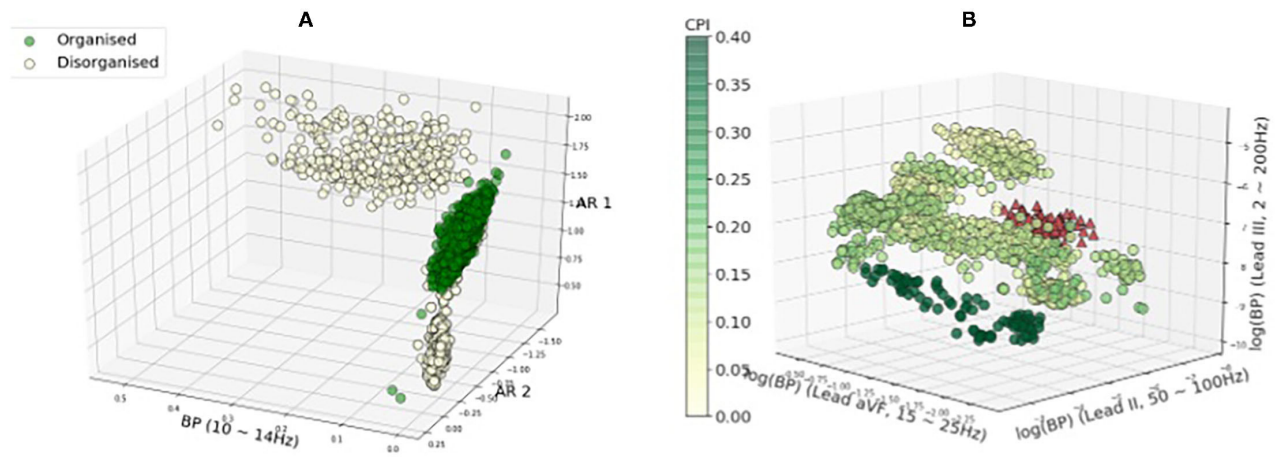

FIGURE 7 | Feature distribution regarding the fibrillatory organisational level. The three best features selected by mutual information were plotted. The colour of the features are corresponding to the CPI values except features of subject clinical-10 in red. In General, the features with the high and low CPI are separated. However, features of subject clinical-10 with high CPI (in red triangles) tend to be overlapped with features from the low-CPI group. **(A)** Rat VF features. **(B)** Clinical AF features.

levels were shown in **Figure 6**. For the subject-level prediction, the sensitivities are 75 and 80%, the specificities are 80 and 91.67% and the accuracies are 77.78 and 88.24% for rat VF and clinical AF, respectively.

Figures 7A,B show the distribution of the three most discriminative features selected using mutual information for rat VF ECG and clinical AF ECG, respectively. In both panels, each circle represents one feature calculated from a 2 s data segment. Note that the feature selection was only applied for illustrative purposes. For the rat VF ECG in **Figure 7A**, most segments from the organised class fell within one cluster, separated from the two clusters of disorganised features. For Rat-7, the duration of VF is shorter, resulting in a much smaller number of available segments than the other rat subjects. Thus, the short ECG segment may not be able to fully represent the fibrillatory characteristic, which could be the reason for its incorrect classification with high P_w = 100%.

Figure 7B shows the features of the clinical AF ECG, which formed more sub-clusters. The colour of the features are corresponding to the CPI values except for features of subject clinical-10 in red, as clinical-10 is the only organised subject that is classified as disorganised. Generally, the features with the highest and lowest CPI tended to be separated from each other, while the features with intermediate CPI tended to have more overlapping. Clinical-10 has a CPI of 0.22 and stable RD identified, however, the features of this subject tend to be closer to features from the disorganised class, which could be the reason for the wrong classification. Clinical-9 has a CPI of 0.15 and was labelled as disorganised because no RD is detected for this subject. The reason for the subject being classified wrongly could be the CPI is very close to the median CPI that is used to binarise the data into two groups.

Figures 8A,B show examples of the rat VF ECG segments from organised and disorganised classes based on the phase mapping. In **Figures 8C–F**, examples of clinical AF ECG segments of lead I are shown with the corresponding CPI. Generally, there are no clear morphological patterns associated with CPI level and subsequently, it is difficult to discern the organisation level of a given data segment by visual evaluation alone.

5. DISCUSSION

Experimental results showed that the proposed classification methods can differentiate fibrillation of different organisation

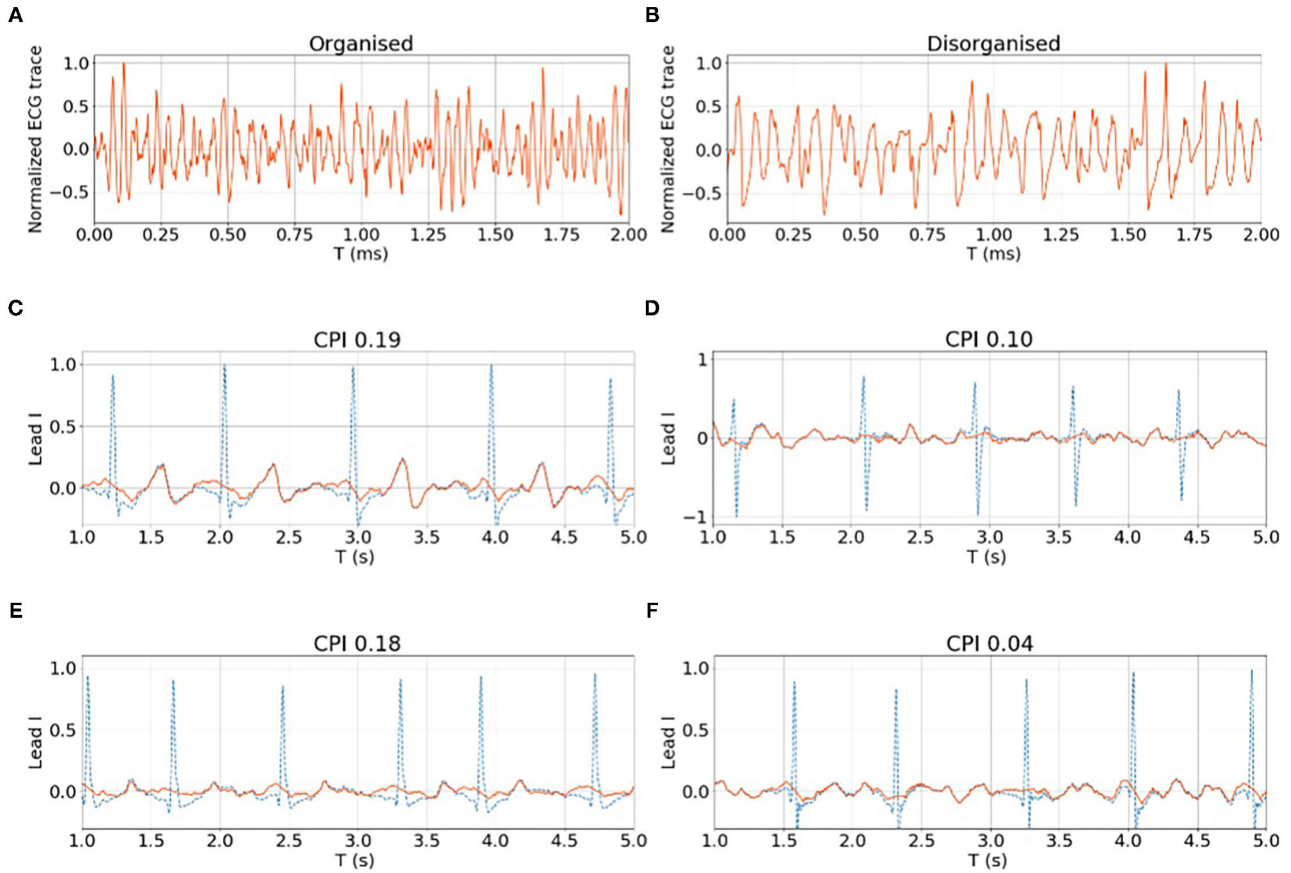

FIGURE 8 | (A,B) show examples of organised and disorganised rat VF ECG. **(C–F)** shows examples of clinical AF ECG with different CPI levels calculated from the corresponding EGM data. For both rat and clinical data, it is difficult to differentiate the organised and disorganised data by visual evaluation alone.

levels using the surface ECG an with accuracy of 78% for the rat VF data and an accuracy of 88% for the clinical AF data. Based on the results, this method has the potential to non-invasively the determine degree of organisation to aid mechanism-directed treatment decisions for patients with AF and in VF survivors.

The concept of 'organisation' within AF is not fully established or defined, in part due to a limited understanding of the underlying mechanisms. The degree of complexity within AF has been analysed previously by both local and multi-site analysis of EGMs in time and frequency domains (Ravelli and Masè, 2014). Some groups have looked at analysing the repetitive nature of wavefronts in AF using techniques such as similarity index (Ravelli et al., 2005) and Retro-Mapping (Mann et al., 2019). These techniques require intracardiac electrogram analysis from invasive mapping. Lankveld et al. (2014) previously showed that the spatiotemporal organisation of the AF ECG as measured by techniques such as F-wave complexity, harmonic decay, and DF analysis could delineate paroxysmal AF from the more disorganised persistent AF (Lankveld et al., 2014). Furthermore, it was shown that these AF complexity parameters derived from surface ECGs could predict procedural outcomes from catheter ablation in patients with persistent AF at long-term follow-up (Lankveld et al., 2016). The proposed methodology in this study for characterising the complexity of fibrillation from ECGs has the strength of being both non-invasive and being validated with detailed optical mapping studies in rat VF. The binary classification of AF ECGs as organised or disorganised with regard to description of the probable underlying mechanism may be useful in selecting appropriate treatment strategies for patients. Patients with disorganised AF are likely better suited for treatment with anti-arrhythmic drugs or extensive compartmentalisation of the atria with a surgical approach, while those with an organised AF may benefit from catheter ablation.

5.1. Implication of High-Frequency Components

This study shows that the power of frequency bands of relatively higher frequency is negatively correlated with the organisation level, which is consistent with existing studies that organised AF tends to have a lower DF (Lankveld et al., 2016).

In **Figure 9**, filtered signals (normalised by the total power) corresponding to bands 25∼50 Hz (i.e., high-frequency components) from one organised and one disorganised subject were compared, and it shows that the power of these high-frequency components from the disorganised subject was consistently higher than that from the organised subject, although high-frequency components (>25 Hz) constitute a

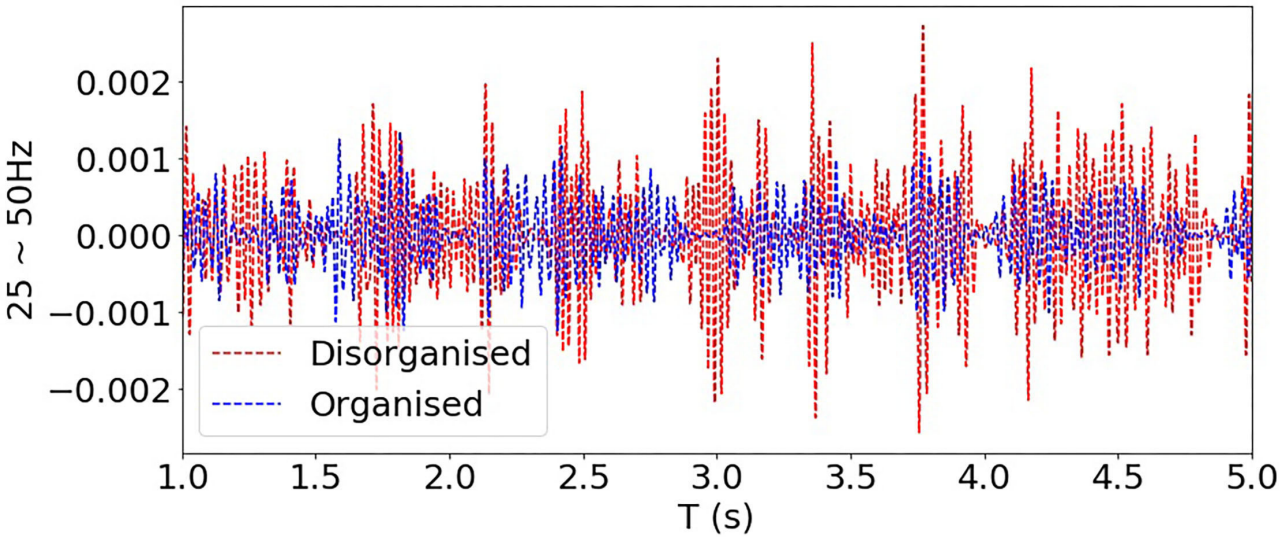

FIGURE 9 | Comparing filtered signals of bands 25∼50 Hz from one organised and one disorganised subjects (clinical AF dataset).

relatively small part of the whole signal spectrum, they may be helpful in distinguishing organised from disorganised AF.

Optical mapping data and EGM recordings can be regarded as sources, and the surface ECG can be regarded as a linear mixture of the sources due to the volume conduction effect. The organised fibrillation driven by one or two stable RDs tends to have activation with consistent and synchronised patterns of activation, yielding the power spectral density (PSD) of the ECG concentrating on a few low-frequency components. When the fibrillation is chaotic with randomly propagating wave-fronts, source signals tend to be more fragmented, resulting in the surface ECG with more high-frequency components.

It is also worth noting that the temporal morphological characteristics of ECG signals are only one aspect of the differences implied by high-frequency bandpower features between the organised and disorganised classes. The significant associations between high frequency bandpower and organisation level were found with only certain leads. Only using features with significant correlations yielded classification accuracies around the chance level. Moreover, using features from all 12 leads but from only one single band, 25∼50 Hz or 50∼100 Hz, also yielded accuracies around 60%. Neither a single band nor a single lead can fully capture the source pattern differences between the organised and disorganised subjects. The different spatial dispersion patterns over the 12 leads of different frequency bands are the key in discriminating the organised and disorganised classes.

5.2. Lead Optimisation

For the 12-lead clinical ECG, we also estimated the lead weights by solving the following optimisation problem

$$\hat{\mathbf{w}} = \arg\min_{\mathbf{w}} \frac{\mathbb{E}[(\mathbf{w}^\top \mathbf{x}_o(t))^2]}{\mathbb{E}[(\mathbf{w}^\top \mathbf{x}_d(t))^2]} \tag{11}$$

where $\mathbf{w} \in \mathcal{R}^{12}$ is the channel weights, and $x_o(t)$ and $x_d(t)$ are the vectors of the band-passed ECG signal at time t of organised and disorganised classes, respectively. $\mathbf{w}^\top \mathbf{x}_o(t)(\mathbf{w}^\top \mathbf{x}_d(t))$ can be regarded as a single virtual channel, and $\mathbb{E}[(\mathbf{w}^\top \mathbf{x}_o(t))^2]$ and $\mathbb{E}[(\mathbf{w}^\top \mathbf{x}_d(t))^2]$ denotes the expectation of the BP of the single virtual channel for organised and disorganised classes, respectively. By solving (Equation 11), the lead weights could be optimised in a way that $\mathbf{w}$ maximises the difference between the BP of the organised and disorganised classes. We have applied (Equation 11) to each band and used the bandpower of the single virtual channel as the feature. This approach was evaluated in the same LOO manner. However, the lead optimisation based on Equation (11) is not as good as that using mutual information for feature selection, possibly due to over-fitting. Selecting the leads yielding BP features with the highest mutual information means that weights of leads could be either 0 or 1. This process involves fewer parameters to be tuned as solving (Equation 11), and subsequently, is more robust against the cross-subjects dissimilarities within the same class.

5.3. Limitations

A limitation of this study is that the AF mapping data were low-resolution sequentially acquired intracardiac EGM data used to label the underlying mechanism, and follow-up data were not available. Thus, the ground truth for the organisation level could not be directly determined and had to be inferred from GC analysis. GC analysis of intracardiac electrogram in patients with AF was established from a methodology developed from analysis of rat VF optical mapping. The outcomes measured in AF in this study may have been influenced by mapping resolution, interelectrode distance, catheter stability, and heterogeneity in mapping. CPI value to determine the fibrillatory organisation, while applied to an unselected population may also have been influenced by the characteristics of this population.

Because the sample size of the clinical AF data is small, it is difficult to infer the true distribution of the CPI of clinical AF. In this study, we combined the RD detection results with median CPI to binarise the data. A more comprehensive data set, e.g., including cardiac imaging data from patients and follow-up data post ablation would be needed for a better binarisation in future study. Furthermore, in this study we have conducted QRS subtraction while it is difficult to fully remove T-waves while keeping the fibrillation signals intact. In our future study, we will seek better signal processing approaches for fibrillation signal extraction.

6. CONCLUSION

Individualised mechanism–directed treatments with better patient selection are needed for myocardial fibrillation treatment. If the mechanism of myocardial fibrillation, specifically AF, can be determined from the surface ECG, patients can be non-invasively screened for specific treatment strategies, whereby only patients with globally organised fibrillation are candidates for targeted ablation of drivers, and those with globally disorganised fibrillation are better treated with anti-arrhythmic drugs or ablation strategies to compartmentalise the atria. In this study, we propose a classification framework for detection of the fibrillation organisation level, and thus, the underlying fibrillation mechanism (stable RD vs. multiple wavelet driven) from the ECG alone, with no need for invasive intracardiac recordings.

Experimental results in this study showed that the proposed classification methods can differentiate fibrillation of different organisation types: for the rat VF ECG, the sensitivity, specificity, and accuracy are 75, 80, and 78%, respectively; and when these methodologies were adapted for the clinical AF ECG, the sensitivity, specific, and accuracy are 80, 92, and 88%, respectively. Therefore, the proposed techniques in this study have the potential to determine fibrillatory mechanisms and may aid non-invasive mechanism-directed tailoring of treatments for patients with AF and in VF survivors.

DATA AVAILABILITY STATEMENT

The raw data supporting the conclusions of this article will be made available by the authors, without undue reservation.

ETHICS STATEMENT

The studies involving human participants were reviewed and approved by Local Research Ethics Committee (Bromley). The patients/participants provided their written informed consent to participate in this study. The animal study was reviewed and approved by Imperial College London Ethical Review Board.

AUTHOR CONTRIBUTIONS

XL and FN: conception. XL, BH, NQ, ZW, NL, PL, PK, NP, and FN: data collection. XL, BH, and BZ: data analysis. XL, XS, BH, AS, and FN: drafting article. All authors: critical revision of the article and final approval.

FUNDING

This work was supported by the British Heart Foundation (RG/16/3/32175) and the National Institute of Health Research (NIHR), Imperial Biomedical Research Centre.

REFERENCES

Ahmad, A. Salinet Jr., J. L., Brown, P., Tuan, J. H., Stafford, P., Ng, G. A., and Schlindwein, F. S. (2011). Qrs subtraction for atrial electrograms: flat, linear and spline interpolations. *Med. Biol. Eng. Comput*. 49, 1321–1328. doi: 10.1007/s11517-011-0829-9

Alcaine, A., Masè, M., Cristoforetti, A., Ravelli, F., Nollo, G., Laguna, P., et al. (2017). A multi-variate predictability framework to assess invasive cardiac activity and interactions during atrial fibrillation. *IEEE Trans. Biomed. Eng*. 64, 1157–1168. doi: 10.1109/TBME.2016.2592953

Alcaraz, R., and Rieta, J. J. (2012). Application of wavelet entropy to predict atrial fibrillation progression from the surface ecg. *Comput Math Methods Med, page* 245213. doi: 10.1155/2012/245213

Ang, K. K., Chin, Z. Y., Wang, C., Guan, C., and Zhang, H. (2012). Filter bank common spatial pattern algorithm on BCI competition IV datasets 2a and 2b. *Front. Neurosci*. 6:39. doi: 10.3389/fnins.2012.00039

Arnold, A., Liu, Y., and Abe, N. (2007). "Temporal causal modeling with graphical granger methods," in *Proceedings of the 13th ACM SIGKDD International Conference on Knowledge Discovery and Data Mining, KDD '07* San Jose, CA.

Attia, Z. I., Noseworthy, P. A., Lopez-Jimenez, F., Asirvatham, S. J., Deshmukh, A. J., Gersh, B. J., et al. (2019). An artificial intelligence-enabled ecg algorithm for the identification of patients with atrial fibrillation during sinus rhythm: a retrospective analysis of outcome prediction. *Lancet* 394, 861–867. doi: 10.1016/S0140-6736(19)31721-0

Bollmann, A., Husser, D., Mainardi, L., Lombardi, F., Langley, P., Murray, A., et al. (2006). Analysis of surface electrocardiograms in atrial fibrillation: techniques, research, and clinical applications. *Europace* 8, 911–926. doi: 10.1093/europace/eul113

Cheng, D., Bahadori, M. T., and Liu, Y. (2014). "Fblg: a simple and effective approach for temporal dependence discovery from time series data," in *KDD '14: Proceedings of the 20th ACM SIGKDD International Conference on Knowledge Discovery and Data Mining* (New York, NY), 382–391.

de Groot, N., van der Does, L., Lanters, E., Teuwen, C., Knops, P., van de Woestijne, P., et al. (2016). Direct proof of endo-epicardial asynchrony of the atrial wall during atrial fibrillation in humans. *Circ. Arrhyth. Electrophysiol*. 9, 1–7. doi: 10.1161/CIRCEP.115.003648

Fan, X., Yao, Q., Cai, Y., Miao, F., Sun, F., and Li, Y. (2018). Multiscaled fusion of deep convolutional neural networks for screening atrial fibrillation from single lead short ECG recordings. *IEEE J. Biomed. Health Inform*. 22, 1744–1753. doi: 10.1109/JBHI.2018.2858789

Handa, B. S., Li, X., Baxan, N., Roney, C. H., Shchendrygina, A., Mansfield, C. A., et al. (2021). Ventricular fibrillation mechanism and global fibrillatory organization are determined by gap junction coupling and fibrosis pattern. *Cardiovasc. Res*. 117, 1078–1090. doi: 10.1093/cvr/cvaa141

Handa, B. S., Li, X., Qureshi, N., Mann, I., Chowdhury, R. A., Kanagaratnam, P., et al. (2020). Granger causality based analysis for classification of fibrillation mechanisms and localization of rotational drivers. *Circ. Arrhyth. Electrophysiol*. 13:e008237. doi: 10.1161/CIRCEP.119.008237

Handa, B. S., Roney, C. H., Houston, C., Qureshi, N. A., Li, X., Pitcher, D. S., et al. (2018). Analytical approaches for myocardial fibrillation signals. *Comput. Biol. Med*. 102, 315–326. doi: 10.1016/j.compbiomed.2018.07.008

Krummen, D. E., Ho, G., Villongco, C. T., Hayase, J., and Schricker, A. A. (2016). Ventricular fibrillation: triggers, mechanisms and therapies. *Future Cardiol.* 12, 373–390. doi: 10.2217/fca-2016-0001

Lankveld, T., Zeemering, S., Crijn, H., and Schotten, U. (2014). The ecg as a tool to determine atrial fibrillation complexity. *Heart* 100, 1077–1084. doi: 10.1136/heartjnl-2013-305149

Lankveld, T., Zeemering, S., Scherr, D., Kuklik, P., Hoffmann, B., Willems, S., et al. (2016). Atrial fibrillation complexity parameters derived from surface ECGs predict procedural outcome and long-term follow-up of stepwise catheter ablation for atrial fibrillation. *Circ. Arrhythm. Electrophysiol.* 9, e003354. doi: 10.1161/CIRCEP.115.003354

Laughner, J. I., Ng, F. S., Sulkin, M. S., Arthur, R. M., and Efimov, I. R. (2012). Processing and analysis of cardiac optical mapping data obtained with potentiometric dyes. *Am. J. Physiol. Heart Circ. Physiol.* 303, H753–765. doi: 10.1152/ajpheart.00404.2012

Lee, S., Sahadevan, J., Khrestian, C. M., Cakulev, I., Markowitz, A., and Waldo, A. L. (2015). Simultaneous biatrial high-density (510-512 electrodes) epicardial mapping of persistent and long-standing persistent atrial fibrillation in patients. *Circ. Arrhythm. Electrophysiol.* 132, 2108–2117. doi: 10.1161/CIRCULATIONAHA.115.017007

Li, X., Roney, C. H., Handa, B. S., Chowdhury, R. A., Niederer, S. A., Peters, N. S., et al. (2019). Standardised framework for quantitative analysis of fibrillation dynamics. *Sci. Rep.* 9, 16671. doi: 10.1038/s41598-019-52976-y

Lin, C.-H. (2008). Frequency-domain features for ecg beat discrimination using grey relational analysis-based classifier. *Comput. Math. Appl.* 55, 680–690. doi: 10.1016/j.camwa.2007.04.035

Luengo, D., Munoz, G. R. R., Elvira, V., and Artes-Rodriguez, A. (2016). "A hierarchical algorithm for causality discovery among atrial fibrillation electrograms," in *2016 IEEE International Conference on Acoustics, Speech and Signal Processing (ICASSP)* (Shanghai: IEEE), 774–778.

Luengo, D., Munoz, G. R. R., Elvira, V., Sanchez, C., and Artes-Rodriguez, A. (2018). Hierarchical algorithms for causality retrieval in atrial fibrillation intracavitary electrograms. *IEEE J. Biomed. Health Inform.* 23, 143–155. doi: 10.1109/JBHI.2018.2805773

Mann, I., Coyle, C., Qureshi, N., Nagy, S. Z., Koa-Wing, M., Lim, P. B., et al. (2019). Evaluation of a new algorithm for tracking activation during atrial fibrillation using multipolar catheters in humans. *J. Cardiovasc. Electrophysiol.* 30, 1464–1474. doi: 10.1111/jce.14033

Martín-Yebra, A., Laguna, P., Cygankiewicz, I., Bayés-de-Luna, A., Caiani, E. G., and Martínez, J. P. (2019). Quantification of ventricular repolarization variation for sudden cardiac death risk stratification in atrial fibrillation. *IEEE J. Biomed. Health Inform.* 23, 1049–1057. doi: 10.1109/JBHI.2018.2851299

Meo, M., Zarzoso, V., Meste, O., Latcu, D. G., and Saoudi, N. (2013). Spatial variability of the 12-lead surface ECG as a tool for noninvasive prediction of catheter ablation outcome in persistent atrial fibrillation. *IEEE Trans. Biomed. Eng.* 60, 20–27. doi: 10.1109/TBME.2012.2220639

Moe, G. K., Rheinboldt, W. C., and Abidskov, J. A. (1964). A computer model of atrial fibrillation. *Am. Heart J.* 67, 200–220. doi: 10.1016/0002-8703(64)90371-0

Morillo, C. A., Banerjee, A., Perel, P., Wood, D., and Jouven, X. (2017). Atrial fibrillation: the current epidemic. j geriatr cardiol. *J Geriatr. Cardiol.* 14, 195–203. doi: 10.11909/j.issn.1671-5411.2017.03.011

Nattel, S., Xiong, F., and Aguilar, M. (2017). Demystifying rotors and their place in clinical translation of atrial fibrillation mechanisms. *Nat. Rev. Cardiol.* 14, 509–520. doi: 10.1038/nrcardio.2017.37

Ng, F. S., Handa, B. S., Li, X., and Peters, N. S. (2020). Toward mechanism-directed electrophenotype-based treatments for atrial fibrillation. *Front. Physiol.* 11:987. doi: 10.3389/fphys.2020.00987

Ng, F. S., Kalindjian, J. M., Cooper, S. A., Chowdhury, R. A., Patel, P. M., Dupont, E., et al. (2016). Enhancement of gap junction function during acute myocardial infarction modifies healing and reduces late ventricular arrhythmia susceptibility. *JACC Clin. Electrophysiol.* 2, 574–582. doi: 10.1016/j.jacep.2016.03.007

Ng, F. S., Shadi, I. T., Peters, N. S., and Lyon, A. R. (2013). Selective heart rate reduction with ivabradine slows ischaemia-induced electrophysiological changes and reduces ischaemia—reperfusion-induced ventricular arrhythmias. *J. Mol. Cell Cardiol.* 59, 67–75. doi: 10.1016/j.yjmcc.2013.02.001

Pandit, S. V., and Jalife, J. (2013). Rotors and the dynamics of cardiac fibrillation. *Circ. Res.* 112, 849–862. doi: 10.1161/CIRCRESAHA.111.300158

Ravelli, F., Faes, L., Sandrini, L., Gaita, F., Antolini, R., Scaglione, M., et al. (2005). Wave similarity mapping shows the spatiotemporal distribution of fibrillatory wave complexity in the human right atrium during paroxysmal and chronic atrial fibrillation. *J. Cardiovasc. Electrophysiol.* 16, 1071–1076. doi: 10.1111/j.1540-8167.2005.50008.x

Ravelli, F., and Masè, M. (2014). Computational mapping in atrial fibrillation: how the integration of signal-derived maps may guide the localization of critical sources. *Europace* 16, 714–723. doi: 10.1093/europace/eut376

Rodrigo, M., Climent, A. M., Liberos, A., Calvo, D., Fernández-Avilés, D., Berenfeld, O., et al. (2016). Identification of dominant excitation patterns and sources of atrial fibrillation by causality analysis. *Ann. Biomed. Eng.* 44, 2364–2376. doi: 10.1007/s10439-015-1534-x

Roney, C. H., Cantwell, C. D., Bayer, J. D., Qureshi, N. A., Lim, P. B., Tweedy, J. H., et al. (2017). Spatial resolution requirements for accurate identification of drivers of atrial fibrillation. *Circ. Arrhythm. Electrophysiol.* 10, e004899. doi: 10.1161/CIRCEP.116.004899

Sau, A., Howard, J. P., Al-Aidarous, S., Ferreira-Martins, J., Al-Khayatt, B., Lim, P. B., et al. (2019). Meta-analysis of randomized controlled trials of atrial fibrillation ablation with pulmonary vein isolation versus without. *JACC Clin. Electrophysiol.* 5, 968–976. doi: 10.1016/j.jacep.2019.05.012

Schreiber, D., Rostock, T., M, M. F., Sultan, A., Servatius, H., Hoffmann, B. A., et al. (2015). Five-year follow-up after catheter ablation of persistent atrial fibrillation using the stepwise approach and prognostic factors for success. *Circ. Arrhythm. Electrophysiol.* 8, 308–317. doi: 10.1161/CIRCEP.114.001672

Song, S., and Bickel, P. J. (2011). Large vector auto regressions. *arXiv* 1–28.

Uetake, S., Miyauchi, Y., Osaka, M., Hayashi, M., Iwasaki, Y., Yodogawa, K., et al. (2014). Frequency analysis of surface electrocardiograms (ecgs) in patients with persistent atrial fibrillation: correlation with the intracardiac ecgs and implications for radiofrequency catheter ablation. *J. Arrhythm.* 30, 453–459. doi: 10.1016/j.joa.2013.12.003

Valdés-Sosa, P. A., Sànchez-Bornot, J. M., Lage-Castellanos, A., Vega-Hernández, M., Bosch-Bayard, J., Melie-García, L., et al. (2005). Estimating brain functional connectivity with sparse multivariate autoregression. *Philos. Trans. R. Soc. Lond.* 360, 969–981. doi: 10.1098/rstb.2005.1654

Zheng, Z. J., Croft, J. B., Giles, W. H., and Mensah, G. A. (2001). Sudden cardiac death in the united states, 1989 to 1998. *Circulation* 104, 2158–2163. doi: 10.1161/hc4301.098254

Conflict of Interest: FN, BH, XL, and NP are inventors on a patent application on Granger Causality mapping.

The remaining authors declare that the research was conducted in the absence of any commercial or financial relationships that could be construed as a potential conflict of interest.

Publisher's Note: All claims expressed in this article are solely those of the authors and do not necessarily represent those of their affiliated organizations, or those of the publisher, the editors and the reviewers. Any product that may be evaluated in this article, or claim that may be made by its manufacturer, is not guaranteed or endorsed by the publisher.

A. APPENDIX

Circular interdependence value for RD identification was validated with optical mapping data of the rat VF model. **Figure A1** shows an example of the down-sampling optical mapping data. In (**Figure 6A**), The background is the ground truth of the rotational activity obtained by phase mapping in the form of a heat map, the value of which is the percentage of the time rotational activities staying at the given location. In particular, the red hotspot is of a value around 10%, which is around 350 ms given that the total duration of this recording is 4 s. The DF of the rat VF data usually ranges from 20∼30 Hz. Thus, the rotation activity at the red hotspot would have approximately 18 times of rotations, making it a relatively very stable RD site. The original optical mapping data were down-sampled as 4-by-4 grids with 1/4 of the original resolution. Each rat heart would generate approximately 75 down-sampled areas.

Two examples of local GC map after down-sampling are shown in (**Figures 6B,C**), and areas 1 and 2 were labelled as RD and non-RD class, respectively, according to the heat map in (**Figure 6A**). The CIV for area 1 is much higher at 0.83 than that of area 2 at 0.27. The RD prediction for all the down-sampled areas using CIV yielded the receiver operating characteristic (ROC) curve shown in (**Figure 6D**), with an area under curve (AUC) of 0.87 and the best operating point at 0.60.

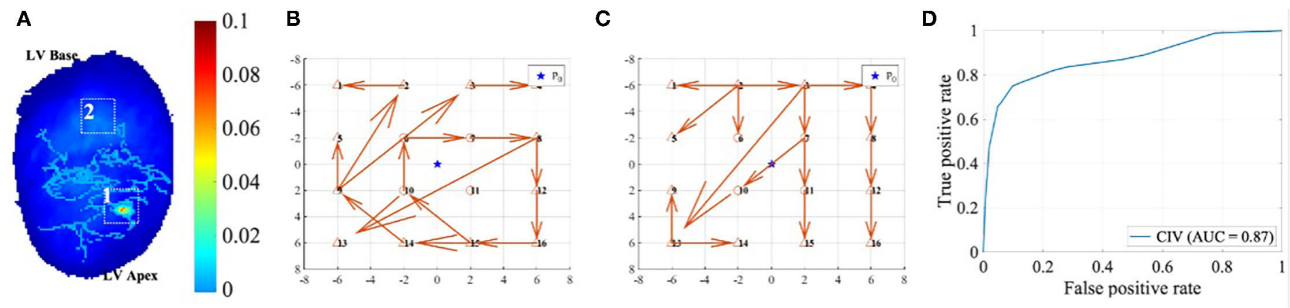

FIGURE A1 | (A) shows the down-sampling of the high-resolution optical mapping data of rat VF. Areas 1 and 2 were labelled according to the RD (RD) heatmap shown as the background, the local GC vector maps of which were shown in **(B)** and **(C)**, respectively. **(D)** shows the ROC of the RD prediction using CIV.

frontiers in Physiology

ORIGINAL RESEARCH
published: 10 December 2021
doi: 10.3389/fphys.2021.787180

Computational Model for Therapy Optimization of Wearable Cardioverter Defibrillator: Shockable Rhythm Detection and Optimal Electrotherapy

Oishee Mazumder, Rohan Banerjee, Dibyendu Roy, Ayan Mukherjee, Avik Ghose, Sundeep Khandelwal and Aniruddha Sinha*

TCS Research, Tata Consultancy Services, Kolkata, India

Wearable cardioverter defibrillator (WCD) is a life saving, wearable, noninvasive therapeutic device that prevents fatal ventricular arrhythmic propagation that leads to sudden cardiac death (SCD). WCD are frequently prescribed to patients deemed to be at high arrhythmic risk but the underlying pathology is potentially reversible or to those who are awaiting an implantable cardioverter-defibrillator. WCD is programmed to detect appropriate arrhythmic events and generate high energy shock capable of depolarizing the myocardium and thus re-initiating the sinus rhythm. WCD guidelines dictate very high reliability and accuracy to deliver timely and optimal therapy. Computational model-based process validation can verify device performance and benchmark the device setting to suit personalized requirements. In this article, we present a computational pipeline for WCD validation, both in terms of shock classification and shock optimization. For classification, we propose a convolutional neural network-"Long Short Term Memory network (LSTM) full form" (Convolutional neural network-Long short term memory network (CNN-LSTM)) based deep neural architecture for classifying shockable rhythms like Ventricular Fibrillation (VF), Ventricular Tachycardia (VT) vs. other kinds of non-shockable rhythms. The proposed architecture has been evaluated on two open access ECG databases and the classification accuracy achieved is in adherence to American Heart Association standards for WCD. The computational model developed to study optimal electrotherapy response is an *in-silico* cardiac model integrating cardiac hemodynamics functionality and a 3D volume conductor model encompassing biophysical simulation to compute the effect of shock voltage on myocardial potential distribution. Defibrillation efficacy is simulated for different shocking electrode configurations to assess the best defibrillator outcome with minimal myocardial damage. While the biophysical simulation provides the field distribution through Finite Element Modeling during defibrillation, the hemodynamic module captures the changes in left ventricle functionality during an arrhythmic event. The developed computational model, apart from acting as a device validation test-bed, can also be used for the design and development of personalized WCD vests depending on subject-specific anatomy and pathology.

Keywords: sudden cardiac death, defibrillation threshold, hemodynamics, myocardial damage, biophysical simulation, deep learning

OPEN ACCESS

Edited by:
Martin Bishop,
King's College London,
United Kingdom

Reviewed by:
Shuang Qian,
King's College London,
United Kingdom
Angel Moreno,
Institut De Rythmologie Et Modélisation Cardiaque (IHU-Liryc),
France

****Correspondence:***
Oishee Mazumder
oishee.mazumder@tcs.com

Specialty section:
This article was submitted to Computational Physiology and Medicine, a section of the journal Frontiers in Physiology

Received: *30 September 2021*
Accepted: *08 November 2021*
Published: *10 December 2021*

Citation:
Mazumder O, Banerjee R, Roy D, Mukherjee A, Ghose A, Khandelwal S and Sinha A (2021) Computational Model for Therapy Optimization of Wearable Cardioverter Defibrillator: Shockable Rhythm Detection and Optimal Electrotherapy. Front. Physiol. 12:787180. doi: 10.3389/fphys.2021.787180

1. INTRODUCTION

Sudden cardiac death (SCD) is a sudden and unpredictable event caused due to loss of cardiac functionality. SCD accounts for the largest cause of natural death in the adult population, causing around 13% of deaths in the overall population and about 36% of deaths in heart failure patients (Smith and Cain., 2006). The leading cause of SCD is primarily attributed to electrical abnormality like ventricular arrhythmia (VA) and ventricular fibrillation (VF) followed by structural cardiac disorders like ischemia. VF is usually lethal within minutes of its inception and if not immediately treated, leads to cardiac arrest (Barraud et al., 2017). Electrical defibrillation is the only effective therapy for such conditions. Electrical defibrillation through wearable cardioverter-defibrillator (WCD) provides a non-invasive therapeutic option for patients during a period when the risk of SCD is changing or unclear (Poole et al., 2008; Sharma et al., 2017).

Wearable cardioverter-defibrillator is mostly recommended to patients who are newly diagnosed with non-ischemic cardiomyopathy with severely reduced left ventricle ejection fraction (LVEF), patients awaiting heart transplantation or in patients with ventricular assist devices, temporary inability to implant an intra-cardiac defibrillator (ICD) or in ambulatory event monitoring, often performed for several weeks in an effort to determine an arrhythmic etiology for syncope (Wan et al., 2013). Similar to ICD, WCD detects ventricular arrhythmic events and delivers a defibrillation shock to terminate VF or tachycardia (>180 bpm) by resetting myocardial potential distribution. Instead of the intracardiac electrogram (EGM) signal, the ECG signal recorded from the body surface is used to detect arrhythmic events. Therapeutic devices like WCD though indispensable, have to maintain very high reliability and accuracies in order to deliver timely and optimal therapy (Epstein et al., 2013). WCD devices are programmed to be autonomous, thus further burdening device complexity. Malfunction in any form while in detection or during shock generation can cause serious injury, which can even be fatal. An effective way of device reliability and performance validation is through computational model aided trials (Ariful et al., 2016). For WCD, computer-aided validation processes could evaluate device performance in virtual trials and benchmark the device settings to suit personalized requirements. In this regard, two separate aspects require validation and bench-marking: the classification accuracy of detecting shockable rhythm from non-shockable rhythm and shock voltage profile optimization based on a personalized requirement to optimize shock efficacy.

The central requirement of autonomous WCD devices is the detection of VF by means of reliable detection algorithms. Over the past decades, special focus has been given toward developing efficient algorithms that can correctly detect VF abnormality, especially in real-time (Ayala et al., 2014; Figuera et al., 2016). Different large-scale machine learning (ML) methods have been explored for ECG beat classification identifying shockable rhythm (Jekova, 2000; Amann et al., 2005). In spite of the high accuracy of classification, incorporating complex feature measurement within the WCD setting is a challenge. WCD shock detection algorithm requires real-time analysis with minimal decision delay, low complexity, and low memory requirement for computations that presents a certain risk of poor feature quality due to inaccurate delineation of ECG waves, filtering, or approximations (Aramendi et al., 2010). As an alternate, several self-learning approaches based on the deep neural network have been proposed recently (Zhong et al., 2020) and are now widely applied on arrhythmia classification using Convolutional Neural Network (CNN) (Lee et al., 2019). The CNN-based arrhythmia classification could eliminate the cumbersome requirement of criteria selections and parameters setting in traditional ML-based arrhythmia detection methods while achieving high detection accuracy. Some notable prior arts (Silva et al., 2019) implementing CNN architecture for arrhythmia classification, reports the use of various architectural layers (Kwon et al., 2018), attention on noise removal, use of LSTM networks (Krasteva et al., 2020), etc. The most recent work reporting the highest accuracy to date uses a bidirectional LSTM (bi-LSTM) instead of unidirectional LSTM (Jeon et al., 2020).

Irrespective of high detection accuracy and type of defibrillator, strong shocks that are required during defibrillation are reported to have serious adverse effects, most prominently *via* electroporation that may initiate post-shock arrhythmia (Colley et al., 2019). Strong shocks can also potentially cause myocardial damage, giving rise to mechanical dysfunction (stunning), increase in contractility, and development of hemodynamically mediated symptoms (Qiana et al., 2018). Hence, it is extremely important to tune and optimize the shock energy to get the desired effect. The mechanism of defibrillation has been studied extensively in recent years, mostly for ICD placements (Stinstra et al., 2008; Onofrio et al., 2018). Computational models analyzing defibrillation mechanism and the after-effect of shock voltage in the myocardium can provide an in-depth understanding of the fibrillation mechanism and help in optimizing the defibrillation threshold (Stinstra et al., 2007). The distribution of electric fields in the heart is closely related to defibrillation outcomes. Three dimensional cardiac models like the volume conductor models coupled with Finite Element Modeling are well suited to reflect the electric field distribution in myocardium substrate (Stinstra et al., 2010; Trayanova et al., 2011; Tate et al., 2018).

Prior art lists sufficient methods of classifying shockable and non-shockable rhythms but for defibrillator performance validation, an integrated pipeline that could classify shockable rhythm as well as validate the shockable energy delivery efficacy is the need of the hour. The shock delivery circuit of WCD generates very strong fields of fixed energy or current to stop the arrhythmic propagation by resetting the myocardial potentials to a depolarized state (Morgan et al., 2009). It has been observed that field distribution required to provide defibrillation effect is greatly dependent on subject-specific parameters like torso geometry, trans-thoracic impedance, cardiac structure, etc. (Hatib et al., 2000). A computational pipeline that could integrate the aspects of shock identification and pre-plan personalized shock delivery can be extremely useful as a WCD device validation. Mathematical modeling and computer simulation can efficiently accelerate the process of optimizing and testing of

WCDs. A computational model-based validation approach could evaluate device performance on virtual trial and benchmark the device setting to suit personalized requirements.

In this article, we propose a computational pipeline for WCD validation, both in terms of shock classification and shock optimization. The schematic representation of the proposed computational framework is shown in **Figure 1**. The computational model is an *in-silico* cardiac model integrating cardiac functionality in terms of hemodynamics and electrophysiology, encompassing biophysical simulation to compute the effect of shock voltage on myocardial potential distribution. We propose a CNN-LSTM architecture for the classification of VF, VT (shockable), and other (non-shockable) rhythms. The proposed network is evaluated on two open-access databases, the CUDB and the VFDB databases. A 3D cardiac computational model in line with the volume conductor model is developed utilizing high definition torso-cardiac MRI. This model is used to study the variation of shock efficacy by varying plausible electrode configurations. A novel metric is designed for quantifying the shock efficacy computed using the energy required to obtain DFT and extent of myocardial damage. Along with the biophysical modeling aspect, the cardiac computational model also integrates the hemodynamics functionality that closely replicates the dynamic changes in left ventricular functions during VF/VT episodes, thus providing key physiological insights. Novelty and uniqueness of the proposed computational pipeline for shock classification and distribution analysis lies in incorporating a CNN-LSTM overlapping window algorithm, deriving defibrillation efficacy metric for optimal electrotherapy, and inclusion of hemodynamic insights during VF initiation and subsequent termination. Such concepts have not been proposed earlier for WCD and have the potential to enhance conventional WCD functioning in terms of device validation and personalization.

2. MATERIALS AND METHODS

The proposed computational framework is divided into three major sections involving the key features of the proposed model which are

- CNN-LSTM based shockable rhythm classifier architecture with both non-overlapping and overlapping window variations
- Biophysical modeling of shock propagation and shock efficacy index generation
- Capturing hemodynamics changes during VF/VT episodes and recovery

Subsequent sections concentrate on the development and integration of each of these features in a computational model incorporating the functionality of a standard WCD. The modeled WCD referred to in this paper is the WCD model of Zoll electronics (WCD system, LifeVest, ZOLL, Pittsburgh, PA, USA) (Reek et al., 2017). The basic working of WCD can be found in the **Supplementary Material**.

2.1. Dataset and ECG Pre-processing

The classification algorithm is designed and validated using two publicly available datasets, the MIT-BIH Malignant Ventricular Arrhythmia database (VFDB) (Greenwald, 1986) and the Creighton University Ventricular Tachycardia database (CUDB) (Nolle et al., 1986). The VFDB dataset contains 30-min long Holter ECG record files belonging to 22 subjects. The CUDB dataset contains 8-min long ECG records collected from 35 patients who have experienced sustained episodes of lethal VA. The sampling rate for all recordings is 250 *Hz*.

A pre-processed version of the ECG recording datasets, as discussed in Krasteva et al. (2010) and Bisera et al. (2008), have been utilized for the design and validation of the proposed algorithm. The preprocessing steps followed are mean subtraction, moving average filtering [$order = 5$], a high-pass filter with $f_c = 1Hz$ to eliminate drift suppression, and low-pass Butterworth filter with $f_c = 30Hz$. Further, noise and artifacts have been excluded from the datasets along with intermediate rhythms like slow VT (<150 bpm) and fine VT. Also, recording segments with minimal electrical activity have also been excluded from the datasets. With all the preceding pre-processing steps applied, the resultant recording is split into windows of different lengths namely, 2, 4, 6, and 8 s. Further, windows with uniform labeling only have been retained for use. The details regarding

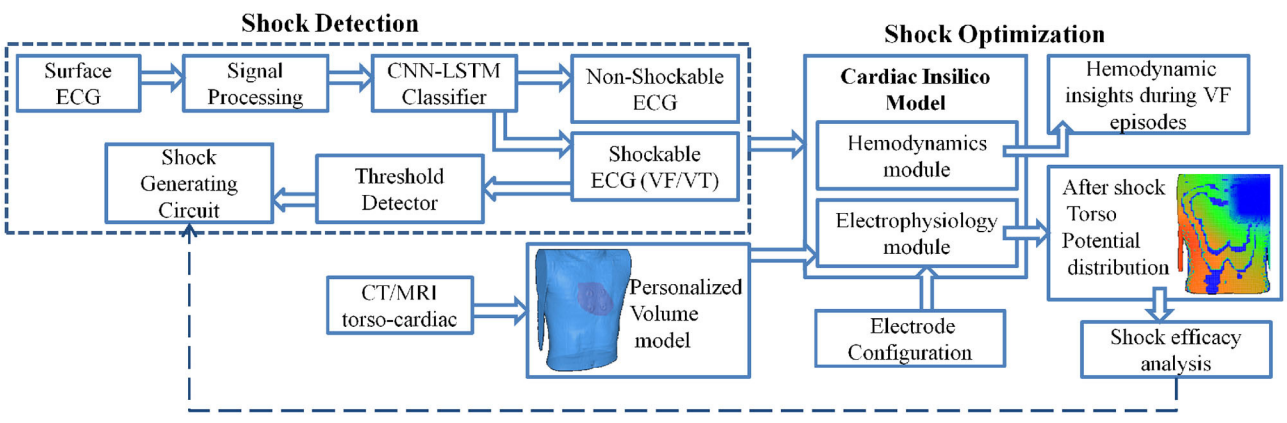

FIGURE 1 | Schematic representation of the computational model to analyze Wearable cardioverter-defibrillator (WCD) efficacy.

the final count of windows generated through the process for the different classes under consideration (VT, VF, and Others) are given in **Table 1**. These instances have been used for training and validation of the proposed algorithm in a k-fold cross-validation framework. Plots of the 8 s recordings with labels VT, VF, and non-shockable rhythm are given in **Figures 2A–C**, respectively.

TABLE 1 | Dataset segmentation details.

	CUDB			VFDB		
Segment length (s)	**NSh**	**VF**	**VT**	**NSh**	**VF**	**VT**
2	6,075	120	1,390	16,005	1,473	1,597
4	2,986	53	663	7,861	702	784
6	1,959	31	422	5172	446	516
8	1,446	21	302	3,823	326	377

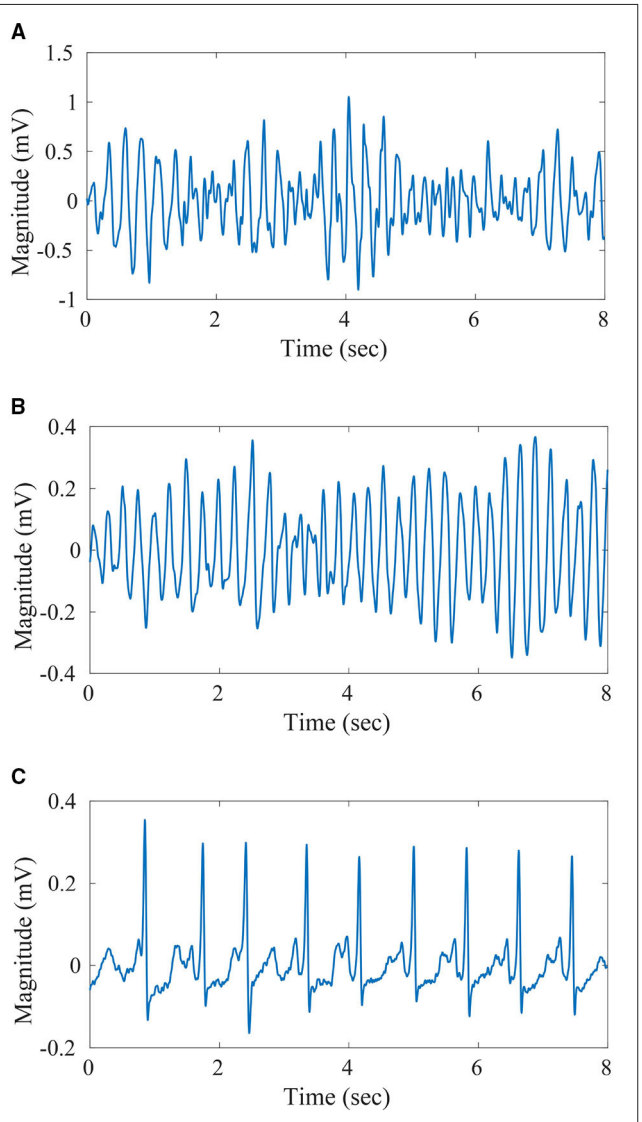

FIGURE 2 | Sample ECG-**(A)** 8 s duration Ventricular Tachycardia (VT) signal, **(B)** 8 s duration VF signal, **(C)** 8 s duration non-shockable signal.

Apart from the above-discussed processing strategy, another approach toward dataset segmentation has been explored. In this second approach, the datasets have been segmented into training and validation subsets in a subject-wise manner. This process ensures that data signatures of a particular subject are not present in both the training and validation sets, thereby ensuring a robust evaluation strategy of the proposed algorithm. This study only considers data with 8 s of data length. In addition, in order to study the impact of over-lapping contiguous windows on classification scores, three overlapping scenarios have been considered under this approach. The three scenarios pertain to 25, 50, and 75% overlapping of contiguous windows. For the different overlapping percentages, the number of windows generated can be expressed in terms of Equation (1).

$$m = (n - r)/(k - r) \tag{1}$$

where, m = number of windows, n = total samples, r = overlap sample, and k = window sample.

2.2. Deep Learning Architecture for Classification

For classifying different arrhythmic rhythms, we propose a deep CNN-LSTM architecture for the classification of VT, VF, and other conditions from ECG. Here, other conditions can include any cardiac condition other than VT and VF, that do not require shock therapy. The block diagram of the proposed network architecture is shown in **Figure 3**.

The CNN-LSTM is a type of LSTM architecture specifically designed for sequence prediction problems for input data with spatial structure that can not be easily modeled with a vanilla LSTM. The architecture contains a series of CNN layers for the extraction of features from the input data which are then applied to an LSTM architecture for temporal modeling and prediction. As shown in **Figure 3**, input ECG data after pre-processing is applied to a series of 1D convolutional layers. For each convolutional layer, the kernel dimension is taken as 5. Batch normalization is applied at the end of the convolution operation for standardizing the inputs to a layer for each mini-batch. The number of filters in the base convolutional layers is selected as 16. As we go deeper, the number of filters in the convolutional layers are gradually increased by a factor of 2 to extract more detailed features. However, the dimension of the feature is reduced by applying the stride length of 2 in every alternate layer for doing the convolution operation. The neurons in the convolutional layer are activated using the non-linear Rectified linear unit (Relu) activation function. The output of the final convolutional layer is applied to an average-pooling layer having a window size of 4 to select a representative feature set at a reduced dimension. This is applied to a pair of LSTM layers having 128 and 64 units, respectively, followed by a dense layer having 3 neurons for classification of VT, VF, and other rhythms using a softmax activation function.

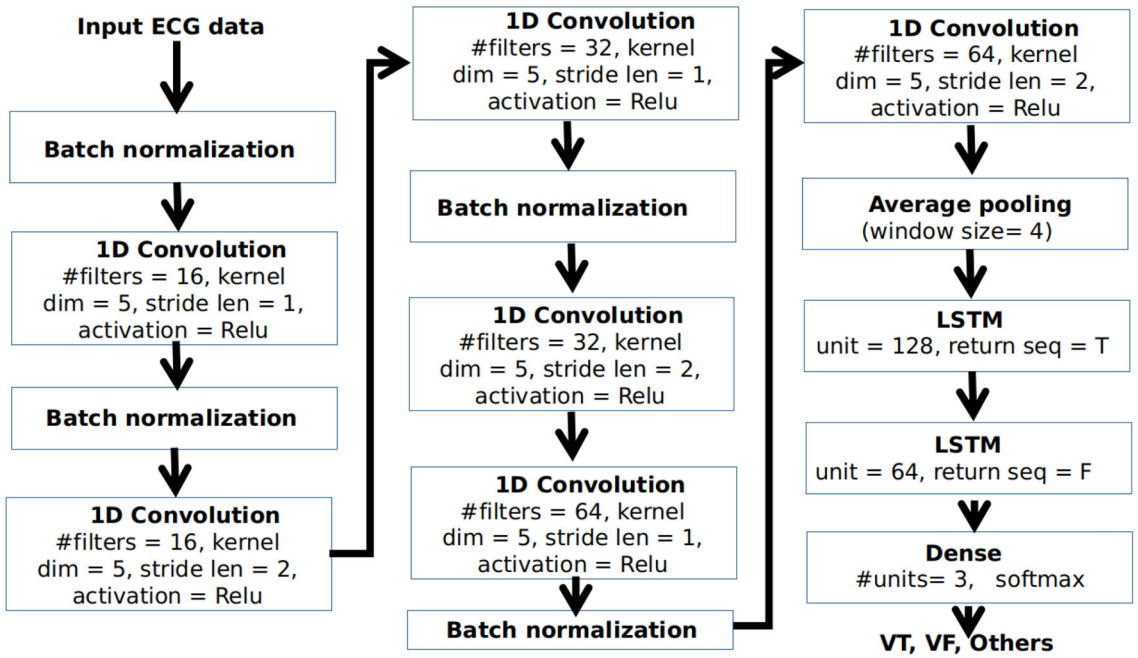

FIGURE 3 | Block diagram of the proposed convolutional neural network-"full form of LSTM" (CNN-LSTM) architecture.

2.2.1. Network Parameters

Selection of the optimum network hyper-parameters becomes a major challenge in designing a neural network architecture. In our architecture, we focused on a few parameters while designing the optimum architecture including, (1) number of filters in the base convolutional layer, (2) dimension of the filter kernel, (3) the stride length, and (4) number of hidden units in the LSTM layers. We opted for a randomized search as the hyper-parameter selection strategy, where the possible values of different hyper parameters are randomly selected from a pre-defined range to train and evaluate the network on a small representative dataset obtained from the CUDB database. The evaluation is done based on 5-fold cross-validation on the representative dataset. The combination of hyper-parameters producing the maximum median accuracy in the cross-validation approach is selected as the optimum combination for designing the network. The duration of instances in the representative dataset is considered as 4 s.

2.2.2. Training of the Proposed Network

The proposed architecture is implemented in python 3.6.9 using TensorFlow 1.5. The platform where the network was trained contains an Intel Core i7 processor and 8 GB of primary memory. The mini-batch size is selected as 32. During training, the categorical cross-entropy loss of the network is minimized using an Adam optimizer with learning a rate of 0.005 and 300 epochs limit are used before stopping the training. The initial weights are set using Xavier initialization. In this process, the values are randomly assigned from a Gaussian distribution of zero mean and a finite variance $var = \frac{2}{n_{in}+n_{out}}$, where n_{in} and n_{out} are the number of input and output neurons in that layer, respectively. The bias terms are initialized by zeros.

2.3. Cardiac *in-silico* Model

The cardiac *in-silico* model is a computational model encompassing a 0D lumped hemodynamic model and a 3D volume conductor model enabling biophysical simulation. There is also electrophysiology (EP) block that can synthesize ECG template and is responsible for the initiation of cardiac contraction and pulsating behavior of heart chambers that drives the hemodynamic block. In this particular work, the ECG signal is used directly from the database or it can be the signal measured by sensing leads of WCD. If required, synthesized VF/VT ECG can also be generated using the proposed *in-silico* model (Mazumder et al., 2021).

2.3.1. Hemodynamics Module

The Hemodynamic block consists of a four-chambered heart with lumped pulmonary and systemic circulations. The pressure variations across the cardiac chambers are modulated through time-varying compliance functions. Heart valves are modeled to replicate the functionality of each cardiac phase, capturing the pressure difference across the cardiac chambers to ensure unidirectional blood flow through the heart and maintain the pressure-volume dynamics. The model is also coupled with central nervous system modulation in terms of a baroreflex control, which regulates pressure autonomously through sympathetic and parasympathetic interaction of heart rate, contractility, and systemic vascular resistance, explained in detail in our prior works (Mazumder et al., 2019; Roy et al., 2021).

The dynamic equations to replicate the pressure dynamics of the model at various chambers and pulmonary and aortic arteries can be represented by state-space equations, depicting the flow variation due to resistance to blood flow from the vessel along with the compliance property of the chambers. As an example, the flow equation of the left ventricle is expressed in Equation (2).

$$\dot{P}_{lv} = \frac{1}{C_{lv}(t)}\left[U_{mi} \times \frac{P_{la} - P_{lv}}{R_{mi}} - U_{ao} \times \frac{P_{lv} - P_{sa}}{R_{ao}} - \dot{C}_{lv}(t)P_{lv}\right] \tag{2}$$

Here P_{la}, P_{lv}, P_{sa} are the pressure variables in the left-atrium, left-ventricle, systemic arteries, respectively, R_{mi}, R_{ao} are the valvular resistances across the mitral and aortic valve, C_{lv} is the left ventricle compliance. The symbols U_{mi}, U_{ao} are the control functions to mimic the opening or closing of the respective cardiac valves. Pulsating action of the heart is driven by a compliance function, which determines the time-varying compliance of auricles and ventricles and brings about the pumping action of the heart, utilizing time and morphological metrics from ECG signal. This compliance adjustment is the most crucial part of this study as the effect of VF is modeled by decoupling atrium and ventricular compliance and then modulating the ventricular compliance to emulate the effect of VA.

In generic ECG signal, for one cardiac cycle, the characteristic cardiac electrical events like PQ (auricular depolarization), QRS (ventricular depolarization), ST duration (ventricular repolarization), and R-R intervals are marked by a specific set of PQRST peaks whose amplitudes and time-instances can be represented as $\left[(P_p, T_p)\ (P_q, T_q)\ (P_r, T_r)\ (P_s, T_s)\ (P_t, T_t)\right]$

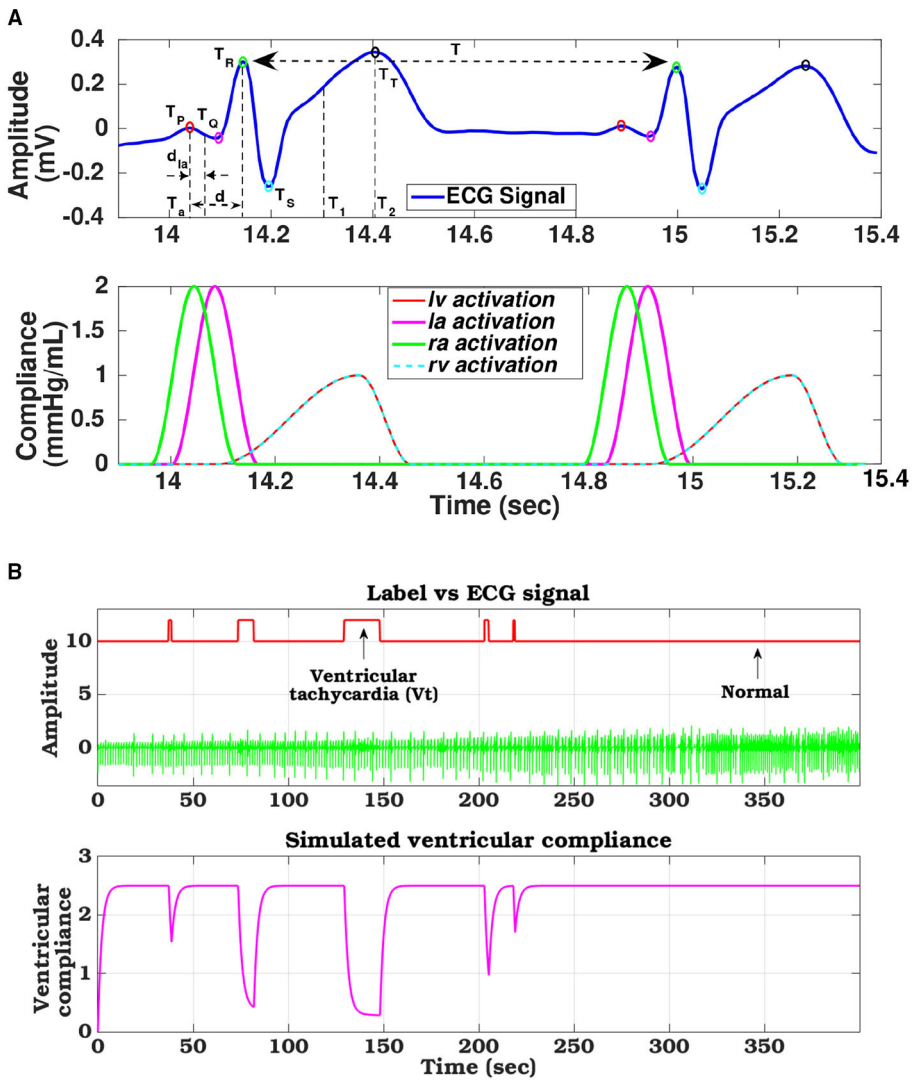

FIGURE 4 | (A) ECG signal decomposed to its constituent components and phase matched cardiac chamber compliance functions, **(B)** Compliance variation of left ventricle tuned with arrhythmia ECG signal levels derived from the database.

(**Figure 4A**). These electrical instances are encoded to modulate compliance function and timing information to control the synchronized operation of four heart chambers (Roy et al., 2021). Compliance function of the left ventricle can be modeled as follows:

$$C_i(t) = C_i \times u_v(t-d), \quad i \in \{lv, rv\} \tag{3}$$

$$u_v(t) = \begin{cases} 0.5 - 0.5\cos\left(\pi \frac{t}{T_1}\right), & 0 \le t < T_1 \\ 0.5 + 0.5\cos\left(\pi \frac{t-T_1}{T_2-T_1}\right), & T_1 \le t < T_2 \\ 0, & T_2 \le t < T \end{cases} \tag{4}$$

where $u_v(t)$ is the activation function, and $d = (T_r - T_p)$ represents the delay in activation of ventricles from the right-atrium, $T_1 = (T_r + T_t)/2$ and $T_2 = T_t$ are the systolic and diastolic duration of the cardiac cycle (T), respectively. Similarly, compliance for the other chambers can also be modeled. The ventricular compliance ($C_i; \forall i \in \{lv, rv\}$) are computed by the ratio between the R-peak and T-peak, expressed as $C_i = \frac{P_r}{P_t}$. Compliance functions estimated from ECG template for a healthy heart for all the 4 chambers are shown in **Figure 4A**.

Ventricular fibrillation is an abnormal heart rhythm, where irregular heart signals cause the ventricles to twitch uselessly. As a result, the cardiac elasticity across the ventricles increases, and hence, those cardiac chambers get stiff with decreased compliance (Arts et al., 2005). Subsequently, the heart does not pump blood to the rest of the body. To hemodynamically simulate this effect, the compliance function during the VF condition has been remodeled. Let us assume that $C^i_{(v,Nor)}(t)$, where, $(i \in RV, LV)$ is the compliance across the ventricles (right and left) during normal conditions at the t^{th} time. When the VF episode starts, $C^i_{(v,Nor)}(t)$ starts decreasing. To model this effect analytically, we have formulated the following equation:

$$C^i_v(t) = \begin{cases} C^i_{v,Nor} \times exp(-\frac{t}{\tau}), & \text{if } VF = 1 \\ C^i_{v,Nor}, & \text{else} \end{cases}; \quad \forall i \in \{RV, LV\} \tag{5}$$

where, t is the duration of the VF/VT episode, and τ defines the time constant of that VF episode. Thus, during the VF occurrence, the ventricular compliance starts decreasing exponentially. One such instance of remodeled ventricular compliance phase tuned with VF/VT occurrence is shown in the **Figure 4B**. The raw ECG signal along with the annotated labels, derived from the CUDB dataset is used as a reference to show the modulation of ventricular compliance with changes in ECG morphology and arrhythmic patterns.

2.3.2. Biophysical Modeling

Understanding and replication of defibrillator behavior need reconstruction of torso-cardiac anatomy with bio-physically detailed realistic-geometry models. We have used an MRI scan of a 19-year-old healthy subject, obtained from a dataset developed by an Open Source software project of the SCI Institute's NIH/NIGMS CIBC Center (SCI, 2016) to create a 3D torso-cardiac model. Conductivity levels of various organs and tissues in the torso section, like the skin, skeletal muscles, fat, bones, lungs, spleen, liver, stomach, kidneys, and spinal cord are defined as per standard values reported in the literature (Lim et al., 2018). Finite element meshes are created in the 3D cardiac-torso model to help in solving the biophysical model associated with the application of external fibrillation. This is similar to forward electrophysiology, the only difference being that instead of using cardiac potential as the source model, defibrillator voltage is acting as the source. We have used monodomain equations to solve the biophysical model. Shocking electrodes are placed in the torso section for various possible configurations. Effect of an external voltage applied at the electrodes is captured through the modified torso and cardiac potential generation. The standard shocking configuration in WCD is *via* Apex-Posterior shock. In one of our previous works (Mazumder and Sinha, 2021), we compared three other shocking electrode configurations to obtain optimized defibrillation, expressed in terms of the critical mass hypothesis. In that analysis, Front-Back configuration resulted as the most optimized electrotherapy. In this work, we extend our previously designed defibrillator efficacy concept and focus on analyzing electrotherapy responses at various sub-locations in Apex-Posterior and Front-Back configurations.

The governing equation for biophysical simulation is the modified steady state electrical potential in an inhomogeneous volume conductor described by Laplace equation:

$$\nabla(\sigma \nabla\phi) = 0 \tag{6}$$

where, σ is the conductivity tensor field and ϕ is the electric potential. This is subjected to two boundary conditions, Dirichlet boundary condition, defined as $\phi(x, y, z) \ |_{\Omega_k} = \ V_k$ applied anywhere the electric potential is known (V_k is the known potential of electrode k, and Ω_k specifies the domain coincident with electrode k) and Neumann boundary condition, defined as $\frac{\partial\phi}{\partial n} \ |_{\Omega} = \ 0$, applied on the surface of the object being simulated, not defined by Ω. In this implementation, we assume a linear and isotropic volume conductor model, with negligible capacitance and inductance, and applied the Galerkin finite element formulation with tri-linear interpolation (Colley et al., 2019). All the processes involved in a biophysical simulation like monodomain equation solving, mesh model generation, and their visualization were done using SCIRun software (Burton et al., 2011). For computing the biophysical equation, the torso model and the electrode model (defined over any place in Ω) are integrated into a computational mesh composed of hexahedral elements suitable for finite element modeling. Mesh created for the cardiac structure consists of 34,927 elements with 1,17,649 nodes, while the torso structure has 45,328 elements and 8,25,871 nodes, build around a lattice volume of 50 x 50 x 75 cm. SCIRun uses BioPSE modeling library and packages like TetGen for generating mesh structure (Stinstra et al., 2007).

During simulations, boundary conditions are specified on all finite element nodes within the geometrical regions defined by the electrodes above. Electrodes are assigned a constant potential over their surface. For shocking electrodes (anode), the extracellular potential was fixed at the specified values to define the strength of the applied shock (500 V); for ground

electrodes (cathode), the extracellular potential was defined to be 0 V throughout.

There are various theories to define defibrillation efficacy, but the underlying principle for all of them suggests that for fibrillation to be effective, the Defibrillation threshold voltage (DFT) value should be high enough to stop the fibrillation effect but lower than upper threshold level (ULV), that is capable of regenerating fibrillation mechanism through reentry (Karagueuzian and Chen, 2001). We have implemented the Critical point theorem (Zipes et al., 1975) which considers DFT value capable of changing at least 95% myocardial mass to a potential gradient of $5V/cm$ as a measure of complete defibrillation. After the potential distribution is solved using the finite element method, the gradients of the potential field are evaluated for the full thorax using tri-linear spatial derivatives and DFT values are computed. The DFT surrogate intrinsically obtains extracellular potential fields throughout the 3D volume of the myocardium making it inherently convenient for use in computational modeling studies in real-time (Morgan et al., 2009). Along with DFT, ventricular mass with voltage gradient distributions are also calculated. Higher voltage gradient (>30 V/cm) causes irreversible damage to the myocardium (Dosdall et al., 2010). Defibrillation energy is calculated using the formulation for energy type defibrillator, defined as $E = \frac{1}{2}CV^2$ where $C = 130\,\mu F$ and V is the required voltage DFT for the particular electrode configuration (Reek et al., 2017). In **Figure 5**, the electrode locations in the 3D volume model (cardiac-torso integrated), torso potential and cardiac potential just after defibrillation, and the myocardial voltage gradient for Apex-Posterior and Front-Back configurations are shown. Apex-Posterior is the default standard shocking electrode configuration used in WCD. Out of the two posterior electrodes, only one is functional at any given time. For our analysis, we have considered the right electrode as the shocking electrode. The cardiac potential reflects the state of complete cardiac depolarization, indicating effective defibrillation. The histogram representation of voltage gradient distribution gives an idea of the defibrillation pattern and efficacy.

2.3.3. Defibrillation Evaluation

Defibrillation threshold value reaching the critical mass is capable of stopping the VA but the shock magnitude itself has sufficient energy to damage the myocardium. We calculate the ventricular mass with a voltage gradient >30, >45, and > $60V/cm$, to assess possible myocardial damage. A new measure combining DFT and myocardial damage is formulated using probabilistic distribution and weighted KL divergence (KLD) (Mazumder and Sinha, 2021). We define an ideal distribution of myocardial voltage gradient after defibrillation by combining two exponential functions, one rising and the other decaying in amplitude for below and above of $5V/cm$, respectively. The distribution is defined such that the required critical mass defibrillation is achieved ideally around the 5 V/cm mark and the decay component diminishes for a value of the voltage

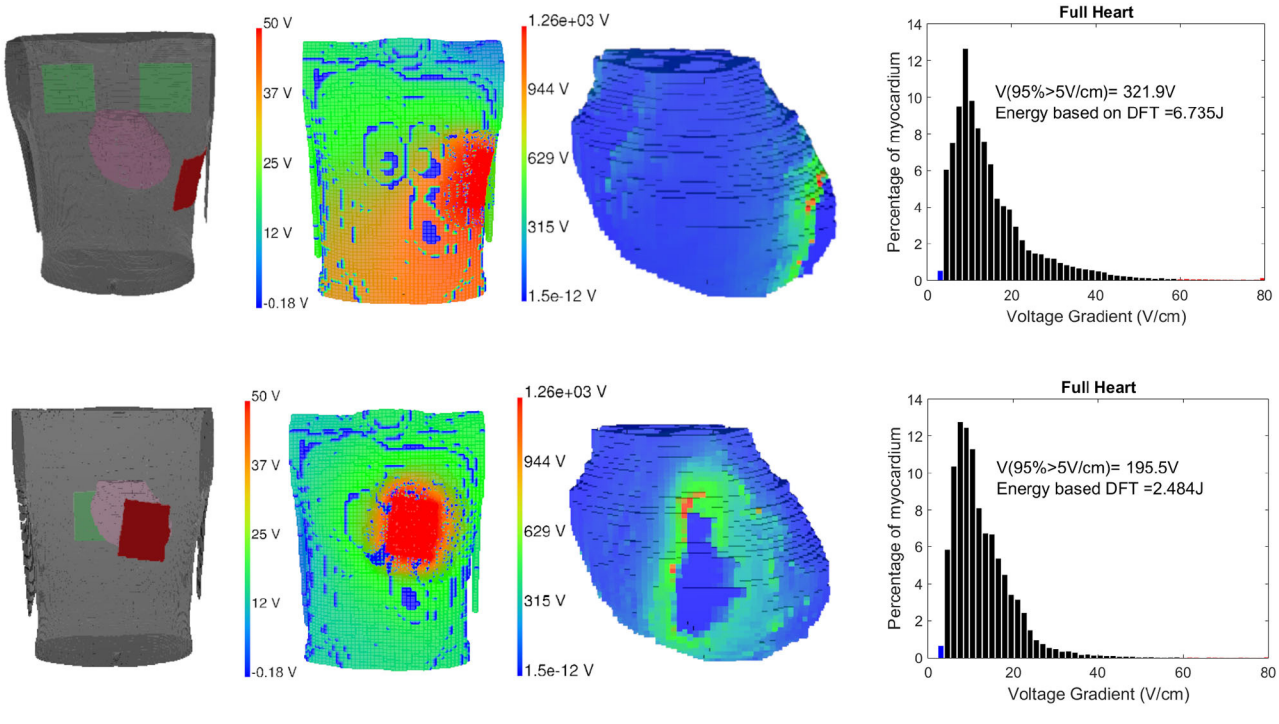

FIGURE 5 | Left to right: Electrode location, torso potential distribution just after defibrillation, cardiac potential indicating complete myocardial de-polarization state and defibrillation threshold (DFT) histogram representation for Apex-Posterior **(upper)** and Front-Back configuration **(lower)**.

gradient $(x) \geq 30V/cm$ (Zipes et al., 1975). Considering the modeled distribution as M and the defibrillation Voltage gradient distribution as C, the divergence or the information gain from M to C can be computed using KLD (Sekeh et al., 2013). Higher voltage gradient leads to greater myocardial damage, hence we have proposed the error measure reflecting the efficacy of the defibrillation (ED) using weighted KLD (WKLD) D_{KL}^{w}. Here, the weight $(W = x)$ allows the regions with a higher myocardial gradient to be penalized more in the computation of the error measure (ED). Lower the measure, lower is the difference in entropy between M and C, making the actual defibrillation function closer to the modeled or ideal one. This difference can be considered as the error between these two distributions and provide an informative efficacy measure (ED) combining both DFT and myocardial damage information expressed as follows:

$$WKLD(C) = D_{KL}^{w}(C||M) = \sum_{x=0}^{\infty} x.C(x)ln\frac{C(x)}{M(x)} \tag{7}$$

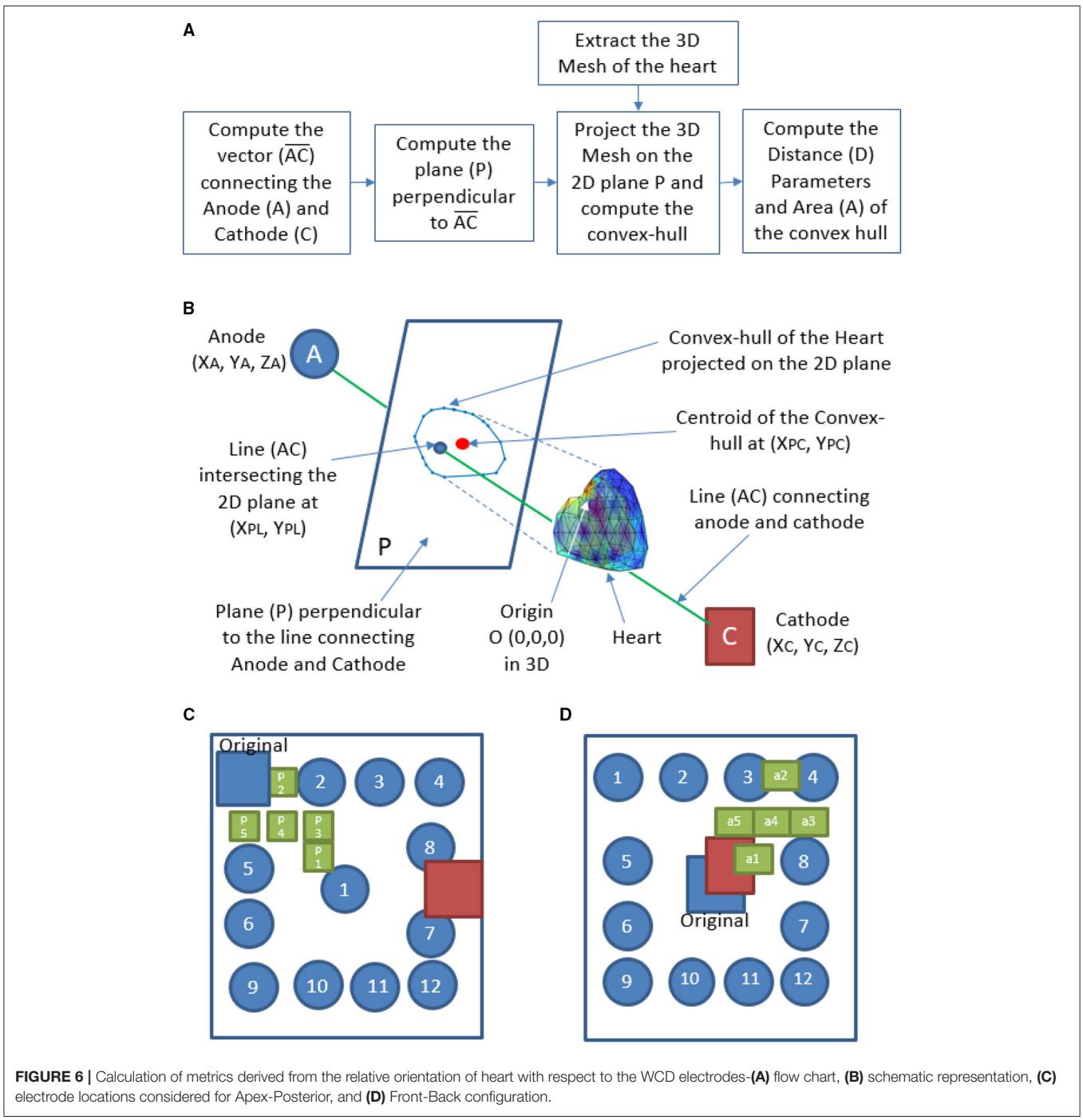

FIGURE 6 | Calculation of metrics derived from the relative orientation of heart with respect to the WCD electrodes-**(A)** flow chart, **(B)** schematic representation, **(C)** electrode locations considered for Apex-Posterior, and **(D)** Front-Back configuration.

Defibrillation threshold, energy, and WKLD values are calculated for two standard shocking electrode orientations (Apex-Posterior and Front-Back) as well as in between various plausible subspaces of the specified configurations. WCD electrodes are all of similar shape and size (0.1 m × 0.1 m). For the Apex-Posterior configuration, the "apex" electrode acting as the cathode is positioned at the mid-axillary line at the level of the 5*th* intercostal space, apex coordinates being (0.1420, –0.074, and 0.0224) with respect to 3D world co-ordinate center (0,0,0). Here the representation is (X,Y, and Z), where X is along the medio-lateral, Y is along anterio-posterior and Z is along the vertical direction, the units are in meter (m). The center (0, 0, and 0) is taken as the center of torso at the transverse plane aligned center to the heart. Anode electrodes are placed under the right clavicle at the 4*th* intercostal level (−0.099, 0.0744, and 0.1225). The cathode electrode is placed on the left precordium, in front of the chest at coordinates (−0.0301, −0.0744, and 0.0225), and an anode is placed on the back behind the heart in between the scapulas (−0.0301, 0.0744, and 0.0225) for the Front-Back configuration (shown in **Figure 5**). For each of these configuration, we create a subspace of probable electrode locations to study the variation in defibrillation efficacy. We examine the variation of the defibrillation energy (E) and WKLD for each such electrode locations to find the location which minimizes the WKLD, while having a low and acceptable value of E. For a given configuration (Apex-Posterior or Front-Back), the variation in the position of the anode, leads to a different view point from which the electric field is propagated through the myocardium. Such change in the relative view point, with respect to the orientation of the heart, is quantified using certain distance and area metrics. In total, four metrics are defined namely, three distance metrics $D1, D2, D3$, and one area metric $A1$. The flow chart of the computation is given in **Figure 6A**. A schematic representation of the axes, planes, and projections used to define the metrics is shown in **Figure 6B**. $D1$ is the perpendicular distance from the origin of the world 3D coordinate "O" to line "AC" connecting the center of the anode and cathode. $D2$ is the distance between "O" and the center of the anode "A." To compute the remaining metrics, the structure of the 3D heart is projected on the plane perpendicular to the line connecting the anode and cathode. The vector $\vec{AC}$ is computed using the centers of the anode (X_A, Y_A, Z_A) and cathode (X_C, Y_C, Z_C), which defined the view direction of the electrodes. Next, a projective transformation matrix (T_O) is derived (given by Equation 8) to project any data point from the world 3D coordinate to a plane (P) perpendicular to the vector $\vec{AC}$.

$$T_O = \begin{bmatrix} m_{11} & m_{12} & m_{13} & 0 \\ m_{21} & m_{22} & m_{23} & 0 \\ m_{31} & m_{32} & m_{33} & 0 \\ 0 & 0 & 0 & 1 \end{bmatrix} \tag{8}$$

The m_{ii} indicates the rotation and scaling related parameters and the entries in the last row and last column, except m_{44} are zeros indicating no translation and the scenario of orthographic projection (Hu et al., 2014). Recently, the orthographic projection was also used to analyze the structure of various parts of the human heart (Sherknies et al., 2003; Liu et al., 2019). We have considered such a projection to preserve the relative distances between a pair of points from the 3D space to the plane, which is required for the computation of the distance and area metrics on the plane P. A 3D mesh of the heart is created and then the V vertices of the mesh, with coordinates $(v^i_{xh}, v^i_{yh}, v^i_{zh})$, $\forall 1 \leq i \leq V$, are projected to the 2d plane P using the transformation matrix T_O as shown in Equation (9).

$$\begin{bmatrix} v^i_{xp} \\ v^i_{yp} \\ v^i_{zp} \\ 1 \end{bmatrix} = T_O \times \begin{bmatrix} v^i_{xh} \\ v^i_{yh} \\ v^i_{zh} \\ 1 \end{bmatrix} \tag{9}$$

The vertices of the 3D mesh are used as homogeneous form $([v^i_{xh}\ v^i_{yh}\ v^i_{zh}\ 1]^T)$, where T denotes the transpose. The projected coordinates $[v^i_{xp}\ v^i_{yp}]^T$ lies on the 2D plane P perpendicular to the view vector $\vec{AC}$. A convex-hull (C_H) is derived using the 2D co-ordinates $[v^i_{xp}\ v^i_{yp}]^T$ on the plane P. The centroid of the C_H is computed as X_{PC}, Y_{PC}, and the line AC intersects the plane P (atX_{PL}, Y_{PL}) as shown in **Figure 6B**. The metric $D3$ is the distance between (X_{PL}, Y_{PL}) and X_{PC}, Y_{PC}, and the metric A is the area of the convex hull.

Along with the standard Apex-Posterior and Front-Back configuration, 12 similar orientations are recreated by placing the anode electrode in different locations and recomputing the mesh and biophysical simulations, keeping the cathode fixed. The top-most right location being (–0.1025, 0.0744, and 0.1025) and bottom left location being (0.1025,0.0744, and –0.1025). The other 10 electrodes are distributed in a symmetrical pattern with a 0.05 m gap in both "X" and "Z" axes. From the findings of these 12 new locations for each configuration, a finer distribution is studied by introducing 5 separate electrode locations in places translating to a better defibrillation index. The electrode sub-locations throughout the torso space are shown in **Figures 6C,D**.

3. RESULTS

Initially, we present the results regarding the accuracy of detection of the shockable rhythms based on two datasets namely, CUDB and the VFDB. Then, the characteristics of the hemodynamics obtained from the cardiovascular simulation model, during both shockable and non-shockable segments, are given. Finally, results on the defibrillation metrics are presented for different electrode positions in two configurations namely, Apex-Posterior and Front-Back.

3.1. Detection of Shockable Rhythm

This sub-section details the performance of the proposed deep learning classifier in identifying VT, VF, and other classes on both CUDB and VFDB datasets based on a 5-fold cross-validation approach. The ECG measurements from all subjects, as available in the original dataset, are first segmented into small non-overlapping windows of equal length. Every single window is considered as an independent training or test instance for the

classifier. The objective of this study is not only to measure the classification accuracy but also to estimate the optimum window length required for robust classification performance. **Table 2** summarizes the classification performance of the proposed CNN-LSTM architecture on the CUDB and the VFDB datasets on different window lengths of 2, 4, 6, and 8 s. Here, we report the median classification performance in terms of precision, recall, and F1-score of detecting various target classes across 5-fold cross-validation.

Precision, recall, and F1-score are popularly used for measuring the performance of a classifier. In theory, precision measures the number of correct positive predictions, and recall measures the number of correct positive predictions made out of all positive predictions that could have been made by the classifier. For a multi-class classifier, these two are defined for every target class in terms of true positive (TP), true negative (TN), false positive (FP), and false negative (FN), across all classes in one vs. all method:

$$precision = \frac{TP}{TP + FP} \qquad recall = \frac{TP}{TP + FN} \tag{10}$$

F1-score is a method of measuring the classification accuracy based on the combined effect of precision and recall. Mathematically, it measures the harmonic mean of precision and recall as follows:

$$F1 = 2\frac{(precision * recall)}{precison + recall} \tag{11}$$

As mentioned in Section 2.1, both our target datasets are largely imbalanced. Among the 3 different classes (VT, VF, and other), the instances corresponding to the other conditions occupy the major portion of both CUDB and VFDB datasets, whereas the number of instances related to VT is the least in number. It can be observed from **Table 2** that the overall F1-score of detecting various classes tends to improve with the increased window-length and the optimum performance is achieved at a window-length of 8 s. It is to note that the overall signal quality of the CUDB datasets is better than the VFDB dataset, which contains many noisy instances where the classifier does not yield reliable performance. Hence, the proposed classifier produces a better classification accuracy on the CUDB dataset compared to VFDB.

Table 2 summarizes the classification performance of our proposed approach on the CUDB and the VFDB databases. Similar to the existing approaches in the literature, the classification approach is evaluated by applying cross-validation on the entire dataset and the accuracy is reported against a fixed window length. However, this approach does not reveal the utility of the classifier in detecting the onset of a VT or a VF event on a long data stream recorded from a subject. Hence, in the second part of our experiment, we perform a detailed subject-wise analysis.

Typically, a shock is applied within 32 s of detecting a VT or a VF event. Hence, in this stage we evaluate our classification performance on every 32 s long data segment. The decision window is fixed at 8 s and a final decision corresponding to a 32 s data stream is made based on majority voting on the prediction labels on the continuous 8 s long windows within the 32 s long data stream. For the subject-wise analysis, we completely separate the train and test subjects on both datasets considered in this article. About 80% of all subjects form the training set and the remaining 20% of the subjects form the test set. The

TABLE 2 | Classification performance of the proposed deep learning classifier on CUDB and VFDB dataset (*P* = precision, *R* = recall, *F*1 = *F*1 score).

	2 s			4 s			6 s			8 s		
Target label	***P***	***R***	***F*1**	***P***	***R***	***F*1**	***P***	***R***	***F*1**	***P***	***R***	***F*1**
VF (CUDB)	0.96	0.92	0.94	0.94	0.99	0.97	0.97	0.96	0.96	0.97	0.98	0.98
VT (CUDB)	0.89	0.66	0.76	0.67	0.47	0.55	0.50	0.83	0.62	1.00	0.69	0.82
Others (CUDB)	0.98	0.99	0.99	1.00	0.99	0.99	1.00	0.99	0.99	0.99	1.00	1.00
VF (VFDB)	0.73	0.81	0.77	0.75	0.85	0.80	0.85	0.70	0.77	0.82	0.78	0.80
VT (VFDB)	0.80	0.69	0.74	0.78	0.70	0.74	0.70	0.83	0.76	0.74	0.81	0.77
Others (VFDB)	0.99	0.99	0.99	1.00	0.99	0.99	0.99	1.00	0.99	1.00	0.99	1.00

TABLE 3 | Subject-Wise classification performance overlapping windows of 8 s on CUDB and VFDB dataset (*P* = precision, *R* = recall, *F*1 = *F*1 score).

Overlappingwindow	0%			25%			50%			75%		
Target label	***P***	***R***	***F*1**	***P***	***R***	***F*1**	***P***	***R***	***F*1**	***P***	***R***	***F*1**
VF (CUDB)	0.93	0.96	0.94	0.98	0.98	0.98	0.98	1.00	0.99	0.99	0.99	0.99
VT (CUDB)	0.95	0.60	0.74	0.98	0.75	0.85	0.98	0.90	0.94	0.97	0.92	0.90
Others (CUDB)	0.98	0.98	0.98	1.00	0.99	0.99	1.00	1.00	1.00	1.00	1.00	1.00
VF (VFDB)	0.82	0.78	0.80	0.90	0.82	0.86	0.97	0.90	0.93	0.99	0.90	0.93
VT (VFDB)	0.71	0.80	0.75	0.77	0.89	0.83	0.88	0.94	0.91	0.80	0.94	0.85
Others (VFDB)	1.00	0.98	0.99	1.00	1.00	1.00	1.00	1.00	1.00	1.00	1.00	1.00

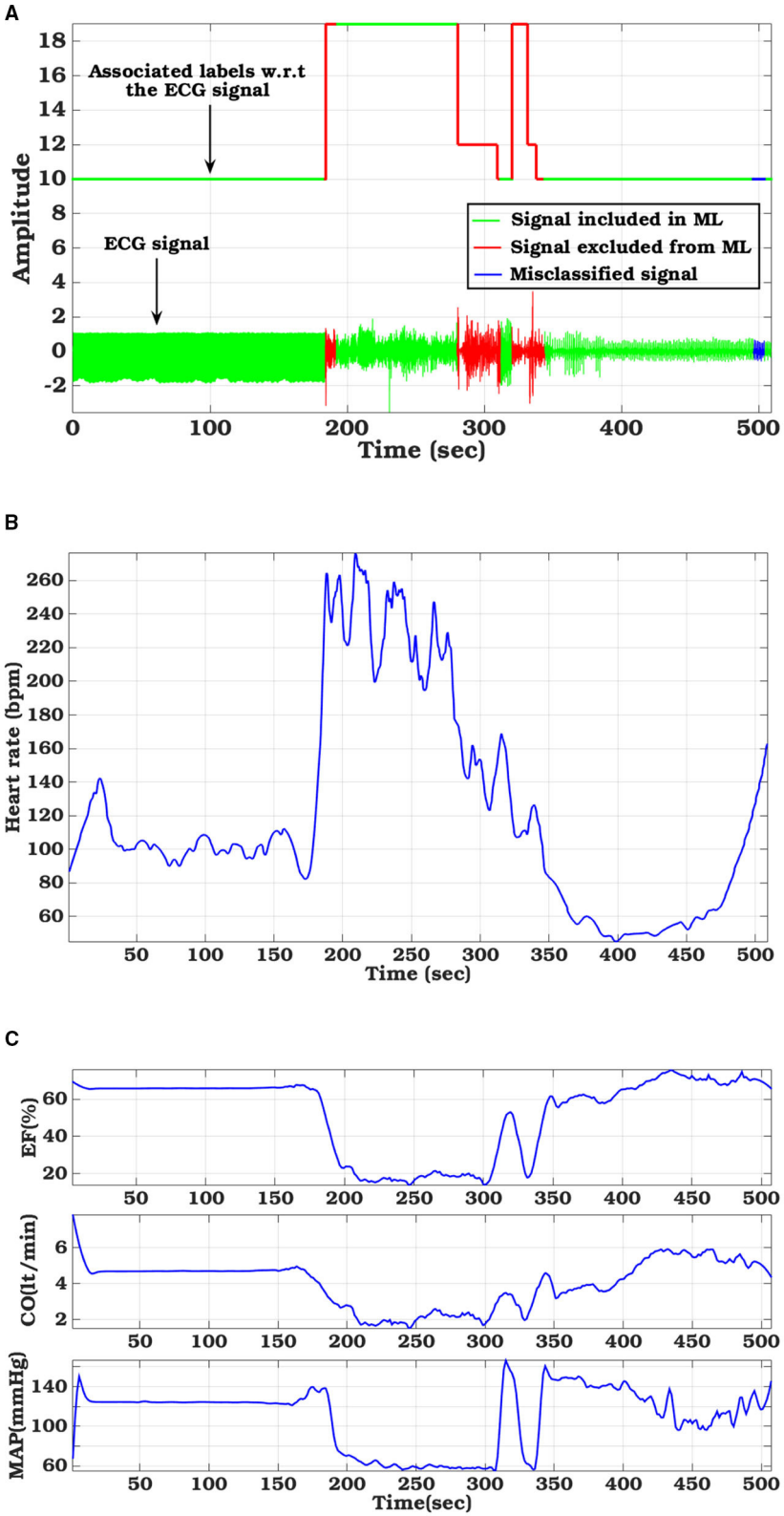

FIGURE 7 | Hemodynamic parameter variations tuned with sample ECG signal from CUDB database: **(A)** ECG signal with ground truth label and classifier derived labels, **(B)** Variation in Heart Rate, **(C)** left-ventricular functional metrics (Ejection fraction, Cardiac output, and Mean arterial pressure).

deep learning model is retrained on the new training set and is individually applied on every test subject for prediction. Different hyper-parameters of the neural networks are kept unchanged. To analyze the detection accuracy of the onset of an event, we applied overlapping on the successive 8 s-long windows, in a 32 s long data-stream. **Table 3** shows the impact of overlapping in classification performance based on non-overlapping, 25, 50, and 75% overlapping. Depending upon the amount of overlapping, a 32 s long data stream contains 4, 5, 7, and 13 data windows.

3.2. Hemodynamic Parameter Variations

The hemodynamic module takes ECG signal as the driving parameter and based on the morphological variation, apparent during VF/VT, adjusts the left ventricular compliance, as explained in Section 2.3.1. **Figure 7A** shows particular instances of ECG waveform variation along with the ground truth label and the performance of our proposed classifier. Heart rate (**Figure 7B**), calculated from the ECG signal is also displayed. Based on the detected VF/VT regions, compliance is modulated. Left ventricle compliance, as shown in Equation (2), dictates the pressure-flow dynamics of the systemic circulation. As C_{lv}, heart rate, and flow parameters vary due to change in cardiac contractility, there is a marked effect on inherent cardiac parameters like ejection fraction (EF), cardiac output (CO), mean arterial pressure (MAP), etc. (**Figure 7C**). These parameters are of paramount medical importance in analyzing cardiac function. LVEF is the most important factor in stratifying SCD. EF, as captured from the computational model, shows a marked reduction during VF/VT period, which if left uncorrected will lead to SCD. In the dataset used, the VF episodes were occurring randomly for a short duration along with normal sinus rhythm. The hemodynamic module adapts to these changes in conduction dynamics and computes left ventricle information in real-time, without any additional delay. Along with EF, CO and MAP also follow pathological trends observed during VF/VT episodes. MAP calculated takes into account the change in cardiac contractility, heart rate variation, and also change in systemic resistance, regulated through a baroreflex mechanism. Hence, these observations are not just reflections of the initiation of pathological conditions, some level of modulation offered by the Central nervous system in an attempt to regularize the hemodynamic turbulence is also encoded in it. This trend is especially evident in post-VF episodes, where the ground truth label is normal but there are fluctuations in MAP trying to maintain the homeostasis.

3.3. Defibrillation Metrics

The results provided for defibrillation efficacy computation are an extension of our previously published work (Mazumder and Sinha, 2021), where we compared four different shock electrode configurations, naming Apex-Anterior, Apex-Posterior, Side-Side, and Front-Back, and found that the unconventional Front-Back configuration yielded better defibrillation efficacy compared to the other configurations. In this work, we extend the concept of varying the electrode location in a sub-plane around the Apex-Posterior and Front-Back configuration to analyze the effect of inter-electrode distance and effect of electrode location in overall defibrillation efficacy. **Table 4** tabulates 4 different distance metric vectors along defibrillation efficacy metrics in terms of WKLD and Energy for 13 locations in Apex-Posterior and 13 Front-Back configurations. The configurations are shown in **Figures 6B,C**. It is interesting to note that apart from the original standard location, there are other locations that reports even lower WKLD and energy value, pointing to location where fibrillation is more efficient. For Apex-Posterior configuration, locations 2, 5 coinciding with the upper right quadrant, and for Front-Back, locations 3, 4, and 8, coinciding with the upper left quadrant shows the most decreased WKLD and DFT energy trend. Similarly, electrodes lying in lower torso quadrants show increased defibrillation energy. For defibrillation, an optimal position is defined as the position of anode and cathodes that allow maximum current path. Current conduction, apart from

TABLE 4 | Defibrillation efficacy analysis on varying electrode location (loc-location, O-original, E-Energy, J-Joule, the units of $D1, D2, and\ D3$ are meter (m) and $A1$ is m^2).

	Apex-Posterior						Front-Back					
loc	D1	D2	D3	A1	WKLD	E(J)	D1	D2	D3	A1	WKLD	E(J)
O	0.096	0.099	0.053	0.009	11.085	6.735	0.052	0.030	0.057	0.009	4.854	2.483
1	0.084	0.050	0.062	0.007	24.256	5.283	0.083	0.103	0.069	0.010	5.982	11.906
2	0.066	0.053	0.056	0.009	7.578	5.847	0.077	0.053	0.068	0.010	5.827	5.595
3	0.088	0.053	0.064	0.007	19.168	4.800	0.040	0.053	0.023	0.008	4.664	2.471
4	0.137	0.103	0.060	0.008	29.414	13.121	0.052	0.103	0.033	0.009	4.443	4.882
5	0.098	0.103	0.054	0.010	8.274	9.399	0.083	0.103	0.069	0.010	6.583	9.615
6	0.098	0.103	0.054	0.010	46.953	25.437	0.083	0.103	0.069	0.010	5.982	11.906
7	0.137	0.103	0.060	0.008	126.765	43.836	0.052	0.103	0.033	0.009	20.696	11.143
8	0.137	0.103	0.060	0.008	55.518	16.087	0.052	0.103	0.033	0.009	3.597	3.530
9	0.098	0.103	0.054	0.010	57.113	36.115	0.083	0.103	0.069	0.010	15.478	18.736
10	0.066	0.053	0.056	0.009	60.734	29.313	0.077	0.053	0.068	0.010	16.600	14.800
11	0.088	0.053	0.064	0.007	85.297	33.501	0.040	0.053	0.023	0.008	20.777	13.214
12	0.137	0.103	0.060	0.008	92.375	49.465	0.052	0.103	0.033	0.009	21.686	16.757

TABLE 5 | Defibrillation efficacy analysis on upper torso concentrated sections, M1 = $\%myo > 30V/cm$, M2 = $\%myo > 45V/cm$, M3 = $\%myo > 60V/cm$, (loc-location, O-original, E-Energy, J-Joule, the units of $D1, D2,$ *and* $D3$ are meter (m) and $A1$ is m^2).

loc	D1	D2	D3	A1	DFT(V)	E(J)	WKLD	M1	M2	M3
p1	0.066	0.052	0.056	0.009	268.5	4.687	8.099	6.092	0.868	0.129
p2	0.042	0.030	0.067	0.008	269.9	4.734	10.535	6.568	1.007	0.138
p3	0.066	0.052	0.056	0.009	272.0	4.809	6.204	4.756	0.564	0.102
p4	0.083	0.075	0.053	0.009	326.9	6.944	5.340	4.584	0.576	0.111
p5	0.098	0.102	0.053	0.009	387.3	9.750	5.721	5.109	0.612	0.102
a1	0.040	0.052	0.022	0.008	159.0	1.642	3.260	1.556	0.252	0.0667
a2	0.046	0.075	0.029	0.008	205.3	2.740	4.792	3.177	0.646	0.182
a3	0.051	0.102	0.032	0.009	255.2	4.234	3.745	2.232	0.611	0.249
a4	0.046	0.075	0.029	0.008	184.4	2.209	4.095	2.643	0.405	0.118
a5	0.040	0.052	0.022	0.008	173.1	1.946	3.798	2.174	0.342	0.104

the geometry of electrodes and voltage applied, also largely depends on the trans-thoracic Impedance (TTI) and intra-thoracic impedance. TTI is dependent on numerous factors like torso geometry, respiration rate and phase, electrode size, etc. and varies from person to person while intra-thoracic impedance, dictated by thoracic organs and tissue may remain fairly constant in normal physiology but gets changed drastically in cardiac conditions like heart failure (Wang, 2007). As we are considering only a single subject scan data, TTI is assumed to be constant. So the current conduction path is mostly a function of a distance vector and tissue conductivity in the thoracic chambers. Out of the four distance metrics defined, D1 and D3 values are less in the Front-Back configuration as compared to Apex-Posterior. Metric A1 and D2 do not show much variations in changing the electrode locations. It is interesting to note that as the electrodes are organized throughout the torso in a geometric fashion, electrodes in the upper and lower quadrants have fairly equivalent distance metrics calculated from the center of the heart, yet, defibrillation energy required in some quadrants is comparatively higher than others. This is mainly due to the high conductivity indices of tissues in the upper torso, decreasing the impedance in the current pathway, and paving the way for efficient defibrillation. In **Table 5**, a more concentrated torso area is analyzed. Based on the deduction from **Table 4** on the possible optimal electrode location, 5 new electrode locations both for Apex-Posterior and Front-Back configurations are analyzed. The distance metrics, DFT voltage, defibrillation energy, WKLD value, and Percentage of myocardial volume (%myo) above critical gradient capable of causing myocardial damage are shown.

4. DISCUSSION

In this article, we present a computational pipeline integrating shockable rhythm detection and shock voltage field optimization for evaluation, testing, and personalization of a WCD design and operation.

In general, machine learning classifiers like an SVM or a random forest can be successfully deployed to predict cardiac events, where the clinical markers/ features are well-known and are relatively simple to compute from the ECG signals (Figuera et al., 2016). However, deep learning approaches are typically preferred in large scale analysis where the disease-specific markers are not very easy to compute in terms of numeric features to train a classifier. A deep learning approach can also deal with the internal noise present in the signal. Both CNN and LSTM based deep architectures have been successfully used in prior literature (Silva et al., 2019). Finding the optimum window length for decision making is an important parameter in biomedical classification problems. In general, a shorter window is preferred due to low latency in inference. However, a small window may not always contain the discriminating markers for accurate decision making. On the other hand, a longer window length may ensure the presence of a discriminating marker. However, there remains a risk of latency in inference which may delay in applying the shock. We evaluated classifier performance on varying the window length from very small windows of 2 s to larger windows of 8 s. As tabulated in **Table 2**, there is a trend of improved precision, recall, and F1 score for VF, VT, and all other rhythms were grouped as non-shockable with the increase in window length. Our proposed CNN-LSTM architecture achieves a sensitivity of 96.10%, specificity of 98.34% for shockable rhythms (VF and VT) detection on a very small window size of 2 s for CUDB data and sensitivity of 94.68%, specificity of 92.77% for the VFDB dataset. For 8-s window size, which is the standard size reported in many prior arts, our algorithm attains sensitivity of 99.21%, specificity of 99.68% for the CUDB dataset and sensitivity of 98.56%, specificity of 99.08% for the VFDB dataset. As per guidelines established by the American heart association (AHA) (Kerber et al., 1997), a sensitivity (Se) higher than 90% for shockable rhythms, and specificity (Sp) higher than 95% for non-shockable rhythms is the benchmark for WCD detection algorithms and our proposed method exceeds the benchmark requirement. Also while comparing with the state-of-the-art, as tabulated in **Table 6**, our sensitivity-specificity values are closely comparable to the highest accuracy reported by Jeon et al. (2020) for WCD applications. Although our reported accuracy is fractionally lower, it is important to note that apart from 8 s standard window-based classification, we have also implemented an overlapping window-based detection that actually spans over 32 s long data that may contain up to 13 windows depending upon the amount of overlapping.

Table 3 shows the classification performance on the ECG data-stream obtained on individual test subjects. Here, the training and the test data were created based on different subjects. The decision was made by combining multiple 8 s long windows in a 32 s time frame. Just like any other time signal, an ECG data-stream is not entirely stationary. Breaking a 32 s long block into multiple non-overlapping windows may cause information loss at the junction of two consecutive windows. Hence, we analyse the impact of overlapping windows by a applying various percentage of overlapping starting with non-overlapping to 25, 50, and 75% of overlapping. The number of 8 s long windows increases with the increased overlapping

TABLE 6 | Comparison of existing algorithms for detection of shockable rhythms.

Reference	Brief approach	Dataset used	Accuracy reported
Figuera et al. (2016)	An ML-algorithms with built-in feature selection capabilities were used to determine the optimal feature subsets for classification. Patient-wise bootstrap techniques were used to evaluate algorithm performance on public database	Validated on the VFDB and the CUDB datasets	Sensitivity = 96.6%, Specificity = 98.8%
Kwon et al. (2018)	The authors proposed an embedded microcontroller where an ECG sensor is used to capture, filter and process data, run a real-time VF detection algorithms developed a VF detection algorithm, via Time Delay (TD), based on phase space reconstruction.	Open access MIT-BIH dataset	Sensitivity = 96.56%, Specificity = 81.53%
Krasteva et al. (2020)	A deep convolutional network was proposed and studied on Holter ECG recordings for detection of shockable and non-shockable rhythms. The impact of various network hyper-parameter tuning was reported	The data used in the study contains a wide variety of non-shockable and shockable rhythms from two sources: public Holter ECG databases from continuously monitored patients with ventricular arrhythmias, and OHCA databases recorded by AEDs from patients in cardiac arrest.	For analysis on short windows (2 s): Sensitivity 97.6% =, Specificity = 98.7%. For analysis on long windows (5 s) : Sensitivity = 99.6 % Specificity = 99.4 %
Jeon et al. (2020)	A deep architecture comprising convolutional layers and recurrent networks for classification of ECG beats. Furthermore, a lightweight model is proposed with fused RNN for speeding up the prediction time on central processing units (CPUs)	The authors used 48 ECGs from the open access MIT-BIH Arrhythmia Database, and 76 ECGs were collected with S-Patch devices developed by Samsung SDS	For the baseline model: Sensitivity = 99.86%, Specificity = 98.31% for the light-weight model: Sensitivity = 99.92%, Specificity = 99.11%
Our proposed approach	A CNN-LSTM architecture is proposed for classification of VF, VT and other rhythms from ECG	The approach is evaluated on CUDB and VFDB datasets	Detection rate of shockable rhythms (VF and VT) on CUDB: very small windows (2 s) Sensitivity = 96.10%, Specificity = 98.34% for large windows (8 s) Sensitivity = 99.21%, Specificity = 99.68% Detection rate of shockable rhythms (VF and VT) on VFDB: very small windows (2 s) Sensitivity = 94.68%, Specificity = 92.77% for large windows (8 s) Sensitivity = 98.56%, Specificity = 99.08%

percentage which is able to capture more detailed features from the data stream. **Table 3** clearly indicates that there is a positive impact on classifier accuracy due to overlapping. Overall classification performance in terms of precision, recall, and F1-score significantly improves over the non-overlapping scenario and reaches the optimum performance when a 50% overlapping is applied between successive windows.

A completely novel aspect of our proposed computational pipeline is the capability of generating hemodynamic parameters during VA. SCD though initiated by different causes is ultimately governed by the left ventricle EF (Sun et al., 2014). ICD/WCD requirement stratification is also modulated based on left ventricle functions (Arts et al., 2005). As such, only understanding the electrical aspects of cardiac functioning through arrhythmia propagation, without giving due importance to its mechanical functioning, results in a partial understanding of the disease etiology and defibrillation response. The proposed *in-silico* cardiac model captures the flow-pressure-volume relationship for each cardiac chamber and for all cardiac phases, thus providing a holistic understanding of the pathophysiological changes occurring as VF/VT initiates, propagates, and subsequently gets terminated naturally or through the application of shock. As the hemodynamic module is controlled *via* ECG signals (either simulated or captured in real-time or used from database), real-time phase matched comparative hemodynamic metrics like cardiac output, mean arterial pressure, cardiac compliance, ejection fraction, etc. can be studied with ECG signal variations due to arrhythmia or any other cardiac disease that changes the ECG morphology, like myocardial ischemia. Another important rationale for introducing the hemodynamic module is evident in **Figure 7**. The ECG signals may be misclassified at several small window locations, however, this has no impact on the outcome of hemodynamic variables as the hemodynamic parameters are not dependent on the classified signal annotations but reflect the true physiological changes during arrhythmic events. The cardiac compliance value gets modulated through heart rate extracted after ECG processing along with physiologically matched mathematical derivations of systemic and pulmonary resistance, aortic and chamber compliance etc. So even if the

classification algorithm fails for any particular window, by judging the hemodynamic parameter variations, initiation of VA can be well speculated and analyzed offline.

We have tabulated some common hemodynamic parameters like CO, EF, MAP, end-systolic pressure volume ratio (ESPVR), and end-diastolic pressure volume ratio (EDPVR) for shockable and non-shockable rhythms utilizing labels and ECG signals from CUDB and VFDB datasets. As indicated in **Table 7**, there is a marked difference between VA hemodynamic parameters compared to other non fatal group. 'Other'class compiled from VFDB and CUDB datasets are not healthy but agglomeration of different supra-ventricular, normal, atrial fibrillation type rhythm grouped as non-shockable. CO, indicative of the volume of blood pumped by the heart in a cardiac cycle, gets heavily reduced during VA, indicating LV failure. EF also gets lowered to a dangerous level indicating impaired LV functionality and subsequent heart failure, if left untreated. The MAP also drops significantly due to low CO. ESPVR is commonly used as a marker for cardiac contractility (Yaxin et al., 2017) and the tabulated value clearly shows the reduction in LV contractility under VA conditions. Similarly, EDPVR is a marker for chamber compliance (reciprocal relation) and is used to judge ventricular stiffness (Yaxin et al., 2017), which during our simulation, also followed a medically correlated trend. The hemodynamic insights not only provides a better understanding of the disease progression but also provide an idea about the operable timeline, to take necessary corrective action in case of heart failure trends. In real time operation of WCD, implementing such a hemodynamic module might not be practical in the embedded circuit used for arrhythmia detection. However, a cloud based implementation of such modules could aid physicians better, in assessing overall cardiac functionality during VF/VT episodes and/or other arrhythmic episodes and may help in generating revised treatment plans with a more subject-specific personalized focus.

In **Table 4**, where we tabulate the variations in electrode location and corresponding defibrillation metric, apart from the trend established in terms of optimized electrode positioning, additional important insights can be inferred. For both Front-Back and Apex-Posterior configuration in various sub spacing, the minimum energy requiring location is not the location that reports the minimum WKLD value. As WKLD integrates both DFT voltage and myocardial damage probability, it becomes quite evident that lower defibrillation energy does not necessarily suffice to minimum cardiac tissue damage. Overall, in all possible location variations, the Front-Back configuration results in better efficacy. Judging by the WKLD value, the most optimal location is "location 8" in Front-Back (FB) configuration and location 2 in Apex-Posterior (AP) configuration, while the least effective location is location 12 and location 7 for Front-Back and Apex-Posterior, respectively. The DFT voltage and % myocardium $> 45V/cm$ and $>60V/cm$ for location 8 (in FB) and 2 (in AP) are 233V, 0.46, 0.191 and 299.9V, 0.72, 0.12, respectively, while for location 12 (in FB) and 7 (in AP), the respective metric values are 507.7V, 1.884, 0.5189 and 821.2, 19.60, 12.67. As observed, the far-away electrode locations require excessive DFT voltage, associated with a greater extent of myocardial damage. The observations from these metrics can indicate locations to avoid while placing electrodes and then can guide areas where optimal defibrillation efficacy can be expected.

TABLE 7 | Hemodynamic parameter variation for shockable and non-shockable pathological conditions.

Parameters	Shockable (VF/VT)	Non-shockable
CO (lt/min)	2 ± 0.5	4.5 ± 1.2
EF (%)	25 ± 7.5	60 ± 5
MAP (mmHG)	60 ± 15	118.9 ± 20
ESPVR	0.36 ± 0.32	2.5 ± 0.5
EDPVR	0.4 ± 0.29	0.16 ± 0.04

In **Table 5**, the myocardial voltage gradient values are also generated to provide an indication of the relation between DFT voltage, energy, and distance metric in the specific torso area where optimal defibrillation pattern is expected, as deduced from **Table 4**. Location p4 in Apex-Posterior and a1 in Front-Back provided the least WKLD value and negligible probability of myocardial damage. Judging 18 locations each for both the configuration, Location 2 and a1 provide the best outcome in Apex-Posterior and Front-Back configurations, respectively. **Figure 8** represents the myocardial voltage gradient histogram for location a1 (in FB), 2 (in AP) and 12 (in FB), 7 (in AP) as two best and two least desired electrode configurations, respectively. In the concentrated areas, situated in the upper thorax, the intra-thoracic conductivity parameters for both Apex-Posterior configuration as well as Front-Back configurations are fairly constant, the current path has to navigate mostly through the skin, skeletal structure, and lungs region. However, due to variation in the anode location, metric D1 and D3 are relatively shorter in Front-Back as compared to Apex-Posterior configurations, yielding a better current pathway and effective defibrillation.

Use of computational pipeline for shock distribution analysis and deriving metrics that can be incorporated in WCD vest and shock generating circuit for optimized defibrillation is a unique solution aimed at providing WCD shock efficacy validation and personalization. Such concepts have not been proposed earlier for WCD and have the potential to enhance conventional WCD functioning.

In this article, we have integrated two different aspects of WCD working in a biophysical computational framework for better understanding and validation of WCD performance both in terms of arrhythmia detection and shock efficacy computation through the DFT principle. While the hemodynamic module of the cardiac *in-silico* model provides additional insights into pathophysiological changes in cardiac functionality during arrhythmic episodes, the 3D volume conductor cardiac model and FE analysis with changeable electrode configuration provided an understanding of the defibrillator efficacy parameter variation with change in shocking electrode configuration and location. This is particularly useful for obese patients or pediatric users where the use of standard configuration may provide successful defibrillation but at the cost of higher myocardial damage. As our proposed

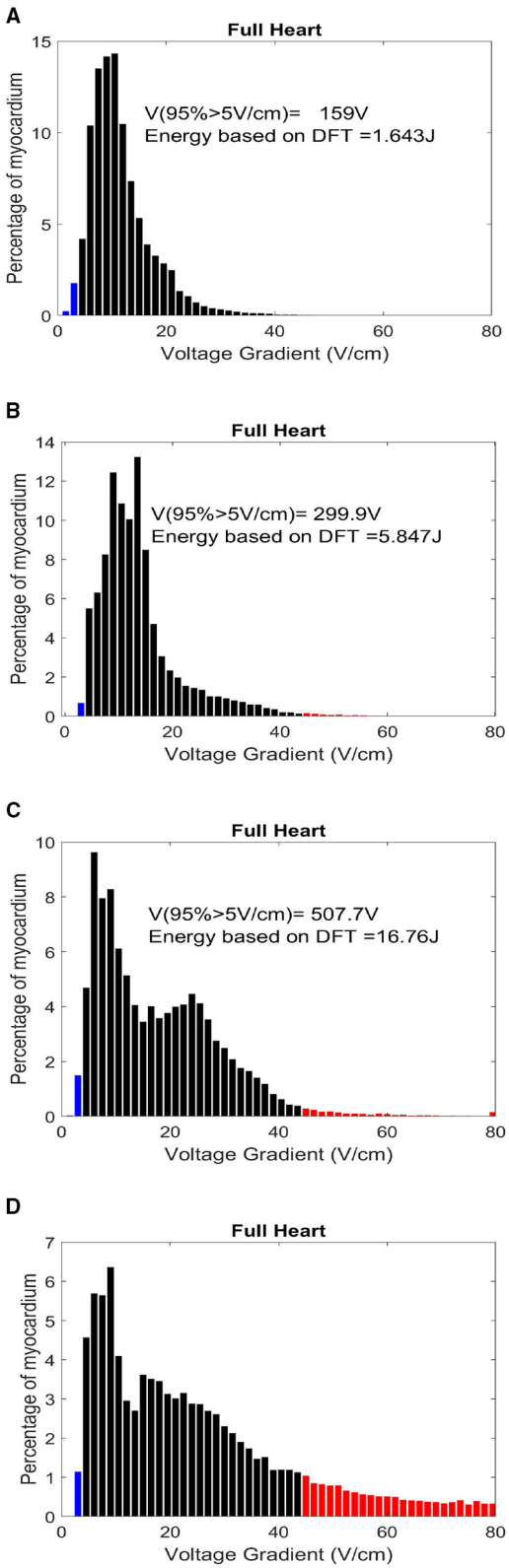

FIGURE 8 | Histogram distribution of myocardial potential gradient for location **(A)** a1-FB, **(B)** 2-AP, **(C)** 12-FB, and **(D)** 7-AP. The red zones indicate a potential gradient harmful enough to create permanent myocardial damage.

model incorporates a monodomain modeling approach rather than a bi-domain, the realistic myocardial tissue behavior during defibrillation is not captured. However, as we do not intend to calculate absolute defibrillation response in myocardial tissue but aim to use the platform to provide an estimate by which the intra-thoracic field strength over the myocardium can be compared given differing electrode configurations, the computationally less extensive monodomain model is suitable. A particular drawback of this study is that the defibrillation efficacy simulation is based on single subject data and MRI data for multiple subjects with varying torso geometry would help to consolidate the electrode location variations observed. In future, for the classification of shockable rhythm, we would integrate the proposed algorithm in an embedded platform to make it suitable for real-time applications.

5. CONCLUSION

In this article, we present a computational pipeline for WCD performance validation, both in terms of shockable arrhythmia classification and optimal electrotherapy generation. We also derived some useful insights regarding the physiological changes in cardiac hemodynamics during Ventricular arrhythmic patterns leading to compromised LV functions. In the classification domain, our proposed CNN-LSTM architecture detection accuracy surpassed AHA recommended accuracy. The inclusion of the novel overlapping window approach guarantees a minimum loss of vital information in between detection windows, increasing the reliability of detection.

Cardiac defibrillators are lifesaving therapeutic devices with potentially harmful capacity if not tuned properly. With the growing demand for WCD, the creation of a personalized energy distribution model based on a patient's anatomy, rather than a 'one size fits all' approach, is the need of the hour. Our proposed optimal electrotherapy assessment using biophysical modeling compares the efficiency of standard (Apex-Posterior) and non-standard (Front-Back) WCD electrode placement along with different plausible electrode locations variation throughout the torso, demonstrating significant differences in defibrillation efficacy associated with different strategies. The proposed approach of tuning defibrillation parameters coupled to a physical cardiac model that provides insights regarding the hemodynamic and electrophysiological changes at initiation or after the termination of an arrhythmic event could enable therapeutic device validation and testing, better patient stratification for ICD or similar invasive procedures, and creating subject-specific treatment plan providing a personalized approach toward cardiac care.

DATA AVAILABILITY STATEMENT

The original contributions presented in the study are included in the article/**Supplementary Material**,

further inquiries can be directed to the corresponding author.

AUTHOR CONTRIBUTIONS

OM and AS conceptualized the overall study, methodology, and formulated defibrillation parameters. RB, AM, and AG contributed in data processing and deep learning architecture. OM and DR contributed in hemodynamic modeling. SK provided clinical viewpoints. OM, AS, RB, AM, DR, AG, and SK drafted the manuscript. All authors have contributed to the manuscript and approved the final version.

FUNDING

This study received funding from Tata Consultancy Services Ltd. (TCS). The funder was not involved in the study design, collection, analysis, interpretation of data, the writing of this article, or the decision to submit it for publication.

SUPPLEMENTARY MATERIAL

The Supplementary Material for this article can be found online at: https://www.frontiersin.org/articles/10.3389/fphys.2021.787180/full#supplementary-material

REFERENCES

Amann, A., Tratnig, R., and Unterkofler, K. (2005). "A new ventricular fibrillation detection algorithm for automated external defibrillators," in *Computers in Cardiology* (Lyon: IEEE), 559–562.

Aramendi, E., Irusta, U., Pastor, E., Bodegas, A., and Benito, F. (2010). Ecg spectral and morphological parameters reviewed and updated to detect adult and paediatric life-threatening arrhythmia. *Physiol. Meas.* 31, 749–761. doi: 10.1088/0967-3334/31/6/002

Ariful, I., Hyunkyung, L., Nicola, P., Houssam, A., Zhihao, J., Jacek, C., et al. (2016). "Cybercardia project: modeling, verification and validation of implantable cardiac devices," in *2016 IEEE International Conference on Bioinformatics and Biomedicine (BIBM)* (Shenzhen: IEEE), 1445–1452.

Arts, T., Delhaas, T., Bovendeerd, P., Verbeek, X., and Prinzen, F. (2005). Adaptation to mechanical load determines shape and properties of heart and circulation: the circadapt model. *Am. J. Physiol. Heart Circ. Physiol.* 288, 1943–1954. doi: 10.1152/ajpheart.00444.2004

Ayala, U., Irusta, U., and Kramer Johansen, A.-A. (2014). A reliable method for rhythm analysis during cardiopulmonary resuscitation. *Biomed. Res. Int.* 2014:872470. doi: 10.1155/2014/872470

Barraud, J., Cautela, J., Bonello, L., and Peyrol, M. (2017). Wearable cardioverter defibrillator: bridge or alternative to implantation?,. *World J. Cardiol.* 9, 531–538. doi: 10.4330/wjc.v9.i6.531

Bisera, L., Geheb, J., and Weil, M. (2008). Identifying potentially shockable rhythms without interrupting cardiopulmonary resuscitation. *Crit. Care Med.* 36, 198–203. doi: 10.1097/01.CCM.0000295589.64729.6B

Burton, B., Tate, J., Erem, B., Swenson, D., Wang, D., Steffen, M., et al. (2011). "A toolkit for forward/inverse problems in electrocardiography within the scirun problem solving environment," in *2011 Annual International Conference of the IEEE Engineering in Medicine and Biology Society* (Boston, MA: IEEE), 267–270.

Colley, A., Williams, S., Rhode, K., Rinaldi, C., and Bishop, M. (2019). Conceptual intra-cardiac electrode configurations that facilitate directional cardiac stimulation for optimal electrotherapy. *IEEE Trans. Biomed. Eng.* 66, 1259–1268. doi: 10.1109/TBME.2018.2871863

Dosdall, D., Fast, V., and Ideker, R. (2010). Mechanisms of defibrillation. *Annu. Rev. Biomed. Eng.* 12, 233–258. doi: 10.1146/annurev-bioeng-070909-105305

Epstein, A., Abraham, W., Bianco, N., Kern, K., Solomon, S., and Szymkiewicz, S. (2013). Wearable cardioverter-defibrillator use in patients perceived to be at high risk early post-myocardial infarction. *J. Am. Coll. Cardiol.* 62, 2000–2007. doi: 10.1016/j.jacc.2013.05.086

Figuera, C., Irusta, U., Ayala, U., and Wik, L. (2016). Machine learning techniques for the detection of shockable rhythms in automated external defibrillators. *PLoS ONE* 11:e0159654. doi: 10.1371/journal.pone.0159654

Greenwald, S. (1986). *The Development and Analysis of a Ventricular Fibrillation Detector*. Massachusetts Institute of Technology, Department of Electrical Engineering and Computer Science. Cambridge, MA.

Hatib, F. A., Trendafilova, E., and Daskalov, I. (2000). Transthoracic electrical impedance during external defibrillation: comparison of measured and modelled waveforms. *Cardiovasc. Res.* 21, 145–153. doi: 10.1088/0967-3334/21/1/318

Hu, Y., Wang, J., Jiang, T., and Lin, S. (2014). "Semantic feature extraction of 3d human model from 2d orthographic projection," in *2014 5th International Conference on Digital Home* (Guangzhou: IEEE), 53–57.

Jekova, I. (2000). Comparison of five algorithms for the detection of ventricular fibrillation from the surface ecg. *Physiol. Meas.* 21, 429–439. doi: 10.1088/0967-3334/21/4/301

Jeon, E., Kyusam, O., and Jung, E. (2020). A lightweight deep learning model for fast electrocardiographic beats classification with a wearable cardiac monitor: development and validation study. *JMIR Med. Inform.* 8:e17037. doi: 10.2196/17037

Karagueuzian, H. S., and Chen, P.-S. (2001). Cellular mechanism of reentry induced by a strong electrical stimulus: Implications for fibrillation and defibrillation. *Cardiovasc. Res.* 50, 251–262. doi: 10.1016/S0008-6363(00)00298-4

Kerber, R., Becker, L., Bourland, J. R., Cummins, A. H., and Michos, M. (1997). Defibrillators for public access defibrillation: Recommendations for specifying and reporting arrhythmia analysis algorithm performance, incorporating new waveforms, and enhancing safety a statement for health professionals from the american heart association task force on automatic external defibrillation, subcommittee on aed safety and efficacy. *Circulation* 95, 1677–1682. doi: 10.1161/01.CIR.95.6.1677

Krasteva, V., Jekova, I., and Dotsinsky, I. (2010). Shock advisory system for heart rhythm analysis during cardiopulmonary resuscitation using a single ecg input of automated external defibrillators. *Ann. Biomed. Eng.* 38, 1326–1336. doi: 10.1007/s10439-009-9885-9

Krasteva, V., Ménétré, S., and Jekova, J. (2020). Fully convolutional deep neural networks with optimized hyperparameters for detection of shockable and non-shockable rhythms. *Sensors* 20:2875. doi: 10.3390/s20102875

Kwon, S., Kim, J., and Chu, C. (2018). Real-time ventricular fibrillation detection using an embedded microcontroller in a pervasive environment. *Electronics* 7:88. doi: 10.3390/electronics7060088

Lee, J., Lee, S., Choi, M., Seo, M., and Kim, S. (2019). Qrs detection method based on fully convolutional networks for capacitive electrocardiogram. *Expert. Syst. Appl.* 134, 66–78. doi: 10.1016/j.eswa.2019.05.033

Lim, H., Cun, W., Wang, Y., Gray, R., and Glimm, J. (2018). The role of conductivity discontinuities in design of cardiac defibrillation. *Chaos* 28, 013106. doi: 10.1063/1.5019367

Liu, M., Rong, X., and Jiang, T. (2019). Representative discovery of structure cues for coronary heart disease recognition based on quality assessment. *J. Vis. Commun. Image Represent.* 64:102607. doi: 10.1016/j.jvcir.2019.102607

Mazumder, O., Roy, D., Bhattacharya, S., Sinha, A., and Pal, A. (2019). "Synthetic ppg generation from hemodynamic model with baroreflex autoregulation: a digital twin of cardiovascular system," in *41th Annual International Conference of the IEEE Engineering in Medicine and Biology Society (EMBC)* (Berlin: IEEE), 5489–5492.

Mazumder, O., Roy, D., and Sinha, A. (2021). "*In silico* cardiac model to evaluate myocardial ischemia effect on hemodynamic parameters," in *2020 28th European Signal Processing Conference (EUSIPCO)* (Amsterdam, Dublin, Ireland: IEEE), 1105–1109.

Mazumder, O., and Sinha, A. (2021). "*In silico* evaluation of wearable cardiac defibrillator: personalized therapy planning to prevent sudden cardiac

death," in *2021 29th European Signal Processing Conference (EUSIPCO)* (IEEE).

Morgan, S., Plank, G., Irina, V., and Vadim, N. (2009). Low energy defibrillation in human cardiac tissue: a simulation study. *Biophys. J.* 96, 1364–1373. doi: 10.1016/j.bpj.2008.11.031

Nolle, F., Badura, F., and Catlett, J. (1986). Crei-gard, a new concept in computerized arrhyth mia monitoring systems. *Comput. Cardiol.* 13, 515–518

Onofrio, A., Russo, V., Bianchi, V., Cavallaro, C., Leonardi, S., Mocavero, P., et al. (2018). Effects of defibrillation shock in patients implanted with a subcutaneous defibrillator: a biomarker study. *Europace* 20, 233–239. doi: 10.1093/europace/eux330

Poole, J., Johnson, G., Hellkamp, A., Anderson, J., and Raitt, D. C. M. (2008). Prognostic importance of defibrillator shocks in patients with heart failure. *N. Engl. J. Med.* 359, 1009–1017. doi: 10.1056/NEJMoa071098

Qiana, L., Wanga, J., Jina, L., Songa, B., and Wua, X. (2018). Effect of ventricular myocardium characteristics on the defibrillation threshold. *Technol. Health Care* 26, 241–248. doi: 10.3233/THC-174599

Reek, S., Burri, H., Roberts, P. R., Perings, C., Epstein, A., and Klein, H. (2017). The wearable cardioverter-defibrillator: current technology and evolving indications. *Europace* 19, 335–345. doi: 10.1093/europace/euw180

Roy, D., Mazumder, O., Sinha, A., and Khandelwal, S. (2021). Multimodal cardiovascular model for hemodynamic analysis: Simulation study on mitral valve disorders. *PLoS ONE* 16:e0247921. doi: 10.1371/journal.pone.0247921

SCI (2016). Scirun: A scientific computing problem solving environment, scientific computing and imaging institute. Available online at: https://www.sci.utah.edu/cibc-software/scirun.html

Sekeh, Y., Borzadaran, S., Reza, G., and Abdolhamid (2013). *On Kullback-Leibler Dynamic Information*. Available online at: https://ssrn.com/abstract=2344078

Sharma, P., Bordachar, P., and Ellenbogen, K. (2017). Indications and use of the wearable cardiac defibrillator. *Eur. Heart J.* 38, 258–267. doi: 10.1093/eurheartj/ehw353

Sherknies, D., Meunier, J., and Tardif, J.-C. (2003). "3d path recovery of an ivus transducer with single-plane angiography," in *CCECE 2003-Canadian Conference on Electrical and Computer Engineering. Toward a Caring and Humane Technology (Cat. No. 03CH37436)*, *Vol. 3* (Montreal, QC, Canada: IEEE), 1489–1492.

Silva, P., Luz, E., Wanner, E., Menotti, D., and Moreira, G. (2019). Qrs detection in ecg signal with convolutional network. *Lect. Notes Comput. Sci* 11401, 802–809. doi: 10.1007/978-3-030-13469-3_93

Smith, T., and Cain., M. (2006). Sudden cardiac death: epidemiologic and financial worldwide perspective. *J. Interv. Card Electrophysiol.* 17, 199–203. doi: 10.1007/s10840-006-9069-6

Stinstra, J., Jolly, M., Callahan, M., Weinstein, D., Cole, M., Brooks, D., et al. (2007). Evaluation of different meshing algorithms in the computation of defibrillation thresholds in children. *Conf. Proc. IEEE Eng. Med. Biol. Soc.* 2007, 1422–1425. doi: 10.1109/IEMBS.2007.4352566

Stinstra, J., Pieper, S., MacLeod, R., Brooks, D., Cecchin, F., and Triedman, J. (2008). A computer modeling tool for comparing novel icd electrode orientations in children and adults. *Heart Rhythm. J.* 5, 565–572. doi: 10.1016/j.hrthm.2008.01.018

Stinstra, J., Tat, J., Pieper, S., MacLeod, R., Chu, L., Wang, P., et al. (2010). Finite element modeling of subcutaneous implantable defibrillator electrodes in an adult torso. *Heart Rhythm. J.* 7, 692–698. doi: 10.1016/j.hrthm.2010.01.030

Sun, W., Martin, C., and Pham, T. (2014). Computational modeling of cardiac valve function and intervention. *Annu. Rev. Biomed. Eng.* 16, 53–76. doi: 10.1146/annurev-bioeng-071813-104517

Tate, J., Stinstra, J., Pilcher, T., Poursaida, A., Jolley, M., Saarelc, E., et al. (2018). Measuring defibrillator surface potentials: the validation of a predictive defibrillation computer model. *Comput. Biol. Med.* 102, 402–410. doi: 10.1016/j.compbiomed.2018.08.025

Trayanova, N., Constantino, J., and Plank, G. (2011). Modeling defibrillation of the heart: approaches and insights. *IEEE Rev. Biomed. Eng.* 4, 89–102. doi: 10.1109/RBME.2011.2173761

Wan, C., Jess, W., Steven, O., and Szymkiewicz, J. (2013). Successful use of wearable cardioverter defibrillator in a patient with dextrocardia and persistent left superior vena cava. *Ann. Noninvasive Electrocardiol.* 18, 487–490. doi: 10.1111/anec.12059

Wang, L. (2007). Fundamentals of intrathoracic impedance monitoring in heart failure. *Am. J. Cardiol.* 99, 3G–10G. doi: 10.1016/j.amjcard.2007.02.009

Yaxin, W., Smith, P., De-Sciscio, P., Sampaio, L., Cohn, W., Liping, X., et al. (2017). Replication of pressure-volume loop with controllable espvr and edpvr curves on a personalized mock circulatory loop based on elastance function. *Annu. Int. Conf. IEEE Eng. Med. Biol. Soc.* 2017, 1282–1286. doi: 10.1109/EMBC.2017.8037066

Zhong, W., Guo, X., and Wang, G. (2020). Non-invasive fetal electrocardiography denoising using deep convolutional encoder-decoder networks. *Lect. Notes Electr. Eng* 592, 1–10. doi: 10.1007/978-981-32-9682-4_1

Zipes, D., Fischer, J., King, R., Nicoll, A., and Jolly, W. (1975). Termination of ventricular fibrillation in dogs by depolarizing a critical amount of myocardium. *Am. J. Cardiol.* 36, 37–44. doi: 10.1016/0002-9149(75)90865-6

Conflict of Interest: OM, RB, DR, AM, AG, SK, and AS are employed by Tata Consultancy Service Ltd. (TCS).

Publisher's Note: All claims expressed in this article are solely those of the authors and do not necessarily represent those of their affiliated organizations, or those of the publisher, the editors and the reviewers. Any product that may be evaluated in this article, or claim that may be made by its manufacturer, is not guaranteed or endorsed by the publisher.

frontiers in Physiology

ORIGINAL RESEARCH
published: 24 December 2021
doi: 10.3389/fphys.2021.749430

A Divergence-Based Approach for the Identification of Atrial Fibrillation Focal Drivers From Multipolar Mapping: A Computational Study

Michela Masè[1,2], Alessandro Cristoforetti[1], Maurizio Del Greco[3] and Flavia Ravelli[1,4]**

[1] Laboratory of Biophysics and Translational Cardiology, Department of Cellular, Computational and Integrative Biology – CIBIO, University of Trento, Trento, Italy, [2] Institute of Mountain Emergency Medicine, EURAC Research, Bolzano, Italy, [3] Division of Cardiology, Santa Maria del Carmine Hospital, Rovereto, Italy, [4] CISMed – Centre for Medical Sciences, University of Trento, Trento, Italy

The expanding role of catheter ablation of atrial fibrillation (AF) has stimulated the development of novel mapping strategies to guide the procedure. We introduce a novel approach to characterize wave propagation and identify AF focal drivers from multipolar mapping data. The method reconstructs continuous activation patterns in the mapping area by a radial basis function (RBF) interpolation of multisite activation time series. Velocity vector fields are analytically determined, and the vector field divergence is used as a marker of focal drivers. The method was validated in a tissue patch cellular automaton model and in an anatomically realistic left atrial (LA) model with Courtemanche–Ramirez–Nattel ionic dynamics. Divergence analysis was effective in identifying focal drivers in a complex simulated AF pattern. Localization was reliable even with consistent reduction (47%) in the number of mapping points and in the presence of activation time misdetections (noise <10% of the cycle length). Proof-of-concept application of the method to human AF mapping data showed that divergence analysis consistently detected focal activation in the pulmonary veins and LA appendage area. These results suggest the potential of divergence analysis in combination with multipolar mapping to identify AF critical sites. Further studies on large clinical datasets may help to assess the clinical feasibility and benefit of divergence analysis for the optimization of ablation treatment.

Keywords: atrial fibrillation, mapping, signal processing, computational models, vector field analysis, conduction velocity, focal activity, wave propagation patterns

OPEN ACCESS

Edited by:
Xin Li,
University of Leicester,
United Kingdom

Reviewed by:
Joakim Sundnes,
Simula Research Laboratory, Norway
Vincent Jacquemet,
Université de Montréal, Canada

****Correspondence:***
Michela Masè
michela.mase@eurac.edu
Flavia Ravelli
flavia.ravelli@unitn.it

Specialty section:
This article was submitted to Computational Physiology and Medicine, a section of the journal Frontiers in Physiology

Received: *29 July 2021*
Accepted: *30 November 2021*
Published: *24 December 2021*

Citation:
Masè M, Cristoforetti A, Del Greco M and Ravelli F (2021) A Divergence-Based Approach for the Identification of Atrial Fibrillation Focal Drivers From Multipolar Mapping: A Computational Study. Front. Physiol. 12:749430. doi: 10.3389/fphys.2021.749430

INTRODUCTION

Atrial fibrillation (AF) is the most common arrhythmia in the clinical practice, with increasing prevalence due to population aging and high morbidity associated to a fivefold increase in the risk of stroke (Fuster et al., 2006; Virani et al., 2021). The most promising approach for AF treatment is represented by catheter ablation, which performs targeted lesions on the atrial surface aiming to isolate arrhythmia sources and to interrupt critical activation pathways. Following the seminal work of Haissaguerre et al. (1998), pulmonary veins (PVs) isolation has become the cornerstone of AF ablation procedures and the common approach to treat patients with paroxysmal and persistent AF. However, given the ineffectiveness of the sole PVs ablation, especially in persistent AF, novel

methodologies and approaches have been proposed to identify and ablate AF drivers located outside the PVs (Stiles et al., 2018; Buist et al., 2021; Parameswaran et al., 2021; Quintanilla et al., 2021). In parallel with the expanding role of catheter ablation, novel mapping strategies have been developed to guide the procedure and improve efficacy (Mahida et al., 2014). Multipolar mapping catheters, such as the PentaRay catheter, have been introduced to guide substrate modification and to identify extra-PV foci. These systems allow reduced mapping times and greater spatiotemporal resolution. In addition, the temporal and directional information provided by the simultaneous multisite electrograms allows, in principle, the reconstruction of activation patterns during AF.

Despite the variety of signal analysis techniques available for the point-by-point analysis of single electrograms (Nollo et al., 2008; Ravelli and Masè, 2014; Baumert et al., 2016; Almeida et al., 2018, 2021; Baher et al., 2019), fewer approaches have been proposed for the analysis of simultaneous multisite electrograms and the characterization of propagation patterns. These comprise, for instance, techniques based on computation of conduction delays and wave directions (Ganesan et al., 2015, 2018, 2019), cosine model fitting (Weber et al., 2010, 2011; Roney et al., 2019), probabilistic interpolation (Coveney et al., 2020), and physics-informed neural network (Sahli Costabal et al., 2020) applied to activation time series, as well as multivariate approaches based on causality analysis applied to atrial electrograms (Richter et al., 2011; Rodrigo et al., 2016; Alcaine et al., 2017; Luengo et al., 2019; Handa et al., 2020; Masè et al., 2020).

The present study introduces a novel framework for the reconstruction of wave activation patterns and the identification of focal drivers from clinically available multipolar mapping systems. The method is based on a radial basis function (RBF) interpolation approach (Franke, 1982; Fornefett et al., 2001), which reconstructs the activation patterns in the mapping area from scattered multisite activation time series. Propagation pattern properties are quantitatively characterized by an analytical determination of the conduction velocity (CV) vector fields, providing information on conduction heterogeneity and slow conduction areas. Finally, focal activation patterns are localized by the analysis of the vector field divergence, which marks the presence of centrifugal propagation from a localized source. After presenting the methodology, the capability of the method to accurately reconstruct activation patterns and CV fields and to identify focal drivers is tested in two different simulation models. RBF reconstruction of various propagation patterns and localization of focal activity is evaluated in a tissue patch cellular automaton (CA) model (Lammers et al., 1991; Masè et al., 2005), where the reliability of the procedure is tested against electrogram loss and activation time misdetection. The localization of focal drivers in a realistic AF context is then evaluated on synthetic electrograms from an anatomically realistic and ionically detailed left atrial (LA) model (Courtemanche et al., 1998; Cristoforetti et al., 2013). Finally, we show a proof-of-concept application of the method to clinical multipolar AF mapping data.

MATERIALS AND METHODS

Conduction Velocity Vector Field Approach for the Analysis of Multipolar Electrograms

Reconstruction of Activation Maps by Radial Basis Function Interpolation

The reconstruction of the activation process in the mapping plane was addressed as a multivariate interpolation problem and solved by RBFs. Let's consider a set of N mapping points, with positions $\vec{X}_i = [x_i, y_i]$ in the 2D catheter mapping area, where i indicates the recording site, and the activation time series $t_i(n)$ extracted from the corresponding mapping electrograms, where n numbers subsequent atrial beats. For each beat n, the task of the RBF interpolation is to determine a continuous and sufficiently differentiable interpolation function $f = f\left(\vec{X}\right)$, describing the variation of the activation time as a function of a generic 2D spatial position $\vec{X} = [x, y]$ (Franke, 1982). The function $f(\vec{X})$ must fulfill the interpolation constraints at the mapping point positions $\vec{X}_i$, given by:

$$f\left(\vec{X}_i\right) = t_i(n) \qquad i = 1, \ldots N \tag{1}$$

In the RBF approach the interpolation function $f(\vec{X})$ takes the form:

$$f\left(\vec{X}\right) = \sum_{i=1}^{N} \alpha_i R\left(||\vec{X} - \vec{X}_i||\right) \tag{2}$$

where $R\left(||\vec{X} - \vec{X}_i||\right)$ are radially symmetric functions, centered on the mapping points $\vec{X}_i$, $||\vec{X} - X_i||$ is the Euclidean distance between interpolation and mapping points, and α_i are the weights of the RBF base elements.

From condition (1), it follows that:

$$f\left(\vec{X}_i\right) = \sum_{j=1}^{N} \alpha_j R\left(||\vec{X}_i - \vec{X}_j||\right) = t_i \text{ for } i=1,\ldots, N \tag{3}$$

Equation 3 can be written in matrix form as:

$$\begin{bmatrix} R\left(||\vec{X}_1 - \vec{X}_1||\right) & R\left(||\vec{X}_2 - \vec{X}_1||\right) & \cdots & R\left(||\vec{X}_N - \vec{X}_1||\right) \\ R\left(||\vec{X}_1 - \vec{X}_2||\right) & R\left(||\vec{X}_2 - \vec{X}_2||\right) & \cdots & R\left(||\vec{X}_N - \vec{X}_2||\right) \\ \vdots & \vdots & & \vdots \\ R\left(||\vec{X}_1 - \vec{X}_N||\right) & R\left(||\vec{X}_2 - \vec{X}_N||\right) & \cdots & R\left(||\vec{X}_N - \vec{X}_N||\right) \end{bmatrix} \begin{bmatrix} \alpha_1 \\ \alpha_2 \\ \vdots \\ \alpha_N \end{bmatrix} = \begin{bmatrix} t_1 \\ t_2 \\ \vdots \\ t_N \end{bmatrix} \tag{4}$$

Or in compact form:

$$\boldsymbol{R\alpha} = \boldsymbol{t}, \tag{5}$$

where **R** is a real-symmetric N × N matrix and α and **t** are N × 1 vectors.

It is sometimes useful to add a low order polynomial term to the interpolant function in Eq. 2 to gain polynomial precision for some portions of f (e.g., to reproduce linear and constant parts of the function) and to ensure solvability of the interpolation problem.

Defining p_j, $j = 1, 2, \ldots, M$ as a basis of the polynomial space and adding it to Eq. 2, we obtain the following expression for the interpolant function:

$$f\left(\overrightarrow{X}\right) = \sum_{i=1}^{N} \alpha_i R\left(||\overrightarrow{X} - \overrightarrow{X}_i||\right) + \sum_{j=1}^{M} \beta_j p_j\left(\overrightarrow{X}\right) \tag{6}$$

with additional constraints for the polynomial part (Fornefett et al., 2001):

$$\sum_{i=1}^{N} \alpha_i p_j\left(\overrightarrow{X}_i\right) = 0, j = 1, \ldots, M \tag{7}$$

Adding the polynomial in the interpolant function and considering these extra-constraints in Eq. 7 leads to the linear system of equations:

$$\begin{bmatrix} \mathbf{R} & \mathbf{P} \\ \mathbf{P^T} & \mathbf{0} \end{bmatrix} \begin{bmatrix} \boldsymbol{\alpha} \\ \boldsymbol{\beta} \end{bmatrix} = \begin{bmatrix} \mathbf{t} \\ \mathbf{0} \end{bmatrix} \tag{8}$$

where **P** is a N × M matrix and $\mathbf{P}^T$ indicate the transposed form of **P**.

It can be demonstrated that with proper choice of the RBFs and of the polynomial term, the left-hand side matrix in Eq. 8 is non-singular and thus the system of equations is solvable and unique values for α and β can be determined (Fornefett et al., 2001; Kybic et al., 2002a,b).

In the present study, the Duchon's radial cubic function was used as basis:

$$R_i\left(\overrightarrow{X}\right) = \left(||\overrightarrow{X} - \overrightarrow{X}_i||\right)^3 \tag{9}$$

and a first-order polynomial term was added to the interpolant function:

$$P\left(\overrightarrow{X}\right) = \beta_1 + \beta_2 x + \beta_3 y \tag{10}$$

Interpolation with Duchon's functions has an elegant theory in a Hilbert space setting, where Eqs 6–8 were derived as the solution of a variational problem targeting minimization of Duchon's semi-norm and the interpolant curvature (Duchon, 1977). Duchon's functions were shown to display excellent accuracy when interpolating scattered data, visual pleasantness and smooth appearance, low complexity, and reduced computational and memory costs (Franke, 1982). In addition, in contrast to multiquadratic or Gaussian RBFs they do not require the subjective choice of additional tuning parameters (Franke, 1982).

Analytical Determination of Conduction Velocity Vector Fields

Conduction velocity vector fields were analytically computed from the RBF reconstructions of the activation process $f\left(\overrightarrow{X}\right)$. The interpolant function $f\left(\overrightarrow{X}\right)$ describes activation as a function of position and sections of the function at constant time describes local isochronal contours. The gradient vector ∇f, whose components are given by the partial derivatives of $f\left(\overrightarrow{X}\right)$:

$$\nabla f = \left[\frac{\partial f}{\partial x}, \frac{\partial f}{\partial y}\right] \tag{11}$$

is, by definition, normal to isochrone contours and thus it defines the direction of wavefront propagation (i.e., it is parallel to the velocity vector).

The components of the 2D velocity vector $\overrightarrow{v} = \left[v_x, v_y\right]$ are given by:

$$\begin{aligned} v_x &= \frac{dx}{dt} = \frac{\partial x}{\partial t} + \frac{\partial x}{\partial y}\frac{\partial y}{\partial t} \\ v_y &= \frac{dy}{dt} = \frac{\partial y}{\partial t} + \frac{\partial y}{\partial x}\frac{\partial x}{\partial t} \end{aligned} \tag{12}$$

As detailed in Bayly et al. (1998), Eq. 12 can be solved by assuming that the direction of propagation is specified by the normal to the isochronal contours (i.e., the direction of propagation is parallel to the gradient in Eq. 11), resulting in the following relationship for the two velocity components:

$$v_y = \frac{\dfrac{\partial f}{\partial y}}{\dfrac{\partial f}{\partial x}} v_x \tag{13}$$

Combining Eqs 11–13 an expression for velocity estimates can be obtained, which is directly linked to the partial derivatives of the interpolant function:

$$\begin{aligned} v_x &= \frac{dx}{dt} = \frac{\dfrac{\partial f}{\partial x}}{\left(\dfrac{\partial f}{\partial x}\right)^2 + \left(\dfrac{\partial f}{\partial y}\right)^2} \\ v_y &= \frac{dy}{dt} = \frac{\dfrac{\partial f}{\partial y}}{\left(\dfrac{\partial f}{\partial x}\right)^2 + \left(\dfrac{\partial f}{\partial y}\right)^2} \end{aligned} \tag{14}$$

Velocity estimates can be analytically computed through Eq. 14, once $f\left(\overrightarrow{X}\right)$ has been determined (i.e., once α and β have been calculated from Eq. 8). This means that the computation of the velocity vector field requires no additional manual operations with respect to the determination of an activation map.

Localization of Focal Drivers by Divergence Analysis

Focal activation sites are defined as sites or regions, which centrifugally activate the surrounding atrial tissue (Haissaguerre et al., 1998). CV vector fields corresponding to centrifugal

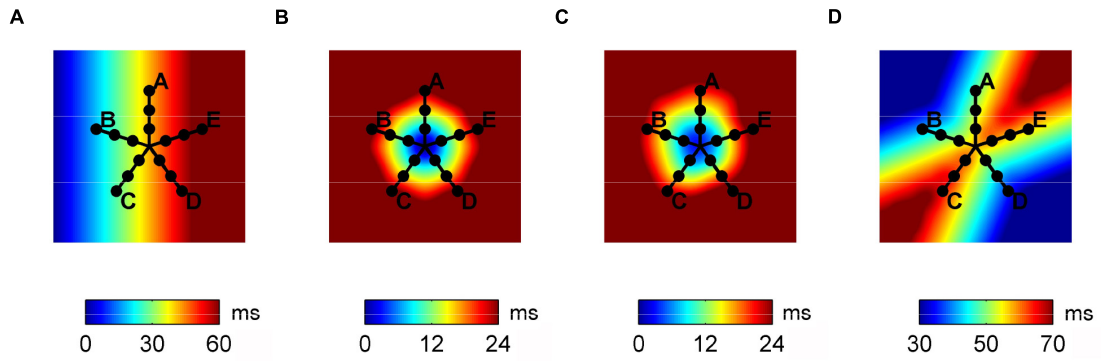

FIGURE 1 | Activation maps of the propagation patterns simulated on the tissue patch cellular automaton model and position of the simulated multipolar catheter. From left to right, plane wave propagation **(A)**, focal propagation in tissues with homogeneous **(B)** and heterogeneous **(C)** conduction properties, and wave collision **(D)**.

activation present well-defined angular properties, resulting in positive divergence values. To identify focal activation, the divergence operator was applied to the analytically determined CV vector field. Before divergence computation, CV vectors were normalized to unit vectors $\vec{v} = [v_x, v_y]$, to consider the sole contribution of vector angular properties. The divergence (D) of the vector field $\vec{v}$ on the mapping plane in Cartesian coordinates is given by:

$$D = \nabla \cdot \vec{v} = \frac{\partial v_x}{\partial x} + \frac{\partial v_y}{\partial y} \tag{15}$$

where $\nabla\cdot$ represents the divergence operator. D yields a signed scalar with positive values in presence of field sources and negative values for field sinks. Focal activation sites are thus located in correspondence of the local maxima of D.

Validation of Radial Basis Function Framework by Computer Simulations

Validation on a Simulated Tissue Patch

The capability and accuracy of the method to reconstruct activation patterns, quantify propagation properties, and detect focal activation sites were evaluated in a bidimensional tissue patch CA model (Lammers et al., 1991; Masè et al., 2005), where the method was tested against the effects of missing electrograms and activation time misdetections.

A previously detailed bidimensional CA model of excitable tissue was used to simulate basic propagation patterns (Lammers et al., 1991; Masè et al., 2005). The model consisted of a bidimensional patch of 1000 × 1000 cell units (4 cm × 4 cm), each assigned with an evolving excitation state. As shown in **Figure 1**, four basic activation patterns were simulated: planar wave propagation (a), focal propagation in a tissue with homogeneous (b) and heterogeneous (c) conduction properties, and wavefront collision (d). Conduction properties were homogeneous and isotropic in patterns (a), (b), and (d) with CV values reported in **Table 1**. In pattern (c), eight areas with different normally distributed conduction properties were created around the focal site, resulting in a CV of 59.9 ± 12.5 cm/s. The simulation output consisted of the activation time series at each cell element, which were down-sampled on a 200 × 200 element grid to limit grid artifacts on propagation patterns. Multipolar activation time series were thus acquired from 15 mapping points, corresponding to the position of the electrode bipoles in a PentaRay catheter-like configuration, as displayed in **Figure 1**.

The accuracy of the reconstruction of CV fields was determined in the four propagation scenarios by comparing exact and estimated pointwise CV vector magnitudes and directions on the 200 × 200 grid. The localization of the focal source was evaluated in simulated scenarios (b) and (c), calculating the cell-distance between the exact position of the focal source and the maximal divergence site identified by the algorithm. The localization was considered accurate for average distances less than a distance threshold r = 2.7 mm (equivalent to 13.5 cells in the down-sampled 200 × 200 grid). The threshold value r was determined based on a statistical principle, so that the ratio between the circular area of radius r and the circular area swept by the simulated catheter was equal to 0.05. This corresponded to a probability <0.05 of locating the source by chance.

A stability analysis was led to test the method against factors that might corrupt clinical mapping data. The effect of electrogram loss (e.g., due to poor catheter displacement or inadequate contact) was evaluated by performing the analysis when removing a progressively larger number of randomly selected mapping points. The method stability against activation time misdetections was tested by adding random jitters to the simulated activation times series. Jitters were uniformly distributed around zero with distribution amplitude ε, varying from 0 to 20% (step 0.5%) of the activation cycle length (150 ms). The stochastic procedure was repeated 100 times for each number of sites removed and noise level. For the assessment of source localization, the catheter center was randomly moved over the patch at different repetitions.

Validation on an Anatomically Realistic Left Atrial Model

The capability of the method to localize AF focal drivers was tested on synthetic electrograms, obtained from an anatomically

TABLE 1 | Effects of electrogram removal on the estimation of median velocity, velocity vector magnitudes, and directions.

Simulated pattern	Removed electrograms	Exact median speed (cm/s)	Estimated median speed (cm/s)	Absolute single value speed error (%)	Absolute angle error (rad)
Plane wavefront (pattern a)	0	60.4	60.4	0.16	0.002
	2	60.4	60.4 (60.4, 60.4)	0.16 (0.14, 0.18)	0.002 (0.001, 0.002)
	4	60.4	60.4 (60.4, 60.4)	0.18 (0.15, 0.24)	0.002 (0.001, 0.002)
	6	60.4	60.4 (60.3, 60.4)	0.21 (0.16, 0.27)	0.002 (0.001, 0.002)
	8	60.4	60.4 (60.4, 60.5)	0.18 (0.14, 0.24)	0.002 (0.001, 0.003)
	10	60.4	60.4 (60.3, 60.5)	0.17 (0.12, 0.27)	0.002 (0.001, 0.003)
Focal source in homogeneous tissue (pattern b)	0	54.6	54.2	7.6	0.059
	2	54.6	53.6 (53.0, 54.1)	7.9 (7.5, 8.5)	0.065 (0.061, 0.067)
	4	54.6	53.2 (52.5, 54.2)	9.3 (8.3, 10.4)	0.074 (0.068, 0.081)
	6	54.6	54.8 (53.1, 56.6)	12.7 (10.2, 14.4)	0.098 (0.083, 0.144)
	8	54.6	59.3 (56.1, 63.1)	16.7 (14.7, 19.2)	0.167 (0.142, 0.202)
	10	54.6	66.7 (63.4, 74.6)	25.7 (20.3, 38.3)	0.265 (0.210, 0.376)
Focal source in heterogeneous tissue (pattern c)	0	59.9	59.4	7.1	0.092
	2	59.9	58.7 (57.7, 59.4)	7.8 (7.0, 8.5)	0.097 (0.093, 0.098)
	4	59.9	58.2 (56.9, 59.2)	9.2 (8.2, 10.0)	0.101 (0.096, 0.108)
	6	59.9	59.1 (56.8, 60.9)	12.0 (10.4, 13.6)	0.121 (0.106, 0.150)
	8	59.9	61.5 (57.5, 66.1)	17.0 (14.1, 19.7)	0.170 (0.140, 0.196)
	10	59.9	70.2 (63.0, 79.4)	25.2 (19.3, 36.1)	0.255 (0.201, 0.396)
Colliding wavefronts (pattern d)	0	55.8	56.6	11.4	0.088
	2	55.8	56.7 (56.4, 58.8)	12.3 (11.6, 13.1)	0.102 (0.092, 0.115)
	4	55.8	57.8 (55.9, 59.7)	13.7 (12.7, 15.4)	0.130 (0.110, 0.158)
	6	55.8	59.7 (55.1, 63.7)	18.7 (15.3, 22.5)	0.190 (0.145, 0.272)
	8	55.8	64.6 (59.4, 74.7)	23.6 (18.4, 33.1)	0.352 (0.208, 0.675)
	10	55.8	73.3 (64.3, 87.5)	31.2 (22.5, 53.2)	1.015 (0.679, 1.402)

Data are median (IQR) over 100 stochastic repetitions.

realistic LA model, based on Courtemanche–Ramirez–Nattel (CRN) cell formulation (Courtemanche et al., 1998; Cristoforetti et al., 2013). Ionic dynamics were described by the CRN human atrial cell model in monodomain formulation (Courtemanche et al., 1998). The ionic model was implemented on a realistic LA anatomy, segmented from cardiac tomography images (Cristoforetti et al., 2008). A remodeled version of the CRN model (Jacquemet et al., 2003) with an isotropic diffusion tensor of 0.2 cm^2/s was used to obtain spiral breakups and multiple wavelet formation. After stabilization of the multiple wavelet pattern, a localized focal driver was activated in the region of the PVs. The resulting pattern comprised a centrifugal propagation in proximity of the focal driver (**Figure 2**, upper panels) combined with a more complex propagation with transient rotors and colliding wavefronts in the region dominated by multiple wavelets (**Figure 2**, lower panels).

ODE–PDE system integration was performed by a fully adaptive multi-resolution algorithm (Cristoforetti et al., 2013), which dynamically restricted computation to a set of active nodes. Reaction and diffusion were integrated with time step Δt = 0.1 ms, using the Rush Larsen non-standard finite difference forward Euler method and explicit node-centered finite difference stencils (Jacquemet and Henriquez, 2005), respectively.

Synthetic electrograms were generated according to the current source approximation (Jacquemet et al., 2003) and acquired at different locations of the LA, using a PentaRay catheter configuration (see **Figure 2**). Specifically, 20 recording electrodes were arranged in five splines (with interelectrode distance of 4 mm), located at 0.5 mm from the atrial surface, and bipolar electrograms were computed as differences between neighboring unipolar electrograms on the same spline. Simulated signals of 5 s length, sampled at 1 kHz, were used for method evaluation.

Proof-of-Concept Application to Clinical Mapping Data

Conduction velocity vector field reconstruction and divergence analysis were applied to clinical electrograms, retrospectively available from one patient with persistent AF, who underwent a pre-ablation electrophysiological study. The study was approved by the local Ethical Committee and performed in accordance with the principles outlined in the Declaration of Helsinki. The patient gave written informed consent. During the electrophysiological study, a 20 pole PentaRay mapping catheter (Biosense Webster, Inc., Diamond Bar, CA, United States), composed of five radiating splines, each carrying four electrodes was sequentially moved in the LA. Twenty-one atrial regions were mapped in the patient, sampling the PVs and LA body areas. Three hundred and fifteen atrial electrograms (i.e., 15 bipolar electrograms × 21 sites) of 2 s length were recorded during the study and exported for off-line analysis. Electrograms with inadequate

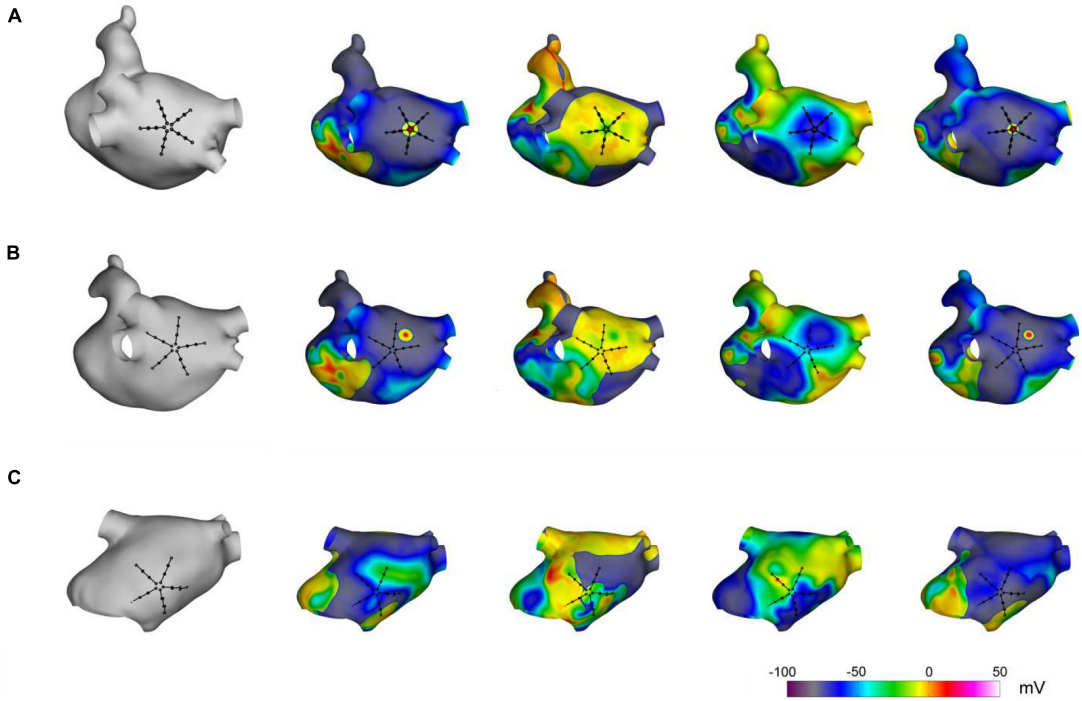

FIGURE 2 | Simulation of atrial fibrillation in a realistic left atrial model. In gray, anatomical model of the left atrium and positions of the simulated multipolar catheter. In color, sequential snapshots of the membrane voltage at three mapping sites: at the focal driver **(A)**, at the boundary between the focal driver and multiple wavelets region **(B)**, and in the multiple-wavelets region **(C)**.

signal-to-noise ratio were excluded from subsequent analysis. Activation time series were automatically extracted from each bipolar electrogram as previously reported (Faes et al., 2002; Masè et al., 2015). Briefly, electrograms were pre-processed to remove ventricular interference, local atrial activation waves were identified by signal filtering and adaptive threshold crossing (Faes et al., 2002; Masè et al., 2015) and atrial activation times were estimated by measuring the barycenter of local activation waves (Faes et al., 2002).

Statistical Analysis

Data are expressed as mean ± standard deviation (SD) or median [interquartile range (IQR)], as appropriate. Divergence values are given as median, maximal, minimal, and/or range values, as appropriate.

RESULTS

Conduction Velocity Vector Field Representation of Propagation Patterns

Figure 3 displays RBF reconstructions (top panels) and superimposed normalized CV fields (arrows) corresponding to the simulated patterns in **Figure 1**. The angular properties of the fields are quantified by divergence maps (bottom panels). All propagation patterns were precisely reconstructed by RBF interpolation. CV vectors, which were analytically determined by RBF approach, clearly indicated the direction of wavefront propagation, being orthogonal to isochronal lines. CV values estimated from RBF reconstructions approximated well the set values, resulting of 60.4, 54.2, 59.4, and 56.6 cm/s for patterns (a) to (d). Propagation pattern properties were quantitatively distinguished in terms of divergence analysis. Indeed, planar wave propagation (a) was characterized by almost-zero values of the divergence [range ($-7.5{\cdot}10^{-3}$, $7.5{\cdot}10^{-3}$ mm^{-1}), in green]. Focal sites (b and c), acting as sources of the field, were marked by maximal positive divergence values (D_{max} = 10 mm^{-1}, in red) versus the almost-zero values of the surrounding area (D_{median} = 0.125 mm^{-1}). The collision line, acting as a field sink, displayed negative divergence values (D_{min} = -5.5 mm^{-1}, in blue, versus $D_{median} = 6.25{\cdot}10^{-3}$ mm^{-1}).

Stability Analysis

The results of the stability analysis are summarized in **Tables 1**, **2**, where reconstruction errors of CV vector magnitudes and directions are reported for the four patterns at the progressive removal of mapping sites (**Table 1**) and at increasing noise in activation time detection (**Table 2**). Reliable estimations of CV magnitudes and directions were obtained even with reduced electrogram sets (**Table 1**), although the number of sites necessary for the reconstructions increased with pattern complexity. The reconstruction of the plane wave pattern was not affected by the progressive removal of the electrograms. Focal patterns in homogeneous/heterogeneous tissues were reconstructed from

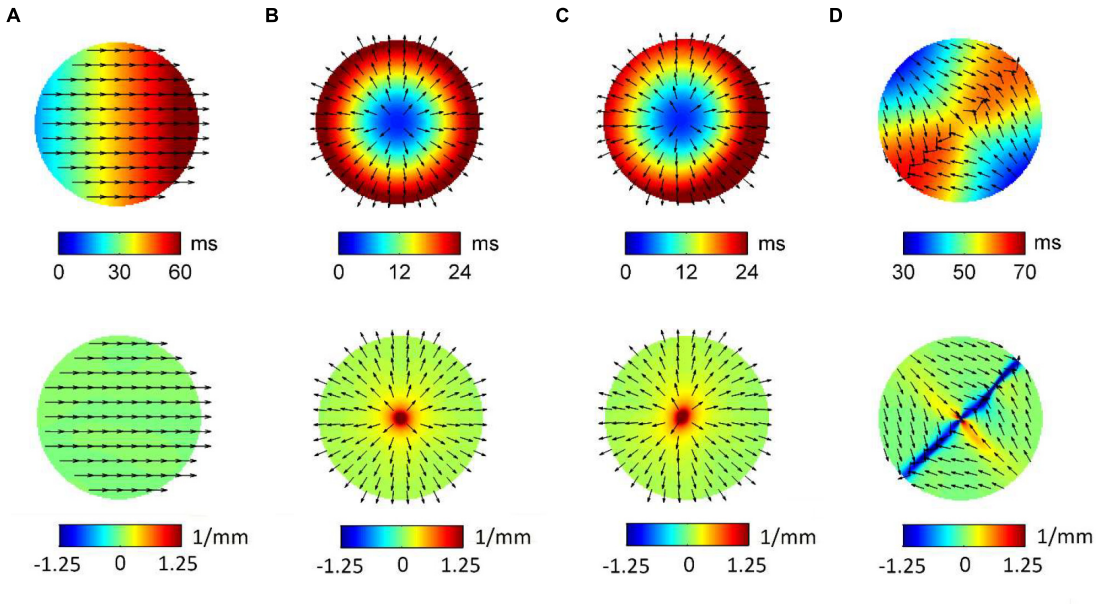

FIGURE 3 | Radial basis function-reconstructed activation (top) and divergence maps (bottom) corresponding to the simulated patterns in **Figure 1**. Analytically determined conduction velocity vector fields are displayed on the maps as normalized arrows indicating the direction of wave propagation. Divergence maps quantify pattern properties, assigning zero divergence values (green) to planar wave propagation **(A)**, positive divergence values (red) to focal sources **(B,C)**, and negative divergence values (blue) to collision lines **(D)**.

a minimum of nine sites (six sites removed) with pointwise CV magnitude errors ∼12% and direction errors of ∼0.12 rad. Wavefront collision pattern were reconstructed from a minimum of 11 sites (four sites removed) with magnitude errors of ∼14% and direction errors of ∼0.13 rad. Median CV estimates were less affected than pointwise velocities by the reduction of sites, with percentage errors of 0.2 and −1.4% for focal and of 3.5% for collision patterns.

Activation time misdetection affected the reconstruction of all the patterns (**Table 2**), with a progressive increase of the estimation errors at increasing levels of noise. Noise had more severe effects on the estimation of CV vector magnitudes than on median CV estimates. Absolute errors on CV vector magnitudes for focal source patterns raised from 7.6 and 7.1% at 0% noise to 32.3 and 33.9% at 10% noise, and for wavefront collision patterns errors raised from 11.4 to 28.8%. Median CV values underestimated true CV values at a progressively higher extent with increasing noise levels. At 10% noise, median CV estimates decreased to 50.5 and 52.2 cm/s (error of −7.5 and −12.8%) in focal patterns and to 49.6 cm/s (error of −11.1%) in the wavefront collision pattern. In terms of CV vector directions, angle errors for the simulated patterns increased from a range of 0.002–0.09 rad at 0% noise levels to 0.27–0.43 rad at 10% noise. Noise effects on vector magnitudes and directions were significantly reduced by averaging CV values over few beats. At 10% noise amplitude, a 10-beat average reduced CV magnitude errors to 14–16% for focal patterns, and to 18% for the collision pattern, keeping direction estimation errors <0.18 rad in all patterns.

The precision of divergence analysis to locate focal sources in tissues with homogeneous and heterogeneous conduction properties is reported in **Figure 4** for changing number of recording sites (left) and noise levels (right). The localization strategy was stable against a reduction in the number of recording sites. Accurate identification was maintained with a minimum of nine sites available (i.e., seven sites removed). Focal drivers were precisely localized from single-beat divergence maps in presence of mild levels of noise (<11 and <10%, for homogeneous and heterogeneous conduction properties, respectively). Accurate identification at higher levels of noise (<17 and <14%) could be accomplished by averaging divergence maps over 10 beats (gray lines).

Identification of Focal Drivers in Simulated Atrial Fibrillation

The capability of the RBF framework to locate focal sources in a realistic, but controlled AF context, was evaluated by analyzing synthetic AF electrograms (**Figures 5A**, **6A**, **7A**), generated by a detailed LA model. **Figures 5B**, **6B**, **7B** show the activation and divergence maps obtained by moving the catheter from the region dominated by the focal driver (**Figure 5**) to the region with prevailing multiple-wavelet propagation (**Figure 7**).

In **Figure 5** the presence of the focal driver at the center of the mapping system resulted in a centrifugal sequence of activation from internal to external recording points (i.e., from A_{34} to A_{12} and from C_{1112} to C_{910}). Focal activation was apparent from the reconstructed activation maps (**Figure 5B**, top) and was accompanied by high positive values in the divergence maps (e.g., at time T1, D_{max} = 3.91 mm^{-1}, in red, versus D_{median} = 0.10 mm^{-1}). The regularity of the focal pattern could

TABLE 2 | Effects of temporal noise (expressed as percentage of atrial cycle length) on the estimation of median velocity, velocity vector magnitudes, and directions.

Simulated pattern	Noise level (%)	Exact median speed (cm/s)	Estimated median speed (cm/s)	Absolute speed error (%) 1 beat	Absolute angle error (rad) 1 beat	Absolute speed error (%) 10 beats	Absolute angle error (rad) 10 beats
Plane wavefront (pattern a)	0	60.4	60.4	0.16	0.002	0.158	0.002
	1	60.4	60.2 (59.8, 60.9)	3.6 (3.1, 4.3)	0.037 (0.030, 0.044)	1.4 (1.2, 1.6)	0.014 (0.012, 0.016)
	2	60.4	59.7 (58.7, 60.8)	6.9 (6.1, 8.2)	0.072 (0.060, 0.088)	2.8 (2.4, 3.2)	0.027 (0.024, 0.032)
	5	60.4	57.3 (55.4, 59.8)	16.9 (15.0, 19.0)	0.190 (0.160, 0.225)	7.0 (6.2, 8.0)	0.072 (0.065, 0.082)
	10	60.4	51.1 (47.7, 55.5)	28.3 (25.1, 33.0)	0.353 (0.292, 0.410)	16.4 (14.3, 18.0)	0.143 (0.121, 0.173)
	15	60.4	43.1 (40.0, 47.3)	37.1 (33.1, 41.2)	0.488 (0.423, 0.613)	28.1 (25.8, 30.0)	0.223 (0.188, 0.253)
	20	60.4	37.4 (34.0, 39.9)	44.2 (40.9, 48.6)	0.677 (0.527, 0.814)	38.4 (35.8, 40.5)	0.299 (0.258, 0.354)
Focal source in homogeneous tissue (pattern b)	0	54.7	54.2	7.6	0.059	7.6	0.059
	1	54.7	54.5 (53.7, 55.2)	8.7 (7.9, 9.4)	0.078 (0.073, 0.085)	7.7 (7.5, 8.0)	0.064 (0.062, 0.066)
	2	54.7	54.6 (53.3, 56.5)	11.7 (10.4, 13.1)	0.103 (0.094, 0.111)	8.4 (7.8, 8.6)	0.073 (0.070, 0.077)
	5	54.7	54.5 (51.5, 57.9)	21.5 (18.5, 24.3)	0.160 (0.142, 0.179)	10.5 (9.1, 11.3)	0.094 (0.085, 0.099)
	10	54.7	50.5 (44.8, 56.2)	32.3 (27.5, 36.0)	0.273 (0.228, 0.319)	14.0 (12.4, 15.9)	0.122 (0.106, 0.133)
	15	54.7	43.9 (39.2, 48.7)	38.6 (34.2, 43.1)	0.381 (0.311, 0.482)	22.2 (18.9, 24.0)	0.176 (0.145, 0.197)
	20	54.7	37.8 (33.2, 42.6)	44.2 (38.9, 47.5)	0.488 (0.389, 0.661)	30.4 (27.9, 32.6)	0.213 (0.182, 0.241)
Focal source in heterogeneous tissue (pattern c)	0	59.9	59.4	7.1	0.092	7.1	0.092
	1	59.9	58.7 (57.7, 59.9)	8.3 (7.8, 9.1)	0.102 (0.098, 0.104)	7.3 (7.1, 7.6)	0.095 (0.093, 0.097)
	2	59.9	58.3 (56.7, 60.7)	11.3 (10.0, 12.8)	0.115 (0.108, 0.124)	7.9 (7.4, 8.4)	0.099 (0.096, 0.103)
	5	59.9	57.1 (52.8, 59.3)	20.8 (17.9, 23.4)	0.168 (0.154, 0.193)	10.2 (8.9, 11.2)	0.112 (0.103, 0.123)
	10	59.9	52.2 (46.7, 56.5)	33.9 (29.2, 37.4)	0.276 (0.232, 0.326)	16.0 (14.1, 18.8)	0.135 (0.116, 0.156)
	15	59.9	43.5 (40.2, 48.9)	39.8 (36.9, 44.9)	0.390 (0.319, 0.519)	25.6 (21.8, 27.9)	0.166 (0.148, 0.190)
	20	59.9	38.9 (33.3, 42.6)	46.1 (41.4, 50.1)	0.521 (0.401, 0.699)	33.8 (31.4, 36.3)	0.207 (0.175, 0.243)
Colliding wavefronts (pattern d)	0	55.8	56.6	11.4	0.088	11.4	0.088
	1	55.8	56.4 (55.7, 57.0)	12.2 (11.7, 12.8)	0.096 (0.088, 0.107)	11.3 (11.1, 11.5)	0.089 (0.085, 0.093)
	2	55.8	56.0 (54.6, 57.4)	14.2 (13.1, 15.0)	0.116 (0.102, 0.130)	11.4 (11.0, 11.7)	0.093 (0.086, 0.098)
	5	55.8	55.8 (53.3, 58.8)	19.3 (17.5, 22.0)	0.230 (0.199, 0.266)	12.9 (12.0, 14.0)	0.114 (0.103, 0.125)
	10	55.8	49.6 (45.3, 54.1)	28.8 (25.7, 31.1)	0.428 (0.350, 0.518)	18.0 (16.0, 19.7)	0.172 (0.150, 0.200)
	15	55.8	42.2 (38.6, 47.4)	36.2 (31.5, 40.6)	0.590 (0.483, 0.688)	26.3 (24.0, 28.6)	0.253 (0.209, 0.289)
	20	55.8	37.1 (33.3, 42.4)	43.4 (38.1, 47.1)	0.701 (0.563, 0.835)	35.5 (32.9, 38.0)	0.337 (0.287, 0.408)

Data are median (IQR) over 100 stochastic repetitions.

be observed comparing successive single-beat activation and divergence maps and resulted in a consistent average divergence map (D_{max} = 3.45 mm^{-1}, in red, versus D_{median} = 0.10 mm^{-1}).

Figure 6 displays signals and maps from an intermediate region, with the focal driver located at the top right corner of the mapping system. Here, the presence of the focal driver was less apparent from visual inspection of the recorded signals, but it was revealed by single-beat and average divergence maps, displaying maximal positive values at the focal source (e.g., in the average map, D_{max} = 3.44 mm^{-1}, in red, versus D_{median} = 0.06 mm^{-1}). Single-beat activation and divergence maps showed that the area was invaded by wavefronts from the multiple wavelet region, which collided with wavefronts originating from the focal driver. The presence of collision lines resulted in negative divergence values (e.g., at time T4, D_{min} = −3.02 mm^{-1}, in blue, versus D_{median} = 0.07 mm^{-1}).

Figure 7 shows the complex propagation patterns observed in the multiple wavelet region. The activation sequence of the simulated electrograms suggested that the area was activated by wavefronts of changing directions. This was apparent in the beat-to-beat activation and divergence maps, which showed the presence of collision lines marked by minimal negative divergence values (e.g., at time T1, D_{min} = −4.40 mm^{-1}, in blue, versus D_{median} = −0.07 mm^{-1}). The irregularity of the patterns and the changing position of collision lines resulted in an average divergence map with almost-zero values [range = (−0.19, 0.08) mm^{-1}, in green].

Proof-of-Concept Application to Clinical Atrial Fibrillation Data

The methodology was applied to multipolar catheter electrograms acquired in the LA of a patient with persistent AF. Three representative examples of activation and divergence maps observed in the patient in different LA regions are displayed in **Figure 8**. The observed patterns can be directly compared to the simulated maps of **Figures 5–7**.

Figure 8A displays the activation and divergence maps reconstructed from the mapping of the LA appendage region. The regular activation sequence from the internal to the external bipoles (i.e., from A_{34} to A_{12} and from C_{1112} to C_{910}) and the repetitive morphology of the signals suggested the presence of a stable focal activation pattern. The reconstructed map identified the focal site at the center of the mapping area. Wavefronts

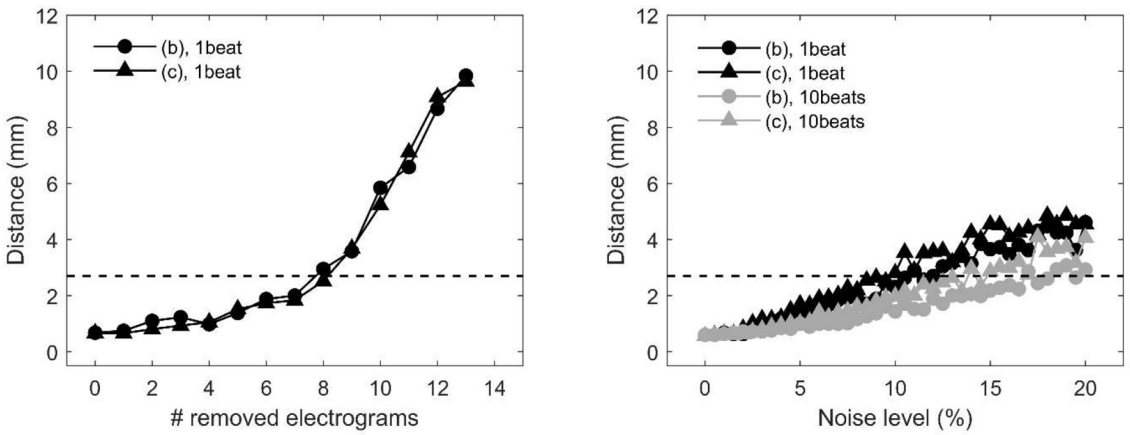

FIGURE 4 | Effects of missing or corrupted data on the accuracy of localization of focal drivers by divergence analysis in a tissue patch with homogeneous (pattern b) and heterogeneous conduction properties (pattern c) in the presence of partially corrupted data. Distance between exact and estimated focal driver position as a function of the progressive removal of electrograms (left) and at increasing levels of noise in activation time series (right). The horizontal dotted line indicates the threshold for accurate localization. In the right panel, black and gray lines correspond to single-beat and 10-beat position estimation, respectively. Data are median over 100 stochastic repetitions.

propagated centrifugally from the focal site with an average CV of 44.0 ± 4.3 cm/s and activated the region at a mean cycle length of 147 ms. The stability of the focal pattern was testified by the average divergence map, which displayed a maximal positive value at the center of the mapping area (D_{max} = 1.03 mm^{-1} versus D_{median} = 0.08 mm^{-1} in the surrounding area).

The mapping of the right superior PV ostium in **Figure 8B** showed a regular, but more complex pattern. Activation and divergence maps suggested the presence of a focal activation site at the top corner of the mapping area (D_{max} = 0.78 mm^{-1}), firing at a cycle length of 150 ± 16 ms. Wavefronts from the focal site activated the mapping area from top to bottom (i.e., from A_{12} to A_{34} to C_{1112}) at an average CV of 49.8 ± 8.7 cm/s and collided with wavefronts from the bottom. Collision lines were suggested by the fragmentation of electrogram C_{1112} (**Figure 8B**) and were marked by negative values in the average divergence map (D_{min} = −0.82 mm^{-1}).

Maps from the LA floor (**Figure 8C**) evidenced a complex activation process. Single-beat activation/divergence maps suggested that the region was invaded by colliding wavefronts, propagating with an average CV of 48.0 ± 4.9 cm/s. The region was characterized by an average cycle length of 160 ms and higher variability (cycle length SD of 14 ms). The average divergence map displayed almost-zero values [range = (−0.24, 0.11) mm^{-1}], reflecting the instability of the activation process and the absence of a prevalent propagation pattern.

Overall, the patient's mapping data showed an average LA cycle length of 150.1 ± 7.5 ms, with the fastest activity (136.9 ± 2.7 ms) recorded in the region of the vein of Marshall and the slowest (159.6 ± 2.9 ms) on the LA floor. Reconstructed CV vector fields showed that CV values in the LA ranged from 40.8 to 58.5 cm/s, with a mean value of 47.2 ± 4.5 cm/s. Beat-averaged divergence maps evidenced the presence of focal activation patterns in the region of the LA appendage, right superior PV and vein of Marshall, where maximal divergence values were observed (D_{max} = 1.00 ± 0.28 mm^{-1}). Collision lines were observed in proximity of focal sites and in ostial regions, where average divergence maps displayed minimal negative values (D_{min} = −1.03 ± 0.64 mm^{-1}). Differently, mapping sites on the LA body were prevalently characterized by complex and variable propagation patterns with more uniform divergence maps.

DISCUSSION

This study introduced and validated by computer simulations a novel approach for the characterization of wave propagation and the identification of focal drivers in AF, based on a RBF reconstruction of local CV vector fields from multipolar mapping electrograms. Computer simulations demonstrated the method flexibility in reconstructing continuous activation patterns and CV fields corresponding to different propagation patterns from scattered activation time series, and its accuracy in localizing focal drivers even in the presence of partially corrupted data. The proof-of-concept application to clinical multipolar mapping data detected focal activation patterns in the PVs and LA appendage region and more complex propagation patterns on the LA body, suggesting the potential of the approach for identifying critical sites in human AF.

Radial Basis Function-Based Conduction Velocity Vector Approach for the Characterization of Propagation Patterns

Our approach was based on a RBF reconstruction of activation patterns and corresponding CV vector fields in the mapping area. The RBF approach presents several features, which makes it suitable for integration with clinically available mapping systems. RBF interpolation does not require any assumptions on the spacing and/or density of the interpolation

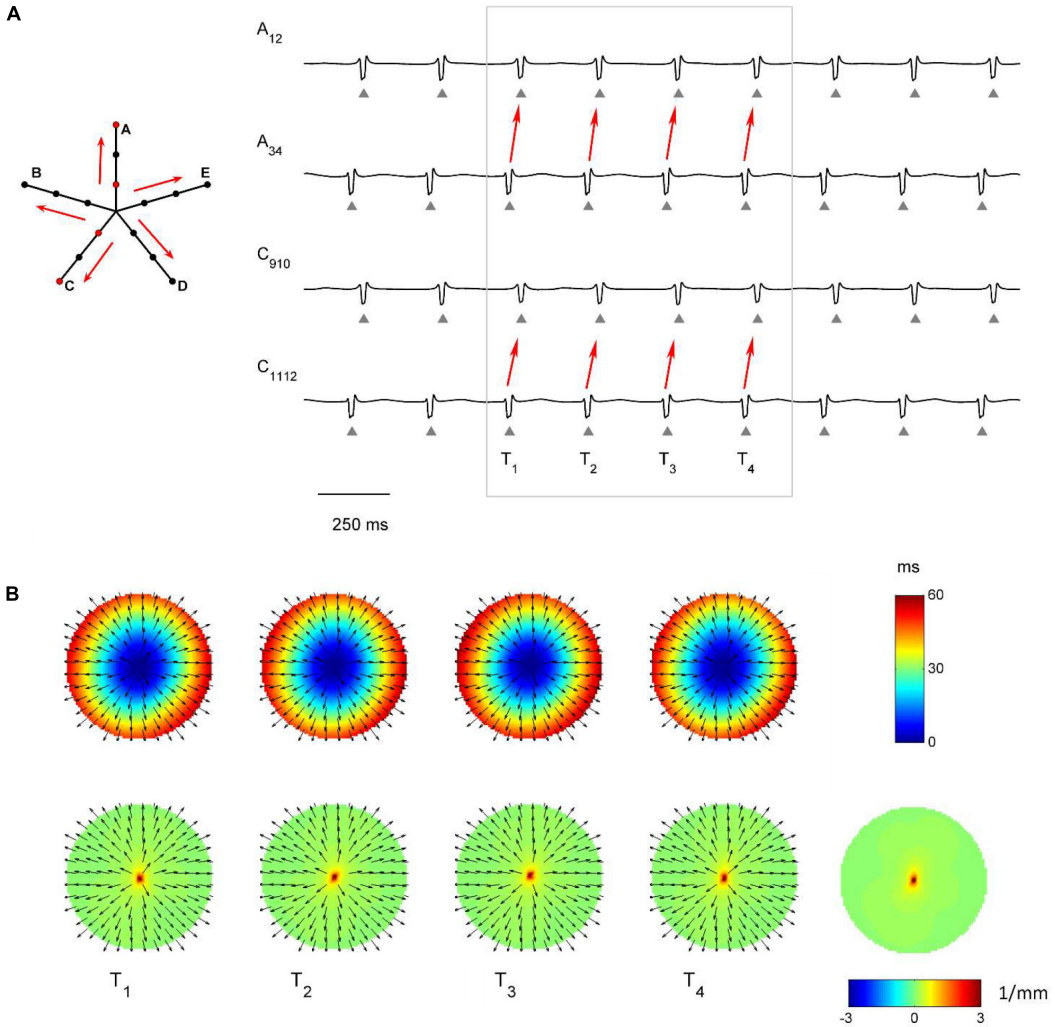

FIGURE 5 | Application of divergence analysis during simulated atrial fibrillation in a region activated by a focal driver. **(A)** Schematic representation of the multipolar mapping system, indicating the central position of the bipoles, and representative synthetic electrograms corresponding to the red bipoles of the catheter. Arrows indicate the prevalent activation sequence. **(B)** Beat-to-beat reconstructed activation (top) and divergence maps (bottom) corresponding to the evidenced beats. The average divergence map over the analyzed epoch is displayed in the bottom right panel. The presence of the focal driver is evidenced by maximal positive divergence values (red).

points (Fornefett et al., 2001; Kybic et al., 2002a,b). This allows integration with different clinically available mapping systems, with respect to other approaches (Rogers et al., 1997; Bayly et al., 1998; Alcaine et al., 2014; Zeemering et al., 2020) proposed in the experimental setting, which instead require regularly spaced and/or high-density latency data. In this study we demonstrated the capability of RBFs to accurately reconstruct CV fields from the analysis of simultaneous electrograms from multipolar catheters and we showed that the application of operators, such as the divergence, to the calculated CV fields could be used to identify focal drivers in the presence of complex propagation patterns. This extends our preliminary work (Masé and Ravelli, 2010), where we suggested the possibility of using RBFs to reconstruct activation patterns and CV fields from scattered latency data, consecutively acquired by electro-anatomic mapping system, during atrial pacing. In addition, in the present work we corroborated the stability of the reconstructions at a progressive reduction of the mapping sites, suggesting that the method may be able to cope with partial information loss due to inappropriate deployment and/or poor electrode contact with the endocardial surface.

A second advantage of RBF interpolation is that the methodology displays a certain degree of flexibility in reconstructing continuous activation patterns that can be present during atrial arrhythmias, such as focal activation, multiple wavelet propagation, and wave collision. This may represent an advantage with respect to previously proposed algorithms, such as cosine or ellipse model fitting

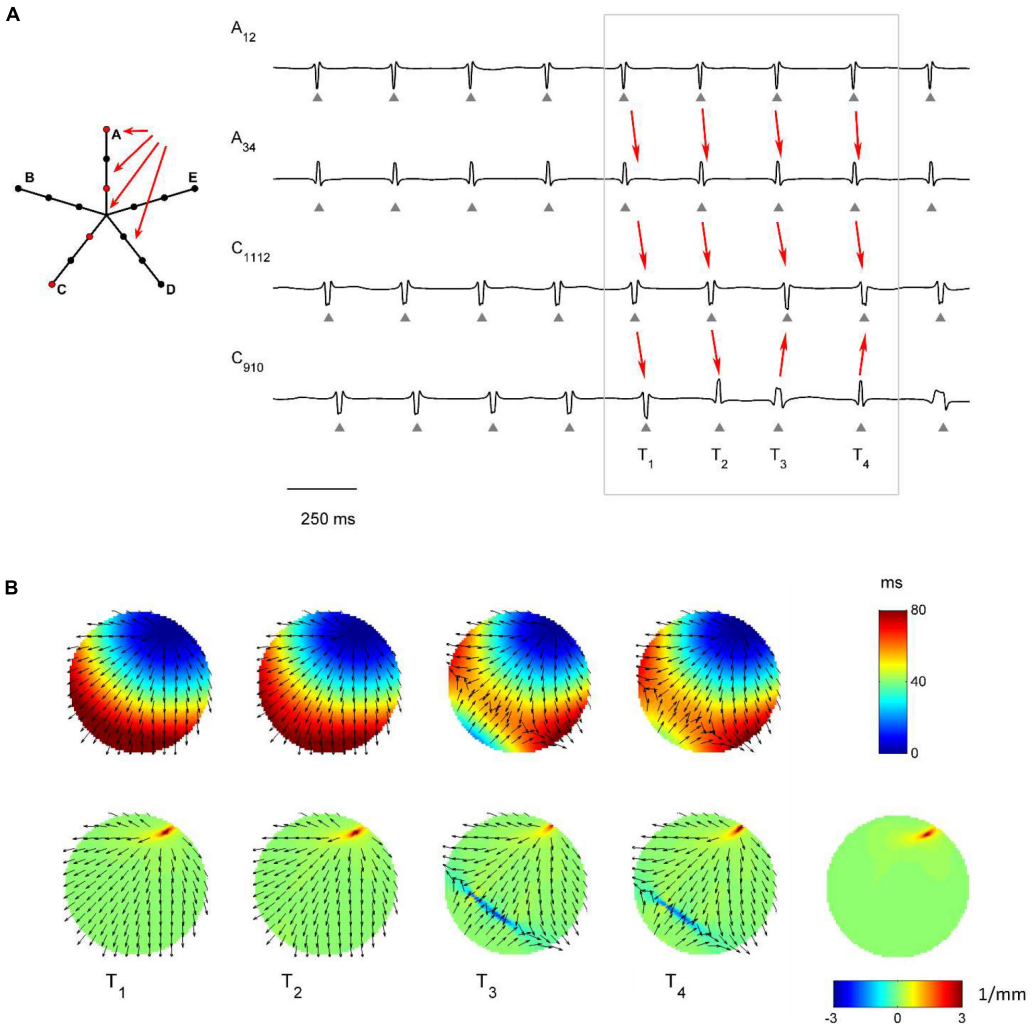

FIGURE 6 | Application of divergence analysis to simulated atrial fibrillation at the boundary between the focal driver and multiple wavelets region. **(A)** Schematic representation of the multipolar mapping system, indicating the central position of the bipoles, and representative synthetic electrograms corresponding to the red bipoles of the catheter. Arrows indicate the prevalent activation sequence. **(B)** Beat-to-beat reconstructed activation (top) and divergence maps (bottom) corresponding to the evidenced beats. The average divergence map over the analyzed epoch is displayed in the bottom right panel. The presence of the focal driver is evidenced by positive divergence values (red), while collision lines are indicated by negative values (blue).

(Weber et al., 2010, 2011; Roney et al., 2019) and triangulation approaches (Kojodjojo et al., 2006; Ravelli et al., 2011), which display accuracy in the estimation of wavefront speed, direction, and conduction anisotropy in the presence of a single propagating wavefront, but are not able to operate in the presence of other propagation patterns. Flexibility in reproducing different activation patterns, such as focal activation and wave collision, has been recently demonstrated by physically informed neural network, which may represent a promising approach also to quantify the epistemic uncertainty associated with these predictions (Sahli Costabal et al., 2020). Despite the flexibility of RBFs to reproduce different propagation patterns, it should be noticed that the definition of the interpolant function as a sum of continuous functions makes RBFs incapable to accurately reconstruct patterns where discontinuities and/or abrupt changes in activation time are present. Thus, although capable to reconstruct wavefronts with different curvature, RBFs may not be suitable to trace the head-meet-tail region and phase singularity of rotors, where discontinuities in phase values are present. This is exemplified in **Figure 9**, which displays the RBF reconstruction of a transient rotor observed in the complex activity region of the simulated AF. In the displayed time window, the electrical activity in the PentaRay mapped area was characterized by a rotational wave activating the tissue in a counterclockwise direction (**Figure 9A**). The RBF reconstruction (**Figure 9B**) was able to track the sequence of activation, showing a wave entering from the upper left region and turning to the right, but it could not reliably map the head-meet-tail part of the reentrant

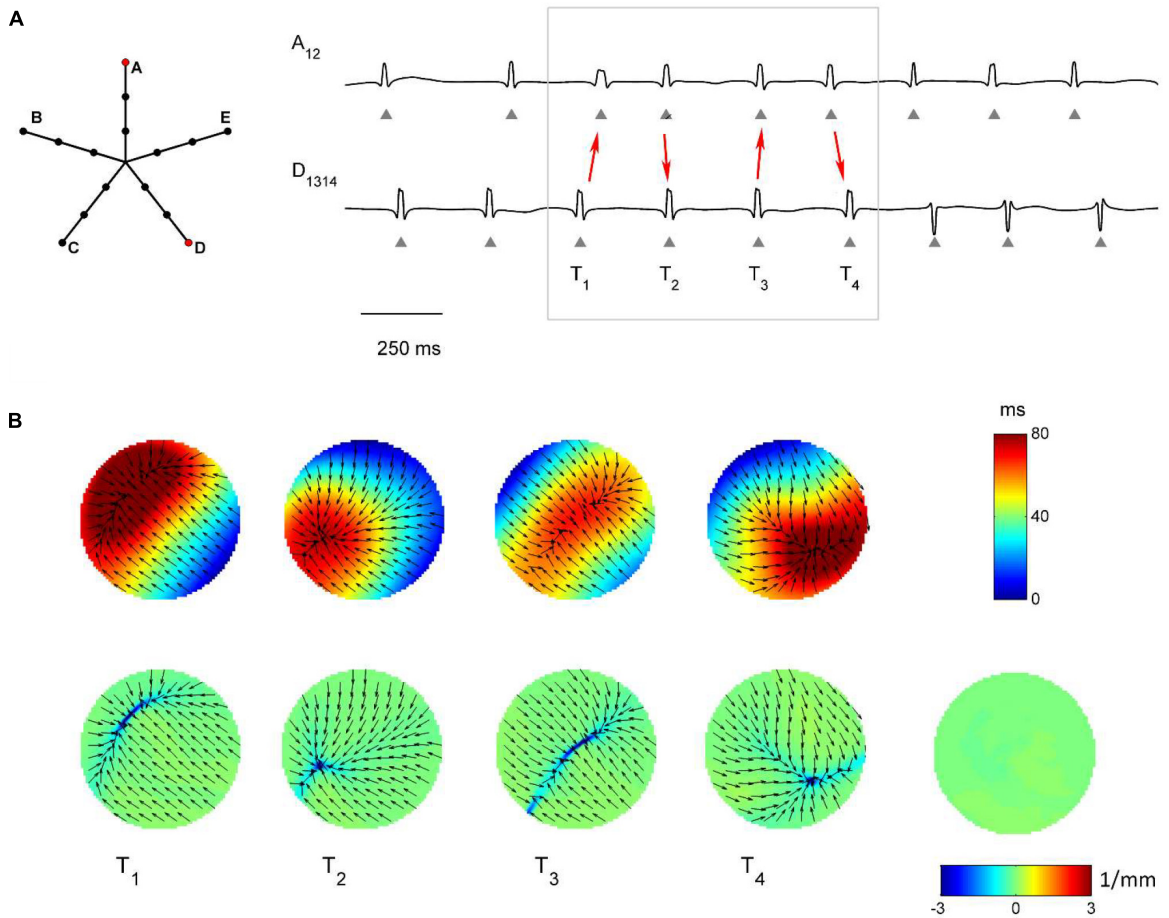

FIGURE 7 | Application of divergence analysis to simulated atrial fibrillation in the region dominated by multiple wavelets propagation. **(A)** Schematic representation of the multipolar mapping system, indicating the central position of the bipoles, and representative synthetic AF electrograms corresponding to the red bipoles of the catheter. Arrows in the electrograms indicate changes in the activation sequence. **(B)** Beat-to-beat reconstructed activation (top) and divergence maps (bottom), corresponding to the evidenced beats. The average divergence map over the analyzed epoch is displayed in the bottom right panel. The absence of a stable propagation pattern is evidenced by the almost-zero values of the average divergence map (green).

circuit. Given this limitation, specific techniques available in the literature, which detect rotors by examining the characteristics of the electrograms obtained from catheters (Roney et al., 2017; Ganesan et al., 2018, 2019; Orozco-Duque et al., 2019; Li et al., 2020), should be used to supplement our approach when the aim is the precise localization of rotors' critical sites. Another pattern that may not be correctly reproduced by our method is the occurrence of conduction block. Indeed, our reconstruction algorithm assumes that activation times are correctly identified and aligned per beat at different atrial sites. In the presence of conduction block and missed activations at some space locations, direct RBFs interpolation may wrongly extrapolate a continuous electrical activation in these areas. To address this problem, in future implementations, missed activation times should be properly marked on the activation map and restrictions to interpolate activation patterns in these regions may be posed. Alternatively, imposition of late activation times at these sites may be considered to mimic conduction blocks in terms of extremely slow conduction areas.

Radial basis functions provide an analytical formulation of the activation patterns, which can be directly used for the analytical determination of the CV vector field and its properties in the mapping area. CV fields integrate and complete the information content of activation maps, providing quantitative data on local CVs and directions of propagating wavefronts. In combination with spatial and/or anatomical information, CV maps evidence spatial heterogeneities in conduction and slow conduction areas. As well, specific angular properties of CV vectors mark areas of focal activation and/or wave collision (Fitzgerald et al., 2005). Of note, in a study performing a quantitative comparison of the use of vector maps and isochrone cardiac activation maps to identify patterns and features associated with arrhythmias, the former displayed superior performance in mapping simple arrhythmias, reducing the number of measurements necessary to select the correct ablation target and presenting more rapid learning curves (Fitzgerald et al., 2004). Despite the potentiality of CV vector field representation of activation patterns (Fitzgerald et al., 2004), CV field maps have been mostly limited to experimental models

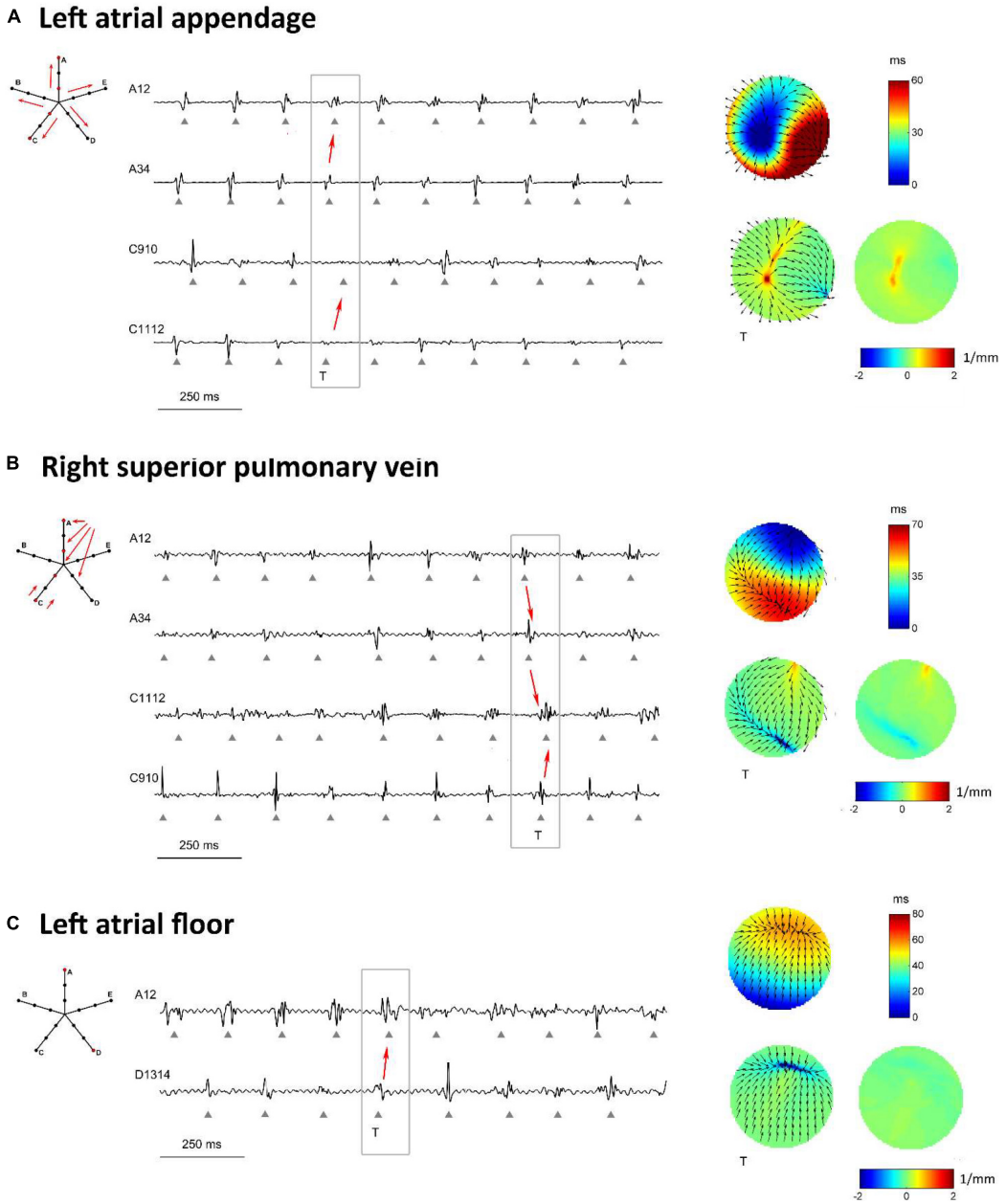

FIGURE 8 | Proof-of-concept application of divergence analysis to multipolar electrograms acquired during left atrial mapping in an AF patient. The displayed multipolar mapping data were collected at the left atrial appendage **(A)**, PVs region **(B)**, and left atrial floor **(C)**. For each mapped region, the left panels show a schematic representation of the multipolar mapping system with arrows indicating the prevalent activation sequence and the representative electrograms corresponding to the red bipoles of the catheter. The right panels show single-beat reconstructed activation and divergence maps for the evidenced beat and the average divergence map calculated over the analyzed epoch.

(Bayly et al., 1998; Eijsbouts et al., 2003; Fitzgerald et al., 2003) and open-heart surgery settings (Hansson et al., 1998), and are only recently entering electrophysiological mapping data software (O'Shea et al., 2019; Williams et al., 2021). Our approach makes the construction of a CV vector maps equivalent to that of an activation map, in terms of both clinician skill and time expenditure, which supports clinical applications. Indeed, the analytical formulation derived from RBFs allows the automatic determination of the direction of propagation (given by the gradient of the function), solving the problem of precisely delineating the activation front. The interpolation function is globally estimated from all latency data, without need of point latency grouping as required by triangulation and bilinear fit model approaches (Fitzgerald et al., 2003; Kojodjojo et al., 2006; Ravelli et al., 2011). The potential of RBF approaches to measure CV is testified by a recent study, where RBFs were chosen to

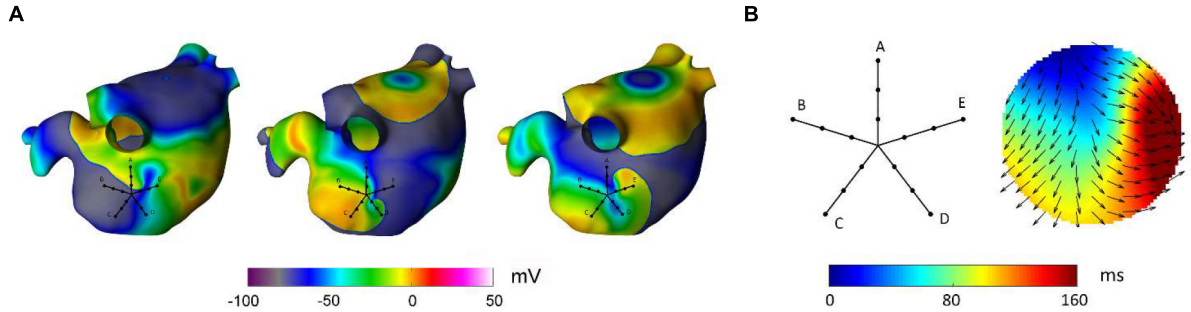

FIGURE 9 | Reconstruction of a rotational pattern by radial basis functions during simulated atrial fibrillation in a realistic left atrial model. In panel **(A)**, the sequential snapshots of the membrane voltage show the presence of a transient rotor, which activates the PentaRay mapping area in a counterclockwise direction. Panel **(B)** shows the activation map reconstructed from RBF interpolation of the activation times recorded at the PentaRay bipoles, with the normalized conduction velocity vectors indicating the direction of wave propagation. The RBF activation map tracked the activation sequence, but it was not able to reproduce the head-meet-tail part of the circuit **(B)**.

estimate CV values in an open software for mapping data analysis (Williams et al., 2021). Together with the computation of CV fields by RBFs, the present study implemented the application of operators, such as the divergence, to the CV fields. We showed the divergence able to reveal and quantify important arrhythmia features, such as the presence of focal sources or wave collision lines. These features may thus be used to inform the mapping strategy in order to accelerate the detection of these critical sites in the absence of human pattern recognition. Few previous studies have proposed algorithms to navigate the mapping catheter toward focal or early activation sites (Roney et al., 2014; Weber et al., 2017; Ganesan et al., 2019). An algorithm based on iterative regression analyses displayed high accuracy to predict the earliest activation site during focal tachycardias, requiring a significantly lower number of mapping points with respect to an operator-guided mapping (Weber et al., 2017). However, the method was developed to work in combination with a point-by-point acquisition mapping and thus with a single bipole at each catheter location, while instead our approach has the advantage of condensing in the divergence index the collective information from a multipolar catheter at each mapping location. Collective information from multipolar mapping systems was extracted in another study (Roney et al., 2014) by fitting a single planar or circular wave model to the activation times of the bipoles. The direction of the estimated wave was used to guide the catheter toward the earliest activation focal source. As our approach, this method had the advantage not to be limited to a specific catheter configuration, although better detection of focal sources was obtained in combination with PentaRay or spiral catheters than with circular catheters. While the approach in Roney et al. (2014) provided a global evaluation of the direction of propagation in the mapped area by a single-wave fit, our method allows a more local and precise description of the actual wave propagation patterns. In the absence of a source in the mapped area, local RBF-estimated CV vectors may be nonetheless easily combined in a macroscopic average vector to determine a prevalent propagation direction and thus direct the mapping process. More recently, a multiparameter algorithm was proposed to iteratively guide the incremental movement of circular catheter through the atrium until source (either focal or reentrant) detection (Ganesan et al., 2019). The detection was based on the computation of four indices describing the propagation pattern and the fulfillment of source detection criteria. In particular, focal sources were detected based on the "so-called" wave divergence index, which was approximated as the SD of the direction of the velocity vectors computed through subgrouping of the mapping points into triads (Ganesan et al., 2019). Differently from this method, our divergence approach may have the advantage of not requiring any subgroup of electrodes nor specific catheter configurations or symmetries, and of providing a divergence evaluation directly based on a physical definition. Our method may be conveniently integrated into these mapping navigation schemes, where the RBF-based detection of focal sources would complement the rules for the identification of rotors (Ganesan et al., 2019). However, the implementation would require the estimation of reliable threshold values for the divergence index, which may be determined by receiver-operating characteristic analysis or statistical approaches (Schreiber and Schmitz, 2000).

It is important to notice that our approach shares with all these methods the necessity of a correct detection of activation times. Indeed, although the use of an interpolation approach allows flexibility for pattern reconstruction, interpolation is more sensitive to activation time misdetections and noise effects, with respect to techniques based on model fitting (Bayly et al., 1998; Fitzgerald et al., 2003; Weber et al., 2010; Alcaine et al., 2014) or approaches that do not require activation time detection (Richter et al., 2011; Rodrigo et al., 2016; Alcaine et al., 2017; Luengo et al., 2019; Handa et al., 2020). In order to reduce inaccuracy in activation time estimations, activation waveforms from patient data were automatically identified by a well-established technique (Botteron and Smith, 1995; Faes et al., 2002), and activation times were set at the waveform barycenter (Faes et al., 2002; Masè et al., 2005, 2015). As suggested in several works (Holm et al., 1996; Faes et al., 2002; El Haddad et al., 2013; Ravelli and Masè, 2014), the use of a morphology-based activation detection, such as the barycenter method, improves estimation accuracy in the presence of fragmented electrograms. In addition, the barycenter identifies the central point of the activation waveform

and thus can be spatially associated with the midpoint of the bipole, where bipolar electrogram coordinates were set. The importance of an accurate estimation of activation series was pointed out by our computer simulations, which showed a progressive deterioration of estimation accuracy at increasing noise levels. Noise affected at a higher extent the estimation of CV vector magnitudes, while vector directions (and thus divergence analysis) were less affected. On the other hand, median CV displayed a decreasing trend with increasing noise, which may be partially related to a minimization of the wavefront curvature performed by RBF. Since simulations showed the method to be more robust against electrogram loss than misdetection, it should be preferable to exclude activation series from noisy or excessively fragmented electrograms, although extrapolation of activation patterns to poorly mapped regions should be considered with caution. Alternatively, uncertainty in local activation times may be profitably addressed using novel approaches based on probabilistic interpolation, able to keep into account activation time errors at different sites and to pin the activation map more strongly at site with higher precision measurements (Coveney et al., 2020). Consistently with previous works (O'Shea et al., 2019), our simulations also suggested that, in the presence of stable patterns, noise effects on CV estimation and source localization could be reduced by averaging values over few beats. Thus, although the method is potentially able to work on a beat-to-beat basis, sequential divergence maps should be computed to distinguish transient instances of focal activation [e.g., due to epicardial breakthroughs (de Groot et al., 2010)] from the presence of a stable localized source, whose activity should be repetitive and persist over longer periods (Takahashi et al., 2006; de Groot et al., 2010; Ravelli et al., 2012, 2014). Assuming an atrial cycle length <200 ms during AF, averaging of 10 beats would require very short (<2 s) signal windows, which are consistent with clinical mapping times. The method may thus be used to complement other descriptors of the fibrillatory patterns, such as causality-based approaches (Richter et al., 2011; Rodrigo et al., 2016; Alcaine et al., 2017; Luengo et al., 2019; Handa et al., 2020), which may require longer signal windows for the analysis.

Divergence-Based Identification of Focal Patterns in Human Atrial Fibrillation

The proof-of-concept application of divergence analysis to clinical multipolar electrograms revealed the presence of stable focal activation patterns at the PVs, vein of Marshall, and LA appendage during AF. The position of the detected focal sites is consistent with previous studies in AF patients (Haissaguerre et al., 1998; Hwang et al., 2000; Schmitt et al., 2002; Nitta et al., 2004; Sanders et al., 2005; Ravelli et al., 2012, 2014). Arrhythmic episodes of multifocal origin, with triggers located outside the PV region, were observed in AF patients by multisite biatrial mapping using a basket catheter or a non-contact mapping system (Schmitt et al., 2002). Rapid repetitive activity from the LA veins, including the PVs (Haissaguerre et al., 1998) and the vein of Marshall (Hwang et al., 2000), were reported to trigger paroxysmal AF. Dominant frequency analysis applied to atrial electrograms in paroxysmal AF showed that the PVs and ostial regions were most likely to harbor a high frequency source (42%), while the probability decreased in other atrial regions and in the coronary sinus (Sanders et al., 2005). In patients with permanent AF and mitral valve disease (Nitta et al., 2004), intraoperative mapping of the entire atrial epicardium showed LA focal activation from the posterior region adjacent to the PVs and the LA appendage. Consistently, electro-anatomic mapping and combined cycle length/wave similarity analysis in patients with persistent AF localized AF sources in the PV region in 47% of patients and in the LA appendage area in 12% of patients (Ravelli et al., 2012). Our analysis revealed the presence of collision areas and more complex propagation patterns in proximity of the focal sites, as observed at the right superior PV (see **Figure 8B**) and in other ostial regions. This is consistent with experimental (Kalifa et al., 2006) and clinical studies (Stiles et al., 2008; Ravelli et al., 2014; Kochhäuser et al., 2017), which identified zones characterized by propagation pattern variability and fractionated activity alongside areas of fast and regular atrial activation.

In the present study the analysis of clinical data was restricted to a proof-of-concept, being limited to the LA mapping of a single AF patient. Nonetheless, the consistency of our results with previous studies suggests the potential of the approach and fosters the performance of systematical studies on larger patient groups to investigate the spatial distribution of focal activation patterns in AF and their correlation with ablation outcomes. In addition, the developed techniques may be useful to map more organized forms of AF, as well as secondary atrial tachycardias at re-do procedures (Haissaguerre et al., 2006). Further validation of the method in larger clinical datasets, including different types of atrial arrhythmias, is necessary to clinically validate the method and to assess its applicability and benefit for the optimization of ablation strategies.

CONCLUSION

This paper introduced a novel methodology for the characterization of wave propagation and the identification of focal drivers in AF, which is based on the reconstruction of CV vector fields and the application of divergence analysis. Tests led by computer simulations suggested that accurate reconstruction of propagation patterns and localization of focal sites was feasible with clinically available catheter configurations. The proof-of-concept application of the methodology to human AF signals consistently identified focal patterns in the PVs and LA appendage area. The combination of RBF and divergence analysis with other methods for the extraction of collective information from multipolar mapping data may allow a more robust interrogation of cardiac conduction patterns, potentially leading to the optimization of ablation treatment.

DATA AVAILABILITY STATEMENT

The datasets generated and analyzed in this study are available from the corresponding authors on reasonable request.

ETHICS STATEMENT

The part of the study involving human participants was reviewed and approved by the Ethical Committee for Clinical Experimentation of the Provincial Agency for Health Services of the Autonomous Province of Trento. The patients/participants provided their written informed consent to participate in this study.

AUTHOR CONTRIBUTIONS

MM designed the study, performed the simulations and analysis, and wrote the manuscript. AC performed the simulations. MD collected the clinical data. FR designed and supervised the study, and critically revised the manuscript for important intellectual content. All authors contributed to manuscript revision, read, and approved the submitted version.

FUNDING

This study was supported by the Fondazione Cassa di Risparmio di Trento e Rovereto (Grants: 2014.0349 and 2016.0273).

ACKNOWLEDGMENTS

The authors thank the Department of Innovation, Research, University and Museums of the Autonomous Province of Bozen/Bolzano for covering the Open Access publication costs.

REFERENCES

Alcaine, A., Masè, M., Cristoforetti, A., Ravelli, F., Nollo, G., Laguna, P., et al. (2017). A multi-variate predictability framework to assess invasive cardiac activity and interactions during atrial fibrillation. *IEEE Trans. Biomed. Eng.* 64, 1157–1168. doi: 10.1109/TBME.2016.2592953

Alcaine, A., Soto-Iglesias, D., Calvo, M., Guiu, E., Andreu, D., Fernandez-Armenta, J., et al. (2014). A wavelet-based electrogram onset delineator for automatic ventricular activation mapping. *IEEE Trans. Biomed. Eng.* 61, 2830–2839. doi: 10.1109/TBME.2014.2330847

Almeida, T. P., Schlindwein, F. S., Salinet, J., Li, X., Chu, G. S., Tuan, J. H., et al. (2018). Characterization of human persistent atrial fibrillation electrograms using recurrence quantification analysis. *Chaos* 28:085710. doi: 10.1063/1.5024248

Almeida, T. P., Soriano, D. C., Mase, M., Ravelli, F., Bezerra, A. S., Li, X., et al. (2021). Unsupervised classification of atrial electrograms for electroanatomic mapping of human persistent atrial fibrillation. *IEEE Trans. Biomed. Eng.* 68, 1131–1141. doi: 10.1109/TBME.2020.3021480

Baher, A., Buck, B., Fanarjian, M., Paul Mounsey, J., Gehi, A., Chung, E., et al. (2019). Recurrence quantification analysis of complex-fractionated electrograms differentiates active and passive sites during atrial fibrillation. *J. Cardiovasc. Electrophysiol.* 30, 2229–2238. doi: 10.1111/jce.14161

Baumert, M., Sanders, P., and Ganesan, A. (2016). Quantitative electrogram-based methods for guiding catheter ablation of atrial fibrillation. *Proc. IEEE* 104, 416–431. doi: 10.1109/jproc.2015.2505318

Bayly, P. V., KenKnight, B. H., Rogers, J. M., Hillsley, R. E., Ideker, R. E., and Smith, W. M. (1998). Estimation of conduction velocity vector fields from epicardial mapping data. *IEEE Trans. Biomed. Eng.* 45, 563–571. doi: 10.1109/10.668746

Botteron, G. W., and Smith, J. M. (1995). A technique for measurement of the extent of spatial organization of atrial activation during atrial fibrillation in the intact human heart. *IEEE Trans. Biomed. Eng.* 42, 579–586. doi: 10.1109/10.387197

Buist, T. J., Zipes, D. P., and Elvan, A. (2021). Atrial fibrillation ablation strategies and technologies: past, present, and future. *Clin. Res. Cardiol.* 110, 775–788. doi: 10.1007/s00392-020-01751-5

Courtemanche, M., Ramirez, R. J., and Nattel, S. (1998). Ionic mechanisms underlying human atrial action potential properties: insights from a mathematical model. *Am. J. Physiol.* 275, H301–H321. doi: 10.1152/ajpheart.1998.275.1.H301

Coveney, S., Corrado, C., Roney, C. H., Wilkinson, R. D., Oakley, J. E., Lindgren, F., et al. (2020). Probabilistic interpolation of uncertain local activation times on human atrial manifolds. *IEEE Trans. Biomed. Eng.* 67, 99–109. doi: 10.1109/TBME.2019.2908486

Cristoforetti, A., Faes, L., Ravelli, F., Centonze, M., Del Greco, M., Antolini, R., et al. (2008). Isolation of the left atrial surface from cardiac multi-detector CT images based on marker controlled watershed segmentation. *Med. Eng. Phys.* 30, 48–58. doi: 10.1016/j.medengphy.2007.01.003

Cristoforetti, A., Masè, M., and Ravelli, F. (2013). A fully adaptive multiresolution algorithm for atrial arrhythmia simulation on anatomically realistic unstructured meshes. *IEEE Trans. Biomed. Eng.* 60, 2585–2593. doi: 10.1109/TBME.2013.2261815

de Groot, N. M., Houben, R. P., Smeets, J. L., Boersma, E., Schotten, U., Schalij, M. J., et al. (2010). Electropathological substrate of longstanding persistent atrial fibrillation in patients with structural heart disease: epicardial breakthrough. *Circulation* 122, 1674–1682. doi: 10.1161/CIRCULATIONAHA.109.910901

Duchon, J. (1977). "Splines minimizing rotation-invariant semi-norms in Sobolev spaces," in *Constructive Theory of Functions of Several Variables. Lecture Notes in Mathematics*, eds W. Schempp and K. Zeller (Berlin: Springer).

Eijsbouts, S., Van Zandvoort, M., Schotten, U., and Allessie, M. (2003). Effects of acute atrial dilation on heterogeneity in conduction in the isolated rabbit heart. *J. Cardiovasc. Electrophysiol.* 14, 269–278. doi: 10.1046/j.1540-8167.2003.02280.x

El Haddad, M., Houben, R., Stroobandt, R., Van Heuverwyn, F., Tavernier, R., and Duytschaever, M. (2013). Algorithmic detection of the beginning and end of bipolar electrograms: implications for novel methods to assess local activation time during atrial tachycardia. *Biomed. Signal Process. Control* 8, 981–991. doi: 10.1016/j.bspc.2012.11.005

Faes, L., Nollo, G., Antolini, R., Gaita, F., and Ravelli, F. (2002). A method for quantifying atrial fibrillation organization based on wave morphology similarity. *IEEE Trans. Biomed. Eng.* 49, 1504–1513. doi: 10.1109/TBME.2002.805472

Fitzgerald, T. N., Brooks, D. H., and Triedman, J. K. (2004). Comparative psychometric analysis of vector and isochrone cardiac activation maps. *IEEE Trans. Biomed. Eng.* 51, 847–855. doi: 10.1109/TBME.2004.826670

Fitzgerald, T. N., Brooks, D. H., and Triedman, J. K. (2005). Identification of cardiac rhythm features by mathematical analysis of vector fields. *IEEE Trans. Biomed. Eng.* 52, 19–29. doi: 10.1109/TBME.2004.839636

Fitzgerald, T. N., Rhee, E. K., Brooks, D. H., and Triedman, J. K. (2003). Estimation of cardiac conduction velocities using small data sets. *Ann. Biomed. Eng.* 31, 250–261. doi: 10.1114/1.1543936

Fornefett, M., Rohr, K., and Stiehl, H. S. (2001). Radial basis functions with compact support for elastic registration of medical images. *Image Vis. Comput.* 19, 87–96. doi: 10.1109/IEMBS.2010.5628055

Franke, R. (1982). Scattered data interpolation: tests of some methods. *Math. Comput.* 38, 181–200. doi: 10.1090/s0025-5718-1982-0637296-4

Fuster, V., Ryden, L. E., Cannom, D. S., Crijns, H. J., Curtis, A. B., Ellenbogen, K. A., et al. (2006). ACC/AHA/ESC 2006 guidelines for the management of patients with atrial fibrillation: a report of the American college of cardiology/American heart association task force on practice guidelines and the European society of cardiology committee for practice guidelines. *Circulation* 114, e257–e354.

Ganesan, P., Cherry, E. M., Huang, D. T., Pertsov, A. M., and Ghoraani, B. (2019). Locating atrial fibrillation rotor and focal sources using iterative navigation of multipole diagnostic catheters. *Cardiovasc. Eng. Technol.* 10, 354–366. doi: 10.1007/s13239-019-00414-5

Ganesan, P., Cherry, E. M., Pertsov, A. M., and Ghoraani, B. (2015). Characterization of electrograms from multipolar diagnostic catheters during atrial fibrillation. *Biomed. Res. Int.* 2015:272954. doi: 10.1155/2015/272954

Ganesan, P., Cherry, E. M., Pertsov, A. M., and Ghoraani, B. (2018). Development of a rotor-mapping algorithm to locate ablation targets during atrial fibrillation. *IEEE Life Sci. Conf.* 2018, 41–44. doi: 10.1109/LSC.2018.8572271

Haissaguerre, M., Hocini, M., Sanders, P., Takahashi, Y., Rotter, M., Sacher, F., et al. (2006). Localized sources maintaining atrial fibrillation organized by prior ablation. *Circulation* 113, 616–625. doi: 10.1161/CIRCULATIONAHA.105.546648

Haissaguerre, M., Jais, P., Shah, D. C., Takahashi, A., Hocini, M., Quiniou, G., et al. (1998). Spontaneous initiation of atrial fibrillation by ectopic beats originating in the pulmonary veins. *N. Engl. J. Med.* 339, 659–666. doi: 10.1056/NEJM199809033391003

Handa, B. S., Li, X., Aras, K. K., Qureshi, N. A., Mann, I., Chowdhury, R. A., et al. (2020). Granger causality-based analysis for classification of fibrillation mechanisms and localization of rotational drivers. *Circ. Arrhythm. Electrophysiol.* 13:e008237. doi: 10.1161/CIRCEP.119.008237

Hansson, A., Holm, M., Blomstrom, P., Johansson, R., Luhrs, C., Brandt, J., et al. (1998). Right atrial free wall conduction velocity and degree of anisotropy in patients with stable sinus rhythm studied during open heart surgery. *Eur. Heart J.* 19, 293–300. doi: 10.1053/euhj.1997.0742

Holm, M., Johansson, R., Olsson, S. B., Brandt, J., and Luhrs, C. (1996). A new method for analysis of atrial activation during chronic atrial fibrillation in man. *IEEE Trans. Biomed. Eng.* 43, 198–210. doi: 10.1109/10.481989

Hwang, C., Wu, T. J., Doshi, R. N., Peter, C. T., and Chen, P. S. (2000). Vein of marshall cannulation for the analysis of electrical activity in patients with focal atrial fibrillation. *Circulation* 101, 1503–1505. doi: 10.1161/01.cir.101.13.1503

Jacquemet, V., and Henriquez, C. S. (2005). Finite volume stiffness matrix for solving anisotropic cardiac propagation in 2-D and 3-D unstructured meshes. *IEEE Trans. Biomed. Eng.* 52, 1490–1492. doi: 10.1109/TBME.2005.851459

Jacquemet, V., Virag, N., Ihara, Z., Dang, L., Blanc, O., Zozor, S., et al. (2003). Study of unipolar electrogram morphology in a computer model of atrial fibrillation. *J. Cardiovasc. Electrophysiol.* 14, S172–S179. doi: 10.1046/j.1540.8167.90308.x

Kalifa, J., Tanaka, K., Zaitsev, A. V., Warren, M., Vaidyanathan, R., Auerbach, D., et al. (2006). Mechanisms of wave fractionation at boundaries of high-frequency excitation in the posterior left atrium of the isolated sheep heart during atrial fibrillation. *Circulation* 113, 626–633. doi: 10.1161/CIRCULATIONAHA.105.575340

Kochhäuser, S., Verma, A., Dalvi, R., Suszko, A., Alipour, P., Sanders, P., et al. (2017). Spatial relationships of complex fractionated atrial electrograms and continuous electrical activity to focal electrical sources: implications for substrate ablation in human atrial fibrillation. *JACC Clin. Electrophysiol.* 3, 1220–1228. doi: 10.1016/j.jacep.2017.05.013

Kojodjojo, P., Kanagaratnam, P., Markides, V., Davies, D. W., and Peters, N. (2006). Age-related changes in human left and right atrial conduction. *J. Cardiovasc. Electrophysiol.* 17, 120–127. doi: 10.1111/j.1540-8167.2005.00293.x

Kybic, J., Thierry, B., and Unser, M. (2002a). Generalized sampling: a variational approach. Part I – theory. *IEEE Trans. Signal Process.* 50, 1965–1976. doi: 10.1109/tsp.2002.800391

Kybic, J., Thierry, B., and Unser, M. (2002b). Generalized sampling: a variational approach. Part II – applications. *IEEE Trans. Signal Process.* 50, 1977–1985. doi: 10.1186/s12868-016-0283-6

Lammers, W. J. E. P., Ravelli, F., Disertori, M., Antolini, R., Furlanello, F., and Allessie, M. A. (1991). Variations in human atrial flutter cycle length induced by ventricular beats: evidence of a reentrant circuit with a partially excitable gap. *J. Cardiovasc. Electrophysiol.* 2, 375–387. doi: 10.1111/j.1540-8167.1991.tb01337.x

Li, X., Almeida, T. P., Dastagir, N., Guillem, M. S., Salinet, J., Chu, G. S., et al. (2020). Standardizing single-frame phase singularity identification algorithms and parameters in phase mapping during human atrial fibrillation. *Front. Physiol.* 11:869. doi: 10.3389/fphys.2020.00869

Luengo, D., Rios-Munoz, G., Elvira, V., Sanchez, C., and Artes-Rodriguez, A. (2019). Hierarchical algorithms for causality retrieval in atrial fibrillation intracavitary electrograms. *IEEE J. Biomed. Health Inform.* 23, 143–155. doi: 10.1109/JBHI.2018.2805773

Mahida, S., Berte, B., Yamashita, S., Derval, N., Denis, A., Shah, A., et al. (2014). New ablation technologies and techniques. *Arrhythm. Electrophysiol. Rev.* 3, 107–112.

Masé, M., and Ravelli, F. (2010). Automatic reconstruction of activation and velocity maps from electro-anatomic data by radial basis functions. *Annu. Int. Conf. IEEE Eng. Med. Biol. Soc.* 2010, 2608–2611. doi: 10.1109/IEMBS.2010.5626616

Masè, M., Faes, L., and Ravelli, F. (2020). Letter by Masè et al regarding article, "Granger causality-based analysis for classification of fibrillation mechanisms and localization of rotational drivers". *Circ. Arrhythm. Electrophysiol.* 13:e008675. doi: 10.1161/CIRCEP.120.008675

Masè, M., Faes, L., Antolini, R., Scaglione, M., and Ravelli, F. (2005). Quantification of synchronization during atrial fibrillation by Shannon entropy: validation in patients and computer model of atrial arrhythmias. *Physiol. Meas.* 26, 911–923. doi: 10.1088/0967-3334/26/6/003

Masè, M., Marini, M., Disertori, M., and Ravelli, F. (2015). Dynamics of AV coupling during human atrial fibrillation: role of atrial rate. *Am. J. Physiol. Heart Circ. Physiol.* 309, H198–H205. doi: 10.1152/ajpheart.00726.2014

Nitta, T., Ishii, Y., Miyagi, Y., Ohmori, H., Sakamoto, S., and Tanaka, S. (2004). Concurrent multiple left atrial focal activations with fibrillatory conduction and right atrial focal or reentrant activation as the mechanism in atrial fibrillation. *J. Thorac. Cardiovasc. Surg.* 127, 770–778. doi: 10.1016/j.jtcvs.2003.05.001

Nollo, G., Marconcini, M., Faes, L., Bovolo, F., Ravelli, F., and Bruzzone, L. (2008). An automatic system for the analysis and classification of human atrial fibrillation patterns from intracardiac electrograms. *IEEE Trans. Biomed. Eng.* 55, 2275–2285. doi: 10.1109/TBME.2008.923155

O'Shea, C., Holmes, A. P., Yu, T. Y., Winter, J., Wells, S. P., Correia, J., et al. (2019). ElectroMap: high-throughput open-source software for analysis and mapping of cardiac electrophysiology. *Sci. Rep.* 9:1389. doi: 10.1038/s41598-018-38263-2

Orozco-Duque, A., Tobón, C., Ugarte, J. P., Morillo, C., and Bustamante, J. (2019). Electroanatomical mapping based on discrimination of electrograms clusters for localization of critical sites in atrial fibrillation. *Prog. Biophys. Mol. Biol.* 141, 37–46. doi: 10.1016/j.pbiomolbio.2018.07.003

Parameswaran, R., Al-Kaisey, A. M., and Kalman, J. M. (2021). Catheter ablation for atrial fibrillation: current indications and evolving technologies. *Nat. Rev. Cardiol.* 18, 210–225. doi: 10.1038/s41569-020-00451-x

Quintanilla, J. G., Shpun, S., Jalife, J., and Filgueiras-Rama, D. (2021). Novel approaches to mechanism-based atrial fibrillation ablation. *Cardiovasc. Res.* 117, 1662–1681. doi: 10.1093/cvr/cvab108

Ravelli, F., and Masè, M. (2014). Computational mapping in atrial fibrillation: how the integration of signal-derived maps may guide the localization of critical sources. *Europace* 16, 714–723. doi: 10.1093/europace/eut376

Ravelli, F., Masè, M., Cristoforetti, A., Del Greco, M., Centonze, M., Marini, M., et al. (2012). Anatomic localization of rapid repetitive sources in persistent atrial fibrillation: fusion of biatrial CT images with wave similarity/cycle length maps. *JACC Cardiovasc. Imaging* 5, 1211–1220. doi: 10.1016/j.jcmg.2012.07.016

Ravelli, F., Masè, M., Cristoforetti, A., Marini, M., and Disertori, M. (2014). The logical operator map identifies novel candidate markers for critical sites in patients with atrial fibrillation. *Prog. Biophys. Mol. Biol.* 115, 186–197. doi: 10.1016/j.pbiomolbio.2014.07.006

Ravelli, F., Masè, M., Del Greco, M., Marini, M., and Disertori, M. (2011). Acute atrial dilatation slows conduction and increases AF vulnerability in the human atrium. *J. Cardiovasc. Electrophysiol.* 22, 394–401. doi: 10.1111/j.1540-8167.2010.01939.x

Richter, U., Faes, L., Cristoforetti, A., Mase, M., Ravelli, F., Stridh, M., et al. (2011). A novel approach to propagation pattern analysis in intracardiac atrial fibrillation signals. *Ann. Biomed. Eng.* 39, 310–323. doi: 10.1007/s10439-010-0146-8

Rodrigo, M., Climent, A. M., Liberos, A., Calvo, D., Fernández-Avilés, F., Berenfeld, O., et al. (2016). Identification of dominant excitation patterns and sources of atrial fibrillation by causality analysis. *Ann. Biomed. Eng.* 44, 2364–2376. doi: 10.1007/s10439-015-1534-x

Rogers, J. M., Usui, M., KenKnight, B. H., Ideker, R. E., and Smith, W. M. (1997). A quantitative framework for analyzing epicardial activation patterns during ventricular fibrillation. *Ann. Biomed. Eng.* 25, 749–760. doi: 10.1007/BF02684159

Roney, C. H., Cantwell, C. D., Qureshi, N. A., Ali, R. L., Chang, E. T. Y., Lim, P. B., et al. (2014). An automated algorithm for determining conduction velocity, wavefront direction and origin of focal cardiac arrhythmias using a multipolar catheter. *Annu. Int. Conf. IEEE Eng. Med. Biol. Soc.* 2014, 1583–1586. doi: 10.1109/EMBC.2014.6943906

Roney, C. H., Cantwell, C. D., Qureshi, N. A., Chowdhury, R. A., Dupont, E., Lim, P. B., et al. (2017). Rotor tracking using phase of electrograms recorded during atrial fibrillation. *Ann. Biomed. Eng.* 45, 910–923. doi: 10.1007/s10439-016-1766-4

Roney, C. H., Whitaker, J., Sim, I., O'Neill, L., Mukherjee, R. K., Razeghi, O., et al. (2019). A technique for measuring anisotropy in atrial conduction to estimate conduction velocity and atrial fibre direction. *Comput. Biol. Med.* 104, 278–290. doi: 10.1016/j.compbiomed.2018.10.019

Sahli Costabal, F., Yang, Y., Perdikaris, P., Hurtado, D. E., and Kuhl, E. (2020). Physics-informed neural networks for cardiac activation mapping. *Front. Phys.* 8:42. doi: 10.3389/fphy.2020.00042

Sanders, P., Berenfeld, O., Hocini, M., Jais, P., Vaidyanathan, R., Hsu, L. F., et al. (2005). Spectral analysis identifies sites of high-frequency activity maintaining atrial fibrillation in humans. *Circulation* 112, 789–797. doi: 10.1161/circulationaha.104.517011

Schmitt, C., Ndrepepa, G., Weber, S., Schmieder, S., Weyerbrock, S., Schneider, M., et al. (2002). Biatrial multisite mapping of atrial premature complexes triggering onset of atrial fibrillation. *Am. J. Cardiol.* 89, 1381–1387. doi: 10.1016/s0002-9149(02)02350-0

Schreiber, T., and Schmitz, A. (2000). Surrogate time series. *Physica D* 142, 346–382.

Stiles, M. K., Brooks, A. G., Kuklik, P., John, B., Dimitri, H., Lau, D. H., et al. (2008). High-density mapping of atrial fibrillation in humans: relationship between high-frequency activation and electrogram fractionation. *J. Cardiovasc. Electrophysiol.* 19, 1245–1253. doi: 10.1111/j.1540-8167.2008.01253.x

Stiles, M. K., Sanders, P., and Lau, D. H. (2018). Targeting the substrate in ablation of persistent atrial fibrillation: recent lessons and future directions. *Front. Physiol.* 9:1158. doi: 10.3389/fphys.2018.01158

Takahashi, Y., Hocini, M., O'Neill, M. D., Sanders, P., Rotter, M., Rostock, T., et al. (2006). Sites of focal atrial activity characterized by endocardial mapping during atrial fibrillation. *J. Am. Coll. Cardiol.* 47, 2005–2012. doi: 10.1016/j.jacc.2005.12.068

Virani, S. S., Alonso, A., Aparicio, H. J., Benjamin, E. J., Bittencourt, M. S., Callaway, C. W., et al. (2021). Heart disease and stroke statistics-2021 update: a report from the American heart association. *Circulation* 143, e254–e743. doi: 10.1161/CIR.0000000000000950

Weber, F. M., Luik, A., Schilling, C., Seemann, G., Krueger, M. W., Lorenz, C., et al. (2011). Conduction velocity restitution of the human atrium–an efficient measurement protocol for clinical electrophysiological studies. *IEEE Trans. Biomed. Eng.* 58, 2648–2655. doi: 10.1109/TBME.2011.2160453

Weber, F. M., Schilling, C., Seemann, G., Luik, A., Schmitt, C., Lorenz, C., et al. (2010). Wave-direction and conduction-velocity analysis from intracardiac electrograms–a single-shot technique. *IEEE Trans. Biomed. Eng.* 57, 2394–2401. doi: 10.1109/TBME.2010.2055056

Weber, T., Katus, H. A., Sager, S., and Scholz, E. P. (2017). Novel algorithm for accelerated electroanatomic mapping and prediction of earliest activation of focal cardiac arrhythmias using mathematical optimization. *Heart Rhythm* 14, 875–882. doi: 10.1016/j.hrthm.2017.03.001

Williams, S. E., Roney, C. H., Connolly, A., Sim, I., Whitaker, J., O'Hare, D., et al. (2021). OpenEP: a cross-platform electroanatomic mapping data format and analysis platform for electrophysiology research. *Front. Physiol.* 12:646023. doi: 10.3389/fphys.2021.646023

Zeemering, S., van Hunnik, A., van Rosmalen, F., Bonizzi, P., Scaf, B., Delhaas, T., et al. (2020). A novel tool for the identification and characterization of repetitive patterns in high-density contact mapping of atrial fibrillation. *Front. Physiol.* 11:570118. doi: 10.3389/fphys.2020.570118

Conflict of Interest: The authors declare that the research was conducted in the absence of any commercial or financial relationships that could be construed as a potential conflict of interest.

frontiers in Physiology

ORIGINAL RESEARCH
published: 25 January 2022
doi: 10.3389/fphys.2022.816865

Electro-characteristics of Myocardial Pouches and Reduction of the Frequency of Steam Pops During Radiofrequency Ablation

*Jianfeng Luo[1], Fei Guo[1], Hongjun Zhu[1], Hao Su[1], Yuanbo Wu[2], Jing Zhu[1], Can Zhang[1] and Jian Xu[1]**

[1]Department of Cardiology, The First Affiliated Hospital of USTC, Division of Life Sciences and Medicine, University of Science and Technology of China, Hefei, China, [2]Department of Neurology, The First Affiliated Hospital of USTC, Division of Life Sciences and Medicine, University of Science and Technology of China, Hefei, China

OPEN ACCESS

Edited by:
Xin Li,
University of Leicester,
United Kingdom

Reviewed by:
Jason Chinitz,
Northwell Health, United States
Sachin Nayyar,
University Health Network (UHN),
Canada

***Correspondence:**
Jian Xu
ahslyyxujian@163.com

Specialty section:
This article was submitted to Cardiac Electrophysiology, a section of the journal Frontiers in Physiology

Received: *17 November 2021*
Accepted: *04 January 2022*
Published: *25 January 2022*

Citation:
Luo J, Guo F, Zhu H, Su H, Wu Y, Zhu J, Zhang C and Xu J (2022) Electro-characteristics of Myocardial Pouches and Reduction of the Frequency of Steam Pops During Radiofrequency Ablation. Front. Physiol. 13:816865. doi: 10.3389/fphys.2022.816865

Background: Radiofrequency ablation (RFA) effectively treats arrhythmia. Steam pop (SP) is a dangerous complication of RFA, which can lead to pericardial tamponade or even death.

Objective: This study aimed to explore the electro-characteristics of myocardial pouches, and the relationship between SP, pouch, and impedance.

Methods: Swine myocardium was divided into the pouch group and smooth myocardium group. Continuous RFA at 50 W was applied. The initial impedance reduction within the first 3 s of ablation and the time from the start of ablation to SP were recorded. After enabling the delta impedance cutoff function, RFA was performed at different percentage of delta impedance (PDI) cutoff thresholds.

Results: The impedance was higher for the pouch myocardium compared to the smooth myocardium ($123.22 \pm 8.63\,\Omega$ and $95.75 \pm 4.75\,\Omega$, respectively; $p < 0.001$). The RFA duration before SPs was shorter in the pouch group compared to the smooth myocardium group [9 s (interquartile range, IQR: 6.25–13 s) and 33 s (IQR: 26.25–40.75 s), respectively; $p < 0.001$]. Within the first 3 s of RFA, impedance reduction ($24.65 \pm 6.57\,\Omega$ and $12.78 \pm 3.35\,\Omega$, respectively; $p < 0.001$) and PDI [19.18% (IQR: 16.39–24.20%) and 12.96% (IQR: 11.17–14.39%), respectively; $p < 0.001$] were greater in the pouch group compared to the smooth myocardium group. A PDI of 15% and delta time of 3 s effectively reduced the frequency of SPs without seriously affecting RFA use.

Conclusion: SPs occur more frequently in the pouch area during RFA. Appropriate delta impedance cutoff settings (PDI: 15%; delta time: 3 s) can reduce the frequency of SPs and improve the RFA safety.

Keywords: arrhythmia, atrial fibrillation, radiofrequency ablation, impedance, pouch, steam pop

INTRODUCTION

Radiofrequency ablation (RFA) is an effective treatment for patients with arrhythmia (Hindricks et al., 2021). However, there is concern regarding the safety of RFA, especially with the recently introduced high-power, short-time RFA and left atrial isolation (Eichenlaub et al., 2021; Zedda et al., 2021).

During RFA, coagulation necrosis begins at temperatures higher than 50°C. As the tissue temperatures rise, steam is formed within the myocardium, leading to a steam pop (SP). SP refers to the audible sound produced by an intramyocardial explosion when the intra-tissue steam is rapidly produced, causing pressure buildup (Nakagawa et al., 1998). SPs are relatively infrequent (0.1–1.5%) but are a potentially severe complication of RFA; SPs may result in myocardial wall disruption and increased risk for cardiac perforation, pericardial tamponade, embolic stroke, and even death (Seiler et al., 2008; Tokuda et al., 2011). It is difficult to achieve the optimal balance between sufficient energy to penetrate deep myocardial tissues and avoiding excessive heat and SPs. Therefore, it will be useful to develop technology that prevents this potentially life-threatening complication (Kondo et al., 2017; Viles-Gonzalez et al., 2017).

SPs often occur after the changes in myocardial tissue impedance (Theis et al., 2015; Alfonso-Almazán et al., 2019). During RFA, the impedance gradually decreases, sometimes with a steep decrease at the very beginning (Ikeda et al., 2014; Viles-Gonzalez et al., 2017). SP is associated with more rapid impedance reduction at the initial stage (Cooper et al., 2004; Theis et al., 2015; Nguyen et al., 2018). RFA may be interrupted due to impedance changes, based on several important principles. First, the application of radiofrequency produces lesions through resistive heat, which depends on tissue electrical resistivity and is inversely related to tissue water content. Second, tissue impedance initially decreases due to increased mobility of ions. Third, thermal lesions are associated with decreased impedance, and the magnitude of the decrease depends on tissue temperature and area of the heated cardiac tissue. Thus, higher tissue temperature and faster rise in temperature correlate with faster and earlier decrease in impedance. Finally, a rapid increase in temperature (resulting in a rapid and significant decrease in impedance) produces gas from the ablated tissue through vaporization.

If impedance is rapidly reducing or has reduced to a great, it is reasonable to interrupt RFA. However, the cutoff values to guide this decision and prevent SPs have not been determined.

There are many pocket-shaped indentations of various sizes in the human endocardium, called pouches (**Figure 1**; Costa et al., 2004; Shimizu et al., 2018). Pouches can interfere with RFA, resulting in prolonged RFA duration (Chen et al., 2011; Shimizu et al., 2018). The sub-Eustachian pouch depth was independently associated with total RFA duration and radiofrequency energy delivered during cavotricuspid isthmus ablation (Shimizu et al., 2018). Some experts believe that resistive heating and impedance reduction at the beginning of RFA are associated with the amount of cardiac tissue surrounding the catheter tip (Viles-Gonzalez et al., 2017). When the catheter is placed in the pouch, its tip is surrounded by more cardiac tissue; therefore, a large amount of heat is rapidly generated. The rapid blood flow through the heart removes some of the heat, which is important to lower the temperatures of the catheter tip and cardiac tissue. However, blood flows slowly through the pouches. Therefore, theoretically, SP is more likely to occur in the pouches, but this assumption has not evaluated in previous studies.

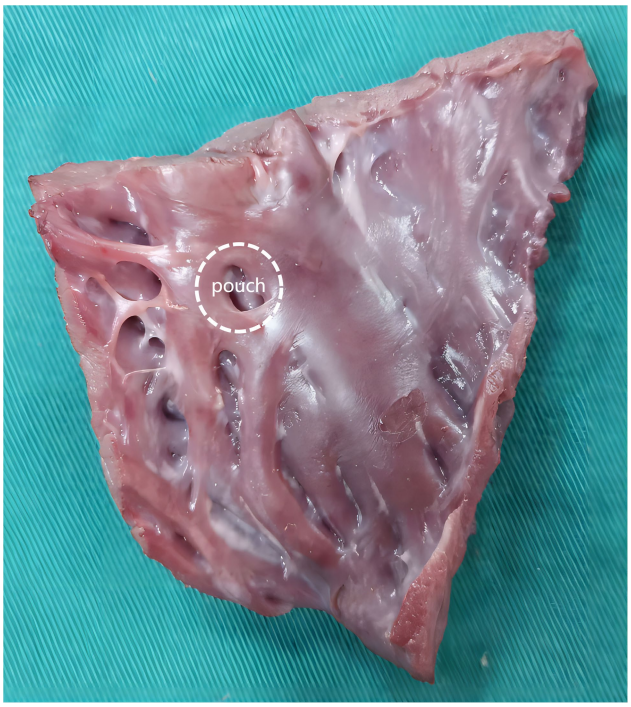

FIGURE 1 | A figure to show pouch.

Large pouches, such as those in the cavotricuspid isthmus and atrial septum, can be detected by intracardiac echocardiography, transesophageal echocardiography, intracardiac imaging, and multislice computed tomography (Shimizu et al., 2018). However, there is no effective, safe, and easily applicable method to detect small pouches, such as those in the left atrium.

To explore the relationships between pouch, impedance, and SP, we aimed to determine whether SPs occur more frequently in pouches, whether impedance differs between the pouch and the smooth myocardium, and whether impedance-related settings can be used to improve the safety of RFA.

MATERIALS AND METHODS

Experimental Instruments

The experimental instruments consisted of a container with saline, a thermostat, a water circulator, and an RFA system (**Figure 2**). The thermostat maintained the temperature of the saline at 37°C, and the water circulator continuously circulated the saline. Swine hearts were obtained from

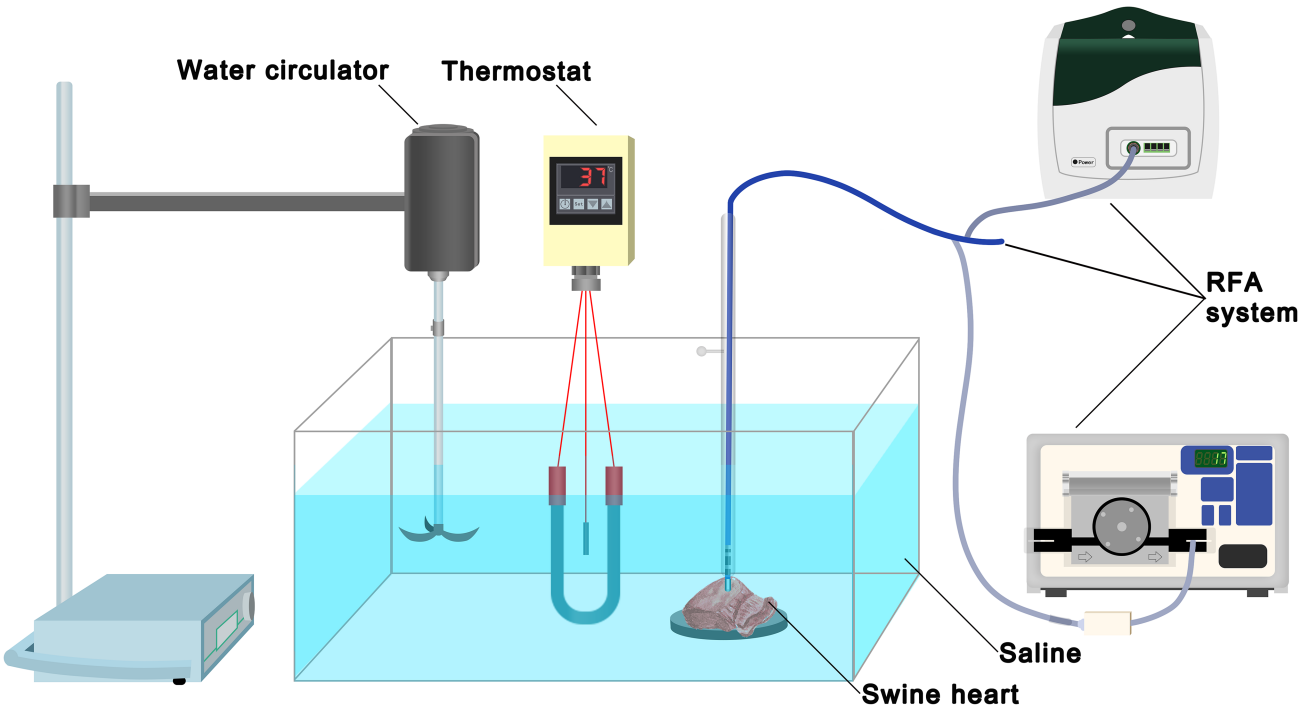

FIGURE 2 | Experimental set-up. The experimental instruments consisted of a container with 0.9% saline, a thermostat, a water circulator, and an RFA system. The thermostat maintained the temperature of saline at 37°C and the water circulator continuously circulated the saline. Swine heart tissue was secured on a rubber plate in the saline container. RFA, radiofrequency ablation.

commercial vendors and transported to the laboratory on ice immediately after the slaughter. The myocardium was cut into small pieces (5 × 5 cm), which were spread out and fixed on a rubber plate in saline. A total of 37 swine hearts were used.

The EnSite Precision system (St. Jude Medical Inc., St. Paul, MN, United States) and an Ampere™ radiofrequency generator were used for RFA. The TactiCath™ quartz contact force-sensing ablation catheter (75/65) was fixed in a plastic tube perpendicular to the tissue to maintain stability. The dynamic force sensor (TactiSys Quartz) was used to maintain a stable force (15–20 g) at the distal end of the catheter. The rate of irrigation flow of cold saline was 17 ml/min at the distal end of the catheter end (Cool Point Irrigation Pump).

Experiment Design

Pouch and smooth myocardium were identified by observing the myocardial shape. Parts of the pouch and regular smooth myocardium co-existed in the same sections; multiple ablations were performed in the pouch and smooth myocardial areas on the same tissue sections.

The experiment comprised of four parts. First, continuous RFA at 50 W was applied until SP occurred. The RFA duration before SP was recorded for 40 RFAs performed in the pouch group and regular smooth myocardium group each. Second, impedance of the pouch group and smooth myocardial group without RFA was recorded. Third, continuous RFA at 50 W was applied to the pouch and smooth myocardial tissues, and impedance reduction within the first 3 s was recorded. The percentage of delta impedance (PDI, %) was calculated as (delta impedance/initial impedance) × 100. A total of 40 RFAs were performed in the pouch and smooth myocardium groups each. Fourth, continuous RFA at 50 W was applied using the delta impedance cutoff function (i.e., when delta impedance was higher or lower than the set value within the set delta time, the system automatically turned off the RFA). The following setting procedure was completed on the screen of the RF generator: Menu → Ablation Parameters → Delta Impedance Cutoff → Enable. For example, if delta impedance and delta time were set at 20 Ω and 3 s, respectively, the system will automatically terminate the RFA if the delta impedance reached 20 Ω within 3 s. Delta impedance was tested at a range of 1–50 Ω, and delta time was tested at a range of 1–10 s. Because the initial myocardial impedance varies between different locations, subgroups based on PDI are better able to reflect the changes in impedance. RFA was performed 40 times at each cutoff value in each group.

Statistical Analysis

Normally distributed data are expressed as mean ± standard deviation (SD); data with a skewed distribution are expressed as median (interquartile range, IQR: P_{25}–P_{75}). A two-sample *t*-test was used to compare the data with normal distribution and homogeneity of variance. The Mann–Whitney *U*-test was used for data with a non-normal distribution. Categorical and grade data are expressed as number, rate, or percentage.

The Kaplan–Meier method was used to analyze the probabilities of endpoint events. A time-event curve was constructed. A two-sided value of $p < 0.05$ was considered statistically significant.

RESULTS

RFA Duration Before SP Was Shorter in Myocardial Pouches

Continuous RFA at 50 W, without the cutoff function, caused SPs in all ablation lesions in the pouch and smooth myocardium groups. RFA duration before the SP was significantly shorter in the pouch group compared to the smooth myocardium group [9 s (IQR: 6.25–13 s) and 33 s (IQR: 26.25–40.75 s), respectively; $p < 0.001$; **Figure 3A**].

The Kaplan–Meier curves with SP as the endpoint event (**Figure 3E**) confirmed that SP occurred earlier in the pouch group compared to the smooth myocardium group.

Impedance Change Was More Significant in Pouches Than Smooth Myocardium

The initial impedance was significantly higher in the pouch group compared to the smooth myocardium group (123.22 ± 8.63 Ω and 95.75 ± 4.75 Ω, respectively; $p < 0.001$; **Figure 3B**). The impedance significantly decreased in the first 3 s of RFA at 50 W in both groups when the delta impedance cutoff function was disabled. The decrease in impedance was much greater in the pouch group compared to the smooth myocardium group (24.65 ± 6.57 Ω and 12.78 ± 3.35 Ω, respectively; $p < 0.001$; **Figure 3C**), confirming that the pouch areas had a more significant impedance change during RFA. Moreover, PDI was significantly higher in the pouch group compared to the smooth myocardium group [19.18% (IQR: 16.39–24.20%) and 12.96% (IQR: 11.17–14.39%), respectively; $p < 0.001$; **Figure 3D**]. PDI during the first 3 s of RFA was stratified as <5%, 5–10%, 10–15%, 15–20%, 20–25%, and > 25%. Among these PDI-based strata, 0, 1, 6, 15, 10, and 8 ablation lesions, respectively, were

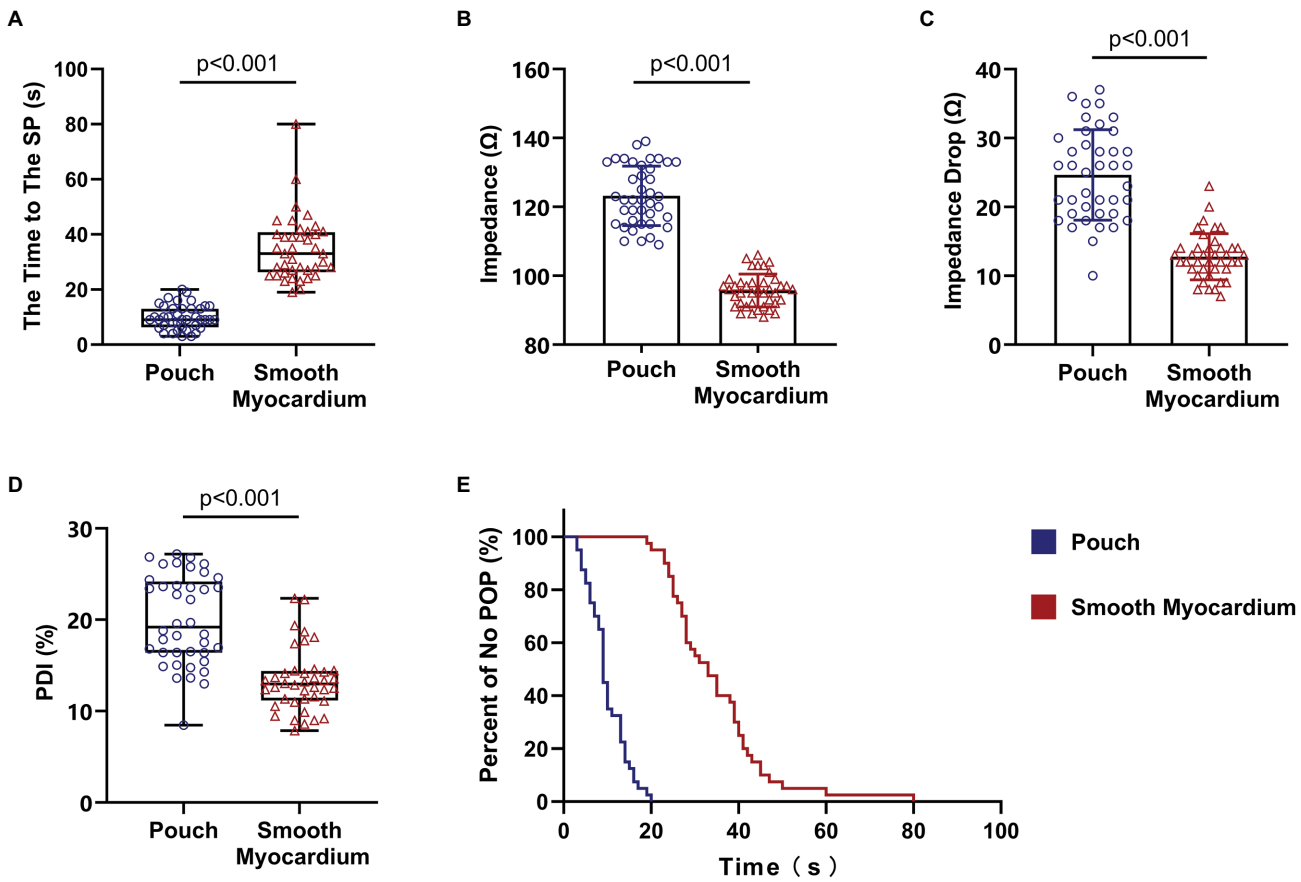

FIGURE 3 | Steam pops occurred earlier in the pouch group. Impedance of the pouch tissue was high and rapidly decreased at the beginning of RFA. **(A)** RFA duration before SPs was shorter in the pouch group compared to the smooth myocardium group. **(B)** Impedance was higher in the pouch group compared to the smooth myocardium group. **(C)** Decrease in impedance in the first 3 s of RFA was faster in the pouch group compared to the smooth myocardium group. **(D)** The PDI of the pouch group was greater than that of the smooth myocardium group. **(E)** Kaplan–Meier curves show that SPs occurred earlier in the pouch group compared to the smooth myocardium group. PDI, percentage of delta impedance.

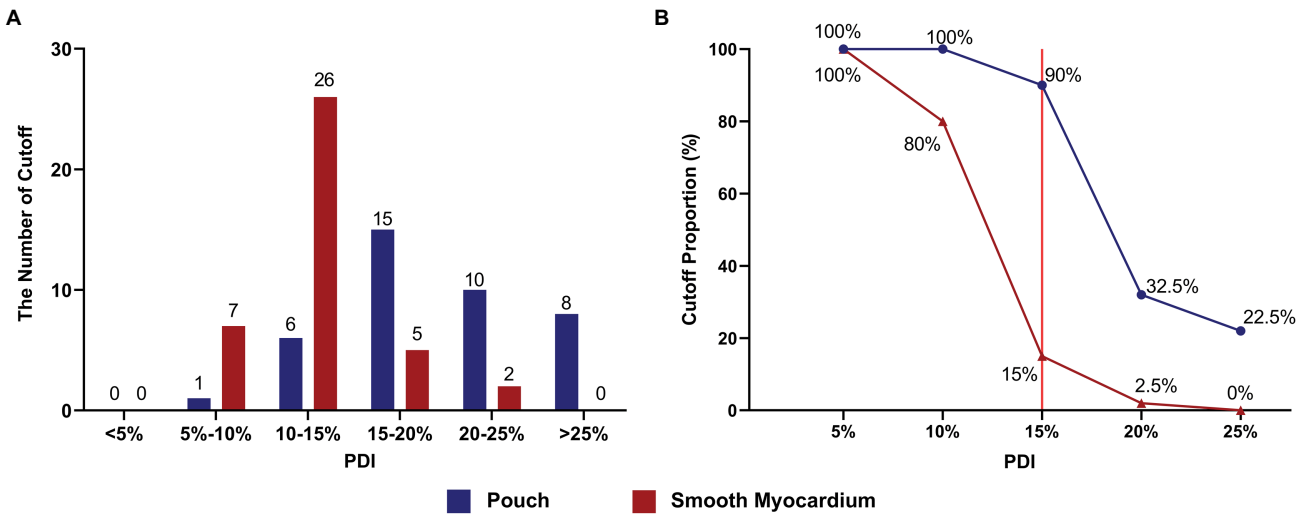

FIGURE 4 | Appropriate PDI cutoff settings effectively prevented SPs. **(A)** The number of ablation lesions with PDI values (< 5%, 5–10%, 10–15%, 15–20%, 20–25%, and > 25%) during the first 3 s of RFA in the pouch group and smooth myocardium group. **(B)** The frequency of invoked cutoffs at different PDI settings. Red line indicates that at the optimal PDI setting of 15%, the cutoff rate in the pouch group was 90%, while RFA application was only terminated in 15% of all cases in the smooth myocardium group.

observed in the pouch group, and 0, 7, 26, 5, 2, and 0 ablation lesions, respectively, were observed in the smooth myocardium group (**Figure 4A**).

SPs Are Prevented With the Use of Delta Impedance Cutoff

Using the delta impedance cutoff function, RFA procedure was continued until the cutoff was reached or SP occurred. RFA was performed using different PDI cutoff values (i.e., 5, 10, 15, 20, and 25%). For example, when a PDI cutoff value of 5% was selected and the delta impedance exceeded 5% of the initial impedance value, RFA was terminated.

The cutoff value was reached and RFA was terminated in some ablation lesions in both groups. No SP occurred in these cases. However, SP occurred in ablation lesions without the cutoff function. Using different PDI cutoff values, the rates of cutoff without SP were 100 and 100% (PDI = 5%), 100 and 80% (PDI = 10%), 90 and 15% (PDI = 15%), 32.5 and 2.5% (PDI = 20%), and 22.5 and 0% (PDI = 25%) in the pouch group and smooth myocardium group, respectively (**Figure 4B**).

Because five cutoff threshold values were set, 200 RFAs were performed (5 thresholds × 40 lesions) in each group. Cutoff was invoked in 138 and 77 RFAs in the pouch group and smooth myocardium group, respectively. The RFA duration before cutoff was 1–5 s (minimum to maximum). In the pouch group, most cutoffs occurred within 1–3 s after the start of RFA (130/138 cutoffs, 94.20%), and a few cutoffs occurred in 4 s (7/138, 5.07%) and 5 s (1/138, 0.72%). In the smooth myocardium group, all cutoffs occurred within the initial 3 s (77/77 cutoffs, 100%; **Figure 5**), confirming that significant impedance changes occurred at the beginning of RFA.

DISCUSSION

SPs Occur More Frequently and Earlier in Pouch Areas

When the catheter tip was placed in a pouch, it was surrounded by more myocardial tissue compared to when it was placed on smooth myocardium, producing a greater amount of heat (Viles-Gonzalez et al., 2017). In addition, less blood flow passes through the pouch to remove the heat. Therefore, heat builds up much faster in pouches compared to the smooth myocardium, causing SPs during RFA. Because the presence of pouches is a risk factor of SP, techniques to detect the presence of pouches or avoid RFA in the pouches will reduce the incidences of SP and other serious complications. Such techniques are especially desirable for high-power, short-time RFA, which involve a rapid increase in temperature and strictly controlled ablation.

In our study, the pouch group and smooth myocardium group were separated based on visual inspection. The characteristics of the pouches that may increase the incidence of SP are as: firstly, the diameter of the pouch is larger than the outer diameter of the ablation catheter so that the catheter can fall into and ablate within the pouch. Currently, the outer diameter of the ablation catheter used commonly is greater than 7F (2.331 mm), so pouch should be greater than 2.331 mm in diameter. Secondly, a shallower and greater pouch is more conducive to heat dissipation and less likely to produce SP.

Impedance of Pouch Myocardium Is Significantly Increased

It is not completely clear why impedance is higher in pouches compared to the smooth myocardium. Marmar et al. suggested that the main determinant of impedance is the cross-sectional area of the lumen where the catheter tip is placed (Vaseghi

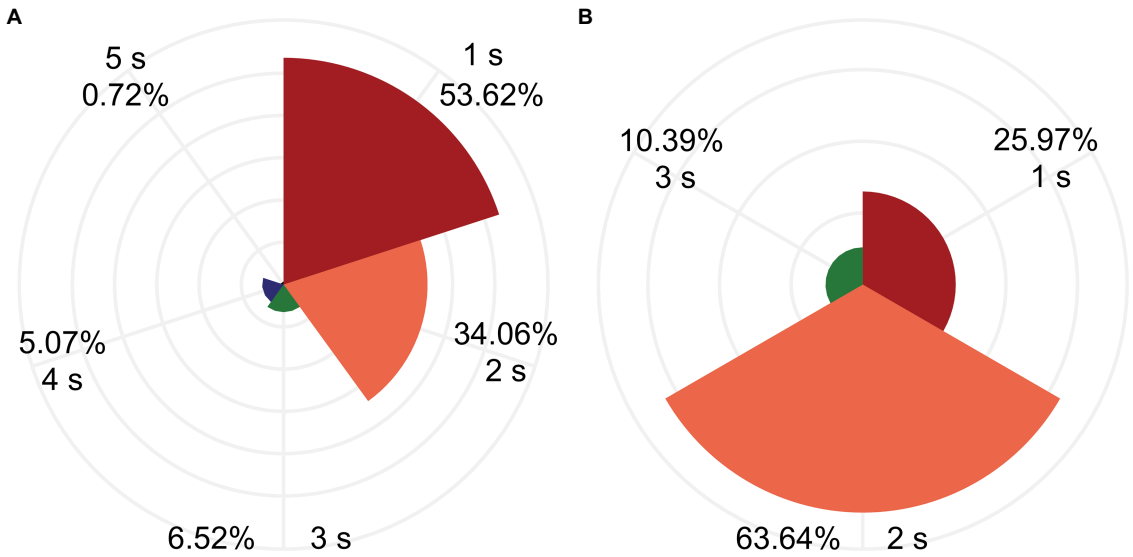

FIGURE 5 | Most cutoffs occurred within the first 3 s of RFA. RFA duration before the cutoff was 1–5 s. Percentage of RFA duration in the pouch group **(A)** and smooth myocardial group **(B)** are depicted.

et al., 2005). The cross-sectional area of a pouch is significantly smaller than that of the smooth myocardium. Therefore, the pouch generally has higher impedance. In addition, blood is an excellent electronic conduction medium, and abundant blood flow decreases the impedance of the myocardial tissue. Pouch cavities in the left atrial/ventricle endocardium have significantly reduced blood flow due to their small size, while the smooth myocardium is rich in blood flow, which increases the difference in the impedance of the two myocardial regions. Cheung et al. (2004) and Vaseghi et al. (2005) reported that the pulmonary veins have relatively high impedance (Cheung et al., 2004; Vaseghi et al., 2005), which may complicate pulmonary vein RFA by causing pulmonary vein stenosis or even occlusion (Teunissen et al., 2017; Fink et al., 2018). In this study, RFA in the pouch was associated with increased risk of SP. Therefore, RFA-related risks are increased in areas with high impedance, such as pouch and the pulmonary vein. A significant increase in impedance during the movement of the catheter suggests that the catheter tip may have entered a special anatomical site, such as a pouch or pulmonary vein. Therefore, in such a case, the catheter should be repositioned until the impedance decreases to the initial level, and RFA can be resumed.

Using the delta impedance cutoff function, cutoff will be invoked when the impedance increases or decreases to a certain value. In China, most RFA procedures are performed under local anesthesia rather than general anesthesia; therefore, the catheter tip is prone to movements during the operation due to unstable breathing, coughing, and body movements. Large abnormal movements of the catheter tip during RFA, such as sliding into the pulmonary vein from the atrial wall, may lead to dramatic impedance changes, which will invoke cutoff and automatically terminate the RFA. The cutoff method can reduce the likelihood of performing ablation under unstable conditions and improve RFA efficiency and safety. However, the optimal cutoff value has not been determined.

In clinical practice, SP is often accompanied by significant changes in impedance. When designing the study protocol, we tried to reduce SP by interfering with this impedance change. However, we gave up finally, because it was found that the interval between these impedance change and SP was very short or even simultaneous, so it was difficult to intervene by impedance cutting. This impedance change may be related to tissue change or catheter displacement during SP occurrence.

Appropriate Cutoff Settings Can Prevent SPs and Ensure Normal RFA Application

During the first 3 s of RFA, the impedance significantly decreased in the pouch group and smooth myocardium group; both the impedance reduction and PDI were greater in the pouch group compared to the smooth myocardium group. A low PDI threshold easily invoked cutoff, thereby preventing SPs and interfering with the normal RFA procedures. Conversely, when a high PDI threshold was used, cutoff was not frequently invoked, thereby rarely interfering with the normal RFA procedures. However, the incidence of SP increased. When the PDI threshold was set to 15% (red reference line in **Figure 4B**) and delta time to 3 s, 90% of RFAs in the pouch group were cutoff, while only 15% of RFAs were terminated in the smooth myocardium group (**Figure 4B**). Therefore, PDI of 15% and delta time of 3 s are the optimal cutoff settings, which significantly reduce the incidence of SPs, while having minimal effect on normal RFAs.

In this study, we observed that the impedance decreased rapidly in the initial stage of continuous RFA and decreased slowly in the later stage, consistent with the previous studies (Nakagawa et al., 1998). In the present study, 96.28% (207/215)

of the cutoffs occurred within the first 3 s of RFA, confirming a significant decrease in impedance in the initial stage. At 50 W, the RFA durations before SP were 9 s (IQR: 6.25–13 s) and 33 s (IQR: 26.25–40.75 s) in the pouch group and the smooth myocardium group, respectively. Both durations were significantly longer than the 3 s required to invoke cutoffs. Therefore, cutoffs usually occurred before SPs, thereby lowering SP incidence and ensuring RFA safety.

Study Limitations

The ablation power we used was 50 W, and the results were obtained under experimental conditions. In clinical practice, parameters may vary according to different conditions. When designing the study protocol, we attempted to conduct a study *in vivo*. However, in this study, the pouch group and smooth myocardium group were separated based on visual inspection, which is difficult to do *in vivo*. Temperature is associated with SP production. In order to simulate temperature changes in the real environment, myocardial tissue needs to be immersed in a large amount of flowing fluid during RFA. We also tried to replace saline with heparinized blood. However, we found that pouch was difficult to visualize in this blood, so we did not use heparinized blood in place of saline in our model ultimately. Therefore, further research is needed to identify the optimal cutoffs settings for RFA in human tissue. With advancements in catheter-based RFA technology, it is likely that no single factor will be able to predict the occurrence of SPs. Therefore, a combination of parameters may be evaluated to predict and prevent SP formation.

CONCLUSION

The endocardial pouch structure has a higher initial impedance and a faster impedance decreases during RFA. The endocardial pouch structure is prone to the occurrence of SPs. The use of an appropriate delta impedance cutoff threshold (PDI of 15% and delta time of 3 s) can effectively prevent SPs without affecting RFA application, thereby increasing RFA safety.

DATA AVAILABILITY STATEMENT

The raw data supporting the conclusions of this article will be made available by the authors, without undue reservation.

ETHICS STATEMENT

Ethical review and approval was not required for the animal study because Swine hearts were obtained from commercial vendors.

AUTHOR CONTRIBUTIONS

JL, JX, and FG conceived and designed the animal experiments. HZ, HS, and YW contributed to the statistical analysis. JX, JL, JZ, and CZ wrote the main body of the manuscript. All authors contributed to the critical reading and approval of the manuscript.

FUNDING

This work was supported by the Central Government Guidance for Local Science and Technology Development (2017070802D145).

REFERENCES

Alfonso-Almazán, J. M., Quintanilla, J. G., García-Torrent, M. J., Laguna-Castro, S., Rodríguez-Bobada, C., González, P., et al. (2019). Lesion index titration using contact-force technology enables safe and effective radiofrequency lesion creation at the root of the aorta and pulmonary artery. *Circ. Arrhythm. Electrophysiol.* 12:e007080. doi: 10.1161/CIRCEP.118.007080

Chen, J. Y., Lin, K. H., Liou, Y. M., Chang, K. C., and Huang, S. K. S. (2011). Usefulness of pre-procedure cavotricuspid isthmus imaging by modified transthoracic echocardiography for predicting outcome of isthmus-dependent atrial flutter ablation. *J. Am. Soc. Echocardiogr.* 24, 1148–1155. doi: 10.1016/j.echo.2011.06.007

Cheung, P., Hall, B., Chugh, A., Good, E., Lemola, K., Han, J., et al. (2004). Detection of inadvertent catheter movement into a pulmonary vein during radiofrequency catheter ablation by real-time impedance monitoring. *J. Cardiovasc. Electrophysiol.* 15, 674–678. doi: 10.1046/j.1540-8167.2004.03562.x

Cooper, J. M., Sapp, J. L., Tedrow, U., Pellegrini, C. P., Robinson, D., Epstein, L. M., et al. (2004). Ablation with an internally irrigated radiofrequency catheter: learning how to avoid steam pops. *Heart Rhythm.* 1, 329–333. doi: 10.1016/j.hrthm.2004.04.019

Costa, A. D., Faure, E., Thévenin, J., Messier, M., Bernard, S., Abdel, K., et al. (2004). Effect of isthmus anatomy and ablation catheter on radiofrequency catheter ablation of the cavotricuspid isthmus. *Circulation* 110, 1030–1035. doi: 10.1161/01.CIR.0000139845.40818.75

Eichenlaub, M., Mueller-Edenborn, B., Minners, J., Jander, N., Allgeier, M., Lehrmann, H., et al. (2021). Left atrial hypertension, electrical conduction slowing, and mechanical dysfunction – the pathophysiological triad in atrial fibrillation-associated atrial cardiomyopathy. *Front. Physiol.* 12:670527. doi: 10.3389/fphys.2021.670527

Fink, T., Schluter, M., Heeger, C. H., Lemes, C., Lin, T., Maurer, T., et al. (2018). Pulmonary vein stenosis or occlusion after catheter ablation of atrial fibrillation: long-term comparison of drug-eluting versus large bare metal stents. *Europace* 20, e148–e155. doi: 10.1093/europace/eux291

Hindricks, G., Potpara, T., Dagres, N., Arbelo, E., Bax, J. J., Blomström, L. C., et al. (2021). 2020 ESC Guidelines for the diagnosis and management of atrial fibrillation developed in collaboration with the European Association for Cardio-Thoracic Surgery (EACTS): the task force for the diagnosis and management of atrial fibrillation of the European Society of Cardiology (ESC) developed with the special contribution of the European Heart Rhythm Association (EHRA) of the ESC. *Eur. Heart J.* 42, 373–498. doi: 10.1093/eurheartj/ehaa612

Ikeda, A., Nakagawa, H., Lambert, H., Shah, D. C., Fonck, E., Yulzari, A., et al. (2014). Relationship between catheter contact force and radiofrequency lesion size and incidence of steam pop in the beating canine heart: electrogram amplitude, impedance, and electrode temperature are poor predictors of electrode-tissue contact force and lesion size. *Circ. Arrhythm. Electrophysiol.* 7, 1174–1180. doi: 10.1161/CIRCEP.113.001094

Kondo, Y., Ueda, M., and Kobayashi, Y. (2017). Visualizing induced silent steam pop with intracardiac echocardiography. *Europace* 19:1145. doi: 10.1093/europace/eux085

Nakagawa, H., Wittkampf, F. H., Yamanashi, W. S., Pitha, J. V., Imai, S., Campbell, B., et al. (1998). Inverse relationship between electrode size and lesion size during radiofrequency ablation with active electrode cooling. *Circulation* 98, 458–465. doi: 10.1161/01.CIR.98.5.458

Nguyen, D. T., Zipse, M., Borne, R. T., Zheng, L. J., Tzou, W. S., and Sauer, W. H. (2018). Use of tissue electric and ultrasound characteristics to predict and prevent steam-generated cavitation during high-power radiofrequency ablation. *J. Am. Coll. Cardiol.* 4, 491–500. doi: 10.1016/j.jacep.2017.10.003

Seiler, J., Roberts-Thomson, K. C., Raymond, J. M., Vest, J., Delacretaz, E., and Stevenson, W. G. (2008). Steam pops during irrigated radiofrequency ablation: feasibility of impedance monitoring for prevention. *Heart Rhythm.* 5, 1411–1416. doi: 10.1016/j.hrthm.2008.07.011

Shimizu, Y., Yoshitani, K., Murotani, K., Kujira, K., Kurozumi, Y., Fukuhara, R., et al. (2018). The deeper the pouch is, the longer the radiofrequency duration and higher the radiofrequency energy needed-cavotricuspid isthmus ablation using intracardiac echocardiography. *J. Arrhythm.* 34, 410–417. doi: 10.1002/joa3.12075

Teunissen, C., Velthuis, B. K., Hassink, R. J., Van der Heijden, J. F., Vonken, E. P. A., Clappers, N., et al. (2017). Incidence of pulmonary vein stenosis after radiofrequency catheter ablation of atrial fibrillation. *JACC Clin. Electrophysiol.* 3, 589–598. doi: 10.1016/j.jacep.2017.02.003

Theis, C., Rostock, T., Mollnau, H., Sonnenschein, S., Himmrich, E., Kämpfner, D., et al. (2015). The incidence of audible steam pops is increased and unpredictable with the thermocool(R) surround flow catheter during left atrial catheter ablation: a prospective observational study. *J. Cardiovasc. Electrophysiol.* 26, 956–962. doi: 10.1111/jce.12721

Tokuda, M., Kojodjojo, P., Epstein, L. M., Koplan, B. A., Michaud, G. F., Tedrow, U. B., et al. (2011). Outcomes of cardiac perforation complicating catheter ablation of ventricular arrhythmias. *Circ. Arrhythm. Electrophysiol.* 4, 660–666. doi: 10.1161/CIRCEP.111.963413

Vaseghi, M., Cesario, D. A., Valderrabano, M., Boyle, N. G., Ratib, O., Finn, J. P., et al. (2005). Impedance monitoring during catheter ablation of atrial fibrillation. *Heart Rhythm.* 2, 914–920. doi: 10.1016/j.hrthm.2005.06.007

Viles-Gonzalez, J. F., Berjano, E., and d'Avila, A. (2017). Complications of radiofrequency catheter ablation: can we prevent steam pops? *JACC Clin. Electrophysiol.* 4, 501–503. doi: 10.1016/j.jacep.2017.11.003

Zedda, A., Huo, Y., Kronborg, M., Ulbrich, S., Mayer, J., Pu, L. Y., et al. (2021). Left atrial isolation and appendage occlusion in patients with atrial fibrillation at end stage left atrial fibrotic disease. *Circ. Arrhythm. Electrophysiol.* 14:e010011. doi: 10.1161/CIRCEP.121.010011

Conflict of Interest: The authors declare that the research was conducted in the absence of any commercial or financial relationships that could be construed as a potential conflict of interest.

Publisher's Note: All claims expressed in this article are solely those of the authors and do not necessarily represent those of their affiliated organizations, or those of the publisher, the editors and the reviewers. Any product that may be evaluated in this article, or claim that may be made by its manufacturer, is not guaranteed or endorsed by the publisher.

frontiers in Physiology

ORIGINAL RESEARCH
published: 16 March 2022
doi: 10.3389/fphys.2022.826449

Simultaneous Whole-Chamber Non-contact Mapping of Highest Dominant Frequency Sites During Persistent Atrial Fibrillation: A Prospective Ablation Study

Gavin S. Chu[1,2†], Xin Li[1,3†], Peter J. Stafford[4], Frederique J. Vanheusden[5], João L. Salinet[6], Tiago P. Almeida[1,3], Nawshin Dastagir[7], Alastair J. Sandilands[4], Paulus Kirchhof[8], Fernando S. Schlindwein[3,4] and G. André Ng[1,4]*

[1] Department of Cardiovascular Science, University of Leicester, Leicester, United Kingdom, [2] Lancashire Cardiac Centre, Blackpool Teaching Hospitals NHS Foundation Trust, Blackpool, United Kingdom, [3] School of Engineering, University of Leicester, Leicester, United Kingdom, [4] National Institute for Health Research Leicester Cardiovascular Biomedical Research Centre, Glenfield Hospital, Leicester, United Kingdom, [5] School of Science and Technology, Nottingham Trent University, Nottingham, United Kingdom, [6] Center for Engineering, Modeling and Applied Social Sciences, University Federal of ABC, Santo André, Brazil, [7] Department of International Foundation, Massey University, Auckland, New Zealand, [8] University Heart and Vascular Centre, University Medical Center Hamburg-Eppendorf, Hamburg, Germany

OPEN ACCESS

Edited by:
Fu Siong Ng,
Imperial College London,
United Kingdom

Reviewed by:
Elena Tolkacheva,
University of Minnesota Twin Cities,
United States
Junaid Zaman,
The Keck School of Medicine of the University of Southern California,
United States

***Correspondence:**
Gavin S. Chu
gc171@le.ac.uk

† These authors have contributed equally to this work

Specialty section:
This article was submitted to Cardiac Electrophysiology, a section of the journal Frontiers in Physiology

Received: 30 November 2021
Accepted: 21 February 2022
Published: 16 March 2022

Citation:
Chu GS, Li X, Stafford PJ, Vanheusden FJ, Salinet JL, Almeida TP, Dastagir N, Sandilands AJ, Kirchhof P, Schlindwein FS and Ng GA (2022) Simultaneous Whole-Chamber Non-contact Mapping of Highest Dominant Frequency Sites During Persistent Atrial Fibrillation: A Prospective Ablation Study. Front. Physiol. 13:826449. doi: 10.3389/fphys.2022.826449

Purpose: Sites of highest dominant frequency (HDF) are implicated by many proposed mechanisms underlying persistent atrial fibrillation (persAF). We hypothesized that prospectively identifying and ablating dynamic left atrial HDF sites would favorably impact the electrophysiological substrate of persAF. We aim to assess the feasibility of prospectively identifying HDF sites by global simultaneous left atrial mapping.

Methods: PersAF patients with no prior ablation history underwent global simultaneous left atrial non-contact mapping. 30 s of electrograms recorded during AF were exported into a bespoke MATLAB interface to identify HDF regions, which were then targeted for ablation, prior to pulmonary vein isolation. Following ablation of each region, change in AF cycle length (AFCL) was documented ($\geq$ 10 ms considered significant). Baseline isopotential maps of ablated regions were retrospectively analyzed looking for rotors and focal activation or extinction events.

Results: A total of 51 HDF regions were identified and ablated in 10 patients (median DF 5.8Hz, range 4.4–7.1Hz). An increase in AFCL of was seen in 20 of the 51 regions (39%), including AF termination in 4 patients. 5 out of 10 patients (including the 4 patients where AF termination occurred with HDF-guided ablation) were free from AF recurrence at 1 year. The proportion of HDF occurrences in an ablated region was not associated with change in AFCL ($\tau = 0.11$, $p = 0.24$). Regions where AFCL decreased by 10 ms or more (i.e., AF disorganization) after ablation also showed lowest baseline spectral organization ($p < 0.033$ for any comparison). Considering all ablated regions, the average proportion of HDF events which were also HRI events was 8.0 $\pm$ 13%. Focal activations predominated (537/1253 events) in the ablated regions on isopotential

maps, were modestly associated with the proportion of HDF occurrences represented by the ablated region (Kendall's $\tau = 0.40$, $p < 0.0001$), and very strongly associated with focal extinction events ($\tau = 0.79$, $p < 0.0001$). Rotors were rare (4/1253 events).

Conclusion: Targeting dynamic HDF sites is feasible and can be efficacious, but lacks specificity in identifying relevant human persAF substrate. Spectral organization may have an adjunctive role in preventing unnecessary substrate ablation. Dynamic HDF sites are not associated with observable rotational activity on isopotential mapping, but epi-endocardial breakthroughs could be contributory.

Keywords: atrial fibrillation, catheter ablation, non-contact mapping, atrial electrograms, dominant frequency, persistent AF, multi-layer, rotors

INTRODUCTION

Atrial fibrillation (AF) is the commonest cardiac arrhythmia in clinical practice, affecting 2% of the population worldwide (Nattel, 2002). AF increases the risk of stroke fivefold and is associated with increased mortality (Nattel, 2002). Catheter ablation is an effective therapy for paroxysmal AF (pAF) (Haissaguerre et al., 1998; Fichtner et al., 2015), but the identification of successful ablation targets in patients with persistent AF (persAF) remains challenging (Jalife et al., 2002; Nattel, 2002, 2003). The electrophysiological mechanisms underlying persAF and current adjunctive ablation strategies beyond pulmonary vein isolation (PVI) lack clear evidence for effectiveness (Providencia et al., 2015; Verma et al., 2015; Mohanty et al., 2018). Recently, endocardial-epicardial interaction has been highlighted as a relevant pathophysiological contributor (Yamazaki et al., 2012; Gutbrod et al., 2015; Hansen et al., 2015), but this has not yet been translated into the clinical arena.

Sheep optical mapping studies (Mandapati et al., 2000; Mansour et al., 2001; Kalifa et al., 2006) first outlined the potential of using dominant frequency (DF) assessment to detect AF driver sites, predicated around the observation of rotors (Mandapati et al., 2000), but the utility of DF is also implicit with other proposed mechanisms (Kumagai et al., 2000; Lin et al., 2005; Kalifa et al., 2006). DF has previously demonstrated good correlation with local cycle length (Earley et al., 2006; Lin et al., 2007; Gojraty et al., 2009). Despite this, human ablation studies based on point-by-point sequential DF mapping were inconclusive (Atienza et al., 2009, 2014; Verma et al., 2011). Highest DF (HDF) sites have since been shown to be spatiotemporally unstable (Lazar et al., 2004; Yokoyama et al., 2009; Habel et al., 2010; Jarman et al., 2012; Salinet et al., 2014); consequently, as a natural corollary, simultaneous multisite mapping is necessary to reliably localize atrial high DF areas.

In this study, we hypothesized that the strategy of prospectively identifying and ablating dynamic left atrial HDF sites would favorably impact the electrophysiological substrate of persAF. We sought in particular to assess the feasibility of prospectively identifying HDF sites by global simultaneous left atrial mapping across long continuous time segments, and to describe the underlying wavefront activation characteristics at these sites.

MATERIALS AND METHODS

Patients

Ten persAF patients with no previous ablation history gave written informed consent to undergo HDF mapping and ablation, on uninterrupted oral anticoagulation. All had undergone successful direct current cardioversion (DCCV) previously, and median AF duration (from the first documented AF post-DCCV up to the time of their procedure) was 219 (range 132–848) days. **Table 1** summarizes the clinical characteristics of the group. The study was independently approved by the United Kingdom national health research ethics service. Procedures were performed under general anesthesia. All anti-arrhythmic drugs (AADs) were stopped for at least 5 half-lives, except amiodarone which was continued. Every patient was in AF at the start of their procedure.

Non-contact Mapping

A non-contact multi-electrode array (Ensite Array, St. Jude Medical, St Paul, MN, United States) was positioned transseptally in the left atrium (LA) alongside an EZ Steer Thermocool ablation catheter (Biosense Webster, Diamond Bar, CA, United States). Patients were heparinized to maintain an activated clotting time > 300 s. 3D electroanatomic mapping was performed using the Velocity platform (St. Jude Medical). 30 s of continuous AF activity were recorded, and the virtual electrograms (vEGMs) of a 2048 node geometry from this period were exported.

Signal Processing

A bespoke MATLAB graphical user interface was created for the study (Li et al., 2017), incorporating our previously published spectral analysis methodology (Salinet et al., 2014; Li et al., 2021), generating 13 sequential DF maps in each patient with 30 s data. The non-contact MEA catheter was used to collect intracardiac signals, as previously described. 2,048 channels of virtual electrograms (vEGMs) were sampled at 2034.5 Hz and exported with a 1–150 Hz filter setting from Ensite system (**Figure 1A**). MATLAB was used to analyze the data offline (Mathworks, United States). As shown in **Figure 1B**, ventricular far-field activity was removed from the recorded vEGMs using a previously described QRST subtraction technique (Salinet et al., 2013). The vEGMs were then divided into 4 s window segments

TABLE 1 | Clinical and procedural characteristics of patients with and AF recurrence within 12 months following ablation.

	All patients	AF free at 12 months	AF-recurrence within 12 months
N	10	5	5
Age/years	57.7 ± 12.1	57.3 ± 9.0	58.2 ± 14.6
Body mass index/kg m^{-2}	31.0 ± 5.7	32.6 ± 6.7	29.5 ± 3.7
Longstanding persistent AF	3	2	1
LA volume/ml	151 ± 38	146 ± 40	156 ± 35
Amiodarone usage	2	2	0
Hypertension	3	1	2
Diabetes mellitus	1	0	1
Previous myocardial infarction	1	1	0
Procedure duration/mins	389 ± 80	386 ± 65	393 ± 92
LA area ablated during HDF targeting/mm^2 (% of LA total)	1362 ± 704 (7.3 ± 3.6)	1055 ± 494 (5.9 ± 3.1)	1670 ± 746 (8.7 ± 3.6)
HDF occurrences ablated (%LA)	559 ± 268 (22.8 ± 8.7)	448 ± 278 (21.6 ± 7.1)	670 ± 205 (23.9 ± 9.9)
Electrical cardioversion required at procedure end to restore sinus rhythm	5	0	5

Numbers are mean ± SD where relevant. HDF, highest dominant frequency; LA, left atrium.

that overlapped by 50%. The fast Fourier transform (FFT) was used to perform spectral analysis on each segment (**Figure 1C**). A Hamming window was applied to the atrial vEGMs to reduce leakage. To improve DF identification, zero padding was used, resulting in a frequency step of 0.05 Hz. The peak in the power spectrum within the physiological range of 4–10 Hz was defined as DF (**Figure 1C**) (Salinet et al., 2014). Regularity index (RI) was defined as the ratio of spectral area (power) under the curve centered at DF peak (0.75 Hz bandwidth) and area under the full physiological spectrum (here 4 – 20 Hz, **Figure 1C**) (Sanders et al., 2005).

Highest Dominant Frequency Ablation Targeting

For each 4 s window, HDF occurrences were defined as all nodes hosting a DF within 0.25 Hz of the maximum DF for that map (shown as purple on the LA geometry in the example in the top panel of **Figure 1D**). To avoid biasing for target size, the spatial centers of the HDF occurrence regions for each map were projected onto the LA geometry in MATLAB (bottom panel, **Figure 1E**). The intended regions of ablation were transcribed on to the Velocity geometry, with the objective of prospectively defining several discrete regions for ablation. Each region where possible would encompass multiple co-localizing HDF spatial centers which would be ablated "en-bloc" (**Figure 1F**). Once this initial map was created, changes or re-mapping were not permitted.

Ablation Protocol

Highest dominant frequency spatial centers were targeted for radiofrequency ablation, with the objective of eliminating local atrial signal. The bipolar signal at the LAA is invariably well demarcated and permits unambiguous manual assessment of AFCL, has been applied as a surrogate of AF organization in many other clinical studies (O'Neill et al., 2006, 2009; Haissaguerre et al., 2007; Rostock et al., 2011; Honarbakhsh et al., 2018a). Following each region of HDF-guided ablation, AFCL in the left atrial appendage (LAA) was measured using the ablation catheter over 10 cycles to evaluate ablation response. A 10 ms change in AFCL was considered *a priori* to be significant (Bezerra et al., 2020). This was repeated until one of the following pre-defined endpoints was reached:

1) Termination of AF to sinus rhythm (SR);
2) Conversion from AF to an organized LA rhythm, or;
3) Operator decision to stop based on satisfactory target coverage or patient safety.

A further post-procedural Velocity data export was performed to capture all radiofrequency (RF) point (lesion) locations corresponding to each ablation region. Every RF point has an associated location on the LA geometry (the closest atrial endocardial surface point). Regularity index (RI) was defined as the ratio of spectral area (power) under the curve of DF peak and area under the full spectrum. Therefore, each point was associated with a DF value and an RI value which both vary over time. The DF and RI values at these LA geometry points were averaged spatially and temporally to generate (scalar) mean DF and RI values for each ablated region individually. There was no attempt to manually filter ablation points.

Finally, the Array was removed and replaced by PVAC (Pulmonary Vein Ablation Catheter, Medtronic, Fridley, MN, United States) to achieve PVI, irrespective of the atrial rhythm. Where necessary, intravenous flecainide followed by DCCV was delivered to restore SR at the end of the procedure.

Associating Post-ablation AF Cycle Length Change With Regional Pre-ablation Spectral Characteristics

Each of the 51 ablated regions across the whole patient cohort was categorized by the AFCL change arising from ablation in the region. The DIS group was pre-defined as regions where ablation resulted in a reduction in AFCL (i.e., DISorganization) by 10 ms or more. The ORG group was pre-defined as regions where ablation resulted in AFCL increase by 10 ms or more, or termination of arrhythmia (i.e., ORGanization). All other regions were classified as EQUivocal (i.e., an AFCL change of 9 ms or less in either direction).

Highest dominant frequency was defined as above, while highest RI (HRI) was defined as the top decile of RI values for the LA within any single given time window. HDF + HRI concurrence was defined whenever a given LA geometry point hosted HDF and HRI in the same time window.

HDF, HRI, and HDF + HRI concurrence was retrospectively compared across the DIS, EQU, and ORG groups.

Isopotential Map Wavefront Analysis

A retrospective analysis of the pre-ablation patterns of activation behavior in HDF regions was performed in the Velocity

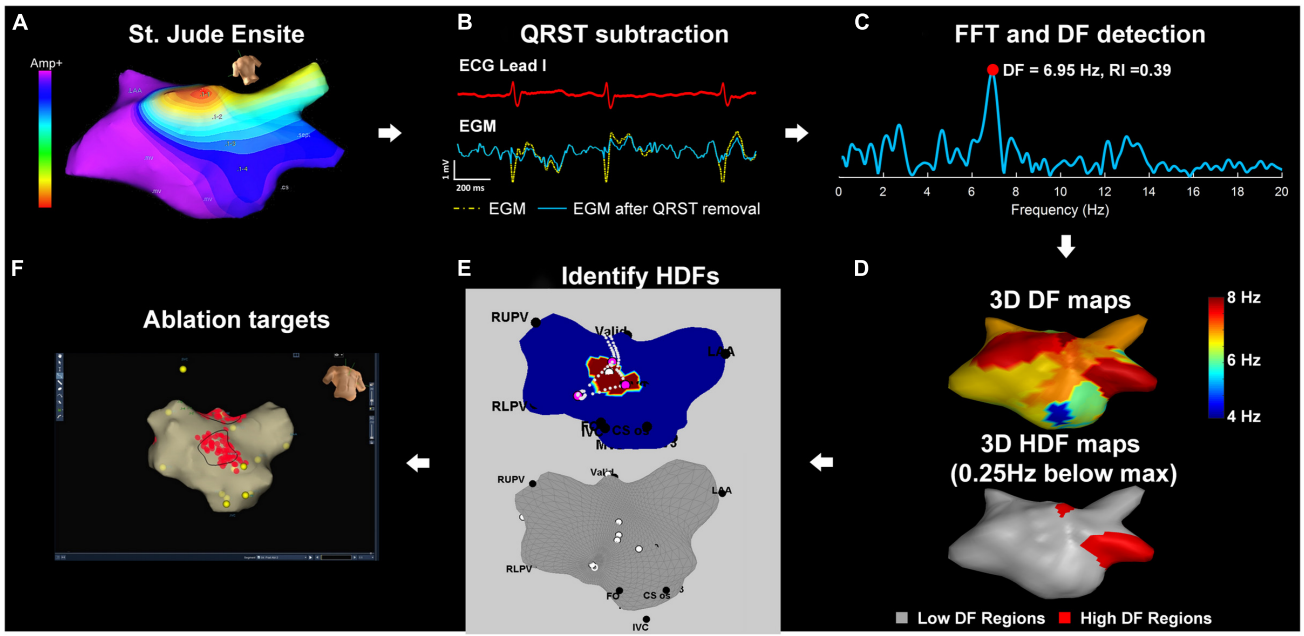

FIGURE 1 | Diagram of the workflow for ablation targets identification. **(A)** St. Jude Ensite: left atrial geometry isopotential map exported from Ensite Velocity System. **(B)** Array data is imported into a bespoke MATLAB user interface. QRST subtraction: Electrograms using one ECG lead as reference. **(C)** FFT and DF detection: power spectrum of the current non-contact atrial signal and DF identification **(D)** 3D and 2D DF/HDF maps: MATLAB reconstructed 3D Atrial geometry with color-coded DF/HDF and transformation to 2D uniform grid. **(E)** The top panel shows an antero-posterior view of the LA, with the region hosting HDF for a single 4 s time window highlighted in purple. The pink dots indicate the HDF spatial centers for all time windows. For better intraprocedural clarity, the bottom panel shows only the HDF spatial centers (white dots) identified across all the mapped time windows. **(F)** Identifying and ablating HDF regions. These are transcribed into the Velocity 3D mapping system and targeted with ablation (red dots). Yellow dots represent anatomical marker points. FFT, fast Fourier transform; HDF, highest dominant frequency.

environment using the following pre-specified protocol. Each discrete region that received ablation was circumscribed on the geometry. The isopotential mapping area was then centered upon this region. Activation was defined when local vEGM voltage fell below the fixed thresholds of either −0.28 or −0.53 mV (Hoshiyama et al., 2016). The rationale for these thresholds is based on the work of Hoshiyama and colleagues, where endocardial mapping of the LA was performed using the same non-contact multielectrode array as the one in the present study (Hoshiyama et al., 2016). In their study, vEGM signals from premature atrial contractions (PACs) were recorded at the time of spontaneous onset of AF. In particular, very short-coupled PACs (VS-PACs) were defined as "PAC with the shortest coupling interval that was observed just before the AF onset." The amplitude of the vEGM during VS-PACs was reported as 0.53 ± 0.25 mV. This threshold represented the smallest amplitude for a PAC that would have been associated with discrete ECG evidence of relevant activation, and was therefore used to define the lower activation threshold of −0.53 mV and the upper threshold of −0.28 mV (one standard deviation above the lower threshold) as used in the present study. The described approach avoided reliance upon more arbitrary amplitude thresholds during AF, with such thresholds inevitably being smaller and hence unfavorably reducing overall signal-noise ratio. Playback of the isopotential map from the 30 s period corresponding to the time of HDF mapping was performed, looking to document specific pre-defined activation trajectories encompassing current mechanistic theories of AF persistence (see **Figure 2** for detailed examples, and also the video links available in **Supplementary Materials**). Examples of the considered behaviors are provided in **Figure 2**, and **Supplementary Video** links are available in **Supplementary Materials**. Events were pre-defined as specific visually observed behaviors of activation encompassing current mechanistic theories of AF:

1) Rotor (Narayan et al., 2012, 2014) – core must remain in the lesion with a circular activation path of at least 360 degrees.
2) Critical pathway involved in single or multiple loop re-entry (Lin et al., 2005) – entry and exit of >50% of the activation wavefront must be from distinct sides of the lesion.
3) Wavelet propagation (Moe and Abildskov, 1959; Moe et al., 1964; Allessie, 1985) – Division of a primary wavefront into two or more separate wavefronts occurring within the lesion.
4) Focal wavefront activation (Haissaguerre et al., 1998; Kumagai et al., 2000) – wavefront spontaneously emerges radially from within an otherwise non-activated lesion.
5) Focal wavefront extinction (de Groot et al., 2010, 2016) – wavefront enters from outside the lesion, reduces radially and extinguishes within the lesion.

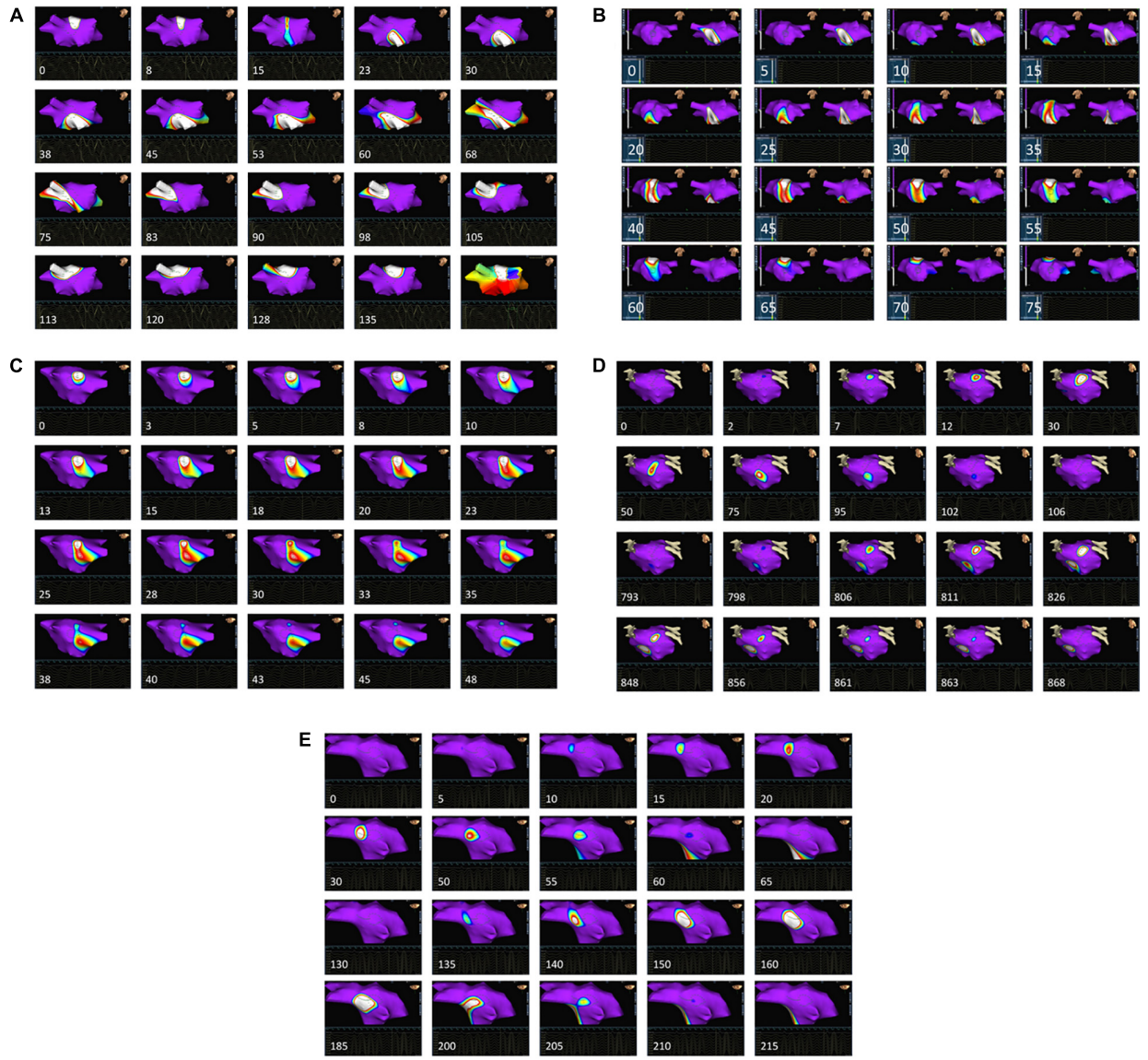

FIGURE 2 | Patterns of pre-ablation isopotential map behavior in and around HDF regions. For each case, the temporal sequence is from left to right and top to bottom. The timing of each frame relative to the first is given in ms. Each image is centered around an area that was subsequently ablated based upon the presence of HDF spatial centers. Purple areas on the map represent atrial myocardium where local activation is absent, as defined by a local vEGM (virtual electrogram) amplitude above –0.28 mV. Voltages of –0.53 mV or less display as white, with the remainder of the color scale defining intermediate values. The appearance and trajectory of color around the maps were used to define the following wavefront activation patterns: **(A)** Rotor-like behavior, seen on the LA roof. The final panel shows an isochronal map of the area during this period, confirming rotational activity. AFCL was not significant altered by ablation in this region. (see also **Supplementary Video 1**). **(B)** Activation passes through the posterior wall of the LA three times consecutively (see **Supplementary Video 2**) within a single TQ period, but ablation here did not alter AFCL. **(C)** A wavefront is seen to split into two independent wavefronts on the LA roof, with the division occurring within the ablated area. AFCL was not significantly affected by ablation here (see also **Supplementary Video 3**). **(D)** Focal activation occurs near the left upper pulmonary vein, migrating out of the ablated area before extinguishing, as also demonstrated in **Supplementary Video 4A**. Later on, the same area is seen to activate again from an identical origin (**Supplementary Video 4B**), this time extinguishing within the lesion. Ablation here terminated AF to an atrial tachycardia. **(E)** A recurring focal extinction event, occurring on the LA roof. Focal activation arises outside the ablated region, then moves into and extinguishes within the ablated area (first 10 images). This behavior is repeated again shortly afterward (last 10 images) within the same TQ interval. See also **Supplementary Video 5**.

For each ablated region, the frequency of each of the above behaviors within the 30 s segment was counted (see **Supplementary Videos** for examples). The observer was blinded to the AFCL change. Events partially or entirely within the QRST period were ignored.

The consistency of focal activation events was evaluated within each ablation region individually by assessing the maximum and minimum number of focal events over the prior 10 TQ intervals, creating a "moving maximum" (MMax) and "moving minimum" (MMin). The difference between the greatest and least

value of MMin and MMax over the 30 s period was designated "diffMMin" and "diffMMax," respectively.

Clinical Follow-Up

Following a 3-month blanking period, patients underwent at least 24 h of continuous ambulatory ECG monitoring, and recurrence was defined as any documented AF of at least 30 s occurring between 3 and 12 months post-procedure, irrespective of ongoing AADs.

Statistical Analysis

Data normality was assessed visually and using the Kolmogorov-Smirnov test. Correlations were performed using Spearman's or Kendall's method depending on the presence of rank ties, within MATLAB or using Prism v7.03 (Graphpad Software, CA, United States). Pairwise comparisons between groups were performed using the "TPB20" percentile bootstrap method with 20% trimmed means (Wilcox, 2012). Non-parametric trends analyses were performed using the Jonckheere-Terpstra test. Statistical significance was defined at the 0.05 level, and further adjusted for multiple comparisons. Both linear and logistic mixed effects regression models were explored but did not add utility ($p = 1.00$ and $p = 0.27$, respectively) for non-zero between-patient variance in AFCL outcome, (R v3.2.1, R Foundation for Statistical Computing, Vienna, Austria).

RESULTS

Clinical Outcomes

All patients completed the study protocol. Procedure duration was 390 ± 57 min, in keeping with a novel mapping and ablation protocol. RF time ablating HDF regions was 54 ± 27 min, covering an LA ablation area of 1447 ± 676 mm^2, corresponding to 7.8 ± 3.6% of the total mapped LA area, prior to PVI.

Five patients converted to SR without the need for DCCV. Patient 1 (longstanding persAF, on amiodarone) converted with flecainide after PVI. Patients 10 (longstanding persAF, on amiodarone), 5 (**Figure 3A**) and 4 converted from AF to atrial flutter, and patient 7 converted transiently to LA silence (**Figure 3B**) before then terminating to SR (all with HDF-guided ablation alone, prior to PVI). AF termination sites were the base of LAA, the LA roof (in 2 patients), and the posterior wall. An example of the ablation performed is shown in **Figure 4A**.

No significant adverse events occurred. During the 12-month follow-up period, all 5 patients requiring DCCV at the end of their procedure experienced AF recurrence, in contrast to zero out of the 5 who ended their procedure in SR without the need for DCCV. **Table 1** lists the clinical characteristics of patients with and without recurrent AF.

Characteristics of 30 s Highest Dominant Frequency-Guided Ablation Regions and AF Cycle Length Responses

The pre-ablation global LA mean DF was strongly correlated with baseline AFCL ($r = 0.88$, $p < 0.001$). A total of 51 discrete regions were ablated during the study, 20 (39%) of which resulted in significant AFCL increase or termination, as summarized in **Table 2**. Ablated region size was 267 ± 290 mm^2. The averaged DF for each ablated region was 5.7 ± 0.7 Hz with an average RI of 0.35 ± 0.06. A median of 4 (range 3–10) regions of ablation were delivered per patient.

Figure 4B shows the AFCL response to prospectively targeted ablation of consecutive HDF regions, demonstrating: (1) higher baseline AFCL conferred greater likelihood of achieving SR without DCCV ($p < 0.01$); (2) HDF-targeted ablation could disorganize as well as organize AF, but; (3) this did not preclude subsequent AF organization and/or termination. Only one patient had a further significant increment in AFCL following PVI (Patient 9, from 195 to 222 ms).

Median lesion size was 166 (21–1380) mm^2. The area of ablation alone (debulking) was not associated with AFCL variation (Kendall's $\tau = 0.05$, $p = 0.64$).

The proportion of HDF occurrences per ablated region (compared with the entire LA across 30 s) ranged from 0 to 14.7% (median 2.6%). Correlation between this and AFCL change was non-significant ($\tau = 0.11$, $p = 0.24$).

Highest Dominant Frequency and Highest RI Occurrences in Ablated Regions

The relationship between the spectral behavior of ablated regions and the AFCL response to ablation was assessed by comparing the number of HDF and HRI occurrences between the AFCL response groups, as shown in **Figure 5**. In view of the prolonged RF delivery times and varying extent of ablation, the possibility of cumulative ablation effects was assessed by evaluating the above metrics for only the first two (indicated in red) and first three (indicated in green) ablated regions for each patient, and finally for all ablated regions (indicated in blue).

Highest RI showed statistically significant trends analyses, as well as differences between the DIS group and the ORG group, for all extents of ablation. A significant difference was also seen in HRI between the DIS and EQU group when considering only the first two lesions. No other trends or comparisons were statistically relevant. Considering all ablated regions, the average proportion of HDF events which were also HRI events was 8.0 ± 13%.

For each patient in this study, DF mapping utilized a total of 13 consecutive time windows of 4 s each, with an overlap of 2 s. The geometry consists of 2048 notes, each of which may or may not host HDF, and may or may not host HRI. Across the 13 time windows, there are therefore 2048 * 13 = 26624 opportunities for HDF + HRI concurrence per patient. A period of HDF + HRI concurrence is considered as a spatially and temporally contiguous period of HDF + HRI concurrence of at least 1 time window, at any single node. With this in mind, the median (range) of HDF + HRI concurrence periods was 128.5 (0–628) out of a possible 26624 occurrences, per patient.

When considering all patients together, in this study there were a total of 1952 periods of HDF + HRI concurrence. The median duration of HDF + HRI concurrence was 1 time

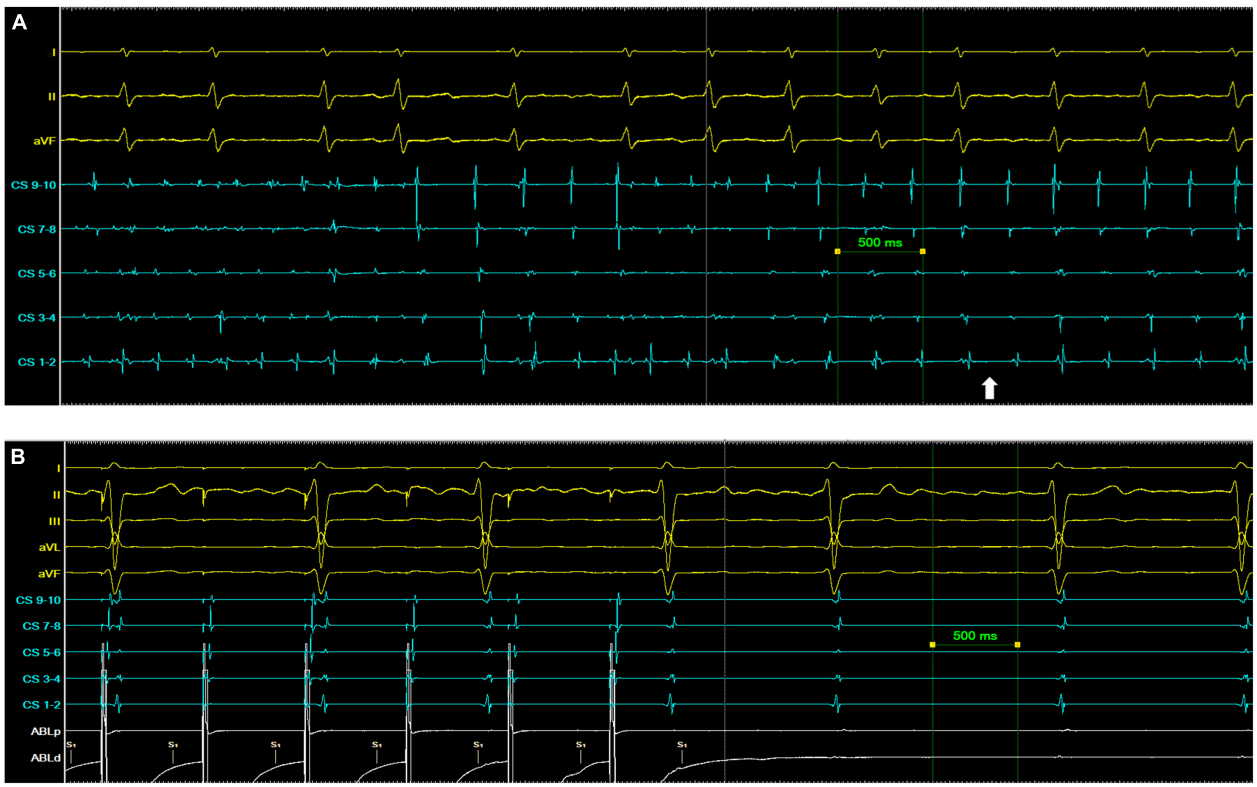

FIGURE 3 | Examples of AF termination following ablation of a region of highest dominant frequency. **(A)** Patient 5. The white arrow indicates the point of transition from AF to a persistent organized atrial tachyarrhythmia. **(B)** Patient 7. The left atrium is silent with no coronary sinus (CS) signal at baseline, but with ECG evidence of ongoing AF. Pacing from the ablation (Abl) catheter captures the CS with organized distal to proximal activation.

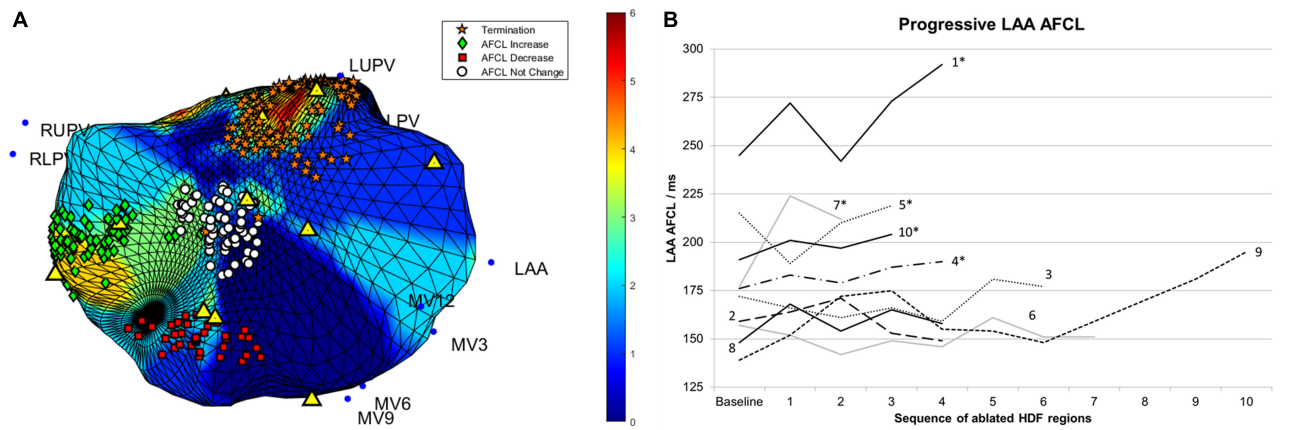

FIGURE 4 | (A) The four HDF targeted ablation regions from patient 5 are shown. The color scale corresponds to occurrences of HDF at the given spatial location. Individual lesions are labeled according to their impact on AFCL, with a change of 10 ms or more considered significant. Yellow triangles indicate the location of HDF spatial centers. **(B)** Changes in AFCL for each consecutive region of HDF-guided LA ablation. Lines are labeled with their respective patient number. Case progression is from left to right. *, patients in whom sinus rhythm was restored without the need for electrical cardioversion; AFCL, atrial fibrillation cycle length; HDF, highest dominant frequency; MV, mitral valve annular locations; LUPV, left upper pulmonary vein; RUPV, right upper pulmonary vein; RLPV, right lower pulmonary vein.

window (of 4 s), range 1–3 windows, i.e., 4–8 s (after accounting for window overlap). Importantly, only 82 out of the 1952 periods (4.2%) of HDF + HRI concurrence lasted for more than 1 time window.

Analysis of Isopotential Maps

The numbers of activation events per patient across all 51 ablation regions observed on 30 s pre-ablation isopotential maps are summarized in **Table 3**.

TABLE 2 | Location of ablated regions targeted using HDF mapping, and their associated left atrial response.

	Termination	AFCL increase	AFCL unchanged	AFCL decrease
Anterior	0	2	2	1
Posterior	1	3	5	3
Roof	2	3	9	0
Septum	0	4	0	1
Left PV region	0	2	3	1
Right PV region	0	0	4	2
Left atrial appendage	1	1	0	0
Lateral	0	1	0	0

AFCL, atrial fibrillation cycle length; PV, pulmonary vein.

A positive association between the proportion of HDF occurrences and all isopotential events within ablated regions was mainly driven by the focal activation group ($\tau = 0.40$, $p < 0.0001$). Focal event rates were indicatively different between ablation response groups (**Figure 6A**), and their ablation was weakly associated with an organizing AFCL response ($\tau = 0.21$, $p = 0.04$).

Focal extinction events were strongly correlated with focal activations in the same region ($\tau = 0.79$, $p < 0.0001$, **Figure 6B**). 0.65 extinction events (95% confidence intervals 0.58–0.71, $p < 0.0001$) were estimated to occur for every activation event in the same region. Rotor behavior was only observed 4 times during this study, and only in one patient (Patient 6). 3 of these 4 rotors occurred in the same ablated region. This particular region also recorded the highest overall number of wavefront activation events (excluding extinction events) in the whole study.

The maximum and minimum number of focal activation events occurring in any given ablation region appeared to be consistent over time (example in **Figure 7A**). diffMMin values ranged from 0 to 1 only, whilst all diffMMax values were 2 or less, except one. Greater variability (i.e., higher diffMMax and diffMMin) tended to occur only with higher mean event rates. ($\tau = 0.73$ and 0.41, respectively, $p < 0.0001$ for both, **Figure 7B**).

DISCUSSION

The present study shows that spatiotemporally dynamic HDF areas throughout the LA during human *in vivo* persAF can be prospectively, feasibly, and efficaciously targeted using a global multisite mapping approach based on an established commercial platform, even before PVI. 39% of HDF-targeted lesions resulted in an AFCL increase of 10 ms or more. The presence of focal activations on isopotential mapping was the most commonly observed electrophysiological behavior, and co-localized with HDF activity during AF in ablation regions. These activations were consistently observed in the same areas. Focal extinction events were strongly associated with focal activation events in these same areas, while rotor events were rare.

Regions with lower HRI occurrences were associated with a negative AFCL response to ablation, but HDF occurrences were not predictive. Simultaneous concurrence of HDF and HRI in the same time window and spatial location was uncommon and short-lived.

Dynamic Highest Dominant Frequency Mapping Does Not Identify Clinically Relevant Rotor Behavior

Dominant frequency is implicated across multiple potential mechanisms of AF persistence including multiple loop re-entry (Lin et al., 2005), focal sources (Takashima et al., 2010) and rotors (Mandapati et al., 2000; Mansour et al., 2001), yet previous results from DF-targeted persAF ablation have been disappointing (Atienza et al., 2009, 2014; Verma et al., 2011). Part of the explanation lies in the temporal-spatial variability in DF (Yokoyama et al., 2009; Habel et al., 2010; Jarman et al., 2012; Salinet et al., 2014) which may have limited the point-by-point approaches that have been employed in many studies to date, and underpinned our belief that a panoramic whole-atrial method would be necessary for robust spectral mapping of persAF. However, despite using such an approach, prospective ablation of dynamic HDF targets in the present study did not predict AF organization.

While previous retrospective data alluded to this possibility (Jarman et al., 2012) the current study is the first to prospectively reach this conclusion. Early data from the cholinergic stimulation of sheep atria (Kalifa et al., 2006; Filgueiras-Rama et al., 2012) first proposed the relevance of micro-reentrant phenomena producing spatial frequency gradients which might be potentially mapped in the frequency domain. Subsequent evidence supported the concept of such "rotor" meandering around anatomical or recurrent functional areas of block (Gianni et al., 2016; Salinet et al., 2017), or varying in response to the autonomic milieu (Atienza et al., 2006), both of which would lead to dynamic DF behavior and hence require similarly dynamic mapping to target successfully.

It was hypothesized that the present study might clarify this through the combination of isopotential activation map analysis alongside HDF. However, during the comprehensive isopotential map analysis of ablated regions in the present work, only 4 rotor-like events were observed, all in the same patient. This is comparable to the published rates of similarly described behavior using the same technology (Yamabe et al., 2016). Our observation suggests that where rotors do arise, they may co-localize with (and could thus confound the targeting of) other activation phenomena. Overall though, the rarity of this type of rotor behavior, coupled to the overall equivocal AFCL outcomes with prospective dynamic HDF targeting, questions the significance of such phenomena in relation to both HDF mapping and human AF persistence, as detected using the current study platform. Direct rotor observation and ablation in humans (Narayan et al., 2012, 2014) has been controversial (Benharash et al., 2015; Gianni et al., 2016) and some groups using direct atrial patch electrodes during cardiac surgery have not observed rotor phenomena at all (Moe et al., 1964; Allessie et al., 2010; Lee et al., 2015).

In addition, the definition of a rotor is still debated. A popular approach is to generate instantaneous phase signals from time series data using the Hilbert transform (Umapathy et al., 2010).

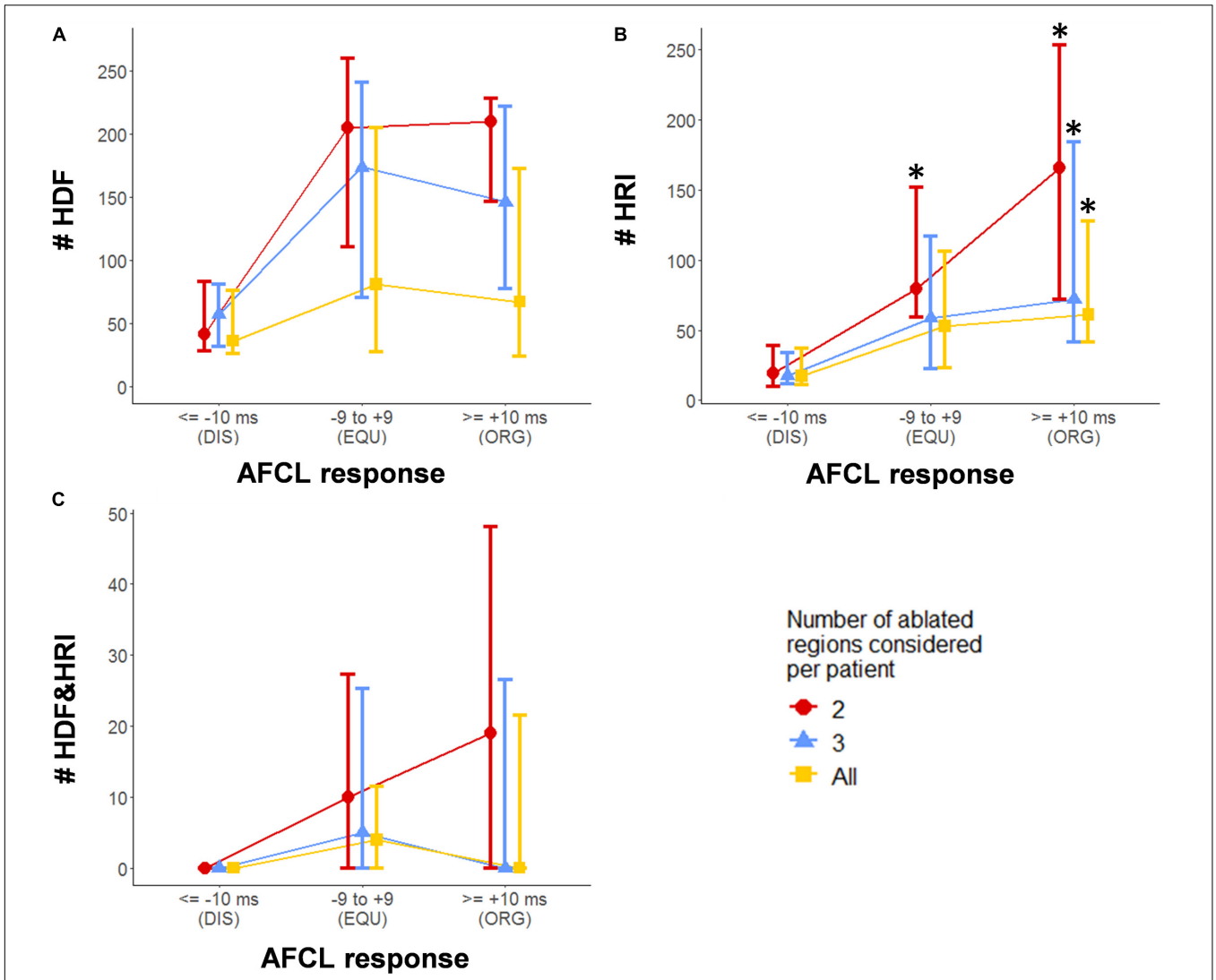

FIGURE 5 | Spectral characteristics of HDF-targeted ablation regions compared with the AFCL response to ablation of that region. **(A)** HDF counts. **(B)** HRI counts. **(C)** HDF + HRI concurrence counts. Values shown are median ± interquartile range. DIS – ablation lesions resulting in an AFCL decrease/disorganization of 10 ms or more; EQU – ablation lesions resulting in equivocal change in AFCL of between –9 and + 9 ms; ORG – ablation lesions resulting in AFCL increase/organization of 10 ms or more; * indicates a statistically significant difference when compared with the corresponding DIS group after correction for multiple comparisons.

To "unmask" the rotational behaviors within narrower frequency ranges, pre-processing methods have been applied to intracardiac data before Hilbert transform. Wavelet/sinusoidal reconstruction and band-pass filters centered on DFs are examples of techniques for filtering out undesirable and/or non-physiologic activations (Rodrigo et al., 2014; Kuklik et al., 2015). Once robust phase mapping has been obtained, another factor to consider is the definition of a rotor in terms of completeness of rotations. While the original idea is of a re-entrant circuit requiring a full rotation with 1 cycle or 360 degrees, in practice, this is usually not achievable due to spatial electrodes sampling. More recently, a rotor with >75% of a full rotation was considered to be generally acceptable (Kowalewski et al., 2018). In the present study, the rotors were defined by visual assessment of isopotential maps in a manner similar to that of Yamabe et al. (2016). It is nevertheless possible that we could have underestimated the number of rotors that were present, as using activation or isopotential maps alone, based on electrograms or activation wavefronts, may have a

TABLE 3 | Frequency of left atrial activation events during lesion-by-lesion visual assessment of isopotential maps within each patient.

Patient	1	2	3	4	5	6	7	8	9	10	Total
Rotor	0	0	0	0	0	4	0	0	0	0	4
Critical pathway	21	0	12	6	7	127	11	3	86	42	315
Wavelet propagation	1	0	0	2	0	10	0	0	5	2	20
Focal activation	23	1	37	60	70	70	27	25	167	57	537
Focal extinction	27	1	18	48	59	41	27	19	121	16	377

See text for definitions of activation behavior.

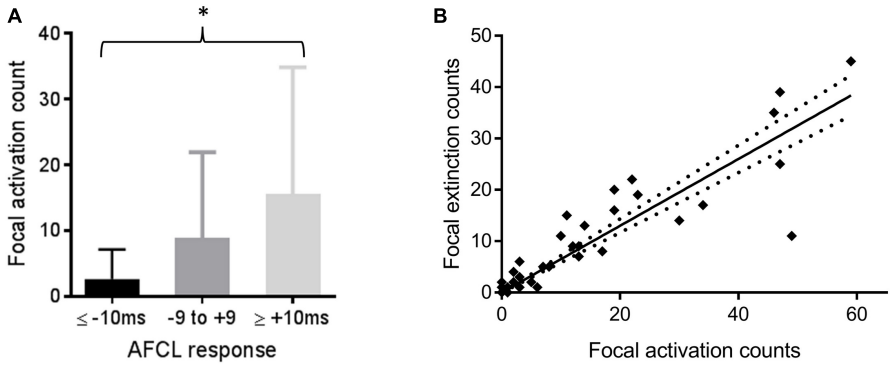

FIGURE 6 | (A) Comparing numbers (mean and SD) of focal activation events with the AFCL response to ablation of that region; *$p < 0.05$ for Kendall's correlation between the variables. **(B)** Counts of focal extinction and activation events within the same regions. Line of best fit and confidence intervals by linear regression are shown ($p < 0.0001$).

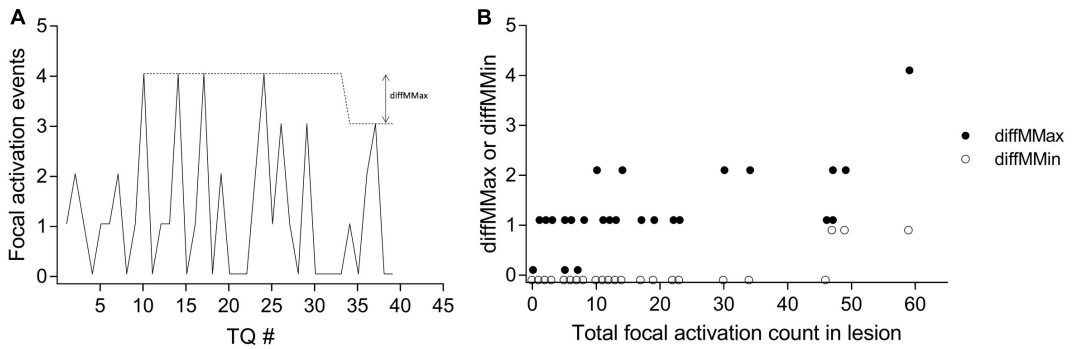

FIGURE 7 | Demonstrating the temporal consistency of focal activation events. **(A)** In one patient, for each consecutive TQ interval, the number of observed focal activation events for one ablated region is shown by the solid line. The dotted line indicates the MMax (moving maximum) for the region, and an example of the derivation of diffMMax is shown. **(B)** The variation in the consistency of focal activation as measured by diffMMax (filled circles) and diffMMin (unfilled circles) across all 51 lesions from all 10 patients are shown. See main text for definitions.

tendency to overlook phase-singularity events that have been used to define rotors (Narayan and Zaman, 2016).

Identifying Spectral Organization May Minimize Excess Ablation

The data in the present study shows that HDF-guided ablation may not always result in AF organization; in another words, HDF-guided mapping results in false-positive substrate identification. Interestingly however, where HDF-guided ablation resulted in AF disorganization, the pre-ablation HRI in these areas was significantly lower than if AF had organized, and to a lesser extent than if there was no AFCL response. Therefore, low HRI may have utility as an adjunctive indicator to avoid the risks of ineffective ablation of false-positive targets identified by HDF, or indeed by other putative substrate markers.

Dominant frequency variability is known to be inversely associated with spectral measures of AF organization (Takahashi et al., 2006; Jarman et al., 2014; Honarbakhsh et al., 2018b). As such, atrial zones with low HRI may be expected to host substantially more DF variation, which would not be consistent with putative source-like behavior. The fact that HDF and HRI were only very rarely spatiotemporally coincident in our cohort thus further supports a significantly lesser role for HDF than was previously assumed.

Relatively few studies have specifically evaluated the spectral assessment of organization in the context of AF ablation. Computer simulation has suggested that OI (organization index, a measure of spectral organization similar to the RI used in the present study) would be superior to DF in localizing focal activity (Everett et al., 2001; Tobon et al., 2012), Tuan et al. (2010) noted a rise in OI prior to AF termination with flecainide, with Takahashi and colleagues observing the same after isolation of a driving PV in pAF (Takahashi et al., 2006). Jarman and colleagues documented in 6 patients, also using a non-contact array in the LA, that where PVI with wide area circumferential ablation had coincidentally crossed areas of higher organization, the organization in a distal part of the LA (around the LAA) also increased (Jarman et al., 2014). However, the organization in adjacent sites did not change significantly which may run counter to the idea of the index area as an AF source.

More recently, Honarbakhsh et al. (2019) used a 64-pole basket contact catheter and CARTOFINDER to evaluate 44

AF driver sites in 29 patients, defined by either rotational or focal activity observed over 30 s. Following PVI, 39 out of 44 prospectively ablated driver sites resulted in AFCL prolongation (of at least 30 ms) or termination. Interestingly the sensitivity (true positive rates) for HDF and HRI were 50 and 95%, while false positive rates were 37 and 33%, respectively.

Epicardial-Endocardial Interaction: An Alternative Hypothesis for Highest Dominant Frequency in Atrial Fibrillation Persistence

Our method of tracking HDF did not assume any specific underlying electrophysiological mechanism other than the relevance of high frequency activation sites in maintaining persAF. To explore this further, we investigated the underlying isopotential patterns within ablated regions, seeking pre-defined mechanistic behaviors that co-localized with or formed the basis for HDF events or for the AFCL response to ablation.

Out of all our pre-defined activation patterns, only focal activation events were found to be associated with AFCL response, and more interestingly also (very strongly) with focal extinction events. The co-localization of focal activation and extinction suggests that the same anatomical regions may act as both source and sink in the electrophysiological environment, where current can both originate from and flow back to. Our results suggest the possibility of other electrophysiologically active tissue permitting the channeling of current both toward and away from the endocardium – in other words, multiple electrophysiologically relevant myocardial layers. To the best knowledge of the authors, this is the first presentation of data from a commercially available mapping system in the LA that is supportive of the multi-layer hypothesis in human persAF (de Groot et al., 2010, 2016). In keeping with this interpretation and their own conclusions, de Groot and colleagues (de Groot et al., 2016) documented highly correlated numbers of focal endocardial and epicardial events measured using contact electrodes in the right atrium during AF in cardiac surgery ($R^2 = 0.89$, $p < 0.0001$, our calculation). Not all focal waves breaking through to the epicardium will originate from the endocardium, which may explain the apparent shortfall of endocardially observed extinction events compared to activation events in the present work. Notably, 57% of our ablated regions demonstrated repetition of focal behavior, often with clear anatomical consistency even within the ablated area (see example in **Supplementary Video 4**), whereas < 10% of focal events in the data from de Groot et al., were repetitive, probably due to differences in detection criteria, and a shorter mapping time of 10s per patient. Our data suggests that 30 s would be sufficient to observe temporally consistent focal activity in humans.

We also show for the first time an association between HDF events and observed focal events. Computer modeling studies (Gharaviri et al., 2017) suggest that reducing the number of epicardial-endocardial breakthrough sites (BTRs) could increase or decrease AF stability. Although this study could not look specifically at BTRs ablation, our finding of a heterogeneous AFCL response to ablation in potentially equivalent areas is supportive of this and may have contributed to the equivocal outcomes from previous DF-targeted persAF ablation studies.

Limitations

We believe our work on a small number of patients offers a number of useful insights into persAF behavior in the context of HDF ablation, but larger patient cohorts would be needed to confirm or otherwise the prospective validity of future similar methodologies.

Isopotential map analysis was voltage thresholded at a level which may have precluded visualization of lower amplitude but electrophysiologically relevant signals. It is however notable that the correlation between focal activation and extinction events was preserved ($\tau = 0.82$, $p < 0.0001$) even when the threshold for activation was reduced (i.e., made more stringent) from −0.28 to −0.53 mV, negating the idea of a noise-driven phenomenon, and suggesting that the −0.28 mV threshold was reasonably specific for the detection of this type of behavior.

An average of 10% of Array geometry points were located more than 40 mm from the Array, at which point signal quality is known to decrease (Kadish et al., 1999). The process of HDF evaluation will be partially resistant to this effect (Gojraty et al., 2009), as it is less dependent on signal amplitude.

Ablation can alter spectral characteristics at distant sites (Jarman et al., 2014; Salinet et al., 2017), therefore it is possible that the cumulative effect of sequentially targeted ablation may be different to each lesion considered individually. The effect of this was partially accounted for with analysis for 2,3 and all available lesions separately as shown in **Figure 5**. In the future, faster generation of global DF maps may increase the feasibility of applying an iterative approach (remapping after each lesion is delivered) to investigate this further.

The current investigation was focused on frequency domain analysis. Future work including other metrics such as entropy and coherence could bring new insights and help to better understand the underlying mechanisms of persAF (Lee et al., 2013; Almeida et al., 2017, 2018; Li et al., 2020, 2021).

In the absence of confirmatory epicardial data, the endo-epi interaction shown through non-contact mapping was observational in nature and hence hypothesis generating only. Computational simulation or pre-clinical experiments may provide more evidence but were not included in the current study.

CONCLUSION

We have shown that the ablation of spatiotemporally dynamic HDF regions guided by global intra-cardiac non-contact mapping is feasible and can acutely organize persAF before PVI. However, HDF alone has inadequate specificity for AF driving sites. During persAF ablation, left atrial areas of low organization in the frequency domain are unlikely to be appropriate substrate targets and should be avoided to reduce excess ablation and its consequences. Whole-chamber non-contact mapping may be able to detect epicardial-endocardial interactions in persAF, but

further studies are needed to better delineate the importance of this in clinical practice.

DATA AVAILABILITY STATEMENT

The raw data supporting the conclusions of this article will be made available by the authors, without undue reservation.

ETHICS STATEMENT

The studies involving human participants were reviewed and approved by United Kingdom NHS National Research Ethics Service. The patients/participants provided their written informed consent to participate in this study.

AUTHOR CONTRIBUTIONS

GC: concept/design study, data analysis/interpretation of results, drafting manuscript, critical revision of manuscript, statistics, and "off-line" data collection. XL: concept/design study, data analysis/interpretation of results, drafting manuscript, critical revision of manuscript, and statistics. PS: EP studies and ablation procedures, concept/design study, EP study, data collection, interpretation of results, and critical revision of manuscript. FV: data analysis/interpretation of results, critical revision of manuscript, and statistics. JS, AS, and PK: data analysis/interpretation of results and critical revision of manuscript. TA: data analysis/interpretation of results, drafting manuscript, and critical revision of manuscript. ND: data analysis/interpretation of results, and critical revision of manuscript. FS: concept/design study, data analysis/interpretation of results, and critical revision of manuscript. GN: EP studies and ablation procedures, concept/design study, interpretation of results, and critical revision of manuscript. All authors contributed to the article and approved the submitted version.

FUNDING

This work was supported by the NIHR Leicester Biomedical Research Centre, United Kingdom. GC has been supported for this work by educational funding from St. Jude Medical (now Abbott, not involved in study conception/design and manuscript preparation). XL received research grants from Medical Research Council United Kingdom (MRC DPFS ref: MR/S037306/1). TA received research grants from the British Heart Foundation (BHF Project Grant No. PG/18/33/33780), BHF Research Accelerator Award funding, and Fundação de Amparo à Pesquisa do Estado de São Paulo (FAPESP, Brazil, Grant No. 2017/00319-8). GN received funding from the British Heart Foundation (BHF Program Grant, RG/17/3/32774). JS was supported by grant 2018/25606-2, São Paulo Research Foundation (FAPESP).

ACKNOWLEDGMENTS

This work falls under the portfolio of research conducted within the NIHR Leicester Biomedical Research Centre. GN – Speaker Honoraria (SJM/Abbott, Biosense Webster), research fellowship funding (SJM/Abbott, Boston Scientific), and support for conference attendance (Boston Scientific, Medtronic, SJM/Abbott). GC supports for conference attendance (Biosense Webster, SJM/Abbott), funding of research fellowship position (SJM/Abbott). PK receives research support from European Union, British Heart Foundation, Leducq Foundation, Medical Research Council (UK), German Centre for Cardiovascular Research, from several drug and device companies active in atrial fibrillation, and has received honoraria from several such companies, and listed as inventor on two patents held by University of Birmingham (Atrial Fibrillation Therapy WO 2015140571, Markers for Atrial Fibrillation WO 2016012783).

SUPPLEMENTARY MATERIAL

The Supplementary Material for this article can be found online at: https://www.frontiersin.org/articles/10.3389/fphys.2022.826449/full#supplementary-material

REFERENCES

Allessie, M. A. (1985). Experimental evaluation of Moe's multiple wavelet hypothesis of atrial fibrillation. *Card. Arrhyth.* 1985, 265–276. doi: 10.1016/j.hrthm.2020.06.017

Allessie, M. A., de Groot, N. M., Houben, R. P., Schotten, U., Boersma, E., Smeets, J. L., et al. (2010). Electropathological substrate of long-standing persistent atrial fibrillation in patients with structural heart disease: longitudinal dissociation. *Circ. Arrhythm. Electrophysiol.* 3, 606–615. doi: 10.1161/CIRCEP.109.910125

Almeida, T. P., Chu, G. S., Li, X., Dastagir, N., Tuan, J. H., Stafford, P. J., et al. (2017). Atrial Electrogram Fractionation Distribution before and after Pulmonary Vein Isolation in Human Persistent Atrial Fibrillation—A Retrospective Multivariate Statistical Analysis. *Front. Physiol.* 8:589. doi: 10.3389/fphys.2017.00589

Almeida, T. P., Schlindwein, F. S., Salinet, J., Li, X., Chu, G. S., Tuan, J. H., et al. (2018). Characterization of human persistent atrial fibrillation electrograms using recurrence quantification analysis. *Chaos* 28:085710. doi: 10.1063/1.5024248

Atienza, F., Almendral, J., Jalife, J., Zlochiver, S., Ploutz-Snyder, R., Torrecilla, E. G., et al. (2009). Real-time dominant frequency mapping and ablation of dominant frequency sites in atrial fibrillation with left-to-right frequency gradients predicts long-term maintenance of sinus rhythm. *Heart Rhythm.* 6, 33–40. doi: 10.1016/j.hrthm.2008.10.024

Atienza, F., Almendral, J., Moreno, J., Vaidyanathan, R., Talkachou, A., Kalifa, J., et al. (2006). Activation of inward rectifier potassium channels accelerates atrial fibrillation in humans: evidence for a reentrant mechanism. *Circulation* 114, 2434–2442. doi: 10.1161/CIRCULATIONAHA.106.633735

Atienza, F., Almendral, J., Ormaetxe, J. M., Moya, A., Martinez-Alday, J. D., Hernandez-Madrid, A., et al. (2014). Comparison of radiofrequency catheter ablation of drivers and circumferential pulmonary vein isolation in atrial fibrillation: a noninferiority randomized multicenter RADAR-AF trial. *J. Am. Coll Cardiol.* 64, 2455–2467. doi: 10.1016/j.jacc.2014.09.053

Benharash, P., Buch, E., Frank, P., Share, M., Tung, R., Shivkumar, K., et al. (2015). Quantitative analysis of localized sources identified by focal impulse and rotor modulation mapping in atrial fibrillation. *Circ. Arrhythm. Electrophysiol.* 8, 554–561. doi: 10.1161/circep.115.002721

Bezerra, A. S., Yoneyama, T., Soriano, D. C., Luongo, G., Li, X., Ravelli, F., et al. (2020). Optimizing Atrial Electrogram Classification Based on Local Ablation Outcome in Human Atrial Fibrillation. *Computing in Cardiology* 2020, 13–16. doi: 10.3389/fphys.2020.00869

de Groot, N., van der Does, L., Yaksh, A., Lanters, E., Teuwen, C., Knops, P., et al. (2016). Direct Proof of Endo-Epicardial Asynchrony of the Atrial Wall During Atrial Fibrillation in Humans. *Circ. Arrhythm. Electrophysiol.* 9:5. doi: 10.1161/CIRCEP.115.003648

de Groot, N. M., Houben, R. P., Smeets, J. L., Boersma, E., Schotten, U., Schalij, M. J., et al. (2010). Electropathological substrate of longstanding persistent atrial fibrillation in patients with structural heart disease: epicardial breakthrough. *Circulation* 122, 1674–1682. doi: 10.1161/CIRCULATIONAHA.109.910901

Earley, M. J., Abrams, D. J., Sporton, S. C., and Schilling, R. J. (2006). Validation of the noncontact mapping system in the left atrium during permanent atrial fibrillation and sinus rhythm. *J. Am. Coll. Cardiol.* 48, 485–491. doi: 10.1016/j.jacc.2006.04.069

Everett, T. H. T., Kok, L. C., Vaughn, R. H., Moorman, J. R., and Haines, D. E. (2001). Frequency domain algorithm for quantifying atrial fibrillation organization to increase defibrillation efficacy. *IEEE Trans. Biomed. Eng.* 48, 969–978. doi: 10.1109/10.942586

Fichtner, S., Sparn, K., Reents, T., Ammar, S., Semmler, V., Dillier, R., et al. (2015). Recurrence of paroxysmal atrial fibrillation after pulmonary vein isolation: is repeat pulmonary vein isolation enough? A prospective, randomized trial. *Europace* 17, 1371–1375. doi: 10.1093/europace/euu389

Filgueiras-Rama, D., Price, N. F., Martins, R. P., Yamazaki, M., Avula, U. M., Kaur, K., et al. (2012). Long-term frequency gradients during persistent atrial fibrillation in sheep are associated with stable sources in the left atrium. *Circ. Arrhythm. Electrophysiol.* 5, 1160–1167. doi: 10.1161/CIRCEP.111.969519

Gharaviri, A., Verheule, S., Eckstein, J., Potse, M., Kuklik, P., Kuijpers, N. H., et al. (2017). How disruption of endo-epicardial electrical connections enhances endo-epicardial conduction during atrial fibrillation. *Europace* 19, 308–318. doi: 10.1093/europace/euv445

Gianni, C., Mohanty, S., Di Biase, L., Metz, T., Trivedi, C., Gokoglan, Y., et al. (2016). Acute and early outcomes of focal impulse and rotor modulation (FIRM)-guided rotors-only ablation in patients with nonparoxysmal atrial fibrillation. *Heart Rhythm.* 13, 830–835. doi: 10.1016/j.hrthm.2015.12.028

Gojraty, S., Lavi, N., Valles, E., Kim, S. J., Michele, J., and Gerstenfeld, E. P. (2009). Dominant frequency mapping of atrial fibrillation: comparison of contact and noncontact approaches. *J. Cardiovasc. Electrophysiol.* 20, 997–1004. doi: 10.1111/j.1540-8167.2009.01488.x

Gutbrod, S. R., Walton, R., Gilbert, S., Meillet, V., Jais, P., Hocini, M., et al. (2015). Quantification of the transmural dynamics of atrial fibrillation by simultaneous endocardial and epicardial optical mapping in an acute sheep model. *Circ. Arrhythm. Electrophysiol.* 8, 456–465. doi: 10.1161/CIRCEP.114.002545

Habel, N., Znojkiewicz, P., Thompson, N., Muller, J. G., Mason, B., Calame, J., et al. (2010). The temporal variability of dominant frequency and complex fractionated atrial electrograms constrains the validity of sequential mapping in human atrial fibrillation. *Heart Rhythm.* 7, 586–593. doi: 10.1016/j.hrthm.2010.01.010

Haissaguerre, M., Jais, P., Shah, D. C., Takahashi, A., Hocini, M., Quiniou, G., et al. (1998). Spontaneous initiation of atrial fibrillation by ectopic beats originating in the pulmonary veins. *New Engl J Med.* 339, 659–666. doi: 10.1056/NEJM199809033391003

Haissaguerre, M., Lim, K. T., Jacquemet, V., Rotter, M., Dang, L., Hocini, M., et al. (2007). Atrial fibrillatory cycle length: computer simulation and potential clinical importance. *Europace* 9(Suppl. 6), vi64–vi70. doi: 10.1093/europace/eum208

Hansen, B. J., Zhao, J., Csepe, T. A., Moore, B. T., Li, N., Jayne, L. A., et al. (2015). Atrial fibrillation driven by micro-anatomic intramural re-entry revealed by simultaneous sub-epicardial and sub-endocardial optical mapping in explanted human hearts. *Eur. Heart J.* 36, 2390–2401. doi: 10.1093/eurheartj/ehv233

Honarbakhsh, S., Schilling, R. J., Dhillon, G., Ullah, W., Keating, E., Providencia, R., et al. (2018a). A Novel Mapping System for Panoramic Mapping of the Left Atrium: Application to Detect and Characterize Localized Sources Maintaining Atrial Fibrillation. *JACC Clin. Electrophysiol.* 4, 124–134. doi: 10.1016/j.jacep.2017.09.177

Honarbakhsh, S., Schilling, R. J., Providencia, R., Keating, E., Chow, A., Sporton, S., et al. (2018b). Characterization of drivers maintaining atrial fibrillation: correlation with markers of rapidity and organization on spectral analysis. *Heart Rhythm.* 15, 1296–1303. doi: 10.1016/j.hrthm.2018.04.020

Honarbakhsh, S., Schilling, R. J., Finlay, M., Keating, E., Ullah, W., and Hunter, R. J. S. T. A. R. (2019). mapping method to identify driving sites in persistent atrial fibrillation: Application through sequential mapping. *J. Cardiovasc. Electrophysiol.* 30, 2694–2703. doi: 10.1111/jce.14201

Hoshiyama, T., Yamabe, H., Koyama, J., Kanazawa, H., and Ogawa, H. (2016). Left atrial electrophysiologic feature specific for the genesis of complex fractionated atrial electrogram during atrial fibrillation. *Heart Vessels* 31, 773–782. doi: 10.1007/s00380-015-0672-2

Jalife, J., Berenfeld, O., and Mansour, M. (2002). Mother rotors and fibrillatory conduction: a mechanism of atrial fibrillation. *Cardiovasc. Res.* 54, 204–216. doi: 10.1016/s0008-6363(02)00223-7

Jarman, J. W., Wong, T., Kojodjojo, P., Spohr, H., Davies, J. E., Roughton, M., et al. (2012). Spatiotemporal behavior of high dominant frequency during paroxysmal and persistent atrial fibrillation in the human left atrium. *Circ. Arrhythm. Electrophysiol.* 5, 650–658. doi: 10.1161/CIRCEP.111.967992

Jarman, J. W. E., Wong, T., Kojodjojo, P., Spohr, H., Davies, J. E. R., Roughton, M., et al. (2014). Organizational index mapping to identify focal sources during persistent atrial fibrillation. *J. Cardiovasc. Electrophysiol.* 25, 355–363. doi: 10.1111/jce.12352

Kadish, A., Hauck, J., Pederson, B., Beatty, G., and Gornick, C. (1999). Mapping of atrial activation with a noncontact, multielectrode catheter in dogs. *Circulation* 99, 1906–1913. doi: 10.1161/01.cir.99.14.1906

Kalifa, J., Tanaka, K., Zaitsev, A. V., Warren, M., Vaidyanathan, R., Auerbach, D., et al. (2006). Mechanisms of wave fractionation at boundaries of high-frequency excitation in the posterior left atrium of the isolated sheep heart during atrial fibrillation. *Circulation* 113, 626–633. doi: 10.1161/CIRCULATIONAHA.105.575340

Kowalewski, C. A. B., Shenasa, F., Rodrigo, M., Clopton, P., Meckler, G., Alhusseini, M. I., et al. (2018). Interaction of Localized Drivers and Disorganized Activation in Persistent Atrial Fibrillation: Reconciling Putative Mechanisms Using Multiple Mapping Techniques. *Circ. Arrhythm. Electrophysiol.* 11:e005846. doi: 10.1161/CIRCEP.117.005846

Kuklik, P., Zeemering, S., Maesen, B., Maessen, J., Crijns, H. J., Verheule, S., et al. (2015). Reconstruction of instantaneous phase of unipolar atrial contact electrogram using a concept of sinusoidal recomposition and Hilbert transform. *IEEE Trans. Biomed. Eng.* 62, 296–302. doi: 10.1109/TBME.2014.2350029

Kumagai, K., Yasuda, T., Tojo, H., Noguchi, H., Matsumoto, N., Nakashima, H., et al. (2000). Role of rapid focal activation in the maintenance of atrial fibrillation originating from the pulmonary veins. *Pace* 23(11 Pt 2), 1823–1827. doi: 10.1111/j.1540-8159.2000.tb07029.x

Lazar, S., Dixit, S., Marchlinski, F. E., Callans, D. J., and Gerstenfeld, E. P. (2004). Presence of left-to-right atrial frequency gradient in paroxysmal but not persistent atrial fibrillation in humans. *Circulation* 110, 3181–3186. doi: 10.1161/01.CIR.0000147279.91094.5E

Lee, J., Nam, Y., McManus, D. D., and Chon, K. H. (2013). Time-varying coherence function for atrial fibrillation detection. *IEEE Trans. Biomed. Eng.* 60, 2783–2793.

Lee, S., Sahadevan, J., Khrestian, C. M., Cakulev, I., Markowitz, A., and Waldo, A. L. (2015). Simultaneous Biatrial High-Density (510-512 Electrodes) Epicardial Mapping of Persistent and Long-Standing Persistent Atrial Fibrillation in Patients: New Insights Into the Mechanism of Its Maintenance. *Circulation* 132, 2108–2117. doi: 10.1161/CIRCULATIONAHA.115.017007

Li, X., Chu, G. S., Almeida, T. P., Vanheusden, F. J., Salinet, J., Dastagir, N., et al. (2021). Automatic Extraction of Recurrent Patterns of High Dominant Frequency Mapping During Human Persistent Atrial Fibrillation. *Front. Physiol.* 2021:12. doi: 10.3389/fphys.2021.649486

Li, X., Salinet, J. L., Almeida, T. P., Vanheusden, F. J., Chu, G. S., Ng, G. A., et al. (2017). An interactive platform to guide catheter ablation in human persistent atrial fibrillation using dominant frequency, organization and phase mapping. *Comput. Methods Progr. Biomed.* 141, 83–92. doi: 10.1016/j.cmpb.2017.01.011

Li, X., Sidhu, B., Almeida, T. P., Ehnesh, M., Mistry, A., Vali, Z., et al. (2020). P439Could regional electrogram desynchronization identified using mean phase coherence be potential ablation targets in persistent atrial fibrillation? *EP Europace* 22:1.

Lin, Y. J., Higa, S., Kao, T., Tso, H. W., Tai, C. T., Chang, S. L., et al. (2007). Validation of the frequency spectra obtained from the noncontact unipolar

electrograms during atrial fibrillation. *J. Cardiovasc. Electrophysiol.* 18, 1147–1153. doi: 10.1111/j.1540-8167.2007.00924.x

Lin, Y. J., Tai, C. T., Kao, T., Tso, H. W., Huang, J. L., Higa, S., et al. (2005). Electrophysiological characteristics and catheter ablation in patients with paroxysmal right atrial fibrillation. *Circulation* 112, 1692–1700. doi: 10.1161/CIRCULATIONAHA.104.512731

Mandapati, R., Skanes, A., Chen, J., Berenfeld, O., and Jalife, J. (2000). Stable microreentrant sources as a mechanism of atrial fibrillation in the isolated sheep heart. *Circulation* 101, 194–199. doi: 10.1161/01.cir.101.2.194

Mansour, M., Mandapati, R., Berenfeld, O., Chen, J., Samie, F. H., and Jalife, J. (2001). Left-to-right gradient of atrial frequencies during acute atrial fibrillation in the isolated sheep heart. *Circulation* 103, 2631–2636. doi: 10.1161/01.cir.103.21.2631

Moe, G. K., and Abildskov, J. A. (1959). Atrial fibrillation as a self-sustaining arrhythmia independent of focal discharge. *Am. Heart J.* 58, 59–70. doi: 10.1016/0002-8703(59)90274-1

Moe, G. K., Rheinboldt, W. C., and Abildskov, J. A. A. (1964). Computer Model of Atrial Fibrillation. *Am. Heart J.* 67, 200–220.

Mohanty, S., Mohanty, P., Trivedi, C., Gianni, C., Della Rocca, D. G., Di Biase, L., et al. (2018). Long-Term Outcome of Pulmonary Vein Isolation With and Without Focal Impulse and Rotor Modulation Mapping: Insights From a Meta-Analysis. *Circ. Arrhythm. Electrophysiol.* 11:e005789. doi: 10.1161/CIRCEP.117.005789

Narayan, S. M., Baykaner, T., Clopton, P., Schricker, A., Lalani, G. G., Krummen, D. E., et al. (2014). Ablation of rotor and focal sources reduces late recurrence of atrial fibrillation compared with trigger ablation alone: extended follow-up of the CONFIRM trial (Conventional Ablation for Atrial Fibrillation With or Without Focal Impulse and Rotor Modulation). *J. Am. Coll. Cardiol.* 63, 1761–1768. doi: 10.1016/j.jacc.2014.02.543

Narayan, S. M., Krummen, D. E., Shivkumar, K., Clopton, P., Rappel, W. J., and Miller, J. M. (2012). Treatment of atrial fibrillation by the ablation of localized sources: CONFIRM (Conventional Ablation for Atrial Fibrillation With or Without Focal Impulse and Rotor Modulation) trial. *J. Am. Coll. Cardiol.* 60, 628–636. doi: 10.1016/j.jacc.2012.05.022

Narayan, S. M., and Zaman, J. A. (2016). Mechanistically based mapping of human cardiac fibrillation. *J. Physiol.* 594, 2399–2415. doi: 10.1113/JP270513

Nattel, S. (2002). New ideas about atrial fibrillation 50 years on. *Nature* 415, 219–226. doi: 10.1038/415219a

Nattel, S. (2003). Atrial electrophysiology and mechanisms of atrial fibrillation. *J. Cardiovasc. Pharmacol. Ther.* 8(Suppl. 1), S5–S11.

O'Neill, M. D., Jais, P., Takahashi, Y., Jonsson, A., Sacher, F., Hocini, M., et al. (2006). The stepwise ablation approach for chronic atrial fibrillation–evidence for a cumulative effect. *J. Interv. Card. Electrophysiol.* 16, 153–167. doi: 10.1007/s10840-006-9045-1

O'Neill, M. D., Wright, M., Knecht, S., Jaïs, P., Hocini, M., Takahashi, Y., et al. (2009). Long-term follow-up of persistent atrial fibrillation ablation using termination as a procedural endpoint. *Eur. Heart J.* 30, 1105–1112. doi: 10.1093/eurheartj/ehp063

Providencia, R., Lambiase, P. D., Srinivasan, N., Ganesh Babu, G., Bronis, K., Ahsan, S., et al. (2015). Is There Still a Role for Complex Fractionated Atrial Electrogram Ablation in Addition to Pulmonary Vein Isolation in Patients With Paroxysmal and Persistent Atrial Fibrillation? Meta-Analysis of 1415 Patients. *Circ. Arrhythm. Electrophysiol.* 8, 1017–1029. doi: 10.1161/CIRCEP.115.003019

Rodrigo, M., Guillem, M. S., Climent, A. M., Pedron-Torrecilla, J., Liberos, A., Millet, J., et al. (2014). Body surface localization of left and right atrial high-frequency rotors in atrial fibrillation patients: a clinical-computational study. *Heart Rhythm.* 11, 1584–1591. doi: 10.1016/j.hrthm.2014.05.013

Rostock, T., Salukhe, T. V., Steven, D., Drewitz, I., Hoffmann, B. A., Bock, K., et al. (2011). Long-term single- and multiple-procedure outcome and predictors of success after catheter ablation for persistent atrial fibrillation. *Heart Rhythm.* 8, 1391–1397. doi: 10.1016/j.hrthm.2011.04.012

Salinet, J., Schlindwein, F. S., Stafford, P., Almeida, T. P., Li, X., Vanheusden, F. J., et al. (2017). Propagation of meandering rotors surrounded by areas of high dominant frequency in persistent atrial fibrillation. *Heart Rhythm.* 14, 1269–1278. doi: 10.1016/j.hrthm.2017.04.031

Salinet, J. L. Jr., Madeiro, J. P., Cortez, P. C., Stafford, P. J., Ng, G. A., and Schlindwein, F. S. (2013). Analysis of QRS-T subtraction in unipolar atrial fibrillation electrograms. *Med. Biol. Eng. Comput.* 51, 1381–1391. doi: 10.1007/s11517-013-1071-4

Salinet, J. L., Tuan, J. H., Sandilands, A. J., Stafford, P. J., Schlindwein, F. S., and Ng, G. A. (2014). Distinctive patterns of dominant frequency trajectory behavior in drug-refractory persistent atrial fibrillation: preliminary characterization of spatiotemporal instability. *J. Cardiovasc. Electrophysiol.* 25, 371–379. doi: 10.1111/jce.12331

Sanders, P., Berenfeld, O., Hocini, M., Jais, P., Vaidyanathan, R., Hsu, L. F., et al. (2005). Spectral analysis identifies sites of high-frequency activity maintaining atrial fibrillation in humans. *Circulation* 112, 789–797.

Takahashi, Y., Sanders, P., Jais, P., Hocini, M., Dubois, R., Rotter, M., et al. (2006). Organization of frequency spectra of atrial fibrillation: relevance to radiofrequency catheter ablation. *J. Cardiovasc. Electrophysiol.* 17, 382–388. doi: 10.1111/j.1540-8167.2005.00414.x

Takashima, H., Kumagai, K., Matsumoto, N., Yasuda, T., Nakashima, H., Yamaguchi, Y., et al. (2010). Characteristics of the conduction of the left atrium in atrial fibrillation using non-contact mapping. *J. Cardiol.* 56, 166–175. doi: 10.1016/j.jjcc.2010.04.004

Tobon, C., Rodriguez, J. F., Ferrero, J. M. Jr., Hornero, F., and Saiz, J. (2012). Dominant frequency and organization index maps in a realistic three-dimensional computational model of atrial fibrillation. *Europace* 14(Suppl. 5), v25–v32. doi: 10.1093/europace/eus268

Tuan, J., Osman, F., Jeilan, M., Kundu, S., Mantravadi, R., Stafford, P. J., et al. (2010). Increase in organization index predicts atrial fibrillation termination with flecainide post-ablation: spectral analysis of intracardiac electrograms. *Europace* 12, 488–493. doi: 10.1093/europace/eup405

Umapathy, K., Nair, K., Masse, S., Krishnan, S., Rogers, J., Nash, M. P., et al. (2010). Phase mapping of cardiac fibrillation. *Circ. Arrhythm. Electrophysiol.* 3, 105–114.

Verma, A., Jiang, C. Y., Betts, T. R., Chen, J., Deisenhofer, I., Mantovan, R., et al. (2015). Approaches to catheter ablation for persistent atrial fibrillation. *New Engl. J. Med.* 372, 1812–1822.

Verma, A., Lakkireddy, D., Wulffhart, Z., Pillarisetti, J., Farina, D., Beardsall, M., et al. (2011). Relationship Between Complex Fractionated Electrograms (CFE) and Dominant Frequency (DF) Sites and Prospective Assessment of Adding DF-Guided Ablation to Pulmonary Vein Isolation in Persistent Atrial Fibrillation (AF). *J. Cardiovasc. Electr.* 22, 1309–1316. doi: 10.1111/j.1540-8167.2011.02128.x

Wilcox, R. R. (2012). *Introduction to robust estimation and hypothesis testing*, 3rd Edn. Amsterdam: Academic Press, 690.

Yamabe, H., Kanazawa, H., Ito, M., Kaneko, S., and Ogawa, H. (2016). Prevalence and mechanism of rotor activation identified during atrial fibrillation by noncontact mapping: Lack of evidence for a role in the maintenance of atrial fibrillation. *Heart Rhythm.* 13, 2323–2330. doi: 10.1016/j.hrthm.2016.07.030

Yamazaki, M., Mironov, S., Taravant, C., Brec, J., Vaquero, L. M., Bandaru, K., et al. (2012). Heterogeneous atrial wall thickness and stretch promote scroll waves anchoring during atrial fibrillation. *Cardiovasc. Res.* 94, 48–57. doi: 10.1093/cvr/cvr357

Yokoyama, E., Osaka, T., Takemoto, Y., Suzuki, T., Ito, A., Kamiya, K., et al. (2009). Paroxysmal atrial fibrillation maintained by nonpulmonary vein sources can be predicted by dominant frequency analysis of atriopulmonary electrograms. *J. Cardiovasc. Electrophysiol.* 20, 630–636. doi: 10.1111/j.1540-8167.2008.01376.x

Conflict of Interest: The authors declare that the research was conducted in the absence of any commercial or financial relationships that could be construed as a potential conflict of interest.

Publisher's Note: All claims expressed in this article are solely those of the authors and do not necessarily represent those of their affiliated organizations, or those of the publisher, the editors and the reviewers. Any product that may be evaluated in this article, or claim that may be made by its manufacturer, is not guaranteed or endorsed by the publisher.

frontiers in Physiology

ORIGINAL RESEARCH
published: 17 March 2022
doi: 10.3389/fphys.2022.846620

Anti-atrial Fibrillation Effects of Pulmonary Vein Isolation With or Without Ablation Gaps: A Computational Modeling Study

*Ze Jin, Inseok Hwang, Byounghyun Lim, Oh-Seok Kwon, Je-Wook Park, Hee-Tae Yu, Tae-Hoon Kim, Boyoung Joung, Moon-Hyoung Lee and Hui-Nam Pak**

Yonsei University College of Medicine, Yonsei University Health System, Seoul, South Korea

Background: Although pulmonary vein isolation (PVI) gaps contribute to recurrence after atrial fibrillation (AF) catheter ablation, the mechanism is unclear. We used realistic computational human AF modeling to explore the AF wave-dynamic changes of PVI with gaps (PVI-gaps).

Methods: We included 40 patients (80% male, 61.0 ± 9.8 years old, 92.5% persistent AF) who underwent AF catheter ablation to develop our realistic computational AF model. We compared the effects of a complete PVI (CPVI) and PVI-gap (2-mm × 4) on the AF wave-dynamics by evaluating the dominant frequency (DF), spatial change of DF, maximal slope of the action potential duration restitution curve (Smax), and AF defragmentation rate (termination or change to atrial tachycardia), and tested the effects of additional virtual interventions and flecainide on ongoing AF with PVI-gaps.

Results: Compared with the baseline AF, CPVIs significantly reduced extra-PV DFs ($p < 0.001$), but PVI-gaps did not. COV-DFs were greater after CPVIs than PVI-gaps ($p < 0.001$). Neither CPVIs nor PVI-gaps changed the mean Smax. CPVIs resulted in higher AF defragmentation rates (80%) than PVI-gaps (12.5%, $p < 0.001$). In ongoing AF after PVI-gaps, the AF defragmentation rates after a wave-breaking gap ablation, extra-PV DF ablation, or flecainide were 60.0, 34.3, and 25.7%, respectively ($p = 0.010$).

Conclusion: CPVIs effectively reduced the DF, increased its spatial heterogeneity in extra-PV areas, and offered better anti-AF effects than extra-PV DF ablation or additional flecainide in PVI-gap conditions.

Keywords: atrial fibrillation, computational modeling, pulmonary vein, gap, dominant frequency

OPEN ACCESS

Edited by:
Martin Bishop,
King's College London,
United Kingdom

Reviewed by:
Mohit Turagam,
Mount Sinai Hospital, United States
Jordi Heijman,
Maastricht University, Netherlands

***Correspondence:**
Hui-Nam Pak
hnpak@yuhs.ac

Specialty section:
This article was submitted to Computational Physiology and Medicine, a section of the journal Frontiers in Physiology

Received: *31 December 2021*
Accepted: *24 February 2022*
Published: *17 March 2022*

Citation:
Jin Z, Hwang I, Lim B, Kwon O-S, Park J-W, Yu H-T, Kim T-H, Joung B, Lee M-H and Pak H-N (2022) Anti-atrial Fibrillation Effects of Pulmonary Vein Isolation With or Without Ablation Gaps: A Computational Modeling Study. Front. Physiol. 13:846620. doi: 10.3389/fphys.2022.846620

INTRODUCTION

Catheter ablation is the most effective rhythm control method for atrial fibrillation (AF; Turagam et al., 2019). The cornerstone of AF catheter ablation (AFCA) is pulmonary vein isolation (PVI; Oral et al., 2006). However, even after AFCA with an adequate PVI, the AF recurrence rate is 40–50% within 5 years (Saguner et al., 2018). In patients with a post-AFCA recurrence

during a repeat procedure, the pulmonary vein (PV) reconnection rate, which is the leading cause of recurrence, reaches 37–95% (Lin et al., 2015). PV reconnections are due to the technical limitations of the PVI durability (Arujuna et al., 2012). On the other hand, extra-PV triggers are also an important AF mechanism in AF patients with significant atrial remodeling (Velagapudi et al., 2013). Because AF is a progressive, degenerative disease, an empirical extra-PV ablation has been attempted, especially in patients with persistent or long-standing AF (Haissaguerre et al., 2005). Nevertheless, there is no evidence that an empirical extra-PV linear, electrogram-guided, or rotor ablation has a rhythm outcome superior to a complete PVI (CPVI) alone for ablating persistent AF (Verma et al., 2015). Indeed, the mechanism by which a CPVI and additional extra-PV ablation provide equivalent rhythm control is unknown. Little is known about the optimal procedure for AF patients with recurrence and an incomplete PVI (Park et al., 2019).

Therefore, this study used realistic human AF computational modeling to explore how a CPVI affects the extra-PV AF wave-dynamics and how a PVI-gap affects the recurrence mechanism. Current AF computational modeling takes advantage of recent improvements in the computational power to precisely simulate human AF by applying a personalized anatomy, histology, and electrophysiology (Lim et al., 2020a). Various virtual interventions and virtual anti-arrhythmic drug tests have become possible using controlled *in silico* conditions (Shim et al., 2017; Kim et al., 2019). In this study, we hypothesized that a CPVI would affect the extra-PV AF wave-dynamics. In addition, we evaluated the effects of a PVI with-gaps on the AF maintenance and compared the interventions and drug challenges to find the optimal anti-AF outcomes.

MATERIALS AND METHODS

Ethical Approval

The study protocol followed the Declaration of Helsinki and was approved by the Institutional Review Board of Severance Cardiovascular Hospital, Yonsei University Health System. All participants were included in the Yonsei AF Ablation Cohort Database (ClinicalTrials.gov Identifier: NCT02138695) and provided written informed consent for us to use their cardiac CT images and clinical electrophysiological mapping data for computational modeling studies.

3D Computational Model of the Left Atrium

Figure 1 illustrates the protocol for the computational atrial modeling and AF simulations used in this study. We developed an ionic currents model according to the human atrial action potential model proposed by Courtemanche et al. (1998). For AF atrial ionic remodeling, the sodium current (I_{Na}), transient outward potassium current (I_{to}), L-type calcium current (I_{CaL}), and ultrarapid outward current (I_{Kur}) decreased by 10, 70, 50, and 50%, respectively, and the inwardly rectifying potassium current (I_{K1}) and Na^+/Ca^{2+} exchanger (I_{NCX}) increased by 100 and 40%, respectively (Lee et al., 2016). The surface of the left atrial (LA) 3D model was composed of triangular meshes containing 400,000–500,000 geometric elements, and the mean distance between adjacent elements was 235.1 ± 32.1 μm. Interpolated voltage data were generated from bipolar electrograms recorded from >500 points on the atrial surface using a circular mapping catheter and CT images (**Figure 1A**). Artifact caused by the patient's breathing was removed by trimming the ostial positions on the PVs and mitral valve. The coordinates of the electroanatomical map (NavX, Abbott, Inc., Chicago, IL, United States; CARTO System, Biosense Webster, Diamond Bar, CA, United States) were precisely aligned with the patients' clinical heart CT images, and then the registration between the electroanatomical maps and clinical CT data was completed. We used the inverse distance weighting method (Ugarte et al., 2015) to represent the interpolation of the electroanatomical map values during the simulation procedures. Our graphical user interface software (Model: SH01, CUVIA ver. 2.5; Laonmed Inc., Seoul, Korea) integrated the fibrosis formation and fiber orientation into the LA surface and enabled a virtual AF induction and AF wave-dynamic changes by using the dominant frequency (DF) and maximal slope of the action potential duration restitution curve (Smax; Lim et al., 2017). The fiber orientations were defined in the meshes of each patient's geometry and adjusted based on the clinical local activation time map (Pashakhanloo et al., 2016). Bipolar voltage data obtained from catheter ablation mapping were matched onto the computational nodes of the LA 3D model, and the locations of the fibrotic areas were determined using the map (**Figure 1B**). The fibrosis status of each node was numerically defined (Hwang et al., 2019). We simulated the clinical local activation data by using the model, which reflected the cardiac structural orientation and fiber orientation (**Figure 1C**). The conductivity of the model was based on the status and shape of the fibrosis (Zahid et al., 2016). For the ion currents of fibrotic cells, the inward rectifier potassium current (I_{K1}), L-type calcium current (I_{CaL}), and sodium current (I_{Na}) were decreased by 50, 50, and 40%, respectively, as compared to normal cells (Zahid et al., 2016). The reaction–diffusion equation for the cardiac wave propagation was solved numerically and adjusted based on the specific conduction velocity in each case to represent personalized AF simulations (Lee et al., 2016).

AF Simulation

Figure 1F shows the process used in the study protocol. We induced AF in each case using AF pacing from 200 to 120 ms with eight beats per cycle lasting a total of 11,520 ms, based on appropriate ion current settings. Each virtual pacing location corresponded to the clinical activation time map for a realistic LA modeling, and the pacing sites were matched precisely to reflect the personalized LA models. AF maintenance was observed for 32 s. We defined a successful AF induction according to the electrograms in each LA model. AF defragmentation involved AF termination and AF conversion to atrial tachycardia.

Virtual Interventions

We applied a virtual ablation and virtual anti-arrhythmia drug to our realistic AF model. For the virtual ablation, the

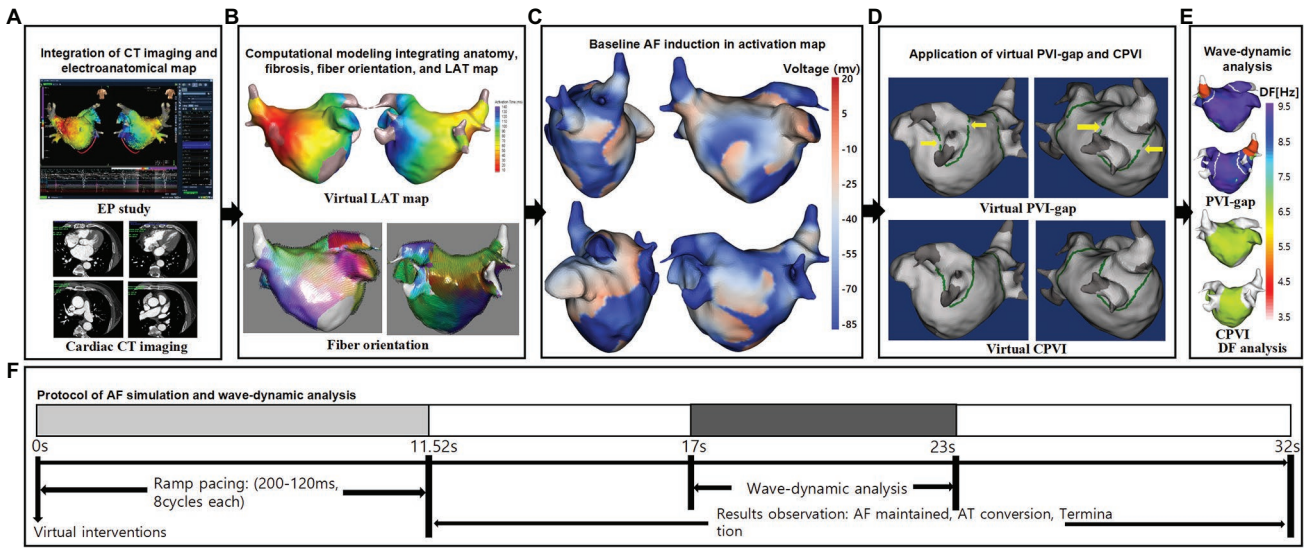

FIGURE 1 | Study protocol of the computational atrial modeling and AF simulation. **(A)** CT merged 3D-clinical electroanatomical map. **(B)** Clinical map integrated computational modeling. **(C)** Baseline AF induction in activation map. **(D)** Application of CPVI and PVI-gap. The yellow arrows indicate gaps in the PVI. **(E)** DF-based wave-dynamics analyses. **(F)** Study protocol. CT indicates computed tomography; EP, electrophysiology; LAT, local activation time; PVI-gap, pulmonary vein isolation with gap; CPVI, complete pulmonary vein isolation; DF, dominant frequency; AF, atrial fibrillation; AT, atrial tachycardia.

membrane potential of the ablated regions was set as zero to produce a permanent conduction block interrupting the cardiac wave propagation. First, we performed a virtual PV isolation with four gaps located on the anterior and posterior sides of each pulmonary vein isolation line (**Figure 1D**). Then we ablated all those gaps to perform a circumferential pulmonary vein isolation. The size of each gap was 2 mm. We initiated AF induction after performing each ablation. We applied high dose virtual flecainide (15 μm) to the failed AF defragmentation cases. With the Courtemanche-Ramirez-Nattel model (Courtemanche et al., 1998; Sossalla et al., 2010; Grandi et al., 2011) as the baseline, the effects of flecainide were implemented by applying the percent changes for the specific ion channels. Compared with baseline AF, the I_{to}, I_{CaL}, I_{Kr}, and I_{Na} were decreased by 5, 5, 30 and 45%, respectively (Wang et al., 1993; Hilliard et al., 2010; Kramer et al., 2013; Crumb et al., 2016; Geng et al., 2018; Sutanto et al., 2019).

Analysis of the Spatial Changes in the AF Wave-Dynamics

We analyzed the wave-dynamics of the DF and Smax from 17 to 23 s. The DF was defined as the frequency with the highest power. It was analyzed using a Fourier transform for 6 s of action potentials at each node and the power spectra density function (Lim et al., 2017). We calculated the DF values for all nodes in the 3D LA model (**Figure 1E**). To examine the stability of the DF after each intervention, the coefficient of variation (COV) of the high-DF was calculated as the standard deviation divided by the mean. The Smax values were defined at every node in the LA regions of each patient.

Statistical Analysis

The continuous variables are represented as the median and range. The proportion of categorical variables was compared among the groups using a Fisher's exact test. Comparisons of the DF, Smax, and COV-DF were conducted using t-testing or Mann–Whitney testing, depending on the distribution. A value of $p < 0.05$ was considered statistically significant. Statistical analyses were conducted using SPSS (Statistical Package for Social Sciences, Chicago, IL, United States) software for Windows (version 26.0).

RESULTS

Wave-Dynamic Changes After the PVI

We induced virtual AF in realistic computational models obtained from 40 patients (**Supplementary Table S1**). PV interventions (40 CPVI and 40 PVI-gap) significantly increased the mean AF cycle-lengths (140.9 ms [129.9, 153.3] to 147.1 ms [131.6, 200.3], $p = 0.045$), but they did not change the mean DF (7.69 Hz [7.31, 8.47] to 7.65 Hz [6.27, 8.30], $p = 0.150$) or Smax (0.97 [0.81, 1.26] to 0.88 [0.66, 1.13], $p = 0.144$). The AF termination and defragmentation rates after the PV interventions were 20 and 46.3%, respectively. Any episode terminated before 17 s was excluded from the AF cycle-length, DF, and Smax analyses.

Effects of the CPVI vs. PVI-Gaps on the Extra-PV Area

Table 1 compares the AF wave-dynamic changes between the CPVI and PVI-gap procedures. Compared with baseline AF, the CPVI significantly increased the mean AF cycle-lengths ($p < 0.001$), but the PVI-gap did not ($p = 0.581$). The

TABLE 1 | Wave-dynamic changes and defragmentation after virtual PV interventions.

	Baseline	PVI-gap	CPVI	*p* value
	(*n* = 40)	(*n* = 40)	(*n* = 40)	
Mean AFCL	140.87 [129.87,153.26]	138.89 [128.21,149.25]	212.77*,† [148.76,242.45]	<0.001
Mean DF (Hz)	7.690 [7.306,8.474]	8.061 [7.566,8.524]	5.760*,† [4.984,7.847]	<0.001
ΔMean DF	NA	0.171 [−0.099,0.441]	−1.482† [−3.184,−0.044]	NA
COV-DF (%)	NA	2.026 [1.190,4.555]	17.162† [1.849,34.705]	NA
Mean Smax	0.974 [0.805,1.259]	0.847 [0.643,1.047]	0.943 [0.707,1.304]	0.208
ΔMean Smax	NA	−0.154 [−0.350,−0.034]	−0.102 [−0.350,0.181]	NA
Defragmentation, % (*n*)	0%(0/40)	12.5%(5/40)	80.0%(32/40)*,†	<0.001
Termination, % (*n*)	0%(0/40)	7.5%(3/40)	32.5%(13/40)*,‡	<0.001
Converted to AT, % (*n*)	0%(0/40)	5.0%(2/40)	47.5%(19/40)*,†	<0.001

*Smax, The maximal slope of the restitution curves; DF, Dominant frequency; COV-DF, Coefficient of variation-dominant frequency; AFCL, Atrial fibrillation cycle lengths. The median (IQ1, IQ3) is displayed in the table. *p < 0.001 vs. Baseline. †p < 0.001 vs. PVI-gap. ‡p = 0.010 vs. PVI-gap.*

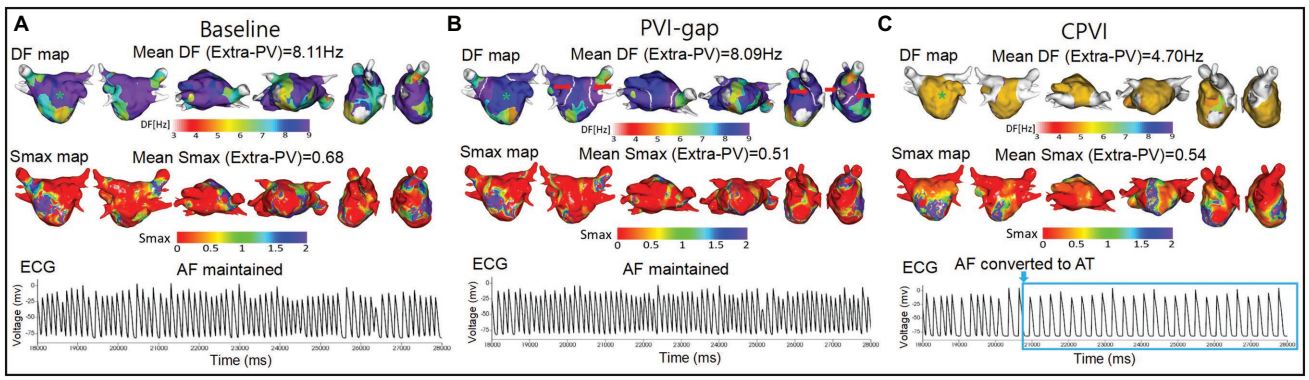

FIGURE 2 | Wave-dynamic changes after the virtual PVI-gap and CPVI. **(A)** The ECGs were obtained at the blue * sites in the DF maps. **(B)** The red arrows indicate gaps in the PVI. **(C)** The 3D DF maps and ECGs indicate that the CPVI reduced the mean DF, increased the AF cycle lengths, and defragmented the AF, but the PVI-gap did not. However, neither the CPVI nor PVI-gap changed the Smax. DF indicates dominant frequency; Smax, the maximal slope of the restitution curves; PVI-gap, pulmonary vein isolation with gaps; CPVI, complete pulmonary vein isolation; AF, atrial fibrillation; AT, atrial tachycardia; ECG, electrocardiogram.

CPVI also reduced the mean DF ($p < 0.001$), but the PVI-gap did not ($p = 0.354$, **Figure 2**). The amount of the DF reduction was significantly greater in the CPVI group than PVI-gap group ($p < 0.001$). The COV-DF, which reflected the spatial instability of the DF, was significantly greater in the CPVI group than PVI-gap group ($p < 0.001$). However, neither the CPVI ($p = 0.445$) nor PVI-gap ($p = 0.078$) changed the mean Smax (**Table 1**).

Defragmentation Rates After the CPVI vs. PVI-Gap and Flecainide

The AF defragmentation and termination rates after the PVI are listed in **Table 1**. There was no AF termination or defragmentation during the 32 s waiting period during the baseline AF. The AF termination rate after the CPVI was 32.5%, and it was 7.5% after the PVI-gap ($p = 0.010$). The AF defragmentation rates were also higher in the CPVI group (80.0%) than PVI-gap group (5%, $p < 0.001$). This finding was consistent after changing the location and number of PVI-gaps (**Supplementary Table S2**).

We added virtual flecainide to the failed defragmented episodes after the CPVI ($n = 8$) and PVI-gap ($n = 35$). The post-flecainide termination rate in the group after the CPVI (25.0%) tended to be higher than that in the PVI-gap group without statistical significance (2.9%, $p = 0.084$, **Table 2**).

Mechanism of the AF Maintenance After the PVI-Gap

We evaluated the PV and extra-PV wave-dynamic interactions in 35 ongoing AF episodes after the PVI-gap

TABLE 2 | Flecainide-induced defragmentation rates of ongoing AF after the CPVI vs. PVI-gap.

	PVI-gap	CPVI	*p* value
	(*n* = 35)	(*n* = 8)	
Defragmentation, % (*n*)	25.7%(9/35)	62.5%(5/8)	0.089
Termination, % (*n*)	2.9%(1/35)	25.0%(2/8)	0.084
Converted to AT, % (*n*)	22.9%(8/35)	37.5%(3/8)	0.401

PVI-gap, Pulmonary vein isolation with gap; CPVI, Complete pulmonary vein isolation; AT, Atrial tachycardia.

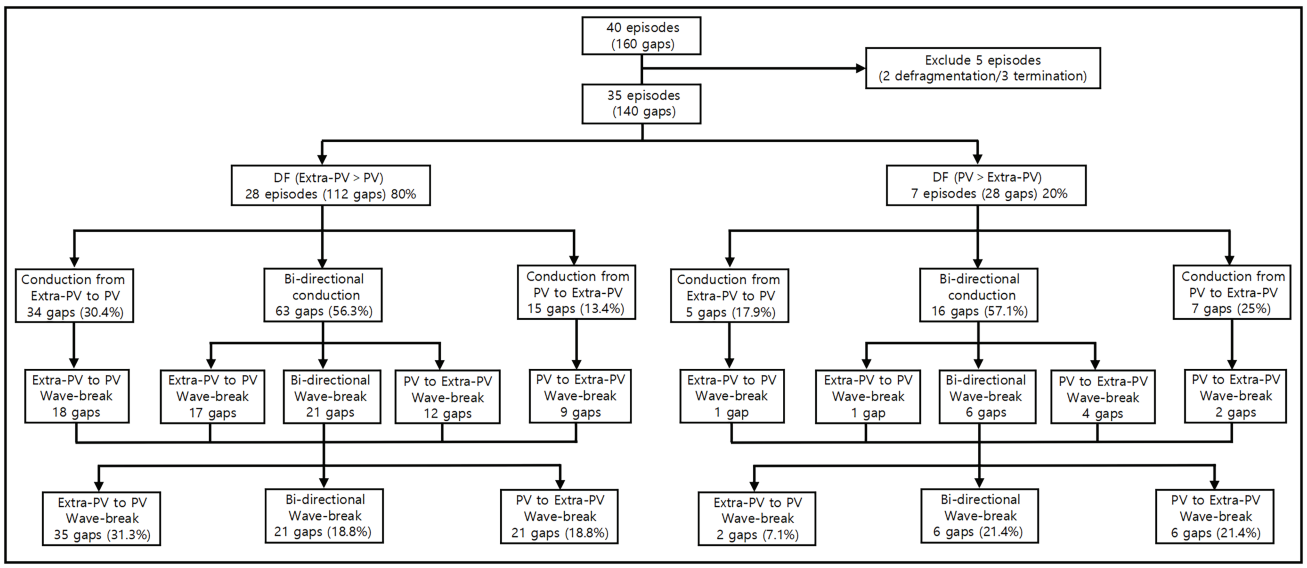

FIGURE 3 | Wave-dynamic interactions between the PVs and extra-PVs in 35 ongoing AF episodes after the PVI-gap intervention. DF indicates dominant frequency; PV, pulmonary vein.

intervention (**Figure 3**). The extra-PV DF was greater than the PV-DF in 28 of those episodes (80%), and the inside PV-DF was greater than the extra-PV DF in 7 episodes (20%). The wavelet interactions were maintained through the PVI-gaps for as long as the AF was maintained. The wave-breaks generally appeared at the wavelet exit of the gaps by a source-sink mismatch (**Figure 4**). The rate of a wave-break did not differ between the episodes in which the wavelet moved from the higher DF site to the lower DF site and that in which it moved from the lower DF site to the higher DF site (48.8% vs. 50%, $p = 1.000$).

Among the 35 episodes of ongoing AF after the PVI-gap, filling the wave-breaking PVI-gaps (total 91 gaps), ablation of the highest DF site without touching the PVI-gaps (112 extra-PV and 51 intra-PV sites), and additional virtual flecainide defragmented the AF in 60.0, 34.3, and 25.7% of cases, respectively ($p = 0.010$, **Figure 5**). The AF termination rate was significantly greater after filling the PVI-gaps than after ablating the highest DF or administering flecainide ($p = 0.010$, **Table 3**).

DISCUSSION

Main Findings

In this study, we used realistic human AF computational modeling to explore how a CPVI affected the extra-PV wave-dynamics and PVI-gaps as a mechanism for AF recurrence. The CPVI significantly reduced the mean extra-PV DF and its spatial stability (increased COV-DF), but it had no effect on the Smax, an index of wave-breakability. In the episodes of ongoing AF after the PVI-gap, wave-breaks commonly occurred at the wavelet exit of the gaps. Additional ablation of wave-breaking PVI-gaps had a greater defragmentation effect than extra-PV DF ablation or virtual flecainide. Therefore, the CPVI effectively reduced the mean DF in the extra-PV area, and under the PVI-gap condition, filling the PVI-gaps had anti-AF effects superior to those of an extra-PV DF ablation or additional flecainide.

Extra-PV Effects of the CPVI

The CPVI has traditionally been the cornerstone of AFCA (Oral et al., 2006), and it has several potential anti-AF

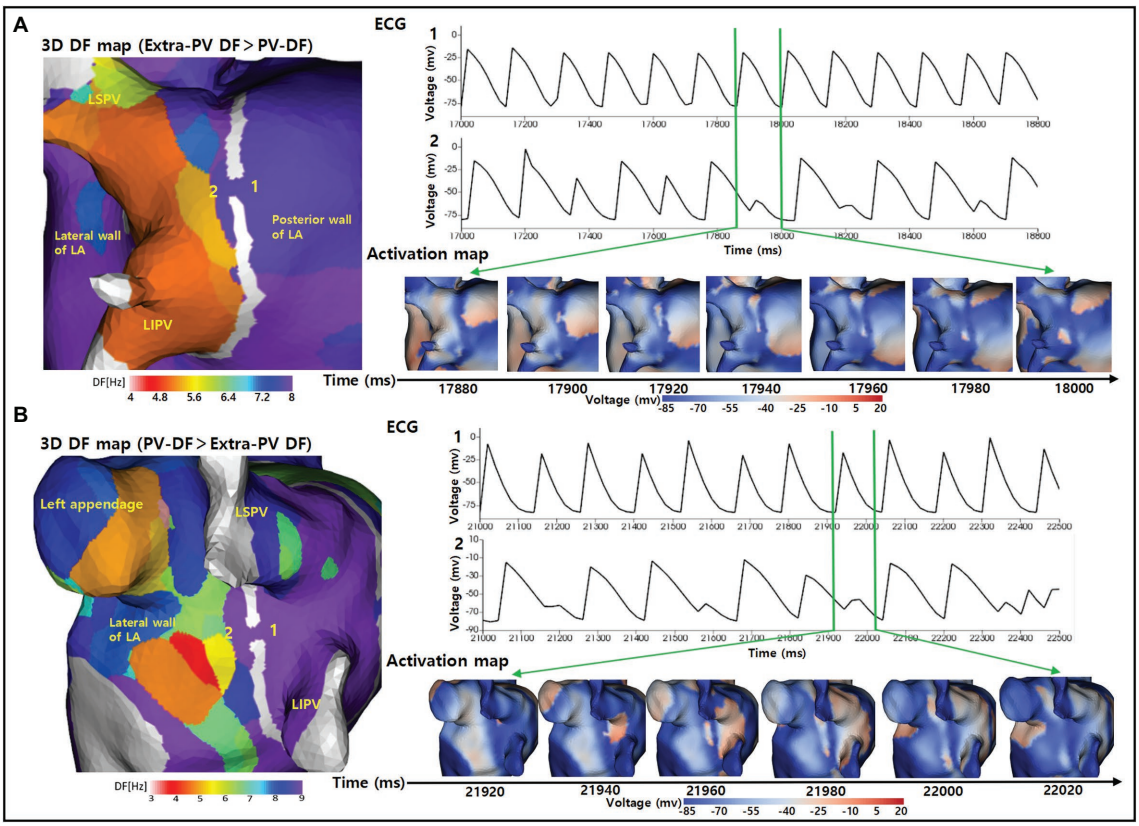

FIGURE 4 | Wave-break at the wavelet exit of the gaps by a source-sink mismatch. **(A)** The 3D DF map indicates that the extra-PV DFs was greater than the PV-DFs. The activation map and ECG indicate that a regular wavelet turned into a wave-break when moving from the posterior wall of the LA to inside the PV through the gap. **(B)** The 3D DF map indicates that the inside PV-DF was greater than the extra-PV DF. The activation map and ECG indicate that a regular wavelet turned into a wave-break when moving from inside the PV to the lateral wall of the LA through the gap. DF indicates dominant frequency; PV, pulmonary vein; LA, left atrium; LSPV, left superior pulmonary vein; LIPV, left inferior pulmonary vein; ECG, Electrocardiogram.

mechanisms. First, the CPVI blocks the PV triggers (Oral et al., 2006). Second, the CPVI partially denervates cardiac autonomic nerves, including the ganglionated plexi around the PV antrum (Po et al., 2009). Third, a wide CPVI significantly reduces the atrial critical mass (Hwang et al., 2012). We have here identified another novel mechanism by which the CPVI significantly reduces the mean DF and spatial heterogeneity of the DF at extra-PV sites. Among the 40 patients who were included in this study, 93% had persistent AF, and we integrated their voltage-activation maps into our realistic computational models. We found that the CPVI still plays an important role in the extra-PV AF maintenance mechanism, even in AF patients with atrial substrate remodeling. To date, no empirical extra-PV LA ablation, including linear, electrogram-guided, or rotor ablation, has shown equivalent rhythm outcomes in patients with a CPVI, despite multiple randomized clinical trials (Verma et al., 2015). Our results reconfirm the importance of a CPVI in the LA, even though extra-PV areas, including the right atrium, contribute to the maintenance mechanisms of AF (Lim et al., 2020b).

Role of PV-Gaps as a Mechanism of Recurrence After a PVI

Irrespective of the uncertain unifying mechanisms of AF, a PV electrical isolation is an objective, standard, and widely accepted minimal requirement for AFCA (Calkins et al., 2012). However, despite advances in the catheter efficiency, a long-term durable PVI still has technical limitations. The rate of PV reconnections during a repeat ablation has been reported to range from 36% to more than 95% in repeat procedures (Lin et al., 2015). Many studies have reported that PV reconnections are the leading cause of arrhythmia recurrences. However, PV reconnections have also been observed in patients without AF recurrence (Nilsson et al., 2006). In this study, we evaluated how PV gaps affected the AF maintenance mechanisms. Of the four 2-mm PV gaps that remained in our model, 65% (91/140) were accompanied by wave-breaks and 19.3% (27/140) contributed to wave-breaks in the PV to LA direction. The PV gap size also had an essential influence on the AF maintenance. Following Herweg's report, we applied 2-mm gaps, which were suitable for generating wave-breaks by a source-sink mismatch (Herweg et al., 2021).

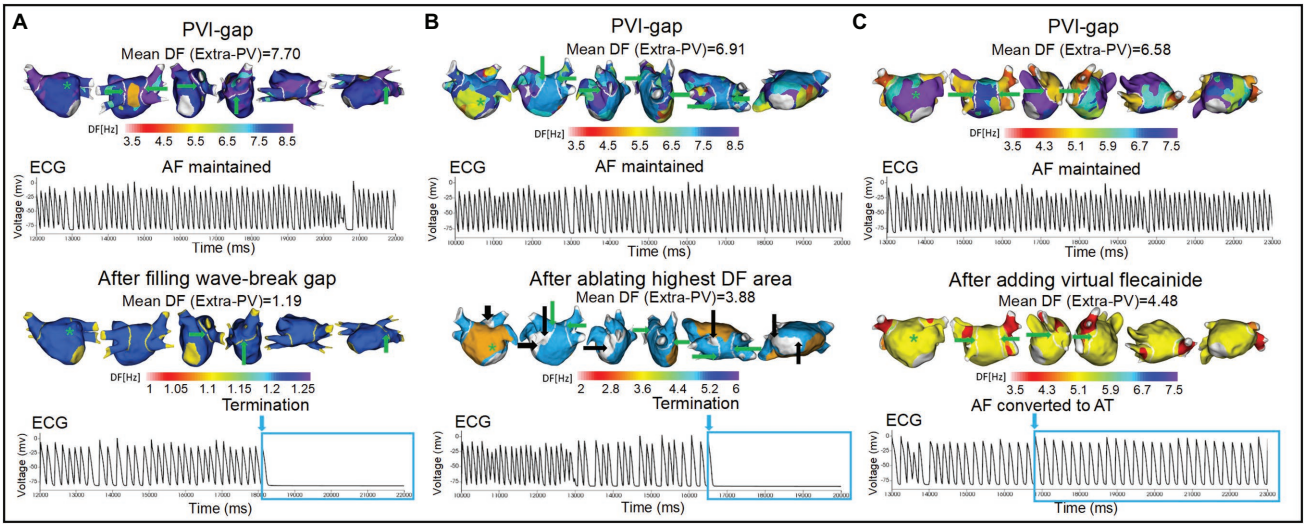

FIGURE 5 | Wave-dynamic changes after filling the wave-breaking PVI-gaps, ablating the highest DF sites, and adding virtual flecainide. ECGs were obtained at the green * sites in the DF map, and the green arrows indicate the gaps in the PVI. **(A)** AF terminated after ablating the two gaps on the posterior wall of the LA. **(B)** AF terminated after ablating the high DF site (white areas indicated by black arrows). **(C)** AF converted to AT after adding virtual flecainide without additional ablation. PVI-gap indicates pulmonary vein isolation with gaps; PV, pulmonary vein; DF, dominant frequency; AF, atrial fibrillation; AT, atrial tachycardia; ECG, Electrocardiogram.

TABLE 3 | Defragmentation rates after interventions for 35 AF PVI-gap episodes.

	Wave-break gap ablation	Highest DF sites ablation	Add virtual flecainide	*P* value
	(*n* = 35)	(*n* = 35)	(*n* = 35)	
AF Defragmentation, % (*n*)	60.0%(21/35)*	34.3%(12/35)	25.7%(9/35)	0.010
AF termination, % (*n*)	25.7%(9/35)†	8.6%(3/35)	2.9%(1/35)	0.010
AF converted to AT, % (*n*)	34.3%(12/35)	25.7%(9/35)	22.9%(8/35)	0.538

*AF, Atrial fibrillation; DF, Dominant frequency; AT, Atrial tachycardia. *p = 0.007 vs. Add virtual flecainide. †p = 0.013 vs. Add virtual flecainide.*

Appropriate Management of Recurrent AF After AFCA

The most effective repeat procedures for patients with recurrence after AFCA is not yet known. Depending on the recurrent AF burden or the operators' discretion, gap fillings for the reconnected PVs or an empirical extra-PV ablation, such as a posterior wall isolation, have been performed (Lee et al., 2019). In patients with a well-maintained PVI during redo-mapping, extra-PV triggers play a significant role in AF recurrence, and the outcomes of a repeat ablation are worse than in patients with PV reconnections (Kim et al., 2021). In this study, we examined the AF maintenance mechanism during the PVI-gap state by using computational models made with the electroanatomical maps of 40 patients, most of whom had persistent AF. Under those controlled conditions, filling the wave-breaking gap produced a more effective AF defragmentation than ablation of the extra-PV DF sites or using antiarrhythmic drugs. That was consistent with the results of a recent randomized clinical trial, suggesting that a durable PVI is more effective than an empirical extra-PV ablation as a repeat AF ablation procedure (Kim et al., 2022).

Limitations

This study had some limitations in its computational simulations. First, bi-atrial modeling manifesting interatrial conduction was not applied in this study. Second, we did not consider the LA wall thickness in our LA model. Third, because we applied fibrosis based on voltage-map, not a magnetic resonance image (Boyle et al., 2019; Baek et al., 2021), it is not clear whether the detailed structure of cardiac fibrosis with microchannels is adequately reflected in our morel. Fourth, our personalized LA model consisted of a monolayer, not bilayers representing the endocardial and epicardial layers. Fifth, the rate-dependent effect of flecainide on I_{Na} may not be reflected sufficiently in this study (Moreno et al., 2011).

Conclusion

The CPVI effectively reduced the mean DF and increased its spatial heterogeneity in the extra-PV areas. Filling the PVI-gaps

had anti-AF effects superior to those of an extra-PV DF ablation or additional flecainide under the PVI-gap condition.

DATA AVAILABILITY STATEMENT

The original contributions presented in the study are included in the article/**Supplementary Material**, further inquiries can be directed to the corresponding author.

ETHICS STATEMENT

The studies involving human participants were reviewed and approved by Institutional Review Board of Severance Cardiovascular Hospital, Yonsei University Health System. The patients/participants provided their written informed consent to participate in this study.

AUTHOR CONTRIBUTIONS

ZJ contributed to the data, statistical analyses, and writing of the manuscript. IH contributed to the statistical analyses and data acquisition. O-SK contributed to the software programming and data acquisition. BL confirmed the data acquisition and references. J-WP contributed the clinical data acquisition. H-TY, T-HK, BJ, and M-HL contributed to the clinical data acquisition and interpretation of clinical data. H-NP contributed to the study design, clinical data acquisition, data interpretation, and revision of manuscript. All authors contributed to the article and approved the submitted version.

FUNDING

This work was supported by grants (HI19C0114) and (H21C0011) from the Ministry of Health and Welfare and grants (NRF-2020R1A2B01001695) and (NRF-2019R1C1C1009075) from the Basic Science Research Program run by the National Research Foundation of Korea (NRF), which is funded by the Ministry of Science, ICT, and Future Planning (MSIP).

ACKNOWLEDGMENTS

We would like to thank Mr. John Martin for his linguistic assistance.

SUPPLEMENTARY MATERIAL

The Supplementary Material for this article can be found online at: https://www.frontiersin.org/articles/10.3389/fphys.2022.846620/full#supplementary-material

REFERENCES

Arujuna, A., Karim, R., Caulfield, D., Knowles, B., Rhode, K., Schaeffter, T., et al. (2012). Acute pulmonary vein isolation is achieved by a combination of reversible and irreversible atrial injury after catheter ablation: evidence from magnetic resonance imaging. *Circ. Arrhythm. Electrophysiol.* 5, 691–700. doi: 10.1161/CIRCEP.111.966523

Baek, Y. S., Kwon, O. S., Lim, B., Yang, S. Y., Park, J. W., Yu, H. T., et al. (2021). Clinical outcomes of computational virtual mapping-guided catheter ablation in patients With persistent atrial fibrillation: A multicenter prospective randomized clinical trial. *Front. Cardiovasc. Med.* 8:772665. doi: 10.3389/fcvm.2021.772665

Boyle, P. M., Zghaib, T., Zahid, S., Ali, R. L., Deng, D., Franceschi, W. H., et al. (2019). Computationally guided personalized targeted ablation of persistent atrial fibrillation. *Nat. Biomed. Eng.* 3, 870–879. doi: 10.1038/s41551-019-0437-9

Calkins, H., Kuck, K. H., Cappato, R., Brugada, J., Camm, A. J., Chen, S. A., et al. (2012). 2012 HRS/EHRA/ECAS expert consensus statement on catheter and surgical ablation of atrial fibrillation: recommendations for patient selection, procedural techniques, patient management and follow-up, definitions, endpoints, and research trial design. *J. Interv. Card. Electrophysiol.* 33, 171–257. doi: 10.1007/s10840-012-9672-7

Courtemanche, M., Ramirez, R. J., and Nattel, S. (1998). Ionic mechanisms underlying human atrial action potential properties: insights from a mathematical model. *Am. J. Phys.* 275, H301–H321. doi: 10.1152/ajpheart.1998.275.1.H301

Crumb, W. J. Jr., Vicente, J., Johannesen, L., and Strauss, D. G. (2016). An evaluation of 30 clinical drugs against the comprehensive in vitro proarrhythmia assay (CiPA) proposed ion channel panel. *J. Pharmacol. Toxicol. Methods* 81, 251–262. doi: 10.1016/j.vascn.2016.03.009

Geng, L., Kong, C. W., Wong, A. O. T., Shum, A. M., Chow, M. Z. Y., Che, H., et al. (2018). Probing flecainide block of INa using human pluripotent stem cell-derived ventricular cardiomyocytes adapted to automated patch-clamping and 2D monolayers. *Toxicol. Lett.* 294, 61–72. doi: 10.1016/j.toxlet.2018.05.006

Grandi, E., Pandit, S. V., Voigt, N., Workman, A. J., Dobrev, D., Jalife, J., et al. (2011). Human atrial action potential and Ca2+ model: sinus rhythm and chronic atrial fibrillation. *Circ. Res.* 109, 1055–1066. doi: 10.1161/CIRCRESAHA.111.253955

Haissaguerre, M., Hocini, M., Sanders, P., Sacher, F., Rotter, M., Takahashi, Y., et al. (2005). Catheter ablation of long-lasting persistent atrial fibrillation: clinical outcome and mechanisms of subsequent arrhythmias. *J. Cardiovasc. Electrophysiol.* 16, 1138–1147. doi: 10.1111/j.1540-8167.2005.00308.x

Herweg, B., Nellaiyappan, M., Welter-Frost, A. M., Tran, T., Mabry, G., Weston, K., et al. (2021). Immuno-electrophysiological mechanisms of functional electrical connections Between recipient and donor heart in patients With Orthotopic heart transplantation presenting With atrial arrhythmias. *Circ. Arrhythm. Electrophysiol.* 14:e008751. doi: 10.1161/CIRCEP.120.008751

Hilliard, F. A., Steele, D. S., Laver, D., Yang, Z., Le Marchand, S. J., Chopra, N., et al. (2010). Flecainide inhibits arrhythmogenic Ca2+ waves by open state block of ryanodine receptor Ca2+ release channels and reduction of Ca2+ spark mass. *J. Mol. Cell. Cardiol.* 48, 293–301. doi: 10.1016/j.yjmcc.2009.10.005

Hwang, M., Kim, J., Lim, B., Song, J. S., Joung, B., Shim, E. B., et al. (2019). Multiple factors influence the morphology of the bipolar electrogram: an in silico modeling study. *PLoS Comput. Biol.* 15:e1006765. doi: 10.1371/journal.pcbi.1006765

Hwang, E. S., Nam, G. B., Joung, B., Park, J., Lee, J. S., Shim, J., et al. (2012). Significant reduction of atrial defibrillation threshold and inducibility by catheter ablation of atrial fibrillation. *Pacing Clin. Electrophysiol.* 35, 1428–1435. doi: 10.1111/j.1540-8159.2012.03517.x

Kim, D., Shim, J., Kim, Y. G., Yu, H. T., Kim, T. H., Uhm, J. S., et al. (2021). Malnutrition and risk of procedural complications in patients With atrial fibrillation undergoing catheter ablation. *Front. Cardiovasc. Med.* 8:736042. doi: 10.3389/fcvm.2021.736042

Kim, D., Yu, H. T., Kim, T.-H., Uhm, J.-S., Joung, B., Lee, M.-H., et al. (2022). Electrical posterior box isolation in repeat ablation for atrial fibrillation: a

prospective randomized clinical study. *J. Am. Coll. Cardiol. Clin. Electrophysiol.* doi: 10.1016/j.jacep.2022.01.003 (in press).

Kim, I. S., Lim, B., Shim, J., Hwang, M., Yu, H. T., Kim, T. H., et al. (2019). Clinical usefulness of computational modeling-guided persistent atrial fibrillation ablation: updated outcome of multicenter randomized study. *Front. Physiol.* 10:1512. doi: 10.3389/fphys.2019.01512

Kramer, J., Obejero-Paz, C. A., Myatt, G., Kuryshev, Y. A., Bruening-Wright, A., Verducci, J. S., et al. (2013). MICE models: superior to the HERG model in predicting torsade de pointes. *Sci. Rep.* 3:2100. doi: 10.1038/srep02100

Lee, Y. S., Hwang, M., Song, J. S., Li, C., Joung, B., Sobie, E. A., et al. (2016). The contribution of ionic currents to rate-dependent action potential duration and pattern of reentry in a mathematical model of human atrial fibrillation. *PLoS One* 11:e0150779. doi: 10.1371/journal.pone.0150779

Lee, J. M., Shim, J., Park, J., Yu, H. T., Kim, T. H., Park, J. K., et al. (2019). The electrical isolation of the left atrial Posterior Wall in catheter ablation of persistent atrial fibrillation. *JACC Clin. Elect.* 5, 1253–1261. doi: 10.1016/j.jacep.2019.08.021

Lim, B., Hwang, M., Song, J. S., Ryu, A. J., Joung, B., Shim, E. B., et al. (2017). Effectiveness of atrial fibrillation rotor ablation is dependent on conduction velocity: An in-silico 3-dimensional modeling study. *PLoS One* 12:e0190398. doi: 10.1371/journal.pone.0190398

Lim, B., Kim, J., Hwang, M., Song, J. S., Lee, J. K., Yu, H. T., et al. (2020a). In situ procedure for high-efficiency computational modeling of atrial fibrillation reflecting personal anatomy, fiber orientation, fibrosis, and electrophysiology. *Sci. Rep.* 10:2417. doi: 10.1038/s41598-020-59372-x

Lim, B., Park, J. W., Hwang, M., Ryu, A. J., Kim, I. S., Yu, H. T., et al. (2020b). Electrophysiological significance of the interatrial conduction including cavo-tricuspid isthmus during atrial fibrillation. *J. Physiol.* 598, 3597–3612. doi: 10.1113/JP279660

Lin, D., Santangeli, P., Zado, E. S., Bala, R., Hutchinson, M. D., Riley, M. P., et al. (2015). Electrophysiologic findings and long-term outcomes in patients undergoing third or more catheter ablation procedures for atrial fibrillation. *J. Cardiovasc. Electrophysiol.* 26, 371–377. doi: 10.1111/jce.12603

Moreno, J. D., Zhu, Z. I., Yang, P. C., Bankston, J. R., Jeng, M. T., Kang, C., et al. (2011). A computational model to predict the effects of class I anti-arrhythmic drugs on ventricular rhythms. *Sci. Transl. Med.* 3:98ra83. doi: 10.1126/scitranslmed.3002588

Nilsson, B., Chen, X., Pehrson, S., Kober, L., Hilden, J., and Svendsen, J. H. (2006). Recurrence of pulmonary vein conduction and atrial fibrillation after pulmonary vein isolation for atrial fibrillation: a randomized trial of the ostial versus the extraostial ablation strategy. *Am. Heart J.* 152, 537.e1–537.e8. doi: 10.1016/j.ahj.2006.05.029

Oral, H., Pappone, C., Chugh, A., Good, E., Bogun, F., Pelosi, F. Jr., et al. (2006). Circumferential pulmonary-vein ablation for chronic atrial fibrillation. *N. Engl. J. Med.* 354, 934–941. doi: 10.1056/NEJMoa050955

Park, J. W., Yang, P. S., Bae, H. J., Yang, S. Y., Yu, H. T., Kim, T. H., et al. (2019). Five-year change in the renal function After catheter ablation of atrial fibrillation. *J. Am. Heart Assoc.* 8:e013204. doi: 10.1161/JAHA.119.013204

Pashakhanloo, F., Herzka, D. A., Ashikaga, H., Mori, S., Gai, N., Bluemke, D. A., et al. (2016). Myofiber architecture of the human atria as revealed by submillimeter diffusion tensor imaging. *Circ. Arrhythm. Electrophysiol.* 9:e004133. doi: 10.1161/CIRCEP.116.004133

Po, S. S., Nakagawa, H., and Jackman, W. M. (2009). Localization of left atrial ganglionated plexi in patients with atrial fibrillation. *J. Cardiovasc. Electrophysiol.* 20, 1186–1189. doi: 10.1111/j.1540-8167.2009.01515.x

Saguner, A. M., Maurer, T., Wissner, E., Santoro, F., Lemes, C., Mathew, S., et al. (2018). Catheter ablation of atrial fibrillation in very young adults: a 5-year follow-up study. *Europace* 20, 58–64. doi: 10.1093/europace/euw378

Shim, J., Hwang, M., Song, J. S., Lim, B., Kim, T. H., Joung, B., et al. (2017). Virtual in-Silico modeling guided catheter ablation predicts effective linear ablation lesion set for longstanding persistent atrial fibrillation: multicenter prospective randomized study. *Front. Physiol.* 8:792. doi: 10.3389/fphys.2017.00792

Sossalla, S., Kallmeyer, B., Wagner, S., Mazur, M., Maurer, U., Toischer, K., et al. (2010). Altered Na(+) currents in atrial fibrillation effects of ranolazine on arrhythmias and contractility in human atrial myocardium. *J. Am. Coll. Cardiol.* 55, 2330–2342. doi: 10.1016/j.jacc.2009.12.055

Sutanto, H., Laudy, L., Clerx, M., Dobrev, D., Crijns, H., and Heijman, J. (2019). Maastricht antiarrhythmic drug evaluator (MANTA): a computational tool for better understanding of antiarrhythmic drugs. *Pharmacol. Res.* 148:104444. doi: 10.1016/j.phrs.2019.104444

Turagam, M. K., Garg, J., Whang, W., Sartori, S., Koruth, J. S., Miller, M. A., et al. (2019). Catheter ablation of atrial fibrillation in patients With heart failure: a meta-analysis of randomized controlled trials. *Ann. Intern. Med.* 170, 41–50. doi: 10.7326/M18-0992

Ugarte, J. P., Tobon, C., Orozco-Duque, A., Becerra, M. A., and Bustamante, J. (2015). Effect of the electrograms density in detecting and ablating the tip of the rotor during chronic atrial fibrillation: an in silico study. *Europace* 17(Suppl. 2), ii97–ii104. doi: 10.1093/europace/euv244

Velagapudi, P., Turagam, M. K., Leal, M. A., and Kocheril, A. G. (2013). Atrial fibrosis: a risk stratifier for atrial fibrillation. *Expert. Rev. Cardiovasc. Ther.* 11, 155–160. doi: 10.1586/erc.12.174

Verma, A., Jiang, C. Y., Betts, T. R., Chen, J., Deisenhofer, I., Mantovan, R., et al. (2015). Approaches to catheter ablation for persistent atrial fibrillation. *N. Engl. J. Med.* 372, 1812–1822. doi: 10.1056/NEJMoa1408288

Wang, Z., Fermini, B., and Nattel, S. (1993). Mechanism of flecainide's rate-dependent actions on action potential duration in canine atrial tissue. *J. Pharmacol. Exp. Ther.* 267, 575–581

Zahid, S., Cochet, H., Boyle, P. M., Schwarz, E. L., Whyte, K. N., Vigmond, E. J., et al. (2016). Patient-derived models link re-entrant driver localization in atrial fibrillation to fibrosis spatial pattern. *Cardiovasc. Res.* 110, 443–454. doi: 10.1093/cvr/cvw073

Conflict of Interest: The authors declare that the research was conducted in the absence of any commercial or financial relationships that could be construed as a potential conflict of interest.

Publisher's Note: All claims expressed in this article are solely those of the authors and do not necessarily represent those of their affiliated organizations, or those of the publisher, the editors and the reviewers. Any product that may be evaluated in this article, or claim that may be made by its manufacturer, is not guaranteed or endorsed by the publisher.

frontiers in Physiology

ORIGINAL RESEARCH
published: 22 March 2022
doi: 10.3389/fphys.2022.850951

Generalizable Beat-by-Beat Arrhythmia Detection by Using Weakly Supervised Deep Learning

Yang Liu[1], Qince Li[1,2], Runnan He[2], Kuanquan Wang[1], Jun Liu[1], Yongfeng Yuan[1], Yong Xia[1] and Henggui Zhang[2,3,4]**

[1]School of Computer Science and Technology, Harbin Institute of Technology (HIT), Harbin, China, [2]Peng Cheng Laboratory, Shenzhen, China, [3]School of Physics and Astronomy, The University of Manchester, Manchester, United Kingdom, [4]Key Laboratory of Medical Electrophysiology of Ministry of Education and Medical Electrophysiological Key Laboratory of Sichuan Province, Institute of Cardiovascular Research, Southwest Medical University, Luzhou, China

Beat-by-beat arrhythmia detection in ambulatory electrocardiogram (ECG) monitoring is critical for the evaluation and prognosis of cardiac arrhythmias, however, it is a highly professional demanding and time-consuming task. Current methods for automatic beat-by-beat arrhythmia detection suffer from poor generalization ability due to the lack of large-sample and finely-annotated (labels are given to each beat) ECG data for model training. In this work, we propose a weakly supervised deep learning framework for arrhythmia detection (WSDL-AD), which permits training a fine-grained (beat-by-beat) arrhythmia detector with the use of large amounts of coarsely annotated ECG data (labels are given to each recording) to improve the generalization ability. In this framework, heartbeat classification and recording classification are integrated into a deep neural network for end-to-end training with only recording labels. Several techniques, including knowledge-based features, masked aggregation, and supervised pre-training, are proposed to improve the accuracy and stability of the heartbeat classification under weak supervision. The developed WSDL-AD model is trained for the detection of ventricular ectopic beats (VEB) and supraventricular ectopic beats (SVEB) on five large-sample and coarsely-annotated datasets and the model performance is evaluated on three independent benchmarks according to the recommendations from the Association for the Advancement of Medical Instrumentation (AAMI). The experimental results show that our method improves the F_1 score of supraventricular ectopic beats detection by 8%–290% and the F1 of ventricular ectopic beats detection by 4%–11% on the benchmarks compared with the state-of-the-art methods of supervised learning. It demonstrates that the WSDL-AD framework can leverage the abundant coarsely-labeled data to achieve a better generalization ability than previous methods while retaining fine detection granularity. Therefore, this framework has a great potential to be used in clinical and telehealth applications. The source code is available at https://github.com/sdnjly/WSDL-AD.

Keywords: cardiac arrhythmia, electrocardiogram, heartbeat classification, weakly supervised learning, generalization ability

OPEN ACCESS

Edited by:
Xin Li,
University of Leicester, United Kingdom

Reviewed by:
Mingfeng Jiang,
Zhejiang Sci-Tech University, China
Mehmet Akif Ozdemir,
Izmir Kâtip Çelebi University, Turkey

****Correspondence:***
Qince Li
qinceli@hit.edu.cn
Henggui Zhang
henggui.zhang@manchester.ac.uk

Specialty section:
This article was submitted to Cardiac Electrophysiology, a section of the journal Frontiers in Physiology

Received: *08 January 2022*
Accepted: *07 March 2022*
Published: *22 March 2022*

Citation:
Liu Y, Li Q, He R, Wang K, Liu J, Yuan Y, Xia Y and Zhang H (2022) Generalizable Beat-by-Beat Arrhythmia Detection by Using Weakly Supervised Deep Learning. Front. Physiol. 13:850951. doi: 10.3389/fphys.2022.850951

1 INTRODUCTION

Cardiac arrhythmia has become one of the leading causes of morbidity and mortality worldwide (Roger et al., 2012). Ambulatory electrocardiogram (ECG) monitoring with prolonged duration (several days or weeks) provides critical information for early detection and treatment of arrhythmias, especially for transient and asymptomatic arrhythmias (Sana et al., 2020). The ambulatory ECG devices have been sufficiently miniaturized, wearable and connected to high-speed mobile networks with the promise to give patients high-quality yet affordable health monitoring services at home. To enable the adoption of remote ECG monitoring services in the general population, reliable automatic ECG analysis and diagnosis technology is necessary as analyzing the vast amount of monitoring data is far beyond the capability of human physicians. Although the technologies for automatic ECG analysis have been developed for decades, current technologies cannot replace human physicians for diagnosis because they have limited generalization ability to cope with the diverse artifacts and inter-patient variations in the ECG signals (Alday et al., 2020; Siontis et al., 2021). Therefore, novel technologies for generalizable detection of arrhythmias are in urgent demand.

Beat-by-beat arrhythmia detection, determining the rhythm type of each heartbeat in an ECG recording, is essential for the analysis of ambulatory ECG. According to the ANSI/AAMI EC57:2012 standard (AAMI, 2012), a beat-by-beat arrhythmia detection software should discriminate five types of heartbeats: ventricular ectopic beat (VEB or V), supraventricular ectopic beat (SVEB or S), ventricular fusion beat (F), ambiguous beat (Q), and beat of all other types (N). In particular, the detection performances of SVEB and VEB are of major interest to health care practitioners and constitute the evaluation metrics for the detectors as recommended by the ANSI/AAMI standard. An accurate beat-by-beat arrhythmia detector has several important implications for clinical practices. The detected beat-wise rhythm types manifest the occurrence time of each arrhythmia episode which is necessary evidence to correlate the detected arrhythmias with the symptoms recorded by the patients. Besides, the detected types of each heartbeat in the recording can be used to measure the burdens (i.e., the proportions in all heartbeats) of VEB and SVEB which are important indicators in evaluating cardiac function (Baman et al., 2010), assessing the effectiveness of treatments (Deyell et al., 2012), and predicting the risk of malignant diseases, such as stroke, heart failure and sudden death (Binici, 2010; Marcus, 2020). Furthermore, the fine-grained beat-wise rhythm types can be further used to identify some complex patterns of arrhythmias, such as ventricular/supraventricular tachycardia, bigeminy, and trigeminy.

The state-of-the-art methods for beat-by-beat arrhythmia detection are generally based on machine learning (ML), a methodology to guide the models to learn detection rules from a training dataset. Typically, the ECG signal is segmented into individual heartbeats, each of which is then fed into a classifier to determine its rhythm type, as shown in **Figure 1A**. The classifier is usually trained in a supervised learning methodology, where each training beat is annotated with a corresponding rhythm type. According to the split of training and test sets, the classifiers can be further categorized into two types: intra-patient classifier, of which the training and test data are from the same group of patients (Kiranyaz et al., 2016; Li et al., 2018; Degirmenci et al., 2021), and inter-patient classifier, of which the training and test data are from non-overlapping patient populations (Raj and Ray, 2018; Guo et al., 2019; Niu et al., 2020). The intra-patient classifiers are suitable to develop personalized arrhythmia

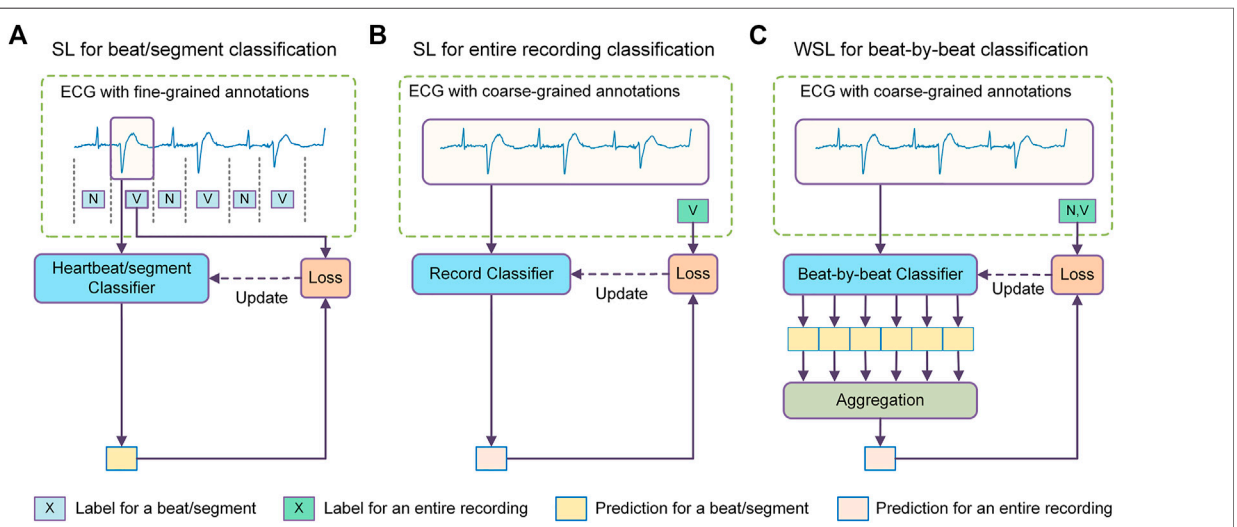

FIGURE 1 | Comparison between different methodologies of machine learning for arrhythmia detection. **(A)** The supervised learning (SL) method for heartbeat/segment classification which uses fine-grained annotations for model training and achieves fine-grained predictions. **(B)** The SL method for ECG recording classification which uses coarse-grained labels as supervision and achieves coarse-grained predictions. **(C)** The weakly supervised learning (WSL) method for beat-by-beat classification which uses coarse recording labels for model training but achieves fine-grained predictions. N = normal or bundle branch block beat. SVEB = supraventricular ectopic beat. VEB = ventricular ectopic beat.

detectors, while the inter-patient classifiers aim to provide diagnostic models for general populations. Intra-patient classifiers usually perform much better than inter-patient classifiers because they have been fine-tuned for the target population. This in turn suggests that it is more challenging to develop models with good generalization abilities to deal with data from unseen patients. In real-world medical settings, the ECGs are obtained from large, diverse populations, which makes the classifier's generalization ability of critical importance.

A key reason for the poor generalization ability of current methods is that the training data come from a small population. For example, the MIT-BIH Arrhythmia Database, a dataset used by dozens of studies for classifier training, contains only 48 ECG recordings collected from 47 subjects (Moody and Mark, 2001). Since the training data only reflect the characteristics of a few people, it is naturally difficult for the model learner to learn the discrimination features applicable to data from general population. For example, it has been demonstrated that patients with COVID-19 exhibit obvious ECG changes, based on which an automatic diagnostic model for COVID-19 has been developed and achieved a quite high accuracy and F1 score (both ≥93.0%) (Ozdemir et al., 2021). These COVID-19-related ECG changes represent a new class of conditions that may not be considered by previous arrhythmia detectors and may affect the generalization ability of those detectors. Besides, the models tend to over-fit the small amount of training data and thus impair their generalization ability. The small sample sizes of the training datasets are partly because of the high cost of the beat-by-beat annotation work. In order to ensure the correctness of the labels, independent labeling by multiple experts is often required and the disputed samples should resort to an expert committee for adjudication. Another challenge of machine learning for arrhythmia detection is class imbalance, where samples of normal sinus rhythm tend to predominate in the datasets. Some strategies have been proposed to address this problem. For example, Lu *et al.* utilized focal loss to address the class imbalance in ECG classification (Lu et al., 2021).

In view of the limitation of annotated training data, some researchers have explored new methods to improve the generalization ability of ECG classifiers, such as unsupervised learning and semi-supervised learning. The unsupervised learning methods have been developed to mine unlabeled ECG data for representative learning (Rajan and Thiagarajan, 2018), domain adaptation (Li et al., 2021; Wang et al., 2021), and data augmentation (Golany and Radinsky, 2019; Wulan et al., 2020). Some semi-supervised learning methods that use both labeled and unlabeled data for model training have also been developed to fine-tune the classifier for the target patient without the need for patient-specific labeled data (Zhai et al., 2020). Although these methods contribute to the improvement of generalization ability, the limited labeled data still plays a very central role in the training of these models and induce a high risk of overfitting.

This study explores the possibility of another learning approach, i.e., weakly supervised learning (WSL), to improve the generalization ability of beat-by-beat arrhythmia detectors. Unlike previous methods that utilize unlabeled samples or synthesize new samples, the WSL approach tries to train a model with incomplete, inexact, or inaccurate annotations that are usually much easier to obtain (Zhou, 2018). In the domain of ECG classification, there are a large amount of ECG data annotated with coarse-grained labels, i.e., a recording (typically several to tens of seconds) is labeled as a whole (Liu et al., 2018; Alday et al., 2020). Since the rhythm types of individual heartbeats in these datasets are not annotated, these datasets are mainly used to train recording classifiers that determine if certain anomalies are present in an ECG recording, as shown in **Figure 1B**, in previous studies. Nevertheless, the recording labels indicate the rhythm types of an unknown subset of heartbeats in the recording, which can provide a form of weak supervision for the model training. In addition, as these datasets reflect diverse signal artifacts and inter-patient variations, they may help prevent overfitting and improve the generalization ability of the heartbeat classifiers.

Several issues need to be addressed for applying WSL to beat-by-beat arrhythmia detection. Firstly, what is the mapping relationship between the target labels of individual heartbeats and the labels of their recording? For this study, the recording labels in datasets such as the PhysioNet/CinC Challenge 2020 datasets clearly reflect the presence of SVEB or VEB in the recordings, which is critical to a successful application of WSL. Secondly, how to construct a beat-by-beat classifier that can be trained under the supervision of recording labels? As the true heartbeat labels are not available, a mechanism is needed to guide the optimization of the heartbeat classifier based on the true recording labels and the mapping relationships between heartbeat labels and recording labels. Finally, how to address the ill-posed problem that the constraints of recording labels can be satisfied by different hypotheses of the heartbeat rhythms? The ill-posed problem usually arises when two types of samples always occur concomitantly (Choe et al., 2020). For example, SVEBs and sinus beats usually occur alternately and have similar waveforms, which may confuse the classifier in discriminating these two kinds of beats since swapping their categories can also map to the same recording labels. Therefore, the ill-posed problem must be addressed to ensure the stability of the heartbeat classifier.

In this study, we propose a deep-learning-based WSL framework for beat-by-beat arrhythmia detection (WSDL-AD), as shown in **Figure 1C**, which can be trained with just coarse record-level labels in an end-to-end manner. In this framework, the model first makes local predictions for each heartbeat, and then maps the heartbeat predictions to the prediction of the recording labels by an aggregation mechanism. The model can be optimized by gradient descent, where the gradients of the recording predictions are back-propagated through the aggregation layer to calculate the gradients of the heartbeat predictions. Thus, the heartbeat classifier can be optimized according to the coarse recording labels. To address the ill-posed problem, we design a two-stage training strategy: a supervised pre-training stage with small amounts of heartbeat labels, and a weakly-supervised training stage with large amounts of recording labels. In addition, we introduce some techniques into the WSDL-AD framework to enhance the model performance. 1) To assist the model in utilizing contextual

TABLE 1 | The mapping between the dataset labels and the classes suggested by the ANSI/AAMI standard. The dataset labels are in the parentheses following their corresponding class names.

ANSI/AAMI	SNOMED CT codes	PhysioBank labels
N	All labels except that mapped to SVEB, VEB	Normal beat (N) Left bundle branch block beat (L) Right bundle branch block beat (R) Atrial escape beat (e) Nodal (junctional) escape beat (j)
SVEB	Premature atrial contraction (284470004) Supraventricular premature beats (63593006)	Atrial premature beat (A) Aberrated atrial premature beat (a) Nodal (junctional) premature beat (J) Supraventricular premature or ectopic beat (S)
VEB	Premature ventricular contractions (427172004) Ventricular premature beats (17338001) Ventricular ectopic beats (164884008)	Premature ventricular contraction (V) Ventricular escape beat (E)

TABLE 2 | The compositions of the datasets.

Datasets	Recording numbers	Recording lengths	Sampling rate (Hz)	Annotations			Annotation unit
				N	VEB	SVEB	
CPSC	6,877	6–144 s	500	5,564	700	616	record
CPSC-Extra	3,453	8–98 s	500	3,150	194	124	record
PTB-XL	21,837	10 s	500	20,194	1,154	555	record
G12EC	10,334	5–10 s	500	9,336	395	640	record
Chapman-Shaoxing-Ningbo	45,152	10 s	500	42,536	1,385	1,321	record
MITBIH-AR-DS1	22	30 min	360	45,869	3,789	945	beat
MITBIH-AR-DS2	22	30 min	360	44,264	3,221	1837	beat
MITBIH-SUP	78	30 min	128	162,368	9,950	12,207	beat
INCART	75	30 min	257	153,673	20,012	1960	beat

CPSC, the China physiological signal challenge; PTB-XL, the Physikalisch Technische Bundesanstalt extension dataset; G12EC, the Georgia 12-lead ECG challenge dataset; MITBIH-AR-DS1, the DS1 of MIT-BIH arrhythmia database; MITBIH-AR-DS2, the DS2 of MIT-BIH arrhythmia database; MITBIH-SUP, the MIT-BIH supraventricular arrhythmia database; INCART, the St. Petersburg INCART arrhythmia database; N, normal or bundle branch block beat; SVEB, supraventricular ectopic beat; VEB, ventricular ectopic beat.

information, two knowledge-based features, namely relative RR interval and RR entropy, are proposed. 2) Considering the heartbeats vary in length and are unevenly distributed over time, we propose a masked aggregation mechanism that can select a representative prediction for each heartbeat for aggregation without the need to split the ECG signal into heartbeat segments.

The remainder of this paper is organized as follows. In **section 2**, the proposed WSDL-AD framework and the datasets for model training and evaluation are described in detail. The experimental setup and results are present in **section 3**. **Section 4** compares our results with that of other studies and discusses the implications and limitations of this work. Finally, we conclude this work in **section 5**.

2 MATERIALS AND METHODS

2.1 Datasets

We use multiple coarsely annotated and finely-annotated datasets in this study. The coarsely-annotated datasets are from the PhysioNet/CinC challenge 2020/2021 (Alday et al., 2020; Reyna et al., 2021), including two China physiological signal challenge datasets (CPSC and CPSC-Extra) (Liu et al., 2018), the Physikalisch Technische Bundesanstalt extension (PTB-XL) dataset (Wagner et al., 2020), the Georgia 12-lead ECG challenge dataset (G12EC), and the Chapman University, Shaoxing People's Hospital and Ningbo First Hospital database (Chapman-Shaoxing-Ningbo) (Zheng et al., 2020). There are a total of 87,653 12-lead ECG records in these datasets. Each record was annotated as a whole using the SNOMED CT codes (Donnelly, 2006). The ANSI/AAMI standard recommends five classes for the arrhythmia detector, namely VEB, SVEB, F, Q, and N (AAMI, 2012). In addition, as recommended by the standard, a detector is neither penalized nor rewarded for its treatment of F and Q. Therefore, in this work, we only deal with the classification of VEB, SVEB, and N. The data of F and Q are excluded from the evaluation. The mapping between the original labels and the ANSI/AAMI classes is available in **Table 1**. Statistics of the datasets are shown in **Table 2**.

The finely annotated datasets used in this study include the MIT-BIH arrhythmia database (MITBIH-AR) (Moody and Mark, 2001), the MIT-BIH supraventricular arrhythmia

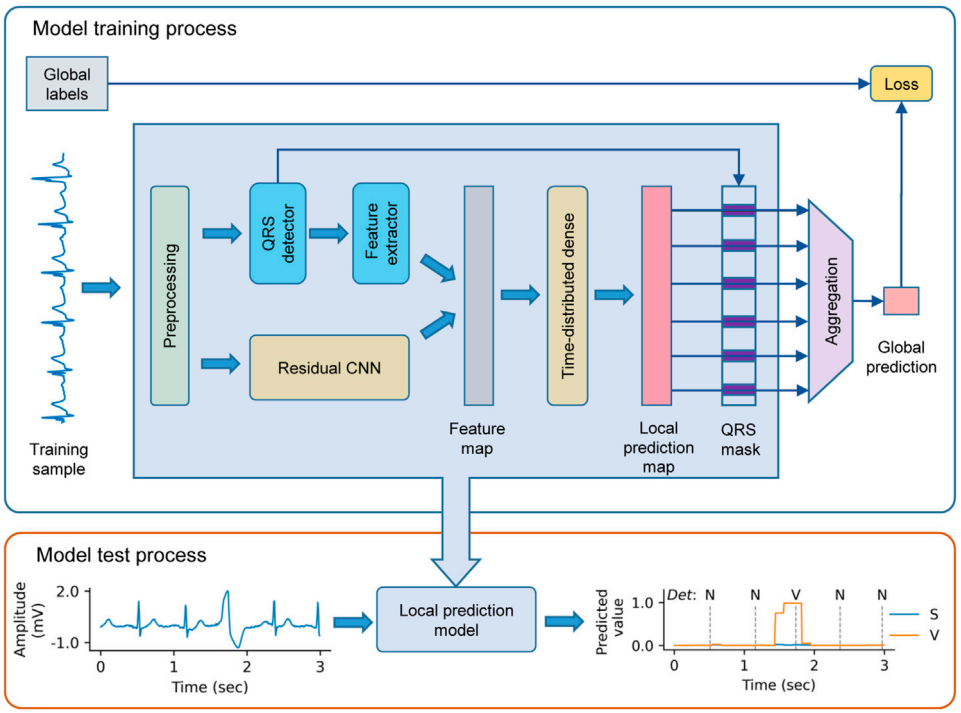

FIGURE 2 | The schematic diagram of the weakly supervised deep learning framework for arrhythmia detection (WSDL-AD). CNN = convolutional neural network. N = normal or bundle branch block beat. S = supraventricular ectopic beat. V = ventricular ectopic beat.

database (MITBIH-SUP) (Greenwald et al., 1990), and the St. Petersburg INCART arrhythmia database (INCART) (Goldberger et al., 2000). The MITBIH-AR dataset is further divided into two subsets as in (De Chazal et al., 2004), namely MITBIH-AR-DS1[1] (or DS1) and MITBIH-AR-DS2[2] (or DS2), which contain ECG records from non-overlapping patient groups and have similar category distributions. This division is widely used in previous studies (Mar et al., 2011; Raj and Ray, 2018; Niu et al., 2020), where the models are trained on DS1, and tested on DS2. For comparison purposes, we also adopt this division in this study. All these datasets contain two-lead ECG signals with physician-reviewed beat-by-beat annotations in the PhysioBank labels, which can be mapped to the AAMI classes as in **Table 1**. The compositions of the datasets are shown in **Table 2**.

In this study, the signal in the lead II of each recording is used for beat-by-beat arrhythmia detection. For recordings in MITBIH-AR, the modified lead II (MLII) is used instead. If the lead configurations are unavailable, such as in MITBIH-SUP, the signal in the first lead is used.

[1]MITBIH-AR-DS1 comprises recordings 101, 106, 108, 109, 112, 114, 115, 116, 118, 119, 122, 124, 201, 203, 205, 207, 208, 209, 215, 220, 223, and 230.

[2]MITBIH-AR-DS2 comprises recordings 100, 103, 105, 111, 113, 117, 121, 123, 200, 202, 210, 212, 213, 214, 219, 221, 222, 228, 231, 232, 233, and 234.

2.2 Overview of the WSDL-AD Framework

We propose the WSDL-AD framework for beat-by-beat arrhythmia detection, as shown in **Figure 2**. The framework is input with an ECG signal of variable length. The input signal is first preprocessed to unify the signal configurations (such as sampling rate and amplitude) and eliminate noise. Then, feature maps are extracted from the signal by a residual convolutional neural network (ResNet) and domain-knowledge-based methods respectively. Based on the features, the framework makes local predictions in the granularity of a sampling point. Then the predicted rhythm for each heartbeat is obtained by selecting the prediction at its R peak. Finally, the beat-level predictions are aggregated into the global prediction, whereby the loss value for the prediction can be calculated according to the global annotations to enable the model to be trained end-to-end.

2.3 Preprocessing

The preprocessing is mainly aimed to eliminate the noise and unify the sampling rate and amplitude of the ECG signals. Each ECG recording is first processed by a moving average filter (the window size is one second) to estimate the baseline wander which mainly originated from the offset and low-frequency noises in the signal. The estimated baseline wander is then removed by subtracting it from the signal. The signal is also processed by a band-pass filter (0.1–30 Hz) to suppress noises in other bands. In addition, we resample the signal to 125 Hz and normalize the signal to have mean zero and variance one. Among these datasets, the MITBIH-SUP has a frequency (128 Hz) very similar to our target frequency, so signals

of this dataset are not resampled. But the frequencies of other datasets are all much higher than the target frequency, so signals in these datasets are downsampled to 125 Hz.

For the coarsely-annotated training data, a tricky situation is that if a recording contains both sinus and arrhythmia episodes, its annotation usually does not include the label for sinus rhythm. To address this problem, we complement the labels based on the rules of co-occurrence of different rhythms. Specifically, if the label set of a recording contains SVEB or VEB, and contains neither supraventricular tachyarrhythmia nor idioventricular rhythm, it is very likely that beats of N are also present in the recording. So, in this case, we add the label N to the label set of the recording for complementing.

2.4 Knowledge-Based Features

Contextual information, e.g., the variation of RR intervals, is essential for the detection of many arrhythmias. In order to facilitate the utilization of contextual information in arrhythmia detection, we design two context-relative features based on domain knowledge. The extraction of the two features requires the positions of QRS complexes, which are usually not directly available, and need to be detected by some algorithms. In this study, the QRS complexes are detected by a U-net-based model that has been proposed in a previous study (He et al., 2020).

2.4.1 Relative RR Interval

The change of current RR interval relative to the contextual normal sinus RR intervals supplies important information for the detection of many arrhythmias including SVEB and VEB. So, we design a feature, named relative RR interval, to represent this information: $I_R = (I_N - I_A)/I_N \cdot s$, where I_R is the relative RR interval, I_A is the absolute RR interval, I_N is the representative normal RR interval in the context, and s is a scaling parameter. Here, we use the mean RR interval of the context to approximate I_N for simplicity of calculation: $I_N \approx mean(\mathbb{I})$, where $\mathbb{I}$ is the set of RR intervals in the context. Note that I_R is negatively related with I_A. I_R is positive when $I_A < I_N$, while I_R is negative when $I_A > I_N$. Due to the wide adoption of rectified linear unit (ReLU), many DNN models are more sensitive to positive values. Therefore, our design can induce the DNN to be more sensitive to the shortening of RR interval which is an important indicator of ectopic heartbeats. Besides, I_R is normalized by I_N in the formula to better reflect the degree of relative changes.

In selecting the length of the context for estimating I_N, a trade-off should be considered between the accuracy and robustness: the longer the context is, the more robust the mean RR interval is to local disturbances, but the less accurately it reflects a temporal fluctuation of the sinus RR interval. In this work, we set the context length to 60 RR intervals with the current RR interval at the middle of the context. And when the number of RR intervals in a recording is less than 60, all the RR intervals are used as the context. The scaling parameter, s, is used to increase the feature's contribution in the prediction since the raw value is usually small and easy to be ignored by the classifier. In our implementation, s is set to 10.

The relative RR intervals of a recording are organized in a feature map, which has the same length as the ECG. In this way, the feature map can be easily combined with the DNN-extracted feature maps, and used in the local predictions. The feature map is organized as follows: the points in the region of a heartbeat are assigned the feature value of the corresponding heartbeat. Here, we define the region of a heartbeat as the portion between the midpoint of its preceding RR interval and the midpoint of its succeeding RR interval.

2.4.2 RR Entropy

The regularity and stationarity of the RR intervals in the context also provide important diagnostic information. We measure this information by another feature, named RR entropy. The RR entropy is calculated by the sample entropy (SampEn) method (Richman and Moorman, 2000). SampEn is the negative natural logarithm of the empirical probability that two templates (i.e., segments) of length m+1 from the input sequence match each other given that their sub-templates containing the corresponding first m sampling points match. In our implementation, m is set to 1, and the threshold to determine whether two templates match is set to 0.05. Before the entropy calculation, the RR intervals are divided by their median value for normalization. Since the entropy can fluctuate with time, we calculate its values dynamically in a sliding window. Similar to the selection of the context length for estimating normal RR interval, the selection of window size for entropy calculation should also take into account the balance between accuracy and robustness. The window size is set also to 60 RR intervals in our implementation. And the method for window selection is the same as that for specifying the context in normal RR interval estimation. The calculated RR entropies are also organized in a feature map, where the result of each moving window calculation is mapped to the region of the central heartbeat (typically the 30th heartbeat) of the window. Any sampling point that is not mapped in the above process is assigned the value of its neatest mapped neighbor.

To assess the discriminative abilities of the features, we randomly sample 2,700 heartbeats from the MITBIH-AR-DS1 (900 for each category), and apply one-way ANOVA test on their feature values grouped by categories. The results show that the values of both features are significantly different ($p < 0.0001$) among these categories. We also perform multiple pairwise comparisons on the feature values, and the results are given in **Figure 3**. We found that the feature values are significantly different ($p < 0.0001$) between each pair of categories. Therefore, these knowledge-based features have certain discernibility for categories and will contribute to the classification task.

2.5 DNN-Based Feature Extraction and Local Prediction

The ResNet is used to automatically extract features from the ECG. It consists of a stack of residual convolutional blocks (Res blocks) as shown in **Figure 4**. Each Res block contains two convolutional (Conv) layers and some assistant layers,

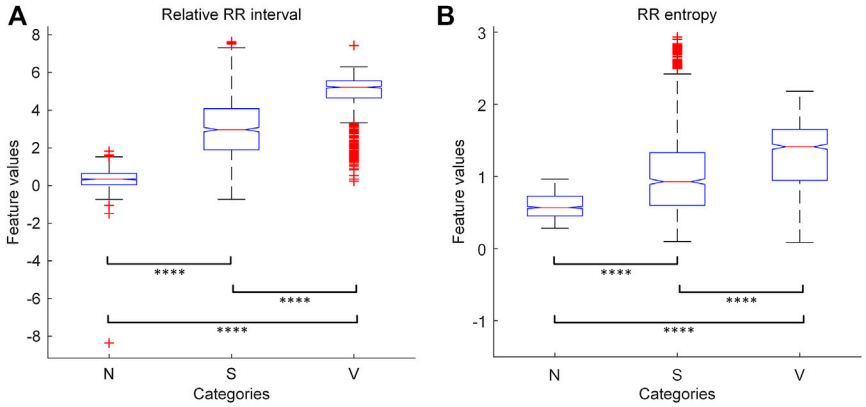

FIGURE 3 | The results of one-way ANOVA with multiple pairwise comparison for the knowledge-based features. **(A)** The results for relative RR interval. **(B)** The results for RR entropy. The symbol "****" indicates that the corresponding two groups are significantly ($p < 0.0001$) different from each other in features values. N = normal or bundle branch block beat. S = supraventricular ectopic beat. V = ventricular ectopic beat.

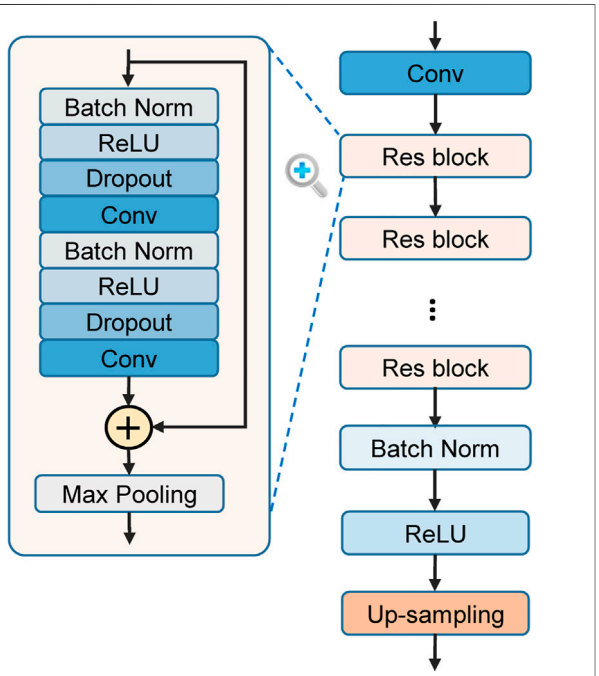

FIGURE 4 | The structure of residual convolutional network (ResNet) for feature learning. Res block = residual block. Conv = convolutional layer. Batch Norm = batch normalization. ReLU = rectified linear unit.

including batch normalization (BN) (Ioffe and Szegedy, 2015), rectified linear unit (ReLU) (Nair and Hinton, 2010), and Dropout (Srivastava et al., 2014). The output of a block's last convolutional layer is merged with the block's input by element-wise addition, as suggested by the original ResNet (He et al., 2016). A max-pooling layer with a pool size of two then compresses the merged output to half of its original length. The blocks are connected in series, with the output of the previous one serving as the input of the latter. The outputs of the last block are a series of feature maps characterizing each temporal slice of the input recording. To align with the knowledge-based features, these DNN-extracted feature maps are up-sampled along the time dimension to the same length of the input. Then, these feature maps are concatenated with the feature maps of knowledge-based features along the feature dimension, and jointly used for the local prediction. This architecture contains several hyperparameters which may affect the model performance. We optimize the hyperparameters by grid search: different choices of residual blocks number (3, 4, 5, and 6), convolutional kernel number (16, 32, and 64), convolutional kernel length (8, 16, and 32), and dropout rate (0, 0.25, and 0.5) are tested to find the combination that achieves the best performance on the validation set (MITBIH-AR-DS1). After the hyperparameters optimization, the ResNet consists of 4 Res blocks. In each Res block, each convolutional layer contains 32 kernels with a kernel length of 8. The parameters of each convolutional layer are initialized by the method proposed in (He et al., 2015), which takes the ReLU into account and allows for very deep models. The dropout rate of each dropout layer is 0.25.

Based on the feature map merged from DNN features and knowledge-based features, the local predictions are made by a time distributed dense (TDD) layer, which leverages a dense layer (i.e., fully-connected layer) to process each temporal element separately. The cell number of the TDD layer is equal to the number of considered rhythm types. The output of the TDD layer at each temporal element is then processed by the softmax function to calculate probability of each considered rhythm occurring at the slice.

2.6 Aggregation for Global Prediction

The aggregation mechanism, mapping the local predictions to the global prediction, is a critical part in the WSDL-AD framework. Here, we introduce the method of applying the traditional aggregation mechanisms to this framework, and also propose the masked aggregation mechanism.

2.6.1 Traditional Aggregation Methods

A series of aggregation methods have been proposed in previous studies for computer vision, including global average pooling (GAP) (Zhou et al., 2016), global maximum pooling (GMP) (Pathak et al., 2014), and Log-Sum-Exp (LSE) (Pinheiro and Collobert, 2015). Here, we formalize these methods for application to the mapping between the local predictions and the global prediction. GAP averages all local predictions to obtain the global prediction: $GAP(\hat{Y})_c = \frac{1}{n}\sum_{i=1}^{n}\hat{y}_{i,c}$, where $\hat{Y}$ is the collection of local predictions, $\hat{y}_{i,c}$ is the prediction for rhythm c at the ith sampling point. We argue that GAP is not suitable for use in the WSDL-AD framework, because some arrhythmias, e.g., ectopic beats, may account for only a very small fraction of a recording, and the predictions for them will be ignored by GAP. In contrast, GMP selects the maximum local prediction for a class as its global prediction: $GMP(\hat{Y})_c = \max_{i\in\{1,\ldots,n\}}\hat{y}_{i,c}$. By using GMP, a rhythm is considered to be present in a recording as long as it occurs at some time in the recording regardless of the duration. One possible problem of GMP is that it may underestimate the true region of an object (Kolesnikov and Lampert, 2016), because the gradient of the prediction loss will be saturated (extremely close to 0) as long as the maximum activation for the existing arrhythmia is extremely close to 1. One solution for this problem is to make a compromise between GAP and GMP. For example, LSE is a convex approximation of the max function (Pinheiro and Collobert, 2015): $LSE(\hat{Y})_c = (1/b)\log((1/n)\sum_{i=1}^{n}\exp(b\hat{y}_{i,c}))$, where $b > 0$ is a hyper-parameter that controls the degree of the approximation to GMP. Increasing b will push the function closer to GMP, while decreasing b will make the function closer to GAP.

However, there are some problems when directly applying these aggregation methods to the local predictions. Firstly, the local predictions are corresponding to sampling points rather than heartbeats. Although we can divide these local features and predictions into individual heartbeats, the variable length and uneven distribution of heartbeats can make an accurate division difficult and increase the complexity of the model structure. Secondly, due to the significant morphological differences between the subwaves (e.g., P wave, QRS complex, and T wave) of a heartbeat, the local predictions at different parts of a heartbeat may be inconsistent, i.e., different parts of a heartbeat are classified to different classes. These inconsistent predictions are unreasonable and will increase the difficulty of model optimization. To address these problems, we propose a masked aggregation mechanism.

2.6.2 Masked Aggregation

The inconsistent predictions within a heartbeat are mainly due to the morphological differences between the subwaves (e.g., P, QRS, and T) of a heartbeat. This problem can be circumvented by selecting the prediction at a certain point in a heartbeat (i.e., the reference point) as the representative prediction for the beat. To ensure the representativeness of the selected predictions, we propose to aggregate only the selected predictions to obtain the global prediction. In this way, only the selected predictions are optimized according to the gradient of the global prediction loss, and thus they will be representative of the beats after the training. Since other predictions are masked out in the aggregation, we call this mechanism masked aggregation. In this work, we choose the R peak as the reference point of a heartbeat because it can be usually accurately recognized by certain algorithms (He et al., 2020). On the selected local predictions, the aggregation methods mentioned above can also be applied. Here, we combine masked aggregation with GMP to get masked global max pooling (MGMP): $MGMP(\hat{Y})_c = \max_{i\in R}\hat{y}_{i,c}$, where R denotes the set of reference points. By selecting only the local predictions at the reference points, the space of possible solutions for local predictions will be significantly reduced, because the reference points in a recording are a few orders of magnitude less than the sampling points. Furthermore, the masked aggregation induces the model to learn features around the reference points so that the learned features at different reference points are semantically comparable between each other.

2.7 Loss Calculation

The global predictions are used for the loss calculation since only record-level labels are available in our WSL setting. The loss function should support multi-label classifications, because multiple rhythms may coexist in a single ECG record. Here, we use the binary cross-entropy as the loss function for the training of our models:

$$L_\theta(X,T) = -\frac{1}{|\mathcal{C}|}\sum_{c=1}^{|\mathcal{C}|}\left(t_c log\left(f(X;\theta)_c\right) + (1-t_c) log\left(1-f(X;\theta)_c\right)\right) \tag{1}$$

where X is a recording of the training set, T is the record-level label set of X, f is the prediction model, and $|\mathcal{C}|$ is the number of considered classes. t_c is an indicator of the presence of class c in the label set T: if $c \in T$, $t_c = 1$; otherwise, $t_c = 0$. Besides, because N is much more common than SVEB and VEB in clinic, there is an extreme imbalance between these classes. For this problem, we assign different weights to the training samples of different classes in the loss calculation:

$$\boldsymbol{L_\theta}(D) = \frac{1}{M}\sum\nolimits_{(X_i,T_i)\in D} w_{(X_i,T_i)} L_\theta(X_i,T_i) \tag{2}$$

where $\boldsymbol{L_\theta}(D)$ is the loss for the training set D, $w_{(X_i,T_i)}$ is the weight for the sample (X_i, T_i), and M is the number of samples in the dataset. In our implementation, after tuning the weight parameters with experiments, the weight for a sample with SVEB or VEB is set to 2, the weight for a sample with both SVEB and VEB is set to 4, while the weight for a sample with neither SVEB nor VEB is set to 0.1.

2.8 Two-Stage Training Strategy

To address the ill-posed problem of WSL, we propose a two-stage training strategy. In the first stage, the model is pre-trained in SL with small amounts of samples with heartbeat labels. Then, in the second stage, the pre-trained model is further trained in WSL with large amounts of coarsely-labeled ECG data. The SL-based pre-training is implemented by omitting the aggregation part of the WSDL-AD framework and applying the supervision directly

to the local predictions. The loss value is calculated using categorical cross-entropy on the predictions at the R peaks, as in **(3)**.

$$L_\theta(X,Y) = -\frac{1}{|R|}\sum_{i\in R}\sum_{c=1}^{|\mathcal{C}|}\left(y_{i,c}\log\left(g(X;\theta)_{i,c}\right)\right) \quad (3)$$

where g is the local prediction model, R denotes the set of heartbeat positions, Y denotes the set of heartbeat labels. $y_{i,c}$ is an element of Y: if the heartbeat at the ith sampling point belongs to category c, $y_{i,c} = 1$; otherwise, $y_{i,c} = 0$. The idea behind this strategy is that the SL-based pre-training can initialize the model with proper parameters that may prevent the subsequent WSL-based training from going in the wrong direction.

3 RESULTS

In this section, we describe the experimental setup and results to evaluate the performance of the WSDL-AD framework in beat-by-beat arrhythmia detection. Ablation studies are also conducted to assess the influence of our proposed techniques on the model's performance.

3.1 Experimental Setup

For comparison between different ML methodologies, we conduct the experiments in three settings: 1) SL setting, where the model is trained with full supervision; 2) WSL setting, where the model is trained with only weak supervision; and 3) the SL + WSL setting, where the model is pre-trained with full supervision on a small dataset, and then trained with weak supervision on a large dataset. Details of each setting are shown in the following subsections.

We implement the models based on the Tensorflow and train the models on a workstation with a CPU running at 3.5 GHz, an NVIDIA Quadro k6000 GPU, and 64 GB of memory. The method used for model optimization is Adaptive Moment Estimation (Adam) (Kingma and Ba, 2014), where β_1 is 0.9, β_2 is 0.999, and the learning rate is 0.001. The training process is terminated when the mean F1 score for all categories on the validation set doesn't increase over 10 epochs. The source code is available at https://github.com/sdnjly/WSDL-AD.

By comparing the model predictions with the annotations, we calculate several metrics to evaluate the model performance. These metrics include sensitivity (*Sen*), specificity (*Spe*), positive predictivity (*Ppr*), accuracy (*Acc*), F_1 score, and average precision (*AP*). Formulas for calculating these metrics are as follows:

$$Sen = \frac{TP}{TP+FN} \quad (4)$$

$$Spe = \frac{TN}{FP+TN} \quad (5)$$

$$Ppr = \frac{TP}{TP+FP} \quad (6)$$

$$Acc = \frac{TP+TN}{TP+FP+TN+FN} \quad (7)$$

$$F_1 = \frac{2\times Sen\times Ppr}{Sen+Ppr} \quad (8)$$

$$AP = \sum_n (Sen_n - Sen_{n-1})Ppr_n \quad (9)$$

where TP denotes true positive predictions, TN denotes true negative predictions, FP denotes false positive predictions, and FN denotes false negatives predictions. Sen_n and Ppr_n are the sensitivity and positive predictivity at the nth threshold of the precision-recall curve (PRC) (Chen, 2003).

3.2 The SL Setting

For training the SL model, recordings of MITBIH-AR-DS1 are split into segments of 20 s 80% of the segments are randomly selected as the training set, and the remaining 20% are used as the validation set. The validation set is just used for hyperparameters tuning and early stopping of the training process. The trained model is tested on the other three completely independent and finely annotated datasets, including MITBIH-AR-DS2, MITBIH-SUP, and INCART. The metric scores on these test sets are used for the final evaluation of the model performance.

The test results on each dataset and the total test data are shown in **Table 3**. For the detection of SVEB, the SL model achieves high scores in *Spe* and *Acc*, but has very low scores in *Sen*, *Ppr*, and F_1. For example, the *Spe* scores of the SL model on MITBIH-AR-DS2, MITBIH-SUP, and INCART are 0.994, 0.981, and 0.993, respectively, whereas its *Sen* scores on these datasets are only 0.066, 0.130, and 0.590, respectively. The high scores of *Spe* and *Acc* can be attributed to the extreme class imbalance of the test sets, where only a tiny minority of the samples belong to SVEB. And the low scores of *Sen*, *Ppr*, and F_1 are a true reflection of the poor ability of the SL model in detecting SVEB. The test scores for VEB detection are much higher than those for SVEB detection. Besides, the model performances are different from dataset to dataset. For example, the scores of *Ppr* and F_1 for VEB detection on the MITBIH-SUP dataset are much lower than that on the other datasets. These differences may result from the diversity of data distribution among these test sets.

3.3 The WSL Setting

The WSL model is trained on the five coarsely-annotated datasets from the PhysioNet/CinC challenge. MITBIH-AR-DS1 is used as the validation set, and the other three finely-annotated datasets are used as the test sets. For ease of batch processing during the model training, all recordings in the training set are padded or truncated at the end to 20 s. The recordings in the validation set are also split into segments of 20 s.

The evaluation results on the test sets are shown in **Table 3**. By comparing the scores with those in the SL setting, we find that the WSL model improves the scores for detecting SVEB, VEB and N on all of the test sets. Especially, the scores for SVEB detection are improved most significantly. For example, on the dataset of MITBIH-AR-DS2, the *Sen*, *Ppr*, and F_1 scores for SVEB detection are improved from 0.066, 0.286, and 0.108 to 0.806, 0.799, and 0.803, respectively. The differences are shown visually by the PRCs in **Figure 5**. In the detection of both VEB (**Figure 5A**) and SVEB (**Figure 5B**), the curves for the WSL

TABLE 3 | Experimental results of different training setting on the evaluation datasets.

Test set	Experimental setting	N					S					V				
		Sen	*Ppr*	*Spe*	*Acc*	F_1	*Sen*	*Ppr*	*Spe*	*Acc*	F_1	*Sen*	*Ppr*	*Spe*	*Acc*	F_1
MITBIH-AR-DS2	SL	0.985	0.959	0.634	0.949	0.972	0.066	0.286	0.994	0.959	0.108	0.935	0.873	0.991	0.987	0.903
	WSL	0.990	0.987	0.883	0.979	0.988	0.806	0.799	0.992	0.985	0.803	0.902	0.950	0.997	0.990	0.925
	SL + WSL	0.990	0.992	0.928	0.983	0.991	0.886	0.785	0.991	0.987	0.832	0.916	0.956	0.997	0.992	0.936
MITBIH-SUP	SL	0.932	0.941	0.574	0.889	0.936	0.130	0.323	0.981	0.924	0.186	0.826	0.434	0.939	0.933	0.569
	WSL	0.991	0.951	0.629	0.947	0.971	0.325	0.776	0.993	0.949	0.458	0.803	0.774	0.987	0.977	0.788
	SL + WSL	0.986	0.962	0.717	0.954	0.974	0.452	0.705	0.987	0.951	0.551	0.795	0.768	0.986	0.976	0.782
INCART	SL	0.991	0.978	0.844	0.973	0.985	0.590	0.487	0.993	0.989	0.534	0.826	0.945	0.994	0.975	0.882
	WSL	0.990	0.988	0.914	0.981	0.989	0.852	0.575	0.993	0.991	0.687	0.886	0.950	0.994	0.982	0.917
	SL + WSL	0.993	0.990	0.933	0.986	0.992	0.927	0.519	0.990	0.990	0.665	0.880	0.976	0.997	0.984	0.926
The Total Test Set	SL	0.964	0.959	0.701	0.932	0.961	0.179	0.371	0.988	0.956	0.242	0.837	0.696	0.968	0.957	0.760
	WSL	0.990	0.971	0.782	0.965	0.981	0.445	0.721	0.993	0.972	0.550	0.862	0.893	0.991	0.980	0.878
	SL + WSL	0.990	0.978	0.835	0.971	0.984	0.560	0.669	0.989	0.972	0.610	0.858	0.906	0.992	0.981	0.882

N, normal or bundle branch block beat; S, supraventricular ectopic beat; V, ventricular ectopic beat; SL, supervised learning; WSL, weakly supervised learning; Sen, sensitivity; Ppr, positive predictivity; Spe, specificity; Acc, accuracy; F_1, F_1 score.

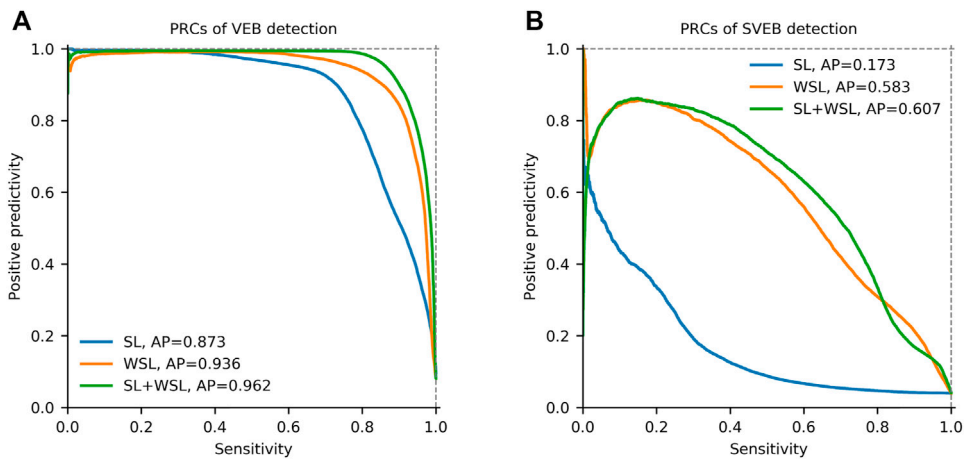

FIGURE 5 | Precision-recall curves (PRCs) of the detection for ventricular ectopic beats (VEB) and supraventricular ectopic beats (SVEB) on the total dataset in different learning settings. **(A)** PRCs of VEB detection. **(B)** PRCs of SVEB detection. SL = supervised learning. WSL = weakly supervised learning. AP = average precision.

model (in orange) cover significantly larger areas than that for the SL model (in blue), especially in the detection of SVEB.

3.4 The SL + WSL Setting

In this two-stage training setting, the model is pre-trained in SL for 10 epochs on the segments from the first half of each recording in the MITBIH-AR-DS1. Then the model is trained in WSL on the same data in the WSL setting, with the last-half recordings in the MITBIH-AR-DS1 as the validation set. Finally, the model is tested on the three test sets, with the results shown in **Table 3**. These results are very close to that in the WSL setting, which is also shown in **Figure 5**. The WSL and SL + WSL models have superiority over each other in different datasets and metrics. For example, the WSL model outperforms the SL + WSL model in *Ppr* and F_1 for detecting SVEB on the INCART, whereas the SL + WSL model outperforms the WSL model in *Sen* and F_1 for detecting SVEB on the MITBIH-SUP. On the total test set, the overall performance (indicated by F_1 and *AP*) of the SL + WSL model is superior to that of the WSL model in detecting both SVEB and VEB. Especially, in the detection of SVEB, the SL + WSL model achieves obvious better scores (F_1 of 0.610, *AP* of 0.601) than the WSL model (F_1 of 0.550, *AP* of 0.583) on the total test set.

3.5 Stability Assessment

Due to the ill-posed problem of WSL, there is a chance that the rules learned by a WSL model deviate from the ground truth. To assess the stability of the model performance from training to training, we train the model independently 50 times in each of the WSL and SL + WSL settings. In the WSL setting, the F_1 scores for SVEB detection and VEB detection are 0.370 ± 0.260 and 0.740 ± 0.187, respectively, whereas in the SL + WSL setting, the F_1 scores

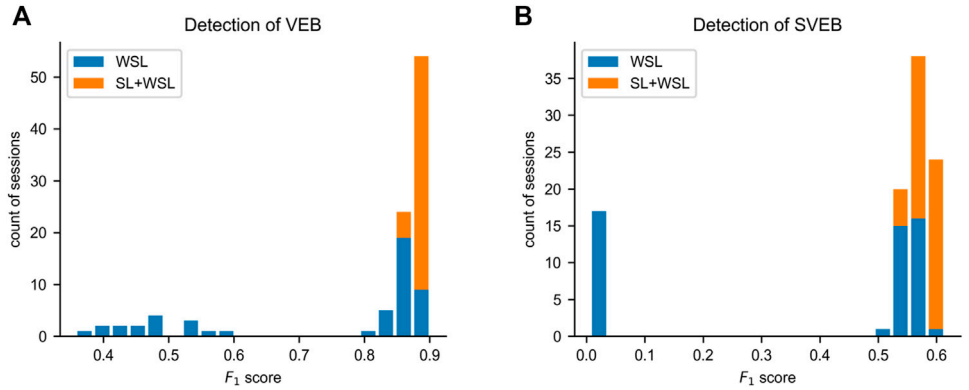

FIGURE 6 | Distributions of the F_1 scores on the total test data in multiple independent training sessions. **(A)** The histogram of the results for ventricular ectopic beat (VEB) detection. **(B)** The histogram of the results for supraventricular ectopic beat (SVEB) detection. SL = supervised learning. WSL = weakly supervised learning.

for SVEB detection and VEB detection are 0.582 ± 0.019 and 0.886 ± 0.009, respectively. The distribution of the scores on the total test data are shown by the histograms in **Figure 6**. The results show that the performance of the WSL model in detecting both arrhythmias fluctuates wildly from training to training. The distribution of the scores for SVEB detection is polarized: some scores are clustered at the top pole, while other scores are located near the bottom pole. This suggests that different hypotheses of the detection model can satisfy the weak constraints of the recording labels and cause the instability of the model performance from training to training. By contrast, the performance of the SL + WSL model is very stable in multiple training sessions. The SL-based pre-training only initializes the model with a few training samples. It indicates that proper initialization can avoid the unstable performance of a WSL model.

3.6 Ablation Studies

Several ablation studies are conducted to evaluate the effects of the proposed knowledge-based features, DNN-based feature extraction and masked aggregation on the performance of the WSDL-AD framework. And all of the ablation studies are in the SL + WSL setting.

3.6.1 Knowledge-Based Features

Ablation experiments are conducted to evaluate the contributions of knowledge-based features to the prediction. Four configurations are studied in the experiments, including *none* (using only DNN features), *RR entropy* (using DNN features and RR entropy), *relative RR interval* (using DNN features and relative RR interval), *both features* (using DNN features and both of the knowledge-based features). The test results on the total test data are shown by PRCs in **Figures 7A,B**. The PRCs of VEB detection are very similar among different configurations, so the knowledge-based features have little effect on the VEB detection. In contrast, there are significant differences among the PRCs for the SVEB detection. The model with no knowledge-based features has an AP score of 0.485, while applying the RR entropy and relative RR interval alone improves the score to 0.512 and 0.529 respectively. The joint application of both knowledge-based features further improves the score to 0.607. Therefore, the knowledge-based features have positive effects on the model's performance in detecting SVEB.

3.6.2 DNN-Based Feature Extraction Methods

In our framework, the DNN-based features are extracted using the ResNet. But our framework is also compatible with other kinds of networks for feature extraction. To evaluate the impacts of the network structure on the model performance, we conduct ablation experiments with different types of networks for feature extraction. Besides the ResNet, several well-known networks are tested for comparison, including AlexNet (Krizhevsky et al., 2012), VGG-19 (Simonyan and Zisserman, 2014) and U-Net (Ronneberger et al., 2015). Since these networks are all originally designed for processing 2D images, we replace the 2D convolutional and pooling layers with their 1D counterparts to adapt to the processing of 1D ECG signals. The recommended hyperparameters of these networks are adopted in our experiments. Some dimension-related hyperparameters (such as, convolutional kernel size and pool size) are converted to the 1D counterparts. For example, the convolutional kernel size (3×3) of the VGG-19 is converted to 3. The test results on the total test set are shown in **Figures 7C,D**. From the results, we can find that the performances of models with different network structures are obviously different. Among these networks, ResNet achieves the best performance in both SVEB ($AP = 0.607$) and VEB ($AP = 0.962$) detections on the total test data. The performance of VGG-19 is very close to that of ResNet, and the main difference lies in the detection of VEB ($AP = 0.943$). By contrast, the performances of models with AlexNet and U-Net are much lower than that of ResNet. These results indicate that the structure of the feature-extraction network has important impacts on the model performance. To obtain good performance, it is necessary to choose a proper network structure for feature extraction.

3.6.3 Aggregation Mechanisms

Four aggregation mechanisms are compared in our ablation studies, including GAP, GMP, LSE ($b = 5$), and MGMP. The

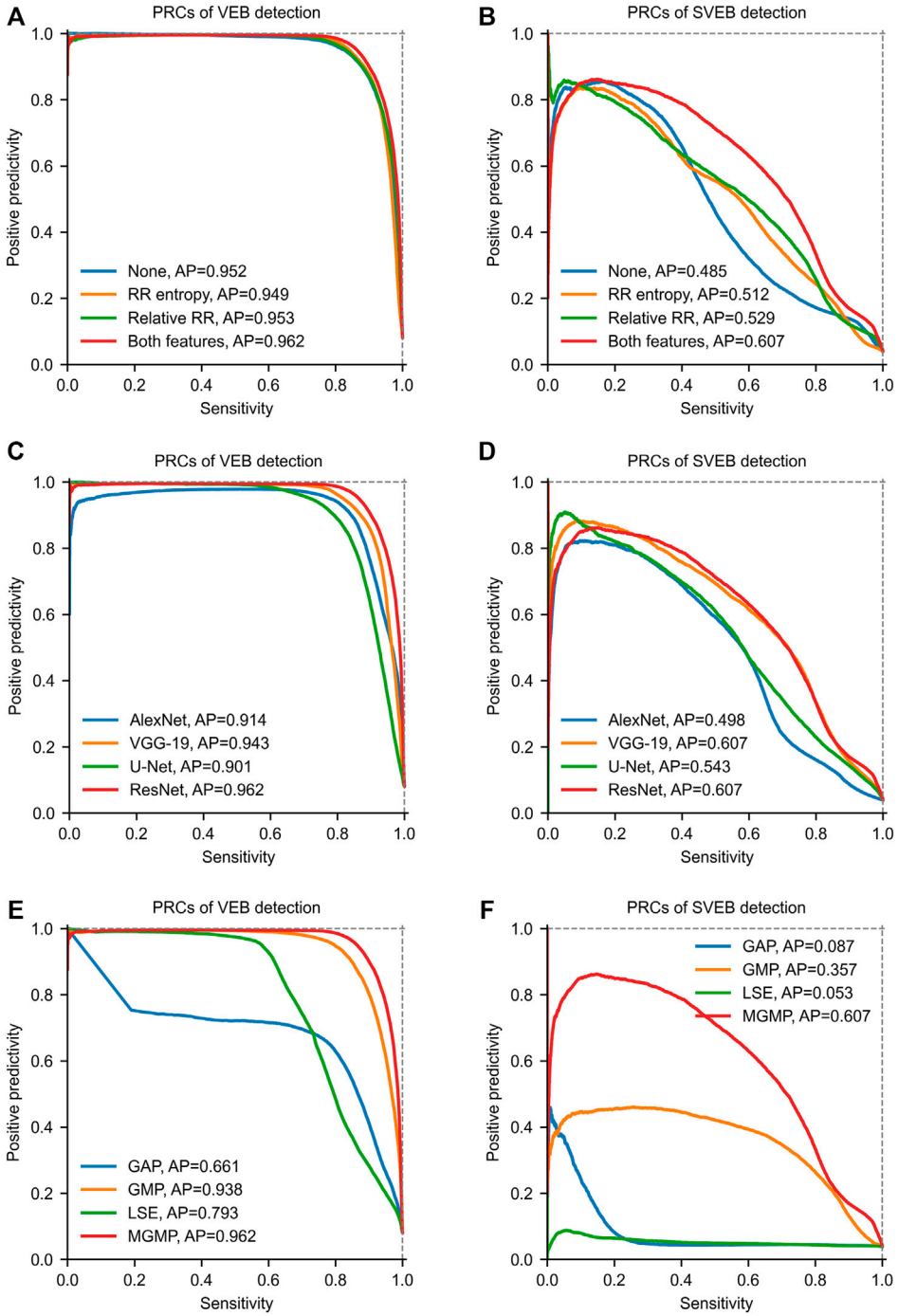

FIGURE 7 | Precision-recall curves (PRCs) of the ablation studies on the total test data. **(A)** and **(B)** show PRCs of models with different knowledge-based features. **(C)** and **(D)** show PRCs of models with different feature extraction networks. **(E)** and **(F)** show PRCs of models with different aggregation mechanisms. GAP = global average pooling. GMP = global max pooling. LSE = Log-Sum-Exp. MGMP = masked global max pooling. AP = average precision. The parameter *b* of LSE is set to 5.

test results on the total test data are shown in **Figures 7E,F**. In detecting VEB, GAP achieves the poorest performance (AP = 0.661) among all of the tested mechanisms, which may be attributed to the fact that an arrhythmia epoch may only account for a small portion of a recording. The performance of LSE (AP = 0.793) is better than GAP since it makes a compromise between GAP and GMP. Much better performances are achieved by GMP (AP = 0.938) and MGMP (AP = 0.962). It may be because that these two mechanisms are consistent with the basic principle that an arrhythmia should be

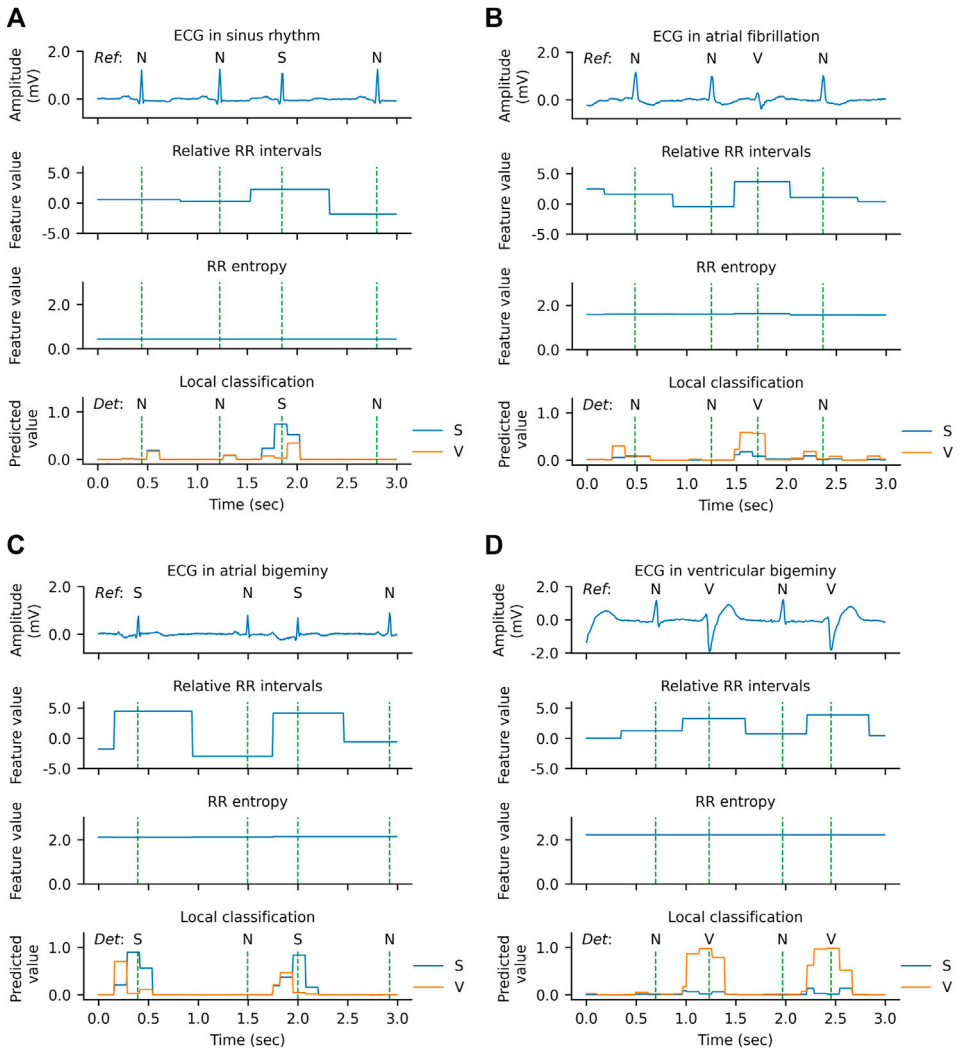

FIGURE 8 | Qualitative results of arrhythmia detection on the MITBIH-AR-DS2 in the SL + WSL setting. **(A)** An example during normal rhythm. **(B)** An example during atrial fibrillation. **(C)** An example during atrial bigeminy. **(D)** An example during ventricular bigeminy. The vertical dashed lines indicate the positions of R peaks. In the ECG waveform charts, the reference category of each heartbeat is labeled above the ECG. In the local classification charts, the predictions for supraventricular ectopic beats (S) are drawn in blue, the predictions for ventricular ectopic beats (V) are drawn in orange, and the detected categories are labeled above the prediction lines. N denotes a normal or bundle branch block beat. Since the probabilities of N, S, and V add up to one at each sampling point, the predictions for N are not plotted in the figure for clarity.

included in the global prediction as long as it exists somewhere in the recording. As for the detection of SVEB, the performances of GMP and MGMP are also significantly better than GAP and LSE. Especially, the MGMP, achieving an AP of 0.607, outperforms all other mechanisms by a large margin. This indicates that the masked mechanism is indeed helpful to improve the performance of WSL-based arrhythmia detection, especially for arrhythmias with subtle morphological changes, e.g., SVEB.

3.7 Analysis of Detection Examples

The qualitative results of the WSDL-AD model in detecting SVEB and VEB are shown in **Figure 8**. In this figure, both the ECG signal and the knowledge-based feature maps (including relative RR interval and RR entropy) of each example are present. The local classifications contain the rhythm-wise probability distribution at each sampling point. The beat-by-beat detections are derived from the local predictions by selecting the predictions at the R peaks. The local classifications indicate that the WSL models have learned the ability to detect SVEBs and VEBs in various contextual rhythms, such as normal sinus rhythm, atrial fibrillation (AF), atrial bigeminy (AB), and ventricular bigeminy (VB). And, in most cases, the model has adequate confidence for the classification, where the predicted probability for some class is significantly higher than that for other classes. The value of the relative RR interval exhibits a positive correlation with the occurrence of SVEB and VEB, which is in line with our expectations and thus can serve as an effective indicator. However, a shortened RR interval, manifested by the

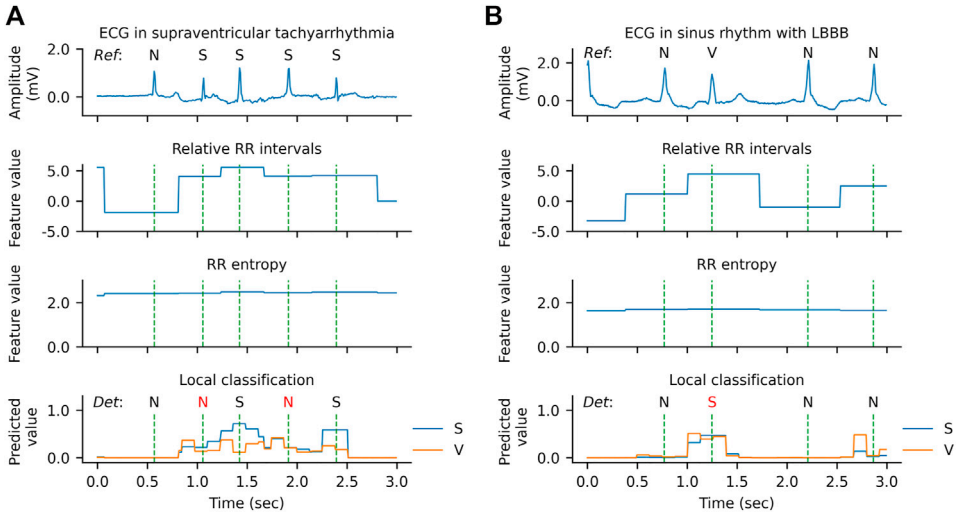

FIGURE 9 | Qualitative results of error predictions. **(A)** An example of misclassifying supraventricular ectopic beats (S) as normal or bundle branch block beats (N) during supraventricular tachyarrhythmia. **(B)** An example of misclassifying a ventricular ectopic beat (V) as an S during left bundle branch block (LBBB).

high value of relative RR interval, doesn't necessarily indicate an ectopic beat, because it may be caused by other arrhythmias, such as AF. The RR entropy, on the other hand, reflects the variation of RR intervals in the context: when the RR interval changes greatly (e.g., during AF, AB, or VB), the entropy value is at a high level, and vice versa (e.g., during sinus rhythm). Therefore, the joint application of relative RR interval and RR entropy can supply the information about the significance of a local RR-interval change, and help to increase the precision of the detection.

However, there are also some cases where the model has low confidence in the classification or even makes errors, as shown in **Figure 9**. In the example of **Figure 9A**, two SVEBs during supraventricular tachyarrhythmia (SVTA) are misclassified as N. This can be attributed to the successive occurrence of SVEBs during SVTA, where the change of RR intervals from beat to beat is not significant, and especially most SVEBs are followed by noncompensatory pauses. **Figure 9B** presents an example that a VEB during the left bundle branch block (LBBB) is misclassified as SVEB. At the beat, the predicted probability for VEB is slightly less than that for SVEB, and both probabilities are significantly higher than that for N. It implies that the model has enough confidence to classify the beat as an ectopic beat, but has not enough confidence to distinguish whether it is an SVEB or VEB. One possible reason for this is that the QRS complex of the VEB is not significantly wider than that of the neighboring beats.

4 DISCUSSION

In this study, we propose a WSL framework (WSDL-AD) for the beat-by-beat detection of arrhythmias, which requires only coarse-grained record-level annotations during the model training. The evaluation on independent datasets shows that a WSDL-AD model is able to learn the ability to detect VEB and SVEB from the coarsely annotated ECGs. In particular, our WSL model outperforms its SL counterpart by a large margin on multiple external test sets, which indicates that the WSL framework can facilitate the generalization ability of arrhythmia detection by exploring the large amount of coarsely-annotated ECG data. The biggest improvement is in the detection of SVEB, which is more difficult to detect because its waveform variation is usually very subtle. In this section, we will compare the results of our method with that of other state-of-the-art studies, and discuss the implications and limitations of this study.

4.1 Comparison With Other Studies

We compare our results with that of representative previous studies. The previous studies on the heartbeat classification can be categorized into two types: inductive learning (or induction), which learns general rules from labeled training samples and applies the rules to test samples; and transductive learning (or transduction), which learns the detection rules from both the labeled training samples and the unlabeled test samples, and applies the rules on the same test samples. This study and most previous studies are in inductive learning. Some studies that based on unsupervised domain adaptation are in transductive learning (Li et al., 2021; Wang et al., 2021). Although the models of transductive learning usually achieve better performance than inductive learning models, their requirement for the unlabeled target samples during the model training stage is hard to satisfy, since there are always new patients in routine clinical practice.

The MITBIH-AR-DS2 dataset is mostly used by previous studies for model evaluation, and the results of some representative studies are shown in **Table 4**. On the dataset, the test scores of our WSL models (in both WSL and SL + WSL settings) in detecting SVEB and VEB are significantly superior to that of the state-of-the-art methods of supervised inductive

TABLE 4 | Comparison of our method with other studies on DS2 of the MITBIH-AR dataset.

Studies	Learning type	N			S			V		
		Se	*Ppr*	F_1	*Se*	*Ppr*	F_1	*Se*	*Ppr*	F_1
De Chazal et al. (2004)	Induction	0.869	0.992	0.926	0.759	0.385	0.511	0.777	0.819	0.794
Llamedo and Martínez. (2010)	Induction	0.776	**0.995**	0.872	0.765	0.413	0.536	0.829	0.880	0.854
Mar et al. (2011)	Induction	0.896	0.991	0.841	0.832	0.335	0.478	0.868	0.759	0.809
Zhang et al. (2014)	Induction	0.889	0.990	0.937	0.791	0.360	0.495	0.855	0.928	0.890
Raj and Ray. (2018)	Induction	0.909	0.994	0.950	0.808	0.488	0.608	0.822	0.854	0.838
Garcia et al. (2017)	Induction	0.940	0.980	0.959	0.620	0.530	0.571	0.873	0.594	0.707
Guo et al. (2019)	Induction	—	—	—	0.627	0.612	0.619	0.913	0.883	0.898
Niu et al. (2020)	Induction	0.989	0.974	0.981	0.765	0.766	0.766	0.857	0.941	0.897
Wang et al. (2021)	Transduction	0.991	0.984	0.990	0.765	0.902	0.830	**0.940**	0.923	0.930
Li et al. (2021)	Transduction	**0.994**	0.983	0.989	0.772	**0.934**	**0.845**	0.906	0.944	0.924
This work (WSL setting)	Induction	0.990	0.987	0.988	0.806	0.799	0.803	0.902	0.950	0.925
This work (SL + WSL setting)	Induction	0.990	0.992	**0.991**	**0.886**	0.785	0.832	0.916	**0.956**	**0.936**

N, normal or bundle branch block beat; S, supraventricular ectopic beat; V, ventricular ectopic beat; Se, sensitivity; Ppr, positive predictivity; F_1, F_1 score.
The bold text indicates the maximum of each column.

TABLE 5 | Comparison of our method with other studies on the MITBIH-SUP dataset.

Studies	Learning type	S			V		
		Se	*Ppr*	F_1	*Se*	*Ppr*	F_1
Al Rahhal et al. (2016)	Induction	0.088	0.143	0.109	0.652	0.093	0.163
Guo et al. (2019)	Induction	0.079	0.645	0.141	**0.868**	0.588	0.701
Wang et al. (2021)	Transduction	0.236	0.539	0.33	0.844	0.563	0.68
Li et al. (2021)	Transduction	0.238	0.472	0.316	0.785	0.724	0.753
This work (WSL setting)	Induction	0.325	**0.776**	0.458	0.803	**0.774**	**0.788**
This work (SL + WSL setting)	Induction	**0.452**	0.705	**0.551**	0.795	0.768	0.782

S, supraventricular ectopic beat; V, ventricular ectopic beat; Se, sensitivity; Ppr, positive predictivity; F_1, F_1 score.
The bold text indicates the maximum of each column.

TABLE 6 | Comparison of our method with other studies on the INCART dataset.

Studies	Learning type	S			V		
		Se	*Ppr*	F_1	*Se*	*Ppr*	F_1
Llamedo and Martínez. (2010)	Induction	0.77	0.39	0.52	0.81	0.87	0.84
Al Rahhal et al. (2016)	Induction	0.156	0.025	0.04	0.751	0.376	0.501
Wang et al. (2021)	Transduction	0.711	0.435	0.54	**0.901**	0.903	0.90
This work (WSL setting)	Induction	0.852	**0.575**	**0.687**	0.886	0.950	0.917
This work (SL + WSL setting)	Induction	**0.927**	0.519	0.665	0.880	**0.976**	**0.926**

N, normal or bundle branch block beat; S, supraventricular ectopic beat; V, ventricular ectopic beat; Se, sensitivity; Ppr, positive predictivity; F_1, F_1 score.
The bold text indicates the maximum of each column.

learning (Guo et al., 2019; Niu et al., 2020), and comparable to the state-of-the-art results of unsupervised transductive learning (Li et al., 2021; Wang et al., 2021). Compared with previous inductive models, the improvements of F_1 scores are >8% (from 0.766 to 0.832) for SVEB and >4% (from 0.898 to 0.936) for VEB. The test results of previous studies on the MITBIH-SUP dataset and the INCART dataset are present in **Tables 5**,**6** respectively. On the MITBIH-SUP dataset, our WSL models substantially outperform previous studies of induction (increasing the F_1 scores by >290% for SVEB and >11% for VEB) and transduction methods (increasing the F_1 scores by >66% for SVEB and >3% for VEB). Similar improvements are also observed for the INCART dataset. In particular, for the detection of SVEB, our WSL models have a big superiority over the transduction methods on these two datasets, although the transduction methods have optimized their models according to the test samples. These improvements indicate that the proposed WSL method can learn robust rules from a large amount of coarsely annotated data and has a better generalization ability.

4.2 Implications of the Proposed Method

This study shows that the WSL approach is effective to improve the generalization ability of beat-by-beat arrhythmia detectors by leveraging the large amounts of coarsely-annotated ECG data. An arrhythmia detector with both fine detection granularity and good generalization ability has important implications for clinical practice. The fine granularity is necessary for measuring the burden and pattern (e.g., bigeminy and trigeminy) of

arrhythmias, which can be used to assess critical risks (e.g., stroke and heart failure) in clinic (Boriani et al., 2014; Marcus, 2020). On the other hand, the generalization ability is a necessary prerequisite for an algorithm to be trusted for clinical use, because ECG is susceptible to environmental and individual differences. The diagnoses made by currently used algorithms still need to be reviewed by doctors. However, with the explosion of ECG data from mobile devices, it is not practical to rely on doctors to review every record. With the improvements in generalization ability, our WSL method can deal with more situations and make more reliable detections independently, which are of significance to prompt the revolution of automatic ECG diagnosis.

This superiority of the WSL models may source from the fact that their training data are from a much larger patient group than that of the SL models. The coarse-grained annotations usually take much less time and effort than fine-grained annotations. And to ensure the correctness of the annotations, fine annotation needs multiple experts to reach a consensus on the labels of each beat, while coarse annotation only needs a consensus on the global labels. In addition, in many medical institutions, the electronic medical records, containing both physiological signals and diagnostic reports, are inherent coarsely annotated data and could be used to train the WSL models. Therefore, the amount of coarsely annotated data could be accumulated rapidly in the future, which provides essential substrates for continually improving the reliability of automatic arrhythmia detectors.

As demonstrated by the ablation experiments, the proposed knowledge-based features and masked aggregation mechanism also play an important role in improving the performance of the WSL models. One of the advantages of the knowledge-based features is that they integrate the information in a very wide context, which is usually difficult to learn by the model self, especially under weak supervision. By fusing the knowledge-based features and the DNN-extracted features, the representative ability of the feature vector might be enhanced, thus causing the detection performance to be improved. On the other hand, the masked aggregation mechanism selects the representative prediction for each heartbeat at the specified reference point, which greatly reduces the space of possible local predictions. Besides, because the reference points belong to the same type of ECG subwave, e.g., the R peak, the features aligned to the reference points are also semantic comparable with each other. Consequently, the masked aggregation mechanism helps to improve the performance of ectopic beat detection. Furthermore, the results of multiple independent training sessions reveal the instability of the training process of WSDL-AD. We also demonstrate that SL-based pre-training on a few finely-annotated samples can effectively improve the stability of the training process. It implies that the initialization has a critical effect on the training process of the WSL model. These methods proposed in this study may also be enlightening to further studies in arrhythmia detection and even other fields.

The computational complexity of our framework can be divided into several parts, which are corresponding to preprocessing, QRS complexes detection, knowledge-based features extraction, DNN-based features extraction, local prediction, and aggregation, respectively. Among these parts, the part of DNN-based features extraction dominates the computational complexity of the framework. The network for feature extraction is a 1D ResNet whose computational complexity mainly comes from the convolutional layers in it. The computational complexity of each convolutional layer is $O(K \times M \times N)$, where K is the kernel number, M is the kernel size (kernel length × channels), and N is the signal length. By putting the hyperparameters in the formula, we get $O(K \times M \times N) = O(32 \times 16 \times 32 \times N) = O(N)$. There are only nine convolutional layers in our 1D ResNet, and the feature maps are gradually down-sampled. Taken together, the computational complexity of the 1D ResNet is $O(9 \times 32 \times 16 \times 32 \times N) = O(N)$. Thus, the computational complexity of the 1D ResNet is linear to the signal length. Besides, the number of layers and the number of convolutional kernels in our network are much smaller than that of other well-known networks, such as VGG-19 (Krittanawong et al., 2019) and U-Net (Ronneberger et al., 2015). Therefore, the computational complexity of our framework is moderate, which is critical for scenarios where computing resources are scarce, such as mobile ECG monitoring.

4.3 Limitations

This work also has some limitations. First, the WSL models have a high error rate for SVEB detection. The waveform patterns of SVEB are usually subtle and therefore difficult to be recognized by the model. To address this problem, collecting more training data or improving the design of the WSL framework (e.g., extracting features of the P wave) would be helpful. Second, the WSDL-AD framework is not evaluated for detecting other kinds of ECG abnormalities, such as branch bundle blocks and ST segment changes. Future work is required to assess the effectiveness of WSL in detecting more diverse ECG abnormalities.

5 CONCLUSION

In conclusion, this study develops and evaluates a WSDL framework for beat-by-beat arrhythmia detection, by which we demonstrate the feasibility of training a fine-grained arrhythmia detector on only coarsely-labeled ECG data. The evaluations on multiple external datasets show that the proposed framework has a significant superiority in generalization ability over previous SL-based methods. The knowledge-based features and masked aggregation mechanism also have important contributions to the performance of the model, while the SL-based pre-training helps to improve the stability of the training process. Furthermore, the computational complexity of our framework is moderate, which permits the models to be deployed on hardware with limited computing resources. Our approach would substantially reduce the burden of data annotation and enhance the reliability of beat-by-beat arrhythmia detection, and therefore has a great potential to promote the application of automatic cardiac monitoring both in and out of hospitals.

DATA AVAILABILITY STATEMENT

The original contributions presented in the study are included in the article/supplementary material, further inquiries can be directed to the corresponding authors.

AUTHOR CONTRIBUTIONS

YL: Conceptualization, Data curation, Formal analysis, Methodology, Software, Validation, Visualization, Writing—original draft, Writing—review and editing. QL: Conceptualization, Supervision, Validation, Writing—review and editing. RH: Validation, Writing—review and editing. KW: Resources, Project administration, Writing—review and editing. JL: Validation, Writing—review and editing. YY: Supervision, Validation, Writing—review and editing. YX: Funding acquisition, Supervision. HZ: Conceptualization, Funding acquisition, Supervision, Validation, Writing—review and editing.

FUNDING

This work was supported by the National Natural Science Foundation of China (NSFC) under Grant No. 62133009 (to QL), and by the Collaborative Innovation Center for Prevention and Treatment of Cardiovascular Disease of Sichuan Province (CICPTCDSP) under Grant No. xtcx2019-01 (to HZ), and by Shandong Provincial Natural Science Foundation (SPNSF) under Grant No. ZR2020MF050 (to YX).

REFERENCES

AAMI (2012). "Testing and Reporting Performance Results of Cardiac Rhythm and ST Segment Measurement Algorithms," in ANSI/AAMI EC57. *Association for the Advancement of Medical Instrumentation*.

Baman, T. S., Lange, D. C., Ilg, K. J., Gupta, S. K., Liu, T.-Y., Alguire, C., et al. (2010). Relationship between burden of Premature Ventricular Complexes and Left Ventricular Function. *Heart Rhythm* 7 (7), 865–869. doi:10.1016/j.hrthm.2010.03.036

Binici, Z., Intzilakis, T., Nielsen, O. W., Køber, L., and Sajadieh, A. (2010). Excessive Supraventricular Ectopic Activity and Increased Risk of Atrial Fibrillation and Stroke. *Circulation* 121 (13), 1904–1911. doi:10.1161/CIR.0b013e3181f3321810.1161/CIRCULATIONAHA.109.874982

Boriani, G., Glotzer, T. V., Santini, M., West, T. M., De Melis, M., Sepsi, M., et al. (2014). Device-detected Atrial Fibrillation and Risk for Stroke: an Analysis of >10 000 Patients from the SOS AF Project (Stroke preventiOn Strategies Based on Atrial Fibrillation Information from Implanted Devices). *Eur. Heart J.* 35 (8), 508–516. doi:10.1093/eurheartj/eht491

Chen, Z. (2003). Assessing Sequence Comparison Methods with the Average Precision Criterion. *Bioinformatics* 19 (18), 2456–2460. doi:10.1093/bioinformatics/btg349

Choe, J., Oh, S. J., Lee, S., Chun, S., Akata, Z., and Shim, H. (2020). "Evaluating Weakly Supervised Object Localization Methods Right," in Proceedings of the IEEE/CVF Conference on Computer Vision and Pattern Recognition, 3133–3142.

deChazal, P., O'Dwyer, M., and Reilly, R. B. (2004). Automatic Classification of Heartbeats Using ECG Morphology and Heartbeat Interval Features. *IEEE Trans. Biomed. Eng.* 51 (7), 1196–1206. doi:10.1109/tbme.2004.827359

Degirmenci, M., Ozdemir, M. A., Izci, E., and Akan, A. (2021). Arrhythmic Heartbeat Classification Using 2D Convolutional Neural Networks. *Irbm*. doi:10.1016/j.irbm.2021.04.002

Deyell, M. W., Park, K.-M., Han, Y., Frankel, D. S., Dixit, S., Cooper, J. M., et al. (2012). Predictors of Recovery of Left Ventricular Dysfunction after Ablation of Frequent Ventricular Premature Depolarizations. *Heart Rhythm* 9 (9), 1465–1472. doi:10.1016/j.hrthm.2012.05.019

Donnelly, K. (2006). SNOMED-CT: The Advanced Terminology and Coding System for eHealth. *Stud. Health Technol. Inform.* 121, 279–290.

Garcia, G., Moreira, G., Menotti, D., and Luz, E. (2017). Inter-patient ECG Heartbeat Classification with Temporal VCG Optimized by PSO. *Sci. Rep.* 7 (1), 10543–10611. doi:10.1038/s41598-017-09837-3

Golany, T., and Radinsky, K. (2019). "Pgans: Personalized Generative Adversarial Networks for Ecg Synthesis to Improve Patient-specific Deep Ecg Classification," in Proceedings of the AAAI Conference on Artificial Intelligence, 557–564.

Goldberger, A. L., Amaral, L. A., Glass, L., Hausdorff, J. M., Ivanov, P. C., Mark, R. G., et al. (2000). PhysioBank, PhysioToolkit, and PhysioNet: Components of a New Research Resource for Complex Physiologic Signals. *Circulation* 101 (23), e215–20. doi:10.1161/01.cir.101.23.e215

Greenwald, S. D., Patil, R. S., and Mark, R. G. (1990). "Improved Detection and Classification of Arrhythmias in Noise-Corrupted Electrocardiograms Using Contextual Information," in *Computers in Cardiology* (Chicago, IL.

Guo, L., Sim, G., and Matuszewski, B. (2019). Inter-patient ECG Classification with Convolutional and Recurrent Neural Networks. *Biocybernetics Biomed. Eng.* 39 (3), 868–879. doi:10.1016/j.bbe.2019.06.001

He, K., Zhang, X., Ren, S., and Sun, J. (2016). "Deep Residual Learning for Image Recognition," in IEEE/CVF Conference on Computer Vision and Pattern Recognition, 770–778.

He, K., Zhang, X., Ren, S., and Sun, J. (2015). "Delving Deep into Rectifiers: Surpassing Human-Level Performance on Imagenet Classification," in International Conference on Computer Vision, 1026–1034.

He, R., Liu, Y., Wang, K., Zhao, N., Yuan, Y., Li, Q., et al. (2020). Automatic Detection of QRS Complexes Using Dual Channels Based on U-Net and Bidirectional Long Short-Term Memory. *IEEE J. Biomed. Health Inform.* PP (4), 1052–1061. doi:10.1109/JBHI.2020.3018563

Ioffe, S., and Szegedy, C. (2015). "Batch Normalization: Accelerating Deep Network Training by Reducing Internal Covariate Shift," in International conference on machine learning, 448–456.

Kingma, D. P., and Ba, J. (2014). *Adam: A Method for Stochastic Optimization*. *arXiv preprint*.

Kiranyaz, S., Ince, T., and Gabbouj, M. (2016). Real-time Patient-specific ECG Classification by 1-D Convolutional Neural Networks. *IEEE Trans. Biomed. Eng.* 63 (3), 664–675. doi:10.1109/tbme.2015.2468589

Kolesnikov, A., and Lampert, C. H. (2016). "Seed, Expand and Constrain: Three Principles for Weakly-Supervised Image Segmentation," in European Conference on Computer Vision, 695–711.

Krittanawong, C., Johnson, K. W., Rosenson, R. S., Wang, Z., Aydar, M., Baber, U., et al. (2019). Deep Learning for Cardiovascular Medicine: a Practical Primer. *Eur. Heart J.* 40 (25), 2058–2073. doi:10.1093/eurheartj/ehz056

Krizhevsky, A., Sutskever, I., and Hinton, G. E. (2012). "Imagenet Classification with Deep Convolutional Neural Networks," in Adv. Neur. Inf. Process. Syst., 1097–1105.

Li, J., Wang, G., Chen, M., Ding, Z., and Yang, H. (2021). Mixup Asymmetric Tri-training for Heartbeat Classification under Domain Shift. *IEEE Signal. Process. Lett.* 28, 718–722. doi:10.1109/lsp.2021.3066068

Li, Y., Pang, Y., Wang, J., and Li, X. (2018). Patient-specific ECG Classification by Deeper CNN from Generic to Dedicated. *Neurocomputing* 314, 336–346. doi:10.1016/j.neucom.2018.06.068

Liu, F., Liu, C., Zhao, L., Zhang, X., Wu, X., Xu, X., et al. (2018). An Open Access Database for Evaluating the Algorithms of Electrocardiogram Rhythm and Morphology Abnormality Detection. *J Med. Imaging Hlth Inform.* 8 (7), 1368–1373. doi:10.1166/jmihi.2018.2442

Llamedo, M., and Martinez, J. P. (2010). Heartbeat Classification Using Feature Selection Driven by Database Generalization Criteria. *IEEE Trans. Biomed. Eng.* 58 (3), 616–625. doi:10.1109/TBME.2010.2068048

Lu, Y., Jiang, M., Wei, L., Zhang, J., Wang, Z., Wei, B., et al. (2021). Automated Arrhythmia Classification Using Depthwise Separable Convolutional Neural Network with Focal Loss. *Biomed. Signal Process. Control.* 69, 102843. doi:10.1016/j.bspc.2021.102843

Mar, T., Zaunseder, S., Martínez, J. P., Llamedo, M., and Poll, R. (2011). Optimization of ECG Classification by Means of Feature Selection. *IEEE Trans. Biomed. Eng.* 58 (8), 2168–2177. doi:10.1109/tbme.2011.2113395

Marcus, G. M. (2020). Evaluation and Management of Premature Ventricular Complexes. *Circulation* 141 (17), 1404–1418. doi:10.1161/circulationaha.119.042434

Moody, G. B., and Mark, R. G. (2001). The Impact of the MIT-BIH Arrhythmia Database. *IEEE Eng. Med. Biol. Mag.* 20 (3), 45–50. doi:10.1109/51.932724

Nair, V., and Hinton, G. E. (2010). "Rectified Linear Units Improve Restricted Boltzmann Machines," in International Conference on Machine Learning, 807–814.

Niu, J., Tang, Y., Sun, Z., and Zhang, W. (2020). Inter-patient ECG Classification with Symbolic Representations and Multi-Perspective Convolutional Neural Networks. *IEEE J. Biomed. Health Inform.* 24 (5), 1321–1332. doi:10.1109/jbhi.2019.2942938

Ozdemir, M. A., Ozdemir, G. D., and Guren, O. (2021). Classification of COVID-19 Electrocardiograms by Using Hexaxial Feature Mapping and Deep Learning. *BMC Med. Inform. Decis. Mak* 21 (1), 170. doi:10.1186/s12911-021-01521-x

Pathak, D., Shelhamer, E., Long, J., and Darrell, T. (2014). "Fully Convolutional Multi-Class Multiple Instance Learning," in International Conference on Learning Representations.

Perez Alday, E. A., Gu, A., Shah, A. J., Robichaux, C., Wong, A. I., Liu, C., et al. (2020). Classification of 12-lead ECGs: the Physionet/computing in Cardiology challenge 2020. *Physiol. Meas.* 41 (12). Article 124003. doi:10.1088/1361-6579/abc960

Pinheiro, P. O., and Collobert, R. (2015). "From Image-Level to Pixel-Level Labeling with Convolutional Networks," in IEEE/CVF Conference on Computer Vision and Pattern Recognition, 1713–1721.

Rahhal, M. M. A., Bazi, Y., AlHichri, H., Alajlan, N., Melgani, F., and Yager, R. R. (2016). Deep Learning Approach for Active Classification of Electrocardiogram Signals. *Inf. Sci.* 345, 340–354. doi:10.1016/j.ins.2016.01.082

Raj, S., and Ray, K. C. (2018). Sparse Representation of ECG Signals for Automated Recognition of Cardiac Arrhythmias. *Expert Syst. Appl.* 105, 49–64. doi:10.1016/j.eswa.2018.03.038

Rajan, D., and Thiagarajan, J. J. (2018). "A Generative Modeling Approach to Limited Channel ECG Classification," in Annual International Conference of the IEEE Engineering in Medicine and Biology Society, 2571–2574.

Reyna, M. S., NadiGu, A., Alday, P., Andres, E., Liu, C., Seyedi, S., et al. (2021). *Will Two Do? Varying Dimensions in Electrocardiography: The PhysioNet - Computing in Cardiology Challenge 2021*. Online. PhysioNet: PhysioNet. AvailableAccessed Feb. 25 2021]. doi:10.13026/jz9p-0m02

Richman, J. S., and Moorman, J. R. (2000). Physiological Time-Series Analysis Using Approximate Entropy and Sample Entropy. *Am. J. Physiology-Heart Circulatory Physiol.* 278 (6), H2039–H2049. doi:10.1152/ajpheart.2000.278.6.h2039

Roger, V. L., Go, A. S., Lloyd-Jones, D. M., Benjamin, E. J., Berry, J. D., Borden, W. B., et al. (2012). Executive Summary: Heart Disease and Stroke Statistics--2012 Update: a Report from the American Heart Association. *Circulation* 125 (22), 188–197. doi:10.1161/CIR.0b013e3182456d46

Ronneberger, O., Fischer, P., and Brox, T. (2015). "U-net: Convolutional Networks for Biomedical Image Segmentation," in 18th International Conference on Medical Image Computing and Computer-Assisted Intervention (MICCAI), 234–241.

Sana, F., Isselbacher, E. M., Singh, J. P., Heist, E. K., Pathik, B., and Armoundas, A. A. (2020). Wearable Devices for Ambulatory Cardiac Monitoring. *J. Am. Coll. Cardiol.* 75 (13), 1582–1592. doi:10.1016/j.jacc.2020.01.046

Simonyan, K., and Zisserman, A. (2014). *Very Deep Convolutional Networks for Large-Scale Image Recognition. arXiv preprint*.

Siontis, K. C., Noseworthy, P. A., Attia, Z. I., and Friedman, P. A. (2021). Artificial Intelligence-Enhanced Electrocardiography in Cardiovascular Disease Management. *Nat. Rev. Cardiol.* 18 (7), 465–478. doi:10.1038/s41569-020-00503-2

Srivastava, N., Hinton, G., Krizhevsky, A., Sutskever, I., and Salakhutdinov, R. (2014). Dropout: a Simple Way to Prevent Neural Networks from Overfitting. *J. Mach. Learn. Res.* 15 (1), 1929–1958.

Wagner, P., Strodthoff, N., Bousseljot, R. D., Kreiseler, D., Lunze, F. I., Samek, W., et al. (2020). PTB-XL, a Large Publicly Available Electrocardiography Dataset. *Sci. Data* 7 (1), 154–215. doi:10.1038/s41597-020-0495-6

Wang, G., Chen, M., Ding, Z., Li, J., Yang, H., and Zhang, P. (2021). Inter-patient ECG Arrhythmia Heartbeat Classification Based on Unsupervised Domain Adaptation. *Neurocomputing* 454, 339–349. doi:10.1016/j.neucom.2021.04.104

Wulan, N., Wang, W., Sun, P., Wang, K., Xia, Y., and Zhang, H. (2020). Generating Electrocardiogram Signals by Deep Learning. *Neurocomputing* 404, 122–136. doi:10.1016/j.neucom.2020.04.076

Zhai, X., Zhou, Z., and Tin, C. (2020). Semi-supervised Learning for ECG Classification without Patient-specific Labeled Data. *Expert Syst. Appl.* 158, 113411. doi:10.1016/j.eswa.2020.113411

Zhang, Z., Dong, J., Luo, X., Choi, K.-S., and Wu, X. (2014). Heartbeat Classification Using Disease-specific Feature Selection. *Comput. Biol. Med.* 46, 79–89. doi:10.1016/j.compbiomed.2013.11.019

Zheng, J., Zhang, J., Danioko, S., Yao, H., Guo, H., and Rakovski, C. (2020). A 12-lead Electrocardiogram Database for Arrhythmia Research Covering More Than 10,000 Patients. *Sci. Data* 7 (1), 48–8. doi:10.1038/s41597-020-0386-x

Zhou, B., Khosla, A., Lapedriza, A., Oliva, A., and Torralba, A. (2016). "Learning Deep Features for Discriminative Localization," in IEEE/CVF Conference on Computer Vision and Pattern Recognition, 2921–2929.

Zhou, Z.-H. (2018). A Brief Introduction to Weakly Supervised Learning. *Natl. Sci. Rev.* 5 (1), 44–53. doi:10.1093/nsr/nwx106

Conflict of Interest: The authors declare that the research was conducted in the absence of any commercial or financial relationships that could be construed as a potential conflict of interest.

Publisher's Note: All claims expressed in this article are solely those of the authors and do not necessarily represent those of their affiliated organizations, or those of the publisher, the editors and the reviewers. Any product that may be evaluated in this article, or claim that may be made by its manufacturer, is not guaranteed or endorsed by the publisher.

frontiers | Frontiers in Physiology

ORIGINAL RESEARCH
published: 02 May 2022
doi: 10.3389/fphys.2022.873821

Electrocardiography is Useful to Predict Postoperative Ventricular Arrhythmia in Patients Undergoing Cardiac Surgery: A Retrospective Study

Weichao Li, Weihua Liu and Heng Li*

The Sixth Affiliated Hospital of Guangzhou Medical University, Department of Anesthesiology, Qingyuan People's Hospital, QingYuan, China

OPEN ACCESS

Edited by:
Xin Li,
University of Leicester, United Kingdom

Reviewed by:
Ioana Mozos,
Victor Babes University of Medicine and Pharmacy, Romania
Sharen Lee,
The Chinese University of Hong Kong, China
Lütfü Bekar,
Hittite University, Turkey

***Correspondence:**
Weichao Li
215344404@qq.com

Specialty section:
This article was submitted to Cardiac Electrophysiology, a section of the journal Frontiers in Physiology

Received: *11 February 2022*
Accepted: *07 March 2022*
Published: *02 May 2022*

Citation:
Li W, Liu W and Li H (2022) Electrocardiography is Useful to Predict Postoperative Ventricular Arrhythmia in Patients Undergoing Cardiac Surgery: A Retrospective Study. Front. Physiol. 13:873821. doi: 10.3389/fphys.2022.873821

Background: Preoperative detection of high-/low-risk postoperative ventricular arrhythmia (POVA) patients using a noninvasive method is an important issue in the clinical setting. This study mainly aimed to determine the usefulness of several preoperative electrocardiographic (ECG) markers in the risk assessment of POVA with cardiac surgery.

Method: We enrolled 1024 consecutive patients undergoing cardiac surgery, and a total of 823 patients were included in the study. Logistic regression analysis determined preoperative ECG markers. A new risk predicting model were developed to predict occurrence of POVA, and the receiver operating characteristic curve (ROC) was used to validate this model.

Results: Of these, 337 patients experienced POVA, and 485 patients did not experience POVA in this retrospective study. Among 15 ECG markers, a univariate analysis found a strong association between POVA and preoperative VA, the R-wave in lead aVR, the QRS wave, index of cardiac electrophysiological balance (iCEB), QT interval corrected (QTc), Tpeak–Tend interval (Tpe) in lead V_2, the J wave in the inferolateral leads, pathological Q wave, and $S_{V1}+R_{V5}>35$ mm. Multivariate analysis showed that a preoperative J wave [adjusted odds ratio (AOR): 3.80; 95% CI: 1.88–7.66; $p < 0.001$], Tpe >112.5-ms (AOR: 2.80; 95% CI: 1.57–4.99; $p < 0.001$), and $S_{V1}+R_{V5}$ >35 mm (AOR: 2.92; 95% CI: 1.29–6.60; $p = 0.01$) were independently associated with POVA. A new risk predicting model were developed in predicting POVA.

Conclusion: The ECG biomarkers including J wave, Tpe >112.5 ms, and $S_{V1}+R_{V5}$ >35 mm were significantly predicted POVAs. A risk predicting model developed with electrocardiographic risk markers preoperatively predicted POVAs.

Keywords: postoperative ventricular arrhythmia, electrocardiographic markers, model, J wave, abnormal repolarization

INTRODUCTION

Postoperative ventricular arrhythmia (POVA) is a frequent complication after surgery. Some clinical studies have suggested that POVA increases short- and long-term mortality and further deteriorates heart failure postprocedure (El-Chami et al., 2012; Valderrábano et al., 2016a). It is important to identify patients at high risk of developing POVA so that targeted prophylactic therapy or alternative strategies can be given. Many clinical markers for the development of malignant arrhythmia in ischemic heart diseases have been reported, including episodes of conduction disturbance postprocedure, T wave peak and end (Tpe) as an independent predictor of arrhythmic events (Maury et al., 2015), fragmented QRS (fQRS) (Morita et al., 2008), an early repolarization (ER) pattern (Pieroni et al., 2008), short- or long-QT intervals (Schwartz and Ackerman, 2013; Bjerregaard, 2018), the existence of late potential, and the index of cardiac electrophysiological balance (iCEB: QT/QRS) (Lu et al., 2013). In addition, the markers can also be used to stratify patients for short- and long-term outcomes and to predict sudden cardiac death due to malignant ventricular arrhythmia (SCD-VA) (Erikssen et al., 2012; Tse et al., 2018). However, the evidence on whether preoperative markers can predict an increased risk of POVA is not clear in the surgical setting. In this study, we chiefly aimed to identify preoperative risk markers for POVA by paying attention to surface electrocardiographic parameters.

METHODS

Design, Setting, and Ethical Statement

Ethical approval for this retrospective cohort study (Ethical Committee approval number: IRB-202108-K4-amendment review-01) was provided by the Ethical Committee of the Sixth Affiliated Hospital of Guangzhou Medical University, QingYuan, GuangDong (Chairperson Prof JiFang Liu) on 12 November 2021. We registered the study protocol with the Chinese Clinical Trial Registration (identifier: ChiCTR2100052496).

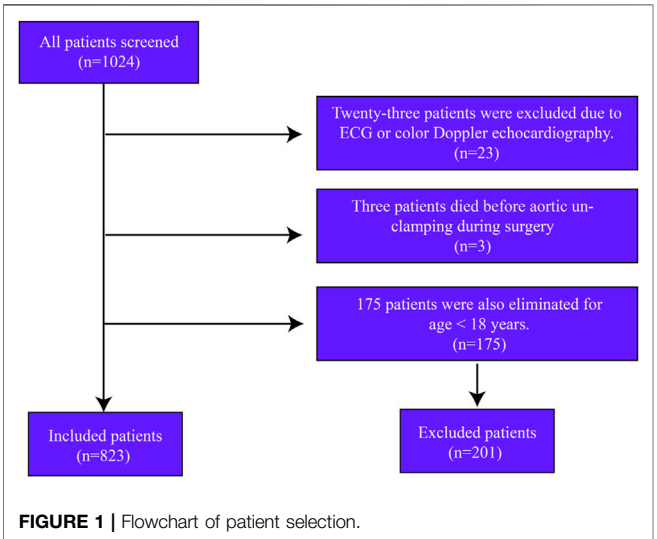

FIGURE 1 | Flowchart of patient selection.

Data Source

The current study used the data archived in the electronic medical record system of Southern Huiqiao and in the anesthesia care system database in the operating room. The exact date of death of in-hospital patients was recorded explicitly.

Study Population and Inclusion and Exclusion Criteria

In this retrospective cohort study, we screened 1024 consecutive patients undergoing open cardiac surgery from January 2013 to October 2021. Twenty-three patients were excluded due to the loss of ECG data. Only three patients who died during surgery were excluded from the analysis. Another 175 patients were excluded for age <18 years. A total of 823 patients were included in the study (**Figure 1**).

Postoperative Ventricular Arrhythmia

Rhythm disturbances were evaluated by continuous electrocardiographic monitoring from the time of the removal of the aortic clamp to 72 h postoperatively. POVA was defined as any premature ventricular beats, ventricular fibrillation, and bradyarrhythmias during the reperfusion period or in the postoperative period (Valderrábano et al., 2016b).

Electrocardiographic Measurements

After a quality check assessing recording speed (>25 mm/s), standard 12-lead ECGs (MedEx-ECG workstation, Madicks Co., Ltd., BeiJing, China) were recorded in the same way and were evaluated for the QRS width, QT or QTc interval, ST-segment level at the J point, Tpeak–Tend interval (Tpe), iCEB, $S_{V1}+R_{V5}$ >35 mm, QT/QTc ratio, and fQRS. The Tpeak–Tend interval (Tpe) is defined as the interval from the peak to the end of the T-wave in the V_2 lead; this interval was measured in three beats and then averaged (Demidova et al., 2019). The QT interval was automatically measured in lead II and corrected for the heart rate with the Bazett method. An S-wave in lead I was defined as a depth >0.1 mV and/or a width >40 ms (Calò et al., 2016). An R-wave in lead aVR was defined as an R-wave height >0.3 mV and/or an R-wave/q-wave ratio >0.75 (BabaiBigi et al., 2007). Regarding the defined short- or long-QT intervals, the current guideline recommends an upper normal limit of a corrected QT (QTc) interval of 440 ms and a lower limit of 340 ms (Schwartz and Ackerman, 2013; Campuzano et al., 2018). The presence of fQRS was defined as abnormal fragmentation within the QRS complex as four spikes in several leads as described previously. Based on the American Heart Association's scientific statement, the J wave or J point was defined as the amplitude of the elevation that had to be at least 1 mm above the baseline level at the ST-segment level, either as QRS slurring or notching (Patton et al., 2016). Atrial fibrillation was diagnosed as previously reviewed. The voltage sum $S_{V1}+R_{V5}$

TABLE 1 | Baseline Characteristics in patients with POVA and POVA-free.

	POVA (*n* = 338), % (*n*)	POVA-free (*n* = 485), % (*n*)	*p* Value
Age, yrs	52.2 ± 12.8	46.8 ± 11.6	0.062
Male	48.7% (165)	33.3% (160)	<0.001
Weight, kg	58.3 ± 11	54.3 ± 11.2	0.69
NYHA class ≥ III	53.8% (182)	66% (320)	<0.001
Medical history			
Dyslipidemia	9.5% (48)	5.3% Tse et al. (2021)	0.545
Hypertension	20.5% (69)	8.9% (43)	0.91
Diabetes	5.7% Takagi et al. (2013)	5.3% Tse et al. (2021)	0.027
Stroke	12.8% (43)	2.6% Calò et al. (2016)	0.023
COPD	3.2% Valderrábano et al. (2016b)	6.2% Shenasa et al. (2015)	0.057
Previous MI	10.2% Valderrábano et al. (2016a)	4.4% Rosenthal et al. (2015)	0.28
Cardiac cardioplegia			
HTK solution	64.7% (219)	19.1% (93)	0.038
Cold blood cardioplegia	35.2% (119)	80.8% (392)	0.038
Surgery variables			
GABG	27.4% (93)	10.7% (93)	0.005
Heart valve surgery	62.1% (210)	69.1% (336)	<0.001
Ventricular septal defect repair	2.5% Erikssen et al. (2012)	4% Takagi et al. (2013)	0.005
Auricular septal defect repair	7.6% Tse et al. (2021)	9.3% (45)	<0.001
Cardiac myxoma removal	3.8% Calò et al. (2016)	3.1% (Schwartz and Ackerman, 2013)	0.18
Others	6.8% Valderrábano et al. (2016a)	0.8% Erikssen et al. (2012)	0.14

MI, myocardial infarction; COPD, chronic obstructive pulmonary disease; GABG, coronary artery bypass grafting.

>35 mm using the Sokolow-Lyon voltage criteria was diagnosed as left ventricular hypertrophy (LVH) (Antikainen et al., 2003). iCEB was defined as QRS/QT.

Selection of Preoperative ECG Markers

We selected 15 potential ECG markers (**Figure 1**) of POVA risk according to previous reviews. Four potential markers were associated with depolarization/conduction disorders, including a QRS width>120 ms, a fragmented QRS in the precordial leads (fQRS), an S wave in lead I, and an R-wave in lead aVR. Five potential markers were implicated in repolarization disorders: the J wave or J point, short- or long-QT intervals, QT/QTc, and Tpe. One potential marker was related to an imbalance between repolarization and depolarization, that is, the iCEB. The following remaining potential markers were unclassified: atrial fibrillation (AF), ST-segment change, and $S_{V1}+R_{V5}$ >35 mm representing LVH.

Statistical Analysis

Data are expressed as the mean ± SD or median (interquartile range). Student's *t* test was performed to compare variables between groups, and categorical data and percentage frequencies were compared with the chi-square or Fisher exact test as appropriate. Univariate analysis was performed for associated POVA events. Multivariate analysis was used to estimate the occurrence risk for those predictors and identified independent risk factors relative to POVA. Receiver operating characteristic (ROC) curve and area under the curve (AUC) analyses were used to estimate the usefulness of preoperative Tpe for the prediction of POVA. Candidate variables were defined as a *p* value < 0.10 in univariate analysis and the 2-group comparison of each model. A *p* value <0.05 was considered statistically significant.

RESULTS

Population Characteristics

Altogether, 823 patients from the same hospital were included in this analysis, with women accounting for 51.3% of the entire cohort and a mean age of 54.7 years. A total of 546 patients underwent isolated valve surgery (66.3%), and 186 patients underwent isolated coronary artery bypass grafting (CABG) [22.6%]. Ventricular and auricular septal defect repair was conducted in 28 and 71 patients, respectively, and 28 patients underwent cardiac myxoma removal. In total, 44 patients underwent other isolated surgeries. POVA occurred in 338 patients (41%). **Table 1** shows the characteristics of patients with and without POVA. The proportions of patients with diabetes, stroke, and undergoing CABG or valve surgery were higher among patients with POVA than among patients without POVA. Patients with ventricular and auricular septal defect were, more often, POVA free. **Table 2** shows preoperative electrocardiographic data in patients with POVA and POVA-free. The proportions of patients with the presence of S-wave in lead I, R-wave in lead aVR, Tpe interval >112.5-ms, ST-segment change, J wave, Preoperative AF, and $S_{V1}+R_{V5}$ > 35 mm were higher among patients with POVA than among patients without POVA. Compared with the patients with POVA-free, the duration of QRS complex, Tpe interval, and QTc duration in the patient with POVA were prolonged.

TABLE 2 | Preoperative electrocardiographic data in patients with POVA and POVA-free.

	POVA (n = 338), % (n)	POVA-free (n = 485), % (n)	*p* Value
Depolarization/conduction disorders markers			
Duration of QRS complex, ms	96.2 ± 17.7	89.3 ± 14.9	<0.001
Fragmented QRS	17.9% (61)	12.0% (58)	0.054
S-wave in lead I	29.4% (100)	26.3% (128)	<0.001
R-wave in lead aVR	95.5% (323)	86.6% (420)	<0.001
Repolarization disorders markers			
Tpe interval in lead V_2, ms	115.1 ± 36.8	87.0 ± 24.1	<0.001
Tpe interval >112.5-ms	53.8% (182)	13.8% (67)	<0.001
QT duration, ms	382.6 ± 61.7	369.5 ± 50.1	0.024
QTc duration, ms	435.2 ± 50.1	415.6 ± 40.8	<0.001
QT/QTc ratio	0.9 ± 0.1	0.9 ± 0.1	0.486
Long- or short- QT intervals	55.7% (188)	39.7% (193)	0.189
ST-segment change	17.3% (58)	12.0% (58)	<0.001
J wave	69.2% (234)	18.7% (91)	<0.001
Abnormal depolarization-repolarization			
Combination of the J wave and fQRS	16.6% (56)	7.5% Moss et al. (2002)	<0.001
Unclassified markers			
Preoperative AF	19.8% (67)	25.4% (123)	<0.001
Preoperative VA	29.4% (100)	16.5% (80)	0.07
iCEB (QRS/QT)	0.3 ± 0.1	0.2 ± 0.1	0.081
Pathological Q wave	4.4% Schwartz and Ackerman, (2013)	0.8% (Morita et al. (2008)	0.092
$S_{V1}+R_{SV5}$ > 35 mm	16.6% (56)	4.9% Panikkath et al. (2011)	<0.001
Heart rate, bpm	80.8 ± 19.9	79.5 ± 19.3	0.485

AF, atrial fibrillation; VA, ventricular arrhythmia; iCEB, the index of cardiac electrophysiological balance.

Univariate Analysis in Preoperative ECG

Table 3 shows the results of the univariable analysis. In univariate analysis, heart rate, fQRS, the S wave in lead I, QT/QTc, ST-segment change, and preoperative AF did not predict POVA. Preoperative VA, the R-wave in lead aVR, QRS duration, iCEB, QT interval, QTc interval, Long- or short- QT intervals, Tpe in lead V_2, inferolateral J wave, J wave + fQRS, Q wave, and $S_{V1}+R_{V5}$ > 35 mm were associated with POVA.

Multivariate Analysis of Preoperative ECG Parameters and Receiver Operating Characteristic Analysis

The multivariate logistic regression analysis identified the following preoperative factors that could predict POVA: the J wave (AOR: 3.80; 95% CI: 1.88–7.66; $p < 0.001$), and $S_{V1}+R_{V5}$ > 35 mm (AOR: 2.92; 95% CI: 1.29–6.60; $p = 0.01$). Each 10-ms decrease in Tpe was associated with a 16% increase in the risk for POVA (AOR: 0.984; 95% CI: 0.97–0.99; $p < 0.001$). In addition, ROC curve analysis revealed the utility of Tpe for the prediction of POVA. The AUC was 0.724 (95% CI 0.67–0.77, $p < 0.0001$), with discrimination at 112.5-ms yielding a sensitivity of 54.5% and specificity of 87.5% (**Supplementary Figure S1**). Subsequently, multivariate analysis again identified that preoperative Tpe >112.5 ms was independently associated with POVA (AOR: 2.80; 95% CI: 1.57–4.99; $p < 0.001$).

Construction and Validation of a POVA Risk Prediction Model

Points were assigned to each risk predictor according to its number, enabling the development of a model that predicted the risk of POVA. The presence of the J wave was assigned 1 point, the presence of the $S_{V1}+R_{V5}$ > 35 mm wave was assigned 1 point, and the presence of the Tpe >112.5-ms wave was assigned one point. Thus, the POVA risk prediction model was developed with a range of 0–3 points based on this calculation. The rates of POVA and the risk scores in the cohorts are shown in **Figure 2**. In addition, the established ROC curve and AUC were validated in the model for the total cohort (Supplement Figure 1). The AUC for this model was 0.797 ($p < 0.0001$).

DISCUSSION

The present study showed the following findings (El-Chami et al., 2012): a preoperative J wave, $S_{V1}+R_{V5}$ >35 mm, and Tpe >112.5 ms were independently associated with POVA, and (Valderrábano et al., 2016a) the risk prediction model could preoperatively predict the risk of POVA.

Preoperative Electrocardiographic Markers of POVA.

A preoperative J wave was independently associated with POVA. There is a long-established concept that the J wave is benign. This concept has been significantly contradicted in recent years. Some studies have shown that the presence of the J wave was associated with a higher incidence of ventricular tachyarrhythmia (VT/VF) in patients with Brugada syndrome (Takagi et al., 2013), short QT syndrome, noncompaction cardiomyopathy (Caliskan et al., 2012), and ischemic heart disease (Patel et al., 2012). This evidence implies that more arrhythmogenic susceptibility appears in patients with the

TABLE 3 | Analyses of independent electrocardiographic markers of POVA using logistic regression models.

Variables	Univariate		Multivariable	
	Adjusted OR (95% CI)<	*p* Value	Adjusted OR (95% CI)	*p* Value
J wave	9.75 (6.04–15.72)	<0.001	3.80 (1.88–7.66)	<0.001
Tpe >112.5 ms	7.26 (4.43–11.89)	<0.001	2.80 (1.57–4.99)	<0.001
$S_{V1}+R_{SV5}$ > 35 mm	3.87 (1.85–8.10)	<0.001	2.92 (1.29–6.60)	0.01
Preoperative VA	2.11 (1.29–3.45)	0.003	—	—
R-wave in lead aVR	3.29 (1.40–7.70)	0.006	—	—
QRS duration	0.97 (0.96–0.98)	<0.001	—	—
ICEB	0.057 (0.002–1.51)	0.087	—	—
QT interval	0.99 (0.992–1.00)	0.027	—	—
QTc interval	0.99 (0.985–0.995)	<0.001	—	—
Combination of the J wave and fQRS	2.43 (1.27–4.66)	0.007	—	—
Q wave	5.21 (1.06–25.4)	0.041	—	—
Heart rate, bpm	0.99 (0.98–1.00)	0.484	—	—
FQRS	1.59 (0.89–2.83)	0.11	—	—
the S wave in lead I	1.16 (0.74–1.84)	0.500	—	—
QT/QTc	1.94 (0.29–12.65)	0.486	—	—
ST-segment change	1.52 (0.85–2.72)	0.151	—	—
Preoperative AF	0.72 (0.44–1.19)	0.206	—	—

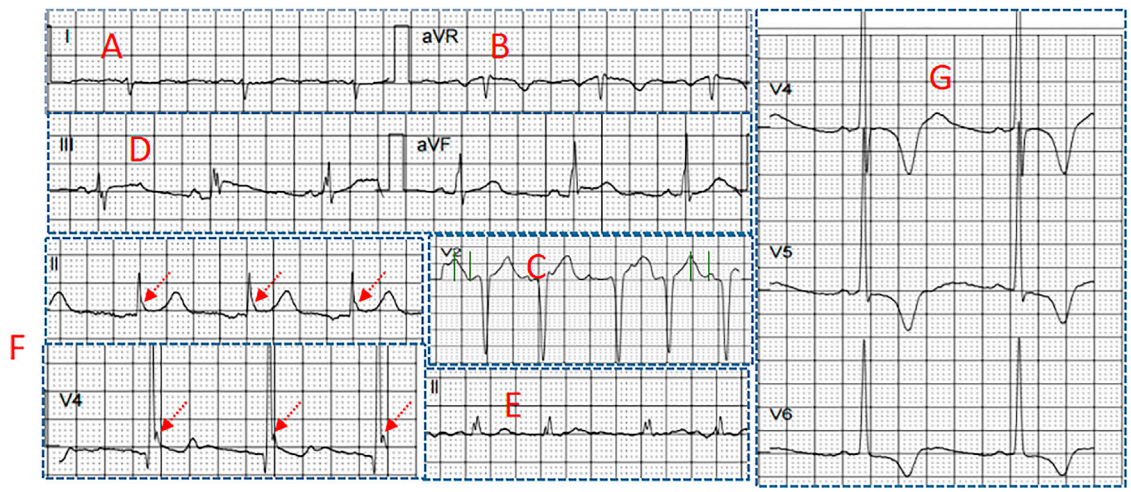

FIGURE 2 | Several electrocardiographic markers for POVA **(A)** S-wave in lead I **(B)** R-wave in lead aVR **(C)** Tpeak-Tend interval in lead V_2 **(D)** Combination of fragmented QRS and J wave **(E)** fragmented QRS **(F)** J wave in the inferior leads, and (G) $S_{V1}+R_{V5}$ >35 mm.

presence of the J wave. Under surgical conditions and global cardiac ischemic factors, there is a general risk of POVA in patients. Our finding that a preoperative J wave was more common in patients experiencing POVA is in agreement with these previous findings. The underlying mechanism may be that the disparity of outward Ito current density between segments of the ventricular epicardium has the potential to cause ventricular tachyarrhythmias.

In addition, Tpe, representing cardiac repolarization inhomogeneity, was implicated in POVA, and ROC curve and multivariate analyses considered that Tpe >112.5 ms was independently associated with POVA. Todd et al. suggested that the T-peak to T-end interval predicts ventricular tachyarrhythmia in a primary prevention population with systolic cardiomyopathy (Rosenthal et al., 2015). The T peak-Tend interval was previously associated with endothelial dysfunction, arterial stiffness and impaired coronary perfusion (Mozos, 2015). Ragesh et al. considered that a prolonged Tpeak-to-Tend interval on resting ECG was associated with increased VF for sudden cardiac death (Panikkath et al., 2011). Tpeak-Tend interval was reported to be prolonged in hypertensive, overweight and obese patients, smokers, and persons with prolonged exposure to shift work (Mozos and Filimon, 2013). Some studies suggested that repolarization variability predict ventricular arrhythmogenesis in mouse or human hearts (Castro-Torres et al., 2015; Tse et al., 2021). Our finding is in accordance with previous reviews of Tpe predicting cardiac arrhythmias. The ventricular myocardium includes three electrophysiologically distinct cell types-endocardial, epicardial,

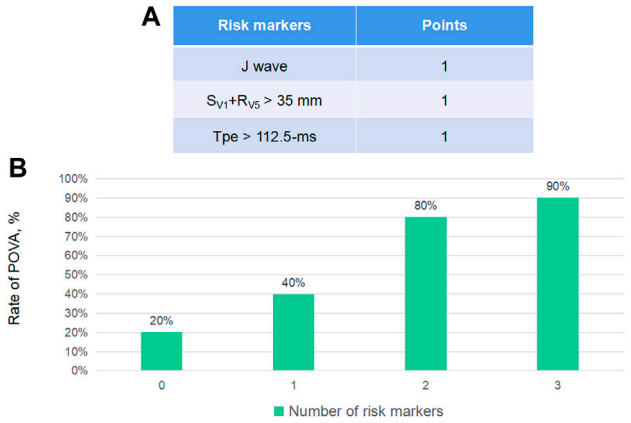

FIGURE 3 | Electrocardiographic markers for POVA and the development of the POVA risk score model, According to the number of risk markers, we assigned points **(A)** and subsequently developed a model predicting POVA **(B)**.

and subendocardial M cells. Tpe corresponds to the transmural dispersion of repolarization in the ventricular myocardium, a period during which the epicardium has repolarized and is fully excitable, but the M cells are still in the process of repolarization and are vulnerable to the occurrence of early afterdepolarizations. If conditions permit, these early afterdepolarizations can lead to reentry, resulting in polymorphic ventricular tachycardia or ventricular fibrillation (Antzelevitch, 2007).

$S_{V1}+R_{V5}$ >35 mm was considered a risk marker of POVA. $S_{V1}+R_{SV5}$ >35 mm represents left ventricular hypertrophy (LVH) according to the Sokolow-Lyon ECG criteria. Seth R. et al. found that ECG LVH was an independent predictor of nonoperative arrhythmic events (Bender et al., 2012). A previous review suggested that left ventricular hypertrophy (LVH) poses an independent risk of increased morbidity and mortality, including atrial arrhythmias, ventricular arrhythmias, and sudden cardiac death (Shenasa et al., 2015). The gap junction surface area is reduced, and its unusual distribution may decrease the threshold of arrhythmogenesis in patients when undergoing cardiac surgery (Wolk, 2000).

A POVA Risk Prediction Model

According to the number of risk markers, we assigned points and subsequently developed a model predicting POVA. The POVA risk prediction model was developed with a range of 0–3 points based on this calculation in **Figure 3A**. The rates of POVA and its risk scores in the cohorts were the highest in the two-point position and did rise by points increased in **Figure 3B**. Subsequently, ROC curve analysis was performed for the validation of the model. The AUC for this model was 0.797 ($p < 0.0001$). The model is simple, efficient and practical. Patients with ventricular and auricular septal defect were, more often, POVA free. There is rarely the relationship between some types of operation including ventricular and auricular septal defect and postoperative arrhythmia. Potential reasons probably were that the patients undergoing the mentioned types of surgery were younger.

Prediction Factors and Clinic Outcomes of a POVA

An abundant study suggested that POVA is associated with increased short- and long-term mortality after cardiac surgery (CS). Previous studies have suggested that have shown that POVA predicts higher (21.7–28.9%) in-hospital mortality compared with control (1.4–1.9%) (Ascione et al., 2004; Yeung-Lai-Wah et al., 2004). Besides, Most deaths in patients with POVA occur in the hospital and within the first year after discharge (El-Chami et al., 2012). Rodrigo et al. have suggested that developing a new POVA increases the risk of in-hospital mortality independently in the medical intensive care unit (Valderrábano et al., 2016a). Older age, female sex, systemic hypertension, peripheral vascular disease (PVD), lower ejection fraction (EF), and emergent surgery are associated with a higher risk of POVA, whereas off-pump surgery seems to be protective (Yeung-Lai-Wah et al., 2004; El-Chami et al., 2012). Some studies looking at risk of POVA after CS found that patients with POVA are older than patients without POVA (Steinberg et al., 1999). Ascione et al. reported a trend toward a reduction in POVA with the use of off-pump surgery compared with on-pump. A group of patients with LV dysfunction associated with a previous MI have been reported that common POVA (Moss et al., 2002). The presence of PVD in some studies is found to be predictive of POVA and operative mortality (Loponen et al., 2002; Bonacchi et al., 2020). Our previous study has been suggested that systemic hypertension was an independent risk factor of post-operative ventricular fibrillation. The need for emergent CABG also strongly predicted POVA. Emergency CABG generally carries a higher risk of in-hospital mortality and added requirements for hemodynamic support (Yang et al., 2005).

Limitations

These electrocardiographic markers are dynamic; thus, the true prevalence of this coexistence is difficult to evaluate. Various methods to measure the Tpe interval have been used in other studies. Our results may not be reproducible with other Tpe measurement methods. In addition, limits of the Bazett formula and the heterogeneity of the studied population also were considered necessarily. This retrospective study evaluated patients from a single hospital, existing the observational bias. There is the limited clinical applicability of the findings in the absence of other clinical and biochemical markers.

CONCLUSION

The ECG biomarkers including J wave, Tpe >112.5 ms, and $S_{V1}+R_{SV5}$ >35 mm were significantly predicted POVAs. A risk predicting model developed with electrocardiographic risk markers preoperatively predicted POVAs.

DATA AVAILABILITY STATEMENT

The raw data supporting the conclusion of this article will be made available by the authors, without undue reservation.

ETHICS STATEMENT

The studies involving human participants were reviewed and approved by the Ethical approval for this retrospective cohort study (Ethical Committee approval number: IRB-202108-K4-amendment review-01) was provided by the Ethical Committee of the Sixth Affiliated Hospital of Guangzhou Medical University, QingYuan, GuangDong (Chairperson JiFang Liu) on 12 November 2021. We registered the study protocol with the Chinese Clinical Trial Registration (identifier: ChiCTR2100052496). The patients/participants provided their written informed consent to participate in this study.

AUTHOR CONTRIBUTIONS

Author contributions: WLi designed the research; HLconducted the review and editing; and WLiu wrote the paper.

SUPPLEMENTARY MATERIAL

The Supplementary Material for this article can be found online at: https://www.frontiersin.org/articles/10.3389/fphys.2022.873821/full#supplementary-material

REFERENCES

Antikainen, R., Grodzicki, T., Palmer, A. J., Beevers, D. G., Coles, E. C., Webster, J., et al. (2003). The Determinants of Left Ventricular Hypertrophy Defined by Sokolow-Lyon Criteria in Untreated Hypertensive Patients. *J. Hum. Hypertens.* 17 (3), 159–164. doi:10.1038/sj.jhh.1001523

Antzelevitch, C. (2007). Role of Spatial Dispersion of Repolarization in Inherited and Acquired Sudden Cardiac Death Syndromes. *Am. J. Physiology-Heart Circulatory Physiol.* 293 (4), H2024–H2038. doi:10.1152/ajpheart.00355.2007

Ascione, R., Reeves, B. C., Santo, K., Khan, N., and Angelini, G. D. (2004). Predictors of New Malignant Ventricular Arrhythmias after Coronary Surgery. *J. Am. Coll. Cardiol.* 43 (9), 1630–1638. doi:10.1016/j.jacc.2003.11.056

Babai Bigi, M. A., Aslani, A., and Shahrzad, S. (2007). aVR Sign as a Risk Factor for Life-Threatening Arrhythmic Events in Patients with Brugada Syndrome. *Heart Rhythm* 4 (8), 1009–1012. doi:10.1016/j.hrthm.2007.04.017

Bender, S. R., Friedman, D. J., Markowitz, S. M., Lerman, B. B., and Okin, P. M. (2012). Electrocardiographic Left Ventricular Hypertrophy Predicts Arrhythmia and Mortality in Patients with Ischemic Cardiomyopathy. *J. Interv. Card. Electrophysiol.* 34 (3), 237–245. doi:10.1007/s10840-011-9661-2

Bjerregaard, P. (2018). Diagnosis and Management of Short QT Syndrome. *Heart Rhythm* 15 (8), 1261–1267. doi:10.1016/j.hrthm.2018.02.034

Bonacchi, M., Parise, O., Matteucci, F., Tetta, C., Moula, A. I., Micali, L. R., et al. (2020). Is Peripheral Artery Disease an Independent Predictor of Isolated Coronary Artery Bypass Outcome? *Heart Lung Circ.* 29 (10), 1502–1510. doi:10.1016/j.hlc.2020.01.013

Caliskan, K., Ujvari, B., Bauernfeind, T., A.M.J. Theuns, D., Van Domburg, R. T., Akca, F., et al. (2012). The Prevalence of Early Repolarization in Patients with Noncompaction Cardiomyopathy Presenting with Malignant Ventricular Arrhythmias. *J. Cardiovasc. Electrophysiol.* 23 (9), 938–944. doi:10.1111/j.1540-8167.2012.02325.x

Calò, L., Giustetto, C., Martino, A., Sciarra, L., Cerrato, N., Marziali, M., et al. (2016). A New Electrocardiographic Marker of Sudden Death in Brugada Syndrome: The S-Wave in Lead I. *J. Am. Coll. Cardiol.* 67 (12), 1427–1440. doi:10.1016/j.jacc.2016.01.024

Campuzano, O., Sarquella-Brugada, G., Cesar, S., Arbelo, E., Brugada, J., and Brugada, R. (2018). Recent Advances in Short QT Syndrome. *Front. Cardiovasc. Med.* 5, 149. doi:10.3389/fcvm.2018.00149

Castro-Torres, Y., Carmona-Puerta, R., and Katholi, R. E. (2015). Ventricular Repolarization Markers for Predicting Malignant Arrhythmias in Clinical Practice. *Wjcc* 3 (8), 705–720. doi:10.12998/wjcc.v3.i8.705

Demidova, M. M., Carlson, J., Erlinge, D., Azarov, J. E., and Platonov, P. G. (2019). Prolonged Tpeak-Tend Interval Is Associated with Ventricular Fibrillation during Reperfusion in ST-Elevation Myocardial Infarction. *Int. J. Cardiol.* 280, 80–83. doi:10.1016/j.ijcard.2019.01.008

El-Chami, M. F., Sawaya, F. J., Kilgo, P., Stein, W., Halkos, M., Thourani, V., et al. (2012). Ventricular Arrhythmia after Cardiac Surgery. *J. Am. Coll. Cardiol.* 60 (25), 2664–2671. doi:10.1016/j.jacc.2012.08.1011

Erikssen, G., Liestøl, K., Gullestad, L., Haugaa, K. H., Bendz, B., and Amlie, J. P. (2012). The Terminal Part of the QT Interval (T Peak to T End): a Predictor of Mortality after Acute Myocardial Infarction. *Ann. Noninvasive Electrocardiol.* 17 (2), 85–94. doi:10.1111/j.1542-474x.2012.00493.x

Loponen, P., Taskinen, P., Laakkonen, E., Nissinen, J., Peltola, T., Wistbacka, J.-O., et al. (2002). Peripheral Vascular Disease as Predictor of Outcome after Coronary Artery Bypass Grafting. *Scand. J. Surg.* 91 (2), 160–165. doi:10.1177/145749690209100205

Lu, H. R., Yan, G.-X., and Gallacher, D. J. (2013). A new biomarker - index of Cardiac Electrophysiological Balance (iCEB) - plays an important role in drug-induced cardiac arrhythmias: beyond QT-prolongation and Torsades de Pointes (TdPs). *J. Pharmacol. Toxicol. Methods* 68 (2), 250–259. doi:10.1016/j.vascn.2013.01.003

Maury, P., Sacher, F., Gourraud, J.-B., Pasquié, J.-L., Raczka, F., Bongard, V., et al. (2015). Increased Tpeak-Tend Interval Is Highly and Independently Related to Arrhythmic Events in Brugada Syndrome. *Heart Rhythm* 12 (12), 2469–2476. doi:10.1016/j.hrthm.2015.07.029

Morita, H., Kusano, K. F., Miura, D., Nagase, S., Nakamura, K., Morita, S. T., et al. (2008). Fragmented QRS as a Marker of Conduction Abnormality and a Predictor of Prognosis of Brugada Syndrome. *Circulation* 118 (17), 1697–1704. doi:10.1161/circulationaha.108.770917

Moss, A. J., Zareba, W., Hall, W. J., Klein, H., Wilber, D. J., Cannom, D. S., et al. (2002). Prophylactic Implantation of a Defibrillator in Patients with Myocardial Infarction and Reduced Ejection Fraction. *N. Engl. J. Med.* 346 (12), 877–883. doi:10.1056/nejmoa013474

Mozos, I., and Filimon, L. (2013). QT and Tpeak-Tend Intervals in Shift Workers. *J. Electrocardiol.* 46 (1), 60–65. doi:10.1016/j.jelectrocard.2012.10.014

Mozos, I. (2015). The Link between Ventricular Repolarization Variables and Arterial Function. *J. Electrocardiol.* 48 (2), 145–149. doi:10.1016/j.jelectrocard.2014.11.008

Panikkath, R., Reinier, K., Uy-Evanado, A., Teodorescu, C., Hattenhauer, J., Mariani, R., et al. (2011). Prolonged Tpeak-To-Tend Interval on the Resting ECG Is Associated with Increased Risk of Sudden Cardiac Death. *Circ. Arrhythm Electrophysiol.* 4 (4), 441–447. doi:10.1161/circep.110.960658

Patel, R. B., Ilkhanoff, L., Ng, J., Chokshi, M., Mouchli, A., Chacko, S. J., et al. (2012). Clinical Characteristics and Prevalence of Early Repolarization Associated with Ventricular Arrhythmias Following Acute ST-Elevation Myocardial Infarction. *Am. J. Cardiol.* 110 (5), 615–620. doi:10.1016/j.amjcard.2012.04.042

Patton, K. K., Ellinor, P. T., Ezekowitz, M., Kowey, P., Lubitz, S. A., Perez, M., et al. (2016). Electrocardiographic Early Repolarization. *Circulation* 133 (15), 1520–1529. doi:10.1161/cir.0000000000000388

Pieroni, M., Bellocci, F., and Crea, F. (2008). Sudden Cardiac Arrest Associated with Early Repolarization. *N. Engl. J. Med.* 359 (7), 761–762. doi:10.1056/NEJMc081272

Rosenthal, T. M., Stahls, P. F., 3rd, Abi Samra, F. M., Bernard, M. L., Khatib, S., Polin, G. M., et al. (2015). T-peak to T-End Interval for Prediction of Ventricular Tachyarrhythmia and Mortality in a Primary Prevention Population with Systolic Cardiomyopathy. *Heart Rhythm* 12 (8), 1789–1797. doi:10.1016/j.hrthm.2015.04.035

Schwartz, P. J., and Ackerman, M. J. (2013). The Long QT Syndrome: a Transatlantic Clinical Approach to Diagnosis and Therapy. *Eur. Heart J.* 34 (40), 3109–3116. doi:10.1093/eurheartj/eht089

Shenasa, M., Shenasa, H., and El-Sherif, N. (2015). Left Ventricular Hypertrophy and Arrhythmogenesis. *Card. Electrophysiol. Clin.* 7 (2), 207–220. doi:10.1016/j.ccep.2015.03.017

Steinberg, J. S., Gaur, A., Sciacca, R., and Tan, E. (1999). New-onset Sustained Ventricular Tachycardia after Cardiac Surgery. *Circulation* 99 (7), 903–908. doi:10.1161/01.cir.99.7.903

Takagi, M., Aonuma, K., Sekiguchi, Y., Yokoyama, Y., Aihara, N., and Hiraoka, M. (2013). The Prognostic Value of Early Repolarization (J Wave) and ST-Segment Morphology after J Wave in Brugada Syndrome: Multicenter Study in Japan. *Heart Rhythm* 10 (4), 533–539. doi:10.1016/j.hrthm.2012.12.023

Tse, G., Gong, M., Meng, L., Wong, C. W., Bazoukis, G., Chan, M. T. V., et al. (2018). Predictive Value of Tpeak - Tend Indices for Adverse Outcomes in Acquired QT Prolongation: A Meta-Analysis. *Front. Physiol.* 9, 1226. doi:10.3389/fphys.2018.01226

Tse, G., Hao, G., Lee, S., Zhou, J., Zhang, Q., Du, Y., et al. (2021). Measures of Repolarization Variability Predict Ventricular Arrhythmogenesis in Heptanol-Treated Langendorff-Perfused Mouse Hearts. *Curr. Res. Physiol.* 4, 125–134. doi:10.1016/j.crphys.2021.04.001

Valderrábano, R. J., Blanco, A., Santiago-Rodriguez, E. J., Miranda, C., Rivera-Del Rio Del Rio, J., Ruiz, J., et al. (2016 Jan 22). Risk Factors and Clinical Outcomes of Arrhythmias in the Medical Intensive Care Unit. *J. Intensive Care* 4, 9. doi:10.1186/s40560-016-0131-x

Valderrábano, R. J., Blanco, A., and Santiago-Rodriguez, E. J. (2016). Risk Factors and Clinical Outcomes of Arrhythmias in the Medical Intensive Care Unit. *J. Intensive Care* 4, 9.

Wolk, R. (2000). Arrhythmogenic Mechanisms in Left Ventricular Hypertrophy. *Europace* 2 (3), 216–223. doi:10.1053/eupc.2000.0110

Yang, E. H., Gumina, R. J., Lennon, R. J., Holmes, D. R., Rihal, C. S., and Singh, M. (2005). Emergency Coronary Artery Bypass Surgery for Percutaneous Coronary Interventions. *J. Am. Coll. Cardiol.* 46 (11), 2004–2009. doi:10.1016/j.jacc.2005.06.083

Yeung-Lai-Wah, J. A., Qi, A., McNeill, E., Abel, J. G., Tung, S., Humphries, K. H., et al. (2004). New-onset Sustained Ventricular Tachycardia and Fibrillation Early after Cardiac Operations. *Ann. Thorac. Surg.* 77 (6), 2083–2088. doi:10.1016/j.athoracsur.2003.12.020

Conflict of Interest: The authors declare that the research was conducted in the absence of any commercial or financial relationships that could be construed as a potential conflict of interest.

frontiers | Frontiers in Physiology

ORIGINAL RESEARCH
published: 12 August 2022
doi: 10.3389/fphys.2022.794761

Circle Method for Robust Estimation of Local Conduction Velocity High-Density Maps From Optical Mapping Data: Characterization of Radiofrequency Ablation Sites

Jimena G. Siles-Paredes[1,2], Christopher J. Crowley[3], Flavio H. Fenton[3], Neal Bhatia[4], Shahriar Iravanian[4], Italo Sandoval[2], Stefan Pollnow[5], Olaf Dössel[5], João Salinet[1,2†] and Ilija Uzelac[3†]*

[1]Graduate Program in Biotechnoscience, Federal University of ABC, São Paulo, Brazil, [2]HEartLab, Federal University of ABC, São Paulo, Brazil, [3]Georgia Institute of Technology, School of Physics, Atlanta, GA, United States, [4]Division of Cardiology, Section of Electrophysiology, Emory University Hospital, Atlanta, GA, United States, [5]Karlsruhe Institute of Technology (KIT)/Institute of Biomedical Engineering, Karlsruhe, Germany

OPEN ACCESS

Edited by:
Xin Li,
University of Leicester,
United Kingdom

Reviewed by:
Caroline Helen Roney,
Queen Mary University of London,
United Kingdom
Gil Bub,
McGill University, Canada

***Correspondence:**
Jimena G. Siles-Paredes
jimena.gabriela@ufabc.edu.br

†These authors have contributed equally to this work and share senior authorship

Specialty section:
This article was submitted to Cardiac Electrophysiology, a section of the journal Frontiers in Physiology

Received: 14 October 2021
Accepted: 15 June 2022
Published: 12 August 2022

Citation:
Siles-Paredes JG, Crowley CJ, Fenton FH, Bhatia N, Iravanian S, Sandoval I, Pollnow S, Dössel O, Salinet J and Uzelac I (2022) Circle Method for Robust Estimation of Local Conduction Velocity High-Density Maps From Optical Mapping Data: Characterization of Radiofrequency Ablation Sites. Front. Physiol. 13:794761. doi: 10.3389/fphys.2022.794761

Conduction velocity (CV) slowing is associated with atrial fibrillation (AF) and reentrant ventricular tachycardia (VT). Clinical electroanatomical mapping systems used to localize AF or VT sources as ablation targets remain limited by the number of measuring electrodes and signal processing methods to generate high-density local activation time (LAT) and CV maps of heterogeneous atrial or trabeculated ventricular endocardium. The morphology and amplitude of bipolar electrograms depend on the direction of propagating electrical wavefront, making identification of low-amplitude signal sources commonly associated with fibrotic area difficulty. In comparison, unipolar electrograms are not sensitive to wavefront direction, but measurements are susceptible to distal activity. This study proposes a method for local CV calculation from optical mapping measurements, termed the circle method (CM). The local CV is obtained as a weighted sum of CV values calculated along different chords spanning a circle of predefined radius centered at a CV measurement location. As a distinct maximum in LAT differences is along the chord normal to the propagating wavefront, the method is adaptive to the propagating wavefront direction changes, suitable for electrical conductivity characterization of heterogeneous myocardium. In numerical simulations, CM was validated characterizing modeled ablated areas as zones of distinct CV slowing. Experimentally, CM was used to characterize lesions created by radiofrequency ablation (RFA) on isolated hearts of rats, guinea pig, and explanted human hearts. To infer the depth of RFA-created lesions, excitation light bands of different penetration depths were used, and a beat-to-beat CV difference analysis was performed to identify CV alternans. Despite being limited to laboratory research, studies based on CM with optical mapping may lead to new translational insights into better-guided ablation therapies.

Keywords: conduction velocity (CV), optical mapping, delayed activation, catheter ablation, local activation time, conduction slowing

1 INTRODUCTION

Persistent cardiac arrhythmia can lead to heart failure, and heart failure can lead to arrhythmia. atrial fibrillation (AF) is the most common sustained cardiac arrhythmia, affecting 2.9% of the worldwide population (Benjamin et al., 2019). AF is associated with significant hemodynamic and thromboembolic complications (Zimerman et al., 2009). In comparison, ventricular tachycardia (VT) usually occurs in structurally diseased hearts.

Conduction velocity (CV) slowing is one of the determinants for AF vulnerability (Narayan et al., 2011), preceding AF initiation (Lalani et al., 2012), and is responsible for AF perpetuation (Shinagawa et al., 2000). VT initiation and persistence also depend on CV slowing (Moe et al., 1964; Allessie et al., 1977; Rensma et al., 1988). When an excitation wave encounters a zone of conduction block, it may propagate around the zone and reenter the previously unexcited region, reexciting it, repetitively (Rudy, 2012). As such, CV slowing facilitates reentry (Nattel et al., 2005) as for a reentrant wave to encounter an excitable tissue recovered from refractory phase, the propagating time around the block zone must be longer than the refractory period (Spector, 2013).

At the cellular level, CV slowing results from ionic remodeling or cell-to-cell uncoupling, leading to decreased excitability. For example, dilatation of the left atrium results in gap junctions remodeling (Takeuchi et al., 2006) and formation of atrial interstitial fibrosis, resulting in CV slowing due to reduced electrical conductivity between myocytes and fibroblasts (Vasquez et al., 2010; Thompson et al., 2011). Dilatation of ventricular tissue also reduces electrical conductivity, resulting in CV slowing (El-Sherif et al., 1987). This leads to dispersion of repolarization (Kuo et al., 1983), contributing to spatially discordant alternans (Chen et al., 2017; Uzelac et al., 2017, 2021), and arrhythmia susceptibility. Among these reasons, it is important to identify local CV changes at the high spatiotemporal resolution to identify and characterize regions of delayed activation to better understand the mechanism leading to arrhythmia (Irie et al., 2015b).

Radiofrequency catheter ablation (RFA) is the most effective invasive treatment for the termination and prevention of AF and VT recurrence, creating tissue lesions through thermal injury. Tissue sustains heating damage in direct contact with a catheter tip via resistive heating, while deeper tissue is damaged through convective heat transfer. Lesion formation is based on the assumption that heat transfer has a predictable profile in homogeneous tissue, and the profile of RFA-created lesions depends on many factors such as delivered RFA power and duration, temperature increase, catheter pressure force, catheter–tissue impedance, and the location of the ground patch.

While the lesion profile is predictable for homogeneous myocardium, persistent AF or VT may be caused by the reentrant waves originating from islets of heterogeneous myocardium within the scar, which can be buried inside the myocardial wall. The common RFA strategy is to identify clinically relevant scar tissue and deliver ablative energy to homogenize the scar. However, the effects of RFA on fibrotic tissue are poorly understood, as heat transfer prediction is challenging in contrast to heterogeneous tissue. Lesion formation depends on electric impedance and increases within scar tissue. Only 10% of RFA applications for scar homogenization resemble the expected lesion pattern (Barkagan et al., 2019). Additionally, adipose cells effectively shield the surrounding myocytes from RFA thermal injury (Sasaki et al., 2015). This imposes challenges in ablation treatment for VT, as one of the ablation goals is to create a lesion across the thick ventricular wall, which was significantly improved with the advent of irrigated catheter tips (Wittkampf and Nakagawa, 2006).

1.1 Measurement of CV

1.1.1 Clinical Practice: Catheter Mapping-Based Measurement of CV

CV measurement has multiple potential benefits in clinical practice, especially during ablation procedures of complex arrhythmias. These benefits include mapping and localizing the substrate suitable for ablation and assessing the quality and depth of ablation lesions. However, CV measurement is not a standard part of such procedures despite all the potential benefits due to technical difficulties. Accurate determination of CV changes at a high spatiotemporal resolution to identify and localize areas of delayed activation is challenging in clinical practice. Instead, the focus during ablation is on the amplitude and fractionation of local electrograms. On the electrograms, the areas of interest for ablation commonly present as low-amplitude potentials and are characterized as arrhythmogenic substrates (Fukumoto et al., 2016; Kim et al., 2020). Anatomically, the areas represent islets of heterogeneous myocardium within the scar and can be alternatively identified in late gadolinium enhancement cardiac magnetic resonance imaging in atria (Fukumoto et al., 2016) or ventricles (Malaczynska-Rajpold et al., 2020).

Traditionally, substrate mapping before ablation is performed point by point with the help of a steerable mapping/ablation catheter under the guidance of a 3D electroanatomical mapping system. The success or failure of ablation to terminate persistent AF or VT depends on arrhythmia complexity, electrical catheter mapping type, and the sampling density. Bipolar electrograms are known to exhibit directional dependence on the propagating wavefront (Haines, 1993; Foppen, 2009). In contrast, unipolar electrograms may be contaminated with far-field electrical potential (Prystowsky, 2008; Allessie, 2014; Zaman et al., 2017), masking the myocardial activation time and misrepresenting the true electrophysiological state (Zaman et al., 2017). These technical challenges, along with uncertainties in electrode locations, hinder accurate CV measurement (Berenfeld et al., 2011; Zaman et al., 2017).

Fortunately, there have been recent advances in catheters and electrophysiology systems that render CV measurement in clinical settings feasible. These advances originated from the realization that CV measurement (both velocity and direction) is beneficial and, second, requires the relative geometry of recording electrodes to be tightly constrained. Under these conditions, the lesson learned from CV measurement of optical mapping data (on a grid) can be applied to clinical

recordings. One such system is the Advisor HD grid catheter (Abbott Technologies, Minneapolis, MN), which forms a relatively rigid and flat 4 × 4 electrode array with known geometry and small electrodes (Hong et al., 2019; Hsen et al., 2020).

One emerging application of CV measurement in clinical electrophysiology is mapping VT substrates during sinus rhythm. For example, the isochronal late activation maps (ILAM) method is based on generating isochronal maps from local activation and identifying slow zones from isochronal crowding (Irie et al., 2015a; Aziz et al., 2019). It is expected that a more accurate CV measurement using grid catheters should improve the applicability of this technique.

1.1.2 Basic Science: Optical Mapping-Based Measurement of CV

Conduction depends on fiber direction (anisotropy), tissue heterogeneity such as trabeculated or fibrotic tissue, aging, local ischemia, inflammation, or heart failure. Optical mapping directly measures transmembrane action potential (AP) at a high spatial resolution, achieving sub-millimeter mapping density. Therefore, it is a method of choice in basic science research to study cardiac electrophysiology from cells to tissue and whole heart level. As optical mapping can be used as a tool in studies of different end goals, published methods for CV estimation based on optical mapping differ (Tu et al., 1997; Mironov et al., 2008; Linnenbank et al., 2014; Doshi et al., 2015), with no one-fits-all method. While most CV methods are based on either polynomial surface fitting or a single vector approach, additional enhancements are often needed to tailor a method for the particular study aim.

In this study, we propose a robust method, termed the circle method (CM), for accurate estimation of local CV (both magnitude and direction) to evaluate the effects of RFA from optical mapping measurements. Ablated areas were localized, and spatial extent and depth of RFA-created lesions were characterized by examining the CV maps before and after ablation and identifying beat-to-beat CV alternans after the ablation.

2 METHODS

2.1 Computer Simulations

Simulations were based on Fenton–Karma's three variables model (Fenton and Karma, 1998) and were carried out using the explicit Euler method for the variables. The integration time step was $dt = 0.05\ ms$, space discretization $dx = 200\ \mu m$, and the standard diffusion coefficient of $0.001\ cm/ms^2$ was used. Tissue level simulations were performed in a 2D isotropic monodomain with 256 × 256 cells (~ $26\ cm^2$). The area is large enough to investigate the effect of CV reduction. The ablated region was modeled as the area of decreased excitability by increasing the time constant of the fast inward Na^+ current from 0.4 to 0.55 *ms*. Low excitability is associated with a larger threshold stimulus needed to support AP propagation and is associated with CV slowing. With the model parameter change, modeled RFA area was not excitable. Inside the ablated area, wavefront propagation was only possible due to electronic coupling, significantly decreasing CV.

To test the proposed CM method in predicting RFA size and location as a function of measurement noise, white Gaussian noise was added to the numerical data with different signal-to-noise ratios (SNRs): 5, 10, 15, 20, 25, 30, and 60 dB (the amplitude ratio, respectively: 1.78, 3.16, 5.62, 10, 17.78, 31.62, and 1,000). Then, LAT, CV maps, and estimated ablation area (size and location) are obtained to evaluate the effect of different noise levels. The surrogate CV maps, obtained with different noise levels, were compared with the reference CV map with no added noise, using the 2D Pearson's correlation coefficient. The 2D Pearson's correlation coefficient was calculated by choosing two different segments of the domain, a segment mainly containing the ablated area and a segment containing almost the entire simulation domain, with the ablated area at the center. The Dice similarity coefficient (Dice, 1945) was used to evaluate the impact of noise by comparing cropped CV maps with the reference CV map to test for noise effects on the accuracy in the determination of the ablated area location.

2.2 Heart Excision and Experimental Setup

Optical mapping imaging with transmembrane voltage (V_m) sensitive dyes was used to characterize RFA-created lesions, analyzing high-density CV maps before and after RFA in *ex-vivo* superfused isolated rat atria ($N = 2$), arterially perfused guinea pig heart ($N = 1$), and explanted human hearts ($N = 2$). Motion was suppressed for guinea pig and human hearts with (-)-Blebbistatin (Cayman Chemicals) at 1.8 μM concentration in Tyrode perfusate. All RFA procedures were performed using a high-frequency desiccator (Bowie).

Heart excision and experimental setup for isolated rat atria have been described in detail elsewhere (Pollnow, 2018). In brief, the right atria from two Fisher rats were dissected by cutting along the tricuspid valve to the superior vena cava, fixated in a bath, superfused with Krebs–Henseleit solution, and stained with Di-4-ANEPPS V_m sensitive fluorescent dye. The dye was excited using a green LED of 525 nm center wavelength (Cairn Research). Emitted V_m fluorescence from endocardial tissue was passed through the 635DF55 filter (Omega Optical) on the camera side. The sequence of images was acquired using an EMCCD camera (Evolve Delta 512, Photometrics) at a sampling frequency of 868 Hz with a binning factor of 2 and a resolution of 82 × 82 pixels, equivalent to a spatial resolution of 128 × 128 μm/pixel corresponding to a 10.5 × 10.5 mm field of view (**Figure 1A**). The atrial epicardium was stimulated (6.7 Hz) with a unipolar electrode. The RFA was performed approximately at the center of the epicardium as a sequence of RFA steps, increasing RFA time duration in each step while keeping the RFA power constant at 10 W. The ablation procedure was performed using a tungsten electrode of 0.4 mm diameter (Pollnow, 2018).

Heart excision and experimental setup in Langendorff-based whole heart perfusion using whole isolated guinea pig heart have been described in detail elsewhere (Uzelac et al., 2021). The RFA procedure was performed on the epicardial side of the left

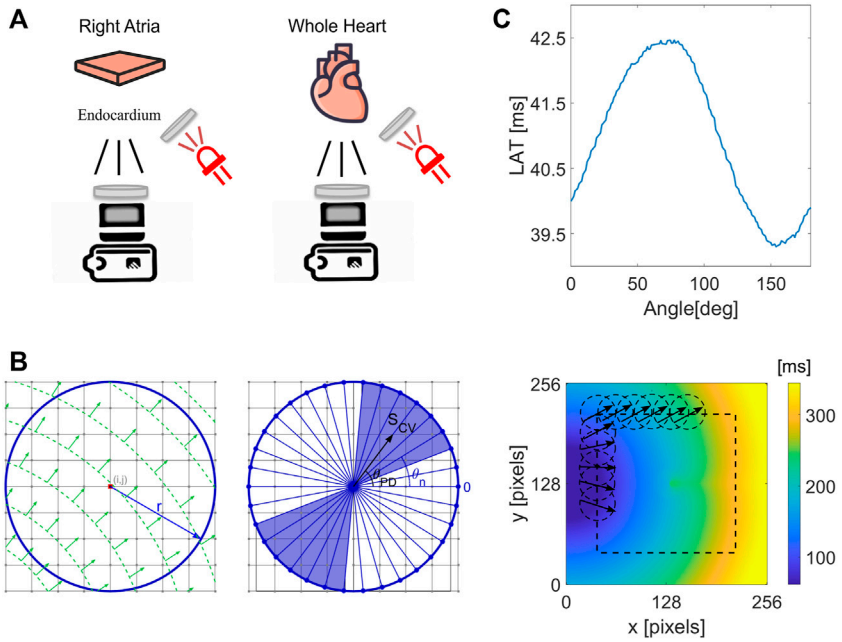

FIGURE 1 | Illustration of the experimental setup and the CM method application to obtain local CV and CV maps. **(A)** For isolated rat atria, RFA was performed in steps of increasing ablation duration of 0.5, 1, 1.5, 2, 2.5, 3, and 4 s, with 2 min pause between the steps. The ablation was performed on the epicardial side with optical mapping measurement on the endocardial side. The ablation was performed on the ventricular tissue for the whole guinea pig heart and human heart preparations. Collimated and bandpass-filtered LED light was used to excite the V_m dye. Emanating fluorescent light was passed through the long-pass filter in front of the EMCCD camera sensor. **(B)** Illustration of the circle method, evaluating LATs differences at the points along a circle of radius r, centered at a grid point (i,j). Left, example of a wave propagating at 45°. Right, a set of test CV values, $S(\theta_n)$, which is evaluated by taking the difference in LATs along diameters (blue lines) at different angles θ_n. The circle method evaluates the resulting conduction velocity by performing a geometrically weighted average of $S(\theta_n)$ over an angular range around θ_{PD} (blue shaded region). **(C)** Top, an example of a set of LAT differences for different chords, with a clear maximum along the chord normal to the propagating wavefront along vector $\mathbf{S_{CV}}$ as in **(B)**. Bottom, application of the CM method at every pixel in the LAT map inside the dashed rectangular region, obtaining local CV directions.

ventricle, using a 0.4-mm-wide tungsten electrode for 20 s with power set to 10 W (**Figure 1A**).

The cardiac surgeon team performed human heart excisions during the heart transplantation procedure. Immediately after receiving the heart from the surgical team, ice-cold cardioplegia solution was flushed through the right and left coronary arteries to protect the myocardium against ischemia during transportation to our optical mapping lab within 20 min while maintaining arrested heart temperature around 4°C. The left and right coronaries were separately perfused in the whole heart preparation for epicardial optical mapping. The human left ventricular wedge preparation was used for optical mapping of the endocardium. The marginal artery was cannulated, and the cannula was secured with a surgical silk ligature. Leaks in the wedge preparation were secured by clamping the wedge preparation around the cut regions. The whole heart and the wedge preparations were placed in an oval heated chamber maintained at 37°C while continuously perfused with oxygenated Tyrode solution (Ng et al., 2014) also kept at 37°C and oxygenated with the mixture of 95% O_2/5% CO_2. Coronary pressure of 70 mmHg was kept constant during the experiments. RFA was performed with power set to 40 W, using a non-irrigated electrode with a blunt tip.

Guinea pig and human hearts were stained with V_m sensitive dye Di-4-ANBDQPQ (JPW-6003) (Potentiometric dyes), with 0.25 mg of the dye for whole guinea pig heart, and 0.5 mg of the dye for each human ventricle. The dye was prepared as a stock solution previously dissolved in pure ethanol at a 1 mg/ml ratio. Two red LEDs with the center wavelength at 660 nm were used as light excitation sources for the V_m dye (**Figure 1A**). The LED light was collimated with a plano-convex lens (ThorLabs) and bandpass filtered with a 660/10 mm filter (Edmund Optics). Additionally, two green LEDs with a center wavelength of 525 nm were used for the optical mapping measurements performed on the human heart endocardium. The LED light was collimated with a plano-convex lens (ThorLabs) and bandpass filtered with a 520/10 mm filter (Edmund Optics). A custom-designed two-channel LED driver was used, with the ability to switch the excitation light bands in sync with the camera frame rate (donated from Aleksa Tech). The emitted fluorescence was passed through a 700 nm long-pass filter (Chroma) on the camera side. The sequence of images was acquired at 500 Hz using an EMCCD camera (Evolve 128, Photometrics) at a resolution of 128 × 128 pixels.

In the post-processing, baseline drift for each pixel trace was removed by applying a low-pass Kaiser Window FIR filter with a stop-band frequency of 1 Hz and a pass-band frequency of 0.5 Hz. The output signal from the FIR filter, representing the baseline drift, was subtracted from the raw pixel trace. The difference was divided with the baseline drift signal, obtaining

the relative change in fluorescence ΔF/F (Uzelac et al., 2019). To boost SNR, approximately 40 optical APs (OAPs) were stacked (ensemble averaged) with a period equaling two beats upon reaching steady-state conditions, significantly reducing the noise (Uzelac and Fenton, 2015). In the next step, the traces were temporally filtered using an anisotropic 1D diffusion filter (Perona and Malik, 1990; Gerig et al., 1992), which preserves the OAP upstroke.

LATs were obtained by linear fit along the OAP upstroke and determining the 50% rise of the OAP upstroke. Contrary to bipolar electrograms, where activation time determination is based on the maximum of the first derivative, OAP signals are inherently spatially averaged across clusters of cells corresponding to a single pixel trace. As the sampling rate is generally lower, the first derivative method is less accurate than the 50% approach (Efimov et al., 2004; Fedorov et al., 2009; Walton et al., 2012; Bastos-Filho, 2021). Obtained LAT maps were subsequently minimally filtered using an anisotropic 2D diffusion filter, which preserves sharp boundaries in LAT maps (Perona and Malik, 1990; Gerig et al., 1992).

2.3 Circle Method (CM)

By assuming a planar wavefront propagation inside a circle of radius r (**Figure 1B**), centered around each LAT grid point, the CV can easily be determined. This can be done by first calculating differences in the LAT across the endpoints of chords passing through the center of the circle. From the LAT differences, an effective conduction speed, $S(\theta)$, can be calculated as a function of the chord's orientation angle, θ. The maximum of $S(\theta)$ corresponds to the true conduction speed along the propagation direction, $S(\theta_{PD})$ (**Figure 1C**). The evaluation of $S(\theta_{PD})$ incorporates measurements along a single path, centered at the LAT grid point. To reduce the effect of LAT measurement uncertainty, CV along neighboring chords can be incorporated.

To reduce noise in the determination of the CV, conduction speeds along chords lying within the range, $(\theta_{\mathrm{PD}} - \frac{1}{2}\Delta\theta, \theta_{\mathrm{PD}} + \frac{1}{2}\Delta\theta)$, are combined to calculate a CV that is spatially averaged over the hourglass-shaped area subtended by these chords (**Figure 1B** right). Because chords within this range do not all lie along the direction of propagation, the conduction speeds are enhanced to account for this geometry before combining. To account for the misalignment, $\vec{S}(\theta)$ is back projected onto $\vec{S}(\theta_{PD})/\|\vec{S}(\theta_{PD})\|$. The resulting conduction speed can be calculated from the average of these back-projected speeds as,

$$S_{\mathrm{CV}} = \frac{1}{N}\sum_{n=1}^{N}\frac{S(\theta_n)}{\cos(\theta_{PD} - \theta_{\mathrm{n}})}, \tag{1}$$

for all N chords lying within the range spanned by $\Delta\theta$. For a detailed discussion of this equation, see **Supplementary Material**.

This method is equivalent to central differences with a separation of $2r$ grid points for waves propagating along the optical mapping grid; however, unlike central differences, the fidelity of the calculation does not depend on the propagating wavefront orientation. Additionally, interpolation is performed for LAT differences calculated along chords with endpoints that do not fall on LAT grid points. Incorporating conduction speed information along with many chords reduces uncertainty in the estimation of local CV.

For comparison with other methods, the CV maps from the numerical simulation, isolated rat atria, guinea pig heart, and whole explanted human heart, obtained with the CM and the finite-difference approach (FiD) (van Schie et al., 2021), were used. The distance between neighbors using the FiD method was set to 20 pixels, corresponding to $r = 10$ used for CM (diameter = 20 pixels). A MATLAB function for implementing the CM for a given LAT map is provided on GitHub at https://github.com/uzelaci/Circle_Method and https://github.com/HEartLab-ufabc/Circle_Method.

3 RESULTS

3.1 Computer Simulations

Figure 2A shows the LAT map of simulated curved wavefront propagation with isochrone lines and superimposed CV vectors, and corresponding CV maps for the entire domain and the selected area with dash line, around the ablated region for improved visibility. The ablated area was modeled as decreased excitability for a circular region, 20 pixels in radius, centered in the domain. Due to decreased excitability in the ablated area, propagation is only due to electrotonic coupling between the excitable and non-excitable (ablated) regions, resulting in a wave block for a large enough ablated area. A point stimulation was used to generate a curved propagating wavefront to capture wavefront effects. A 2D Person correlation (**Figure 2A** upper right) was used to compare the reference noise-free CV map and its surrogates (**Figure 2B**), obtained with different noise levels. Correlation 1 plot refers to the correlation coefficients obtained regarding the referent noise-free CV map of whole domain (236 × 236 pixels), and Correlation 2 for the subdomain around the ablated area (80 × 80 pixels). Dice similarity coefficient is calculated for the subdomain to compare the noise-free reference CV map and its surrogate maps with added noise.

Figure 2B shows the noise effect on the CV maps and ablation area segmentation under different SNR levels of 60, 30, 25, 20, 15, 10, and 5 dB. The correlation coefficients are similar for the SNR range between 60 and 15 dB, varying from 1 to 0.9. Correlation decreases for SNR < 15 dB, with no difference between the two correlation curves, and a significant difference for SNR < 10 dB (0.020). Dice similarity coefficient is less dependent on noise. For SNR = 5 dB, the coefficient is equal to 0.83, and increases to 0.91 for SNR = 60 dB. Even under high levels of noise (i.e., SNR < 5 dB), the ablated area could be segmented (i.e., size and location), showing a high level of similarity between noise corrupted CV maps and the reference noise-free CV map.

3.2 Effects of Ablation on CV: Isolated Rat Atria

Figure 3A shows LAT maps obtained before and after 14.5 s of ablation for two experiments on isolated rat atria. In the experiment A, the wavefront propagates from the upper-right corner, and in the experiment *B* from the left side. The respective

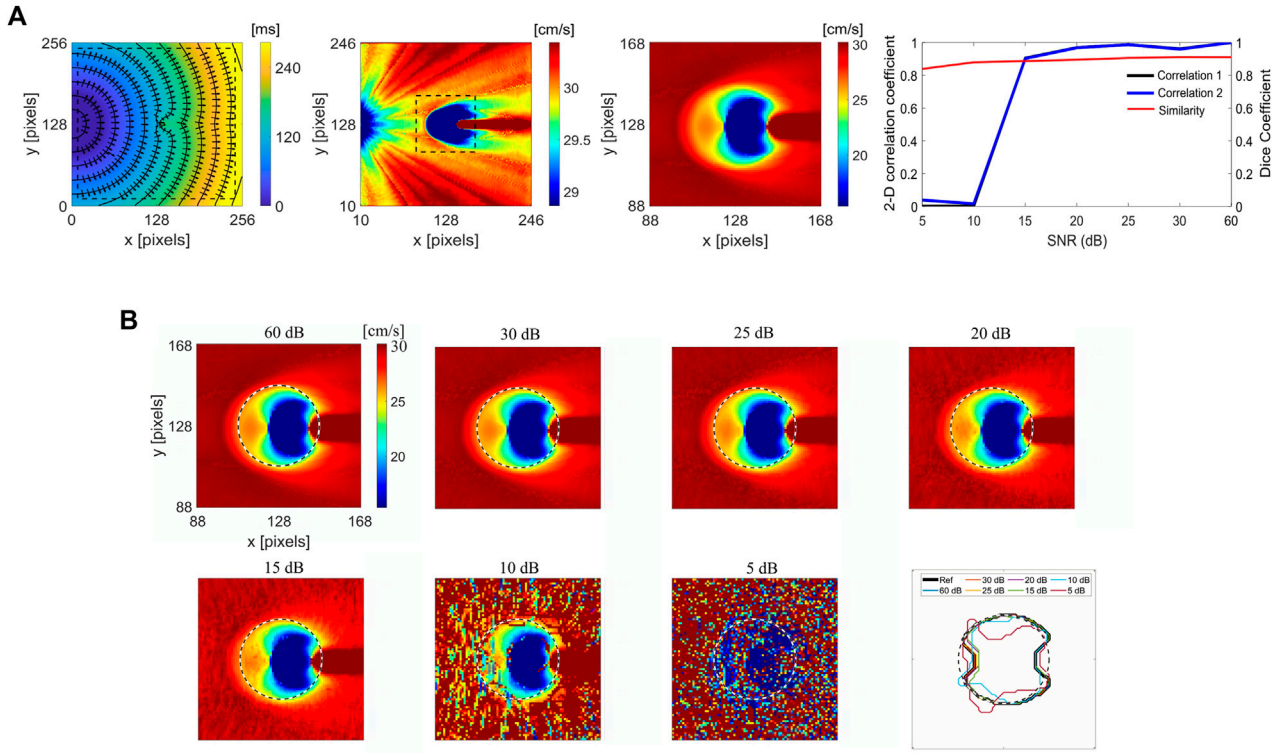

FIGURE 2 | Numerical simulations of the RFA and effects of added noise on CV for the spatial determination of the ablation area. **(A)** Left, the LAT map of a simulated curved wavefront propagation with isochrone lines spaced 20 ms apart, and superimposed CV vector map showing CV magnitude and direction. The ablated area is modeled as a circular region, 20 pixels radius at the center. Middle, the corresponding CV maps from the LAT map for the whole domain and sub-domain (80 × 80 pixels) region around the ablated area outlined with an inscribed dashed rectangle. Right, 2D Pearson's correlation coefficient for different SNR levels ranging from 5 to 60 dB, for the CV maps of different sizes on the left, 236 × 236 (Correlation 1) and 80 × 80 pixels (Correlation 2). The Dice similarity coefficient for the selected 80 × 80 pixels CV map around the ablated area. **(B)** Zoomed-in CV surrogate maps for different SNRs of 60, 30, 25, 20, 15, 10, and 5 dB, with the delineated boundary of the ablated area. The color bar range in all figures is set from the 5th to 95th percentile.

CV maps (**Figure 3B**) are calculated for the area outlined with a dashed line. A region of distinctly lower CV values depicts the location and shape of the ablated tissue, represented by a deep-blue shaded area. The relative difference in CV maps after and before the ablation for both experiments is shown in **Figure 3C**. A well-defined area where CV decreases is observable, delineating the region where ablation was performed. In both experiments, the ablated area resembles an elliptical shape of approximately 24 × 48 pixels for experiment A (2 × 4 mm) and 24 × 72 pixels (2 × 6 mm) for the experiment B. The OAPs inside these areas are presented in **Figure 3D**, depicting a higher amplitude reduction and change in morphological pattern.

3.3 Effects of Ablation on CV: Guinea Pig Ventricle

Wavefront propagation across ventricular tissue is more complex than atrial tissue due to tissue heterogeneity and transmural wave propagation. **Figure 4A** shows the LAT maps obtained at baseline and after application of RFA (initially applied for 3 s and subsequently for 10.5 s). **Figure 4B** shows the respective CV maps, calculated from areas around the ablated region, within the dashed square region from **Figure 4A**. From the figure, it can be inferred that the area representing lower CV values expands in size, with an additional ablation of 10.5 s. Due to the inherent spatial variation in CV, unlike with CV maps of more homogenous rat atria, direct comparison of CV maps is more difficult. A CV map of relative change after and before the ablation, ΔCV map, was calculated for the two ablation steps shown in **Figure 4C**, showing the relative decrease in CV post-ablation. The maps delineate the elliptically shaped red-color-shaded ablated region.

3.4 Effects of Ablation on CV: Human Heart Ventricles

Figures 5, **6** show optical mapping measurements on the whole explanted human heart with epicardial ablation and left ventricle in wedge preparation with endocardial ablation, respectively, using a blunt ablation electrode (Bowie). Hearts were explanted from patients undergoing heart transplantation, suffering from progressive heart failure and recurrent VT as a result of viral myocarditis. As such, ventricular tissue is highly heterogeneous, and the CV maps illustrate challenges in quantifying CV maps. Despite optical mapping achieving high density in comparison to contemporary electroanatomical mapping systems, LAT and CV

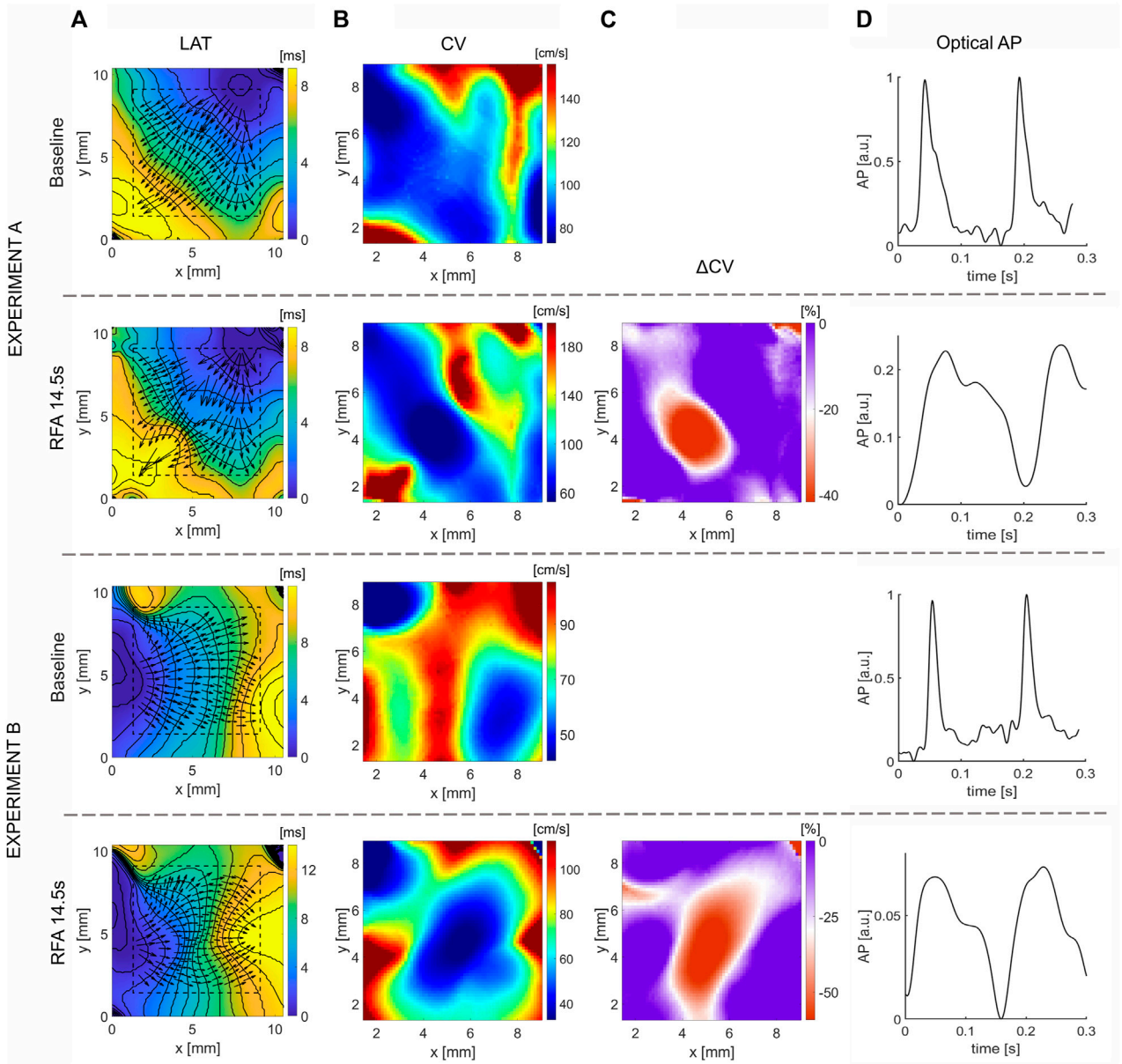

FIGURE 3 | Effect of ablation on CV slowing on isolated rat atria. **(A)** LAT map obtained before (Baseline) and after RFA for the total duration of 14.5 s and power of 10 W, approximately at the center of the map, along with the superimposed CV vector map. **(B)** Respective CV maps obtained with the CM method for selected dashed square regions presented in **(A)** outline the ablated areas as regions of CV reduction. **(C)** Relative change, ΔCV, between the CV maps after and before the ablation, shows a large relative decrease of CV in the ablated areas, delineating the ablated area from non-ablated, suitable for characterization of the ablated area boundary. **(D)** Optical AP traces from a pixel inside the ablated area, normalized before ablation, show the reduction in AP amplitude and morphology changes. The color bar range in all figures is set from the 5th to 95th percentile, except for ΔCV maps' upper boundary that was set to zero. Radius of 10 pixels (1.3 mm), in the CM, was used for CV calculation.

maps illustrate the complex electrophysiology of the human ventricles. This observation is expected as the human endocardium can be highly trabeculated, and the presence of papillary muscle may hinder the mechanism of CV slowing (**Supplemental Figure S2**). For both hearts, epicardial and endocardial LAT and CV maps fail to delineate the ablated region. Moreover, for endocardial ablation (**Figure 6**), even the maps of relative CV difference before and after ablation are not much practical to characterize RFA lesion. Therefore, we modified our optical mapping protocol to overcome these challenges and performed optical mapping with light bands of different penetration depths to study beat-to-beat CV alternans in post-ablation. Analysis of relative CV maps difference for subsequent beats with green light band illumination does not show the presence of CV alternans, indicating a complete surface ablation. However, the same analysis with deeper red-light band illumination of greater tissue penetration

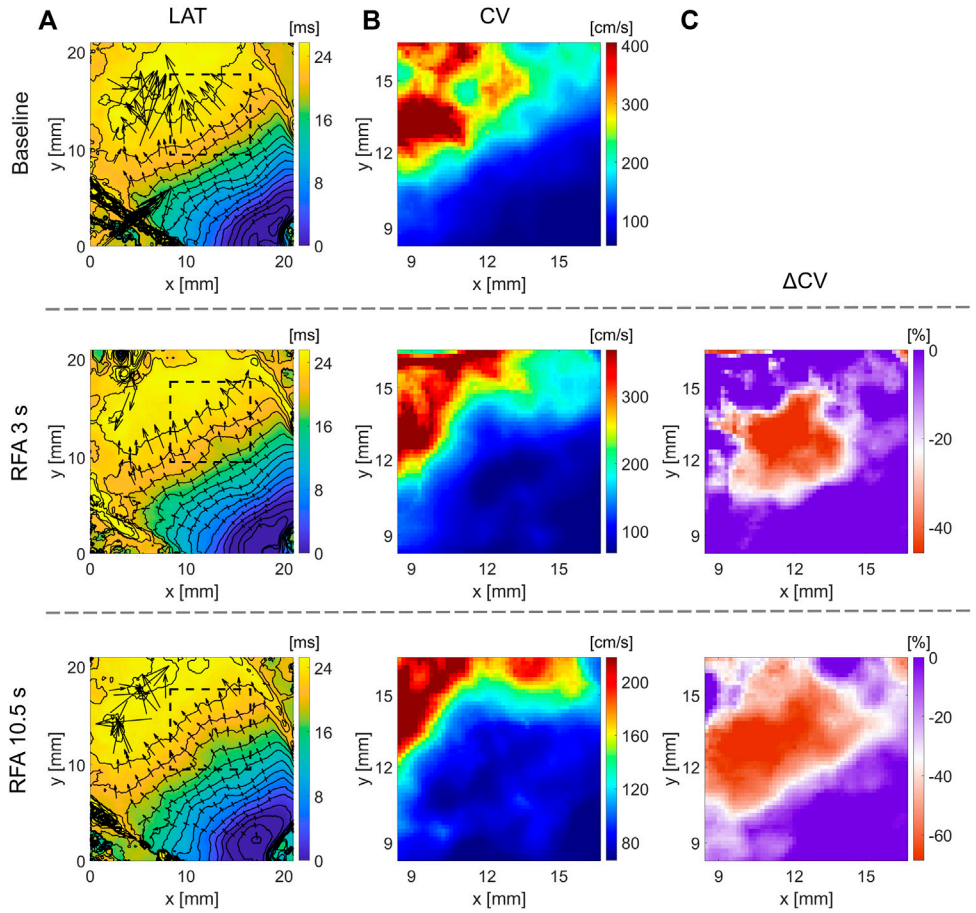

FIGURE 4 | Effect of ablation on CV slowing on guinea pig ventricle for different RFA durations. **(A)** LAT maps obtained at baseline (top) and RFA duration of 3 s (middle) and 10.5 s (bottom), respectively. **(B)** Respective CV maps inside the dashed square regions, where ablation is performed, show CV decrease, with a larger CV decrease after longer RFA. **(C)** Relative difference in CV after and before ablation, ΔCV maps, outlines the ablated region as a distinct decrease of CV. The color bar range in all figures is set from the 5th to 95th percentile, except for ΔCV maps' upper boundary that was set to zero. Radius of 10 pixels (1.6 mm), in the CM, was used for CV calculation.

depth shows CV alternans due to incomplete or non-homogeneous ablation across the ventricular wall. This observation agrees with the images of the RFA lesion taken after the experiment, showing the spatial extent of the lesion and its depth across the ventricular wall (**Supplemental Figure S2**).

4 DISCUSSION

Although the ablated tissue is not excitable, a signal resembling AP can be measured within the ablated area due to electronic coupling between the excitable cardiac cells and a lesion consisting of unexcitable cells (Quinn et al., 2016). APs inside the lesion show characteristic distorted morphology (**Figure 3D**) and decreased amplitude (**Figure 5E**), characteristic of electrotonic coupling. As electrotonic coupling slows wavefront propagation, the ablated region size can be characterized as a CV decrease. The numerical simulations show CV linearly decreases inside the ablation zone toward the ablation center. This allows easy estimation of the lesion size as a knee point deviation from linear CV rise from the ablation center (**Figure 7A**). The same pattern was observed in experiments. The CV increases linearly with the CM radius increase, centered inside the lesion, as long as the radius is smaller than the ablated area (**Figure 7**). The knee points of curves shown in **Figure 7** estimate ablated areas size very well. For example, the CV vs. radius curve for guinea pig ventricular ablation estimates diameter of the ablated area of 5 mm, which is in agreement with the ΔCV map shown in **Figure 4C** for RFA of 3 s. The limitation of this approach is circular-shaped approximation of the ablated area; as for elliptically shaped lesions, the knee point corresponds to the minor axis.

A distinct feature of the proposed CM is its inherent adaptation to the local changes in a propagating wavefront direction, making the method independent of the propagating wavefront direction. CV maps are also obtained through automatized data processing, identifying the wavefront propagation direction upon which the CV's magnitude and angle are obtained. The CM accuracy depends on the chosen circle radius approximating planar wavefront propagation inside the circle. With increased radius, the accuracy

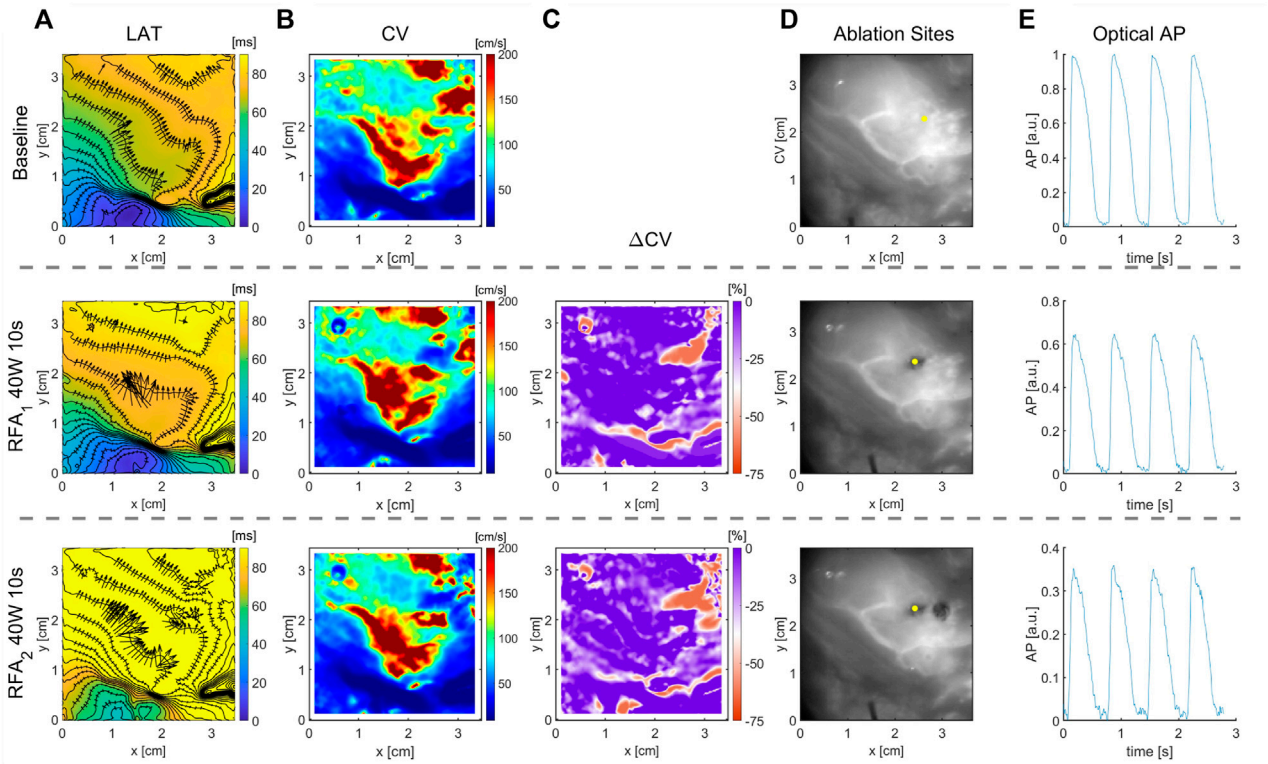

FIGURE 5 | Optical mapping on whole explanted human heart for quantification of RFA-created lesion. RFA was performed on ventricle's epicardial side in two steps, termed RFA_1 and RFA_2, with power set to 40 W for 10 s in each step. **(A)** LAT time maps show wavefront propagation slowing in the upper right region where the ablation was performed. **(B)** CV maps before and after ablation show characteristic CV slowing in the ablated region. **(C)** Change in CV obtained as the relative difference after and before ablation clearly outlines the red area where ablation was performed of a distinct CV decrease. **(D)** Black and white images captured using the optical mapping camera illustrate ablated regions. **(E)** Optical AP traces from a pixel marked with a yellow dot in **D** normalized before ablation. The traces show the relative change in fluorescence corresponding to transmembrane voltage change. The color bar range in all figures is set from the 5th to 95th percentile, except for ΔCV maps' upper boundary that was set to zero. Radius of 4 pixels (1.1 mm), in the CM, was used for CV calculation.

decreases to estimate a true local CV. However, the precision increases as LAT differences are calculated along chords spanning larger spatial differences. In experimental setups, the minimum radius of 1 mm was chosen, to balance the accuracy and precision, resulting in CV maps resolving small conduction heterogeneities with acceptable SNR.

4.1 Comparison With Other CV Methods

In general, optical mapping-based methods estimating local CV differ due to particular study goals. The gold standard for measuring conduction properties (Bayly et al., 1998) is based on a polynomial surface fit over a LAT map to estimate local gradients, whose implementation is available as the Rhythm MATLAB toolkit (Gloschat et al., 2018). However, this method is not ideally suited for heterogeneously conducting tissue, or for those whose activation does not have a continuous pattern, as with calcium imaging in cell cultures. The Ccoffinn method (Tomek et al., 2016) has been developed as an alternative to the standard polynomial surface fit method. The method considers wavefronts from sequential frames, using a graph-based algorithm to find a set of vectors that best describe the direction and velocity of wave propagation. Tissue anisotropy is commonly studied following an activation wavefront spread starting from the central pacing site. Single vector and average vector method (Linnenbank et al., 2014) approaches are helpful to estimate tissue anisotropy by quantifying longitudinal and transversal CV, assuming a homogeneously anisotropic myocardium, and the methods are implemented in ElectroMap open source for analysis of cardiac electrophysiology (O'Shea et al., 2019). The assumption that transverse propagation lies perpendicular to the longitudinal does not consider the influence of irregularity of tissue geometry or heterogeneous discontinuities. The semi-automated ORCA method has been developed to study tissue anisotropy addressing the issue of non-orthogonality (Doshi et al., 2015) to obtain longitudinal and transversal CV and is implemented in the Rhythm toolkit. ORCA employs the single vector method assuming that the CV is constant in an anisotropic 2D sheet at a distance from the pacing site. Longitudinal and transversal CVs were estimated using the linear fits on segments of activation time curves along different directions spanning a complete circle to detect the maximal and minimal slopes of the linear fits corresponding to longitudinal and transverse CVs.

In clinical practice, triangulation is commonly used among many different CV methods, as the method is not constrained by electrode configurations and is suitable for mapping catheters of different

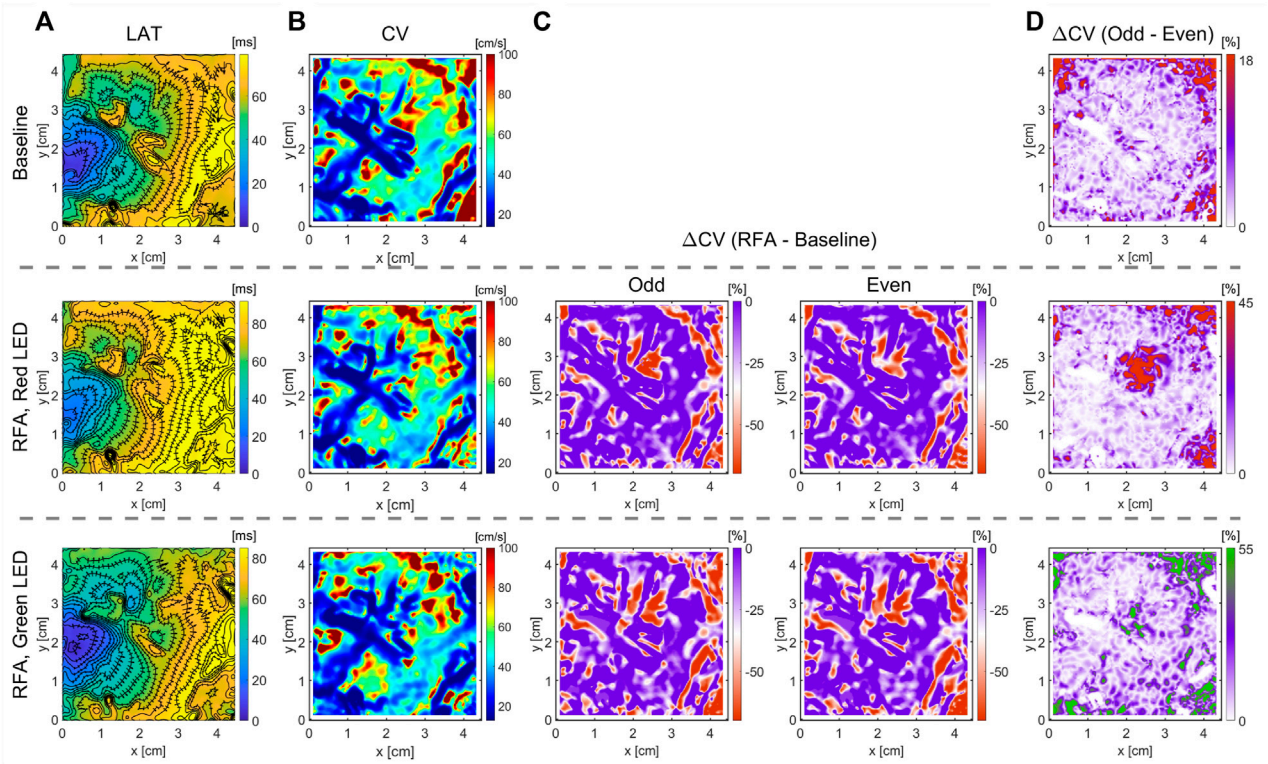

FIGURE 6 | Optical mapping on the LV's endocardium in wedge preparation for quantification of RFA-created lesion. The RFA was performed on a highly trabeculated endocardium for 20 s, and power set to 40 W. Different light excitation bands were used, a green LED of 525 nm center wavelength and a red LED of 660 nm center wavelength, to measure optical APs emanating from the endocardial surface and deeper transmural layers. **(A)** Due to the highly heterogeneous endocardium (**Supplementary Figure S2**), identification of the ablated area from LAT maps is non-trivial. **(B,C)** CV maps and the relative CV difference after and before the ablation do not clearly outline the ablated area, lacking characteristic CV slowing. **(D)** Relative difference in CV maps between subsequent beats (wavefront propagation), termed even and odd, elicits the CV differences due to AP amplitude alternans in the ablated area. Green LED light illumination of penetration depth limited to the endocardial surface layer, and the absence of alternans indicates a complete ablation of the surface layer. Illumination with a deep-red light band of deeper penetration depth enables measuring APs from deeper ventricular wall layers. The presence of CV alternans indicates the non-homogeneous or incomplete ablation across the ventricular wall (**Supplementary Figure S2**). The color bar range in all figures was set from the 5th to 95th percentile, except for ΔCV maps' upper boundary that was set to zero. Radius of 3 pixels (1.05 mm), in the CM, was used for CV calculation.

electrode configurations (Cantwell et al., 2014). The accuracy of the triangulation method depends on the size of a selected triangle, as the CV values are interpolated inside the triangle assuming locally planar wavefront propagation (Cantwell et al., 2015). FiD method is based on a 2D grid layout of measurement points, determining the difference in activation times with known spatial distance between neighboring points and two orthogonal directions, and is suitable for optical mapping measurement. As the CV is calculated using a global coordinate system, the accuracy of the method depends on the wavefront propagating direction. For example, the same activation time of neighboring points results in large CV uncertainties or unphysiological high CV.

The cosine fit is another CV method explicitly developed for atrial mapping. As the arrangement of measurement electrodes in the clinical environment depends on the choice of a catheter, the cosine fit approach (Weber et al., 2010) allows estimation of local CV and the angle of incidence from measured electrograms using electrodes positioned on a circular catheter under sinus or pace mapping. This single-shot analysis is suitable for determining the pacing source, assuming a sufficiently large distance from the wavefront source and assuming planar wavefront propagation inside the circular catheter. A limitation of this analysis is that the locally determined angle of incidence does not necessarily point toward the stimulation origin. As wavefronts may exhibit curvature, particularly if originating from a nearby focal source, the improved cosine-fit method (Roney et al., 2014) allows CV determination and the direction toward the location of a focal source for either circular or planar wavefronts, recorded from the arbitrary arrangements of electrodes. As both methods assume isotropic conductivity to estimate a focal source to address tissue conduction anisotropy and heterogeneities, another cosine-fit-type method (Roney et al., 2018) combines multiple activation maps from different pacing. This technique is suitable for estimating conduction anisotropy and fiber direction from clinically available atrial electrical recordings.

We did not quantitatively compare cosine-based methods with the CM to test for accuracy, as both are developed for different purposes. Cosine-based methods are developed for clinical atrial mapping applications to efficiently extract patient-specific

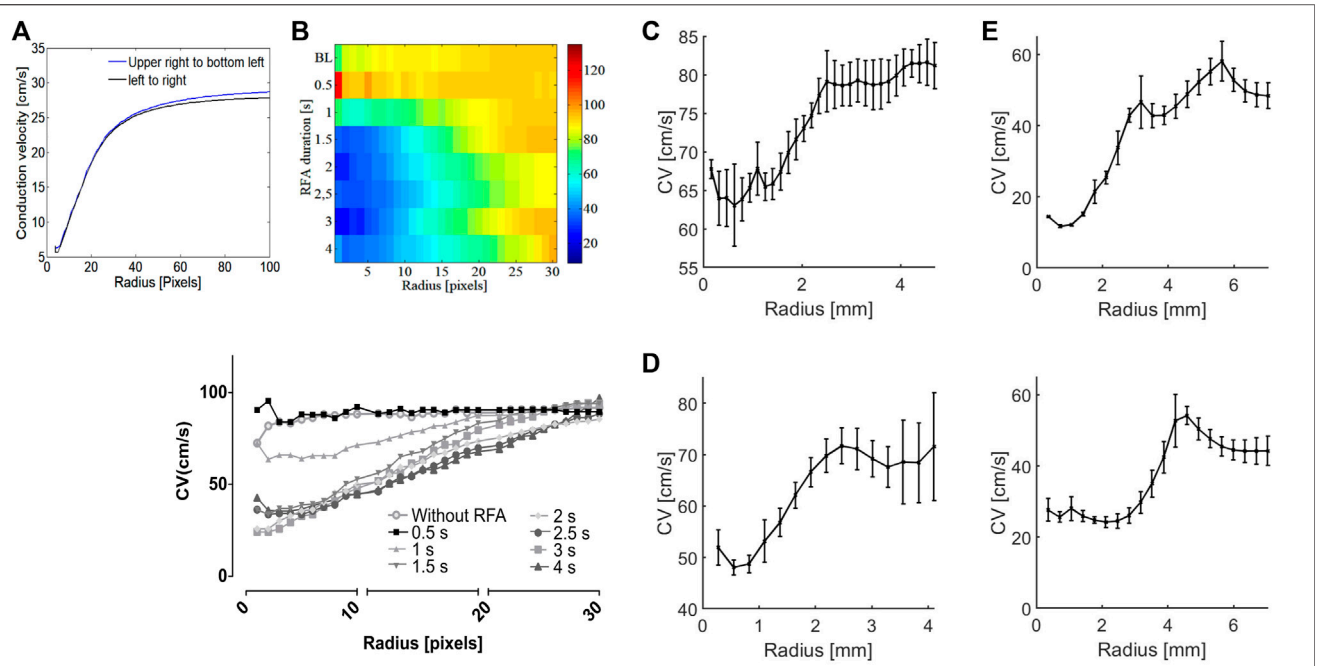

FIGURE 7 | Estimation of the ablated area size based on the CM radius. **(A)** In numerical simulations, CV linearly increases with CM radius inside the ablated area of 20 pixels in radius, reaching a limit value outside the ablated area. The ablated area radius can be estimated as a deviation, the knee point, from a linear rise, independent of wavefront direction. **(B)** Heatmap of CV values at the ablated area center of rat atria as a function of RFA duration and CM radius. The heatmap shows the expansion of the ablated area with each subsequent ablation step characterized by distinctive CV slowing. (Bottom) CV curves are shown for different RFA steps, with a knee point for the approximate radius of 25 pixels, or 2 mm. **(C)** Whole isolated guinea pig heart. The CV curve at the center of ablation (RFA of 3 s) for different CM radii flattens for an approximate radius of 2.5 mm, indicating an RFA-created lesion of 5 mm diameter. **(D)** Human heart epicardium of LV. From the figure, the CV curve, obtained in the same fashion, flattens for an approximate radius of 1.5 mm. **(E)** Human heart endocardium of LV. Upper, for deep-red light excitation, the CV curve flattens for an approximate CM radius of 2.5 mm, and CM radius of 4 mm for green light excitation (lower figure), indicating narrowing of RFA-created lesion across the transmural wall.

substrate parameters for patients undergoing ablation. CM is easy to implement in optical mapping-based ventricular and atrial data experiments to characterize ablated lesions. CM applicability can be extended to determine focal sources, as propagating wavefront direction changes can be tracked. However, optical mapping is currently limited to basic science research.

The CM method can be viewed as an extension of the FiD method as both methods are based on LAT differences over a 2D grid, and the two methods were compared using both numerical and experimental data (**Figures 8A,B**). The relative CV difference between the two methods, (CM-FiD)/CM, is shown in **Figure 8C**. As expected with numerical data, both methods result in similar CV maps with small relative differences. The disparity between the two methods increases significantly for experimental data, ranging from −20% to 10% for rat atria and isolated guinea pig hearts and −40% and 20% for highly trabeculated human ventricular endocardium. We also investigated whether the choice of radius plays a role in the observed differences. We compared the CV maps obtained with the two methods for radius ranging from 5 to 10 pixels. However, the differences between the two methods were consistent. With CM, the local CV is calculated using a locally defined coordinate system with one of the axes coaligning with the automatically identified wavefront direction. In contrast, FiD is based on a globally defined coordinate system, obtaining x and y components separately. If a propagating wavefront line aligns with one of the axes, LAT differences can be zero, resulting in large CV uncertainties. In **Figure 8B**, the FiD overestimates CV values in rat atria for the red-colored region in the middle of the CV map. Since the wavefront is changing its direction and moving down vertically in some parts of the atria (**Figure 3A**), large uncertainties of CV x-axis component result in a rapid rise of local CV.

One of the challenges in ventricular tissue ablation is depth estimation of the created lesions. In this study, we used two different V_m dye excitation bands, a green band centered at 525 nm and a deep red band centered around 660 nm, for optical mapping of the human endocardium. While no measurement of penetration depth for different wavelengths is performed, penetration depth in the skin is generally under 1 mm for the green light and over 3 mm for deep red light (Avci et al., 2013). Using two different light bands allowed us to study the differences in CV maps obtained from AP signals emanating from the surface layer on the epicardial side and AP signals from the deeper layers (**Figure 6D**). A highly trabeculated endocardium of the human left ventricle and the presence of papillary muscle result in a highly heterogeneous CV map which would hinder the ablated area as the zone of decreased CV (**Figures 6B,C**). Amplitude alternans, the beat-to-beat variation in AP amplitudes, occur when the dispersion of AP refractoriness results in decreased excitability and can be

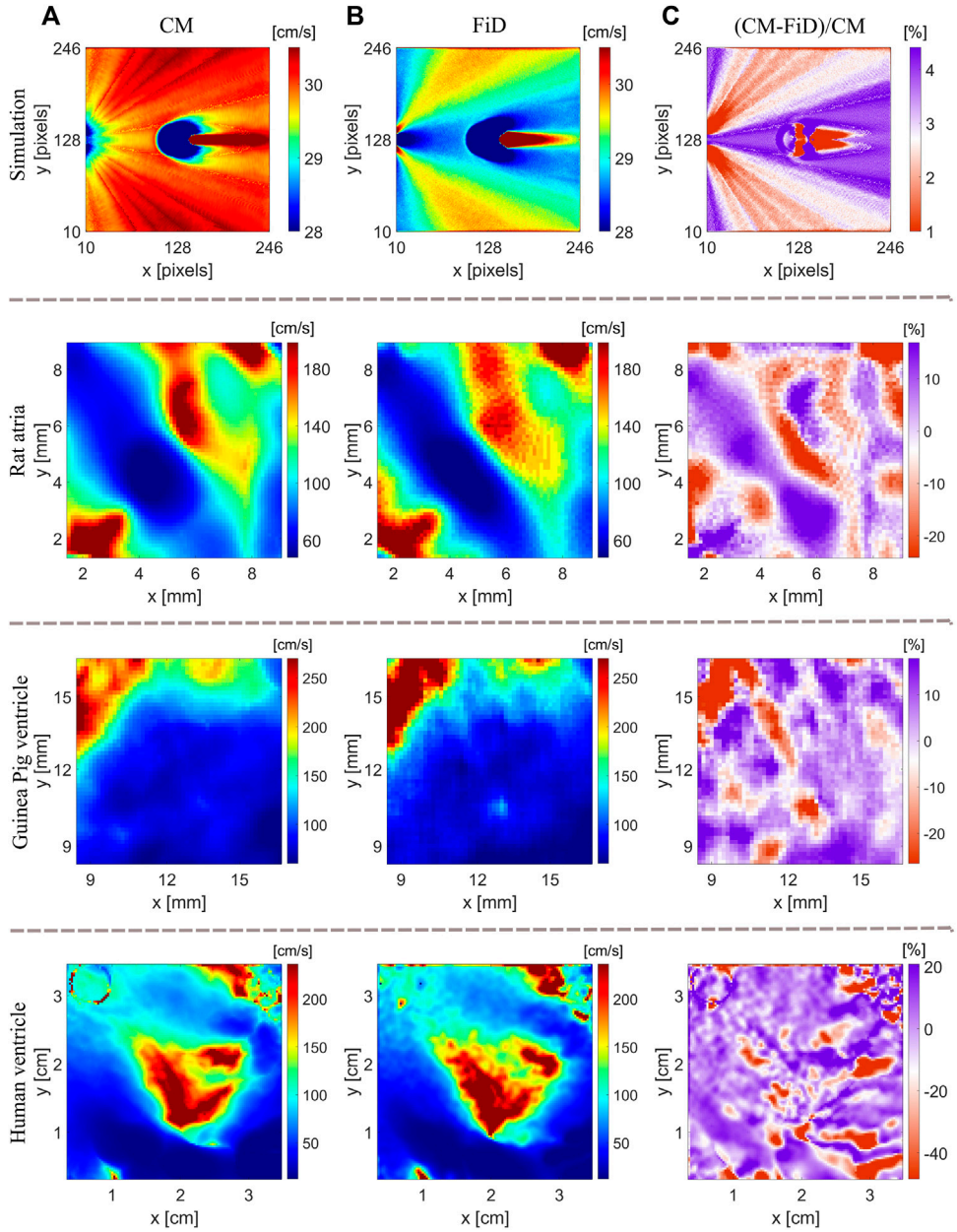

FIGURE 8 | Comparison of CV maps using the CM and FiD method. **(A)** CV maps generated with the CM method for the simulation, rat's atria, guinea pig's ventricle, and human ventricle (epicardium). **(B)** Respective CV maps obtained with the FiD method. **(C)** Relative difference of CV maps obtained with the two methods.

quantified as a decrease in CV. As shown in **Supplemental Figure S2**, the depth of the created lesion is 3–4 mm, measured optical AP traces from the surface layer with green light excitation are solely due to electrotonic coupling between excitable cells and a lesion, resulting in no alternans at PCL of 800 ms. However, deep-red-light excitation shows the presence of CV alternans due to incomplete transmural ablation. One mechanism leading to CV alternans could be due to the presence of unexcitable cells coupled with excitable cells resulting in reduced cell-to-cell coupling, leading to decreased excitability.

5 CONCLUSION

In this study, RFA-created lesions were quantified as local CV decrease using optical mapping measurements with submillimeter spatial resolution. For the application of the CM method, no prior information about the propagating wavefront direction is required, and CM robustness was tested and validated in numerical simulations, and experimentally on isolated rat's atria, whole guinea pig's heart, and human hearts. RFA-created lesion profiles were quantified as the relative change of CV before and after ablation or, as in the case of a human heart with highly trabeculated

endocardium, by analyzing CV alternans using excitation light bands of different penetration depths to estimate lesion depth across the thick transmural wall. As the CV is one of the important parameters for studying heart electrophysiology, CM can be applied to other studies, such as identifying slow zones for mapping VT substrates.

The histopathological features of RFA have been mainly studied in normal myocardia, and its effect on clinically relevant heterogeneous scars is not well understood. For treatment of reentrant VT, reentry typically occurs within the scarred region due to tissue heterogeneities, and the RFA prevents reentry by homogenizing the scared areas. However, studies show that scar tissue is more resistant to thermal injury compared to healthy cardiomyocytes (Barkagan et al., 2019), which may impair the effectiveness of the RFA procedure. Optical mapping with near-infrared V_m dyes enables measurements of transmural wavefront propagation (Herndon et al., 2016; Uzelac et al., 2016) for better depth characterization of the scar area. Although limited to lab research, the high spatial resolution of optical mapping enables quantitatively predictive studies of how local CV changes affect heart electrophysiology. New findings may add toward a better understanding of arrhythmia mechanisms and ablation effects on tissue electrophysiology to develop improved ablation strategies (Jalife et al., 2002; Sanders et al., 2005; Narayan et al., 2012; Clayton and Nash, 2015; Hansen et al., 2015).

6 LIMITATIONS

In this study, experiments were performed at different institutions. Histological evaluations were not performed. Statistical analysis was not possible due to the limited number of experiments. Nevertheless, one of the main objectives of this study is to present the method and results suitable for further investigation of RFA outcome assessment.

DATA AVAILABILITY STATEMENT

The raw data supporting the conclusions of this article will be made available by the authors upon reasonable request.

ETHICS STATEMENT

The animal studies and related procedures were reviewed and approved by their respective regulatory offices. Procedures for isolating rat atria conformed to the European Council guidelines for the care and use of laboratory animals and were approved by the Committee for Animal Welfare at the Karlsruhe Institute of Technology, Germany (35-9185.81/G-61/12). The Office Research and Integrity Assurance approved the procedure on isolated guinea pig heart at the Georgia Institute of Technology under the USDA Animal Welfare Act Regulations and Standards, PHS policy, conforming to the current Guide for Care and Use of Laboratory Animals (protocols A18012 and A15002). The explanted human hearts were obtained through the Emory Hospital Heart transplant program under IRB approval from heart transplant recipients undergoing cardiac transplantation. Written informed consent for participation was not required for this study under the national legislation and the institutional requirements.

AUTHOR CONTRIBUTIONS

JS-P, JS, and IU: conceived the presented idea. JS-P, SP, OD, JS, and IU: contributed to the design and implementation of the research. SP and OD: developed the atria experiments. IU: developed the ventricle experiments. JS-P, JS, CC, IS, and IU: worked out the technical details. JS-P: analyzed the data. JS-P, JS, CC, FH, NB, SI, and IU: contributed to the interpretation and revision of the results. JS-P, JS, CC and IU: wrote the manuscript. JS-P, JS, CC, FF, NB, SI, and IU: contributed to the final manuscript. JS and IU: involved in supervising the work.

FUNDING

JS-P was supported by the Program of Alliances for Education and Training (OEA-GCUB-2017) and currently is supported by grant #2020/03601-9, São Paulo Research Foundation (FAPESP). IU and JS are supported by grant #2018/25606-2, São Paulo Research Foundation (FAPESP). This study was also supported in part by the NIH under grant 1R01HL143450-01, and the NSF under CMMI-1762553.

SUPPLEMENTARY MATERIAL

The Supplementary Material for this article can be found online at: https://www.frontiersin.org/articles/10.3389/fphys.2022.794761/full#supplementary-material

REFERENCES

Allessie, M. A., Bonke, F. I., and Schopman, F. J. (1977). Circus movement in rabbit atrial muscle as a mechanism of tachycardia. III. The "leading circle" concept: a new model of circus movement in cardiac tissue without the involvement of an anatomical obstacle. *Circ. Res.* 41, 9–18. doi:10.1161/01.res.41.1.9

Allessie, M., and de Groot, N. (2014). CrossTalk opposing view: Rotors have Not been demonstrated to be the drivers of atrial fibrillation. *J. Physiol.* 592, 3167–3170. doi:10.1113/jphysiol.2014.271809

Avci, P., Gupta, A., Sadasivam, M., Vecchio, D., Pam, Z., Pam, N., et al. (2013). Low-level laser (light) therapy (lllt) in skin: stimulating, healing, restoring. *Semin. Cutan. Med. Surg.* 32, 41–52.

Aziz, Z., Shatz, D., Raiman, M., Upadhyay, G. A., Beaser, A. D., Besser, S. A., et al. (2019). Targeted Ablation of Ventricular Tachycardia Guided by Wavefront Discontinuities During Sinus Rhythm. *Circulation* 140, 1383–1397. doi:10.1161/CIRCULATIONAHA.119.042423

Barkagan, M., Leshem, E., Shapira-Daniels, A., Sroubek, J., Buxton, A. E., Saffitz, J. E., et al. (2019). Histopathological characterization of radiofrequency ablation in ventricular scar tissue. *JACC Clin. Electrophysiol.* 5, 920–931. doi:10.1016/j.jacep.2019.05.011

Bastos-Filho, T. F. (2021). *XXVII Brazilian Congress on Biomedical Engineering, Vol. 83*. Berlin, Germany: Springer Nature.

Bayly, P. V., KenKnight, B. H., Rogers, J. M., Hillsley, R. E., Ideker, R. E., and Smith, W. M. (1998). Estimation of conduction velocity vector fields from epicardial mapping data. *IEEE Trans. Biomed. Eng.* 45, 563–571. doi:10.1109/10.668746

Benjamin, E. J., Muntner, P., Alonso, A., Bittencourt, M. S., Callaway, C. W., Carson, A. P., et al. (2019). Heart Disease and Stroke Statistics-2019 Update: A Report From the American Heart Association. *Circulation* 139, e56–e528. doi:10.1161/CIR.0000000000000659

Berenfeld, O., Ennis, S., Hwang, E., Hooven, B., Grzeda, K., Mironov, S., et al. (2011). Time- and frequency-domain analyses of atrial fibrillation activation rate: The optical mapping reference. *Heart rhythm.* 8, 1758–1765. doi:10.1016/j.hrthm.2011.05.007

Cantwell, C. D., Roney, C. H., Ali, R. L., Qureshi, N. A., Lim, P. B., and Peters, N. S. (2014). A software platform for the comparative analysis of electroanatomic and imaging data including conduction velocity mapping. *Annu. Int. Conf. IEEE Eng. Med. Biol. Soc.* 2014, 1591–1594. doi:10.1109/EMBC.2014.6943908

Cantwell, C. D., Roney, C. H., Ng, F. S., Siggers, J. H., Sherwin, S. J., and Peters, N. S. (2015). Techniques for automated local activation time annotation and conduction velocity estimation in cardiac mapping. *Comput. Biol. Med.* 65, 229–242. doi:10.1016/j.compbiomed.2015.04.027

Chen, D. D., Gray, R. A., Uzelac, I., Herndon, C., and Fenton, F. H. (2017). Mechanism for amplitude alternans in electrocardiograms and the initiation of spatiotemporal chaos. *Phys. Rev. Lett.* 118, 168101. doi:10.1103/physrevlett.118.168101

Clayton, R. H., and Nash, M. P. (2015). Analysis of cardiac fibrillation using phase mapping. *Card. Electrophysiol. Clin.* 7, 49–58. doi:10.1016/j.ccep.2014.11.011

Dice, L. R. (1945). Measures of the amount of ecologic association between species. *Ecology* 26, 297–302. doi:10.2307/1932409

Doshi, A. N., Walton, R. D., Krul, S. P., de Groot, J. R., Bernus, O., Efimov, I. R., et al. (2015). Feasibility of a semi-automated method for cardiac conduction velocity analysis of high-resolution activation maps. *Comput. Biol. Med.* 65, 177–183. doi:10.1016/j.compbiomed.2015.05.008

Efimov, I. R., Nikolski, V. P., and Salama, G. (2004). Optical imaging of the heart. *Circulation Res.* 95, 21–33. doi:10.1161/01.res.0000130529.18016.35

El-Sherif, N., Gough, W. B., and Restivo, M. (1987). Reentrant ventricular arrhythmias in the late myocardial infarction period: 14. mechanisms of resetting, entrainment, acceleration, or termination of reentrant tachycardia by programmed electrical stimulation. *Pacing Clin. Electrophysiol.* 10, 341–371. doi:10.1111/j.1540-8159.1987.tb05974.x

Fedorov, V. V., Schuessler, R. B., Hemphill, M., Ambrosi, C. M., Chang, R., Voloshina, A. S., et al. (2009). Structural and functional evidence for discrete exit pathways that connect the canine sinoatrial node and atria. *Circulation Res.* 104, 915–923. doi:10.1161/circresaha.108.193193

Fenton, F., and Karma, A. (1998). Vortex dynamics in three-dimensional continuous myocardium with fiber rotation: Filament instability and fibrillation. *Chaos* 8, 20–47. doi:10.1063/1.166311

Foppen, S. (2009). *Experimental and Numerical Analysis of Lesion Growth during Cardiac Radiofrequency Ablation*

Fukumoto, K., Habibi, M., Ipek, E. G., Zahid, S., Khurram, I. M., Zimmerman, S. L., et al. (2016). Association of left atrial local conduction velocity with late gadolinium enhancement on cardiac magnetic resonance in patients with atrial fibrillation. *Circulation Arrhythmia Electrophysiol.* 9, e002897. doi:10.1161/circep.115.002897

Gerig, G., Kubler, O., Kikinis, R., and Jolesz, F. A. (1992). Nonlinear anisotropic filtering of mri data. *IEEE Trans. Med. Imaging* 11, 221–232. doi:10.1109/42.141646

Gloschat, C., Aras, K., Gupta, S., Faye, N. R., Zhang, H., Syunyaev, R. A., et al. (2018). Rhythm: an open source imaging toolkit for cardiac panoramic optical mapping. *Sci. Rep.* 8, 2921. doi:10.1038/s41598-018-21333-w

Haines, D. E. (1993). The biophysics of radiofrequency catheter ablation in the heart: The importance of temperature monitoring. *Pacing Clin. Electro* 16, 586–591. doi:10.1111/j.1540-8159.1993.tb01630.x

Hansen, B. J., Zhao, J., Csepe, T. A., Moore, B. T., Li, N., Jayne, L. A., et al. (2015). Atrial fibrillation driven by micro-anatomic intramural re-entry revealed by simultaneous sub-epicardial and sub-endocardial optical mapping in explanted human hearts. *Eur. Heart J.* 36, 2390–2401. doi:10.1093/eurheartj/ehv233

Herndon, C., Uzelac, I., Farmer, J. T., and Fenton, F. (2016). "Computational ecg reconstruction and validation from high-resolution optical mapping," in 2016 Computing in Cardiology Conference (CinC) (Vancouver, BC, Canada: IEEE), 713–716. doi:10.22489/cinc.2016.208-518

Hong, K. L., Redfearn, D., Chacko, S., Baley, J., Baranchuk, A., and Glover, B. M. (2019). High-resolution mapping of the atria using the hd grid catheter. *Hear. Case Rep.* 5, 351–353. doi:10.1016/J.HRCR.2018.12.012

Irie, T., Yu, R., Bradfield, J. S., Vaseghi, M., Buch, E. F., Ajijola, O., et al. (2015a). Relationship between sinus rhythm late activation zones and critical sites for scar-related ventricular tachycardia. *Circ Arrhythmia Electrophysiol.* 8, 390–399. doi:10.1161/CIRCEP.114.002637

Irie, T., Yu, R., Bradfield, J. S., Vaseghi, M., Buch, E. F., Ajijola, O., et al. (2015b). Relationship Between Sinus Rhythm Late Activation Zones and Critical Sites for Scar-Related Ventricular Tachycardia. *Circ Arrhythmia Electrophysiol.* 8, 390–399. doi:10.1161/circep.114.002637

Jalife, J., Berenfeld, O., and Mansour, M. (2002). Mother rotors and fibrillatory conduction: a mechanism of atrial fibrillation. *Cardiovasc. Res.* 54, 204–216. doi:10.1016/s0008-6363(02)00223-7

Kim, Y. H., Chen, S. A., Ernst, S., Guzman, C. E., Han, S., Kalarus, Z., et al. (2020). 2019 APHRS expert consensus statement on three-dimensional mapping systems for tachycardia developed in collaboration with HRS, EHRA, and LAHRS. *J. Arrhythmia* 36, 215–270. doi:10.1002/joa3.12308

Kuo, C. S., Munakata, K., Reddy, C. P., and Surawicz, B. (1983). Characteristics and possible mechanism of ventricular arrhythmia dependent on the dispersion of action potential durations. *Circulation* 67, 1356–1367. doi:10.1161/01.cir.67.6.1356

Lalani, G. G., Schricker, A., Gibson, M., Rostamian, A., Krummen, D. E., and Narayan, S. M. (2012). Atrial Conduction Slows Immediately Before the Onset of Human Atrial Fibrillation. *J. Am. Coll. Cardiol.* 59, 595–606. doi:10.1016/j.jacc.2011.10.879

Linnenbank, A. C., de Bakker, J. M. T., and Coronel, R. (2014). How to measure propagation velocity in cardiac tissue: a simulation study. *Front. Physiol.* 5. doi:10.3389/FPHYS.2014.00267

Malaczynska-Rajpold, K., Blaszyk, K., Kociemba, A., Pyda, M., Posadzy-Malaczynska, A., and Grajek, S. (2020). Islets of heterogeneous myocardium within the scar in cardiac magnetic resonance predict ventricular tachycardia after myocardial infarction. *J. Cardiovasc Electrophysiol.* 31, 1452–1461. doi:10.1111/jce.14461

Mironov, S., Jalife, J., and Tolkacheva, E. G. (2008). Role of conduction velocity restitution and short-term memory in the development of action potential duration alternans in isolated rabbit hearts. *Circulation* 118, 17–25. doi:10.1161/CIRCULATIONAHA.107.737254

Moe, G. K., Rheinboldt, W. C., and Abildskov, J. A. (1964). A computer model of atrial fibrillation. *Am. Heart J.* 67, 200–220. doi:10.1016/0002-8703(64)90371-0

Narayan, S. M., Franz, M. R., Clopton, P., Pruvot, E. J., and Krummen, D. E. (2011). Repolarization alternans reveals vulnerability to human atrial fibrillation. *Circulation* 123, 2922–2930. doi:10.1161/circulationaha.110.977827

Narayan, S. M., Krummen, D. E., Shivkumar, K., Clopton, P., Rappel, W.-J., and Miller, J. M. (2012). Treatment of Atrial Fibrillation by the Ablation of Localized Sources. *J. Am. Coll. Cardiol.* 60, 628–636. doi:10.1016/j.jacc.2012.05.022

Nattel, S., Shiroshita-Takeshita, A., Brundel, B. J. J. M., and Rivard, L. (2005). Mechanisms of atrial fibrillation: lessons from animal models. *Prog. Cardiovasc. Dis.* 48, 9–28. doi:10.1016/j.pcad.2005.06.002

Ng, F. S., Holzem, K. M., Koppel, A. C., Janks, D., Gordon, F., Wit, A. L., et al. (2014). Adverse Remodeling of the Electrophysiological Response to Ischemia-Reperfusion in Human Heart Failure Is Associated With Remodeling of Metabolic Gene Expression. *Circ Arrhythmia Electrophysiol.* 7, 875–882. doi:10.1161/circep.113.001477

O'Shea, C., Holmes, A. P., Yu, T. Y., Winter, J., Wells, S. P., Correia, J., et al. (2019). Electromap: high-throughput open-source software for analysis and mapping of cardiac electrophysiology. *Sci. Rep.* 9, 1389. doi:10.1038/s41598-018-38263-2

Perona, P., and Malik, J. (1990). Scale-space and edge detection using anisotropic diffusion. *IEEE Trans. Pattern Anal. Mach. Intell.* 12, 629–639. doi:10.1109/34.56205

Pollnow, S. (2018). *Characterizing Cardiac Electrophysiology during Radiofrequency Ablation, Vol. 24*. Karlsruhe, Germany: Karlshure Transactions on Biomedical Engineering.

Prystowsky, E. N. (2008). The history of atrial fibrillation: The last 100 years. *J. Cardiovasc. Electrophysiol.* 19, 575–582. doi:10.1111/j.1540-8167.2008.01184.x

Quinn, T. A., Camelliti, P., Rog-Zielinska, E. A., Siedlecka, U., Poggioli, T., O'Toole, E. T., et al. (2016). Electrotonic coupling of excitable and nonexcitable cells in the heart revealed by optogenetics. *Proc. Natl. Acad. Sci. U.S.A.* 113, 14852–14857. doi:10.1073/pnas.1611184114

Rensma, P. L., Allessie, M. A., Lammers, W. J., Bonke, F. I., and Schalij, M. J. (1988). Length of excitation wave and susceptibility to reentrant atrial arrhythmias in normal conscious dogs. *Circ. Res.* 62 (2), 395–410. doi:10.1161/01.res.62.2.395

Roney, C. H., Cantwell, C. D., Qureshi, N. A., Ali, R. L., Chang, E. T., Lim, P. B., et al. (2014). An automated algorithm for determining conduction velocity, wavefront direction and origin of focal cardiac arrhythmias using a multipolar catheter. *Annu. Int. Conf. IEEE Eng. Med. Biol. Soc.* 2014, 1583–1586. doi:10.1109/EMBC.2014.6943906

Roney, C., Whitaker, J., Sim, I., O'Neill, L., Mukherjee, R., Razeghi, O., et al. (2018). A technique for measuring anisotropy in atrial conduction to estimate conduction velocity and atrial fibre direction. *Comput. Biol. Med.* 104, 278–290. doi:10.1016/j.compbiomed.2018.10.019

Rudy, Y. (2012). *Comprehensive Biophysics*.

Sanders, P., Berenfeld, O., Hocini, M., Jaïs, P., Vaidyanathan, R., Hsu, L.-F., et al. (2005). Spectral analysis identifies sites of high-frequency activity maintaining atrial fibrillation in humans. *Circulation* 112, 789–797. doi:10.1161/circulationaha.104.517011

Sasaki, T., Calkins, H., Miller, C. F., Zviman, M. M., Zipunnikov, V., Arai, T., et al. (2015). New insight into scar-related ventricular tachycardia circuits in ischemic cardiomyopathy: Fat deposition after myocardial infarction on computed tomography-A pilot study. *Heart rhythm.* 12, 1508–1518. doi:10.1016/j.hrthm.2015.03.041

Shinagawa, K., Mitamura, H., Takeshita, A., Sato, T., Kanki, H., Takatsuki, S., et al. (2000). Determination of refractory periods and conduction velocity during atrial fibrillation using atrial capture in dogs. *J. Am. Coll. Cardiol.* 35, 246–253. doi:10.1016/S0735-1097(99)00488-X

Spector, P. (2013). Principles of cardiac electric propagation and their implications for re-entrant arrhythmias. *Circ Arrhythmia Electrophysiol.* 6, 655–661. doi:10.1161/circep.113.000311

Takeuchi, S., Akita, T., Takagishi, Y., Watanabe, E., Sasano, C., Honjo, H., et al. (2006). Disorganization of gap junction distribution in dilated atria of patients with chronic atrial fibrillation. *Circ. J.* 70, 575–582. doi:10.1253/circj.70.575

Tan, V. H., Lyu, M. Z., Tan, P. C., Wong, L. C., Yeo, C., Wong, K. C. K., et al. (2020). Utility of directional high-density mapping catheter (Advisor TM HD Grid) in complex scar-related atrial tachycardia. *J. Arrhythmia* 36, 180–183. doi:10.1002/JOA3.12256

Thompson, S. A., Copeland, C. R., Reich, D. H., and Tung, L. (2011). Mechanical coupling between myofibroblasts and cardiomyocytes slows electric conduction in fibrotic cell monolayers. *Circulation* 123, 2083–2093. doi:10.1161/circulationaha.110.015057

Tomek, J., Burton, R. A. B., and Bub, G. (2016). Ccoffinn: Automated wave tracking in cultured cardiac monolayers. *Biophysical J.* 111, 1595–1599. doi:10.1016/j.bpj.2016.08.049

Tu, Y. X., Wernsdörfer, A., Honda, S., and Tomita, Y. (1997). Estimation of conduction velocity distribution by regularized-least-squares method. *IEEE Trans. Biomed. Eng.* 44, 1102–1106. doi:10.1109/10.641337

Uzelac, I., Herndon, C., Farmer, J., and Fenton, F. (2016). Electrocardiogram reconstruction from high resolution voltage optical mapping. *Annu. Int. Conf. IEEE Eng. Med. Biol. Soc.* 2016, 3941–3944. doi:10.1109/EMBC.2016.7591589

Uzelac, I., and Fenton, F. (2015). "Robust framework for quantitative analysis of optical mapping signals without filtering," in 2015 Computing in Cardiology Conference (CinC) (Nice, France: IEEE), 461–464. doi:10.1109/cic.2015.7408686

Uzelac, I., Iravanian, S., and Fenton, G. (2019). "Parallel acceleration on removal of optical mapping baseline wandering," in 2017 Computing in Cardiology (CinC) (Singapore: IEEE), 1–4. doi:10.22489/cinc.2019.433

Uzelac, I., Ji, Y. C., Hornung, D., Schröder-Scheteling, J., Luther, S., Gray, R. A., et al. (2017). Simultaneous quantification of spatially discordant alternans in voltage and intracellular calcium in langendorff-perfused rabbit hearts and inconsistencies with models of cardiac action potentials and ca transients. *Front. Physiol.* 8, 819. doi:10.3389/fphys.2017.00819

Uzelac, I., Kaboudian, A., Iravanian, S., Siles-Paredes, J. G., Gumbart, J. C., Ashikaga, H., et al. (2021). Quantifying arrhythmic long qt effects of hydroxychloroquine and azithromycin with whole-heart optical mapping and simulations. *Heart Rhythm O2* 2, 394–404. doi:10.1016/j.hroo.2021.06.008

van Schie, M. S., Heida, A., Taverne, Y. J. H. J., Bogers, A. J. J. C., and de Groot, N. M. S. (2021). Identification of local atrial conduction heterogeneities using high-density conduction velocity estimation. *EP Eur.* 23, 1815–1825. doi:10.1093/europace/euab088

Vasquez, C., Mohandas, P., Louie, K. L., Benamer, N., Bapat, A. C., and Morley, G. E. (2010). Enhanced Fibroblast-Myocyte Interactions in Response to Cardiac Injury. *Circ. Res.* 107, 1011–1020. doi:10.1161/circresaha.110.227421

Walton, R. D., Smith, R. M., White, E., Bernus, O., Pertsov, A. M., and Pertsov, A. M. (2012). Extracting surface activation time from the optically recorded action potential in three-dimensional myocardium. *Biophysical J.* 102(1), 30–38. doi:10.1016/j.bpj.2011.10.036

Weber, F. M., Schilling, C., Seemann, G., Luik, A., Schmitt, C., Lorenz, C., et al. (2010). Wave-Direction and Conduction-Velocity Analysis From Intracardiac Electrograms-A Single-Shot Technique. *IEEE Trans. Biomed. Eng.* 57, 2394–2401. doi:10.1109/tbme.2010.2055056

Wittkampf, F. H. M., and Nakagawa, H. (2006). Rf catheter ablation: lessons on lesions. *Pacing Clin. Electro* 29, 1285–1297. doi:10.1111/j.1540-8159.2006.00533.x

Zaman, J. A. B., Baykaner, T., Schricker, A. A., Krummen, D. E., and Narayan, S. M. (2017). Mechanistic targets for the ablation of atrial fibrillation. *Glob. Cardiol. Sci. Pract.* 2017, e201707. doi:10.21542/gcsp.2017.7

Zimerman, L., Fenelon, G., and Martinelli, M. (2009). *Diretrizes Brasileiras de Fibrilação Atrial, vol. 92(6 supl. 1) (Arq Bras Cardiol: Sociedade Brasileira de Cardiologia)*.

Conflict of Interest: The authors declare that the research was conducted in the absence of any commercial or financial relationships that could be construed as a potential conflict of interest.

Frontiers in Physiology

Understanding how an organism's components work together to maintain a healthy state

The second most-cited physiology journal, promoting a multidisciplinary approach to the physiology of living systems - from the subcellular and molecular domains to the intact organism and its interaction with the environment.

Discover the latest Research Topics

See more →

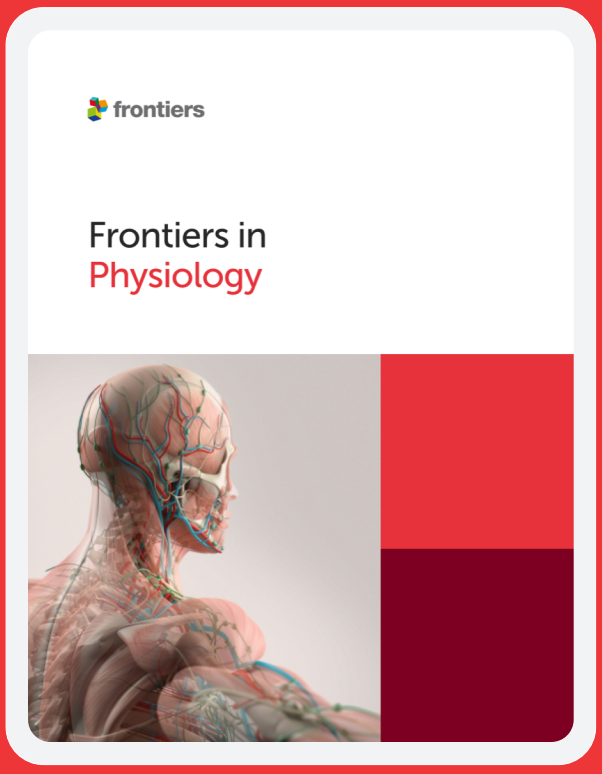

Frontiers

Avenue du Tribunal-Fédéral 34
1005 Lausanne, Switzerland
frontiersin.org

Contact us

+41 (0)21 510 17 00
frontiersin.org/about/contact